

AD-A111 090

KANSAS UNIV/CENTER FOR RESEARCH INC LAWRENCE  
MECHANICAL PROPERTIES OF FOUR HUMAN LONGBONES. (U)  
NOV 81 C R KULP, H W SMITH, H C ANDERSON

F/8 6/16

F49620-79-C-0183

UNCLASSIFIED

AFOSR-TR-82-0040

NL

1 of 5  
42  
4/11/90



**LEVEL II**

(7)

AD A111090

DTIC FILE COPY

F49620-79-C-0183

**DTIC**  
ELECTE  
FEB 18 1982  
**S** **D**  
E



THE UNIVERSITY OF KANSAS CENTER FOR RESEARCH, INC.

2291 Irving Hill Drive—Campus West  
Lawrence, Kansas 66045

450 374

82 02 16 2 03

Approved for public release  
distribution unlimited.

**LEVEL II**

⑦

Accession For	
NTIS GRA&I	<input checked="" type="checkbox"/>
DTIC TAB	<input type="checkbox"/>
Unannounced	<input type="checkbox"/>
Justification	
By _____	
Distribution/	
Availability Codes	
Dist	Avail and/or Special
<b>A</b>	



MECHANICAL PROPERTIES  
OF  
FOUR HUMAN LONGBONES

Carl R. Kulp, Jr. and Howard Wesley Smith, Ph.D.  
University of Kansas  
Aerospace Medical Research Laboratory  
Lawrence, Kansas 66045

H. Clarke Anderson, M.D.  
University of Kansas Medical Center  
Kansas City, Kansas 66103

30 November, 1981

Final Scientific Report



Approved for public release; distribution unlimited

Prepared for  
AIR FORCE OFFICE OF SCIENTIFIC RESEARCH  
Bolling Air Force Base  
Washington, DC 20332

AIR FORCE AEROSPACE MEDICAL RESEARCH LABORATORY  
Wright-Patterson Air Force Base  
Dayton, Ohio 45433

AIR FORCE OFFICE OF SCIENTIFIC RESEARCH (AFOSR)  
NOTICE OF TRANSMITTAL (NOTICE)  
This technical report is approved and  
approved for public release under AFOSR 100-12  
Distribution is unlimited.  
MATTHEW J. KERPER  
Chief, Technical Information Division

REPORT DOCUMENTATION PAGE		READ INSTRUCTIONS BEFORE COMPLETING FORM
1. REPORT NUMBER <b>AFOSR-TR-82-0040</b>	2. GOVT ACCESSION NO. <b>AD-A111090</b>	3. RECIPIENT'S CATALOG NUMBER
4. TITLE (and Subtitle) <b>MECHANICAL PROPERTIES OF FOUR HUMAN LONGBONES</b>		5. TYPE OF REPORT & PERIOD COVERED <b>Final Report</b>
		6. PERFORMING ORG. REPORT NUMBER
7. AUTHOR(s) <b>Carl Kulp Howard Wesley Smith H. Clarke Anderson</b>		8. CONTRACT OR GRANT NUMBER(s) <b>F 49620-79-C-0183</b>
9. PERFORMING ORGANIZATION NAME AND ADDRESS <b>University of Kansas Center for Research, Inc. Aerospace Medical Research Laboratory 4022E Learned Hall, Lawrence, Kansas 66045</b>		10. PROGRAM ELEMENT, PROJECT, TASK AREA & WORK UNIT NUMBERS <b>61102F 2312-A2</b>
11. CONTROLLING OFFICE NAME AND ADDRESS <b>Director of Life Sciences Air Force Office of Scientific Research/NL Building 410, Bolling AFB, D.C. 20332</b>		12. REPORT DATE <b>30 Nov. 1981</b>
		13. NUMBER OF PAGES <b>413</b>
14. MONITORING AGENCY NAME & ADDRESS (if different from Controlling Office)		15. SECURITY CLASS. (of this report) <b>Unclassified</b>
		15a. DECLASSIFICATION/DOWNGRADING SCHEDULE
16. DISTRIBUTION STATEMENT (of this Report)  <b>Approved for public release; distribution unlimited.</b>		
17. DISTRIBUTION STATEMENT (of the abstract entered in Block 20, if different from Report)		
18. SUPPLEMENTARY NOTES		
19. KEY WORDS (Continue on reverse side if necessary and identify by block number) <b>Ejection Seat Injury, Windblast, Flail, Extremity Injury, Longbone Fracture, Bone Stresses, Structural Analysis, Human Bone Properties, Bending, Torsion, Osteology, Histology, Anthropometry, Mineral content, Femur, Tibia, Fibula, Humerus, SEM, Interaction, Osteoclast, Cadaver, Osteometry, Diaphysis, Brittle lacquer, Strain gage, Ash, Morphology</b>		
20. ABSTRACT (Continue on reverse side if necessary and identify by block number) <b>The four human long bones (femur, tibia, humerus, and fibula) were fractured under bending loading conditions, torsion loading conditions, and combinations of bending and torsion. Forty-eight fresh bones, 12 of each type (left and right sides of 6 cadavers), were loaded until fracture occurred. Forty-six bones of all types were loaded quasi-statically while two humeri were fractured at a more rapid rate. All testing was accomplished with a specially designed testing machine, named an Osteoclast which applied the bending and</b> (continued on back)		

20. ABSTRACT (continued from reverse side)

torsion loads separately or combined, as desired. End slopes, mid-diaphyseal deflections, and twist angles of the deforming bones were recorded during all tests. Forty-three of the bones, including all of the types, were strain gaged with axial and rosette resistance strain gages. Interaction boundaries are presented which allow the prediction of fracture loads from various combinations of bending and torsion loadings given the bone type and the geometry at a particular location along the bone diaphysis. With the fracture loads known, graphs depicting end slopes, mid-diaphyseal deflections, and twist angles as functions of load, which are also presented, may be used to estimate fracture displacements. Fracture patterns expected from each of the three types of loadings are discussed and illustrated. The states of strain and stress at specific locations along the diaphyses of the different bone types are described. An osteometry study compares the bones tested with the general population. A brittle lacquer test describes the areas of highest strain for a femur subjected to pure torsion. A scanning electron microscope study presents fracture appearances of tension as well as suspected shear surfaces and illustrates graphically the difficulty involved with modeling bone microstructure, mathematically, in terms of its constituents. Finally, a medical evaluation of the morphology and ash content of the bone tissue involved in the study qualifies the findings presented. Included in the discussions are the osteometry procedures, the strain gaging techniques and a detailed description of the equipment and its employment.

## TABLE OF CONTENTS

Acknowledgments.....	vii
List of Symbols.....	viii
List of Figures.....	xi
List of Tables.....	xviii
1.0 Introduction.....	1
References.....	6
2.0 Studies.....	10
2.1. Osteometry.....	10
2.1.1. Anthropometric Techniques.....	10
2.1.2. Osteometric Measurements.....	12
2.1.2.1. Humerus.....	12
2.1.2.2. Femur.....	14
2.1.2.3. Tibia.....	17
2.1.2.4. Fibula.....	18
2.1.3. Error in Measurement.....	19
2.1.4. Comparisons with Other Osteometric Populations....	20
2.1.4.1 Males.....	21
2.1.4.2 Females.....	21
2.1.4.3 Sexual Dimorphism.....	21
2.1.4.4 Platymeria.....	34
2.1.4.5 Platycnemia.....	35
2.1.4.6 Racial Variation.....	35
2.1.5 References.....	36
2.2 Fracturing.....	37
2.2.1 Introduction.....	37
2.2.2 Theory.....	38
2.2.2.1 Bending Only.....	39
2.2.2.2 Torsion Only.....	44
2.2.2.3 Combined Loading Conditions.....	47
2.2.2.4 General Remarks.....	47
2.2.2.5 Anisotropy of Bone.....	49
2.2.2.6 Microstructure.....	49

2.2.3	Equipment.....	51
2.2.3.1	Introduction.....	51
2.2.3.2	Osteoclast.....	51
	SELF-EQUILIBRATING TEST WINDOW.....	53
	FIXED-END CLAMP.....	57
	SUSPENDED-END CLAMP, DISK AND REACTION POINT....	58
	BENDING LOAD APPLICATION MECHANISM.....	59
	TORSION LOAD APPLICATION.....	64
	HUMIDITY CHAMBER.....	65
	AUXILIARY EQUIPMENT.....	66
	<u>Clamps and Trolleys</u> .....	66
	<u>Dial Indicators</u> .....	66
2.2.3.3	Load Indication.....	67
2.2.3.4	Strain Measurement.....	68
2.3.3.5	Video Record.....	75
2.2.3.6	Molding Device.....	75
2.2.4	Test Procedure.....	76
2.2.4.1	Test Flow.....	76
2.2.4.2	Rentgenography.....	80
2.2.4.3	Molding and Osteometrics.....	81
	PREPARATION FOR MOLDING.....	81
	MOLDING.....	81
2.2.4.5	Strain Gages.....	82
	CAGE PLACEMENT.....	84
	STRAIN GAGE APPLICATION PROCEDURE.....	84
	<u>Removal of Extraneous Tissue</u> .....	93
	<u>Marking and Recording Gage Locations</u> .....	93
	<u>Bonding</u> .....	96
	<u>Attachment of Conductors</u> .....	100
	<u>General Remarks</u> .....	103
2.2.4.6	Equipment Setup.....	103
	OSTEOCLAST.....	103
	<u>Bending</u> .....	103
	<u>Torsion</u> .....	105
	<u>Combined Loads</u> .....	106

BLH SYSTEM.....	106
VISHAY.....	107
VIDEO.....	110
2.2.4.7 Written and Photographic Records.....	110
LOADING PLAN.....	110
DEFLECTION DATA SHEET.....	111
STRAIN DATA SHEET.....	111
STRAIN GAGE LOCATION AND FRACTURE PATTERN.....	111
PHOTOGRAPHIC RECORDS.....	112
2.2.4.8 Test Schedule.....	113
2.2.4.9 General Test Plan.....	117
GENERAL LOADING SCHEDULE.....	123
BENDING ONLY LOADING SCHEDULE.....	126
TORSION ONLY LOADING SCHEDULE.....	127
COMBINED CONDITIONS.....	127
RAPID RATE CONDITIONS.....	128
GENERAL REMARKS.....	128
2.2.4.10 Bone Sectioning.....	128
2.2.5 Results.....	136
2.2.5.1 Data Reduction.....	136
DATA CORRECTIONS.....	136
STRAIN ROSSETTE ANALYSIS.....	139
NONDIMENSIONALIZATION.....	142
<u>X-ray Tracings</u> .....	143
<u>Computations</u> .....	146
<u>Discussion</u> .....	148
SECTION PROPERTIES.....	150
2.2.5.2 Observations.....	151
FRACTURE PATTERNS.....	151
<u>Torsion Only Fractures</u> .....	151
Femora.....	152
Tibiae.....	152
Humeri.....	160
Fibulae.....	169

<u>Bending Only Fractures</u> .....	169
Femora.....	169
Tibiae.....	174
Humeri.....	174
Fibulae.....	186
<u>Combined Loadings</u> .....	186
Torsion Dominant.....	190
Bending Dominant.....	201
<u>Summary</u> .....	207
STRESS STATES.....	209
<u>Bending Only Stress States</u> .....	210
Femora.....	210
Tibiae.....	261
Humeri.....	267
Fibulae.....	274
<u>Torsion Only Stress States</u> .....	275
Femora.....	275
Tibiae.....	279
Humeri.....	281
Fibulae.....	282
Anisotropic Behavior.....	284
<u>Combined Loadings</u> .....	286
Femora.....	286
Tibiae.....	289
Humeri.....	292
Fibulae.....	296
LOADS.....	299
<u>Fracture Loads and Displacements</u> .....	299
<u>Estimation of Fracture Loads</u> .....	304
2.2.6 References.....	316

2.3	Brittle Coat.....	316
2.3.1	Introduction.....	316
2.3.2	Theory.....	323
2.3.3	Test Specimen.....	323
2.3.3.1	Surface Preparation.....	323
2.3.3.2	Coating.....	323
2.3.4	Equipment.....	324
2.3.5	Test Procedures.....	324
2.3.6	Observations.....	324
2.3.7	Data Reduction.....	324
2.3.8	Results.....	330
2.3.9	References.....	330
2.4	Scanning Electron Microscope (SEM) Study.....	331
2.4.1	Introduction.....	331
2.4.2	Theory.....	331
2.4.3	Specimen Preparation.....	335
2.4.4	Equipment/Technique.....	337
2.4.5	Results.....	337
2.4.5.1	Tension Surfaces.....	337
2.4.5.2	Shear Surfaces.....	345
2.4.5.3	Fracture Surfaces of Unknown of Unknown Origin.....	350
2.5	Medical Analysis.....	364
2.5.1	Methods.....	364
2.5.1.1	Mineral Content.....	364
	ACID HYDROLYSIS.....	364
2.5.2	Results.....	366
2.5.2.1	Bone Ash.....	366
2.5.2.2	Protein and Hydroxyproline Content.....	366
2.5.2.3	Morphometric Analysis.....	371
2.5.3	Discussion.....	371
2.5.4	References.....	374
3.0	Conclusions.....	375
3.1	Introduction.....	375
3.2	Osteometry.....	375

3.3	Fracturing.....	375
3.3.1	Fracture Patterns.....	375
3.3.1.1	Torsion Only.....	375
3.3.1.2	Bending Only.....	377
3.3.1.3	Combined Loading.....	384
3.3.2	Strain States.....	384
3.3.3	Fracture Loads.....	386
3.4	Brittle Coat.....	389
3.5	SEM Analysis.....	390
3.6	Medical Analysis.....	390
3.7	General.....	390
3.8	References.....	391
4.0	Recomendations.....	392

#### ACKNOWLEDGMENTS

We wish to express our appreciation to the many individuals, students and faculty who have contributed to this report. Dana Cope, who wrote the osteometry section as well as advised us concerning the osteometrics and human skeletal morphology, has been of great service. Doug Nelson, who accomplished the medical analysis, worked unrelentingly to complete the ash and morphology study at the end of the program. We also wish to express our sincere thanks to Drs. Melvin Mohr and Floyd Foltz who arranged and supervised the bone resection, Dr. Albert Chapman who supervised the scanning electron microscope study, Dr. DeSmet who arranged and supervised the roentgenography and Dr. Ross Stein who consulted with us on numerous pathological and anatomy matters. We also wish to thank Mr. Ray Hassig who performed the bone resection, Mr. Dave Nelson who manufactured the Osteoclast and Mr. Jerry Hanson who set up our electronic equipment. Lastly we wish to thank the students, Jim Hunt, Jean Scott, Steve Koontz and Mike Johnson who worked with us during the experimentation as well as composed sections of the report concerning the work that they did.

LIST OF SYMBOLS

Symbols

Specimen Numbering

F	Femur
T	Tibia
H	Humerus
Fb	Fibula
L	Left Side
R	Right Side

Loading Conditions

B	Bending
T, Tor	Torsion
C	Combined bending and torsion
CB	Combined, bending dominant
CT	Combined, torsion dominant
N	Narrow load spacing
M	Medium load spacing
W	Wide load spacing
E	Eversive rotation
I	Inversive rotation

Reference Planes

A	Anterior
D	Distal
L	Lateral
M	Medial
P	Posterior
Pr	Proximal

General Symbols

A.L.	Anatomical length
CSO	Clam Shell Opening mode
E	Young's modulus of elasticity
Fixed	Fixed end while in the Osteoclast

G	Shear Modulus
J	Polar moment of inertia
L	Length
$I_{xx}$	Second moment of inertia about the x (centroidal) axis
$M_b$	Bending moment
M.C.	Medical Center
M.L.	Maximum length
P	Total bending load as sensed by the bending load cell
$R_o$	Outside radius of a tubular section
$R_i$	Inside radius of a tubular section
T	Twisting moment or torque
V	Shear force
$\delta_b$	Deflection at the mid-diaphysis due to bending
$\gamma_{ij}$	Shear strain in a plane normal to the i axis whose vector points in the j direction
$\epsilon$	Normal strain in the i direction
$\nu_{ij}$	Poisson effect in the plane i due to strain in the plane j
$\rho$	Distance from the axis of twist to a point on a twisted cross-section
$\sigma_i$	Normal stress in the i direction
$\tau_{ij}$	Shear stress in a plane normal to the i axis whose vector points in the j direction

#### Subscripts

A,B	Principal stress axes
b	Bending
T	Twisting moment or torque
$\tau$	Shear
1,2	Material axes
I,II	Principal strain axes

#### Angles

$\alpha$	Angle between the material axes and gage axes
$\beta$	Angle between the ith gage leg and gage axes of the rosette
$\theta$	Angle between the principal strain axes and the material axes
$\xi$	Angle between the principal stress axes and the material axes
$\psi$	Angle of slope at the supports of the bending bone

Picture symbols

-  Mid-diaphyseal dial gage sensing bending deflection
-  Support (pin)
-  Axial strain gage
-  Delta rosette strain gage
-  Rectangular rosette strain gage
-  Stacked rosette strain gage
-  Location of the endosteal surface
- [ ] Denotes references

## LIST OF FIGURES

- Figure 2.1 Shear and moment diagrams for four point bending.
- Figure 2.2 Principal axes of inertia for a mid-diaphyseal cross-section of the humerus.
- Figure 2.3 Fracture modes possible in bones.
- Figure 2.4 Strain and stress due to pure torsion.
- Figure 2.5 Twisting moments resulting from cross-sectional shapes.
- Figure 2.6 Induced bending due to the curvature.
- Figure 2.7 Osteoclast
- Figure 2.8 Parts of the assembled osteoclast.
- Figure 2.9(a) Fixed-end clamp.
- Figure 2.9(b) Bending load application mechanism.
- Figure 2.10 Torsional load applications mechanism.
- Figure 2.11 Large bending carriage and bending load application mechanism.
- Figure 2.12 Small bending carriage and bending load application mechanism.
- Figure 2.13 Bottom view of the large bending carriage showing "centering" design of the loading rollers.
- Figure 2.14 BLH 826A switch and balance and BLH 800 SW.
- Figure 2.15 Rewiring of LBH system to allow calibration in terms of force.
- Figure 2.16 Vishay strain measuring system.
- Figure 2.17 Junction board.
- Figure 2.18 Molding device.
- Figure 2.19 Molding of a right femur.
- Figure 2.20 Femora gage arrangement and type.
- Figure 2.21 Tibiae gage arrangement and type.
- Figure 2.22 Humeri gage arrangement and type.
- Figure 2.23 Fibulae gage arrangement and type.
- Figure 2.24 Marking of the vertical alignment axis for a strain gage.
- Figure 2.25 Plane containing the longitudinal gage axis.
- Figure 2.26 Measurement of the bone surface.
- Figure 2.27(a) Application of adhesive.
- Figure 2.27(b) Application of the gage.
- Figure 2.28 Extention of gage axes.

- Figure 2.29 Attachment of strain gage conductors.
- Figure 2.30 Femora loading conditions.
- Figure 2.31 Tibiae loading conditions.
- Figure 2.32 Humeri loading conditions.
- Figure 2.33 Fibulae loading conditions.
- Figure 2.34 Schematic of an Interaction Boundary
- Figure 2.35 Medical Center section litation -- bending.
- Figure 2.36 Medical Center section litation -- torsion.
- Figure 2.37 Medical Center section litation -- combined.
- Figure 2.38 Marking and cutting of sections using the mold as a clamp.
- Figure 2.39 Tracing a section of bone onto an acetate sheet.
- Figure 2.40 Shifting the data points to obtain a correct load-displacement plot.
- Figure 2.41 Correcting recorded torsional loads for the actual twisting force component.
- Figure 2.42 Strain gage axes in relation to material axes.
- Figure 2.43 Angular relationship between gage axes, material direction and principal axes.
- Figure 2.44 Tracing of x-rays for nondimensionalization, computer program.
- Figure 2.45 Test results for RF3793.
- Figure 2.46 Test results for LF3753.
- Figure 2.47 Test results for LF3792.
- Figure 2.48 Test results for RF3782.
- Figure 2.49 Test results for LT3792.
- Figure 2.50 Test results for RT3793.
- Figure 2.51 Test results for LT3753.
- Figure 2.52(a) Test results for RT3782.
- Figure 2.52(b) Test results for RFb3782.
- Figure 2.53(a) Test results for LT3782.
- Figure 2.53(b) Test results for LFB3782.
- Figure 2.54 Test results for LH3792.
- Figure 2.55 Test results for LH3782.
- Figure 2.56 Test results for RH3793.
- Figure 2.57 Test results for RH3753.
- Figure 2.58 Test results for RFB3793.
- Figure 2.59 Test results for LFB3753.

Figure 2.60	Test results for Lfb3792.
Figure 2.61	Test results for RF3753.
Figure 2.62	Test results for LF3793.
Figure 2.63	Test results for RT3792.
Figure 2.64	Test results for LF3782.
Figure 2.65	Test results for RF3792.
Figure 2.66	Test results for RT3753.
Figure 2.67	Test results for LT3793.
Figure 2.68	Test results for RH3792.
Figure 2.69	Test results for RH3782.
Figure 2.70	Test results for RH3790.
Figure 2.71	Test results for LH3787.
Figure 2.72	Test results for LH3753.
Figure 2.73	Test results for Lfb3793.
Figure 2.74	Test results for Rfb3792.
Figure 2.75	Test results for Rfb3753.
Figure 2.76	Test results for LF3790.
Figure 2.77	Test results for RF3790.
Figure 2.78	Test results for LT3790.
Figure 2.79	Test results for RT3790.
Figure 2.80	Test results for RH3787.
Figure 2.81	Test results for LH3790.
Figure 2.82	Test results for Rfb3790.
Figure 2.83	Test results for RFB3787.
Figure 2.84	Test results for Lfb3790.
Figure 2.85	Test results for RF3787.
Figure 2.86	Test results for LF3787.
Figure 2.87	Test results for LT3787.
Figure 2.88	Test results for RT3787.
Figure 2.89	Test results for LH3793.
Figure 2.90	Test results for RFB3787.
Figure 2.91	Locations of M.C. sections and strain gages for RF3753.
Figure 2.92	Locations of M.C. sections and strain gages for LF3753.
Figure 2.93	Locations of M.C. sections and strain gages for RF3793.
Figure 2.94	Locations of M.C. sections and strain gages for LF3793.
Figure 2.95	Locations of M.C. sections and strain gages for RF3790.

Figure 2.96      Locations of M.C. sections and strain gages for LF3790.  
Figure 2.97      Locations of M.C. sections and strain gages for RF3782.  
Figure 2.98      Locations of M.C. sections and strain gages for LF3782.  
Figure 2.99      Locations of M.C. sections and strain gages for RF3792.  
Figure 2.100     Locations of M.C. sections and strain gages for LF3792.  
Figure 2.101     Locations of M.C. sections and strain gages for RF3787.  
Figure 2.102     Locations of M.C. sections and strain gages for LF3787.  
Figure 2.103     Locations of M.C. sections and strain gages for RT3753.  
Figure 2.104     Locations of M.C. sections and strain gages for LT3753.  
Figure 2.105     Locations of M.C. sections and strain gages for RT3793.  
Figure 2.106     Locations of M.C. sections and strain gages for LT3793.  
Figure 2.107     Locations of M.C. sections and strain gages for RT3790.  
Figure 2.108     Locations of M.C. sections and strain gages for LT3790.  
Figure 2.109     Locations of M.C. sections and strain gages for RT3782.  
Figure 2.110     Locations of M.C. sections and strain gages for LT3782.  
Figure 2.111     Locations of M.C. sections and strain gages for RT3792.  
Figure 2.112     Locations of M.C. sections and strain gages for LT3792.  
Figure 2.113     Locations of M.C. sections and strain gages for RT3787.  
Figure 2.114     Locations of M.C. sections and strain gages for LT3787.  
Figure 2.115     Locations of M.C. sections and strain gages for RH3753.  
Figure 2.116     Locations of M.C. sections and strain gages for LH3753.  
Figure 2.117     Locations of M.C. sections and strain gages for RH3793.  
Figure 2.118     Locations of M.C. sections and strain gages for LH3793.  
Figure 2.119     Locations of M.C. sections and strain gages for RH3790.  
Figure 2.120     Locations of M.C. sections and strain gages for LH3790.  
Figure 2.121     Locations of M.C. sections and strain gages for RH3782.  
Figure 2.122     Locations of M.C. sections and strain gages for LH3782.  
Figure 2.123     Locations of M.C. sections and strain gages for RH3792.  
Figure 2.124     Locations of M.C. sections and strain gages for LH3792.  
Figure 2.125     Locations of M.C. sections and strain gages for RH3787.  
Figure 2.126     Locations of M.C. sections and strain gages for LH3787.  
Figure 2.127     Locations of M.C. sections and strain gages for Rfb3753.  
Figure 2.128     Locations of M.C. sections and strain gages for Lfb3753.  
Figure 2.129     Locations of M.C. sections and strain gages for Rfb3793.  
Figure 2.130     Locations of M.C. sections and strain gages for Lfb3793.  
Figure 2.131     Locations of M.C. sections and strain gages for Rfb3790.

- Figure 2.132 Locations of M.C. sections and strain gages for LFb3790.
- Figure 2.133 Locations of M.C. sections and strain gages for RFb3782.
- Figure 2.134 Locations of M.C. sections and strain gages for LFb3782.
- Figure 2.135 Locations of M.C. sections and strain gages for RFb3792.
- Figure 2.136 Locations of M.C. sections and strain gages for LFb3792.
- Figure 2.137 Locations of M.C. sections and strain gages for RFb3787.
- Figure 2.138 Locations of M.C. sections and strain gages for LFb3787.
- Figure 2.139 Gage strain for LF3793, concave side, proximal end, bending only.
- Figure 2.140 Gage strain for LF3793, concave side, distal end, bending only.
- Figure 2.141 Gage strain for LT3793, concave side, proximal end, bending only.
- Figure 2.142 Gage strain for LT3793, convex side, distal bending only.
- Figure 2.143 Axial strains for LT3793, convex side, near mid-diaphysis, bending only.
- Figure 2.144 Principal stresses for LT3793, convex side, distal end, bending only.
- Figure 2.145 Principal strains RH3782, convex side, mid-diaphysis bending only.
- Figure 2.146 Principal strains LH3753, convex side, mid-diaphysis, bending only.
- Figure 2.147 Axial strains from rapid rate test of LH3787, convex side, mid-diaphysis.
- Figure 2.148 Axial strains from rapid rate test of RH3790, convex side, mid-diaphysis.
- Figure 2.149 Principal stresses for LF3753 at the mid-diaphysis, torsion only.
- Figure 2.150 Principal stresses of RF3782, anterior side, distal end, torsion only.
- Figure 2.151 Principal strains for LH3782, medial side, proximal end, torsion only.
- Figure 2.152 Unexplained increase of lateral strains RT3782.
- Figure 2.153 Mohr's circle depiction of stress alteration under torsion dominant and bending dominant loading conditions.
- Figure 2.154 Gage strains for LT3790, concave side, distal end, torsion dominant.
- Figure 2.155 Gage strains for RH3787, convex side, proximal end, torsion dominant.

- Figure 2.156 Increase in lateral strain due to the rotation of the section.
- Figure 2.157 Effect of bending slope on true torsional force at the suspended end disk/damp.
- Figure 2.158 Nonlinearity of the lateral strains for LH3790, lateral side, proxiaml end.
- Figure 2.159 Calculation of bending moments from fracture loads.
- Figure 2.160 Bending deflections of the four human long bones.
- Figure 2.161 Distal end bending slopes of the four human long bones.
- Figure 2.162 Proximal end bending slopes of the four human long bones.
- Figure 2.163 Twist angles of the four human long bones.
- Figure 2.164 Calculation of fracture bending movements for the interaction boundaries.
- Figure 2.165 Section approximation from the computer output described in section properties.
- Figure 2.166 Interaction boundary for the femur.
- Figure 2.167 Interaction boundary for the tibia.
- Figure 2.168 Interaction boundary for the fibula.
- Figure 2.169 Interaction boundary for the humerus.
- Figure 2.170 First brittle lacquer cracks observed at the proximal end on the posterior side.
- Figure 2.171 Cracks observed at the proximal end anterior surface after additional loading.
- Figure 2.172 Fracture pattern anterior view.
- Figure 2.173 Fracture pattern medial view.
- Figure 2.174 Fracture pattern posterior view.
- Figure 2.175 Fractures expected of tubular shapes subjected to pure torsion.
- Figure 2.176 Fractures expected of tubular shapes under pure bending.
- Figure 2.177 Change in support conditions during fracture causing shear between teh loads in four point bending.
- Figure 2.178 Schematic of the select SEM locations in the study.
- Figure 2.179 Osteon failing normal to its axis in a bending tension state of stress (section 1, 240x).
- Figure 2.180(a) Stepped fracture surface caused by bending tension slightly oblique to the osteon axis (section 2, 100x).
- Figure 2.180(b) Stepped fracture surface caused by bending tension at a more oblique angle to the osteon axis (section 2, 90x).

- Figure 2.181(a) Bending tension fracture on a 45° plane to the osteon axes (section 2, 39x)..
- Figure 2.181(b) Osteon in the frame in Figure 2.181(a) (150x).
- Figure 2.182(a) Torsional-shear tension fracture on a 45° plane to the osteon axes (section 3, 75x).
- Figure 2.182(b) Osteon in the frame in Figure 2.182(a) (430x).
- Figure 2.183 Tilted view of a bending tension's failure on an oblique plane to the osteon axes (section 4, 75x).
- Figure 2.184 Larger scale view of a torsion-shear tension failure on a plane greater than 45° to the osteon axes (section 5, 24x).
- Figure 2.185(a) Shear failure parallel to the osteon axes (section 6, 100x).
- Figure 2.185(b) Osteon in the frame of Figure 2.185(a) (320x).
- Figure 2.186(a) Shear in a plane parallel to the osteon axes (section 7, 110x).
- Figure 2.186(b) Shear in a plane parallel to the osteon axes in lamellar bone (section 7, 150x).
- Figure 2.187(a) Osteon on a torsion-shear tension face (section 8, 100x).
- Figure 2.187(b) End of the same osteon, 220x.
- Figure 2.187(c) End of the same osteon, 1000x.
- Figure 2.187(d) Endosteal lamella showing mineralized collagen fiber bundles (section 8, 5000x).
- Figure 2.187(e) Mineralized collagen fiber bundles (section 8, 11,000x).
- Figure 2.187(f) Fractured end of mineralized fiber bundles (section 8, 9000x).
- Figure 2.188(a) Bending tension failure along a 45° plane (section 9, 90x).
- Figure 2.188(b) Bending tension failure along a plane less than 4° to the osteon axes (section 9, 75x).
- Figure 2.189(a) Shear fracture 45° to the osteon axes (section 10, 100x).
- Figure 2.189(b) Lamellae within the frame in Figure 2.193(a) (360x).
- Figure 2.190 Anterior view of the spiral fracture in a femur.
- Figure 2.191 Lateral view of the CSO mode in a femur.
- Figure 2.192 Posterior view of the spiral fracture in a femur.
- Figure 2.193 Medial view of the change in direction of the spiral fracture.
- Figure 2.194 Lateral view of a typical bending fracture.
- Figure 2.195 Medial view of the same fracture in Figure 2.194.

LIST OF TABLES

- 2.1 Male left femora.
- 2.2 Male right femora.
- 2.3 Female left femora.
- 2.4 Female right femora.
- 2.5 Male left humeri.
- 2.6 Male right humeri.
- 2.7 Female left humeri.
- 2.8 Female right humeri.
- 2.9 Male left tibiae.
- 2.10 Male right tibiae.
- 2.11 Female left tibiae.
- 2.12 Female right tibiae.
- 2.13 Male left fibulae.
- 2.14 Male right fibulae.
- 2.15 Female left fibulae.
- 2.16 Female right fibulae.
- 2.17 Micromasurement strain gages used in the long-bone fracture tests.
- 2.18 Schematic gage locations on the femora.
- 2.19 Schematic gage locations on the tibia.
- 2.20 Schematic gage locations on the humeri.
- 2.21 Schematic gage locations on the fibulae.
- 2.22 Test log
- 2.23 Output from "nondimensionalization" programs.
- 2.24 Mean fracture values for the four human long bones.
- 2.25 Fracture bending moments and bending deflections for bending only loading conditions.
- 2.26 Fracture twisting moments and corresponding angles of twist for the torsion only loading condition.
- 2.27 Fracture loads and displacements for the combined loading conditions.
- 2.28 Synthetic stresses for the femora and tibiae.
- 2.29 Synthetic stresses for the humeri and fibulae
- 2.30 SEM Sections
- 2.31 Proposed causes of fracture Surfaces of unknown origin.
- 2.32 Personal Data of Human Subjects

2.33 Ashing Data.

2.34 Acid Hydrolysis Data

2.35 % Porosity and cortical width (analyzed by MOP 3)

## 1.0 Introduction

Emergency egress from airplanes in flight is almost as old as manned flight itself. As pilots began to "bail out" of their crippled flying machines, they feared banging into exterior parts of the fuselage or having their parachutes entangle with their plummeting craft.

As the speed of flight increased, such contact became inevitable and crewmen were "boosted" away from the aircraft structure with ejection seats. Although the new life prolonging seats avoided one type of injury they invariably led to new and different injuries [1-6]. To alleviate spinal injuries caused by rudimentary ballistic initiators, new rocket powered seats having long load-stroke characteristics were developed; the spinal injuries still persisted and continue to persist [7-10].

During this initial development, a variety of injuries, other than the spinal injuries, also incurred [4-11]. It became more apparent that the low altitude high speed ejections had their own special difficulties. Even if the ejectee escaped contact trauma in the airplane, and survived the spinal injury ( $g_z$ ), there was yet another hazard operating, namely the "q"-force. Dynamic pressures on the limbs can be very high and can cause dislodgement and flail [12-20]. The knee, hip, elbow, and shoulder joints are affected as are all the long bones to varying degrees. Injuries of every type occur: palsies, ligament tears, trabecular bone fractures, and fractures in diaphyses.

Bone fracture is obviously an older study than ejection seat injuries. In fact, fractures occurring during windflail are only a subset of a general topic in orthopedics, with all related subjects, concerning bone strength, a part of this general topic. When an engineer becomes involved with the structural mechanics of bone, he soon realizes that the fracture loads, fracture modes, the geometry and chemistry of bone tissue are as relevant to its strength as the metallurgical equivalents are to the strength of manufactured structures. As his study advances, he is forced once again to focus on the microstructure of bone (hydroxyapatite content [21], collagen quality [22] porosity, etc.) to explain occurrences he observed in his large scale tests -- just as he had to do with lifeless structural materials. Thus, he begins with the simple modeling on a large scale, looks to the

microstructure for reasons to explain observed behaviors, and, finally, returns to a large scale study and attempts to incorporate his small scale findings. So proceeds the usual structural analysis. Fortunately he can turn to other investigations (23-32) for guidance, lightening the burden of this task.

The primary goal of this study is to extend the engineer's involvement in the life sciences in an effort to help others predict the strength and mechanical behavior of bone. Because a great deal has been accomplished to date with small scale experimentation [33-40] -- always the logical, initial approach to any materials study -- while little seems to have been done involving entire skeletal members, the study is aimed at the role of bone tissue in whole bone, specifically the four human long bones; the femora, tibiae, humeri, and fibulae.

As in all structural analyses, the first step necessary in the study of whole bone is the complete definition of geometry. Fortunately for efficiency sake, but unfortunately for the scientist, bones have ridges, bumps, depressions, crests, heads and irregularities of all sorts. They also vary in size as well as shape with some long, some short, some slender and some robust. These variations complicate the search for mathematical representations of bone behavior because the analytical tools available to the engineer produce answers only for simple, uniform shapes. Nonetheless, these simple tools are useful in approximating the responses of the geometrically complex bone shapes if the user realizes their limitations and applies their products judiciously. In fact, if little else is available, they offer the only reasonable estimate of fracture loads and associated displacements necessary for designing test equipment and preparing tests schedules. The use of such simple models is also appropriate if they can organize empirical data for practical application. Although a great deal of data on the geometry of bone exists [41-45], unfortunately little of it applies to the theoretical calculation of bone strength and is not useful directly.

The simple models or "classical theories" are so labeled because they are based on simple shapes that allow further assumptions which lead to closed mathematical solutions. The simple model used in this study to evaluate the response of whole bone, as well as present the

data acquired in a manner useful to the reader, is the round tube of constant diameter and wall thickness. Granted actual bone has neither, with the cortical wall decreasing in thickness as diaphyseal diameters increase and vice versa. However, when corrections are applied and the diaphysis is considered on the whole, the simple model is a good initial approximation.

To use the tube approximation, one is forced to approximate the sectional properties at each station to evaluate the strength of that section since the inside and outside diameters vary from station to station along the diaphyseal axis. This estimation of strength must also include the anisotropic and heterogeneous nature of bone tissue if the strength calculations are to be as accurate as the simple model will allow.

Suppose the simple model, with as many of these parameters considered as is possible, is an acceptable correlation between the geometry of the whole bone and its strength. Then it could allow further correlations between other physical quantities of interest such as torsional strength and bending strength. Thus, if a bone were bent to a certain degree and then twisted, the amount of twist required to cause fracture would be predictable using the bone's geometry.

Such interdependence between loading conditions has been used for years by the aircraft industry to design the sizes and shapes of parts which are to function under biaxial stress conditions. The interdependence is best depicted in terms of an interaction boundary along which a shearing stress influences the effect of a coexisting normal stress or vice versa. For aluminum and steel the boundaries take the form of a circle and are related mathematically as,

$$R_b^2 + R_t^2 = 1$$

where  $R_b$  is the ratio of the current bending stress divided by the ultimate bending stress and  $R_t$  is the current torsional stress divided by the materials ultimate torsional stress. For homogeneous and isotropic materials, nondimensional stress ratios such as these prove advantageous since the interaction formula is unique. However, for anisotropic materials which are also heterogeneous, the formulation is

not as direct and may involve higher order nonlinear functions relating the normal stresses and shearing stresses. These interaction boundaries are best employed graphically.

Obviously, bio-engineers as well as medical specialists would find bone interaction boundaries extremely useful. The human factors engineer could design survival equipment more wisely or, perhaps, the orthopedic surgeon could better restrain a broken limb. The primary intent of this report is the presentation of four such interaction boundaries along with the guidelines necessary to apply them. Each boundary represents one of the four human long bones, femur, tibia, humerus and fibula and, for the first time, allows the prediction of bending and twisting moments necessary to cause fracture when combined.

Secondary to the main goal of predicting fracture loads is the correlation of loading situations with fracture patterns. Such a correspondence is extremely useful to the orthopedic surgeon who is interested in knowing what sort of load caused a particular fracture. If he could determine that this spiral fracture was a result of eversive rotation of humerus, he would be better prepared to build a cast that resists further rotation in that direction. For the human factors engineer such information allows the association of fracture patterns with causal loads even when the trauma was recorded on a roentgenogram 10-15 years earlier. Perhaps, even the bio-engineer could better design a prosthesis knowing that bending load will cause a bifurcated fracture pattern.

Many side studies were conducted in support of the two main goals presented above. Displacements of the four long bones associated with bending and twisting and combinations of bending and twisting were recorded during all the tests and are presented graphically. The graphs are convenient for estimating end slopes, mid-diaphyseal displacements, and angles of twist for any femur, tibia, humerus or fibula when their bending or twisting moments are known. Strain states recorded during the tests offer insight into the magnitudes expected of strains and stresses occurring in the long bones when they are bent or twisted. Scanning electron microscope (SEM) studies depict different types of fracture surfaces as well as a graphic display of the collagen fiber bundles. A brittle coat experiment locates areas of high strain

isolating probable fracture initiation sights. Osteometric analyses were performed to place the specimens tested among the general population. Each of these efforts aided in explaining observed phenomena as well as introduced new phenomena which need study.

Laboratory tests at the University of Kansas Medical Center were performed to evaluate the quality of bone tissue tested in the program. Various analyses established that the bone tissue was indeed representative of the 50 percentile range with respect to the general population. Tests also verified that the tissue had not been degraded by procedures employed during the research program.

Currey [21] has shown bone strength to vary with the tissues' mineral content. Specifically, he reports that a four-fold increase in strength is directly traceable to a seven percent increase, from 63-70%, in mineral content. As a consequence of his findings, an ash analysis study was performed to reference the bone specimens tested with those of the general population.

Because the bones used in this study were resected from cadavers donated to medical science, the cause of death and its effect upon homeostasis was of concern. To obtain a sample more consistent with the aircrew population each cadaver was screened for age and known health problems. Fortunately, individuals were available who were middle-aged and free from any health problems associated with a degradation of bone tissue. To further substantiate the state of health at the time of death gross anatomy autopsies were performed and evaluated.

From experiences with composite materials used frequently in the aerospace industry, voids effect the resilience and strength of these materials and their performance is known to be a function of percent void to volume ratio. Similarly, secondary osteon bone is highly resorbed in the elderly and the increased porosity is known to affect the overall bone strength. So the porosity of the bone tissue tested was also analyzed at the Medical Center using the Zeis MOP III system. The conclusions from this analysis further substantiate the normality of the tissue selected for this study.

All of the data accumulated over the past two years were gathered with the feeling that when organized and analyzed it would offer the science community a few pieces of the puzzle which seemed to be missing.

The predictive capabilities that are offered in this report are considered unique. To date, fracture loads and deflections for whole bone subjected to bending and torsion, not to mention combinations of both bending and torsion, do not exist. Fracture configurations occurring from such loadings also appear missing from literature. In consideration of these facts, it is hoped that the conclusions drawn from this report concerning the primary studies as well as the side studies will prove useful to both the human factors engineer and the medical profession. Even more gratifying would be a continuation of this work by the scientific community based on the merit of this report and the findings disclosed within.

#### References

1. Drew, G. R., "Aircrew Escape and Survival - Problems and Solutions," SAFE, 1976, pp. 137-140, A77-49950.
2. Every, Martin G., "A Summary of Navy Air Combat Escape and Survival," Final Report, ONR, February 1977.
3. Fleck, J. T. and Butler, F. E., Development of an Improved Computer Model of the Human Body and Extremity Dynamics, AMRL-TR-75-14, Aerospace Medical Research Lab, Wright-Patterson Air Force Base, Ohio, July 1975.
4. Fleming, C., "Ejection Problems and Injuries-Their Causes, Effects and Treatments, and Suggestions for Preventive Measures," Aviation, Space, and Environmental Medicine, vol. 50, Aug. 1979, pp. 829-833.
5. Kilgariff, Thomas G., Escape From High-Performance Aircraft. Aeronautical Engineering Review. July, 1957.
6. Kittinger, Donald C., Aeronautical Systems Technology Needs - Escape, Rescue and Survival, ASD-TR-78-21, Aeronautical Systems Division, Air Force Systems Command, Wright-Patterson Air Force Base, Ohio, 1978.
7. Howland, O. E., "Ejection Seat for High G Escape," Final Technical Report for Air Force Dynamics Laboratory, Wright-Patterson AFB, Ohio, 1979.
8. Jones, Capt. Walton L., et al, "Ejection Seat Accelerations and Injuries," Aerospace Medicine 35, 1964, pp. 559-562.
9. Kazarian, Leon E., F/FB-111 Escape Injury Mechanism Assessment, AMRL-TR-77-60, Aerospace Medical Research Laboratory, Wright-Patterson Air Force Base, Ohio, October 1977.
10. Rai, Wg Cdr Kuldip and Gurusiddappa, Wg Cdr G, "Spinal Injury Pattern Due to Ejections," Aviation Medicine 23, 1979, pp., 41-47.

11. Smith, Howard Wesley, "Mechanical Properties of Four Human Longbones," Rev. of AF Sponsored Basic Research, 2-4 Oct. 1979, St. Louis Univ. Med. Center, MO, KU-AMRL-79-2.
12. Belk, Colonel William F., AFOSR-Sponsored Research on Limb Flail Injuries, Letter to Colonel Grant McNaughton, (Personal Communication), November 3, 1980.
13. Combs, Steven P., Mechanism of Extremity Injuries Occurring During Ejection from F-4 Aircraft, Proceedings of the 16th Annual SAFE Symposium, San Diego California, 8-12 October 1978, pp. 52-55.
14. Cummings, R. J. and Drsata, F. E., Exploratory Development of Aircrew Windblast Protection Concepts, AMRL-TR-79-16, Aerospace Medical Research Laboratory, Wright-Patterson Air Force Base, Ohio, 1979.
15. Grood, E., et al., Knee Flail Design Limits: Background, Experimentation and Design Criteria, AMRL-TR-78-58, Aerospace Medical Research Laboratory, Wright-Patterson Air Force Base, Ohio, 1978.
16. Payne, Peter, R., et al., Stability and Limb Dislodgement Force Measurements with the F-105 and Aces-II Ejection Seats, AMRL-TR-75-8, Aerospace Medical Research Laboratory, Wright-Patterson Air Force Base, Ohio, July 1975.
17. Schneck, Daniel J., Aerodynamic Forces Exerted on an Articulated Body Subjected to Windblast, AMRL-TR-76-109, Aerospace Medical Research Laboratory, Wright-Patterson Air Force Base, Ohio, Dec. 1976.
18. Woodward, C. C. and Schwartz, M., "High 'Q' Escape Protection - Pilot Restraint During High Speed Ejection," U.S. Naval Mat. Comm, c54, A79-14428, SAFE Assoc.
19. Zenobi, T. J., Estimation of Dynamic (Windblast) Pressure on Air-Crewman Ejecti--Etc., Naval Air Development Center, Warmister, Pa., Dec. 1979.
20. Anon. Prototype Development Passive, Seat-mounted Limb Retention System, Naval Air Development Center, Rep. No. NADC-79201-60, Stencil Aero Eng'r Corp., May 1979.
21. Currey, J. D., "The Mechanical Consequences of Variation in the Mineral Content of Bone", J. Biomechanics 2, 1969, pp. 1-11.
22. Dequeker, J., "Bone and Aging," Occasional Survey, Annals of Rheumatic Diseases, v. 34, 1975, pp. 100-115.
23. Baker, J. L. and Haugh, C. G., "Mechanical Properties of Bone: A Review." Trans. of the ASAE, v. 22, n. 3, 1979, pp. 678-687.
24. Boyde, Alan and Jones, Sheila J., "Bone and Other Hard Tissues," Principles and Techniques of Scanning Electron Microscopy, (Edited by Hayat, M.A.), Van Nostrand Reinhold Company, New York, 1974, pp. 123-149.
25. Evans, F. Gaynor, Mechanical Properties of Bone. Charles C. Thomas, Springfield, Il.

26. Goss, "Gray's Anatomy," 29th ed., Lea & Febiger.
27. Koch, John C., "The Laws of Bone Architecture," The American Journal of Anatomy, 21-2, 1917, pp. 177-298.
28. Mears, D. C., Materials and Orthopedic Surgery, The Williams & Wilkins Co., Baltimore, 1979, pp. 142-150.
29. Rockwood, Charles A. Jr., and Green, David P., Fractures, Volume I, J. B. Lippincott Company, Philadelphia, PA, 1975.
30. Rockwood, Charles A. Jr., and Green, David P., Fractures, Volume II, J. B. Lippincott Company, Philadelphia, PA, 1975.
31. Vaughan, Janet, The Physiology of Bone, Clarendon Press, Oxford, 1975, pp. 1-3; 10-11; 18-21; 32-37; 40-43; 56-65; 86-87; 96-99; 116-117; 256-257.
32. Yamada, Hiroshi, "Strength of Biological Materials," The Williams and Wilkins Co., Baltimore, 1970.
33. Ascenzi, Antonio and Bonucci, Ermanno, "The Ultimate Tensile Strength of Single Osteons." Acta Anat. 50, 1964, pp. 160-183.
34. Ascenzi, Antonio and Bonucci, Ermanno, "The tensile properties of single osteons." Anat. Rec. 158, 1967, pp. 375-386.
35. Ascenzi, Antonio and Bonucci, Ermanno and Simkin, Ariel, "The Compressive Properties of Single Osteons." Anat. Rec., 161, 1968, pp. 377-392.
36. Ascenzi, Antonio and Bonucci, Ermanno, "The Shearing Properties of Single Osteons." Anat. Rec., 172, 1972, pp. 499-510..
37. Ascenzi, Antonio, Bonucci, Ermanno and Simkin, Ariel, "An Approach to the Mechanical Properties of Single Osteonic Lamellae." J. Biomechanics, 6, 1973, pp. 227-235.
38. Ascenzi, A. and Bonucci, E., "Mechanical Similarities Between Alternate Osteons and Cross-ply Laminates." J. Biomechanics, 9, 1976, pp. 65-72.
39. Ascenzi, A. and Benevenuti, A., "Evidence of a State of Initial Stress in Osteonic Lamellae." J. Biomechanics, 10, 1977, pp. 447-453.
40. Reilly, D. T., Burstein, A. H., "The Elastic and Ultimate Properties of Compact Bone Tissue," J. Biomechanics, 1975, pp. 393-405.
41. Bass, William M., Human Osteology: A Laboratory and Field Manual of the Human Skeleton, Missouri Archaeological Society, Columbia, Missouri, (Second Ed.), 1971, pp. 6-7; 114-115; 168-171.
42. Kroemer, K.H.E., "Functional Anthropometry-A Basis for Biomechanics of the Human Body," Fourth Annual Conference of the American Society of Biomechanics, October 10, 1980.
43. Krogman, Wilton Marion, "Osteology of the Human Skeleton," The Human Skeleton in Forensic Medicine, Charles C. Thomas,

Springfield, 1973, pp. 304-313.

44. Roebuck, J. A., et al., Engineering Anthropometry Methods, John Wiley and Sons, 1975.
45. Anon. United States Air Force, "Anthropometry and Biomechanics" AFSC DH 1-3, Design Note 2B11, 1 Jan. 77.

## 2.0 Studies

### 2.1 Osteometry

#### 2.1.1 Anthropometric Techniques

Anthropometry is a series of more or less standardized techniques for the measurement of living and dead humans [1, 2]. In this study, we have applied osteometry (measurement of the postcranial skeleton) in an attempt to describe quantitatively the external morphology of each long bone. This makes possible comparisons with other skeletal populations and provides quantitative data to correlate with the mechanical properties of long bones.

Osteometric applications have traditionally lagged behind those of other anthropometrics [3]. The measurement of the skull (craniometry) has been used much more widely and consists of a relatively greater repertoire of measurements. This is due in part to the fact that there are simply more morphological landmarks on the skull than there are on the majority of postcranial bones. This is certainly true of the long bones, especially when one's interest is in the properties of the shaft. Another reason is that interest in human bone morphology has been stimulated by the study of fossil man [4]. Human skulls and teeth are much more common in the fossil record than postcranial material, so it is not surprising that craniometry has been emphasized more extensively.

For the purposes of this study, the measurements can be divided into two categories, applied and descriptive. The applied measurements are those being correlated with the mechanical properties of the shaft. They consist mostly of maximum and anatomical lengths, as well as diameters, and circumferences of the shaft. The descriptive measurements are included to form each bone's overall morphological profile. They consist of measurements taken from landmarks on each bone's proximal and distal epiphyses.

Most of the measurements used can be found in the anthropological literature [1, 2, 4, 5, 6]. Those that cannot are extensions of measurements used in the past. For example, medial-lateral diameter, anterior-posterior diameter, and circumferences at the proximal and distal 1/3 points are taken in the same manner as those taken at mid-shaft, where they traditionally have been measured.

The study of human osteology has revealed much about the metric and morphological properties of bone. It is possible to identify age, sex, and racial characteristics based on bone morphology [4]. Some attempts have been made in determining sex from long bone metrics as well [7, 8, 9, 10, 11, 12]. Using Fisher's discriminant function method, Pons reports an accuracy approaching 95% using femur metrics. Krogman [5], using metrics and morphology, believes an 80% accuracy is more realistic. It is also possible to estimate living stature from one or several long bones [1,5]. Generally, accuracy increases with the number of long bones used, especially leg bones. These formula are population specific, however, and accuracy decreases when a formula developed for one population is applied to an individual from another population [13]. For instance, one would not use a formula developed for north American blacks on a known white individual [14]. Although much work remains to be done on the applications of long bone metrics, it is clear that they have a real biological importance. It is also clear that sexual and racial variation has an important effect on bone metrics, and presumably their mechanical properties as well.

The present sample consists of fresh humeri, femora, tibiae, and fibulae from six white individuals whose personal data are described in Section 2.5.1. There are four males and two females ranging in age from 32 to 64 included in the study. Complete sets of long bones were taken from each individual. Each type of bone therefore is represented by two specimens, right and left, from each individual. The total sample for each bone type consists of 12 bones.

The following anatomical terms are useful in understanding the nature of the osteometric measurements used [2].

Anatomical position. In humans, this is an erect posture, with feet running parallel to each other and the arms hanging, elbow straight, and palms facing forward.

Anterior (A). Towards the front of the body.

Posterior (P). Towards the back of the body.

Medial (M). Towards the midline of the body when divided into left and right hemispheres.

Lateral (L). Away from the midline of the body.

Cranial or Superior. Towards the head.

Caudal or Inferior. Towards the foot.

Proximal (Pr). Towards the trunk of the body.

Distal (D). Away from the trunk of the body.

Some indices have been included to give the relationship of two or more measurements. An index is the simplest expression of the geometric relationship between measurements [3]. In this study we have included robusticity indices, which record the relationship between lengths of the bone to its shaft diameters or circumference. The greater a bone's shaft diameters are relative to its total length, the more robust that bone is said to be. The platymeric and platycnemic indices are included as quantitative descriptions of the shaft's shape in cross-section. The flatter a bone is in cross-section, the lower its index value will be. The following is a short description of each measurement.

#### 2.1.2. Osteometric Measurements

##### 2.1.2.1 Humerus

1. Anatomical length osteometric board  
(also called physiological length)  
Distal end is kept parallel to baseline (see Krogman [5] Fig. 113) with total length taken to top of head.
2. Maximum length osteometric board  
(also called morphological length)  
Total distance from head to furthest point on distal end.
3. Head
  - a. Cranial-caudal diameter sliding caliper  
(also called superior-inferior diameter)  
Bone is oriented in anatomical position, take maximum superior-inferior diameter of head.
  - b. Medial-lateral diameter sliding caliper  
In anatomical position, maximum medial-lateral diameter of head.
  - c. Circumference metric tape  
Maximum circumference of head in an anterior-posterior direction.
4. At midshaft (maximum length divided by one half, and marked by measuring on the osteometric board)

- a. anterior-posterior diameter sliding caliper  
(also called sagittal diameter)  
  
Orient bone in anatomical position, take maximum anterior-posterior diameter.
  - b. Medial-lateral diameter sliding caliper  
(also called Transverse diameter)  
Taken at a right angle to previous measurement.
  - c. Circumference metric tape  
Wrap tape around shaft at midpoint.
5. Surgical neck (shaft just below head and greater tuberosity)
- a. Anterior-posterior diameter sliding caliper  
Taken in same manner as at midshaft.
  - b. Medial-lateral diameter sliding caliper  
Taken in same manner as at midshaft.
  - c. Circumference metric tape  
Taken in same manner as at midshaft.
6. Bi-epicondylar breadth sliding caliper  
(also called Bicondylar breadth)  
Distance between medial and lateral epicondyles.
7. At top of olecranon fossa
- a. Medial-lateral diameter sliding caliper  
Taken in same manner as at midshaft.
  - b. Anterior-posterior diameter sliding caliper  
Taken in same manner as a midshaft.
8. Anterior articular surface breadth sliding caliper  
Distance between most medial aspect of trochlea and most lateral aspect of capitulum.
9. As seen from articular surface
- a. Medial ridge height sliding caliper  
Distance from line tangent to trochlea and capitulum to point where medial ridge blends into shaft.
  - b. Lateral ridge height  
Same as above on lateral side.
10. Orientation
- a. One half of the medial-lateral diameter is calculated and marked on the anterior surface of the bone at midshaft.

The bone is then laid on a flat surface with the anterior surface up. The distance from the flat surface to the most anterior aspect of the bone is then added to the distance from the surface to the most posterior aspect at midshaft. The total is then divided by 2 to define a line running along the side of the bone parallel to the flat surface on which the bone rests.

- b. The 1/3 points are defined by dividing the maximum length by 3. The medial-lateral diameters at the proximal and distal 1/3 points are then divided by 2 and marked on the anterior surface of the bone. These points, along with the point marked on the anterior surface at midshaft, define a line which is drawn on the anterior surface of the bone approximately bisecting the shaft.

- 11. At proximal 1/3 point
  - a. Anterior-posterior diameter sliding caliper  
Taken in same manner as at midshaft.
  - b. Circumference metric tape  
Taken in same manner as at midshaft.
- 12. At distal 1/3 point
  - a. Anterior-posterior diameter sliding caliper  
Taken in same manner as at midshaft.
  - b. Circumference metric tape  
Taken in same manner as at midshaft.
- 13. Least circumference of shaft metric tape  
Usually around the distal 1/3 point, repeat trials until least circumference is determined.
- 14. Robusticity Index (least circumference x 100) ÷ maximum length

#### 2.1.2.2 Femur

- 1. Anatomical length osteometric board  
(also called physiological, oblique, or bicondylar length)  
Length is taken with both distal condyles flat against stationary end.

2. Maximum length osteometric board  
 (also called morphological length)  
 Distance between most proximal aspect of head and the most distal aspect of the medial condyle.
3. Femur Head
  - a. Maximum circumference metric tape  
 Maximum circumference possible usually runs from the lateral-superior to the medial-inferior aspects of the head.
  - b. Superior-inferior diameter sliding caliper  
 Maximum diameter available with caliper held along inferior-superior axis and bone oriented in anatomical position.
  - c. Anterior-posterior diameter sliding caliper  
 Taken at right angle to #3b.
4. Femur Neck
  - a. Minimum neck circumference metric tape  
 Usually around constricted part of femur neck.
  - b. Perpendicular neck minimum diameter sliding caliper  
 Minimum diameter possible in a basically superior-inferior direction on neck with bone oriented in anatomical position.
  - c. Horizontal neck minimum diameter sliding caliper  
 Taken at right angle to #4b.
  - d. Biomechanical neck and head length sliding caliper  
 Distance from most lateral aspect of greater trochanter to most medial aspect of head.
  - e. Biomechanical neck length sliding caliper  
 Distance from most lateral aspect of greater trochanter to most lateral aspect of head.
5. At midshaft (1/2 the anatomical length measured on the osteometric board and marked on the anterior surface of the bone)
  - a. Circumference metric tape  
 Wrap tape around shaft at midpoint.

- b. Medial-lateral diameter sliding caliper  
Orient bone in anatomical position, take maximum medial-lateral diameter.
- c. Anterior-posterior diameter sliding caliper  
Taken at a right angle to previous measurement.
- 6. Distal epiphysis
  - a. Maximum breadth of medial condyle sliding caliper  
articular surface  
Repeat trials until maximum distance is ascertained.
  - b. Maximum breadth of lateral condyle sliding caliper  
articular surface  
Same as preceding.
  - c. Maximum bicondylar breadth sliding caliper  
Maximum medial-lateral diameter across the condylar end, at right angle to the long axis of the shaft.
- 7. See Humerus #10 (anatomical length is used to determine 1/3 points)
- 8. Shaft below lesser trochanter
  - a. Circumference metric tape  
Taken in the same manner as at midshaft.
  - b. Anterior-posterior diameter sliding caliper  
Same as at midshaft.
  - c. Medial-lateral diameter sliding caliper  
Same as at midshaft
- 9. Platymeric index (anterior-posterior diameter below lesser trochanter ÷ medial-lateral diameter below lesser trochanter) x 100
- 10. At proximal 1/3
  - a. Anterior-posterior diameter sliding caliper  
Same as at midshaft.
  - b. Circumference metric tape  
Same as at midshaft.
- 11. At distal 1/3
  - a. Anterior-posterior diameter sliding caliper  
Same as at midshaft.

b. Circumference metric tape  
Same as at midshaft.

12. Robusticity index (midshaft medial-lateral diameter + midshaft anterior-posterior diameter x 100) ÷ anatomical length

2.1.2.3 Tibia

1. Anatomical length osteometric board  
(also called physiological lt)

Place tibia at edge of osteometric board, length is taken from depression on the top of the lateral half of the condylar surface to the lower articular surface near the medial malleolus, but excluding it.

2. Maximum length osteometric board  
(also called morphological length)

Total length from intercondylar eminences to tip of medial malleolus.

3. Midshaft (#1 ÷ 2)

a. Circumference metric tape  
Wrap tape around shaft at midpoint.

b. Anterior-posterior diameter sliding caliper  
Orient bone in anatomical position, take maximum anterior-posterior diameter at midshaft.

c. Medial-lateral diameter sliding caliper  
Take at a right angle to the above measurement.

4. Bi-epicondylar breadth sliding caliper  
Maximum medial-lateral breadth across condylar (proximal) end.

5. Minimum perimeter metric tape  
Repeat trials until ascertained, usually found near the distal 1/3 point.

6. At the level of the nutrient foramen

a. Anterior-posterior diameter sliding caliper  
Taken in same manner as at midshaft.

b. Medial-lateral diameter sliding caliper  
Taken in same manner as at midshaft.

- c. Cnemic index (medial-lateral diameter ÷ anterior-posterior diameter) x 100)
7. See humerus #10 (anatomical length is used to determine 1/3 points)
8. Proximal 1/3
- a. anterior-posterior diameter sliding caliper  
Same as at midshaft.
- b. Circumference metric tape  
Same as at midshaft.
9. Distal 1/3
- a. anterior-posterior diameter sliding caliper  
Same as at midshaft.
- b. Circumference metric tape  
Same as at midshaft.
- 2.1.2.4 Fibula
1. Anatomical length osteometric board  
(also called physiological length)  
Length from distal lip of proximal articular facet to tip of lateral malleolus.
2. Maximum length osteometric board  
(also called morphological length)  
Maximum distance from proximal tip to distal tip.
3. Midshaft (#1 ÷ 2)
- a. Circumference metric tape  
Wrap tape around shaft at midpoint.
- b. Anterior-posterior diameter sliding caliper  
Orient in anatomical position, take maximum anterior-posterior diameter.
- c. Medial-lateral diameter sliding caliper  
Taken at a right angle to previous measurement.
4. Fibula lies with facets face down on table (these diameters are therefore close to anterior-posterior axis.) Except for this, the procedure is identical to Humerus #10. Anatomical length is used to calculate 1/3 points.

5. Proximal 1/3
  - a. Anterior-posterior diameter sliding caliper  
Same as at midshaft.
  - b. Circumference metric tape  
Same as at midshaft.
  - c. Medial-lateral diameter sliding caliper  
Same as at midshaft
6. Distal 1/3
  - a. Anterior-posterior diameter sliding caliper  
Same as at midshaft.
  - b. Circumference metric tape  
Same as at midshaft.
  - c. Medial-lateral diameter sliding caliper  
Same as at midshaft.

#### 2.1.3 Error in Measurement

It is usual, in any anthropometric study, to repeat several of the measurements to gain some insight into the degree of intra-observer error inherent in the data. In this case 24 measurements were retaken. The percent error between each repeat measurement and the original was then calculated. The average error between original and repeated measurement was 2.025%.

An error percentage of this magnitude is not overwhelming but it is larger than one would hope for. Under the conditions of this study, however, it is probably unavoidable. Because of the necessity for maintaining our specimens in as fresh a state as possible, it was not feasible to thoroughly remove all the soft tissue from the bone. A common method of removing soft tissue from bone in museums is to allow sand beetles to pick them clean. With human bone, however, this is not possible because of guidelines imposed by the Human Experimentation Board. Another alternative would be boiling in certain chemicals, but this would not leave the bone in a fresh state. For these reasons, it was necessary to clean the bones with scalpel and tweezers. Areas where muscles and ligaments attach are virtually impossible to clean thoroughly by this method. This resulted in the shafts being much cleaner than the proximal and distal epiphyses.

It should be noted that repeated measurements tended to give smaller readings than the original, this is to be expected since any soft tissue would be packed down tighter on the second measurement than on the first. It should also be noted that the error tended to be less on shaft measurements than on measurements on the epiphyses (in several cases it was 0%). This is also to be expected since the diaphysis was always much cleaner than the epiphyses. The measurements on the shaft, therefore, can be considered to be reasonably accurate. Those on the epiphyses, however, should be viewed with more caution.

#### 2.1.4 Comparisons with Other Populations

Any metric comparisons between the present sample and other populations must be viewed with caution because of the small number of individuals used in this study. This difficulty was further exacerbated by the fact that two of the six individuals considered were female and thus could not be included with the males as one sample population [4, 15]. Human skeletal populations exhibit a great deal of sexual dimorphism and so a combined male-female sample cannot be considered a normal distribution.

Fortunately for our purposes, all of the individuals included in this study were white. This eliminated "racial" variation as a potentially confounding source of variation.

Caution must always be exercised when comparing osteometric populations from different sources. Interobserver error can be a factor. Secondly, care must be taken to ascertain whether a given measurement was actually taken in the same manner by both observers. There were many instances in the literature survey of previous osteometric studies where data were not comparable because the method of measurement was not the same.

Despite numerous attempts in this century to standardize osteometric techniques, differences in methods and instrumentation still persist [3, 4]. Some data are available from the literature, however, with which some rough comparisons can be made in order to determine whether the present sample is representative of an average white population [7, 8, 9, 13, 14, 19, 20, 21] (see Tables 2.1 - 2.16).

#### 2.1.4.1. Males

For those measurements which are comparable in the various studies, the males of the present study compare rather well with larger samples from white populations. The dimensions are slightly greater than those of samples taken from individuals who died in the late 19th or early 20th century, but this perhaps is due to a secular trend for increased stature during the 20th century [16]. Trotter and Gleser's military population of WWII Pacific casualties is the only sample yielding consistently greater mean values [13]. This may reflect some bias whereby men assigned combat duty are of greater stature than the general population. Equally as likely, however, is the possibility that this too is a reflection of the secular trend for increased stature in this century. Data from the Terry collection used in this same study yield lower mean values. An examination of the age distribution of both samples reveals that many of the individuals included in the Terry collection were born around or before 1900 while those in the military sample were born mostly in the 1920's. Thus, it may be that the mean values for the present data may be slightly lower than one would find if it were possible to sample a large modern white population.

#### 2.1.4.2. Females

Not much can be said about our female data in comparison with other samples because of inadequate sample size. The dimensions of the present sample are generally larger than those of other white female populations but this is probably due to the small sample size (if 2 individuals can even be considered a sample). The tables will at least give the reader an idea of the differences between male and female mean values.

#### 2.1.4.3. Sexual Dimorphism

The data in Tables 2.1 - 2.16 give a clear impression of the degree of sexual dimorphism present in human skeletal populations. Male skeletons tend to be larger and more robust than female skeletons [6]. Presumably, this is due to a division of labor by sex whereby until the industrial revolution males engaged in more strenuous activities and were more frequently exposed to chance of injury than females. It is

Table 2.1 Male left femora (mean values in mm).\*

	<u>Max lt.</u>	<u>Anat. lt.</u>	<u>Platymeric transverse dia</u>	<u>Robusticity index</u>	<u>Sagittal dia. midshaft</u>
Present Study	460.75(4)	458.50(4)	35.59(4)	13.42(4)	31.34(4)
Parsons (1914)	460(98)	456(102)	36(105)	13.60(105)	32(105)
Ingals (1924)	460.74(100)	457.87(100)	32.465(100)	13.51(100)	29.42(100)
Pearson (1919)	447.70(225)	445.48(214)	31.52(247)	12.71(250)	28.67(250)
Trotter & Gleser Military (1952)	472.90(545)	469.64(545)			
Trotter & Gleser** Terry Collection (1952)	456.60(255)	454.15(255)			
Dupertuis** and Hadden Todd Collection (1951)	453.30(200)				
Holtby (1918)	460(35)	457(35)			
Hrdlicka (1932)		451.1(378)			

\*Sample size in parentheses

\*\*Right and left combined

Table 2.2 Male right femora (mean values in mm).\*

	<u>Max lt.</u>	<u>Anat. lt.</u>	<u>Platymeric transverse dia</u>	<u>Robusticity index</u>	<u>Sagittal dia. midshaft</u>
Present Study	461.13(4)	458.5(4)	34.54(4)	13.30(4)	31.53(4)
Parsons (1914)	456(76)	453(75)	35(80)	13.25(79)	31(79)
Ingals (1924)	460.88(100)	457.83(100)	32.41(100)	13.48(100)	29.29(100)
Pearson (1919)	446.77(218)	444.35(202)	31.68(236)	12.95(237)	29.53(237)
Trotter & Gleser Military (1952)	472.32(545)	468.53(545)			
Trotter & Gleser** Terry Collection (1952)	456.60(255)	454.15(255)			
Dupertuis** and Hadden Todd Collection (1951)	453.3(100)				
Holtby (1917)	453(21)	450(21)			
Hrdlicka (1932) US whites		451.0(378)			

\*Sample size in parentheses

\*\*Right and left combined

Table 2.3 Female left femora (mean values in mm).\*

	<u>Max lt.</u>	<u>Anat. lt.</u>	<u>Platymeric transverse dia.</u>	<u>Robusticity index</u>	<u>Sagittal dia. midshaft</u>
Present Study	437.5(2)	434.5(2)	31.95(2)	12.81(2)	29.5(2)
Parsons (1914)	422(49)	418(51)	33(50)	13.16(51)	28(51)
Pearson (1919)	408.26(181)	405.21(169)	28.68(193)	12.47(196)	25.16(196)
Trotter & Gleser** Terry Collection (1952)	429.59(63)	426.54(63)			
Holtby (1918)	416(24)	414(24)		12.71(24)	27.5(24)
Dupertuis** and Hadden (1951) Todd Collection	422.4(200)				
Hrdlicka (1932)		417.5(133)			

\*Sample size in parentheses

\*\*Right and left combined

Table 2.4 Female right femora (mean values in mm).\*

	<u>Max lt.</u>	<u>Anat. lt.</u>	<u>Platymeric transverse dia.</u>	<u>Robusticity index</u>	<u>Sagittal dia. midshaft</u>
Present Study	439(2)	432.5(2)	31.68(2)	12.72(2)	29.38(2)
Parsons (1914)	416(52)	415(53)	32(55)	13.01(55)	28(55)
Pearson (1919)	410.11(171)	406.43(161)	28.57(178)	12.61(185)	26.05(185)
Trotter & Gleaser** Terry Collection (1952)	429.59(63)	426.54(63)			
Holtby (1918)	414(20)	411(20)		12.51(20)	26.9(20)
Dupertuis** and Hadden Todd Collection (1951)	422.4(200)				
Hrdlicka (1932) US whites		417.6(133)			

\*Sample size in parentheses

\*\*Right and left combined

Table 2.5. Male left humeri.  
(Mean values in mm)\*

	<u>Max lt.</u>	<u>Sagital dia. Midshaft</u>
Present Study	334.38(4)	23.15(4)
Hrdlicka (n) (1932) US whites	323.8(378)	22.2(304)
Trotter & Gleser** (1952) Terry Collection	329.98(255)	
Trotter & Gleser (1952) Military	335.95(545)	
Dupertuis & Hadden** (1951) Todd Collection	328.7(200)	

\*Sample size in parentheses

\*\*Left and right combined

Table 2.6. Male right humeri.  
(Mean values in mm)\*

	<u>Max lt.</u>	<u>Sagital dia. Midshaft</u>
Present Study	335.63	23.375
Hrdlicka (n) (1932) US whites	326.2(378)	23.2(304)
Trotter & Gleser** (1952) Terry Collection	329.98(255)	
Trotter & Gleser (1952) Military	336.4(545)	
Dupertuis & Hadden** (1951) Todd Collection	328.7(200)	

\*Sample size in parentheses

\*\*Left and right combined

Table 2.7. Female left humeri.  
(Mean values in mm)\*

	<u>Max lt.</u>	<u>Sagital dia. Midshaft</u>
Present Study	310.5(2)	20.3(2)
Hrdlicka (1932) US whites	295.6(133)	20.1(97)
Trotter & Gleser** (1952) Terry Collection	304.3(63)	
Dupertuis & Hadden** (1951) Todd Collection	302.3(200)	

\*Sample size in parentheses

\*\*Left and right combined

Table 2.8. Female right humeri.  
(Mean values in mm)\*

	<u>Max lt.</u>	<u>Sagital dia. Midshaft</u>
Present Study	315.5(2)	20.53(2)
Hrdlicka (n) (1932) US whites	298.6(133)	20.7(97)
Trotter & Gleser** (1952) Terry Collection	304.3(63)	
Dupertuis & Hadden** (1951) Todd Collection	302.3(200)	

\*Sample size in parentheses

\*\*Left and right combined

Table 2.9. Male left tibiae (mean values in mm).\*

	<u>Platycnemic transverse dia.</u>	<u>Platycnemic sagittal dia.</u>	<u>Midshaft transverse dia.</u>	<u>Midshaft sagittal dia.</u>	<u>Platycnemic index</u>
Present Study	26.43(4)	38.21(4)	22.94(4)	31.98(4)	69.17(4)
Hrdlicka (1898)	25.0(**)	36.4(**)	22.0(**)	31.4(**)	68.68(**)

Table 2.10. Male right tibiae (mean values in mm).\*

	<u>Platycnemic transverse dia.</u>	<u>Platycnemic sagittal dia.</u>	<u>Midshaft transverse dia.</u>	<u>Midshaft sagittal dia.</u>	<u>Platycnemic index</u>
Present Study	25.18(4)	37.19(4)	22.61(4)	32.54(4)	67.71(4)
Hrdlicka (1898)	25.4(**)	36.3(**)	22.4(**)	31.3(**)	69.97(**)

\*Sample size in parentheses

\*\*Hrdlicka describes his sample as "2,000 normal adult bones of persons of various nations and both sexes."

Table 2.11 Female left tibiae (mean values in mm).\*

	<u>Platycnemic transverse dia.</u>	<u>Platycnemic sagittal dia.</u>	<u>Midshaft transverse dia.</u>	<u>Midshaft sagittal dia.</u>	<u>Platycnemic index</u>
Present Study	23.68(2)	33.90(2)	21.55(2)	29.08(2)	69.85(2)
Hrdlicka (1898)	20.6(**)	27.7(**)	18.6(**)	25.7(**)	74.37(**)

Table 2.12 Female right tibiae (mean values in mm).\*

	<u>Platycnemic transverse dia.</u>	<u>Platycnemic sagittal dia.</u>	<u>Midshaft transverse dia.</u>	<u>Midshaft sagittal dia.</u>	<u>Platycnemic index</u>
Present Study	24.15(2)	32.93(2)	21.28(2)	32.54(2)	73.34(2)
Hrdlicka	22.5(**)	29.2(**)	20.5(**)	27.2(**)	77.05(**)

\*Sample size in parentheses

\*\*Hrdlicka describes his sample as "2,000 normal adult bones of persons of various nations and both sexes."

Table 2.13. Male left fibulae.  
(Mean values in mm)\*

	<u>Maximum length</u>
Present Study	374.25(4)
Trotter & Gleser (1952) Military	381.53(545)
Trotter & Gleser** (1952) Terry Collection	367.82(255)

Table 2.14. Male right fibulae.  
(Mean values in mm)\*

	<u>Maximum length</u>
Present Study	375.5(4)
Trotter & Gleser (1952) Military	381.18(545)
Trotter & Gleser** (1952) Terry Collection	367.82(255)

\*Sample size in parentheses

\*\*Left and right combined

Table 2.15. Female left fibulae.  
(Mean values in mm)\*

	<u>Maximum length</u>
Present Study	360.5(2)
Trotter & Gleser** (1952) Terry Collection	343.35(63)

Table 2.16 Female right fibulae.  
(Mean values in mm)\*

	<u>Maximum length</u>
Present Study	355.5(2)
Trotter & Gleser (1952) Military	343.35(63)

\*Sample size in parentheses  
\*\*Left and right combined

interesting to note that both males and females tend to be more robust in hunting and gathering societies and that such groups exhibit a greater degree of sexual dimorphism than agricultural/ industrial populations [17].

A survey of the range of variation for modern human males and females clearly indicates the degree of sexual dimorphism present. The white populations compared in this study indicate a range of variation for maximum femur length of 543-404 mm for males and 477-358 mm for females [7, 8]. The ranges in the present data for maximum femur length are 468-457 mm and 442-435 mm. Other dimensions, however, are not as variable as lengths. Ranges for the platymeric transverse diameter of the femur are 45-30 mm for males and 39-27 mm for females. Ranges for the present data are 40-32.65 mm for males and 33.6-30 mm for females.

Clearly, sex is a significant source of metric variation in human skeletal populations. Even the small number of individuals measured in this study clearly reflect human sexual dimorphism.

#### 2.1.4.4. Platymeria

Platymeria is the degree of anterior-posterior flattening of the femur shaft, just below the lesser trochanter. Any platymeric index value below 84.9 is said to indicate a femur showing platymeria [15]. Various reasons have been given for this condition including a suggestion that platymeria is an economic adaptation involving the use of material with sufficient strength to support body weight acting on the inclined femur neck. Other explanations suggested for this condition include squatting behavior, osteoarthritis, osteoperiostitis, excessive strain during childhood, or a shortage of bone material due to calcium or vitamin deficiency [15].

Platymeric index values for the present study are probably somewhat inflated due to an excess of soft tissue on the posterior surface, resulting in excessive anterior-posterior diameters. Even so, one of the femora, #3782 (right) yielded an index value indicating platymeria (see femur data sheets, #9 for explanation of index values). Although the platymeric index values for the present data are probably not comparable to those of previous metric studies, they are useful in

quantifying the range of variation in the shape of the shaft in cross-section within the sample population.

According to Brothwell [4], recent groups tend to have higher platymeric index values than fossil groups. It has also been claimed that platymeria is more common in females, and that left femora tend to be more platymeric than right femora.

#### 2.1.4.5. Platycnemia

The platycnemic index expresses the degree of transverse flattening of the upper part of the shaft of the tibia at the level of the nutrient foramen (see tibia data sheets for explanation of index values). Various pathological and muscular reasons have been given, including the old standby, squatting. As with platymeria, ancient and so-called "primitive" recent groups show a higher degree of platycnemia (lower index values) than modern industrial populations [15]. It is perhaps for this reason that squatting is often cited as an explanation. Presumably, individuals in primitive societies exhibit more squatting behavior than those in modern industrial groups. Cameron [18], considers that the persistent adoption of a squatting position when resting results in a retroversion of the upper end of the bone.

The platycnemic index is said to be higher in men than in women [6]. Although both platymeria and platycnemia are said to be related with squatting behavior they are not necessarily found associated [15].

#### 2.1.4.6. Racial Variation

It has been well documented that the metric proportions of long bones vary among the so-called "races" [3, 5, 13]. This fact becomes quite obvious when attempting to predict stature from long bone lengths. For instance, Trotter and Gleser [13] found that in white males a maximum femur length of 482 mm was associated with a stature of 176 cm. In black males a femur of the same length was associated with a stature of 172 cm.

Blacks have on average, longer bones than whites. There is, however, a great deal of overlap in the range of variation between

blacks and whites to the extent that racial classification cannot be made with any great confidence on the basis of long bones exclusively [5].

A survey of Hrdlicka's data on the Humerus [14] reveals consistently higher mean values for lengths among male and female blacks. Diameters of the shaft, however, are about the same for both groups which would indicate that blacks are somewhat less robust than whites.

#### 2.1.5 References (Osteology)

1. Bass, W. M. 1971. Human Osteology. Missouri Archaeological Society, Columbia, Mo.
2. Singh, I. P. and Bhasin, M. K. 1968. Anthropometry. Bharti Bhawan, Delhi.
3. Hrdlicka, A. 1939. Practical Anthropometry. Wistar Inst. of Anat. and Bio., Philadelphia.
4. Brothwell, D. R. 1968. The Skeletal Biology of Earlier Human Populations.
5. Krogman, W. M. 1973. The Human Skeleton in Forensic Medicine, Thomas, Springfield, Il.
6. Oliver, G. 1969. Practical Anthropology. Thomas, Springfield, Il.
7. Holtby, J. R. D. 1918. "Some Indices and Measurements of the Modern Femur." Journal of Anatomy, 52:363-382.
8. Parsons, F. G. 1914. "The Characters of the English Thighbone." Journal of Anatomy, 48:238-267.
9. Pearson, K. and Bell, J. 1919. "A Study of the Longbones of the English Skeleton." The Femur, Draper's Co. Research Mem., U. of London, Biom. Series X.
10. Pons, J. 1955. "The Sexual Diagnosis of Isolated Bones of the Skeleton." Human Biology, 27:12-21.
11. Thieme, F. P. 1957. "Sex in Negro Skeletons." Journal of Forensic Medicine 4(2):72-81.
12. Thieme, F. P. and Schull, W. J. 1957. "Sex Determination from the Skeleton," Human Biology 29(3):242-273.
13. Trotter, M. and Gleser, G. C. 1952. "Estimation of Stature from Longbones of American Whites and Negroes." American Journal of Physical Anthropology, 10:453-514.
14. Hrdlicka, A. 1932. "The Principal Dimensions Absolute and Relative of the Humerus in Whites." American Journal of Physical Anthropology, 16:431-450.
15. Brothwell, D. R. 1963. Digging Up Bones. British Museum, London.

16. Trotter, M. and Gleser, G. C. 1951. "Trends in Stature of American Whites and Negroes born between 1820 and 1924." American Journal of Physical Anthropology, 9:427-440.
17. Frayer, D. W. 1980. "Sexual Dimorphism and Cultural Evolution in the Late Pleistocene and Holocene of Europe." Journal of Human Evolution, 9:399-415.
18. Cameron, J. 1934. The Skeleton of British Neolithic Man, London.
19. Dupertuis, C. W. and Hadden, J. A. 1951. "On the reconstruction of Stature from Long Bones." American Journal of Physical Anthropology, 9:15-53.
20. Hrdlicka, A. 1898. "A Study of the Normal Tibia." American Anthropologist, II:307-310.
21. Ingalls, N. W. 1924. "Studies on the Femur." American Journal of Physical Anthropology, 7:207-255.

## 2.2 Fracturing

### 2.2.1 Introduction

To fracture the four human long bones under controlled conditions, a test apparatus was designed and manufactured which permitted the bending, twisting and combined bending and twisting of each of the four bone types. The machine also provided measurements of the imposed deflections and a means of controlling the environment surrounding the bone diaphysis. Auxillary equipment was purchased to indicate strains from resistance strain gages that were bonded to the diaphyseal surfaces. Other equipment was acquired on loan and modified to indicate the induced loads applied to each of the bone specimens.

Forty-eight bones were fractured using one of the three loading conditions mentioned above. Before testing, the geometry of each bone was recorded as discussed in Section 2.1. Strain gages were applied to forty-three of the bones and their strains recorded during loading. All pertinent deflections and incremental loads were recorded up until fracture. Fracture patterns were sketched as well as photographed. Post-test sectioning of the bone diaphyses was accomplished to locate the strain gages peripherally as well as to remove samples for histological and morphological studies at the Univeristy of Kansas Medical Center.

This section describes the equipment used to fracture the four long bones and the equipment necessary to record load and load response.

Methods of operation of the equipment, including strain gage application procedures and records-keeping, are included. Choices of load conditions, test schedules and loading plans for each bone are explained. Finally, the results and observations are discussed and the certain techniques in reducing data described.

### 2.2.2 Theory

Before actually beginning a test, an investigator should consider the complexities and problems involved in his experimental method as well as the information that is available to help him explain the outcome. The fracturing of the four human long bones, the femur, tibia, fibula and humerus, in the most general sense, involves the bending, twisting and combined bending and twisting of a tube of irregular cross-sectional shape and varying geometry. For those experiments involving bending only, the mechanics of the response can be associated with unsymmetrical bending. For the experiment involving only a twisting moment, the mechanics of response should include section warpage and effects of material constraint. When the two are combined, a biaxial strain and stress state exist and the situation becomes more involved. However, regardless of the loading condition, the principal stresses which exceed the appropriate failure criterion should be the cause of fracture.

As each of these approaches is expounded the complexity of situation evolves. In the case of bending only, the bone diaphyses are not straight, but curved, and, therefore, may cause the bone to twist even though there is no twisting moment applied. If the test machine does not allow total freedom under load, its constraining of this twisting tendency complicates the mechanics modeling the response. In the case of torsion only, the varying cross-section geometry will constrain neighboring material and the warping of the irregular cross-sectional shape becomes complicated. When the two loading conditions are combined, the biaxial strain state is, in actuality, governed by the anisotropic behavior of the bone tissue and the causes for bone response become more subtle.

The discussion to follow attempts to explain the engineering mechanics involved in fracturing the bones when the loading conditions,

bending only, torsion only and combined bending and torsion, are considered.

#### 2.2.2.1 Bending Only

If a tube is subjected to four point bending where a concentrated load is applied symmetrically about the mid-span, the bending shear is restricted to portions of the tube which lie between the loads and the supports (Figure 2.1), with no shear existing between the two applied loads. Consequently, the bending moment increases linearly from the supports to the load points and is constant between the loads. Using this arrangement, the magnitude of the shear involved may be varied by changing the spacing of the applied loads.

Then, assuming the mode of failure to be a tension fracture occurring at mid-span on the convex side of the deflecting tube, the tube should fracture theoretically at the same bending moment regardless of the load spacing. Since the shear does not change and yet the bending moment decreases as the load spacing varies and the load is held constant but the bending moment decreases, the ultimate load causing fracture should increase as the load spacing increases if the fracture is to occur only when the tension stress on the convex side reaches an ultimate stress. Increasing the fracture load then is the only way to maintain a certain bending moment as the load spacing is increased since the bending moment between the loads is equal to area under the shear diagrams. Hence, the amount of shear involved may be increased by increasing the distance between the applied loads.

Considering the irregular shape of the cross-sections of the four long bones, the bending of the diaphysis must occur unsymmetrically with stresses and deflections dependent on the principal axes of inertia of the cross-section. Figure 2.2 shows a cross-section at the mid-diaphysis of a humerus. Included in the figure are the moments of inertia with respect to a reference axis  $x, y$  and the principle axes of inertia  $x', y'$ . If a bending moment were applied whose vector was coincidental with the  $x$  axis and if this cross-section were constant along the span, the bone would bend about both principal axes and the vectorial sum of the two deflections would provide the total deflection. If this model were constrained to bend only about the reference axis  $x$ ,

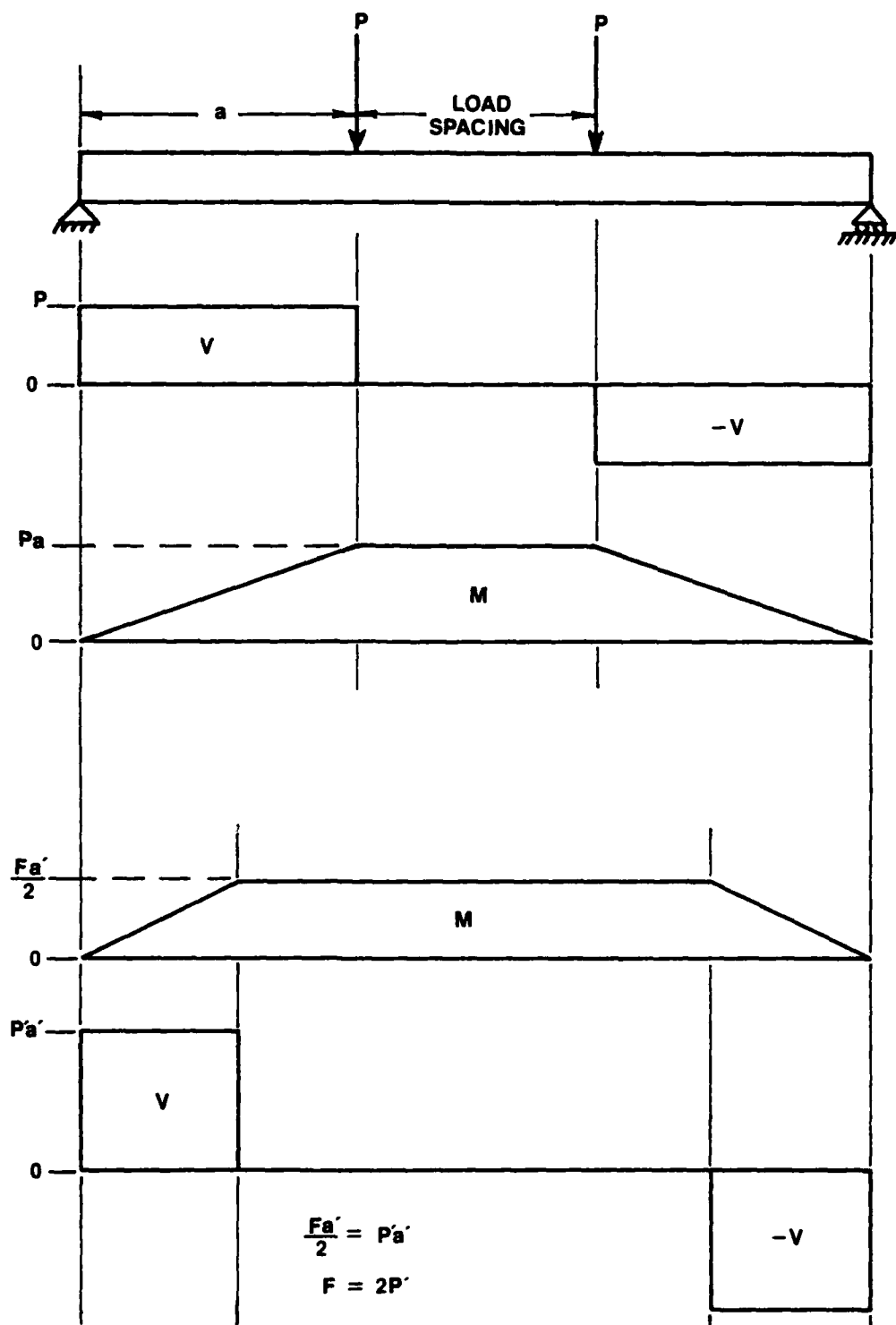
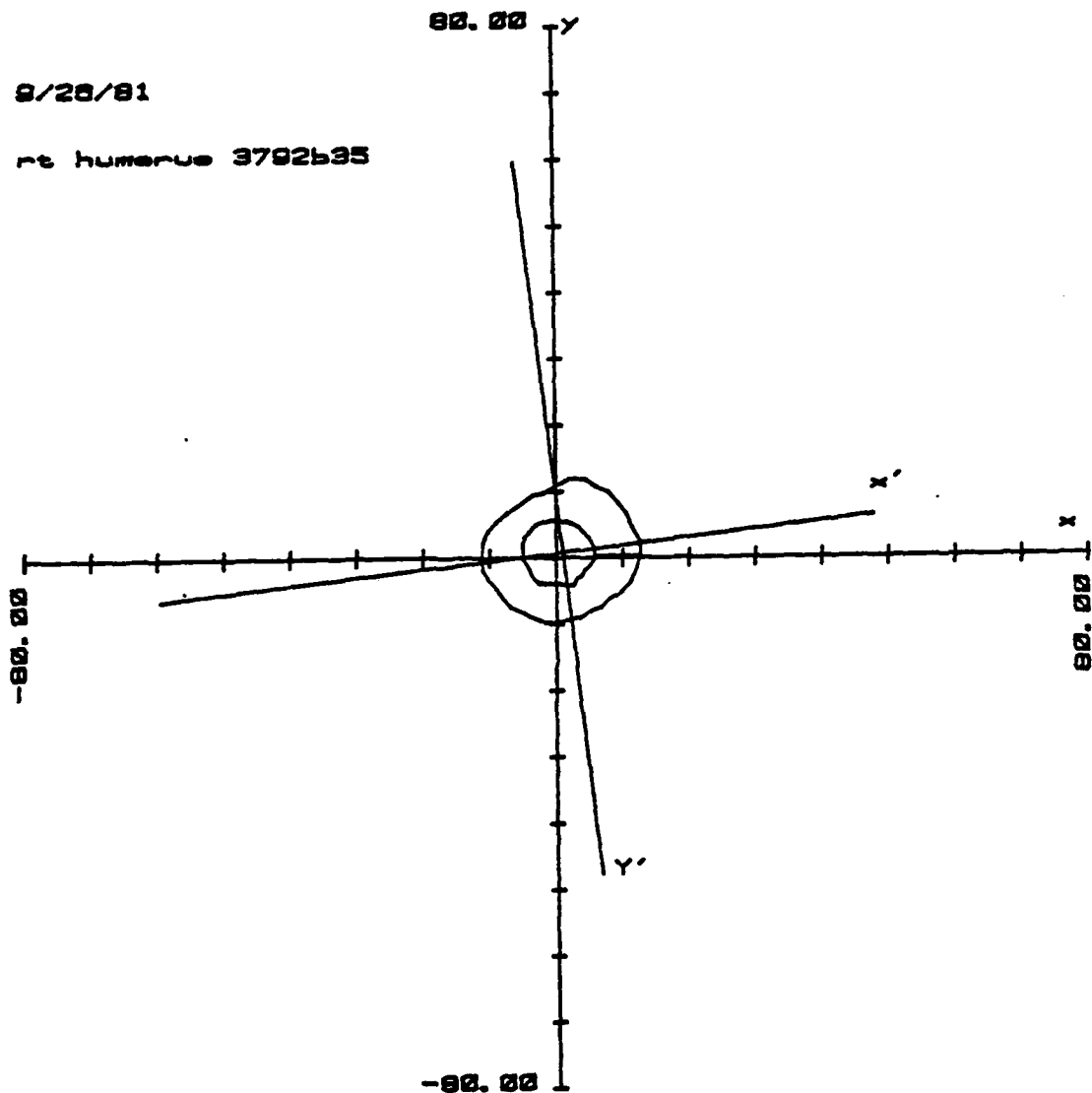


Figure 2.1 Shear and moment diagrams for four point bending.

Figure 2.2 Principal axes of inertia for a mid-diaphyseal cross-section of the humerus.



$$I_{xx} = 9762.24 \text{ mm}^4$$

$$I_{yy} = 12473.66 \text{ mm}^4$$

$$I_{xy} = 1492.06 \text{ mm}^4$$

$$I_{x'} = 0.00 \text{ mm}^4$$

$$I_{x'x'} = 9312.00 \text{ mm}^4$$

$$I_{y'y'} = 12417.04 \text{ mm}^4$$

$$\theta = 6.74 \text{ deg}$$

$$I_{y'y'} = -0.00 \text{ mm}^4$$

$$\text{AREA} = 292.85 \text{ mm}^2$$

the loading configuration would change to include an additional bending moment whose vector is coincidental with the vertical, reference axis  $y$ . Unless the principal axes vary substantially from the reference axis, the effect of constraint should be small. If the principal axes are rotated to a large angle with respect to the reference axes, then the true stress state will be quite different from that of symmetrical bending. In either case, the actual response will not be readily available through observation, but would have to be approached by considering the unsymmetrical bending situation. Furthermore, if such a constraint were imposed, the resulting stresses would not be those associated with simple bending.

The tubular shape of the diaphyses also complicates a thesis describing bone fracture, because the tubular shape tends to collapse beneath the point of the applied load. This behavior along with the contact stresses occurring in the vicinity of the loads further confounds the biaxial state (bending with Poisson's effect) assumed in mechanics of materials when simple bending occurs. Unless the strains and stresses are examined at some distance away from the loading points, in accordance with St. Venant's principle, the strain and stress states will not be easily discernable. Nevertheless, when the fracture occurs in the vicinity of loads, the effect of the collapse mechanism interacting with contact stresses and bending stresses cannot be ignored.

The mechanism of fracture propagation is one of maximum energy release, incorporating the three modes (Figure 2.3 of fracture: opening, shearing and tearing. In the bending only situation, the fracture begins on the tension side, the convex side, of the bending bone as a brittle fracture. It starts when the bending stress reaches a magnitude such that the stress intensity factor in the tensile region approaches a critical value for the bone tissue respective of the stress orientation relative to material directions. This stress intensity factor is related theoretically to the tensile stress and the geometry of the surface and the internal flaws. Once the fracture begins, it follows a path that releases as much of the internal energy as possible to attain a minimum potential energy state. Initially the fracture is of the opening mode but may transform to a shearing or tearing mode. The mode changes because as the fracture progresses the loading

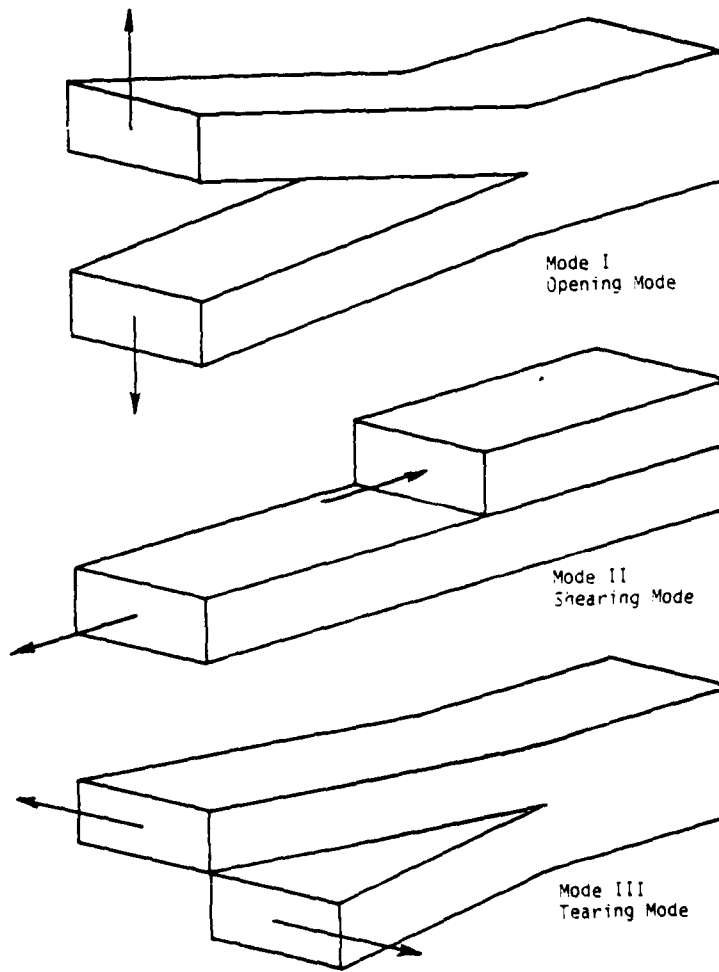


Figure 2.3 Fracture modes possible in bones.

conditions are changed. The fracture behaves in a brittle manner until arrested by load relaxation or until the local redistribution of stresses ahead of the moving crack decreases the stress intensity factor below the critical value, respective again of stress orientation relative to the material direction in the region. The fracture may initiate statically under plastic conditions but propagates dynamically under brittle conditions.

#### 2.2.2.2 Torsion Only

To theorize the mechanics of bone behavior governed by a twisting moment, consider again the simple thick-walled tube of constant cross-section. Mechanics of materials shows us that the only possible strain parallel and perpendicular to the torsional axis is a shearing strain,  $\gamma_{xy}$  (Figure 2.4). However, this shearing strain, when transformed into principal strains, cause a maximum tensile strain in a direction that is 45 deg. to the torsional axis. Normal to this direction of tensile strain is the minimum normal strain, a compressive strain. For this simple model, the three strains have the same magnitude.

The angle of twist of the simple tube is a function of the torque applied as well as the geometry,

$$\phi = \frac{TL}{JG}, \quad \text{simple tube}$$

T - torque

L - length

G - shear modulus

J - polar moment of inertia ( $J = \frac{\pi}{2} (R_o^4 - R_i^4)$  where  $R_o$  and  $R_i$  are the outside and inside radii, respectively.)

Relative to one of the ends of the tube, it increases from zero at that end to a maximum at the other and is proportional to the distance from the referenced end for the simple tube. Therefore, with one end fixed, the free end of a long tube under torsion will undergo a greater angular displacement than will a shorter tube. Similarly, the angle of twist,  $\phi$ , is inversely proportional to the polar moment of inertia; so, the twist of one end relative to the other of a tube with a small cross-

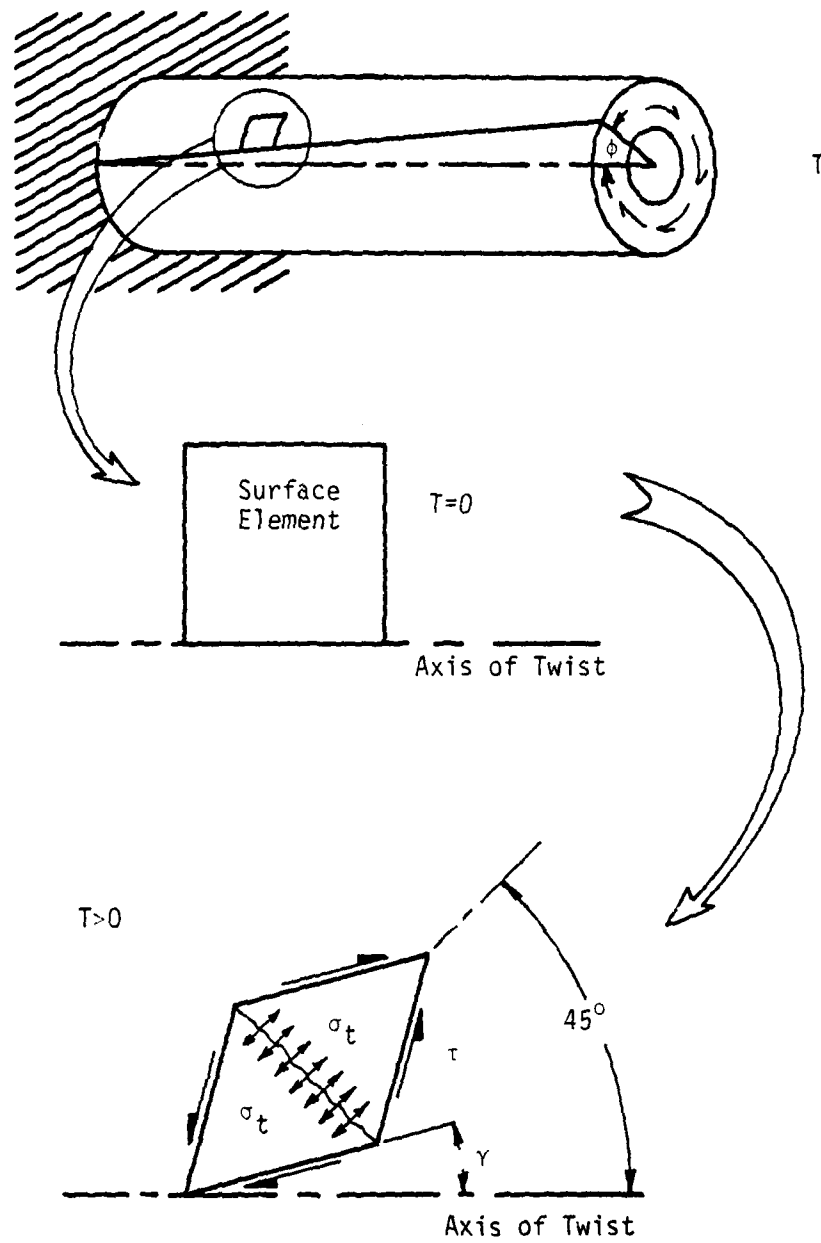


Figure 2.4 Strain and stress due to pure torsion.

section is greater than that of a tube of a large cross-section. These facts for a simple tube infer that the short humerus should twist approximately the same as the longer femur and tibia. Such displacements become evident when cross-sectional shapes and lengths are compared. The humerus has a smaller  $J$  and a shorter length than either the tibia or femur and, therefore, the three should have comparable  $L/J$  values. Conversely, the fibula should twist more than either of the three because its small cross-section and long length result in an  $L/J$  that is large in comparison.

Obviously, bone diaphyses consist of cross-sections which have irregular shapes that vary along the diaphyseal axis. Such geometry no longer behaves in the same manner as the simple tube, but involves warpage of the cross-sections and, consequently, the constraint of the surrounding material introduces complex strain and stress states. Since these cross-sectional shapes are not symmetrical the behavior of a bone twisted eversively will be different from one twisted inversively. The complexity of the situation is not as significant when the macroscopic behavior is of interest as when one is studying the microscopic response; however, the investigator must be aware that modeling a bone as thick-walled tube of constant cross-section is of value only as a rough approximation. Although "rough," such an approximation may still be useful in reducing experimental data for an empirical representation of bone response under a torsional load.

The mechanism of a torsional fracture is again best described as involving a crack initiation followed by instantaneous crack propagation. Different from the bending only situation, the fracture does not necessarily travel from a starting location to a final arrested location or end in complete separation of the diaphysis. It is possible that the fracture could initiate in two regions simultaneously and propagate toward one another meeting at a common point. Regardless, the primary cause of initiation as well as the driving force of crack appears to be the principal stress associated with state of pure shear. This principal stress occurs at an angle of 45 deg. to the torsional axis and results in the classical spiral fracture associated with the twisting of tubular shapes that are weak in tension. The primary fracture mode appears to be the opening mode transferring back and forth between the

other two modes during the progression of the crack. The crack should spiral no more than once around the diaphysis before the remaining tissue ceases to sustain the load and fails in plate bending along a path joining the start and termination of the spiral.

Since the maximum principal stress is 45 deg. to the torsional axis, the fracture plane is generally oblique to osteon axes and the ultimate stress lies between that associated with tension stresses parallel to the osteon axes and that lateral to the axes. Reilly and Burstein [1] have reported this ultimate as 68 MPa [1].

#### 2.2.2.3 Combined Loading Conditions

When the two loads discussed above are combined, the mechanics of the response may be superposed if the deformations are small and the behavior linear. For whole bone neither of these limitations are satisfied. One can speculate, though, that when the combined loading state is dominated by torsion, the failure mode should be primarily a spiral fracture. Likewise if the loading is bending dominant, the fracture should be very similar to a fracture observed for the bending only loading situation.

#### 2.2.2.4 General Remarks

Because each of the long bones, with the exception of the fibula, have curved diaphyses and irregular cross-sections, some twisting should result when the loading condition is bending only. The first effect results from the constraints necessarily imposed on the ends of the bones to prevent rigid body rotation. If there is any lateral curvature of the bone, the offset of the applied bending load relative to the diaphyseal axis becomes a moment arm and the applied force generates a moment acting along the diaphyseal axis with a vector direction parallel to a plane containing the applied loads. Even if the bone diaphysis is relatively straight, twisting may be generated due an irregular cross-section (Figure 2.5). For instance if the bending load is applied at the tibial crest, the bone will tend to rotate about the axis of twist (the shear center which is a function of the thickness of the cortical walls) unless the axis of twist lies in the plane of the applied load.

Conversely, if a bone with a curved diaphysis is twisted, the twisting moment will cause bending of bone if its vector is not applied

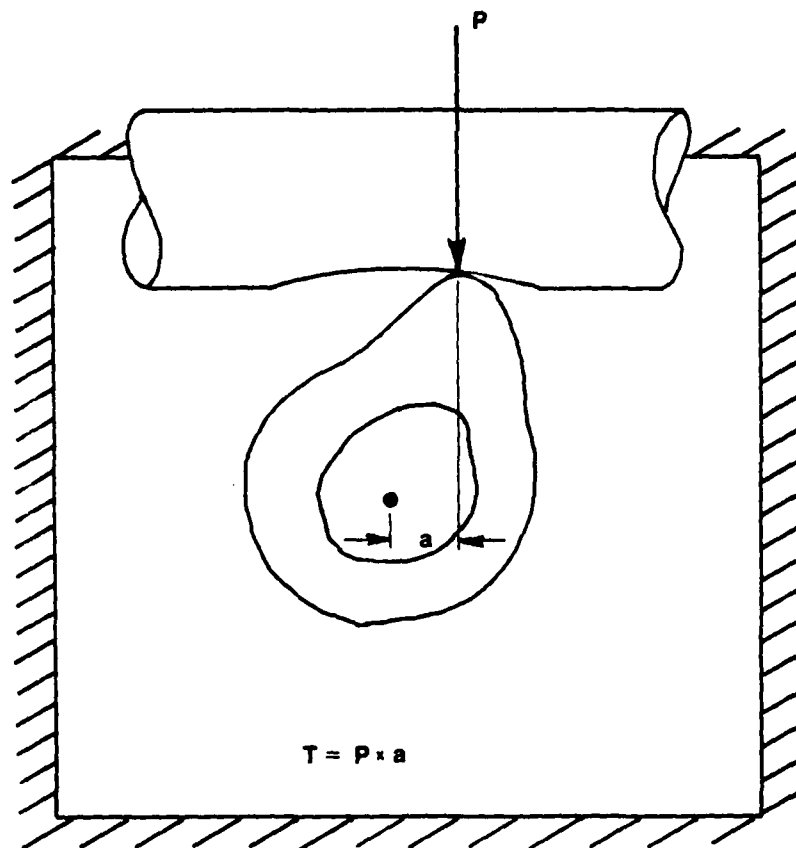


Figure 2.5 Twisting moments resulting from cross-sectional shapes.

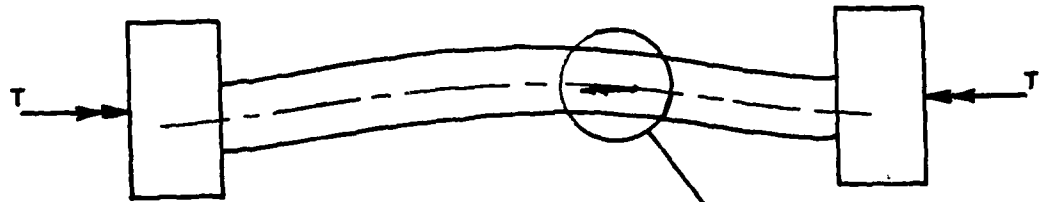
tangent to the axis of twist. The bending results partially from a component of the twisting moment which is normal to the curved axis of twist and partially from the increased separation or "opening up" of the two ends (Figure 2.6). An irregular cross-section can also cause bending through warpage of the section, especially if there is excessive variation in shape along the diaphyseal axis.

#### 2.2.2.5 Anisotropy of Bone

So far the discussion has eluded mentioning one important fact about bone tissue. Bone tissue does not behave isotropically. Many investigators have simplified its anisotropic behavior by assuming the tissue to be transversely isotropic when the more appropriate representation is cylindrical orthotropy as the simplest model. However this simplification is not reasonable when one realistically considers the morphology of Haversian (secondary osteon) bone. The errors in too ideal of a model multiply as the size of the specimen decreases. The small "bricks" tested in the past to determine the bone technical constants are not by any stretch of the imagination homogeneous, and the results when used in formulations of whole behavior will induce errors. The errors result for several reasons. The whole bone has constraining material which regulates the behavior of the tissue it envelopes. The small, free brick specimen then becomes much more stiff when engulfed in surrounding tissue. Furthermore, the material directions vary continuously throughout the cortical wall of the diaphysis. Since the principal stresses in an anisotropic material are not a direct function of strains through Hooke's Law but depend on the material direction, strains alone are not good indications of the stress state. In fact without the material directions, the stress states are indeterminate. Therefore, any attempt to describe analytically the stress state or the fracture load without knowing the material directions becomes a futile effort. Even the calculation of displacements depends on the material direction of the elements involved, and become irrelevant for any anisotropic case if the material directions are not known.

#### 2.2.2.6 Microstructure

Many investigators have tried to model bone tissue as if it were a filamentary composite. Others (authors included) have implied they



$T$  - Applied twisting moment

$T_d$  - Dia-physal twisting component

$M_b$  - Bending component

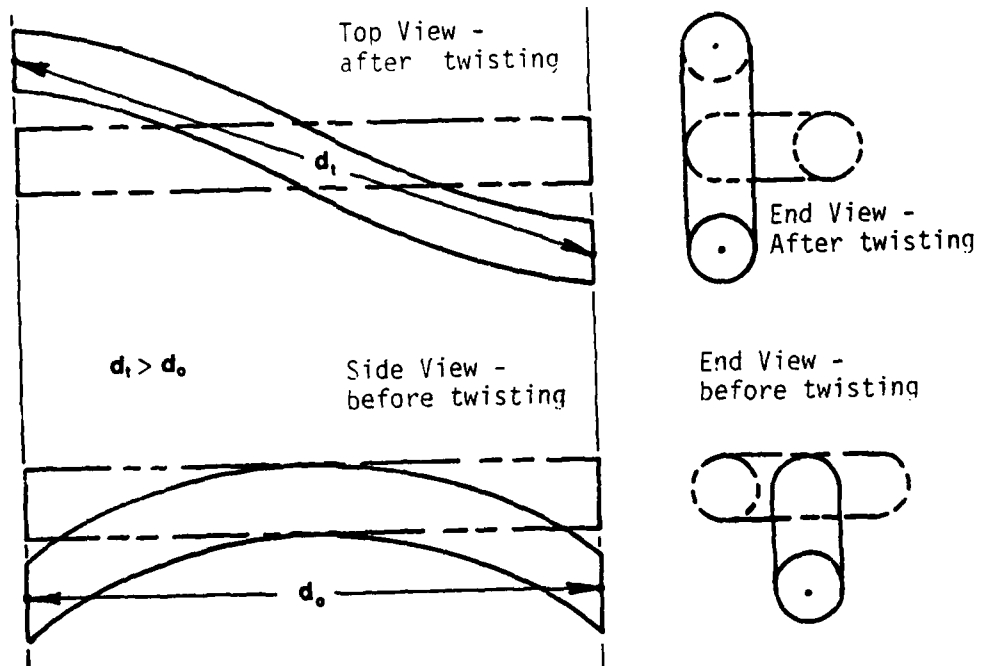


Figure 2.6 Induced bending due to the curvature.

wanted to derive relationships between the technical constants that describe the constituents of the anisotropic matrices similar to the "rule of mixtures" for fiber reinforced plastics. Realistically any representation of bone tissue on a microscopic level is presently absurd when one considers the basic structure of bone. Figure 2.187 depicts mineralized collagen bundles on the endosteum of a Haversian canal. As these bundles are further mineralized and become lamellae in the osteon, they are organized more directionally; still they remain bundles of short fibers which function as would bundles of steel cables, providing strength to the overall system only when packed together in a layered fashion. There is no evidence of a rigid means of shear transfer between bundles or between lamella except through the "cement" substance; each bundle appears to eventually act alone, in tension, (Figure 2.187(f)) when fracture is eminent. How then does the theoretician model bundles of "cables" that are good in tension in order to characterize their macroscopic resistance to shear and compression?

### 2.2.3 Equipment

#### 2.2.3.1 Introduction

The main experimental goal of this investigation is to establish the fracture patterns which are associated with bending failures, torsional failures and failures of combined bending and torsion and, thus, evolve correlations between fracture patterns and the magnitudes of contributing loads. While fulfilling this primary goal, secondary goals were added as a matter of scientific curiosity or to further substantiate and clarify the outcomes of the primary goal. These secondary goals were to establish a stress state at particular locations along the surface of a bone; to determine the large scale material behavior of bone tissue; to determine the micro-mechanical fracture topography and, thus, failure mode (shear, tension, compression); and, finally, to correlate mineral and resorption (porosity) fractions with the failures. This section describes the equipment manufactured or acquired to achieve these experimental goals.

#### 2.2.3.2 Osteoclast (Fig. 2.7)

The osteoclast, a name adopted from Gratten's [2] device for fracturing malformed limbs, is a machine for applying pure bending, pure

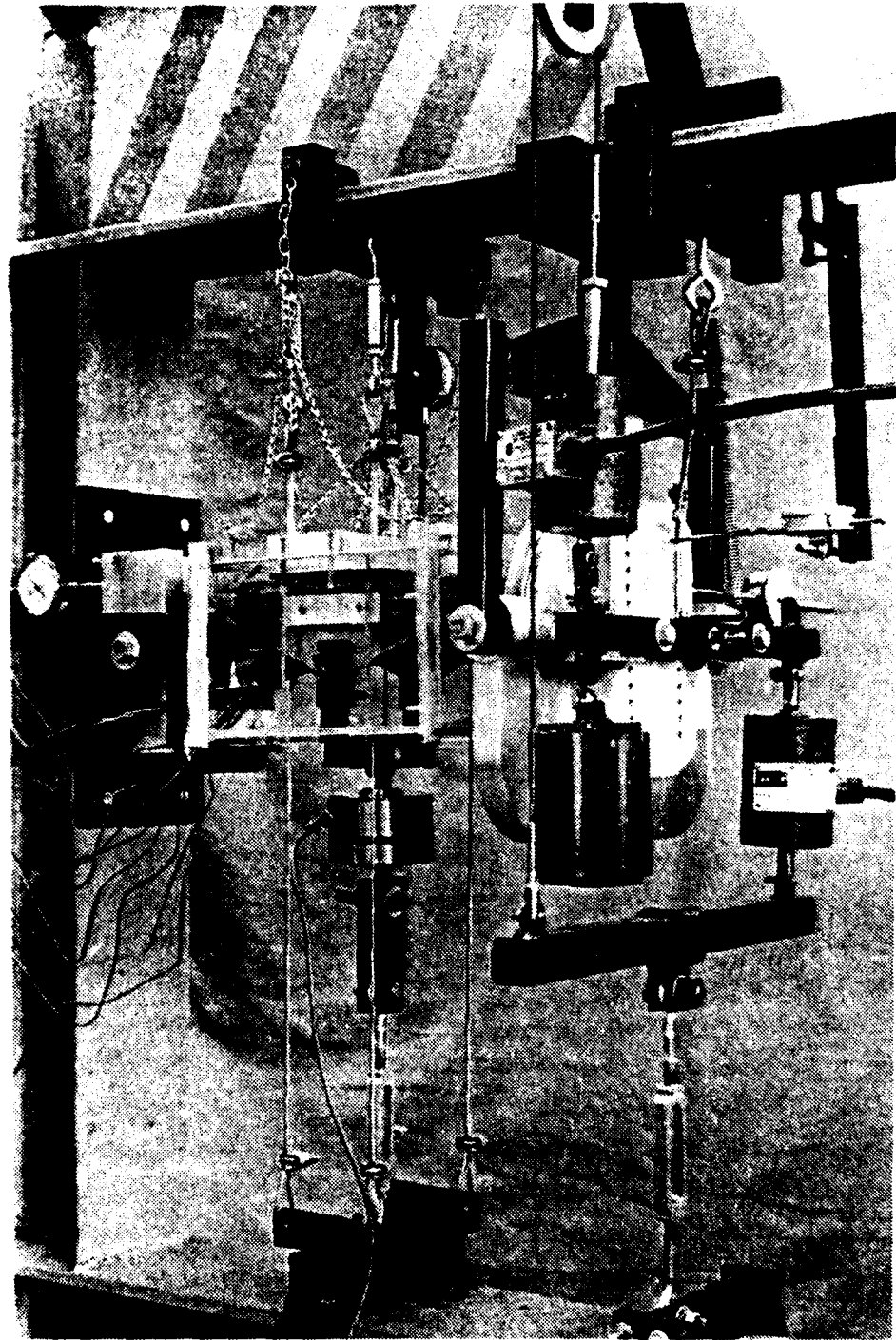


Figure 2.7 Osteoclast

torsion or specific combinations of bending and torsion to the four, human long-bones. It consists of the following main assemblies:

1. Self-equilibrating test window.
2. Fixed end clamp and reaction point.
3. Suspended end clamp, disk, and reaction point.
4. Bending load application mechanism.
5. Torsion load application mechanism.
6. Humidity chamber.

A detailed description of the operation and performance of these assemblies follows. Numbers in parentheses refer to the numbered parts in Figures 2.8 - 2.10.

#### SELF-EQUILIBRATING TEST WINDOW (Figures 2.7, 2.8)

To avoid modifying the building structure of the laboratory and also to provide a testing machine that could be relocated, the osteoclast was designed as a self-contained system. The reaction points for the supports and load applications and mounts for the auxiliary equipment (dial gages, environmental chamber) are all located along or within a 0.914 m high by 1.22 m wide steel "I" beam frame (1). The top and bottom "I" beams (2) have flanges 15.2 cm wide and webs 30.5 cm wide. "I" beams (3) with flanges and webs 15.2 cm wide form the sides of the frame and are welded to the flanges of the top and bottom beams.

The fixed end clamp (4) and reaction point (5) are bolted to one of the side "I" beams, while the suspended-end clamp, disk and reaction point is reacted at a clamp (7) along the bottom flange of the top "I" beam. The bending load application mechanism is reacted at a clamp (6) along the top flange of the bottom "I" beam, while the torsion load application mechanism is reacted at a clamp (8) along the top flange of the bottom "I" beam and by a truss-pulley assembly (9) which clasps the top flange and rests against the web of the top "I" beam. In addition to the clamps, one of two trolleys (10) provides for the suspension of the humidity chamber (11), the attachment of the bending deflection dial indicator (12) and a reaction point for the four stabilizing cables (13). The other trolley (14) provides for the suspension (15) of the "dead" weight of the torsional load mechanism during tests of torsion only. This trolley also allows the attachment of a compensating spring

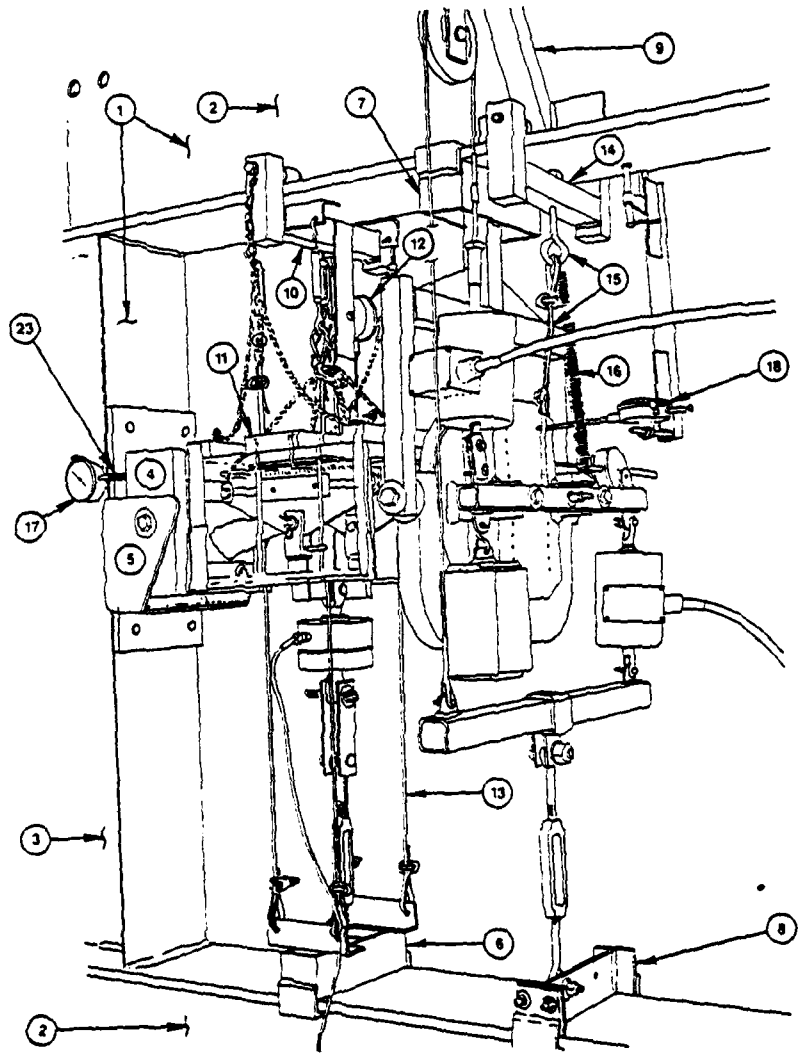


Figure 2.8 Parts of the assembled osteoclast.

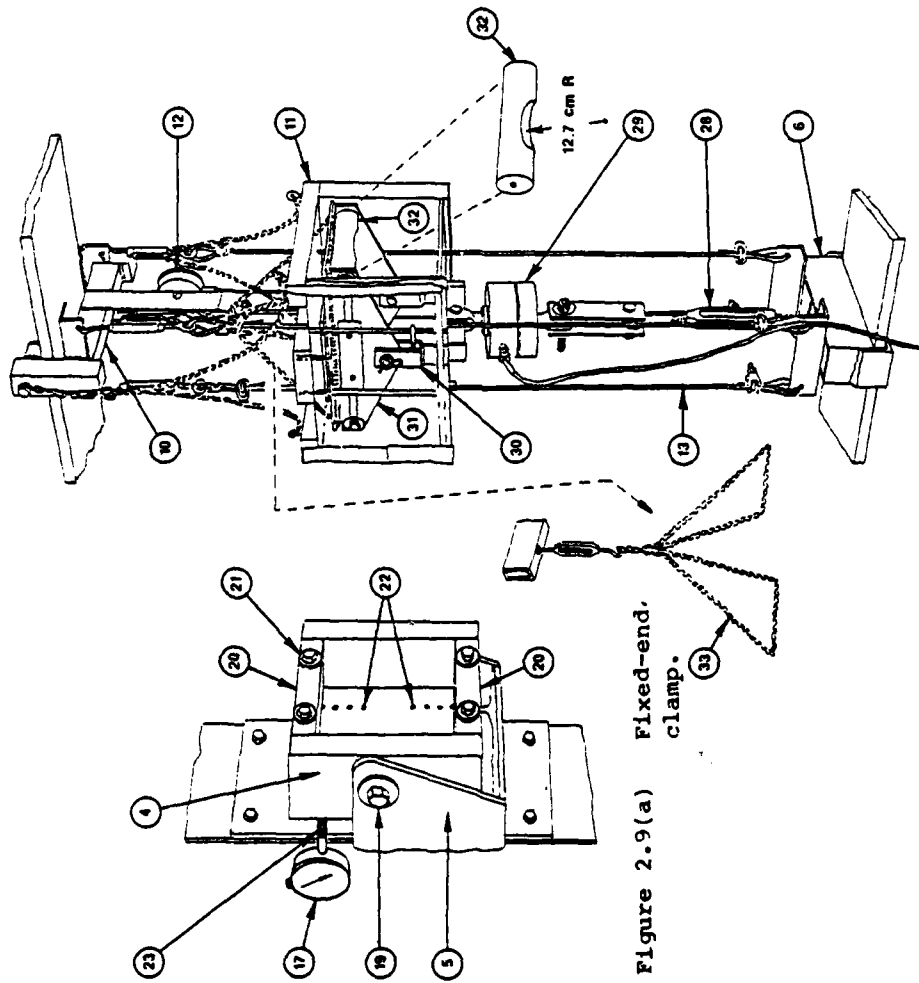


Figure 2.9(b) Bending load application mechanism.

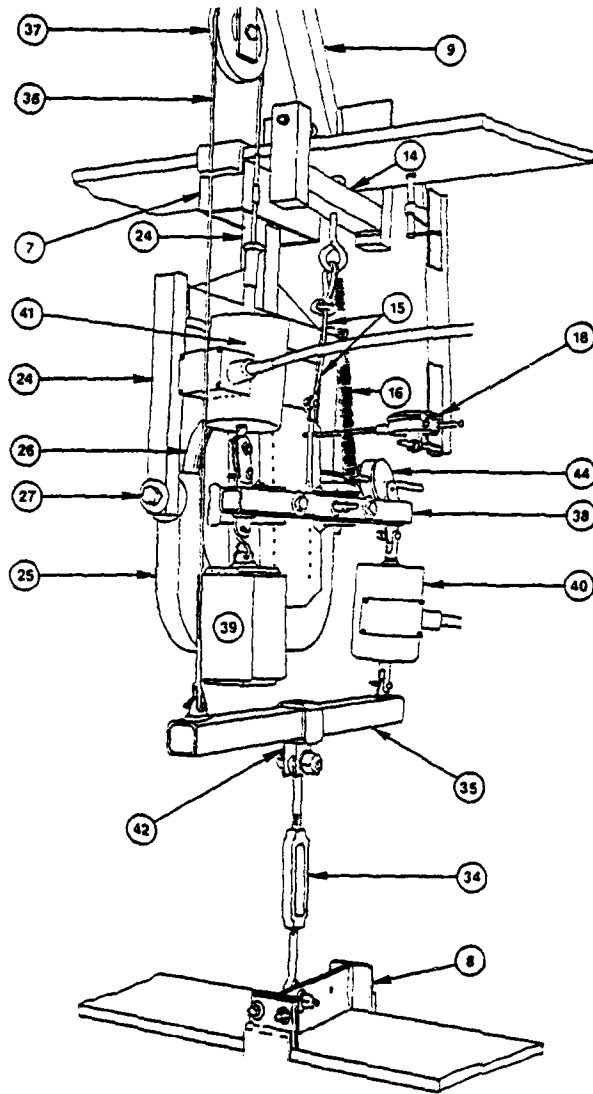


Figure 2.10 Torsional load applications mechanism.

(16) which assists the rotation of the bone at the suspended support during tests of bending only and combination loadings by lifting the "dead" weight of torsional load mechanism. Finally, the frame provides for the mounting of a dial indicator (17) which senses the fixed end rotations of the bone as well as the attachment of another dial indicator (18) which senses the suspended end rotations. When free of loads, all the clamps, the trolleys and the truss-pulley assembly can slide along the flanges to which they attach, and thus, the osteoclast can accommodate bones of various anatomical lengths.

The self-equilibrating frame is fitted with four casters that aid in transporting the osteoclast as well as four screw jacks that permit leveling and immobilization of the machine. The frame was constructed from available materials allowing an over design in stiffness and, thus, avoiding significant deflections of the frame while reacting test loads.

#### FIXED END CLAMP (Figures 2.7, 2.9(a))

The fixed end clamp (4) and reaction point (5) act as a simple support for one end of a bone during bending, and yet prevent the torsional rotation of the same end when the bone is also subjected to a twisting moment along its longitudinal axis. The clamp is bolted (19) to the reaction point (5) on both sides of the clamp and the two bolts ride inside two oil-impregnated, bronze sleeve bearings. The clamp was made from aluminum by welding the two sides to the back and machining to tolerance. The top and bottom (20) of the clamp can be adjusted in 12.7 mm increments from a 12.7 cm maximum separation to a 2.54 cm minimum separation. The desired separation is selected by bolting (21) the top and bottom pieces to the back using a series of paired, tapped holes (22) that run from top to the bottom. The top and bottom pieces are machined from aluminum to a tolerance and have a "√" shaped groove along the back edges on their inside faces. These grooves prevent the ends of bones (when cast in epoxy putty) from sliding out of the clamp under load. The width, height, and depth of the clamp are fixed at 12.7 cm, 12.7 cm and 5.08 cm, respectively.

The clamp gimbals freely in its bearings while reacting all loading situations, and thus, behaves as a simple support. However, because the center of gravity of the clamp does not pass vertically through the

gimbal points (bolt centers) an end moment occurs that tends to oppose the bending moment as well as induce an unwanted load during torsion. To offset this moment, a compression spring (23) was inserted between the slope dial gage (17) and the clamp back. This moment was determined to be significant only when testing the fibula.

#### SUSPENDED END CLAMP, DISK AND REACTION POINT (Figures 2.7, 2.10):

The suspended end clamp, disk and reaction point act as a simple support for the end of the bone opposing the fixed end support, yet permit its rotation about the bone's longitudinal axis. Suspension of the clamp from the top "I" beam, allows horizontal movement of the assembly (gimbaled at the clamp (7)) in the direction of the bone axis eliminating tensile forces that otherwise could be induced during bending. There also is some horizontal movement possible transverse to the bone axis as well as some rotation about the yoke (24) axis. These additional freedoms ease the loading of the bone and also lessen the possibility of other unwanted loads.

The assembly consists of the clamp (7), the steel yoke (24), the aluminum yoke (25), and the disk/clamp (26). The clamp is made of welded steel and clasps the upper "I" beam but allows the entire assembly to slide along the beam flange so that the osteoclast can accommodate bones of various lengths. The aluminum yoke was machined from a solid piece of aluminum stock to receive and hold the disk and clamp. This yoke is fastened to the steel yoke by two bolts (27) (one on each side) resting in oil-impregnated, bronze sleeve bearings which allow the yoke to gimbal freely. The disk/clamp was fabricated from several pieces of aluminum stock that were machined and then welded together to form a single unit. The periphery of the disk and the receiving surface, or race, in the aluminum yoke were machined on a lathe to a "sliding fit" tolerance. Flanges on the front and back of the race prevent the disk from sliding out of the yoke. When assembled the disk slides in the race on a film of lithium grease.

The clamp portion of the disk (not shown in the figures) has selectable inside dimensions of the same magnitude as those in the fixed-end clamp. These dimensions are selected in the same manner as for the fixed-end clamp. (See Figure 2.9(a)).

BENDING LOAD APPLICATION MECHANISM (Figures 2.7, 2.9(b), 2.11, 2.12, 2.13):

The bending load application mechanism is a constant amplitude device which applies a bending load by requiring increases in bending deflections at the load points along the bone diaphysis. A turnbuckle (28) in the mechanism train generates the deflections and the load ensues as a result of the elastic behavior of the bending bone. The tensile force developed in the system follows a path from the reaction point (clamp (6)) through the turnbuckle, load cell (29), clevis/yoke (30), through the sides of the bending carriage (31) to the rollers (32) which then transfer the load to the bone surface. This tensile force along with the stabilizing cables (13) (when taut), assure the stability of the entire mechanism throughout the operating range of osteoclast.

The variation in the lengths of the bones tested required the construction of two bending carriages. One carriage body has an overall length of 22.86 cm and was used for testing the femurs, tibias and fibulas. The other carriage has an overall length of 14.29 cm and was used for testing humeri. Both carriages were made by welding three precut, premachined pieces of aluminum plate, 6.35 mm in thickness, to form a channel. The carriages are 10.48 cm wide and serve as housings for two aluminum rollers (32). To fasten the rollers to the carriage, large bolts pass through slots in sides of the larger carriage and holes in the sides of the smaller carriage and through holes drilled along the axis of the rollers. The slots in the larger carriage allow a variety of roller spacings between a maximum separation of 20.17 cm and a minimum separation of 12.27 cm. The holes in the smaller carriage fix the spacing at 6.35 cm. TEFLON washers inserted between the carriage sides and the ends of the rollers, prevent the two from binding. To keep each carriage centered above the bone, circular cuts (Figure 2.9(b)) were made on each roller, normal to, but below the mid-point of the roller axis.

Four cables (13), each 3.12 mm in diameter, are used to guide the bending carriage as the bending load is applied. Two cables extend past the carriage on each side from the clamp (6) to the roller (10). Each cable is fastened with a cable thimble and clip to cross-members on the clamp (6) at one end, and to the eye of a turnbuckle at the other. The

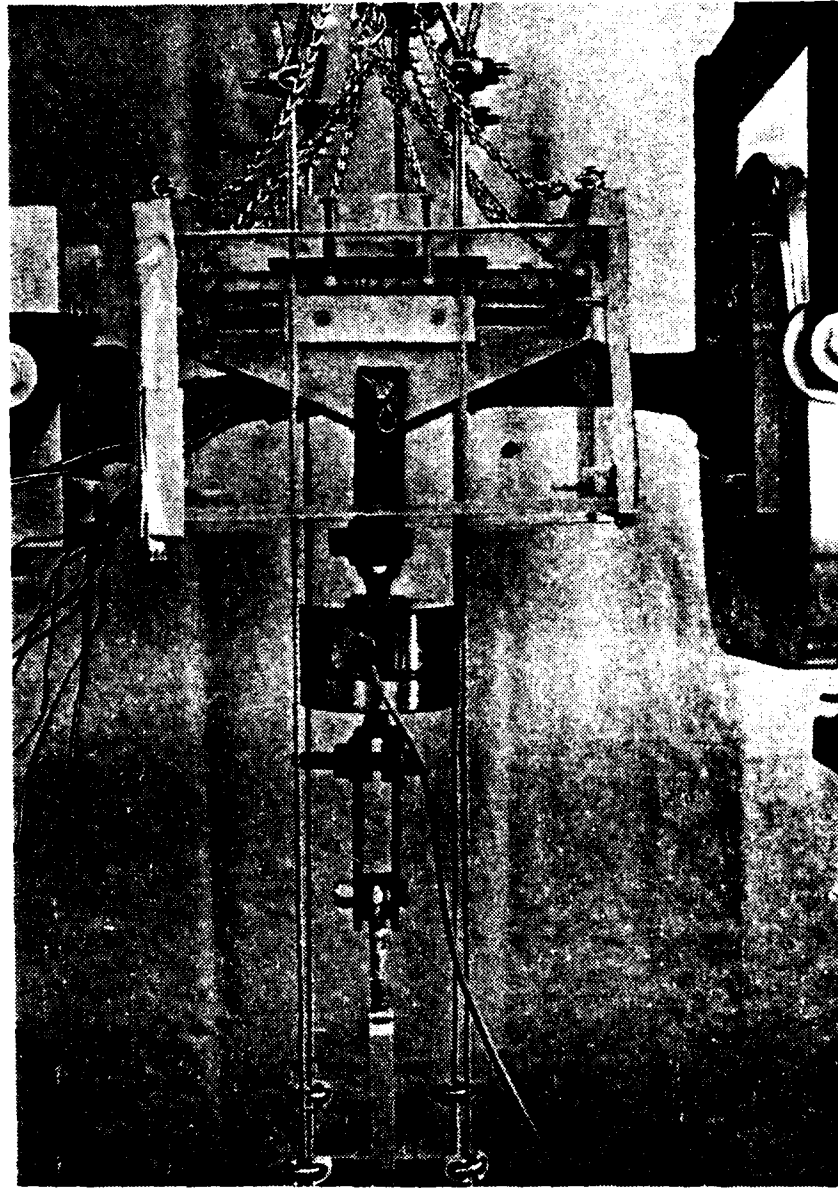


Figure 2.11 Large bending carriage and bending load application mechanism.

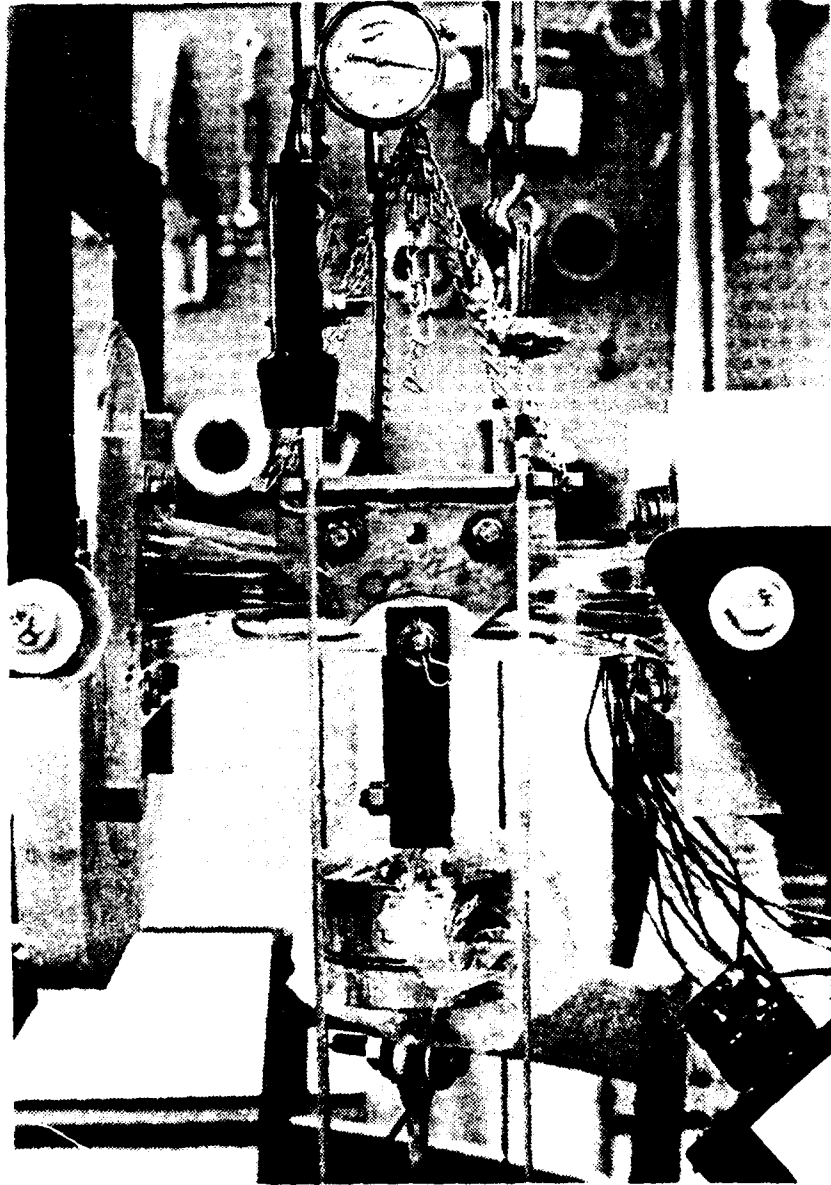


Figure 2.12 Small bending carriage and bending load application mechanism.

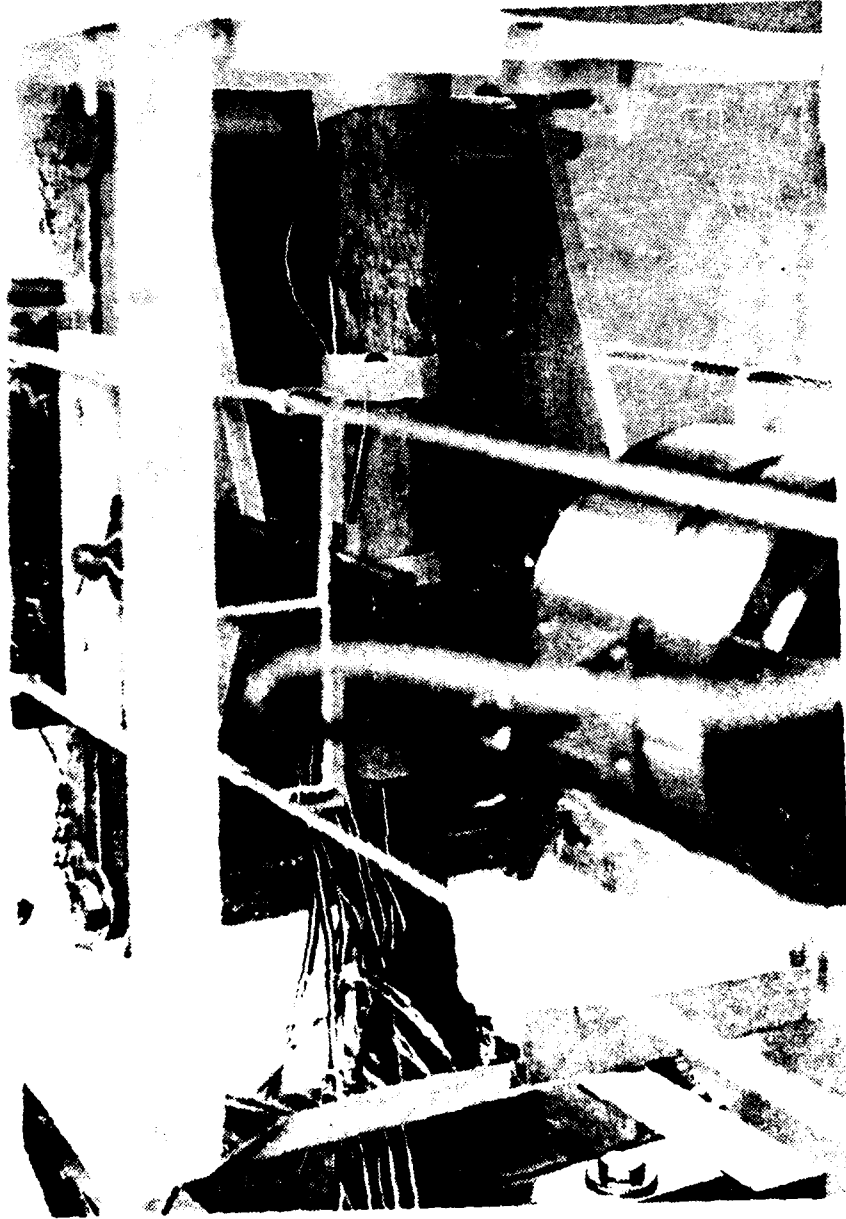


Figure 2.1) Bottom view of the large bending carriage showing "centering" design of the loading rollers.

turnbuckles have hooks at their free end which anchor into cross-members on the roller. The turnbuckles allow the cables to be removed or stretched until taut. Normally, they are stretched until a tensile load of approximately 1335N to 2225N develops which usually is enough to prevent the cables from deflecting more than 7.62 mm in any direction. Slots, machined into opposite edges of a thin steel plate which is bolted to the top of the large carriage, receive the cables and guide the carriage, thus limiting its horizontal motion. The smaller carriage has these slots machined as an integral part of its top. Such restraint prevents the carriage from sliding sideways off the bone or to and fro along its axis. TEFLON tubing covering each cable along the span of travel of the carriage reduces friction and prevents the cables and carriage from binding.

The clevis/yoke connects the bending carriage to the load cell and was made by welding pieces of strap iron together forming a yoke with clevises at its ends. The clevises receive the sides of the bending carriage, and bolts with hairpin cotter pins fasten the two together. Bolts and pieces of strap iron then tie the clevis/yoke, load cell, turnbuckle and clamp together.

A light chain (33) connected to the trolley (10) acts to suspend the bending carriage above and out of the way of the specimen while the specimen is clamped into the osteoclast. The light chain was formed into two equal loops (Figure 2.9(b)) and connected to a heavier chain by passing an "S" hoop through the links at each of the ends of two lengths of light chain and one link of an end of the heavier chain. Each loop of the light chain slips around an overhang at each end of the bending carriage and the heavier chain is hung from a turnbuckle fastened to the trolley. The level of the bending carriage is adjusted by hooking different links of the heavier chain on the hook of the turnbuckle and turning the turnbuckle. Once the rollers of the bending carriage have contacted the bone surface, the heavier chain is hooked on the turnbuckle by the link on its free end. This provides enough slack in the light chain to permit the carriage to travel when the bending bone deflects and, yet, prevents the entire train from collapsing when the specimen breaks. Thus, the bending carriage is kept out of the way

during the clamping of a specimen into the osteoclast, and the bending load mechanism lowered onto the bone for testing.

TORSION LOAD APPLICATION MECHANISM (Figure 2.7, 2.10):

The torsion load application mechanism is also a constant amplitude loading device. As with the bending load mechanism, a turnbuckle is used to generate increasing angles of twist at the end of the bone in the suspended clamp. A torque then results as the bone, governed by its elastic behavior, attempts to resist these increasing twist angles. The mechanism consists of a reaction point (the clamp (8)), a turnbuckle (34), a centering bar (35), a cable, pulley and reacting truss (36, 37, 9), a torque bar and counterweight (38, 39), load cells (40, 41) and the disk/clamp (26) described earlier. To apply a twisting moment, the turnbuckle is turned to pull the centering bar downward. As the centering bar travels downward it pulls down on a load cell (40) and a cable (36). In response, the cable, because it runs up and over the pulley (37), pulls up on the load cell (41). Hence, the torque bar (38) is pulled upward at one end and downward at the other and, since it is fastened to the disk/clamp (26), the end of the bone in the suspended clamp is twisted clockwise for the arrangement shown. All reaction points and connections are designed so that the entire torsion load mechanism can be rotated 180° about a vertical axis and thus change the direction of the torque from clockwise to counterclockwise.

The torsion bar is made from a 3.18 cm square welded-seam steel tube. The turnbuckle attaches to the centering bar via a shackle (42) which can slide along the length of the centering bar. The shackle is made from pieces of strap iron welded together and has two set screws, one on each of its sides. Equal loads on the torque bar (as measured by the load cells (40, 41)) are set by moving the shackle back and forth along the centering bar. Once equal loads exist in the load cells, the shackle is held in place by tightening the set screws on each of its sides. Tabs welded to the upper surface of the centering bar, provide for the attachment of the "falling" load cell (40) and the cable (36).

The pulley (37) and the cable (36) were salvaged from the flight controls of a "scrapped" Beechcraft airplane. The cable has a clevis fitting at one end and a threaded fitting on the other. The clevis end

receives the tab on the centering bar. The threaded end screws into the 1.27 cm diameter bolt, which was bored and tapped to accept the fitting. The bolt then screws into the top end of the "rising" load cell (41). The pulley is suspended from the truss (9) by bolts and pieces of strap iron. The truss was made from 2.54 cm and 3.18 cm square steel tubing welded together to hang from the upper flange while resting against the juncture of the web and bottom flange of the top beam.

The torque tube (38) is made from 2.54 cm square welded-seam steel tubing and bolts to the disk/clamp. The bolts pass through holes in spacer blocks, which are welded to the back of the disk/clamp, and screw into holes drilled and tapped in the disk. Tabs welded on the top and bottom of both ends of the torque tube attach the "falling" load cell, the "rising" load cell and the counter-weight (39). A small steel plate welded to the middle of the top of the torque bar provides for the attachment of the spring (16) described earlier. A bolt passing through the sides at the mid-point of the torque tube allows the attachment of the cable (15) also described earlier. Both the hole for the spring and the bolt holes for the cable are in line with the center of rotation of the disk.

The counter-weight is made of two pieces of round solid steel bar stock welded together with pieces of steel plate. An "S" hook attaches the tab, welded to the top plate, to the bottom tab of the torque tube. The weight of the counter-weight equalizes the weight of the "falling" load cell and the centering bar.

#### HUMIDITY CHAMBER (Figures 2.7, 2.11, 2.9(b)):

The humidity chamber (11) is a rectangular box constructed of plexiglas and polyethylene (PE) plastic sheeting. The top and walls of the chamber are made from five pieces of 2.54 cm thick plexiglass held together with brass machine screws. Three narrow pieces span the top and clamp down on a sheet of PE which has been cut to allow the stabilizing cables (13) and the carriage suspension chain (33) to pass through. After the test specimen has been clamped into the osteoclast, the bottom of the chamber is closed off by sliding two pieces of 6.35 mm plexiglass into grooves cut along the bottom edges of the chamber walls.

Slots cut into these pieces receive the stabilizing cables and the clevis/yoke. Finally, the ends of the chamber are closed either, by sheets of PE that are clamped to its walls or by pieces of thin polyvinyl-chloride plastic (PVC) taped around the chamber ends. The PVC is used when the bone is too small to allow enough clearance between the clamps and the ends of the chamber for the installation of the PE.

Moist air is fed to the chamber through a 6.35 mm copper nipple inserted in a hole in one of the chamber sides. The moist air is generated by forcing compressed laboratory air through cotton batting immersed in distilled water. The batting and water are contained in a corked 4 liter Erlenmeyer flask with glass tubing inserted in the cork to pass the air in and out. Latex tubing connects the flask with the chamber and the compressed air supply. The system, when tested using a hygograph, achieved 83% humidity in 30 minutes, 86% humidity in 1 hour, and stabilized at a maximum of 93% humidity within 21 hours.

#### AUXILIARY EQUIPMENT (Figures 2.7, 2.8, 2.9(b), 2.10)

##### Clamps and trolleys:

All clamps (6, 7, 8) were made by welding together pieces of 6.35 mm thick steel plate and sections of steel angle. The steel angle on one end of each clamp bolts to the clamp and permits its installation onto the osteoclast frame.

The two trolleys (10, 14) were made by welding together sections of 2.54 cm square welded-seam steel tubing. Steel rollers on bolts through the top of the trolleys allow them to roll along the bottom flange of the top "I" beam.

##### Dial Indicators (Figures 2.7, 2.8, 2.9(b), 2.10):

Four dial indicators are used to measure deflections that represent the displacement due to bending of the upper, mid-diaphysal surface of the bone, the bone fixed-end and the suspended-end bending slopes and the bone angle of twist at the suspended-end caused by torsion.

The two indicators that measure bending slope, sense it as horizontal displacements of the backs of the clamps while they rotate about their support points. The fixed end slope indicator (17) is mounted to the inside flange of the side "I" beam and measures the

horizontal deflections of the clamp back a distance of 5.71 cm above the support point. The suspended end slope indicator (18) is mounted on a small steel beam welded to a steel "c"-clamp. This arrangement permits the movement of the indicator along the test window so that the indicator may measure the deflections relative to the test window and yet may be shifted to accommodate the various lengths of bones. The gage is clamped to the bottom flange of the top "I" beam and measures the slope deflections 9.09 cm above the support point.

The bending deflection indicator (12) is bolted to a plate welded to the trolley (10). The bolt can be moved vertically along a slot cut into the plate to obtain the maximum travel of the probe for the various bone sizes. The probe of the indicator has been extended 18.80 cm using an "L" shape rod, 6.35 mm in diameter. The "L" shape allows the probe to contact the bone surface even though the indicator is mounted to the side of the bone out of the way of the bending carriage suspension chain.

The remaining indicator (44) measures the deflections created by the disk/clamp as a bone twists under torsion. It mounts directly to the aluminum yoke (25) with an aluminum bracket and measures the deflections of the side of the clamp as the disk rotates in the racing of the yoke. The measurements are taken 4.24 cm up from the center of rotation of the disk.

#### 2.2.3.3 Load Indication (Figures 2.7, 2.8, 2.9(b), 2.10):

Both the amount of bending load and/or the amount of torque applied to the bone were indicated using strain sensing load cells connected to a manual switch and balance unit and digital display. The torque applied was inferred by the tensile forces indicated by the load cells in the torsional load application mechanism. The concentrated bending loads applied with the rollers in the bending carriage were assumed to be one half the tensile force indicated by the load cell in the bending load mechanism.

Each of the three load cells were the resistance strain gage type and comprised a full Wheatstone bridge. The bending load cell (29) was a LEBOW general purpose cell with a nominal load limit of 4489 N and a static allowable overload of 6734 N. The two load cells (40, 41) in the

torsional load mechanism were BLH general purpose cells, type U-1, with a limit load of 2245 N and a static allowable overload of 2806 N.

The switch and balance unit and digital display were a BLH Model 826 A and a BLH 8000 SW, respectively (Figure 2.14). The display unit generated the excitation current and voltage as well as displayed the signal returned in units of pounds force. The switch and balance unit provided the means of selecting the desired load cell as well as a means of refining the system calibration and balancing the bridges to indicate the desired initial loads.

Originally, the system indicated bridge unbalance in odd units which were different for each of the load cells. By including potentiometers in the circuitry of each bridge, the display was calibrated to read bridge unbalance in pounds force (Figure 2.15). This greatly eased as well as quickened the setting on the recording of loading conditions. The "pots" were set during a calibration run of each cell on a Tinius-Olson universal testing machine. On the top and side of the external surface of the mold, straight lines were incised as guides to orient the bone in the mold. These incisions divide the top and lateral surfaces of the mold into two equal halves.

#### 2.2.3.4 Strain Measurement

To determine states of stress, strain gages were bonded at selected locations on all but five of 48 bones tested. All of the gages used were 120  $\Omega$  foil gages with lead-in-wires attached and a thermal coefficient of 13 parts per million per degree Fahrenheit. They were manufactured by Micromasurements and varied in type from delta and rectangular rosettes, to stacked rosettes, to axial gages. The size of the bone and the type of strain suspected determined the type of gage that was used; axial gages were used to measure bending strains only.

A total of 173 gages were layed down and of these five became unreliable during the tests. A total of 17 came up or were damaged during application. Of the 173 reliable gages, 102 were axial gages, five were delta rosettes, 50 were rectangular rosettes and 16 were stacked rosettes. Table 2.17 lists the specific types of gages used along with the number applied. Figures 2.20-23 show the physical location of each gage on all the bones that were gaged.

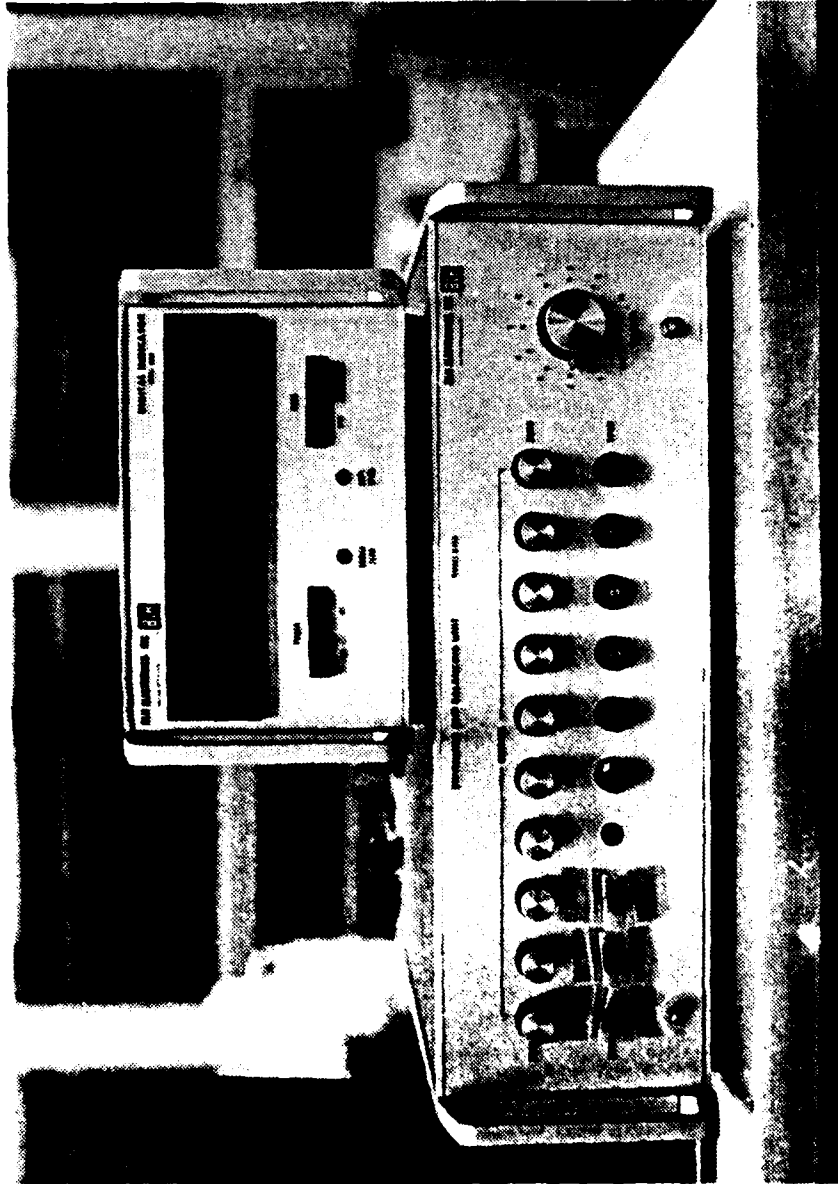


Figure 2.14 BI.H 826A switch and balance and BI.H 800 SW.

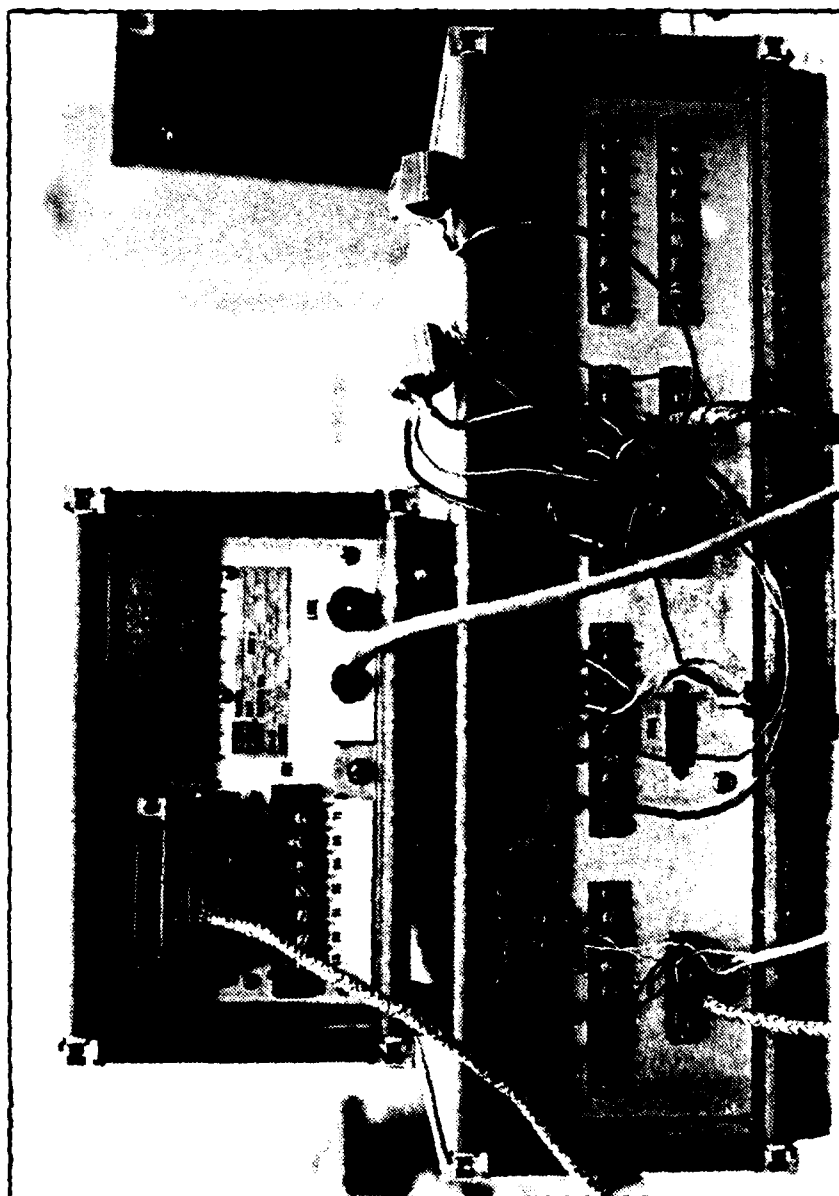


Figure 2.15 Rewiring of LBH system to allow calibration in terms of force.

Table 2.17 Micromasurement strain gages used in the long-bone fracture tests.

<u>Gage Designation</u>	<u>Type</u>	<u>Number Used</u>	<u>Number Damaged during Appl.</u>	<u>Number Unreliable during tests</u>
EA-13-125BT-120	Axial	24	1	3
EA-13-125BT-120-LE	Axial	28	0	0
EA-13-125AD-120	Axial	19	6	0
EA-13-125AD-120-LE	Axial	40	0	0
EA-13-125YA-120	Delta	9	5	0
EA-13-062RB-120	Rect	15	0	0
EA-13-125RA-120	Rect	37	2	1
EA-13-060WR-120	Stacked	16	4	1

In all the tests except for one, the gages functioned singularly as quarters of a Wheatstone bridge without compensations. For the one test, an embalmed bone similar anatomically to the fresh bone tested was gaged geometrically similar and used for temperature compensation.

In all the tests, a Vishay V/E 21A switch and balance module in conjunction with Vishay V/E 20A strain indicator (Figure 2.16) was used to complete and balance the bridge circuits and indicate the strain sensed. By selecting an appropriate "calibration number," this system can provide digital displays of strain in units of microstrain or in terms of units of stress. For all tests performed, strain was read as units of microstrain.

The system is a manual system requiring manual selection of the desired bridge and the visual reading of the strain indicated. Each bridge must be balanced prior to each run during a test and, because of gage heating, requires, on the average, two minutes to stabilize when temperature compensation is not used.

The switch and balance unit provides for ten bridges, or channels (without additional modules), and has a calibration and balance potentiometer for each channel. The bridges are accessed through two 35 pin connectors requiring a MS 3106A-28-15P plug for each. Each pin in the plug corresponds to a particular junction in the overall bridge circuitry and is used depending on the bridge arrangement--whether quarter, half or full bridge--and the channel desired.

The pins of each connector were accessed through a junction board (Figure 2.17) which is wired to the connector plug on the back of the switch and balance. Each terminal on the board corresponds to a particular pin in the plug and, the channel and bridge arrangement desired for the gage is selected according to the color code and letter designation on the board.

To conserve on costs and time, three wiring sets were made at the beginning of the tests and reused until its completion. Each set consisted of ten pieces of three conductor, flat cable 9.14 dm long. One end of each cable was separated and a spade terminal crimped on the end of each conductor. One of these conductors was marked with a numbered, plastic wire marker\* to ease identification of the gage leg when connecting the conductors to the junction board. The individual

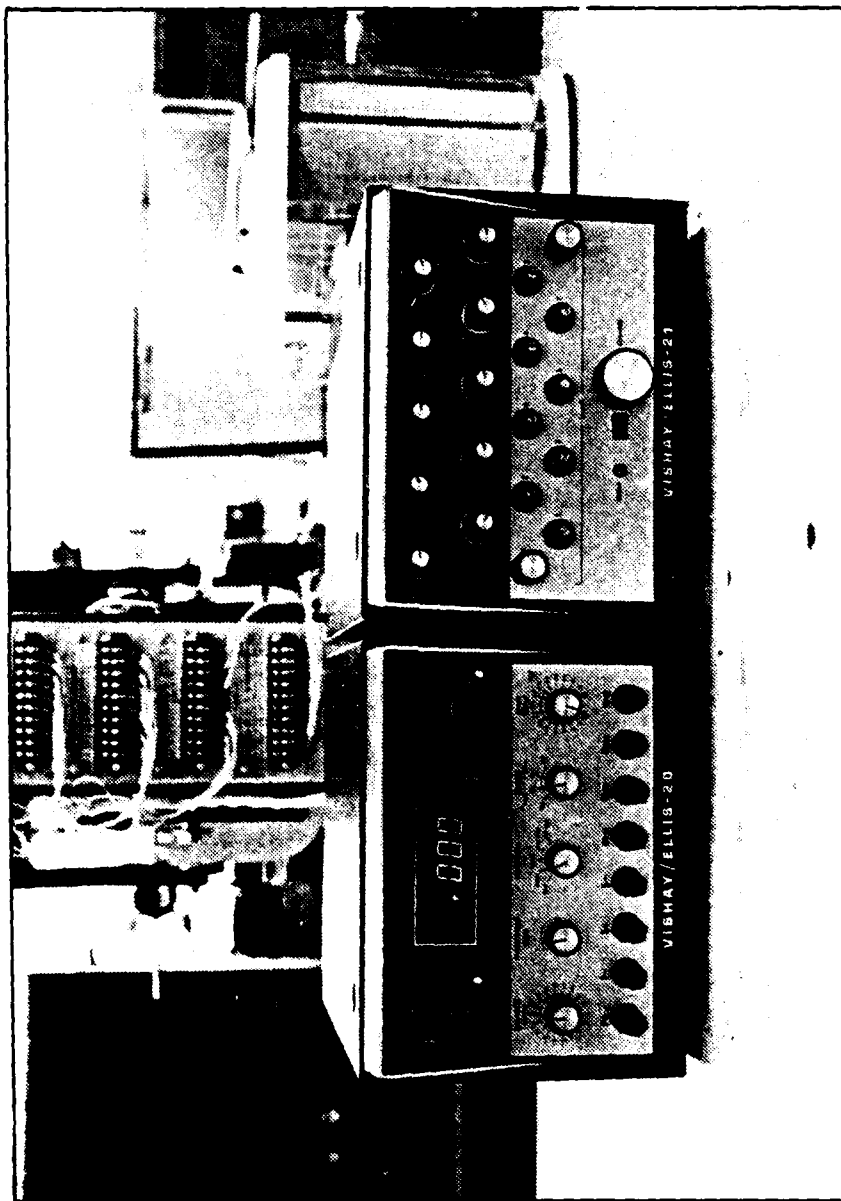


Figure 2.16 Vishay strain measuring system.



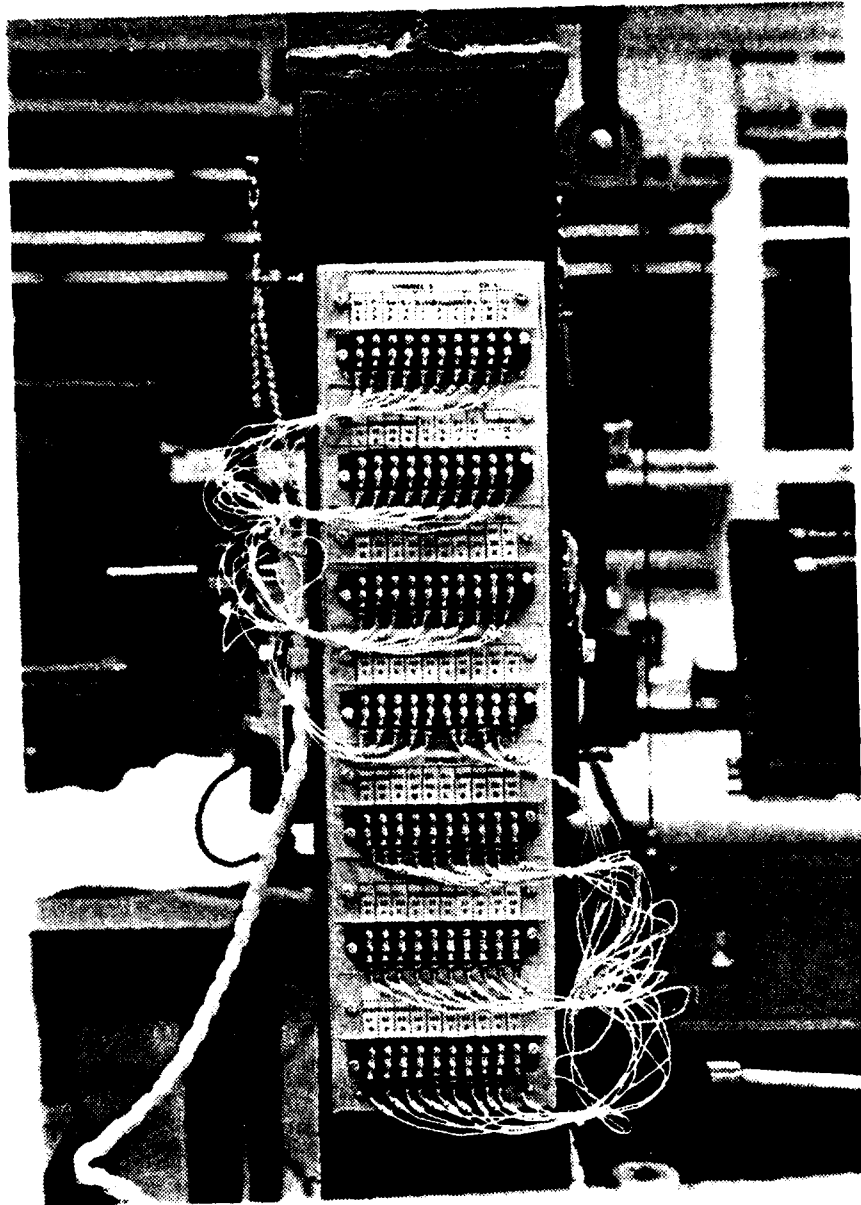


Figure 2.17 Junction board.

conductors on the other end of the cable were stripped and tinned with two conductors made common. The tinned ends were then connected to the strain gages as described in Section 2.3.4.5. Two common conductors were necessary to lessen the resistance differences in the circuitry required for the quarter bridge connections.

#### 2.2.3.5 Video Record

During the first few tests, neither the direction nor the origin of propagating fracture was perceptible--the crack just traveled too quickly to be observed with the naked eye. So, in an attempt to analyze the fracture at a slower rate of propagation, a television camera and video recorder were used to record the failure of the bones in the remaining tests. In thought, if the fracture could be recorded on video tape, then the record could be viewed frame by frame and the direction and origin of the crack determined.

The system used was a Sony AVC-3620 television camera with a Sony 3600 AV video recorder. The lens was a high resolution Cosnucar with a 20.32 CM focal length.

All the tests past the first five were recorded; however, if any of the fractures occurred outside the field of view, the record was erased.

#### 2.2.3.6 The Molding Device

The molding device consists of two, 127 mm square aluminum molds, 50.8 mm deep, facing one another. One end is held stationary and the other can be adjusted by sliding it on a track either toward or away from the stationary end to accommodate the length of the specimen to be molded. The top and bottom plates of each mold have a small groove toward the back of the mold. The resulting prominence in the back of each finished casting then fits into an identical groove in the testing device which prevents the cast from slipping out during testing. These plates are fastened to the mold by bolts. This allows the plates to be adjusted into one of five holes (top and bottom) 12.7 mm apart, depending on the size of the end of the bone to be tested. Bulky femur

\*These markers are commercially sold specifically for identifying electrical wiring. Each conductor had one or two markers. One identified the cable number and the other the set number. One set had only cable markers.

ends and pencil-like fibula ends could thus be molded in the same device. Figure 2.18 shows a right femur in the molding device where the putty is curing.

On the top and side of the external surface of the mold, straight lines were incised as guides to orient the bone in the mold. These incisions divide the top and lateral surfaces of the mold into two equal halves.

#### 2.2.4 Test Procedure

##### 2.2.4.1 Test Flow

The anatomy department at the Kansas University Medical Center (KUMC) furnished all the fresh tissue necessary to complete the static and rapid loads testing part of the proposed research program. In all, 72 fresh unembalmed bones were resected from six cadavers within 24 hours of death and immediately frozen. These bones are the so-called human long-bones--the radius, ulna, humerus, femur, tibia and fibula. Bones from both the right and left sides of each cadaver were resected resulting in 12 bones of each type.

Of the 72 bones, only 46 were tested as whole bones under conditions of static bending, static torsion and combinations of each. The 46 bones included the left and right femora, tibiae, humeri and fibulae. The remaining 24 ulnae and radii were to be sectioned and examined in a small specimen tests for material properties, but time and manpower were insufficient and this part of the program was aborted. Two additional humeri were tested under rapid rate conditions bringing the total number of bones fractured to 48.

The 46 bones in the static loads tests were scheduled so that as many bones as possible could be tested under each type of loading condition. Left and right complements were arranged such that inversive rotations could be compared with eversive rotations. Throughout the testing, as much as possible was done to utilize effectively the small number of bones that were available.

Because the testing plan required each bone to be loaded until fracturing occurred, two sets of records were required before testing could commence on any bone. These were, of course, the osteometrics and roentgenography. Their particular order was immaterial and, with the

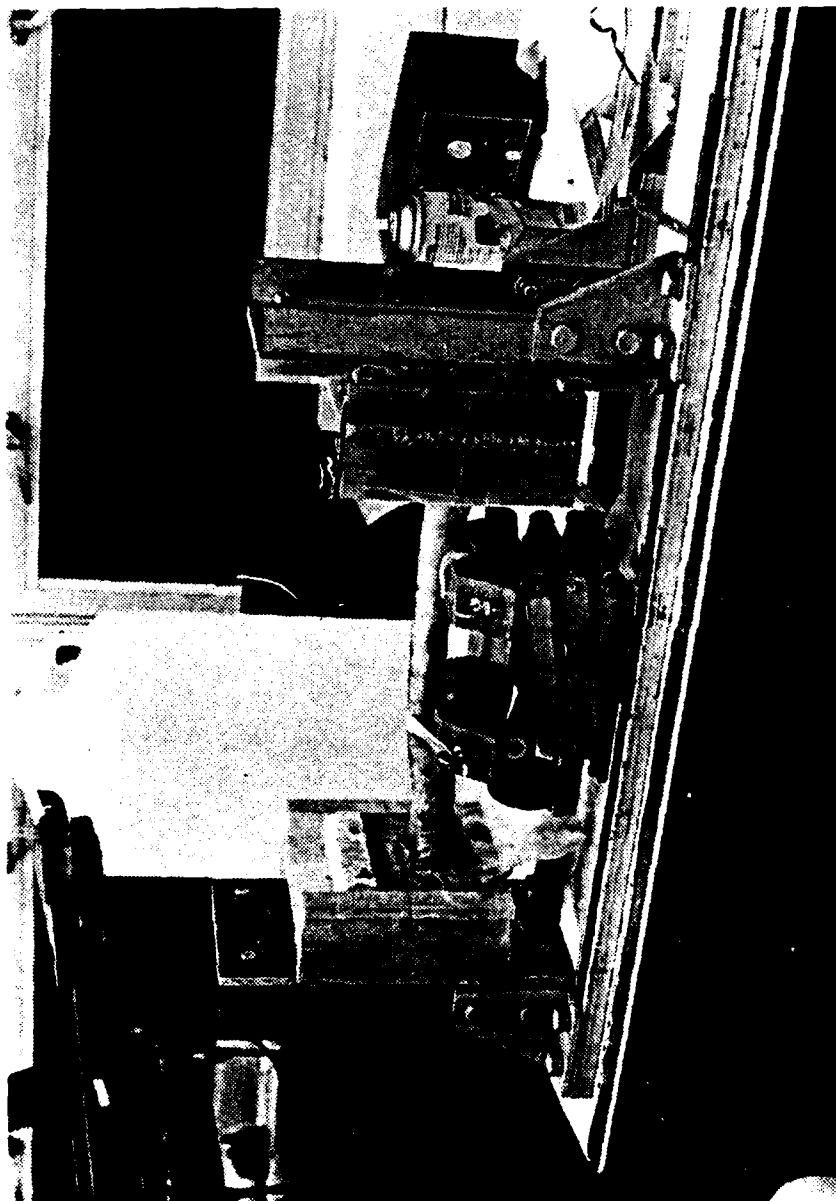


Figure 2.18 Molding device.

first few bones tested, the osteometry was performed before the x-rays were taken. However, because of the tight scheduling required of the KUMC, the remainder of bones were x-rayed on short notice in two, one-day sessions and consequently the osteometrics had to be completed after the x-rays were completed.

After the osteometrics were complete the ends of the bones were cast in epoxy putty for gripping in the osteoclast. Normally, the bones were molded 24 hours prior to the application of the strain gages. Occasionally, bones were molded only six hours prior to gaging, but only during periods when tests were closely scheduled.

Usually, the application of strain gages was begun within 24 hours after molding. There were a few instances, where molding was complete but gaging did not occur for several days for various reasons. If the period of time between molding and gaging was to exceed 24 hours, the bone was refrozen; otherwise it was simply refrigerated.

Every effort was made to complete the strain gaging process within 6-8 hours, including the attachment of the conductors. When more than one day was required, the gages were applied and coated and the bones refrigerated. The conductors were then soldered to the leads the following day.

Testing always followed within 48 hours for all the bones tested except for four. Two of these were the first femora tested and gage corrosion required the reapplication of several gages following aborted tests. The other two bones were humeri planned for the rapid rate tests. These were gaged in expectation of testing but, because of equipment malfunctions, the tests were not completed for several weeks. In all four cases refreezing was impractical--the femora were needed daily for regaging or testing and the humeri were gaged and could not be frozen for fear of gage damage. In none of the cases were the bones left in the refrigerator longer than three weeks.

Testing was considered complete for each bone when it had a set of correct photographs and complete sketches depicting the fracture patterns. In most cases, the remnants of the bones were reassembled, sketched and photographed immediately following the test. Now and then, time was insufficient to complete the sketches and/or photographs; on

these occasions, the bone was either refrigerated or frozen depending on the length of the delay, and the records completed later.

In the course of preparing a bone for testing, it was thawed and refrozen at least twice. After the initial freezing on resection, it partially thawed during roentgenography but the thawing was unintentional. It was refrozen and then totally thawed during the molding of its ends in epoxy putty. The time required for the osteometrics was so short, the bone remained essentially in the frozen state, even though the measurements were taken in the room environment. As mentioned earlier, after molding the bones were rarely refrozen but refrigerated until the strain gages could be applied. On the average, each bone was at room temperature for 13 hours--three hours during molding, seven hours during the gaging process and three hours for testing. The time in a frozen state varied anywhere from eight to ten months.

Whenever exposed to the room environment, each bone was kept as moist as possible by either immersion in Ringer's or by wrapping in gauze soaked in Ringer's solution. However, during the application of the strain gages, keeping the bones in a wet state was impossible if the gages were to be applied in as little time as possible. Although they were not wet during this six hour period every effort was made to prevent the hard tissues from drying. All the periosteum along with other soft tissue was left in place except for an area sufficiently large to successfully apply the gage. If leaving the bone for longer than ten minutes became necessary, it was draped in Ringers' soaked gauze as best as possible and covered with a plastic bag. When the gaging was complete and the silicone rubber coatings fairly thick skinned over the gages, the bones were rehydrated with gauze wrappings wet with Ringers. Because the bones are essentially closed systems, they were considered less susceptible to detrimental drying as are the small, coupon test specimens of bone tissues.

While testing in the osteoclast, as much of the exposed bone as possible was surrounded with an envelop of humid air normally around 80%-90% saturation. Again, although not wet or even damp, the bone was inhibited from drying any further.

As a final step in the fracturing part of the investigation, the bones were sectioned to remove disks for a histological analysis at the

KUMC as well as to locate the strain gages around the periphery of the bone surface. Sections for the scanning electron microscope (SEM) study were also removed at this time.

#### 2.2.4.2 Roentgenography

Each bone was x-rayed in two views prior to testing. Anterior-posterior and medial-lateral roentgenograms were taken. Wedge-shaped sponges were used to orient each bone in the appropriate anatomical position on the x-ray table. Radiographs were taken of the left and right of all humerus, radius, ulna, femur, tibia and fibula specimens. A numbering system was initiated to identify each x-ray. Lead numerals were placed next to each bone being radiographed for identification. The first numeral was to identify the cadaver (individual) as follows:

<u>Cadaver ID</u>	<u>Roentgenograph No.</u>
3753	2
3793	3
3790	4
3782	5
3792	6
3787	7

The second numeral referred to the bone and side. Note that all bones from the right side were odd numbered while all bones from the left were even numbered.

	<u>Right</u>	<u>Left</u>
Humerus	1	2
Radius	3	4
Ulna	5	6
Femur	7	8
Tibia	9	10
Fibula	11	12

Following this system, a radiograph bearing the notation "2-2" would indicate 3753 (left humerus). This system was very helpful in identification, especially with regard to bones such as the fibula. It

is very difficult to distinguish a left from a right with a radiograph only.

Following is the radiography schedule:

3753	July 14, 1980
3787	Feb. 9, 1981
3793, 3790, 3782, 3792	March 11, 1981

#### 2.2.4.3 Molding and Osteometrics

##### PREPARATION FOR MOLDING

In preparing the specimens for testing, two main concerns were considered:

1. To maintain, so far as was possible, the condition of each bone in a fresh state.
2. To orient every specimen of each bone in the mold identically.

Each bone was measured directly after being removed from the freezer in order to assure as little drying as possible during the 20-40 minute interval required for measurement. Fibulae took the least amount of time while femora took the longest.

Upon completion of the measurements, the bone was then placed on a vertically adjustable stand (lab scissor jack), and oriented in the mold by lining up the lines on the anterior and lateral surfaces of the bone with corresponding incisions on the top and sides of the molds. It could then be determined whether the bone fit properly in the molding device. With the femora, it was sometimes necessary to saw off the head to properly align the anterior axis with the lines incised on top of the two molds.

At this point, several small wire nails 15.3 mm were inserted by a small hammer at 10 mm intervals around the proximal and distal ends. This was done to prevent the bone from slipping in the cast during testing. The epoxy putty usually does not adhere directly to the bone because of fatty oils. The bone was then refrozen. The total time out of the freezer was usually less than an hour.

##### MOLDING:

A section of wax paper was cut, folded and taped to fit inside each mold, to prevent the epoxy putty from sticking to the aluminum surfaces.

The bone was then oriented in the mold by adjusting it vertically with the lab jack. The lines incised on the top of the molds were aligned with the one on the anterior surface of the bone. The lines on the side of each bone were aligned with the one on the lateral surface of the bone. The top and bottom plates of each mold could then be adjusted. The bone was then removed and Abbeon epoxy putty was mixed and placed in the grooves and back of the stationary mold.

Following this, the movable mold was translated far enough away from the other end so that the bone could be pushed gently into the back of the stationary mold, but still not be in the movable mold. Putty was then packed into the grooves and back of the movable end. Then, while keeping the bone properly lined up with the stationary end, the movable end was pressed gently toward the bone until it was forced into the putty. The bone was then checked to see if it was in proper alignment. When it was properly aligned, and pressing gently against the back of each mold, the movable end was bolted down. It was then a simple matter to pack putty around the bone on each end. Care was taken to pack putty only around the proximal and distal ends and not around the shaft. Naturally, more putty was required for a femur than for a fibula. Figure 2.19 shows a right femur whose epoxy ends are curing in the mold.

Once molded, the shaft of the bone was wrapped in gauze that had been soaked in Ringer's solution. This was done to prevent drying. At the level of the lines on the sides of the molds, a line was scribed in the soft putty. These lines were later used to center the finished casts in the clamps of the test machine. After setting in the mold for two hours the bone was removed and refrozen.

#### 2.2.4.5 Strain Gages

To determine the state of stress at various locations along the diaphysis as well as around the perimeter of the bones tested in the osteoclast, strain gages were bounded to bone surface at these locations. The strains recorded with these gages were later converted to give principal stresses and strains. This section describes the locations of the gages, the reasoning behind selecting their locations and the methods of actually applying the gages to the bone surface.

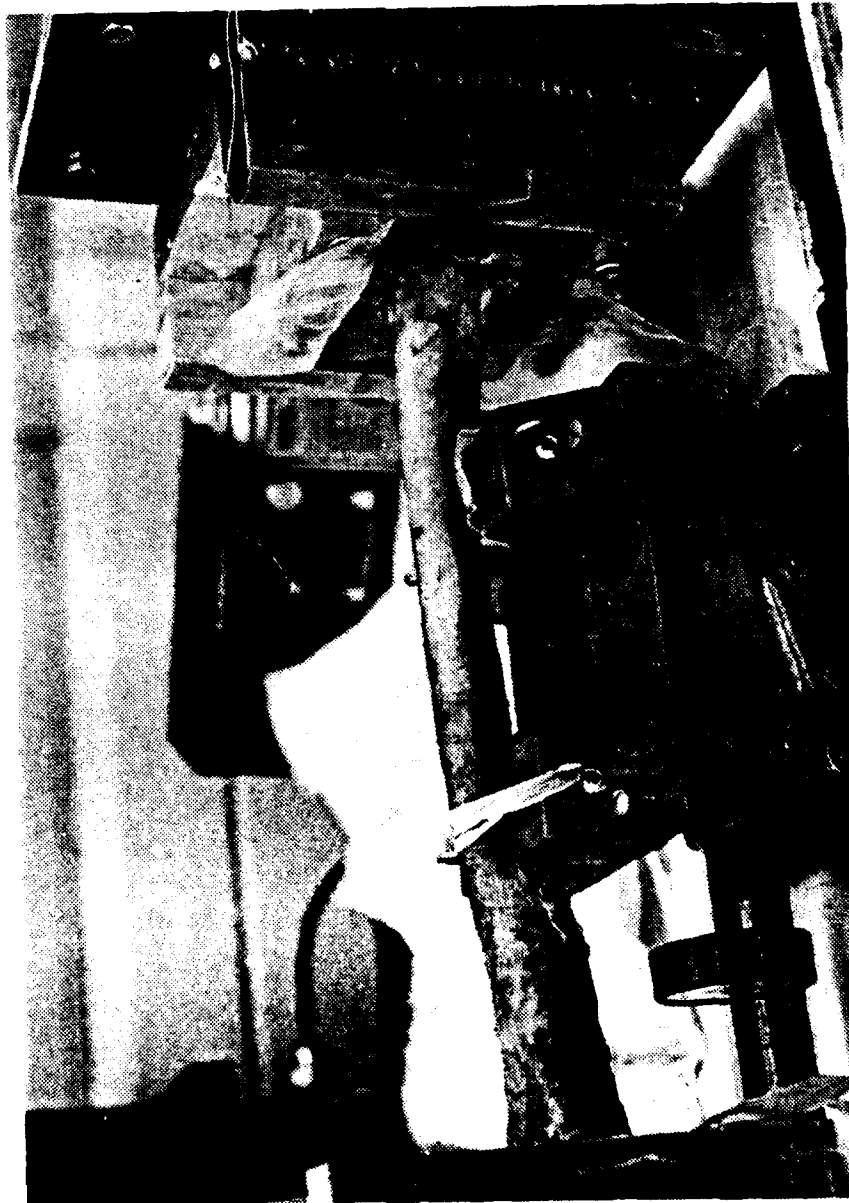


Figure 2.19 Molding of a right femur.

#### GAGE PLACEMENT

Gages were placed at locations around and along the bone surface where strain was considered to be significant. Rosettes were placed at locations where strain was considered biaxial. Axial gages were placed at locations where only normal, unaxial stresses were known to exist parallel to the bone axis. Figures 2.20 - 2.23 and Tables 2.18 - 2.21 and show composite sketches of the gage placement in relation to the bone type and loading conditions. Figures 2.45 - 138 show the precise locations of the gages along the diaphysis and around the periphery of the individual bone surface.

As often as was possible, gages were placed in similar locations, respective of loading conditions, among the types of the long bones tested. Occasionally, gages were placed at locations that were proportional between two bones of different cadavers and different sides, but which were of the same bone type and tested under similar loading conditions. Such placement was to provide a comparison.

As to why specific locations were selected, no defined reasoning is available. Certain points were picked over others to avoid insignificant results. For example, rosettes were not placed near the suspected neutral axis of a bone when the loading condition was bending only. In other instances, rosettes were simply placed near the end of a bone where failure was expected and biaxial stresses were known to exist. But, more often than not, the precise location where a gage was finally bonded was dependent entirely upon the surface condition of the bone. Such conditions were not apparent until the time of gaging.

#### STRAIN GAGE APPLICATION PROCEDURE:

The process of applying the strain gages to a bone before testing involved basically four steps. First the bone is cleared of any extraneous tissue. Next the locations for the strain gages are identified, measured and records made. Then, the gage is bonded. Finally the conductors are soldered to the leads of the gages and taped down and the gages coated. The ends of the bones were always cast in epoxy putty before the gaging process began.

Solid line implies near side  
 Hidden line implies opposite side

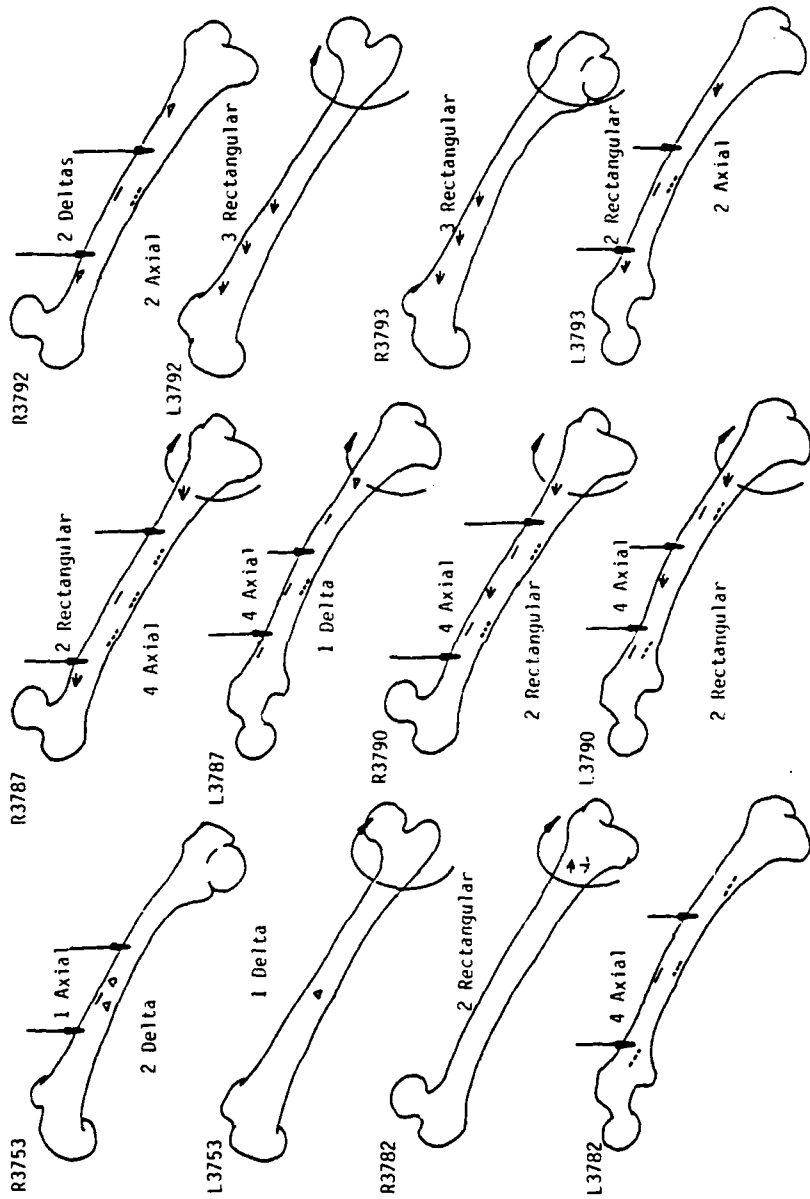


Figure 2.20 Femora gage arrangement and type.

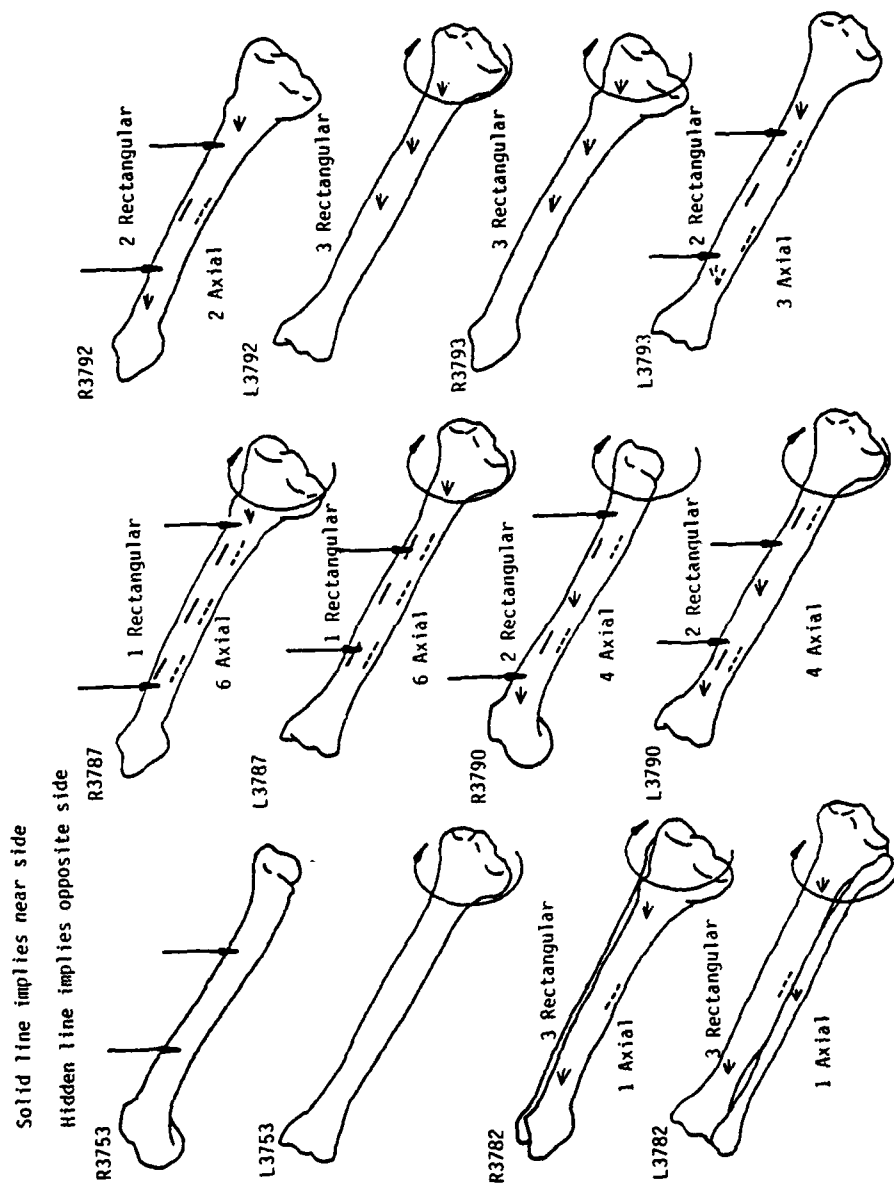


Figure 2.21 Tibiae gage arrangement and type.

Solid line implies near side

Hidden line implies opposite side

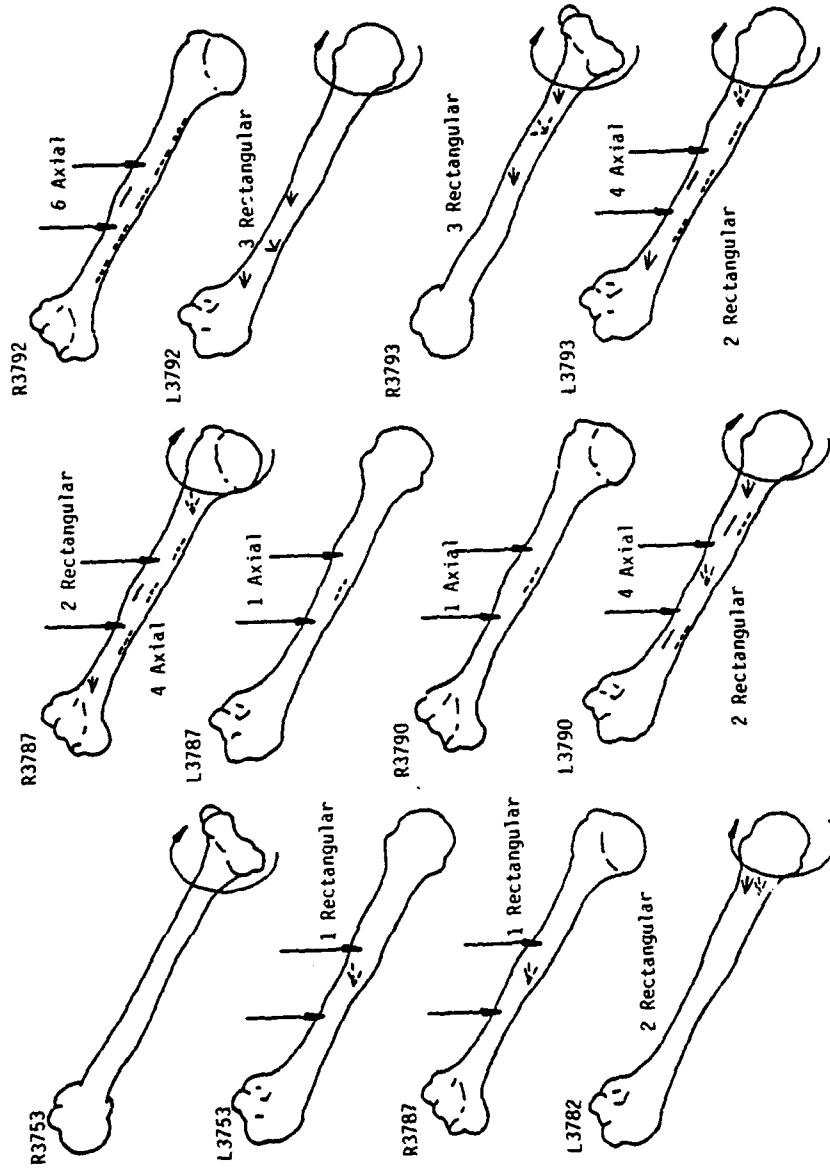


Figure 2.22 Humeri gage arrangement and type.

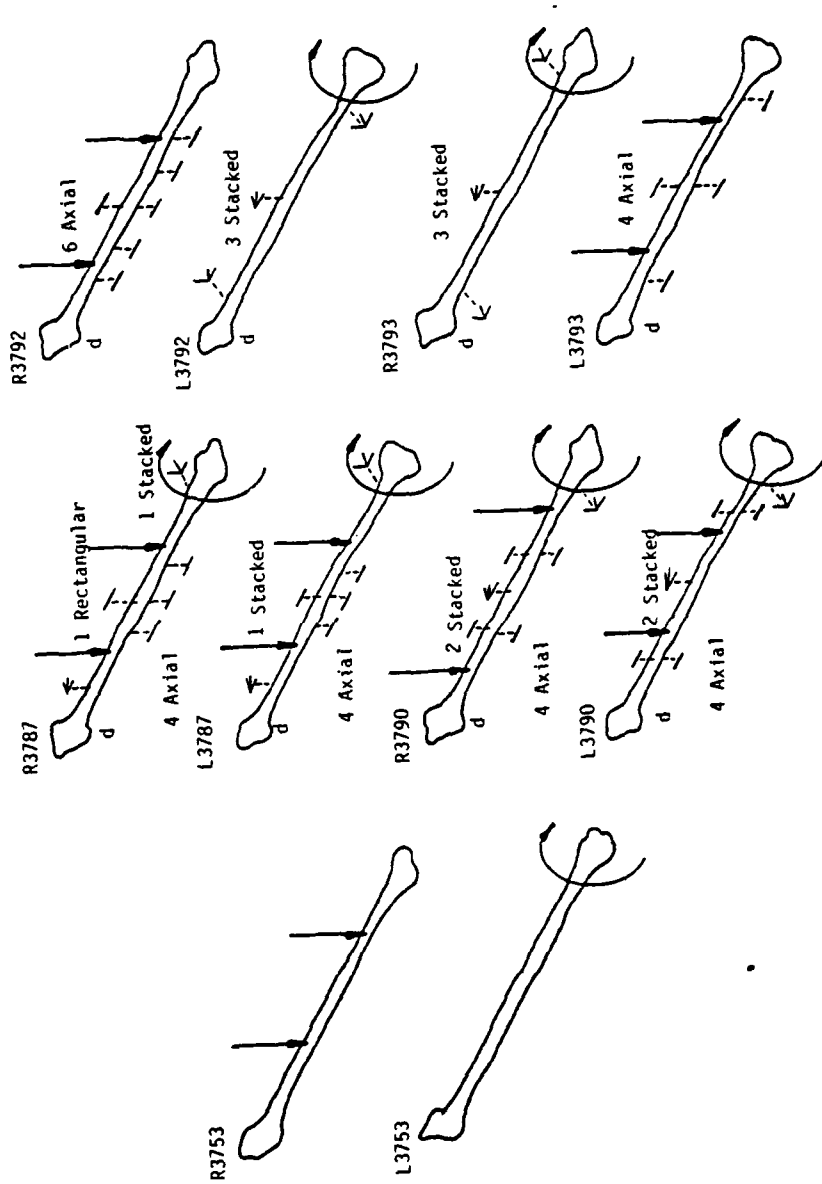


Figure 2.23 Fibulae gage arrangement and type.

Table 2.18 Schematic gage locations on the femora.

TEST NO:	CADAVER NO:	SPECIMEN TYPE:	LOADING	GAGE LOCATION:					DATE:
				R1	R2	L1	L2		
8	3753	LF	T	MD 125YA	○	○	○	○	1981
9	3753	RF	BN	MD 125YA	MD 125YA	MD 125AD	○	○	7/2
10	3792	RF	BM	P 125YA	D 125YA	MD 125AD	○	○	9/2
11	3792	LF	T	MD 125RA	D1/3 125RA	D 125RA	○	○	18/2
12	3787	LF	CBN	D 125YA	D 1/3 4 125AD 3 125BT	MD 6 125AD	○	○	20/2
13	3782	LF	BM	MD 125AD 2 125BT	D1/3 1 125BT	MD 3 125BT	○	○	25/2
14	3790	RF	CTW	D 125RA	MD 125RA	MD 125BT	○	○	28/2
14	3790	LF	CTN	D 125RA	MD 125RA	D 6 125AD 7 125BT	○	○	6/3
15	3782	RF	T	D 125RA	D 125RA	○	○	○	4/3
18	3793	RF	T	D 062RB	D 1/3 062RB	MD R3 062RB	○	○	5/3
19	3793	LF	BM	D 062RB	D 062RB	MD 6 125AD 7 125BT	○	○	16/3
47	3787	RF	CBN	P 125RA	D 125RA	MD 6 125AD 9 125AD	○	○	16/3

R-right  
 L-left  
 T-torsion  
 B-bending  
 N-narrow roller spacing  
 M-medium spacing  
 W-wide spacing  
 CB-combined loading, bending dominate  
 CT-combined loading, torsion dominate  
 P-proximal  
 MD-mid-diaphysis  
 D-distal

Table 2.19 Schematic gage locations on the tibia.

TEST NO:	CADAVER NO:	SPECIMEN TYPE:	LOADING	GAGE LOCATION:				DATE:
				R1	R2	L1	L2	
3	3753	RT	BN	○	○	○	○	1981
5	3753	LT	T	○	○	○	○	18/1
16	3787	LT	CBN	● P	● P	● MD	● D	20/1
17	3787	RT	CBM	● P	● P	● MD	● D	9/3
20	3792	LT	T	● P	● P	● MD	● D	13/3
21	3793	RT	T	● MD	● P	● P	○	17/3
24	3792	RT	BM	● D	● P	● MD	○	17/3
25	3790	RT	CTW	● P	● MD	● MD	● D	30/3
26	3790	LT	CTN	● MD	● D	● MD	● D	1/4
27	3793	LT	BM	● P	● D	● MD	● MD	4/4
31	3782	RT/Fb	T	● P	● D	● MD	● MD	6/4
32	3782	LT/Fb	T	● D	● P	● MD	● MD	15/4

R-right T-torsion P-proximal  
 L-left B-bending N-narrow roller spacing N-mid-diaphysis  
 N-medium spacing N-medium spacing D-distal  
 W-wide spacing CH-combined loading, bending dominate  
 CT-combined loading, torsion dominate

Table 2.2: Schematic gage locations on the humeri.

TEST NO:	CADAVER NO:	SPECIMEN TYPE:	LOADING	GAGE LOCATION:				DATE:
				R1	R2	L1	L2	
6	3753	RH	T	○	○	○	○	1981
22	3792	LH	T	○ <sub>D</sub> 062RB	○ <sub>P</sub> 1/3 062RB	○ <sub>MD</sub> 062RB	○	23/1
23	3793	RH	T	○ <sub>D</sub> 062RB	○ <sub>P</sub> 1/3 062RB	○ <sub>MD</sub> 062RB	○	18/3
28	3782	LH	T	○ <sub>P</sub> 125RA	○ <sub>P</sub> 125RA	○	○	18/3
33	3782	RH	B	○ <sub>MD</sub> 125RA	○	○	○	8/4
34	3753	LH	B	○ <sub>MD</sub> 062RB	○	○	○	22/4
35	3792	RH	B	○ <sub>P</sub> 0 125AD ○ <sub>D</sub> 4 125AD	○ <sub>P</sub> 1/3 1 125AD ○ <sub>D</sub> 1/3 3 125AD	○ <sub>MD</sub> 5 125AD ○ <sub>MD</sub> 2 125AD	○	24/4
36	3793	LH	CB	○ <sub>D</sub> 062RB	○ <sub>P</sub> 062RB	○ <sub>D</sub> 1/3 6 125AD ○ <sub>P</sub> 1/3 9 125AD	○ <sub>MD</sub> 7 125AD ○ <sub>MD</sub> 8 125AD	25/4
38	3787	RH	CT	○ <sub>P</sub> 125RA	○ <sub>D</sub> 125RA	○ <sub>P</sub> 1/3 6 125AD ○ <sub>D</sub> 1/3 9 125AD	○ <sub>MD</sub> 8 125AD ○ <sub>MD</sub> 7 125AD	27/4
40	3790	LH	CT	○ <sub>MD</sub> 125RA	○ <sub>P</sub> 125RA	○ <sub>P</sub> 1/3 6 125AD ○ <sub>D</sub> 1/3 7 125AD	○ <sub>MD</sub> 8 125AD ○ <sub>MD</sub> 9 125AD	1/5
45	3790	RH	Rapid	○ <sub>MD</sub> 0 125AD	○	○	○	6/5
46	3787	LH	Rapid	○ <sub>MD</sub> 0 125AD	○	○	○	29/6

R-right  
 L-left  
 T-torsion  
 B-bending  
 N-narrow roller spacing  
 M-medium spacing  
 W-wide spacing  
 CR-combined loading, bending dominate  
 CT-combined loading, torsion dominate  
 P-proximal  
 MD-mid-diaphysis  
 D-distal

Table 2.21 Schematic gage locations on the fibulae.

TEST NO:	CADAVER NO:	SPECIMEN TYPE:	LOADING	GAGE LOCATION:				DATE:
				R1	R2	L1	L2	
4	3753	Rfb	Bh	○	○	○	○	1981
7	3753	Lfb	T	○	○	○	○	12/1
29	3792	Lfb	T	● P	○ 060MR	○ (R3) 060MR	○	25/1
30	3793	Rfb	T	○ D	○ 060MR	○ (R3) 060MR	○	10/4
37	3793	Lfb	Bm	○ (MD) 2 125BT	○ P 1 125BT	○ D 3 125BT	○	13/4
39	3792	Rfb	Bm	○ (MD) 3 125BT	○ P 1 125BT	○ P (1/3) 2 125BT ○ (1/3) 4	○ D 5 125BT	4/5
41	3790	Rfb	CTN	○ P	○ 060MR	○ P (1/3) 6 125BT ○ 7	○ P (1/3) 8 125BT ○ 9	9/5
42	3790	Lfb	CTN	○ P	○ 060MR	○ P 6 125BT ○ 7	○ D 8 125BT ○ 9	14/5
43	3787	Lfb	CBN	○ P (1/3)	○ 060MR	○ MD 6 125BT ○ 8	○ P (1/3) 7 125BT ○ (1/3) 9	15/5
44	3787	Rfb	CTN	○ D	○ 062RB	○ P (1/3) 6 125BT ○ (1/3) 9	○ MD 7 125BT ○ 8	18/5
				○	○	○	○	
				○ A			○	

R-right  
 L-left  
 T-torsion  
 B-bending  
 N-narrow roller spacing  
 M-medium spacing  
 N-wide spacing  
 CB-combined loading, bending dominate  
 CT-combined loading, torsion dominate  
 P-proximal  
 MD-mid-diaphysis  
 D-distal

#### Removal of Extraneous Tissue:

Prior to beginning the gaging process, each bone was removed from the refrigerator, or freezer, early enough to allow the bone to reach room temperature before bonding took place. If the bone was frozen, this meant removing the bone from the freezer and placing it in the room environment at least 16 hours in advance of beginning the cleaning process. If the bone was only refrigerated, the "warm-up" required only four hours. Each bone had to be at room temperature prior to bonding the first gage, to eliminate any unwanted strains. Such strains occur when the surface warms beyond the temperature occurring at the time of bonding, and, thus, expands, straining the gage. If this straining is sufficient to increase the resistance of the gage beyond balancing units of the switch and balance unit, then external resistors must be added in the bridge circuitry to balance and calibrate the strain indicating system.

Cleaning began with the cutting away of any gross muscle tissue remaining after resection. Such tissue usually occurred only near the ends of the bone and just enough was removed to prevent any interference with the bonding process. Then all the periosteum was scraped away with a scalpel in the vicinity of the gage location to include enough area for alignment marks and the alignment tape. This area was dry sanded with 240 grit silicon carbide paper until it appeared free of soft tissue. Next the area was soaked in micromasurement (MM) acid conditioner, and scrubbed with a gauze sponge. The area was wiped dry with a clean sponge in MM base conditioner. Then it was wiped dry until no debris was evident on the gauze sponge. As a final step to the cleaning process, the area was degreased by soaking a clean gauze sponge in MM Chlorothene NU degreaser and wiping once across the area. Several passes were made across the area with the degreaser using a clean sponge for each pass.

#### Marking and Recording Gage Locations:

General gage placement along and around the diaphysis was always decided in advance of the actual application. Precise placement was not decided until the general area had been cleaned and evaluated as to the curvature and roughness. The final location was picked to be smooth,

not too porous, and flat enough (no ridges) to avoid breaking the backing of the gage.

Once the precise placement was determined, the alignment axes of the gage were marked on the above surface. Both the transverse and the longitudinal alignment axes, were marked on top of a flat, FORMICA topped desk used as a precision table. To mark the transverse axis, the bone was rotated about its longitudinal axis until the areas selected for the gages were most accessible. In this position, the bone would be resting on the epoxy blocks molded to its ends with one of "anatomical" planes parallel to the table top (Figure 2.24). Using a machinist square resting on its wide leg, a vertical mark was made with a drafting pencil at the desired gage center using the vertical edge of the square as a guide (Figure 2.24). The lead in the pencil was 4H in hardness and sharpened to a fine point.

Once located, the longitudinal axis was marked with the same pencil using a small drafting triangle. A line etched in the center of one of the legs of the triangle and at 90 deg. to its edge was aligned with the transverse axis and the mark was then made along the triangle edge.

The transverse axis was located either as a function of the surface condition, as mentioned earlier, or in proportion to the locations of gages on a comparative bone. If in proportion, the distance from the mid-diaphysis was calculated using a proportionality factor and the recorded distances of the gage placement on the comparative bone. The gage placement along the diaphysis of the comparative bone was always determined by the surface conditions. For the transverse axis, proportionality factor was the ratio of either the anatomical or morphological lengths of the two bones under comparison depending on the alignment of the bone in the mold.

The location of the longitudinal axis was also dependent on the surface conditions of the bone surface. The preferred locations of the longitudinal axis was coincidental with a plane that was parallel with the sides of cast epoxy blocks in contact with the table top and also contained the mid point of a diameter of the diaphysis surface area projected on a plane normal to the desk top (Figure 2.25). The location of the axis on the surface of the diaphysis was found as follows:

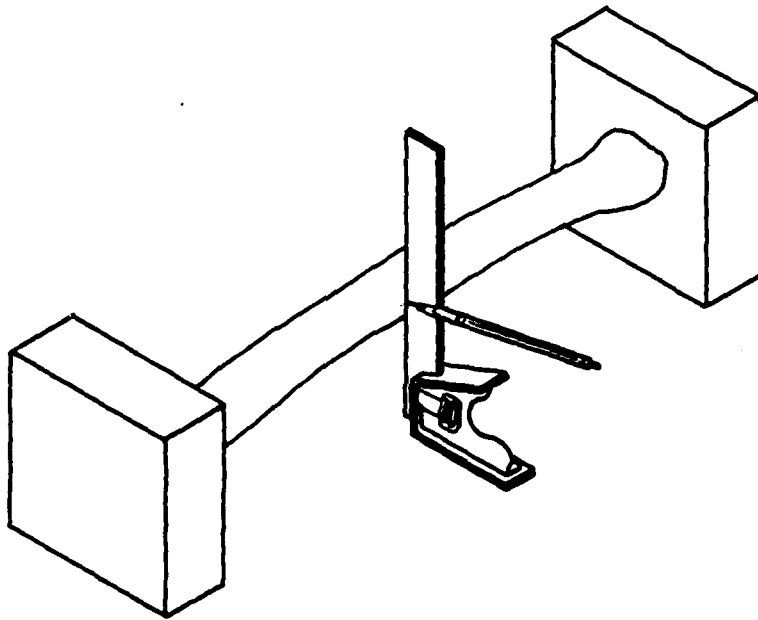


Figure 2.24 Marking of the vertical alignment axis for a strain gage.

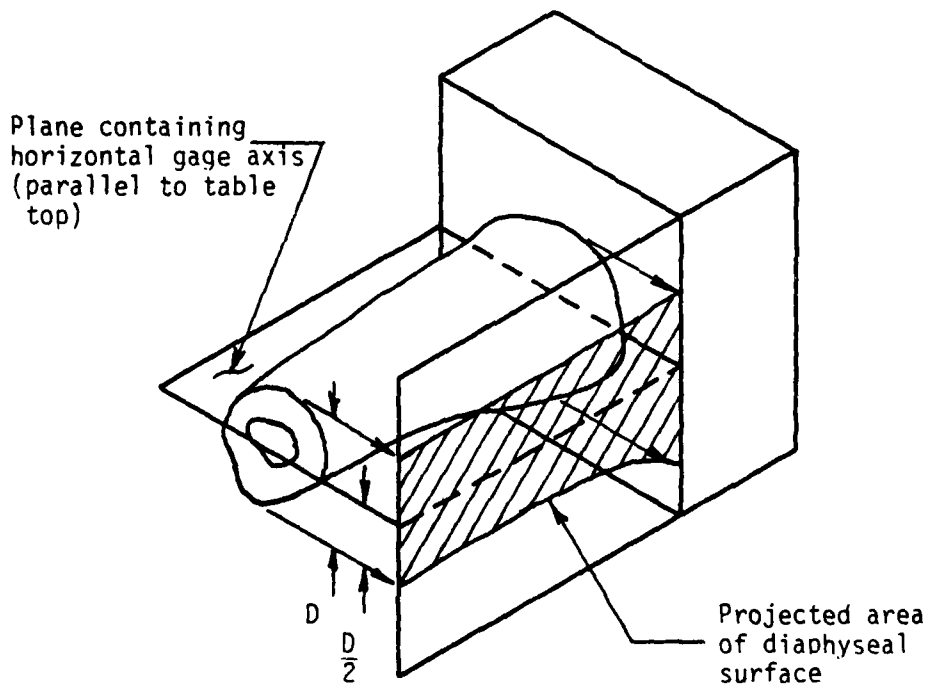


Figure 2.25 Plane containing the longitudinal gage axis.

1. Leaving the bone in the same position used for marking the transverse axes, the distance was measured from the desk top to the point on the top surface of the diaphysis that extends the farthest away from the desk top. This measurement was taken at the transverse axis using a surface gage and a metric scale (Figure 2.26).
2. Similarly, the distance was measured from the desk top to a point on the lower surface of the diaphysis that was closest to the desk top.
3. The average of the two measurements was set on the surface gage and marked scribed across the transverse axis.
4. Each of these distances (with reference to the desk top) were recorded on a worksheet.

If the surface conditions did not permit the placement of longitudinal axis as described in the steps above, steps (1) and (2) were still performed but in place of step (3) the feasible location was marked and measured with the surface gage. If the gages were to be placed at locations proportional to those of a comparative bone, the distance to the axis, with reference to the desk top, was determined authentically using a proportionality factor. This factor was the ratio of the projected diameters of the two as determined by subtracting the distance measured in step (2), above, from that of step (1). The factor was applied to the diameter of the bone being gaged.

When possible, the same side of the bone was kept down during the marking of all the gages on that bone. Obviously, this may not be feasible if gages were to be applied to all sides of the diaphysis; but, usually gages were placed only on opposite sides and keeping the same reference plane made record keeping much simpler.

Bonding:

To ensure a good bond, the surface area directly below the gage had to be free of all fats and oils. This included also those fats and oils just below the surface of bone in the canalicular structure. To remove these oils and fats, the area was first swabbed with cotton-tipped applicators immersed in ether. Then the area was covered with isopropyle alcohol and dried with a hand-held hair dryer. The hair

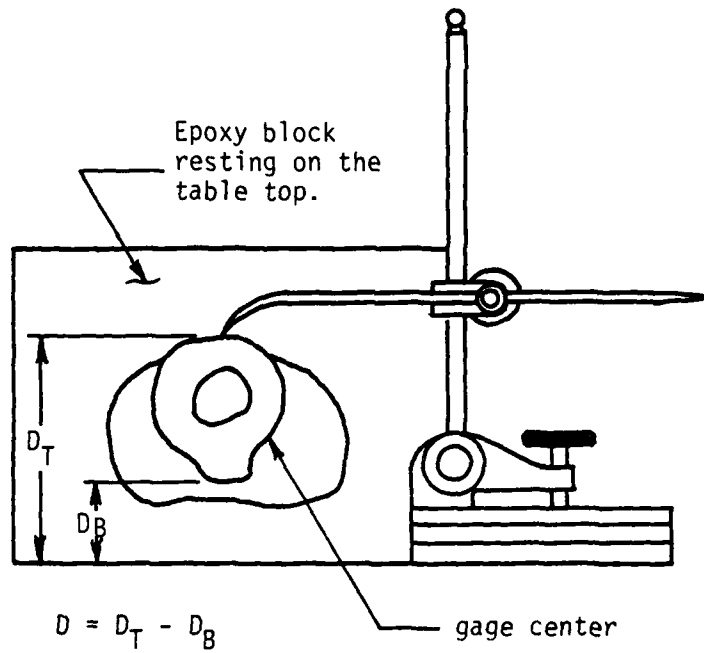


Figure 2.26 Measurement of the bone surface.

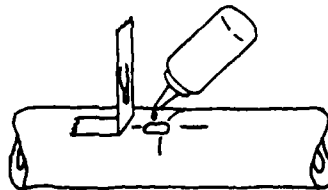


Figure 2.27(a) Application of adhesive.

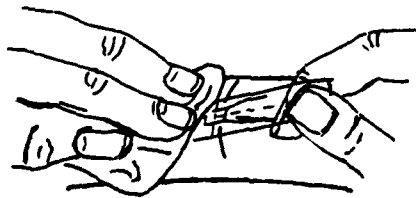


Figure 2.27(b) Application of the gage.

dryer blower was directed at the bone surface for one to two minutes, but only until the bone surface felt warm when touched. Usually, the hot air applied for this period of time was sufficient to dry the subsurface waters and bring up the subsurface oils. These oils were then wiped away with cotton gauze sponges damp with the MM Chlorothene degreaser. Since the oils were brought to the surface with the mild heat and the effect of drying on the capillary action, the remaining liquids remained below the surface as long as the drying temperature was not exceeded. At this point the bone was set aside, draped in a plastic bag and allowed to cool for five to ten minutes. The cooling was again necessary to prevent unwanted strains and their associated high gage resistance.

While the bone was cooling, the gages were prepared for placement. Each gage to be bonded, was placed back down on a glass plate which was free of oils and grease. Each gage, including the lead wires, was then covered with a piece of cellophane tape approximately 8.0 cm in length. Using fine Rapidograph pen, the transverse and longitudinal axes were drawn on the surface of the tape. The axes were marked by aligning the edge of a drafting triangle with the markings on the top of the strain gage. (Refer to Figure 2.28).

To correctly place the gage on the bone surface, the tape with the gage was removed carefully from the glass plate. The tape and gage were then placed over the axis marked on the bone, aligning axes on the tape with those on the bone, and pressed to the bone surface. The end of the tape on the side of the gage opposite the lead wires was then pulled free and folded back onto the end near lead wires which were still stuck in place. Thus, the gage was clear of the bone surface, its back exposed, but it still was aligned with the axes on the bone.

All the gages were bonded to the bones using MM 200 adhesive. The catalyst was applied per instruction and allowed to dry for one minute. Then, the loop of the tape was opened and 2-4 drops of adhesive were placed at the base of the gage between the tape and the bone (Figure 2.27(a)). Finally the tape and gage were repositioned onto the bone surface as shown in Figure 2.27(b). Pressure was applied by placing the pad of the thumb over the gage and pressing down. The pressure was held for one minute.

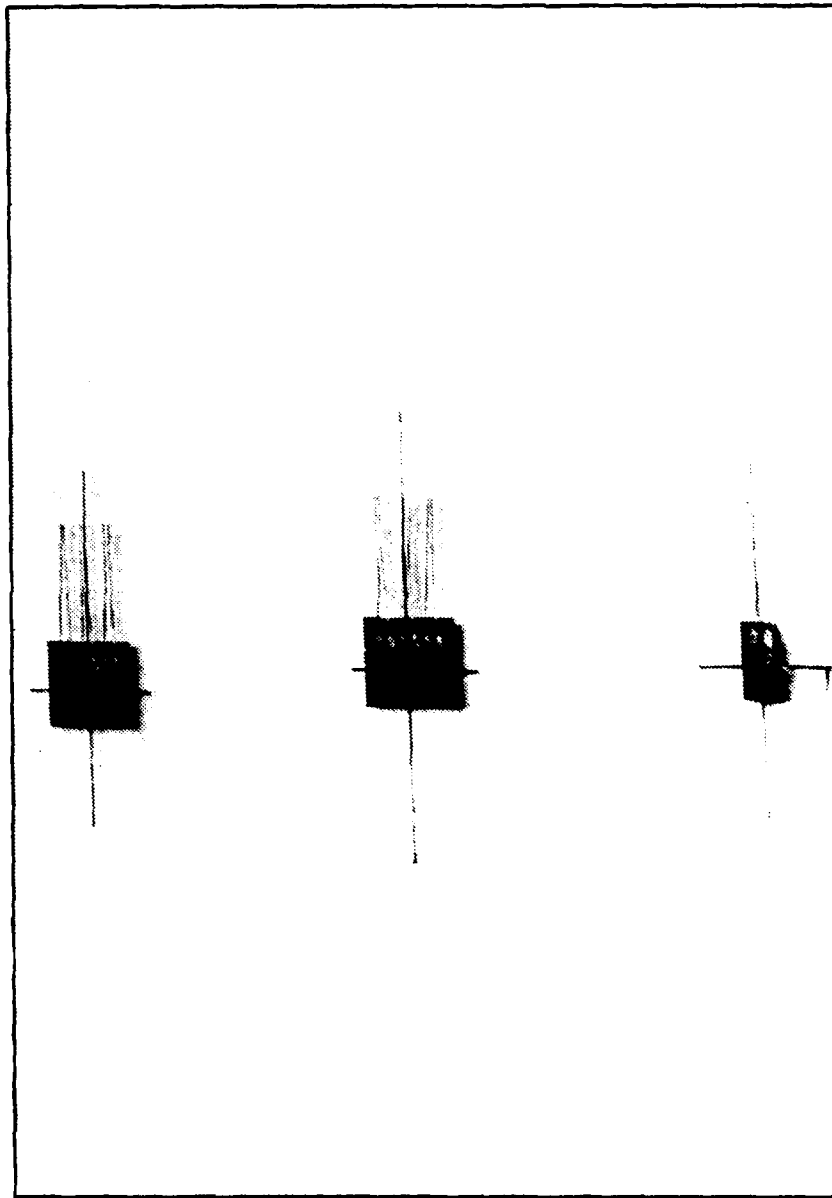


Figure 2.28 Extension of gage axes.

If there was any question as to the quality of the bond, the cellophane tape was removed immediately and the gage backing teased with a spatula. If all appeared well a piece of cellophane tape was reapplied for protection. If only a corner of the backing appeared loose, it was pressed into place with a spatula until the adhesive set. If warranted, more adhesive was applied. However, if any of the grid portion of the gage appeared free of the surface, the gage was removed and a new gage applied.

#### Attachment of Conductors:

Before soldering any conductor to a gage, all conductors were degreased by pulling them through several gauze sponges soaked in the MM degreaser. Then, the insulation was inspected for breaks and the tinned ends cleaned. Because the conductors were reused, the tinned ends had bits of the old silicone coating as well as the remnants of the old gage lead wires. The silicone was removed by pulling the ends through a piece of a nylon floor scrubbing pad. The old pieces of lead wire were removed by clamping the ends of the conductor in a "fly-tying" vise\* and pulling off the lead with a pair of tweezers while heating the tips with a soldering iron. The ends were clipped off and retinned if the insulation appeared melted away from previous solderings.

With the conductors readied, the cellophane tape was removed from each gage and the leads pulled away from the bone surface. The leads were folded back over the gage, out of the way. Care was necessary in order not to pull the leads from their soldered connections at the gage grid.

Conductors were selected, according to the number attached to their spaded end (Section 2.2.3.4), to correspond to a channel number of the Vishay switch and balance. As often as possible, the numbers were arranged among the gages to agree with numbering arrangement called out on the data sheet (Section titled "Strain Data Sheet").

Once the order of the numbering was established, the conductors were taped (Figure 2.29) to the diaphyses with a piece of plastic electrical tape 7 mm wide. When three conductors were necessary for a

\*A vise used for tying fishing flies was found the most convenient for holding delicate electrical wiring for soldering.



Figure 2.29 Attachment of strain gage conductors.

rosette, all three were taped simultaneously. The conductors were held in place with one wrapping of tape and, then, a loop formed in each conductor (Figure 2.29) and the loops taped to the first wrapping with a second wrapping. The loops were necessary to prevent the conductors from pulling the leads off the gage as well as to eliminate the twisting of the conductor beneath the tape. The tinned ends of the conductors were placed about 6 mm from the edge of the gage backing below the lead wires. The tape was wrapped as close as possible to the ends of the insulation on the tinned ends.

When all the tinned ends were pointing up, the individual lead wires on the gage were wrapped one to two turns around the appropriate tinned end (Figure 2.29). One leg of each gage was attached to each three conductor wire with one lead to the two conductors in common and the other to the remaining conductor. After all leads were wrapped around the tinned ends, the wrappings were soldered. The excess lead wire was trimmed away with a small pair of wire cutters. Special care was necessary while wrapping the leads to avoid pulling the leads off the gage grid.

After the soldering was complete for all the gages, the continuity of the wiring was checked with an Ohm-meter. Each short circuit was examined and corrected as necessary. When the wiring was complete, each gage and adjacent soldered connections were cleaned with MM rosin solvent to remove the rosin residue left from the solder. Allowing the solvent to dry for one to three minutes, each gage was liberally coated in MM-C silicone rubber containing an alcohol solvent. Two coats of the silicone were applied with a 20 minute drying time allowed between coats.

With the gaging process complete, the bone was prepared for refrigeration. Areas not gaged along the diaphysis were covered in strips of gauze wet with Ringer's solution. These strips were tied in place with wire "garbage bag" ties. All the conductor wires were gathered and tied together. The ends of the epoxy blocks were marked with the cadaver number, specimen type and side (right, left). The views (lateral, posterior, etc.) and the orientation (distal, proximal) were also marked on the sides of the epoxy blocks. For protection, the entire specimen, bone and epoxy blocks, was covered in a sheet of poly-

ethylene plastic which was scribed and taped together to form a rectangular tube. Finally, the tube with the specimen was placed in a plastic bag and tied closed with a wire tie with the bone identity tag attached. The specimen was then placed immediately in the refrigerator.

General Remarks:

When more than one gage was applied, each step (cleaning, marking, bonding, and soldering) was completed for all the gage locations before advancing to the next step. Specifically, all the locations were scraped clean then sanded. All were degreased, one after the other, before each gage was bonded, one after the other. This method quickened the overall gaging process, but, above all, it was a much cleaner procedure. Since all the difficult preparatory steps such as scraping and sanding were completed early in the process, keeping bonding surfaces clean was much simpler.

All measurements taken during the gaging process were recorded as mentioned earlier. In addition to these, other information was recorded to facilitate data reduction and analysis. The pertinent information on this form was eventually transcribed to several sketches to depict the information in a more physical way.

2.2.4.6 Equipment Setup

OSTEOCLAST:

Generally, the set up of the osteoclast varied only slightly between loading conditions and bone type; however, the humerus did require a shorter bending carriage during its bending tests. The variations that did occur are discussed, below, with respect to the three loading conditions -- bending, torsion and combined bending and torsion.

Bending:

Each bone was removed from the refrigerator and clamped immediately into the osteoclast. The time required to arrange and adjust the osteoclast along with the time required to set up the auxiliary equipment was sufficient to permit the bone to warm up to room temperature.

Before removing the bone from its sealed environment in the plastic bag, the humidity chamber (when required) and the bending carriage were

installed. When femora and tibiae were tested, the chamber was hung first and the stabilizing cables inserted in the cut-outs in its top. The cables were then anchored to the roller but kept slack. Next the bending carriage was hung -- the large carriage for the femora, tibiae and fibulae and the small carriage for the humeri. If the roller spacing had to be changed, this was done before hanging the carriage.

To ensure that the alignment of the bone in the osteoclast agreed with the desired alignment as established in the mold, the bottom pieces of the fixed-end clamp and the disk/clamp were adjusted to correspond to the positions of the bottom pieces of the mold. These positions were determined from the scribe marks on the face of the cast epoxy blocks which were inscribed at the time of molding.

Placing the specimen on its side (with respect to its test orientation), the distance was measured from the bottom of each block to the scribe mark. Using these distances, the pair of holes on the back of the clamp for the correct position of the bottom pieces was found by measuring from center of the clamp back to the top of the bottom piece. Aligned with these pairs of holes, the bottom pieces were bolted to clamp backs, torquing the bolts until they were "snug."

At this point, if the length of the bone did not permit the use of the humidity chamber, the specimen was wrapped in a sheet of poly-vinyl-chloride plastic. This was always the case for the humeri and occasionally for the fibulae. The sheet was taped, sparingly, to the cast epoxy blocks such as not to interfere with the clearance of the blocks in the clamps. The plastic was wrapped once around the specimen taping the sheeting to blocks one side at a time. Some overlap was allowed which was taped down to seal off the bone. This elastic envelop then became the humidity chamber.

To provide room to manipulate the specimen between the clamps during its installation, the suspended support and torsion mechanisms were shifted away from the fixed end clamp. With the fixed end clamp held vertically by the side pin, one of the epoxy blocks on the end of the bone was inserted into the fixed clamp. As to which end was placed in the fixed-end clamp was dependent on the curvature of the diaphysis. The bones were normally oriented so that this curvature would force the bending carriage to slide toward the fixed end when the bone was loaded

in bending. The reason this was desirable was to prevent the bending of the probe of the bending deflection dial indicator with the carriage.

Holding the free end of the bone with one hand, the disk/clamp and torsional load mechanisms were shifted back towards the fixed-end clamp until the epoxy block was set in the disk/clamp. Now both top pieces of the two clamps were bolted snugly into place.

Using the distance measured between the support points, one at each clamp, the bending carriage was positioned in the center of diaphysis. The distance from the fixed-end support to the closest roller axis is half of the difference of the roller spacing subtracted from the distance between the supports. The bending carriage was centered by shifting the trolley and clamps of the bending load mechanism until this distance between the fixed end support and the closest roller was set. Since the cables had to be slack to insert the bottoms of the humidity chamber, the clevis/yoke was now attached and the chamber bottom inserted (if required) before proceeding.

Next, the stabilizing cables were then tightened enough to remove the slack, and the cables aligned visually with the vertical. The distance to the closest roller was checked and the rollers and trolley were again shifted as necessary. When the cables appeared vertical and the distance to the closest roller was satisfactory, the stabilizing cables were tightened until they were loaded approximately 1500 N in tension. Care was taken to ensure the trolley was not cocked off to one side.

To finish the preparation for the bending tests, the bending load cell was suspended from the clevis yoke and the turnbuckle attached to its bottom fitting. As far as the torsional load mechanism was concerned, it was simply aligned with the vertical and any apparent torsional load removed. The moist air was connected to the humidity chamber and the strain gage conductors connected to the junction board. Finally the compensation spring was hooked to the torque tube and the fixed-end-clamp side pin backed off.

#### Torsion:

Clamping the specimen in the osteoclast for a torsion test followed the same procedure as for a bending test. The only difference was the

bending load mechanism, including the stabilizing cables, was not installed only the humidity chamber (when required) was hung. Again for the bones that were too short for the humidity chamber, a plastic envelope was wrapped around the specimen for a substitute.

The only difference between the two types of tests involved the use of the torsional load mechanism; however, nothing special was required to ready its setup. The vertical alignment of the cables, pulley, torque bar and centering bar was assured and the turnbuckle in the mechanism was turned until the rising load cell was neither resting nor pulling on the torque bar. Again the side pin was back off at the fixed-end clamp, but the compensating spring was not connected.

#### Combined Loads:

The setup of the osteoclast involved all the steps discussed for the bending only and torsion only tests. The arrangement of the loading devices, required that the bending steps be accomplished first.

#### BLH SYSTEM:

The BLH switch and balance system was modified to indicate the strains sensed by the loads in osteoclast as pounds force (Section titled "Load Indication"). Since the system remained stationary and connected to the load cells, little was required to set-up the system for a test. All that was necessary was balancing the bridges in each of the three channels. The calibrations were assumed unchanged throughout the tests since the system had not been altered or moved.

Balancing involved corrections of two types. One was to compensate for the weight of the bending load mechanism and the other was to adjust for settling time.

To compensate for the weight of the bending mechanism, the value corresponding to the weight was simply set on channel 1 when the bending carriage was lowered onto the bone. The values varied according to what was included in the mechanism train.

The settling time is the time required for the strain gages to heat to a temperature associated with the current and voltage applied to the gage. In a loaded condition the gage is strained and the resistance has increased. When the gage temperature increases, the gage expands and the strain sensed decreases. Therefore, as the gage heats up, the load (strain) indicated drops off.

Any system which does not maintain a continuous voltage and current on its gages will require a settling time for each channel when first selected. The BLH, which is such a system requires approximately 60 seconds to indicate the "exact" strain or load as sensed. To adjust for this settling time, those channels which would be selected only momentarily were balanced to read their desired "zero" load immediately when selected. Thus during a run, the first value indicated when these channels were selected could be assumed correct and delays waiting for the channels to settle were avoided.

During each test, one channel, or load cell, prevailed as a "control" channel. This channel was monitored a majority of the time and was used as the primary channel for setting the desired load increments. In the torsion tests and the combined tests, the other channels were selected only long enough to read the load first indicated. For the bending tests only one load cell, channel number 1, was involved and it obviously became the control channel. In the torsion tests, two channels were involved -- one for the "falling" load cell and one for the "rising" load cell. Because the falling load cell was monitored and used to set the torsional loads, channel 2 became the "control" channel. Channel 3, the "rising" load cell, was read only momentarily. As to which channel became the control channel during the combined tests was dependent upon which loading condition was dominant. If the bending was held fixed after some point and torsion continued until a fracture occurred, then channel 2 became the control channel and the other two were read only momentarily. If the torsion was held fixed and bending dominated, then channel 1 became the control channel.

VISHAY:

The setup of the Vishay strain indicating system was the same, regardless of the type of loading condition. The only alteration necessary was the setting of the "calibration number" for each channel which was dependent upon the strain gage factor(s). The "calibration number" once entered, varied the gain of the digital display such that the strain sensed was indicated as microstrain.

The "calibration numbers" are published by Vishay in chart form. They are listed in relation to the gage factor and number of active

gages. For all the tests, the legs of each gage were considered as one active gage (one that is mechanically strained).

Once the bone had been clamped into the osteoclast and the humidity chamber sealed, the conductors to the individual strain gages were connected to the junction board. The gage number which was on the end of the conductor (Section 2.2.3.4) was connected to the channel of the same number. This way, the channel numbers corresponded to specific legs of the gages on the bone and allowed later correlation of the strain data with the correct gage leg. As mentioned in Section 2.2.3.4, the legs of all the gages functioned as a quarter of a Wheatstone bridge for all bones tested except one. For this bone, the gages were compensated for temperature and functioned as a leg in a half bridge.

Power was applied to the Vishay system at the beginning of the setting-up of test equipment. At "turn-on," the channel selector was switched to an "open" position to avoid heating any one gage for a long period of time. The selector was then kept in this "open" position except for the actual reaching of the strains indicated and calibration.

When setting the "calibration number," each gage was selected and the gage allowed to settle, or "heat-up", for 5 to 10 minutes. Usually this length of time was sufficient to stabilize the gage leg so that it could be balanced and the balance maintained. If the balance, or zero, appeared steady, the calibration number was set and the channel rebalanced as necessary. When set under these conditions, the calibration needed no refinement and all that was necessary during the tests was to rebalance the bridge of each channel. Of importance, was the necessity that all mechanical alterations of the osteoclast had to be complete before balancing of the Vishay could begin; otherwise, extraneous strains were, or were not, induced and the balance attained would change when these alterations were finally performed.

Before beginning the first run of a test the strains on all the channels were read without load applied. If these values appeared extremely large, greater than  $50 \pm$  microstrain, each channel was rebalanced. The rebalance procedure was different from the initial balance when the calibration numbers were set. When rebalancing, each channel was allowed to settle for 30 seconds, at the most, before its bridge was "balanced." Obviously, under this time limit, the bridges

would not remain balanced if the gages were allowed to fully heat up; however, this procedure lessened the time required for each test and was considered accurate for the method used in rapidly reading the strains at each load increment.

For each run, the strains indicated on each channel were recorded at the beginning without load applied, at each load increment, and at the end of the run with no load applied. As already mentioned, except when reading, the channel selector was left on an open position where there was no current fed to any of the gages. At every reading of the gages, each channel was read following a rapid but consistent pace. This was to assure that, during every pass through the channels, bridge was at the same level of unbalance when its strains were recorded. The same pace was used to read the zero loads condition at the beginning and the end of the run.

This method of recording the indicated strains, if consistent, offered a means of circumventing the need to wait for the gages to settle. If the average of the values read at the zero load conditions are added to the strains read at the load increments, the strains corrected for the unsettled bridge result. Thus, strains were read as rapidly as the operator could physically function and the time between runs necessary to rebalance the gages was reduced from an hour and a half to 10 minutes.

Occasionally, a leg of a strain gage had a resistance after bonding that was outside of the balance limits of the Vishay system. By either shunting various resistances across the bridge leg or inserting them in series with the bridge, the bridge was balanced. Such a practice was considered insignificant since later checks were to show that the small resistance, normally used, would change the indicated strains by no more than 0.8%.

One last matter of importance. When the test was finished, a final comparison was made between the gage legs annotated on the data sheet and their actual arrangement on the bone. This was to assure, that the strains recorded could be later accurately transformed and identified.

## VIDEO

Every test following the first five were recorded with a Sony video recorder system (Section 2.2.3.5). Both sound and video were "taped" in hopes of evaluating crack propagation. Because only the area of the bone expected to fracture was placed in the field of view, some of the fractures were not captured when they occurred in unexpected locations.

Each run was marked by recording on video an index card displaying the test number and run number. Only a portion of a run past a certain load increment was recorded. Each succeeding run was then taped over the preceding run, preserving only the final run showing the fracture. These records have been edited and consolidated onto a single tape.

### 2.2.4.7 Written and Photographic Records

To accurately substantiate and ease later analysis of test results, written records in conjunction with still photography were used throughout this investigation. The written records were used for recording strains, deflections, loads and linear measurements. The written records also include sketches of fractures, of strain gage locations, of SEM locations and of the sections sent to KUMC for their analyses. The photographic records consist of roentgenographs and photographs of equipment, SEM studies, bone fractures and some procedures. The photographs are displayed throughout the report with exception of most of the fractures; only exemplar fractures have been printed for clarity as a part of the text while the rest are in the keeping of the authors. Only the application and purpose of specific, written records and photographs will be discussed below.

#### LOADING PLAN:

The Loading Plan was a listing of the load increments scheduled for each run during a specific test. It was used as a guide by the person setting the load increments to avoid skipping increments and, thus, recording deflections or strains against the wrong load. The form also provided a block for recording problems or changes in testing.

#### DEFLECTION DATA SHEET:

The Deflection Data Sheet was used to record the loads read from the three channels of the BLH and the four deflections read from the dial indicators on the osteoclast. Two columns were provided for each deflection. One was used for writing deflections in hundreds and thousands of an inch as indicated by the large dial. The other was used for writing the indications of the smaller dial which indicated tenths of an inch. Only the deflection indicating angle of twist was an increasing deflection; the deflections indicating slopes and the bending were decreasing.

The sheet also provided a sketch of a bone in the clamps of the osteoclast which dimensioned the distance between support points, the distance from the fixed end to the closest roller, the distance between the farthest roller and the probe of the bending dial indicator and the roller spacings. These measurements were recorded at the time the osteoclast was set up. Also included on the sheet was information establishing the orientation of the bone in the osteoclast.

#### STRAIN DATA SHEET:

Only strain indications and information defining gage configuration were recorded on the Strain Data Sheet. The sheet was arranged for only one configuration -- two rosettes and four axial gages. Whenever there were deviations from this configuration, the old headings were simply crossed out and the new configuration penciled in. The configuration was defined as a location (proximity as proximal, lateral, etc.) and an orientation (what leg of a rosette was toward a specific side of the bone).

#### STRAIN GAGE LOCATION AND FRACTURE PATTERN:

This sheet was used for several purposes: to define strain gage locations along the bone diaphysis and with respect to a datum plane (desk top -- Section titled "Marking and Gage Locations"); to define fracture patterns with reference to the mid-diaphysis; and to define the locations of the sections cut for KUMC as well as the sections cut to locate the gages around the periphery of the diaphysis (Section 2.2.4.10).

The strain gages were located on this sheet as a distance parallel to the longitudinal axis from the mid-diaphysis to the transverse axis of the gage. The location of the gage with respect to the desk top was shown as a distance from the desk top to the longitudinal axis of the gage. The desk top was referenced by distances measured from the top surface of the diaphysis and the bottom surface of the diaphysis to the desk top. These measurements are explained in more detail in section titled "Marking and Gage Locations".

The patterns were sketched as viewed looking normal to the four anatomical planes -- lateral, medial, anterior, posterior. Obvious changes in fracture direction were referenced dimensionally, with respect to the mid-diaphysis as well as to the upper and lower surfaces of the diaphysis, to facilitate the location of the fractures in the photographs.

SEM sections removed for the micromechanical analysis were shown with respect to their location along the fracture line. Distances to their location were considered unnecessary. Disk sections taken from the bone diaphysis (Section 2.2.4.10) were referenced to the mid-diaphysis. Only the cross section of interest was depicted in the sketch.

Because the cross-sectional shapes of the bone diaphysis are so irregular, the specific location of the strain gages around the diaphysis was considered important toward the understanding of the stress state. These cross sections were referenced to mid-diaphysis to assure the person cutting the sections of the correct gage location. This was especially necessary for those gages that had peeled off after or during a test.

#### PHOTOGRAPHIC RECORDS:

Still photographs were taken of all fractures that were observed during the testing. Four views (lateral, anterior, etc.) normal to the anatomical planes (sagittal and coronal) were usually photographed for each bone. A few of the bones were photographed using less than four views if a view(s) did not show any of the fractures.

All views include letters annotating the view, the location of distal end, the loading condition and the test number. The view is

annotated with two letters with a hyphen between them. The surface on the top of the bone is also denoted with a letter. The loading conditions are implied with arrows -- a double-headed arrow for torque and single-headed arrow for a concentrated force. The torque arrow is positioned next to the end of the bone which was clamped in the disk/clamp of the osteoclast and indicates the direction of torque. The force arrows show the direction and points of application of the bending forces as applied by the rollers. The letters represent the first letter in the views: L-lateral, M-medial, A-anterior, P-posterior.

#### 2.2.4.8 Test Schedule

The test program was planned to fracture the bones in groups of the same bone type. The testing was to begin with the femora and progress through the tibiae, fibulae and humeri; however, because of equipment problems this plan was not followed exactly.

In actuality, the tests started by fracturing all of the four long bones of cadaver number 3753 with the exception of one humerus. Originally, all of the bones were to be strain gaged, but because of the need to start testing in January 1981, and because the gaging equipment was still on order, this particular cadaver was chosen for testing without gages rather than all of a particular type of bone. The rationale was that such an approach would offer an opportunity to establish some fracture loads for each bone type and thus avoid early fractures which would result in only a few data points for the bones that were gaged. Fortunately, the gaging equipment arrived before number 3753 was complete, and the femora were fractured gaged. The one humerus was delayed because it was planned as a bending only test and the shorter bending carriage was still under construction.

After cadaver #3753 was complete all the femora were tested with the exception of those of cadaver #3793 and one from #3787. Again strain gages were the problem. Rosettes were required for the loading condition planned for #3793 and they were again on order. Therefore, two tibiae, #3787, were tested instead; they required only axial gages which were on hand.

After the femora (except for one, #3787) were finished, tibiae and humeri were tested in torsion while awaiting axial gages--on order.

Once these were received the tibias were finished with the exception of #3782 which were to be tested articulated with their fibulae. A humerus and two fibulae were tested in torsion before these last two tibiae were finished.

When the fabrication of the short bending carriage was complete, the remainder of the humeri were finished with exception of the two selected for the rapid rate tests. Then the remaining fibulae were completed bringing the static testing to a close except for the right femur #3787 which was at KUMC for CT scans.

Finally, the rapid rates were completed on 29 June 1981 and the last femur was finished as of 2 July 1981. Table 2.22 lists the entries made in the test log which shows the test flow from beginning of the testing until its termination.

Although the testing was often scheduled to utilize existing strain gages while awaiting to receive other gages that were on order, at no time was the supplier at fault. The shortage of gages really resulted from a lack of available information describing the type of strain gages best suited for large-scale whole bone testing. Gages were ordered on a trial and error basis. Before the testing began, certain numbers and types of gages were ordered that were considered best suitable for the tests. If one of these types proved acceptable it was reordered; if it did not it was replaced. Since some of the gages that proved to be the most adaptable were types not always stocked, they were often back ordered. The necessity to reorder and the resulting back orders, was the cause for such an incongruous testing plan.

Problems with the adaptability of the gages to the whole bone testing involved size and configuration mainly. The delta rosette turned out to be too tedious to solder and protect mechanically because two of its legs point in a direction opposite to the middle leg. Some rosettes and axials were too large for the curvature of the humerus and fibulae. These inadequacies along with the necessity for attached lead wires made gage selection more difficult and, because the replacement gages tended toward the unconventional they were often not on hand.

Table 3.1 Test log

1 January 1981 through 30 September 1981										LONG-RUN TEST LOG			
Test No.	Type	Culver No.	Spec. Type	Gages	Date Sched.	Date Comp.	Frac. Sket.	Photo.	Sect'd	Analyzed		Runs	Comments:
										SEM	Chem		
1	T	3753	RT	No	15/1	15/1						1	Last end rotating
2	T	3753	RF	Fully	17/1	---						1	Straining gage corroding
3	BN	3753	RT	No	18/1	18/1	11/3		9/6	22/7	4	4	Valid
4	BN	3753	RFb	No	19/1	19/1	No External Fracture		22/6	---	4	4	Valid
5	T	3753	LT	No	20/1	20/1	18/4	27/5	9/6	---	3	3	Valid
6	T	3753	RH	No	23/1	23/1	18/4	27/5	22/6	24/7	4	4	Valid
7	T	3753	LFb	No	25/1	25/1	18/4	27/5	22/6	23/7	4	4	Valid
8	T	3753	LF	R1	7/2	7/2	7/2	27/5	2/6	---	4	4	Valid
9	BN	3753	RF	R1 R2 1A	9/2	9/2	18/4	27/5	2/16	22/7	4	4	Valid
10	BM	3792	RF	R1 R2 L1	18/2	18/2	19/4	27/5	3/6	23/7	4	4	Valid
11	T	3792	LF	R1 R2 R3	20/2	20/2	19/4	27/5	9/6	23/7	1	1	Valid
12	CBN	3787	LF	R1 4A	25/2	25/2	19/4	27/5	3/6	---	3	3	Valid
13	BM	3782	LF	4A	27/2	28/2	19/4	27/5	9/6	---	3	3	Valid
14	CTN	3790	LF	R1 R2 L1 L2	4/3	4/3	4/3	4/3	15/4	---	3	3	Valid
15	T	3782	RF	R1 R2	5/3	5/3	5/3	5/3	15/4	---	3	3	Valid
14	CTW	3790	RF	R1 R2 L1 L2 6/3	6/3	6/3	6/3	6/3	9/6	23/7	3	3	Valid
16	CBN	3787	LT	R1 L1 L2 L3	9/3	9/3	9/3	7/4	15/4	---	2	2	Valid
17	CBW	3787	RT	R1 L1 L2 L3	13/3	13/3	13/3	7/4	9/6	---	3	3	Valid
18	T	3793	RF	R1 R2 R3	16/3	16/3	16/3	7/4	9/6	---	3	3	Valid
19	B-M	3793	LF	R1 R2 L1	16/3	16/3	16/3	7/4	19/6	---	3	3	Valid
20	T	3792	LT	R1 R2 R3	17/3	17/3	17/3	7/4	16/6	24/7	3	3	Valid
21	T	3793	RT	R1 R2 R3	17/3	17/3	17/3	7/4	15/6	23/7	3	3	Valid
22	T	3792	LH	R1 R2 R3	18/3	18/3	18/3	27/5	21/6	---	3	3	Valid
23	T	3793	RH	R1 R2 R3	18/3	18/3	18/3	27/5	21/6	23/7	3	3	Valid
24	BM	3792	RT	R1 R2 L1	30/3	30/3	30/3	22/6	5/7	---	3	3	Valid

Table 3.22 Test log continued

1 January 1981 through 30 September 1981				LONG-RANGE TEST LOG								
Test No.	Test Type	Cadaver No.	Spec. Type	Gages	Date Sched.	Intr. Comp.	Frac. Sket.	Photo.	Section	Analyzed	Runs	Comments:
25	CTW	3790	RT	R1 R2 L1 L2	1/4	1/4	1/4	29/5	15/6	23/7	3	Valid
26	CTW	3790	LT	R1 R2 L1 L2	4/4	4/4	4/4	27/5	15/6	---	3	Valid
27	BM	3793	LT	R1 R2 3A	6/4	6/4	6/4	27/5	19/6	24/7	3	Valid
28	T	3782	LH	R1 R2	8/4	8/4	8/4	27/5	22/6	---	1	Valid
29	T	3792	Lfb	R1 R2 R3	10/4	10/4	10/4	27/5	22/6	---	3	Valid
30	T	3793	Rfb	R1 R2 R3	13/4	13/4	13/4	27/5	22/6	23/7	3	Valid
31	T	3782	RT/Fb	R1 R2 R3 1A	15/4	15/4	15/4	27/5	16/6	---	3	Valid Tib/Fib Articulated
32	T	3782	LT/Fb	R1 R2 R3 1A	17/4	17/4	18/4	27/5	15/6	---	3	Valid Tib/Fib Articulated
33	B	3782	RH	R1	22/4	22/4	22/4	27/5	22/6	22/7	3	Valid
34	B	3753	LH	R1	24/4	24/4	24/4	27/5	22/6	---	3	Valid Very Plastic
35	B	3792	RH	6 A	25/4	25/4	25/4	27/5	5/7	---	3	Valid Not as plastic
36	CB	3793	LH	R1 R2 L1 L2	27/4	27/4	27/4	29/5	22/6	---	3	Valid
37	B-M	3793	Lfb	4 A	29/4	29/4	29/4	29/5	7/7	---	3	Invalid suspension chain not stick
38	CT	3787	RH	R1 R2 4A	1/5	1/5	1/5	22/6	7/7	---	3	Valid
39	BM	3792	Rfb	5 A	4/5	4/5	4/5	29/5	7/7	22/7	3	Valid
40	CT	3790	LH	R1 R2 L1 L2	6/5	6/5	6/5	29/5	21/6	24/7	3	Valid
41	CTW	3790	Rfb	R1 R2 L1 L2	9/5	9/5	9/5	29/5	8/7	24/7	3	Valid
42	CTN	3790	Lfb	R1 R2 L1 L2	14/5	14/5	14/5	29/5	8/7	24/7	3	Valid
43	CBN	3787	Lfb	R1 R2 4A	15/5	15/5	15/5	29/5	8/7	---	1	Valid
44	CTN	3787	Rfb	R1 R2 4A	18/5	18/5	18/5	22/6	9/7	---	3	Valid
45	Rapid	3790	RH	1 A	29/6	29/6	30/6	5/7	8/7	---	1	Valid
46	Rapid	3787	LH	1 A	29/6	29/6	30/6	5/7	8/7	22/7	1	Valid
47	CBM	3787	RF	R1 R2 L1 L2	2/7	2/7	4/7	5/7	8/7	23/7	2	Valid

#### 2.2.4.9 General Test Plan

Figures 2.30 - 33 show the loading conditions planned for each of the 48 bones. The loading conditions were arranged among each bone type to achieve one purpose, the construction of a bending-stress/shearing-stress interaction curve.

Except for special cases, four bones of each type were selected to establish the fracture moments resulting from torsion only and four to establish the fracture moments from bending only. For the torsion only condition, two of the bones were selected for eversive rotation and two for inversive rotation. For the bending only condition, two of the four bones were tested using a medium load spacing one with a large spacing and one with a small spacing.

For each bone type except the humerus, the combination of torsion and bending involved four bones. Two bones were tested with a narrow load spacing and eversive rotation while the other two were tested using a wide spacing and inversive rotation. One bone from each loading was tested with torsion dominating and bending held constant; the other bone was tested with bending dominant and torsion held constant.

The plan discussed provides just enough data to establish the interaction curves. The torsion only tests and bending only tests provide the data on the axes of the curve (Figure 2.34) while the combination loadings provide two points which lie in the quadrant enclosed by the axes. For the femur, these four points are available to roughly describe an interaction curve for both a wide and a narrow load spacing. However, for the tibiae and fibulae, since one cadaver was tested with the two bones articulated, four data points are available only for a narrow load spacing; the bending only test for the wide roller spacing was not done because the articulated bones were tested in torsion only.

The rationale for testing two bones of each type under bending only conditions with a medium load spacing was to compare the fracture loads for repetition. The tibiae and fibulae from the one cadaver were tested articulated to see what affect, if any, the fibulae would have on the fracture twisting moment. One of these was also tested as an eversive rotation while the other was inversive.

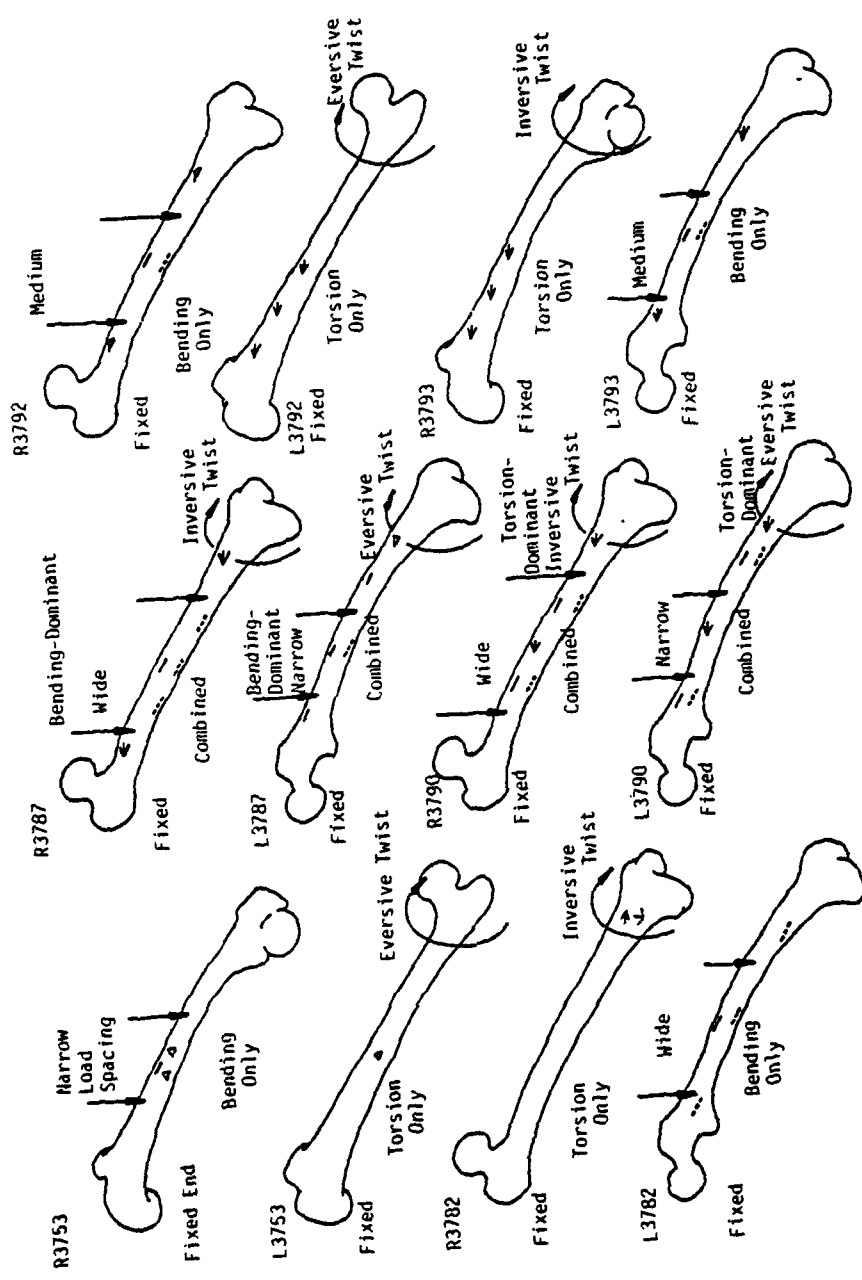


Figure 2.30 Femora loading conditions.

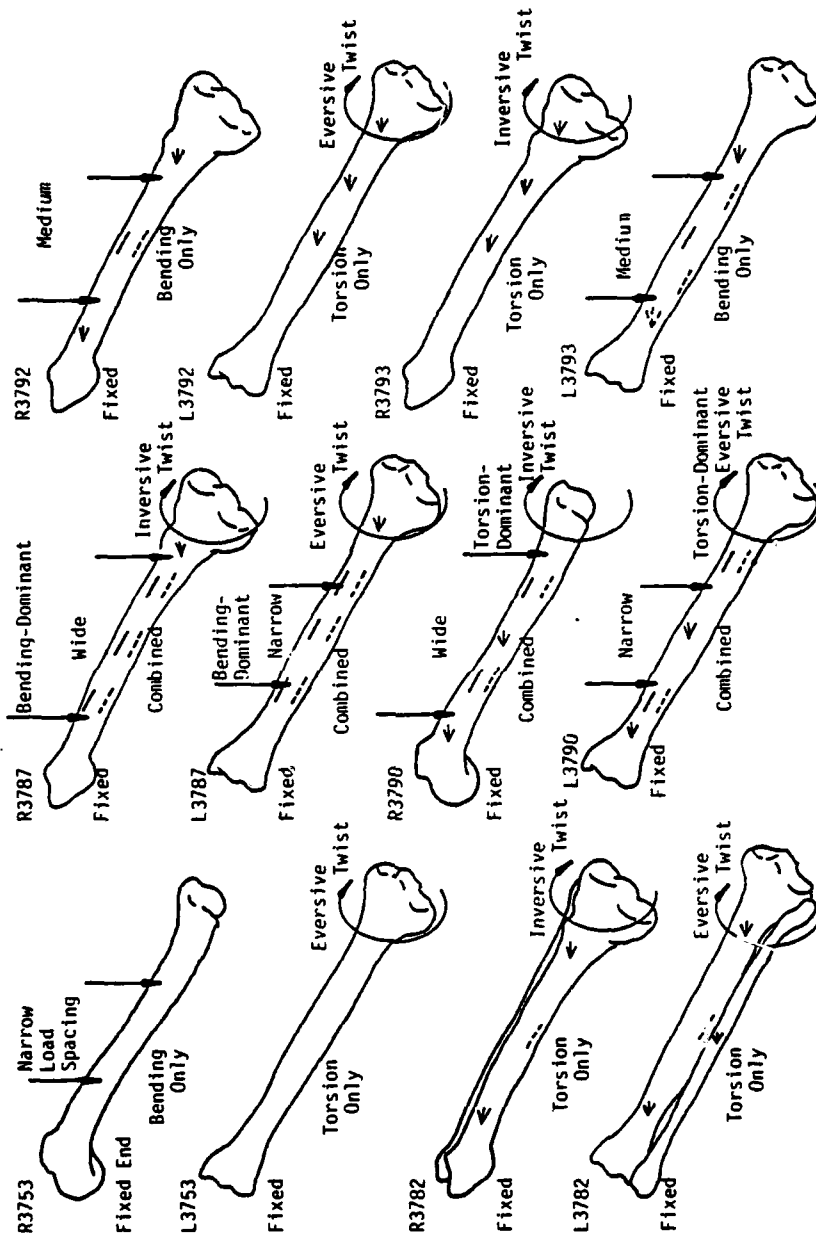


Figure 2.31 Tibiae loading conditions.

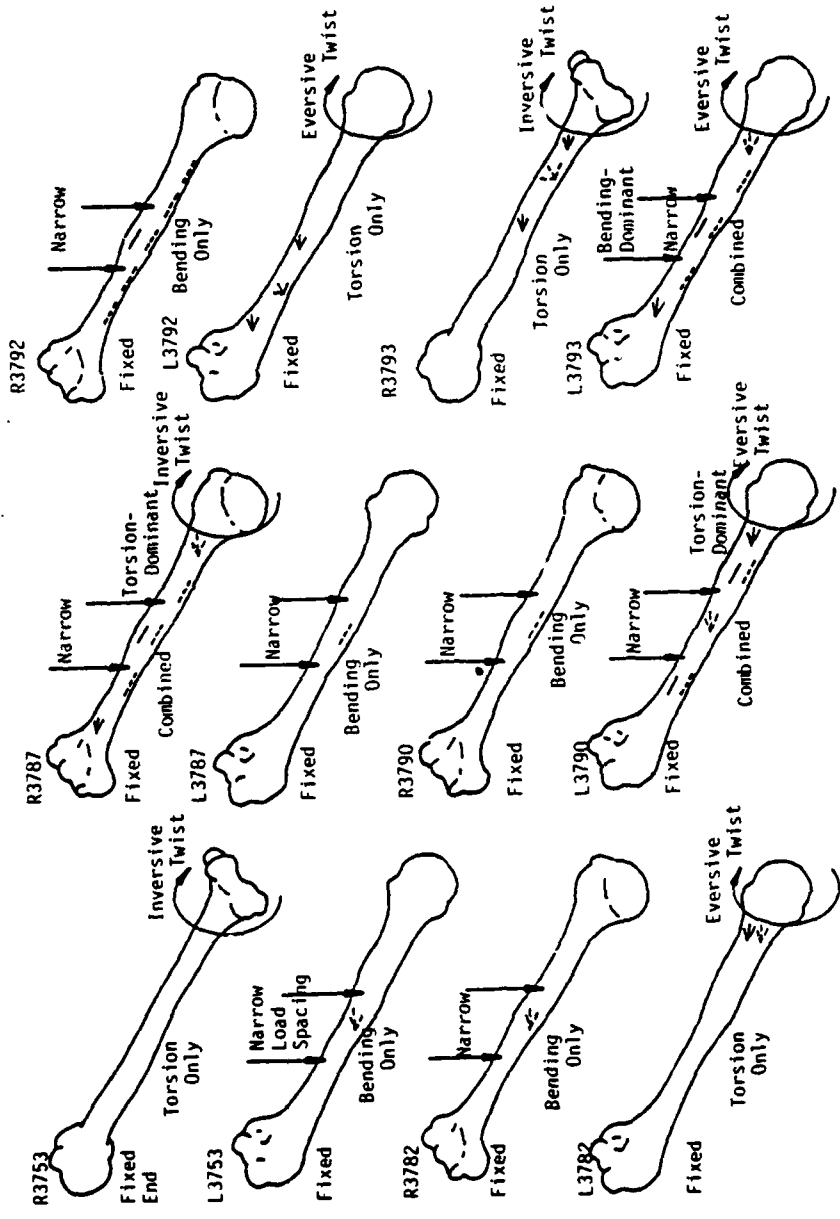


Figure 2.32 Humeri loading conditions.

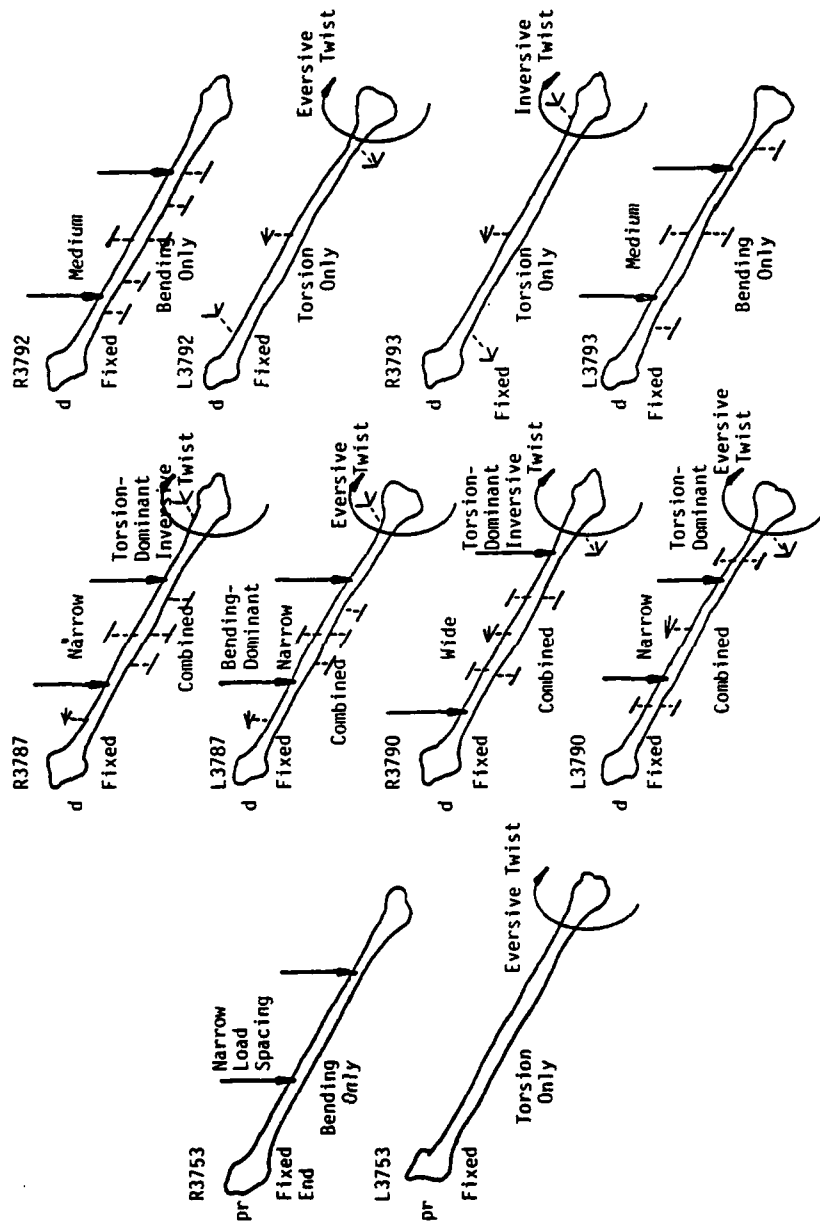


Figure 2.33 Fibulae loading conditions.

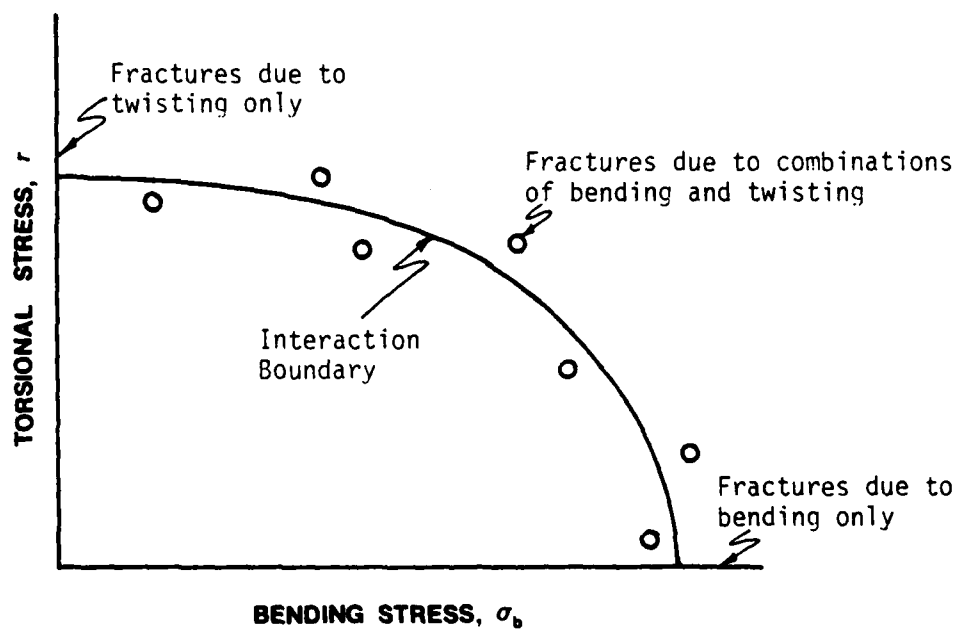


Figure 2.34 Schematic of an Interaction Boundary

The only other major deviation from the above plan was the humerus loading conditions. Since the roller spacing was fixed in the smaller bending carriage, all the tests involving bending used only one load spacing. The one load spacing was planned to provide more data points for a better prediction of the interaction curve as well as for repetition. The humerus was selected over the other bone types for two reasons: (1) its short length limited the roller spacing possible; (2) the humerus is the bone of interest since it fractures most often during ejection as a result of flailing.

With the fixed load spacing, three humeri were available for bending only using a static rate and two for bending only using a "rapid" rate. The combined conditions involved two humeri tested under torsion/dominant loadings using inversive rotation and one bone under a bending dominant condition with eversive rotation. Two humeri were tested under torsion only conditions using eversive rotation and two using inversive rotation. This arrangement provided enough data points for two interaction diagrams -- one representing an eversive rotation and one an inversive rotation.

In summary, two twisting-moment/bending-moment interaction diagrams are available from the data for each bone type -- wide load spacing with eversive rotation and a narrow spacing with inversive rotation for the femur, tibia and fibula and, a narrow spacing with eversive rotation and a narrow spacing with inversive rotation for the humerus. Also available for comparison are twisting moments with an eversive and inversive sense causing fracture in the articulated tibiae/fibulae as well as bending moments causing fractures in humeri under rapid conditions. The rapid rate loading schedule was applied to the humeri to better describe their apparent inelastic behavior as well as illustrate any increase in ultimate values associated with increases strain rates.

#### GENERAL LOADING SCHEDULE:

During the first few tests, each bone was loaded in four cycles. The first cycle was a "wring-out" cycle used to seat the specimen into the clamps. The next two cycles were used to gather additional data points as the limit load was increased for the succeeding cycle. In the fourth cycle the bone was fractured. The procedure was established to

avoid unexpected, early fractures with few data points which might result from inaccurate limit load estimation. After several tests, when the confidence in ultimate load prediction was bolstered, the number of loading cycles per test was reduced from four to three.

Limit loads below the ultimate loads representing fracture causal bending and twisting moments were calculated with the simple mechanics of materials equations. The bending load was determined using the bending stress formula (Section 2.2.2) applied to a round tube under four point bending. The second moment of inertia in the equation was calculated from an average inside and outside diameter measured at a specific location along the diaphysis as depicted by the anterior posterior and mediolateral x-rays taken of the bone. Using the ultimate strength of Reilley and Burstein [1] as the stress in the equation, the fracture load, as sensed by the load cell in the bending load application mechanism, was estimated. This was done at ten stations along the bone and the lowest value found among the stations was assumed the load that would cause initial fracture.

The same approach was taken for the twisting load except the torsional stress equation was used. The bone was again idealized as a round tube whose average inside and outside diameters were determined as described above. These diameters were used to determine the polar moment of inertia for the torsional stress equation. Once again Reilly and Burstein's value for an ultimate shearing stress was used as the stress in the equation to estimate a torsional fracture load; this load corresponds to the load sensed by the "control" load cell (Section 2.2.4.6) in the torsional load mechanism. Even though the bones fail because of the tension that results from the torsional shear, this shearing stress is applicable since it has the same value as this tension stress under torsion only loading conditions. Torsional fracture loads were also calculated at several stations along the diaphysis with the lowest value assumed to cause initial failure.

These estimated fracture loads were used to plan the load schemes for those bones tested from cadaver #3753. (Number 3753 was chosen to establish representative fracture loads for the bending only and torsion only loading conditions.) Using a limit load of 67% of the estimated ultimate load, the test cycles were planned to include 10 steps with

each step equating to approximately 10% of the cycle limit load. Each increment was set at convenient values such as 10 lbs., 25 lbs., 12.5 lbs., etc. Since #3753 was the first set of bones tested, each bone was fractured after four cycles to avoid premature failures and loss of data points. With some of these bones the limit load of each succeeding cycle was increased 10% - 30% above the limit load of the preceding cycle.

Once each of the bone types had been fractured both by bending and by torsion, the actual fracture loads from the test were used to predict the fracture load of the next bone tested respective of bone type. As additional bones were fractured, the new fractured loads were averaged with past fracture loads, respective of loading condition and bone type, to predict future ultimate loads. The limit loads were always 67% of the ultimate.

#### BENDING ONLY LOADING SCHEDULE:

Before the tests were begun, a Load Plan, Strain Data Sheet and Deflection Data Sheet (Section 2.2.4.7) were prepared showing the limit and ultimate loads, the increment load values, the deflections and strain channels involved in the test. Each of these forms were completed for each load cycle.

When all the equipment was properly adjusted and set up and all operators were sure that all preparations were complete, loading for the wring-out cycle would begin. For tests involving bending, the weight of the bending load mechanism was set in the BLH system on the channel connected to the bending load cell; thus, the loads read on the BLH representing bending would include the weight of the mechanism not sensed by the load cell.

Just prior to beginning a cycle, the strains on all the channels of the Vishay were read and recorded. These values represented the unsettled system values that were later deducted from the strains recorded for the various load increments (Section 2.2.4.6).

The next step in a cycle involving bending loads was the recording of the strains induced by the weight of the bending load mechanism. To accomplish this, the bending load mechanism was lowered with its suspension turnbuckle until the suspension chain was slack. The turnbuckle in

the loading mechanism was inspected to ensure that it was slack and not extended, pushing up on the bending load cell. The strains were read and recorded.

Next the load established for setting the dial indicators to zero was applied. Normally for all bending this was 111.2 N. The dial indicators were zeroed at this value, rather than at a zero load, to remove the "dead band" from the osteoclast. The "dead band" existed because of the mechanical connections and tolerances in the osteoclast as well as because the play between the molded specimen and the clamps. At this load increment, strains and loads were read and recorded. The small dial indications on the dial indicators were also recorded to pinpoint the number of sweeps of the larger dials. This was necessary since the indicators show a zero deflection when the indicator probe is fully extended. The use of this small dial reading is fully explained in Section 2.2.4.7.

From this point on the procedure is repetitious until the limit load occurs or the bone fractures. Each load increment is set and the strains, deflections (including changes in the small dial indicating passage of the large dial through zero) and the load indicated are read and recorded. The readings were accomplished as quickly as accuracy would allow. Usually, the loads were read and recorded when the person recording strains was halfway through his readings. This point is significant for the higher loads whenever creep in the bone caused the loads indicated to fall off. Since the loads recorded essentially represented the average of the maximum and minimum load that could occur while at a load increment, the strains\* thus recorded were not associated with a load lower or higher (considering settling time) than that which caused them.

When the limit load was reached, the bending load was quickly but smoothly returned to zero. The bending carriage was raised with its suspension system until the rollers were clear of the bone. Post-cycle strains were then read and recorded for a zero bending load.

\*Because the osteoclast is a constant amplitude device, the strains and deflections remain stable while the load falls because of local creep. Local creep is increasing strain at specific locations of the bone when the load remains relatively constant.

The remaining cycles were accomplished in the same manner. The Vishay was rebalanced between cycles and the BLH was set (balanced) to the appropriate value at the correct point in the cycle. During the last cycle, the BLH control channel (Section 2.2 4.6), was monitored continuously to catch the fracture load when it occurred. Fracture was defined as any substantial drop in the indicated load.

#### TORSION ONLY LOADING SCHEDULE:

Torsion only test cycles progressed much the same as the bending only tests. Strains were read at the start of a cycle with no twisting moment applied and the dial indicators were set to zero with a torsional load of 44.48 N applied. Since there was not a step requiring adjustment of the BLH for the weight of the load mechanism, it was balanced zero. Also, both indications of the two load cells in the torsional load mechanism were read and recorded instead just one. Otherwise the cycles were started and finished in the same manner as the bending only test cycles except another load mechanism was used.

#### COMBINED CONDITIONS:

The combined loading conditions obviously incorporated the steps of both the procedures described above. Strains were read with no bending or torsion applied. The bending mechanism was lowered, the strains read and its weight set into channel 1 of the BLH. A bending load of 111.2 N and a torsional load of 44.48 N were set simultaneously and the dial indicators zeroed. Each advancing load increment was set on each channel of the BLH beginning with the "control" channel and followed by the other channel. The loading devices were adjusted, switching between channels 1 and 2 on the BLH, until the load increments were satisfactorily set. All the required readings were recorded and then the next load increment was begun. When the load increment was passed where the dominating load was increased and the other load was held fixed, the fixed load was still adjusted at each advancing increment of the dominating load to ensure that it remained within 2.5 N of its required value. Such adjustment was necessary because the cross-sectional shapes of the bones (especially the tibia) caused the fixed load to change as the dominant load was increased.

#### RAPID RATE CONDITIONS:

Rapid rate bending was accomplished in the same manner as static bending except for a difference in data acquisition and the loading schedule. Although the loading was far from being an impact, the two humeri were bent as rapidly as possible while contracting the bending turnbuckle manually. Consequently the strain and load indications changed too quickly to record them by hand during the test. Rather than become involved in high response strip recorders, the BLH digital readout for the bending load cell was set on top of the Vishay strain indicator and the two were recorded on video tape simultaneously during the two rapid rate tests. The tape was then simply reviewed, frame by frame, at a later date, and the strains and corresponding loads transcribed to a data sheet by hand.

The loading schedule involved the same steps as the static tests up until the time for the first load after lowering the bending carriage onto the diaphysis. At that point, the turnbuckle in the bending mechanism was contracted in a smooth, quick manner with equal turns until fracture occurred. Thus, the rapid rate tests were completed in 12.0 sec. as compared for 600 seconds for the static tests; this is comparable to strain rates of  $5 \times 10^{-4}$  cm/cm/sec for the rapid rate loadings and  $10^{-5}$  cm/cm/sec for the static tests.

#### GENERAL REMARKS:

At the beginning of the testing programs all deflections were recorded -- even the bending and slope deflections when torsion only was the load condition and the twist angle deflection when bending only was the condition. This was initially done to see if any such deflections would result (within the sensitivity of the equipment) as a result of the bone curvature. Later in the program, only these deflections expected to display significant changes were recorded.

#### 2.2.4.10 Bone Sectioning

All the bones which were strain gaged were cut at specified stations along their length to determine the gage locations on the cross sections. This information was used in the data reduction to provide a qualitative depiction of the location of the strain gages around the

periphery of the diaphysis. These locations were considered important as far as judging the magnitude of the indicated stress relative to other stresses possible around the section. At other stations along the diaphysis, sections of each bone were removed completely for ash and porosity analyses at the Kansas University Medical Center. The stations for the medical sections were chosen by finding the positions along the diaphysis which represented the middle of all the fractures for a specific loading condition (i.e., bending, torsion, or combined bending and torsion) of a particular bone type. The position was approximated as the mean of the fracture mid-point. The mid-points were defined as the middles of the longitudinal distances parallel to the diaphyseal axis and bounded by the ends of the fractures. The means were expressed as percentages of the half diaphyses with respect to bone type and loading condition. Figures 2.35-2.37 show the locations of the mean values with reference to the plotted fracture lengths. The M.C. sections were cut from either side of these specified planes of interest. Each section was approximately one centimeter wide and was cut and handled with great care.

Lastly, small chips were removed along fracture surfaces for study under a scanning electron microscope (SEM) with the intent of determining the type of failure involved. Some examples of these observations are shown and discussed in Section 2.4. In handling the bones and removing the SEM sections, great care was taken not to mar the fracture surfaces. When possible the SEM sections were removed before the bone was reassembled in the mold.

Before cutting, certain reference axes were marked on the diaphyseal surface to relate the strain gage locations with the Osteoclast axis. The different states of fracture required different techniques in locating the reference axes on the bones. If the fractured bone was still in one piece, it was simply placed on a table top and the tops of the mold placed on the tops of epoxy blocks cast on the ends of the bones. The mold tops were positioned on the blocks to mimic their position in the mold. The Osteoclast axes were assumed to coincide with the mold axes and, so, these were transferred to diaphysis using the incised marks on the mold tops. For the bone in one piece, using the mold tops provided a convenient way of marking two of the three

FRACTURE END POINTS:

- |        |   |      |
|--------|---|------|
| ▽ 3753 | × | 3782 |
| □ 3792 | ○ | 3790 |
| ● 3793 |   |      |

DISTAL

FRACTURE LENGTHS: ———

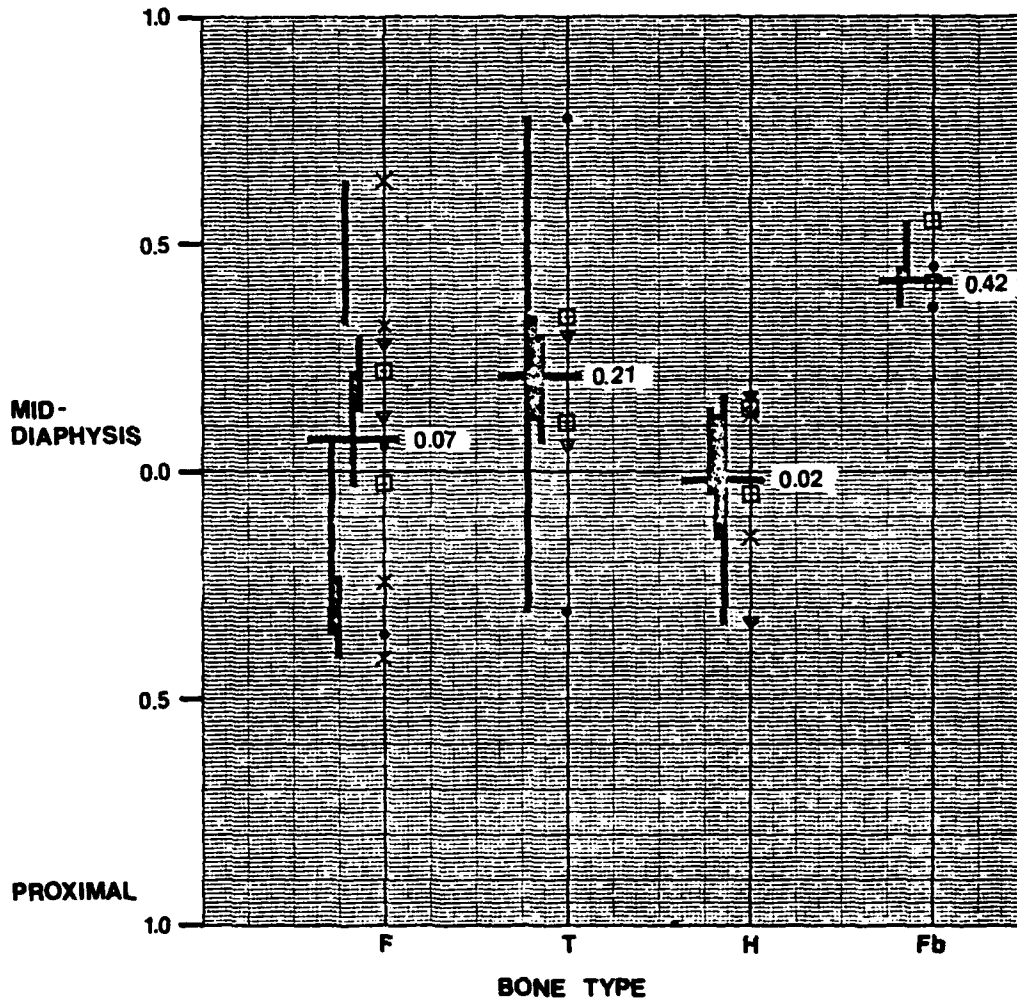


Figure 2.35 Medical Center section litation -- bending.

FRACTURE END POINTS:

▽ 3753

× 3782

● 3793

□ 3792

FRACTURE LENGTHS: ———

DISTAL

MID-DIAPHYSIS

PROXIMAL

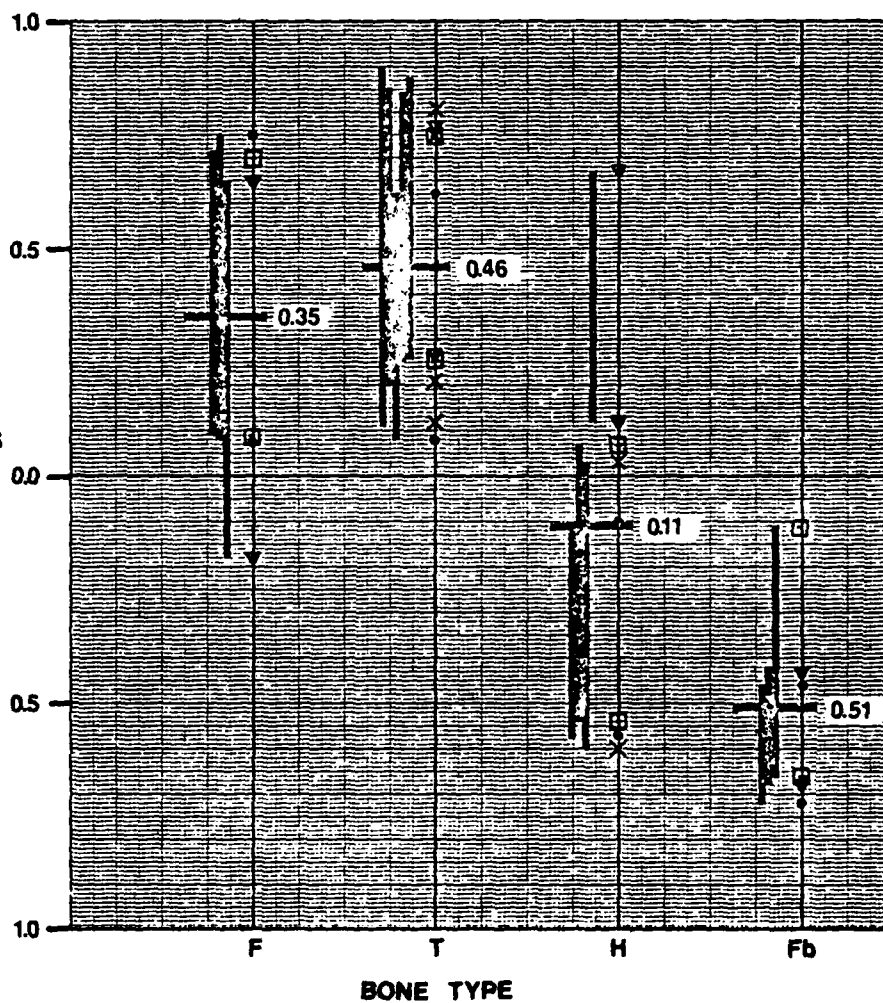


Figure 2.36 Medical Center section litigation -- torsion.

FRACTURE END POINTS:

▽ 3753

× 3782

● 3793

○ 3790

○ 3787

FRACTURE LENGTHS: 

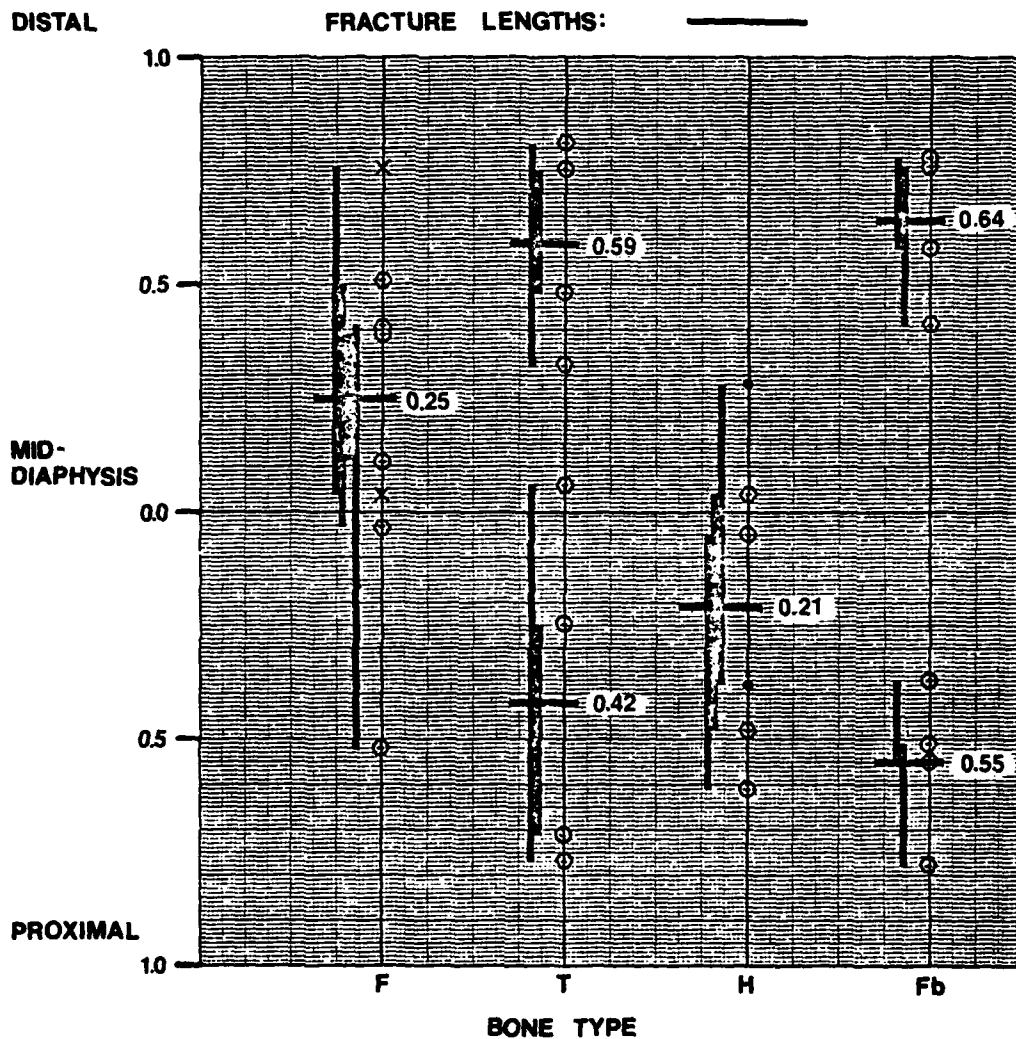


Figure 2.37 Medical Center section litigation -- combined.

reference axes -- one on top and one on the bottom with respect to its orientation in the mold. The third axis was acquired after the bone was clamped back in place in the mold. Its position corresponded to the incised marks on the sides of the mold itself. These were transferred by sight to the diaphysis along a rubber band which was stretched between the mold ends and which was seated in the incised marks (arrow, Figure 2.38). For bones which were in more than one piece, the ends were first clamped in position in the mold. Then the individual pieces were attached and held in place by wires which were wrapped around the shattered diaphysis and twisted together until tight. The axes were marked on the top and two sides of the diaphysis by transferring the incised marks on the mold as described above.

For some of the bones, additional data had to be taken before cutting could occur. One important measurement was that of the material axis which was necessary to calculate the orthotropic principal stresses. These directions were obtained by placing a small, acetate protractor with a scale varying from one to ten degrees over the center of each gage location and estimating the deviation of the "grain" direction in the bone tissue from the longitudinal axis of the gage. Note that there is no established correlation between this grain and the osteon axes; it is simply an intuitive assumption.

After the axes were marked and the material directions acquired, the cross-sections of interest were marked along the diaphysis. Their locations were measured with respect to the mid-diaphysis using a millimeter scale. The locations marked were either a cross-section selected for the M.C. or one that contained one or more strain gages. Cuts were usually made to either side of the mark using a hacksaw. The cut to free each section was then made arbitrarily, approximately one centimeter either side of this first cut. All cuts were made normal to the longitudinal axis of the mold while care was taken not to damage tissue adjacent to the cross-section of interest.

When all the sections had been cut free, they were traced onto a piece of acetate. Each piece of acetate had permanent axes marked on them and these were kept aligned with the axes marked on the section while tracing the section. Figure 2.39 shows the tracing of a section.

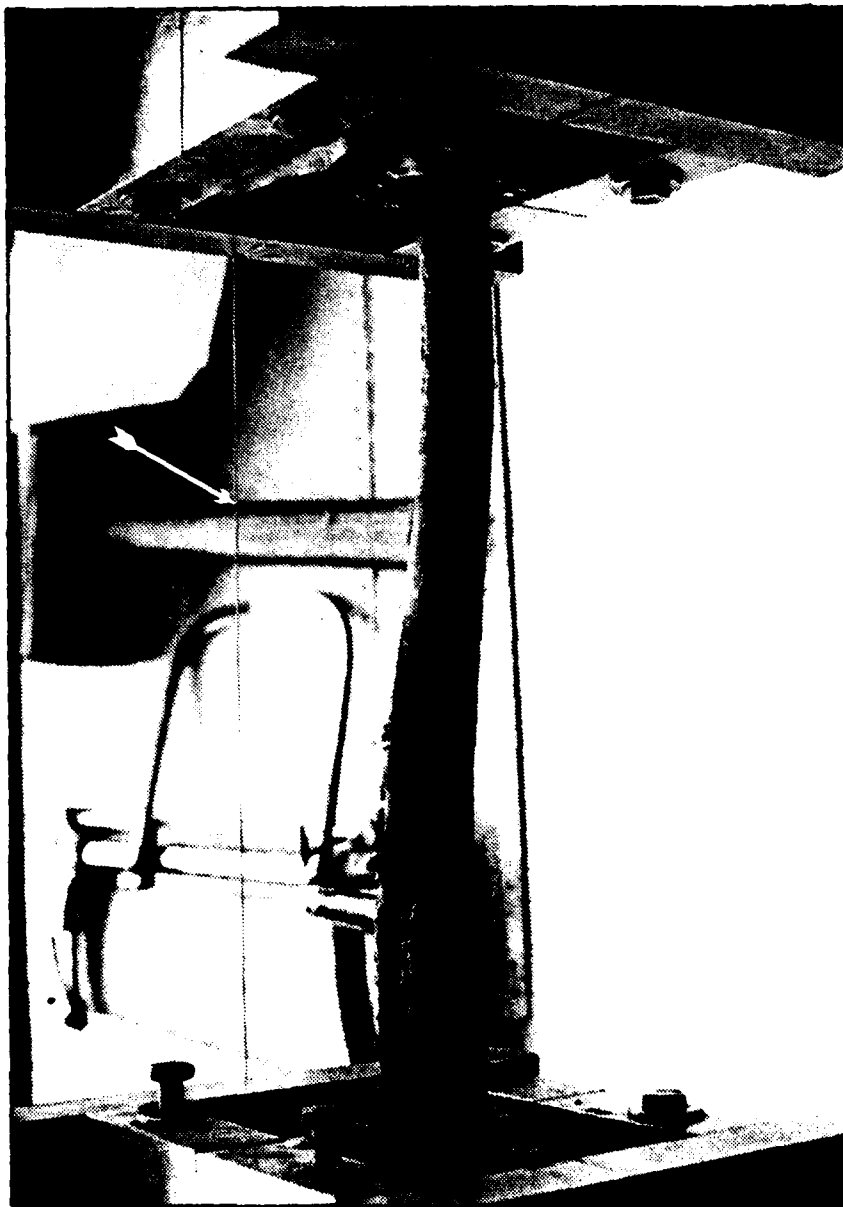


Figure 2.38 Marking and cutting of sections using the mold as a clamp.



Figure 2.39 Tracing a section of bone onto an acetate sheet.

The sections removed for strain gage placement were bagged and refrozen. The M.C. sections were sealed individually in a small plastic bag and sealed and labeled with freezer tape. The SEM chips were placed individually in glass specimen jars with a few drops of Ringer's solution, labeled, and frozen until time for the SEM analysis.

During the marking, cutting and tracing, the orientation of each section was carefully tracked to assure its proper depiction. The tracings were eventually transferred to Figures 2.91 - 2.138.

## 2.2.5 Results

### 2.2.5.1 Data Reduction

#### DATA CORRECTIONS:

Because the deflections were recorded beginning with a load other than zero and because they were read as descending values (dial indicator probe extended as deflections increased), a quick and accurate method was necessary to plot the deflections against their loads from a zero load to fracture. In addition, a method was required to convert the torsional loads to twisting moments and at the same time correct their values for errors introduced at large angles of twist. To make these corrections and conversions, one small computer program was assembled for a Hewlett-Packard 9825A desk top computer and 9872A plotter. The program contained three options providing plots of deflections or strains against their loads. One option converted torsional loads to twisting moments, while correcting the loads for errors and plotted these against the associated twist angles. The second option plots deflections against loads and the third axial strains against loads.

In the first option, a linear regression curve fit is applied to the torsional loads and associated deflections. The resulting curve is used to determine an offset distance (Fig. 2.40) which will shift the deflections toward the right so the load-deflection curve passes through zero. Thus the deflection data is corrected for starting at a specified load rather than zero (Section 2.2.4.9).

Next, the shifted data is converted to angles, in degrees and the twisting moments calculated. During this step, the torsional loads are corrected for errors that occur at large angles of twist. The errors

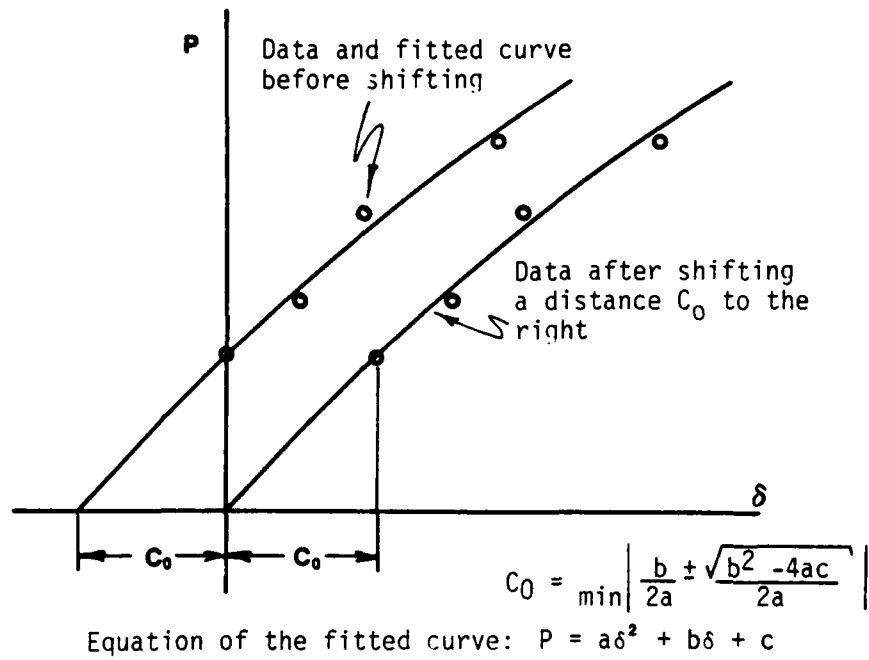


Figure 2.40 Shifting the data points to obtain a correct load-displacement plot.

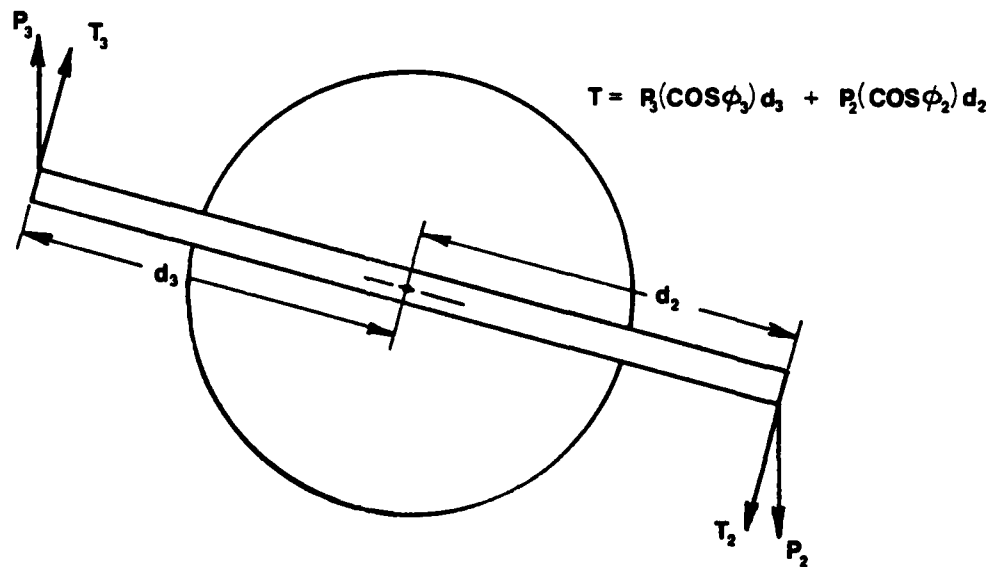


Figure 2.41 Correcting recorded torsional loads for the actual twisting force component.

result from the rotation of the load vectors away from a direction normal to the torque tube as the twist angle increases (Fig. 2.41). Only the component of the load vector normal to the tube contributes to the twisting moment at these large angles and it is this component which is used to determine the actual twisting moment.

To complete the entire process involves curve fits of two kinds. The first is a first order applied to the torsional loads and their respective deflections. This fit is accomplished once and is necessary to determine the twist angles for each load that are required to convert the torsional loads to twisting moments. Once the moments have been found, a second order curve is derived which expresses the twisting moments as a function of twist angles. This curve is then used to determine a new offset for shifting the twist angles to the right. Thus, corrected, the angles are introduced again into the algorithm for converting and correcting the twisting moments to produce an updated set of moments. With these new moments and the twist angles, a new second order curve is found providing an updated offset. The offset is added to the angles and the process repeated. Reiteration occurs until the new twisting moment at the first load increment is within 1% of the previous calculated moment. Once this criteria is met, the final offset is added to the angles and the twisting moments plotted against these corrected angles. Note that the twisting moments and angles plotted are those from the data and not values generated by the least squares polynomial; the curve fit is used only to shift the angles to the right so the curve passes through zero.

The second option also requires a linear regression curve fit of a first and second order; however, there is no conversion of loads to moments or deflections to angles. This option simply expresses the deflections recorded as ascending values and shifts them to the right. There is no reiterative process involved. The first order fit is used for the first pass and the second order fit for the second pass. The data plotted is simply the recorded loads against the recorded displacements which have been shifted to the right and changed to an ascending order.

The third option involves no curve fits. It simply plots recorded loads against recorded strains. The curve fits are not required since strain is recorded from zero load.

To apply the program, the user inputs the loads and deflections as they are recorded. These are echoed, the conversions and/or corrections accomplished and the updated data printed. The updated data is then stored on cassette tape. Before plotting the program selects the range of the axes required and plots the converted or updated data.

#### STRAIN ROSETTE ANALYSIS:

Electrical resistance strain gage rosettes are commonly used for stress analysis at a point on a structural part. These gages sense strain in three directions and allow the determination of stresses using an orthotropic plane stress assumption. To convert the three strain readings to principal stresses and strains, a computer program was written using the methods described in this section. The program was written for use on an HP 9825A desktop calculator with an HP 9872A digital plotter.

The strain data obtained from each of the three legs of the strain rosette were input with the corresponding load and torque values and stored on file for future recall. These strain readings were then corrected for transverse sensitivity [3]. The corrected strains were converted to normal strains and shear strains in a x-y axis system shown in Figure 2.42 using the strain transformation equations, where  $\beta_a$ ,  $\beta_b$  and  $\beta_c$  are the angles of the gages from the x-axis.  $\epsilon_x$ ,  $\epsilon_y$  and  $\gamma_{xy}$  result when the equations,

$$\begin{aligned}\epsilon_a &= \frac{\epsilon_x + \epsilon_y}{2} + \frac{\epsilon_x - \epsilon_y}{2} \cos 2\beta_a + \frac{\gamma_{xy}}{2} \sin 2\beta_a \\ \epsilon_b &= \frac{\epsilon_x + \epsilon_y}{2} + \frac{\epsilon_x - \epsilon_y}{2} \cos 2\beta_b + \frac{\gamma_{xy}}{2} \sin 2\beta_b \\ \epsilon_c &= \frac{\epsilon_x + \epsilon_y}{2} + \frac{\epsilon_x - \epsilon_y}{2} \cos 2\beta_c + \frac{\gamma_{xy}}{2} \sin 2\beta_c\end{aligned}\quad [5]$$

are arranged in a matrix format and the system solved through matrix inversion and multiplication.

The strains in the material direction ( $\epsilon_1$ ,  $\epsilon_2$ ,  $\gamma_{12}$ ) were found by subtracting the material direction angle  $\alpha$ , shown in Figure 2.42, 2.43, from each gage angle and using the resulting angles and  $\epsilon_1$ ,  $\epsilon_2$  and  $\gamma_{12}$  to replace  $\beta$ ,  $\epsilon_x$ ,  $\epsilon_y$  and  $\gamma_{xy}$  in the above equations.

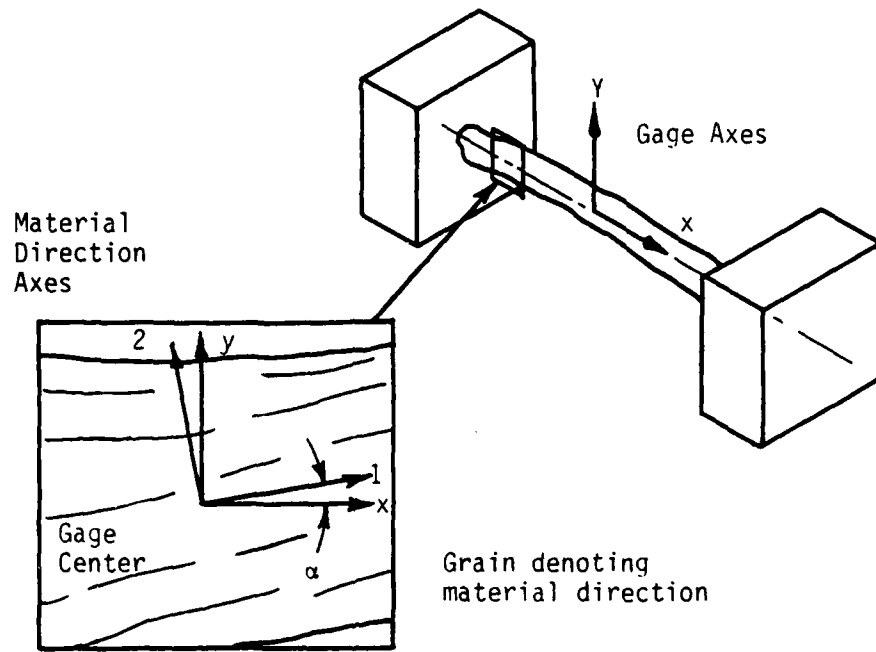


Figure 2.42 Strain gage axes in relation to material axes.

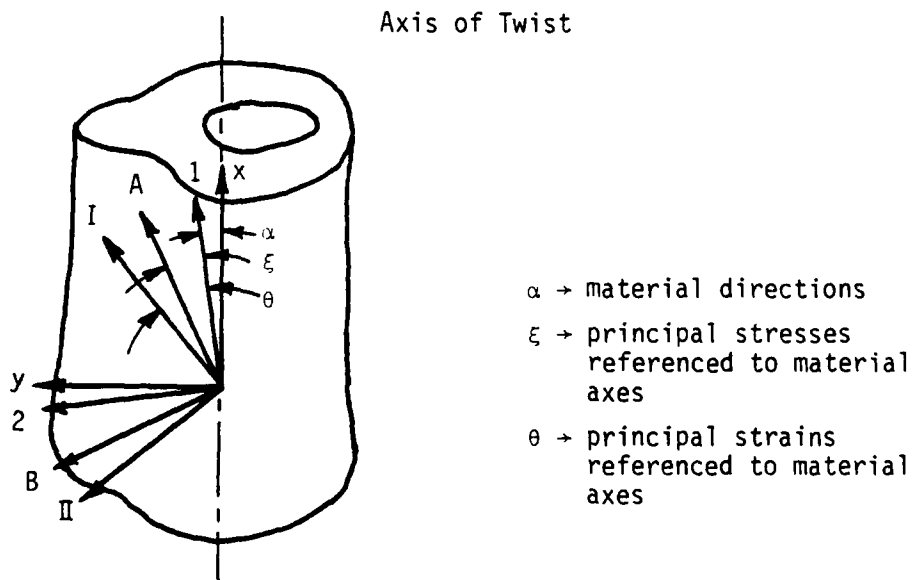


Figure 2.43 Angular relationship between gage axes, material direction and principal axes.

The principal strain axes were located with respect to the 1-2 axes as the angle given by:

$$\tan 2\theta = \frac{\gamma_{12}}{\epsilon_1 - \epsilon_2}$$

Since, relative to these axes, shear strain is zero, the principal strains were found using the strain transformation equation:

$$\begin{pmatrix} \epsilon_I \\ \epsilon_{II} \\ 0 \end{pmatrix} = [T]^{-1} \begin{pmatrix} \epsilon_1 \\ \epsilon_2 \\ \gamma_{12} \end{pmatrix}$$

where

$$\begin{bmatrix} \cos^2\theta & \sin^2\theta & -2\sin\theta\cos\theta \\ \sin^2\theta & \cos^2\theta & 2\sin\theta\cos\theta \\ \sin\theta\cos\theta & -\sin\theta\cos\theta & \cos^2\theta - \sin^2\theta \end{bmatrix} = [T]$$

The maximum shearing strain,  $\gamma_{\max}$ , which occurs at 45 deg. to the principal strain axes was found as:  $\gamma_{\max} = \epsilon_I - \epsilon_{II}$ .

The principal stresses were found by first calculating the stresses in the material direction ( $\sigma_1, \sigma_2, \tau_{12}$ ) using:

$$\begin{pmatrix} \sigma_1 \\ \sigma_2 \\ \tau_{12} \end{pmatrix} = [S] \begin{pmatrix} \epsilon_1 \\ \epsilon_2 \\ \gamma_{12} \end{pmatrix}$$

The S matrix was the reduced stiffness matrix which accounts for the material properties. Since bone is anisotropic, these properties differed with direction. The engineering constants for human femoral compact bone as determined by Reilly and Burstein [1],

$$\begin{aligned}
E_{11} &= 12.0 \text{ GPa} \\
E_{12} &= 11.5 \text{ GPa} \\
G_{12} &= 3.28 \text{ GPa} \\
\nu_{12} &= 0.46
\end{aligned}$$

along with equations 3 + 8 of [4] were used to generate,

$$[S] = E_{11} \begin{bmatrix} 1.16 & .36 & 0 \\ .36 & .79 & 0 \\ 0 & 0 & .19 \end{bmatrix}$$

The angle of transformation of the principal stress axes ( $\xi$ ) was found as,

$$\xi = \frac{1}{2} \tan^{-1} \frac{2\tau_{12}}{\sigma_1 - \sigma_2}$$

The principal stresses were then calculated using the same transformation equation as used to find the principal strains with  $\theta$  replaced by  $\xi$ . Finally, the maximum shearing stress ( $\tau_{\max}$ ) was found by:

$$\tau_{\max} = \frac{\sigma_A - \sigma_B}{2}$$

The results of the calculations were printed in tabular form and plotted versus load or torque whichever was dominant.

#### NONDIMENSIONALIZATION:

A third computer program was written to calculate the theoretical failure loads of four human long bones subjected to either torsion or four-point bending. Failure loads in the program were computed for several stations along the diaphysis of a bone and these were compared to the failure load actually encountered during the bending or torsion tests performed in the laboratory. The load comparison was used to locate a theoretical station along the bone where failure was likely to have occurred.

This theoretical station for failure was then used to define a parameter with which bending-torque interaction diagrams were defined

for each type of bone. For instance, if the data from several femora broken in the bending and torsion laboratory tests were input into the program, the results might indicate that the initial failure location of all bending fractures was ten percent of the total length of the bone as measured from the proximal end. Similarly, the torsional fractures may have been determined to start at sixty percent of the total length. At these locations a parameter such as the average outer diameter of the cross-section of the bone or section modulus could then be selected to "nondimensionalize" the interaction diagrams. Once the interaction diagram for femora (or other types of bones) has been "nondimensionalized" by this parameter, it may be used to predict the bending, torsion, or combination of bending and torsion loads necessary to cause any femur to fail.

Contained within this report are four sections explaining the development and use of the program. The first is a summary of the function of the computer program and the intended use of the output it generates. The second section describes how x-rays of four human long bones are aligned and traced to provide the geometric data input to the program. A third section discussed the output of the program, and identifies the parameters chosen to nondimensionalize the interaction diagrams. The last section identifies some possible sources of error and recommends some procedures that might reduce the chance of error for future use.

#### X-ray Tracings

To determine the inner and outer diameters of a bone, a two-dimensional picture of the bone was digitized with the HP plotter. The picture was a tracing of the inner and outer cortical walls of roentgenograms of the bone. Since one view of a bone does not provide a clear picture of the diameters because they vary, with viewing plane, two different views were traced, and an average of the diameters used for further calculations. A reduced tracing is pictured in Figure 2.44, showing the steps outlined below.

The two views were aligned, one below the other, such that their cross-sections lay in the same plane. This was accomplished by aligning their mid-diaphyses in the same plane and placing the axes of the two views parallel to each other. For the femur, tibia, and numerus, the

Maximum Length: 317 mm  
 Length Ratio: 1  
 % Magnification: 1.3%  
 Roller Spacing: 63.5 mm

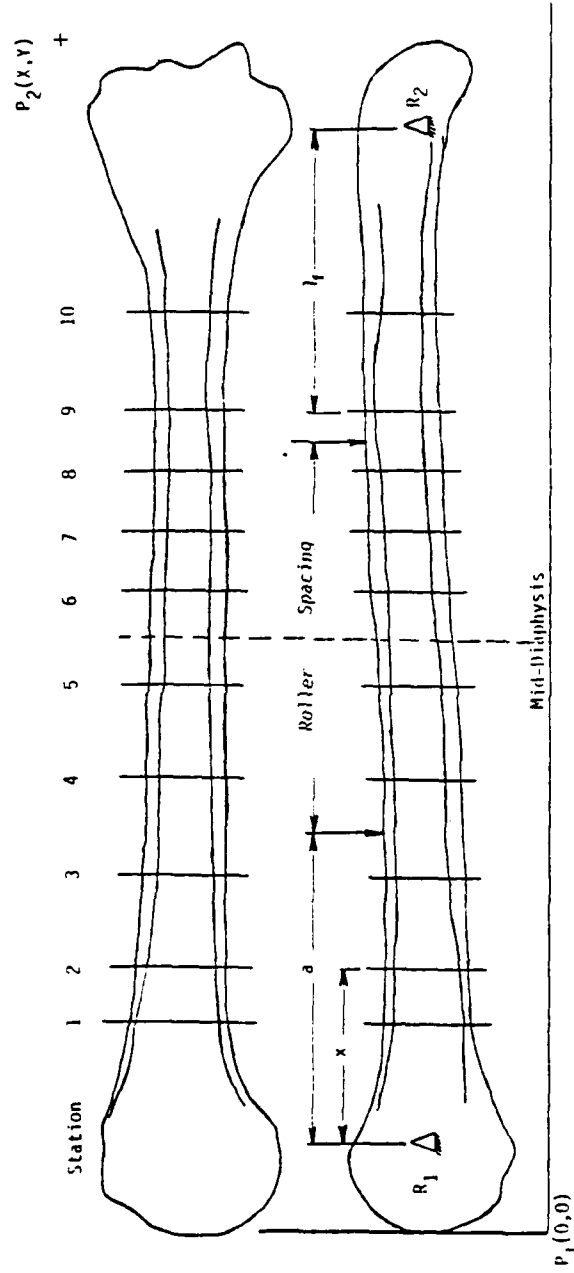


Figure 2.44 Tracing of x-rays for nondimensionalization, computer program.

top view in the tracing was an anterior/posterior (or posterior/ anterior) view with the proximal end to the left. In this view, the axis was located by drawing a line down the center of the diaphysis. The lower view was medial/lateral (or lateral/medial), with the proximal end towards the left of the tracing. Here, the axis was parallel to the plane upon which the bone rests in the mold.

Because the two views were not generally the same length, the mid-diaphyses had to be located in each view by measuring the length and dividing it in half. With the mid-diaphyses and the axes, the x-rays were aligned and then traced.

Tracings of the x-rays of the fibulae differed somewhat from those of the femora, tibiae, and humeri. The lateral/medial view was above the anterior/posterior view with the distal end to the left. The axis for the lateral/medial view was the center line, and the resting plane was in the anterior/posterior view. The fibulae were traced essentially opposite of the others because of their different orientation in the osteoclast during testing.

Once the tracing was completed, stations along the diaphysis were located. This was most easily accomplished by drawing lines perpendicular to the longitudinal axes across both tracings wherever a station was desired. The femora had twelve stations, and the others had ten--half on each side of the mid-diaphysis. The station locations were somewhat arbitrary, however emphasis was made on placing more stations in regions where the diameters changed sharply and fewer stations where they remained essentially constant.

At this point, additional information was added to the tracing as input to the inherent HP operational programs. The digital plotter required coordinates of two points on the tracing with which to scale the points it digitizes. In Figure 2.44, these points are labeled P1 and P2. P1 was located at the intersection of the left end of the bone and its axis, and is assigned coordinates (0,0). P2 was placed at the right end of the lower tracing but above both views. Its two coordinates were the actual length of the bone, and the distance of P2 above the lower bone axis, accounting for magnification in the x-ray. Thus, these two points, which were entered into the plotter, set up a scale for the tracing in terms of the actual bone size.

In the case of femora this scaling procedure had to be altered because the tracings were too long to fit on the plotter. To allow for this, P2 was not placed at the right end of the bone, but was located closer to the mid-diaphysis. It was then assigned the proper coordinates, taking magnification into account. When all stations left of the mid-diaphysis had been digitized, the tracing was shifted to the left, and the remaining stations digitized. The shifting distance was entered to the program, and all affected values adjusted.

The final step in preparing a tracing involved only bending cases. The two support points on the end of the bone about which the ends rotated during testing were also located on the tracing. The distances from the mid-diaphysis to these rotation points were known, and were easily found on the tracing. Other values also necessary as input for the bending calculations were the distance from a rotation point to the location where a load was applied to the bone, and the distance between the applied loads. These distances are shown in Figure 2.44.

#### Computations

The interaction diagrams for four human long bones were nondimensionalized by dividing the torque or bending moment that induced a fracture by the section modulus for a tube approximating the true section at a station along the diaphysis. For the case of bending, the station was found by using the output from the program (as illustrated in Table 2.23) for bones that underwent bending tests. Note that the table specifies the actual fracture load for the bone and two stations whose theoretical loads bracket the experimental load. Also listed are the distances along the diaphysis of the bone to the two stations. Assuming that the load varied linearly between these two stations, an interpolation would result in a single theoretical fracture location. The distance from one end of the bone to this station divided by the length of the bone to yield a percent length. This is done for each of the thirteen cases.

A station,  $l_f$ , for each of the four types of bones was then specified by taking an average of the individual percent lengths found previously. This procedure yields the following values which represent a percent of the maximum length of each bone type:

Table 2.23. Output from "nondimensionalization" programs.

LEFT FEMUR, #3793

STATION	O DIAMETERS		I DIAMETERS		AVG O	AVG I
1	47.55	39.73	36.37	34.58	43.64	35.47
2	39.40	34.91	26.21	27.73	37.15	26.97
3	34.40	32.43	19.52	22.49	33.41	21.00
4	32.73	29.70	16.52	19.64	31.21	18.08
5	31.37	29.49	15.67	22.00	30.43	18.83
6	30.46	30.67	15.52	21.67	30.56	18.59
7	33.21	30.67	21.64	23.12	31.94	22.38
8	38.28	33.82	29.03	24.67	36.05	26.85
9	45.94	36.55	38.52	29.61	41.25	34.06
10	52.67	38.09	47.06	31.76	45.38	39.41
11	61.49	40.18	56.10	32.61	50.84	44.35
12	73.49	40.49	69.10	34.06	56.99	51.58

STATION	I
1	100310.58
2	67563.73
3	51623.23
4	41358.76
5	35893.07
6	36964.38
7	38782.85
8	57375.74
9	75975.34
10	89777.94
11	137924.54
12	170328.12

BENDING FAILURE LOAD = 2194.99

LEFT STATION	X	RIGHT STATION	X	LEFT LOAD	RIGHT LOAD
57.54	1	76.95	2	2653.99	1570.47
105.12	3	136.08	4	976.89	2664.00

Femora	79%
Tibiae	19%
Fibulae	82%
Humeri	77%

For the femura, tibiae, and humeri, these length percentages were taken in reference to the proximal end. However, the fibulae were referenced to the distal end.

Note that in many cases the output listed more than one location where fracture could occur. If this were the case, the location which is closest to others of the same type of bone was used.

The torsion cases presented a special problem in that the theoretical fracture loads calculated for each station were, in general, higher than the actual load, and no fracture location could be found. Therefore, the station with the lowest calculated failure load was chosen as the fracture location. This procedure was used for all of the torsion tests, even for those whose program output listed a fracture location. As in the bending cases, the distance to the fracture location was divided by the length of the bone, and these percentages were averaged for each type of bone. The "nondimensionalizing" stations for torsion are:

Femora	59%
Tibias	65%
Fibulae	76%
Humeri	64%

The ultimate torsional stress used in the program was  $68 \text{ N/mm}^2$ . When using this value, it is assumed that, in torsion, failure will occur at a forty-five degree angle from the axis of twist of the bone in tension. It may be the case that the ultimate stress is lower than the value used here, which would correspondingly lower the calculated failure loads.

#### Discussion

One problem common to many of the bones that were traced for use in the HP program was that the x-rays of two views of the same bone were not the same length. It was agreed that if a difference of ten percent

occurred, a compensating statement in the program would adjust the lengths and diameters of the top view of a tracing to correspond with that of the lower view. The largest length disparity encountered was four percent, and thus the difference was neglected.

This length difference can be explained by noting that an x-ray magnifies the bone. The amount of magnification differs from one x-ray to another. Also, an x-ray may provide a distorted picture of the ends of a bone because the rays travel radially from the source. This is most noticeable in the longer bones, such as femora. Both of these effects most often result in x-rays of the same bone having different lengths.

The error induced by such distortions could be minimized by locating the stations differently than described herein. As mentioned in explaining the x-ray tracings the two views of a bone were positioned by aligning their axes and mid-diaphyses. Stations were located by drawing a line perpendicular to the axes through both views. The stations that are furthest away from the mid-diaphysis will be the most in error. However, if each view was considered separately, and the stations were located as percent of length away from the mid-diaphysis, this error could be reduced. This procedure would result in the station of one view being slightly offset from the same station in another view, however, they would be more accurately located. The ratio of the length of the bone in the lower view divided by the length in the top view could then be entered to the program as its "Length Ratio", and the length disparity would be compensated for.

A second problem that hampered accurate tracing of the x-rays was that the proximal and distal ends were cut off, in a few cases, in the x-ray. This prevented accurate measurements of length, and in the case of the fibulae, it was difficult to identify the views. One way this problem was overcome was by finding landmarks on the actual bone that could be located in the x-ray, then measuring from the landmark to the mid-diaphysis. This distance was then used to find the mid-diaphysis on the x-ray. However, this procedure did not account for magnification. In the case of femora, magnification was usually between four and seven percent, and this is a considerable margin of error. Therefore, in the

future, if x-rays are to be used for this purpose, care should be taken to insure that the entire bone appears in the x-ray.

The program models a bone as a hollow tube and uses the classical bending and torsion formulas to calculate failure loads. The hollow tube approach is clearly an approximation since a bone varies greatly in geometry from a tube. However, since the intent was not to specify failure loads, but to try and recognize a pattern for the failure loads of bones that underwent similar tests, the approximation was adequate.

The program is useful in calculating theoretical failure loads of any irregularly shaped shaft that could reasonably be modeled as a hollow tube. It allows for an unlimited number of stations along the shaft, and with alterations, could digitize as many points as desired at a station.

#### SECTION PROPERTIES:

The second moments of inertia and centroids of the diaphyseal cross-sections were required to improve the accuracy of the interaction boundaries. Since these sectional shapes are highly irregular, the section properties are not explicitly obtained and must be approximated using methods of composite areas.

To conserve time and effort, a computer program for the Hewlett-Packard 9825A desk-top computer and 9872A plotter, was written which calculates the first and second moments of inertia, the product of inertia and the area of an irregular cross-section. These quantities are estimated by discretizing the section into finite trapezoidal shapes for which the exact area and moment and products of inertia are calculated. The values for the trapezoids are then summed to represent the overall values for the section.

As input, points selected around the section using a polar grid are digitized and stored in arrays. The program then operates on the arrays until the areas and moments and products of inertia are estimated with respect to the axis established during digitization. These quantities are then transformed into principal values and the results displayed by the plotter.

The output consists of a plot of the digitized section along with the printing of the second moments and product of inertia with respect

to the axis at digitization and with respect to the principal axes. The principal axes are also drawn locating the centroid of the section. The principal angle as well as the areas of the cross-section are finally printed beneath the inertia values. Figure 2.2 shows an example of the output.

#### 2.3.5.2 Observations

##### FRACTURE PATTERNS:

In general, the observed fracture patterns regardless of bone type were of two basic configurations. One was the result of a tension state of stress caused by pure shear and the other was the result of normal stresses caused by bending moments. Those bones subjected to twisting moments alone failed with a spiral fracture that began at the ends of the bone and spiraled around the diaphysis toward the mid-diaphysis. The end of the bone, distal or proximal, at which the spiral began was dependent on the bone type and direction of rotation (eversive or inversive). The bone ceased to resist the applied torque when the spiral reached the mid-diaphysis and the material between the beginning and end of the fracture failed in a "clam shell opening" (CSO) mode. For the bones that failed due to bending loads acting alone, the fracture began on the convex side of the bending diaphysis, propagated vertically to the neutral axis, bifurcated and then followed a curved path until parallel to the neutral axis. Any observed deviations from these two configurations were either combinations of the two actually exaggerations of one of the two.

##### Torsion Only Fractures:

The fracture configurations resulting from torsion only were very repetitive. They were the classical spiral patterns associated with materials weak in tension which fail along planes perpendicular to axis of rotation; the tension, of course, results from the shear that occurs. With most of the bones exhibiting this type of configuration, regardless of type, a fracture plane parallel to the axis of rotation was also observed. Such a plane infers a failure due to shear. This fracture usually occurred in the distal or the proximal 1/3 of the diaphysis depending on the type of bone.

As mentioned earlier the bone ceased to resist the twisting moment when the fracture had reached the mid-diaphysis and the bone failed due to "plate" bending along a fracture connecting the start and finish of the spiral fracture. This is the "clam shell opening" (CSO) mode; a term coined to identify this final behavior which resulted after the spiral traveled once around the diaphysis.

Occasionally, fractures were observed which ran parallel to the axis of rotation and were not associated with the CSO mode. These are attributed to shear because they occur in pairs and there is no way to cause the second fracture by the CSO mode once the first has occurred.

#### Femora:

Three of the four femora subjected to torsion exhibited the classical spiral fracture in the distal half of the bone. For these fractures the crack was observed to begin at the distal end and travel toward the mid-diaphysis. All of these bones except one, RF3793 (Figure 2.45) separated finally with the CSO mode. The spiral fracture in LF 3753 (Figure 2.46) began at the distal third and traveled to the proximal third. The CSO fracture was observed on the anterior, lateral and posterior surfaces and occurred when the spiral fracture had traveled once around the diaphysis. One femur, LF 3792, also had two longitudinal fractures (Figure 2.47) on the posterior side in the distal half. These are believed due to shear. The fourth femur, RF3782, is shown in Figure 2.48.

Three femora, RF 3793, LF3753, RF3782, had regions of their spiral fracture which were aligned with the torsional axis. Since the fracture is believed to have begun at the distal end and travel to the mid-diaphysis, it apparently propagated, failing in the tension mode, to a section of diaphysis where the principal stresses were insufficient to maintain this mode. The fracture then continued on as a shear failure until the stresses were once again large enough for the crack to propagate as a tension failure.

#### Tibiae:

Five tibiae were tested under torsion only conditions; however, two of these had their fibulae still articulated and will be discussed separately. Of the three left, all, LT3792, RT3793 and LT3753 (Figures 2.49 - 2.51, respectively), exhibited spiral fractures with the CSO

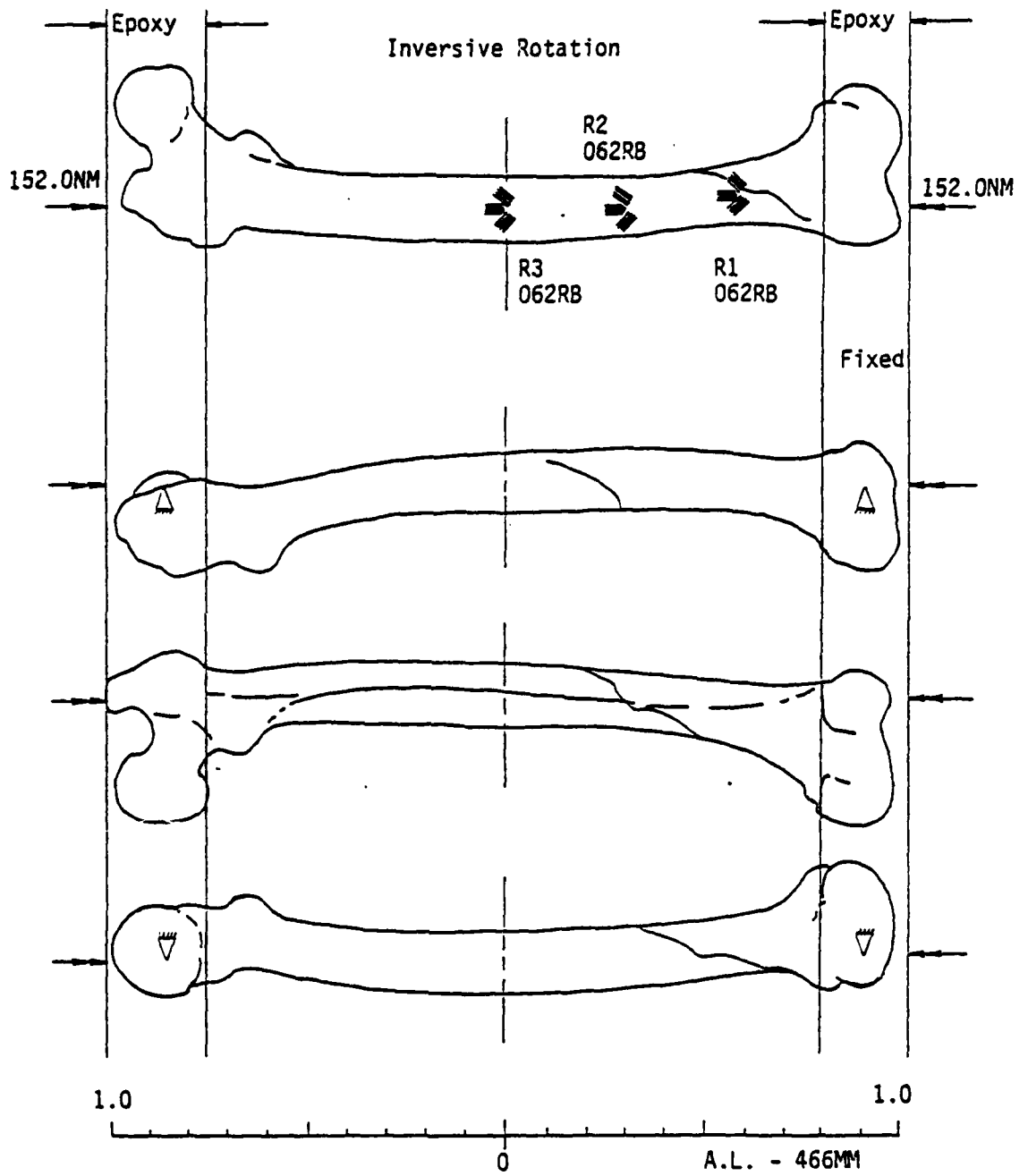


Figure 2.45 Test results for RF3793.

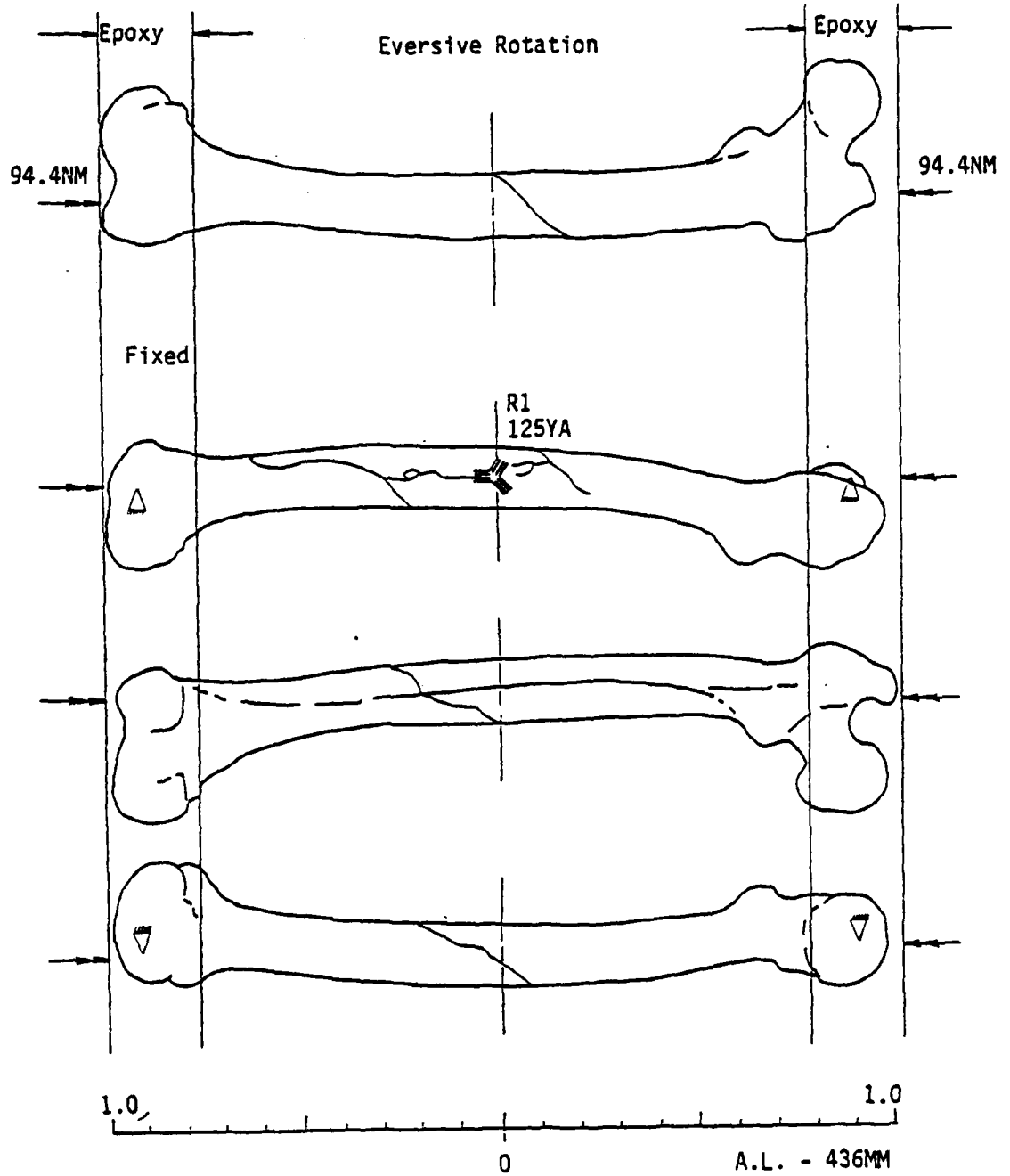


Figure 2.46 Test results for LF3753.

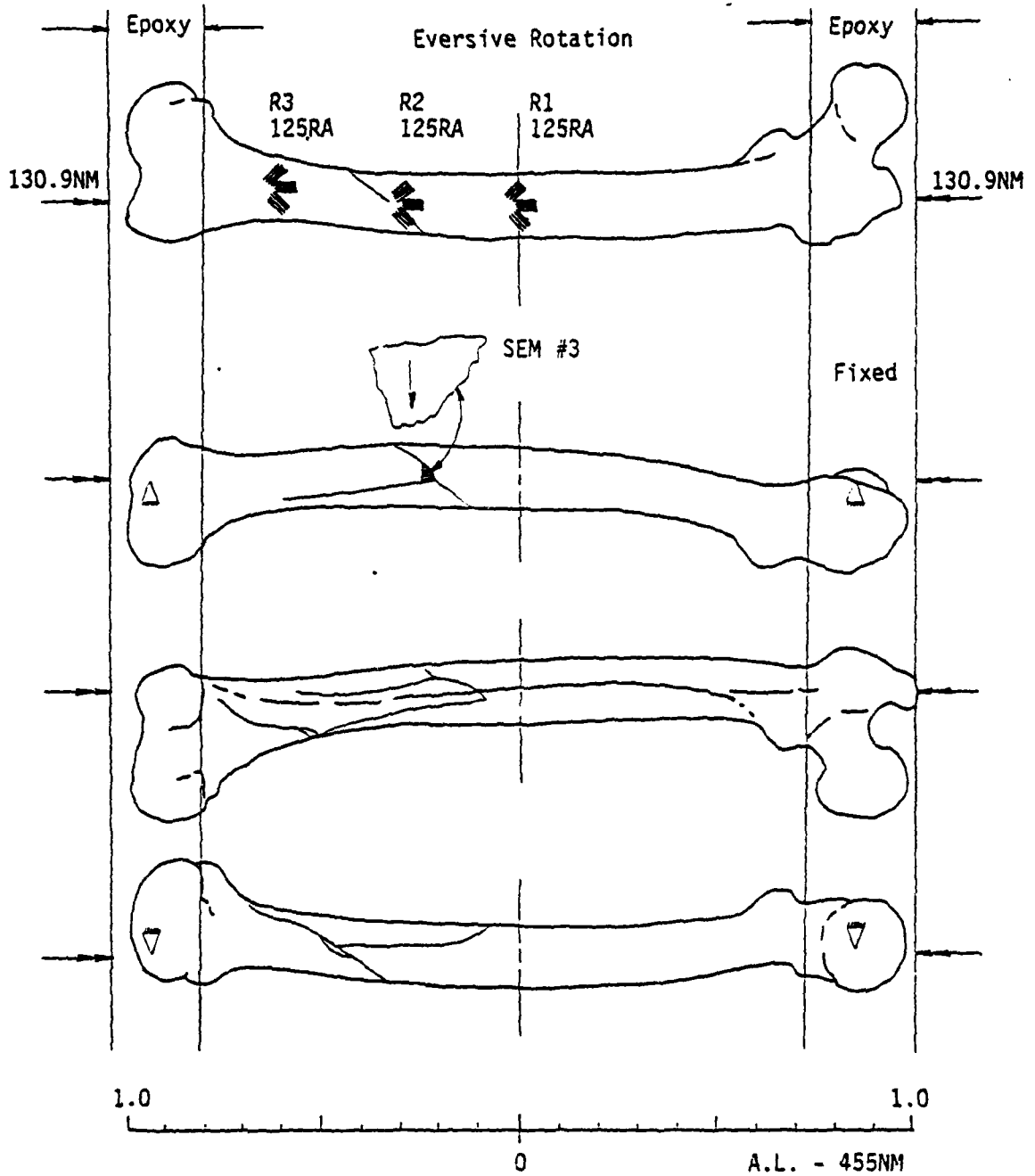


Figure 2.47 Test results for LF3792.

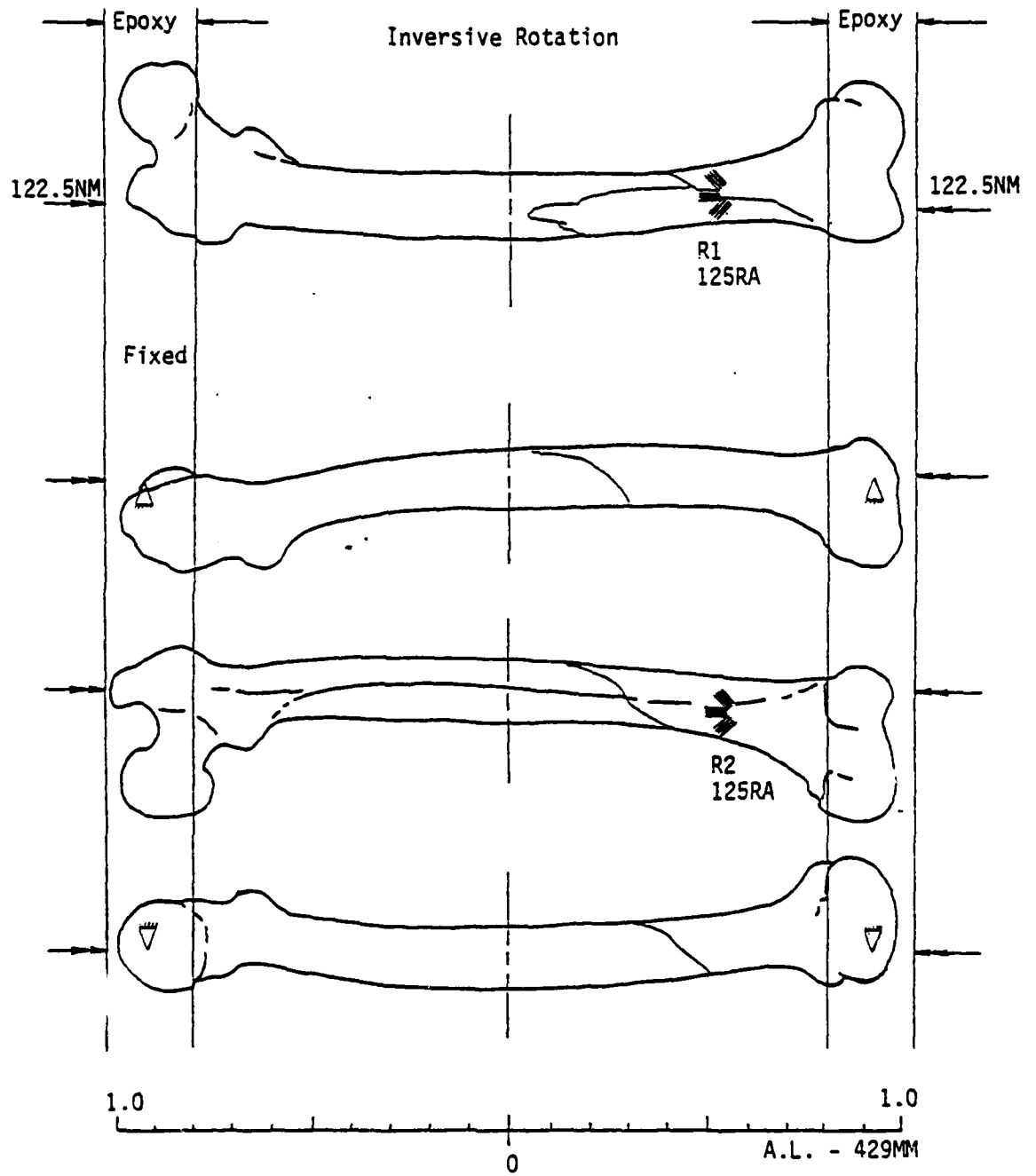


Figure 2.48 Test results for RF3782.

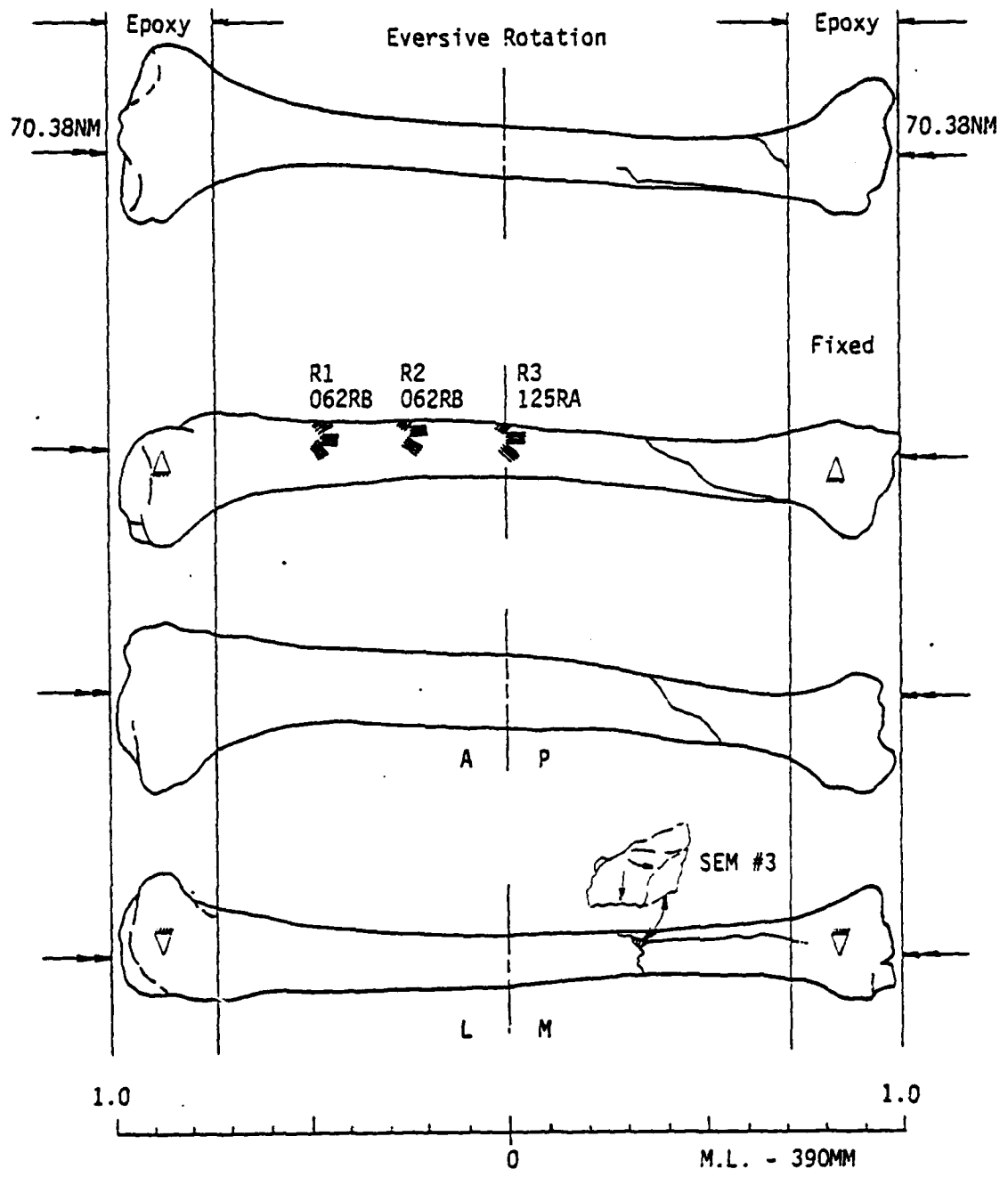


Figure 2.49 Test results for LT3792.

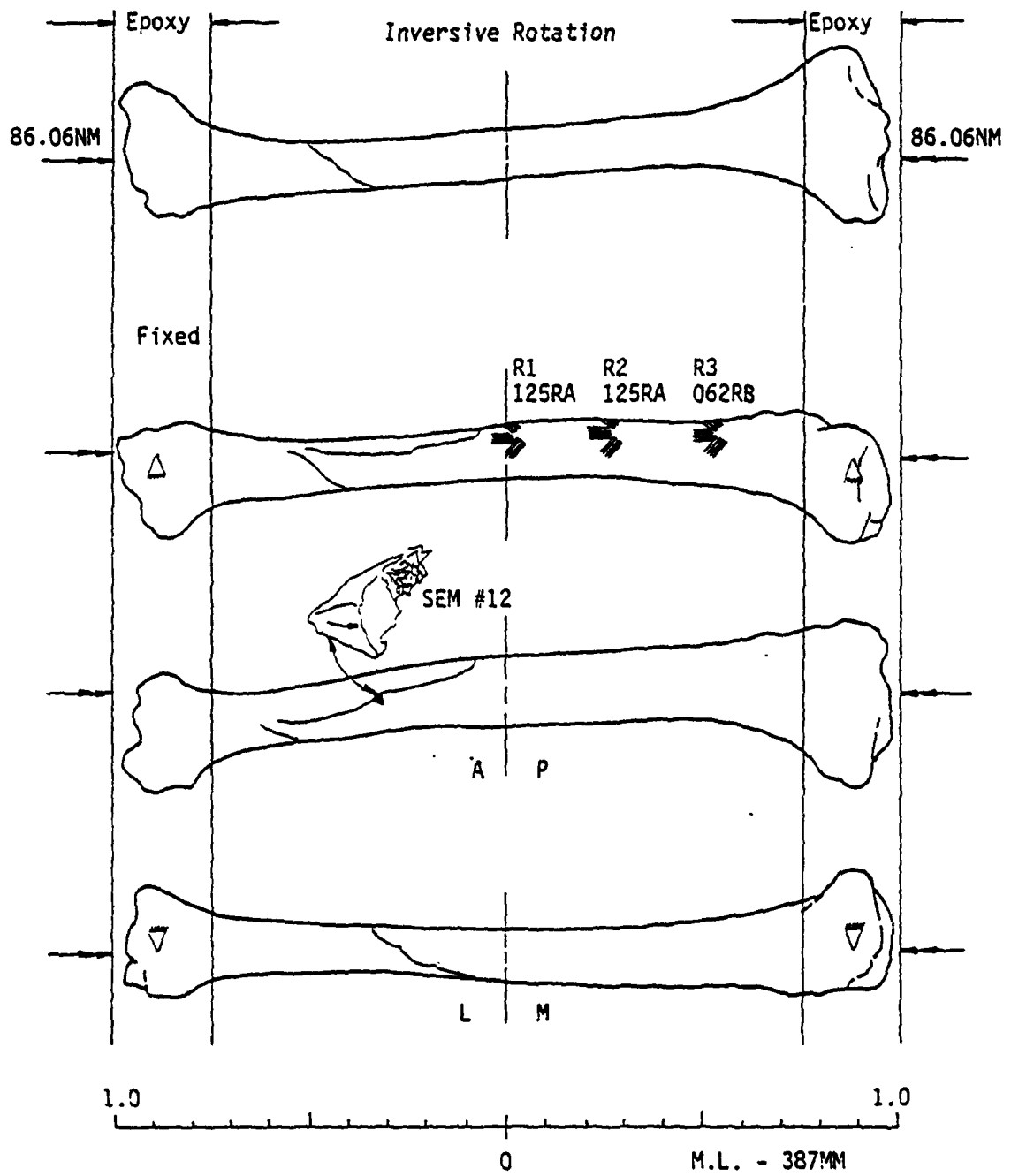


Figure 2.50 Test results for RT3793.

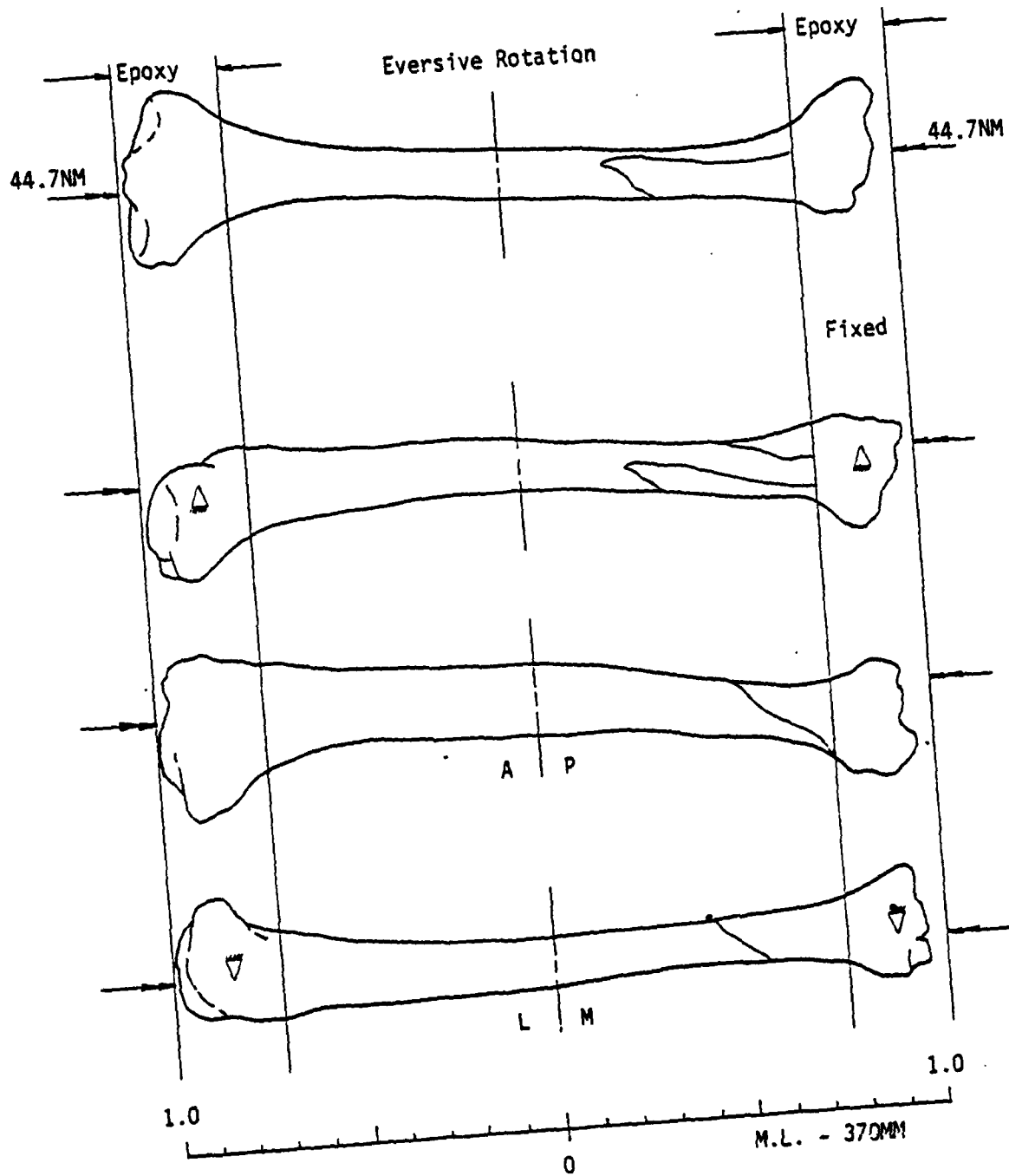


Figure 2.51 Test results for LT3753.

fracture joining the start and finish of the spiral fracture. The spiral fracture on all three bones occurred near the distal half and traveled once around the diaphysis before the CSO mode occurred. If the rotation was inversive, the CSO fracture was on the anterior side and, if eversive, on the posterior side.

The two tibiae, RT3782 and LT3782 (Figures 2.52, 2.53), tested articulated with their fibulae, had similar configurations to those above. However, the axis of torsion for these tibiae did not pass through the "center" of the cross-section at the mid-diaphysis, but was between the fibula and tibia at the tibia mid-diaphysis. If the cast epoxy blocks on the ends are considered to fully constrain the bone they surround, then the condition of pure torsion at the mid-diaphysis no longer exists and some bending should be involved. In addition, with the fibulae present, the tibia should carry less of the load. None of these variations were evident in the fracture patterns observed for the two bone.

Three tibiae had portions of their spiral fractures which were aligned with the axis of rotation. RT3782 and LT3792 had longitudinal region at the distal third while LT3782 had the region at the distal end. These regions are believed the result of shearing failure rather than tension due to shear.

#### Humeri:

Four humeri were tested under torsion only loading conditions. Each exhibited the spiral fracture with the CSO fracture joining the start and finish of the spiral fracture. On three of the humeri, LH3792, LH3782 and RH3793 (Figures 2.54 - 2.56), the fracture occurred in the proximal half of the bone; on the fourth, RH3753 (Figure 2.57), the fracture was on the distal half. There is no explanation as to why the variation in location other than it was simply the result of deviations in geometry.

The spiral fracture traveled once around the diaphysis before the CSO occurred. The CSO fracture was on the lateral side for two of the bones and on the medial side of the other two; no correlation to loading condition (eversive or inversive) is evident.

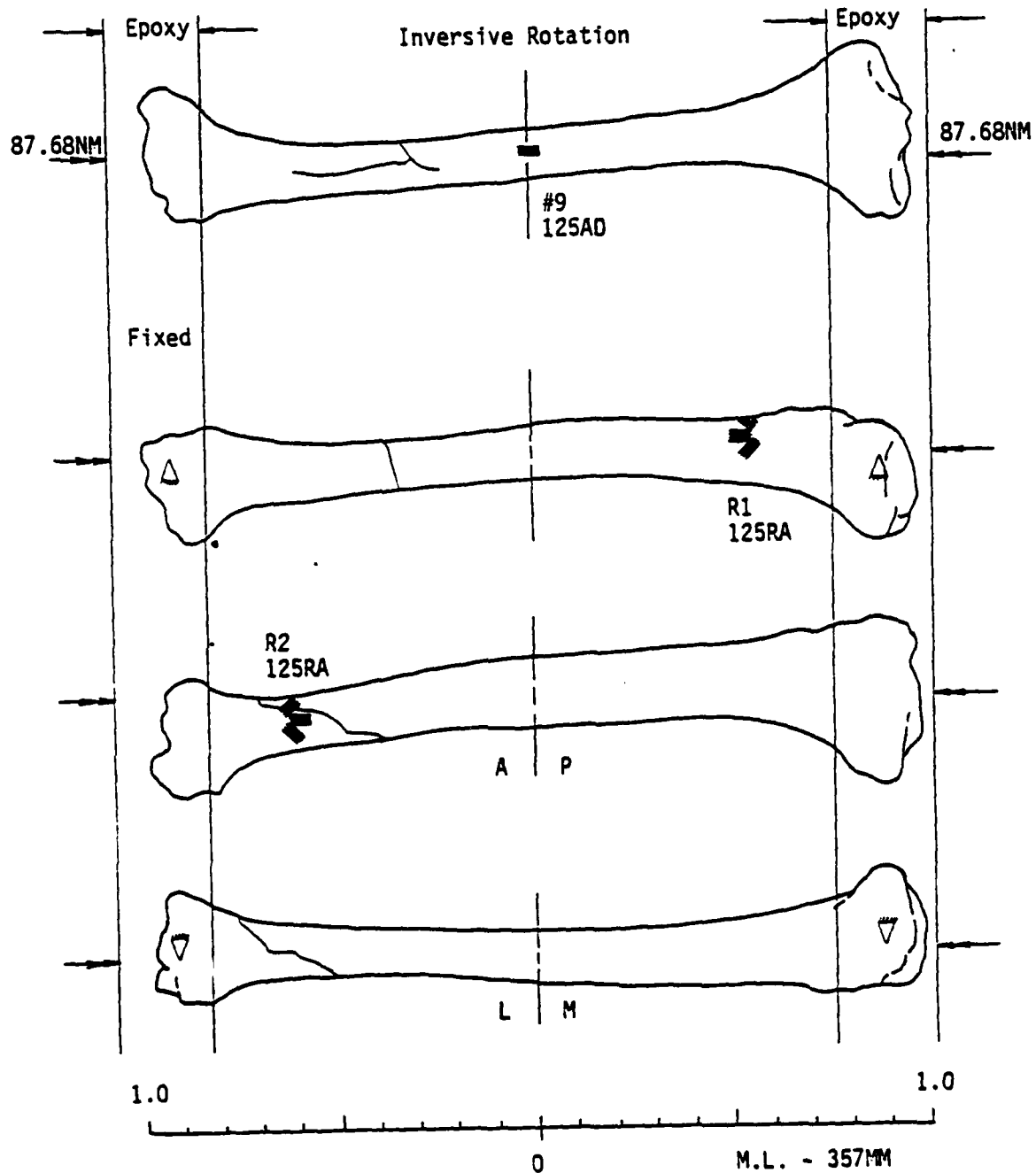


Figure 2.52(a) Test results for RT3782.

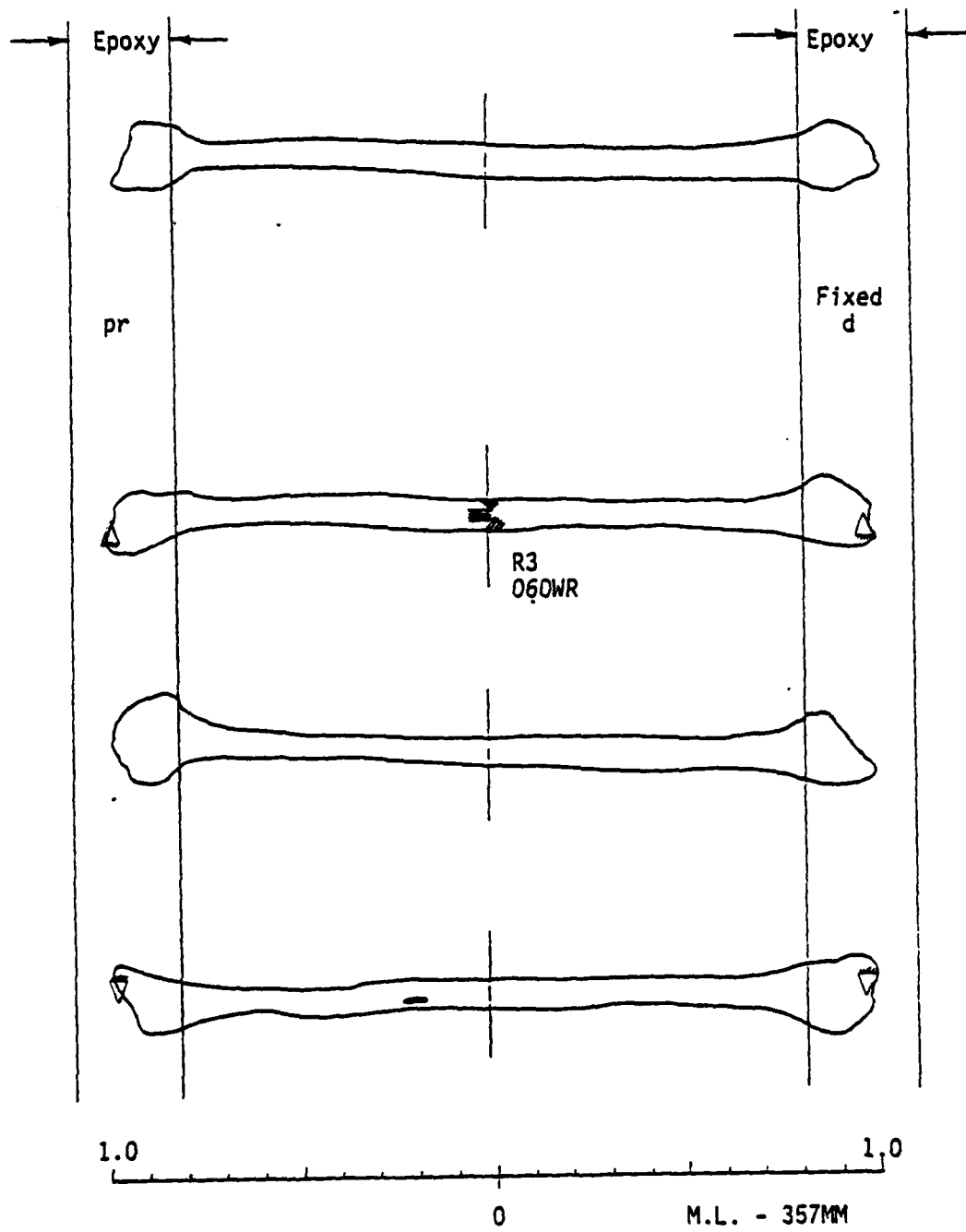


Figure 2.52(b) Test results for Rfb3782.

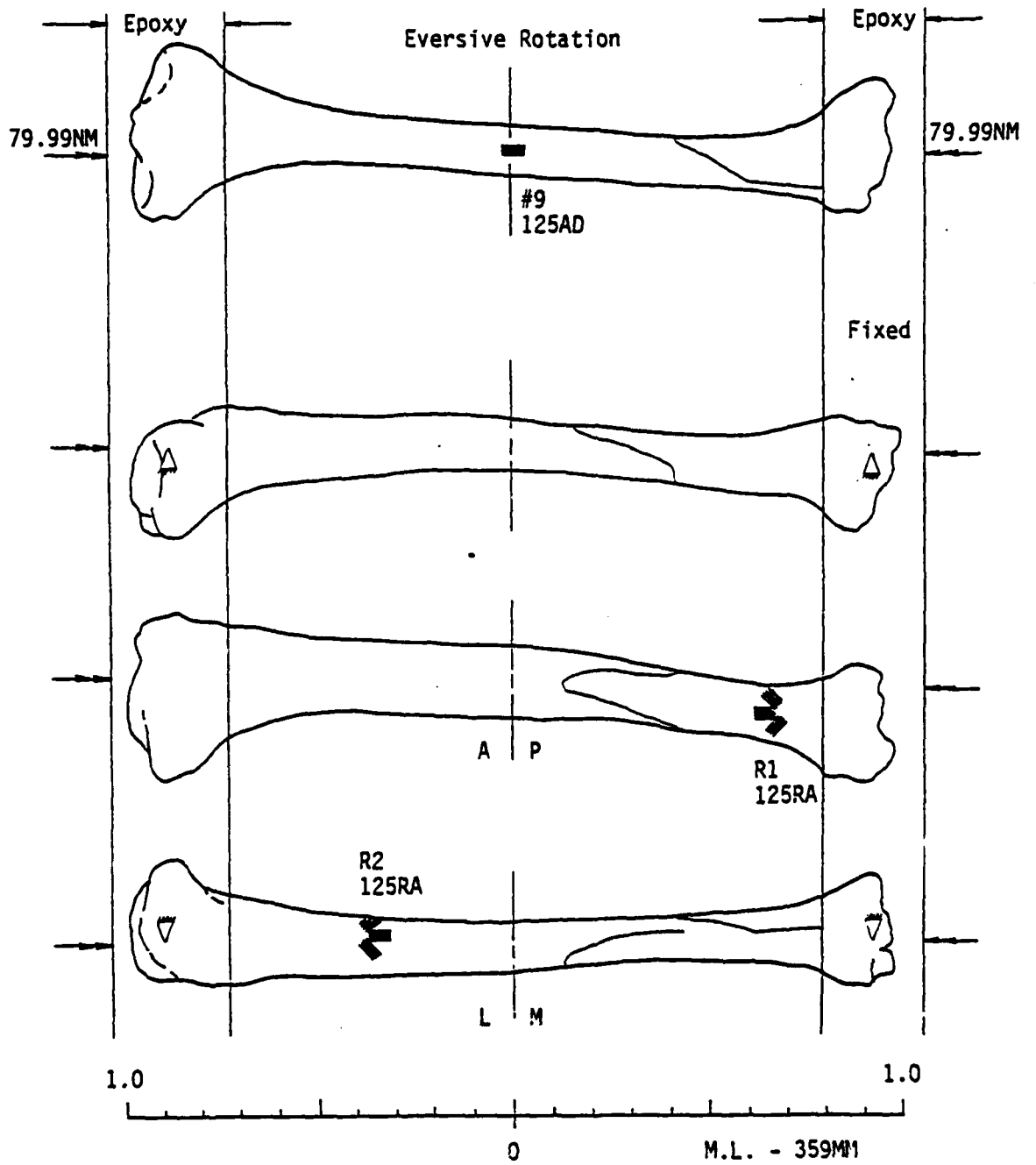


Figure 2.53(a) Test results for LT3782.

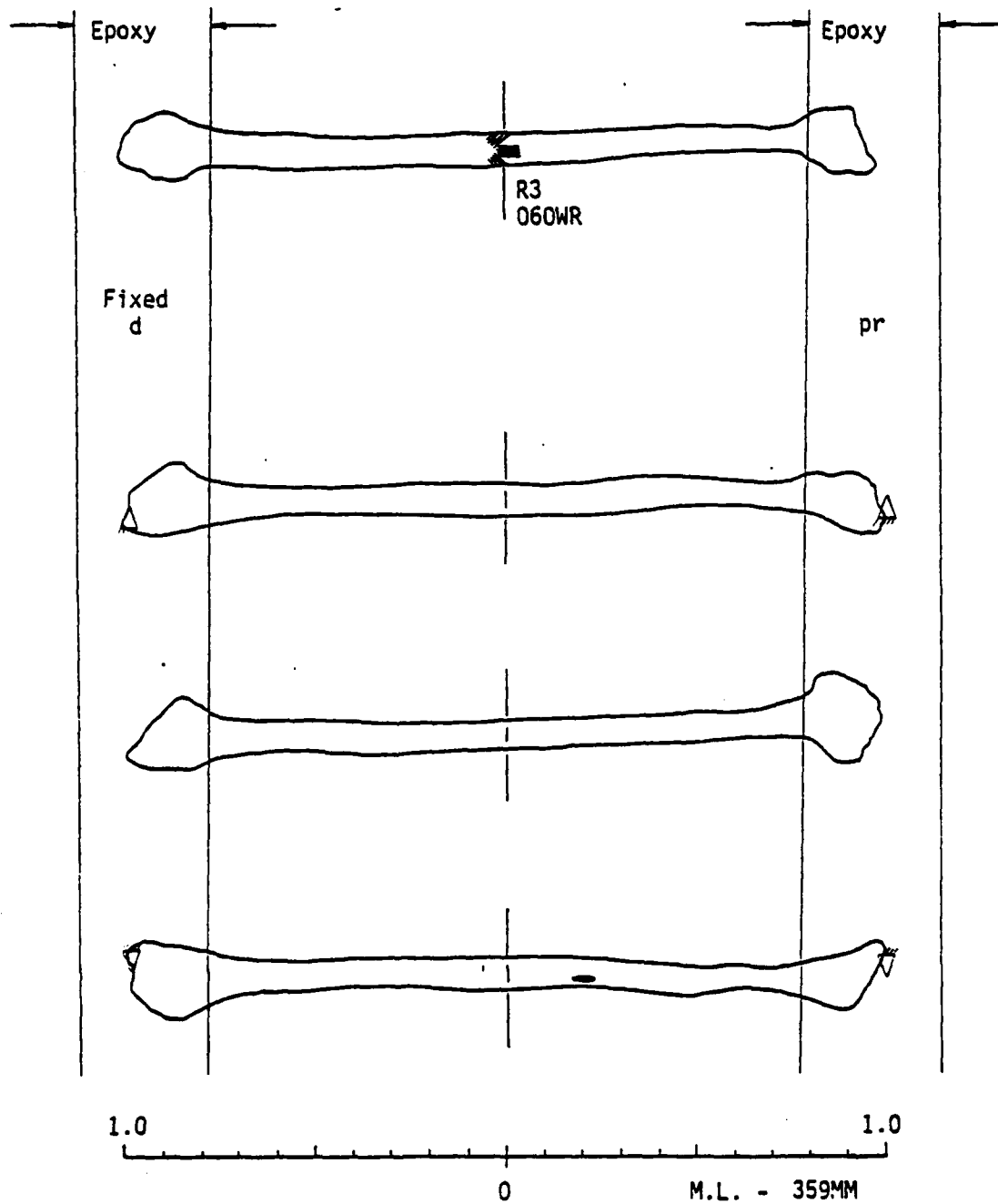


Figure 2.53(b) Test results for LFB3792.

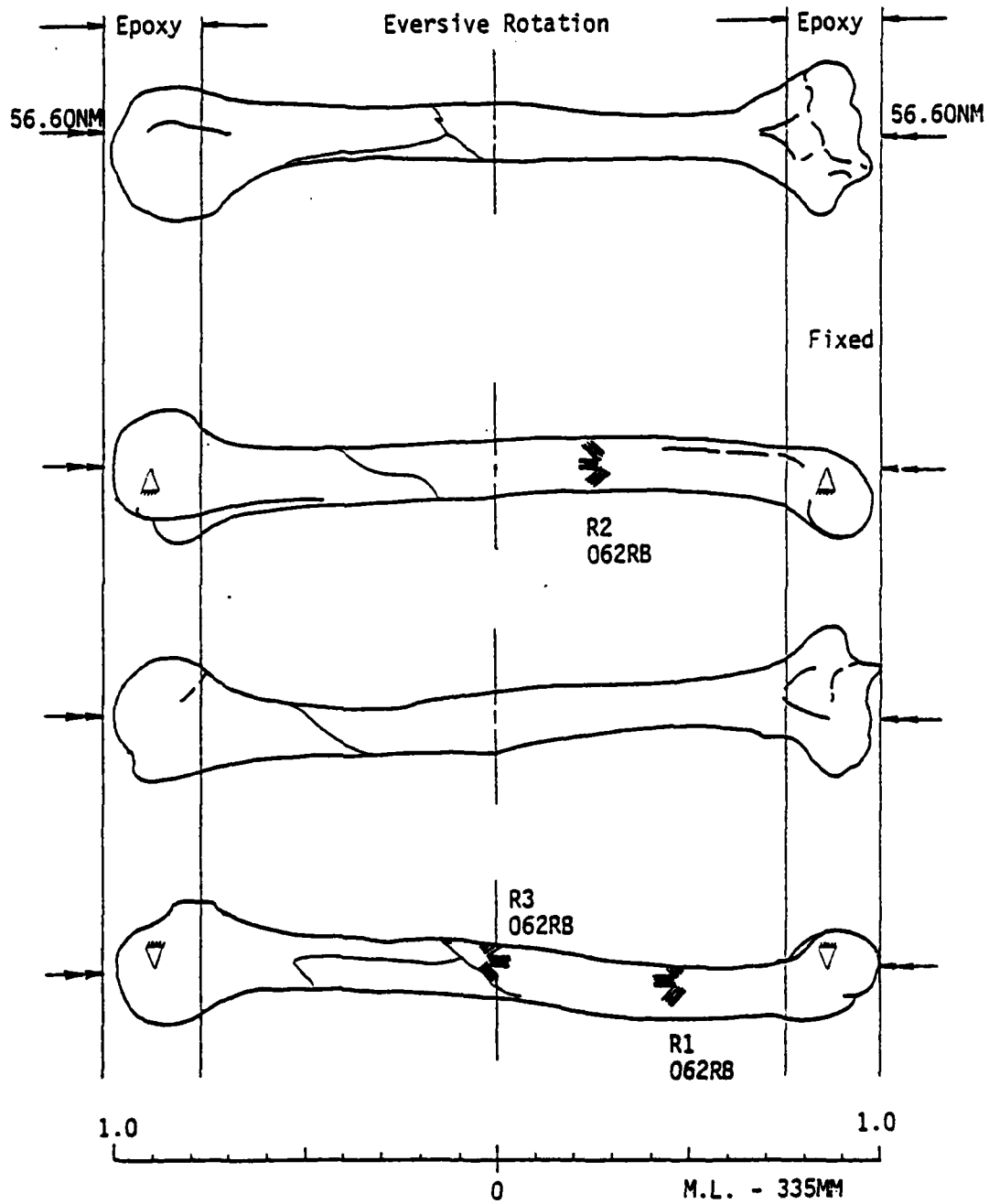


Figure 2.54 Test results for LH3792.

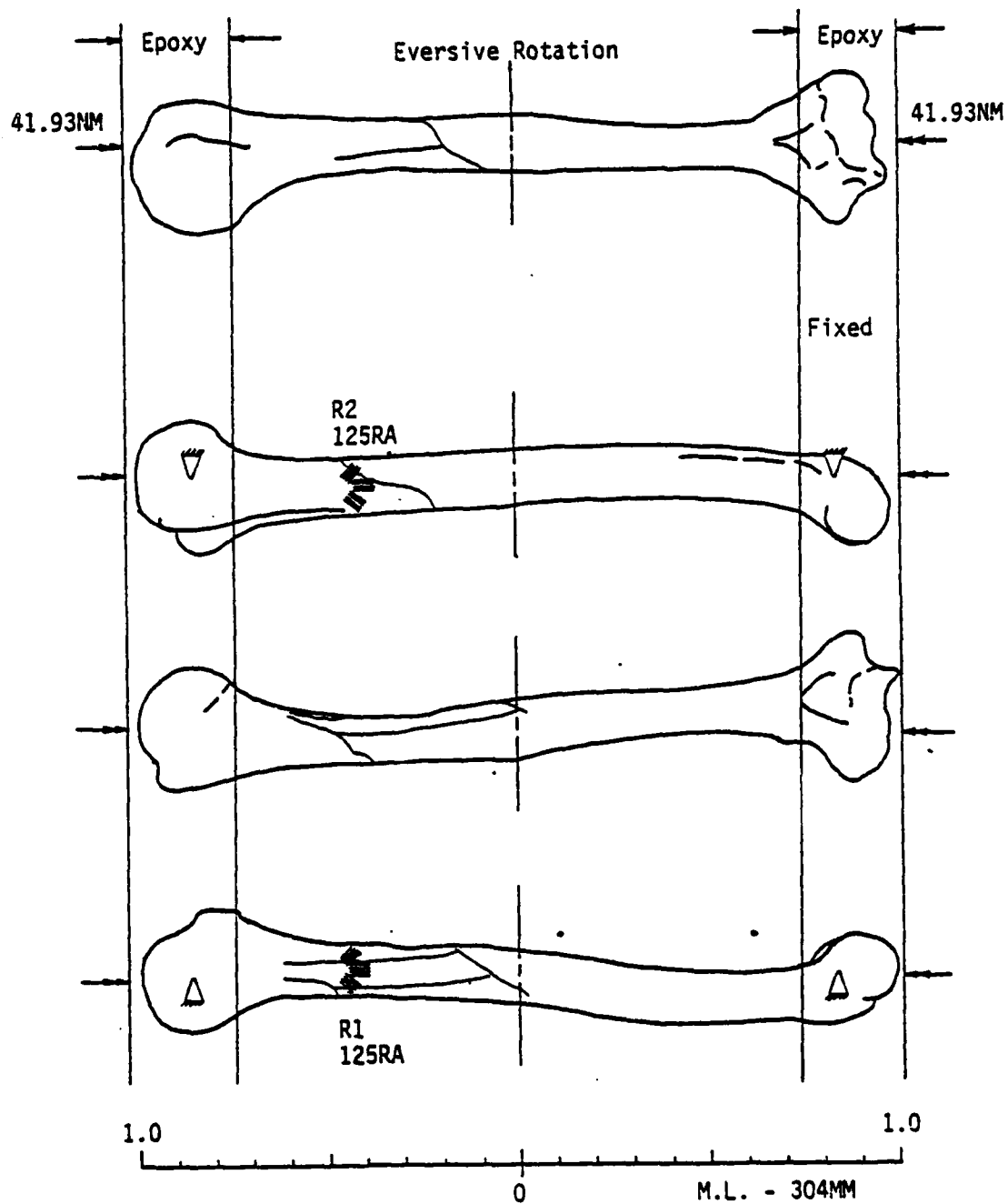


Figure 2.55 Test results for LH3782.

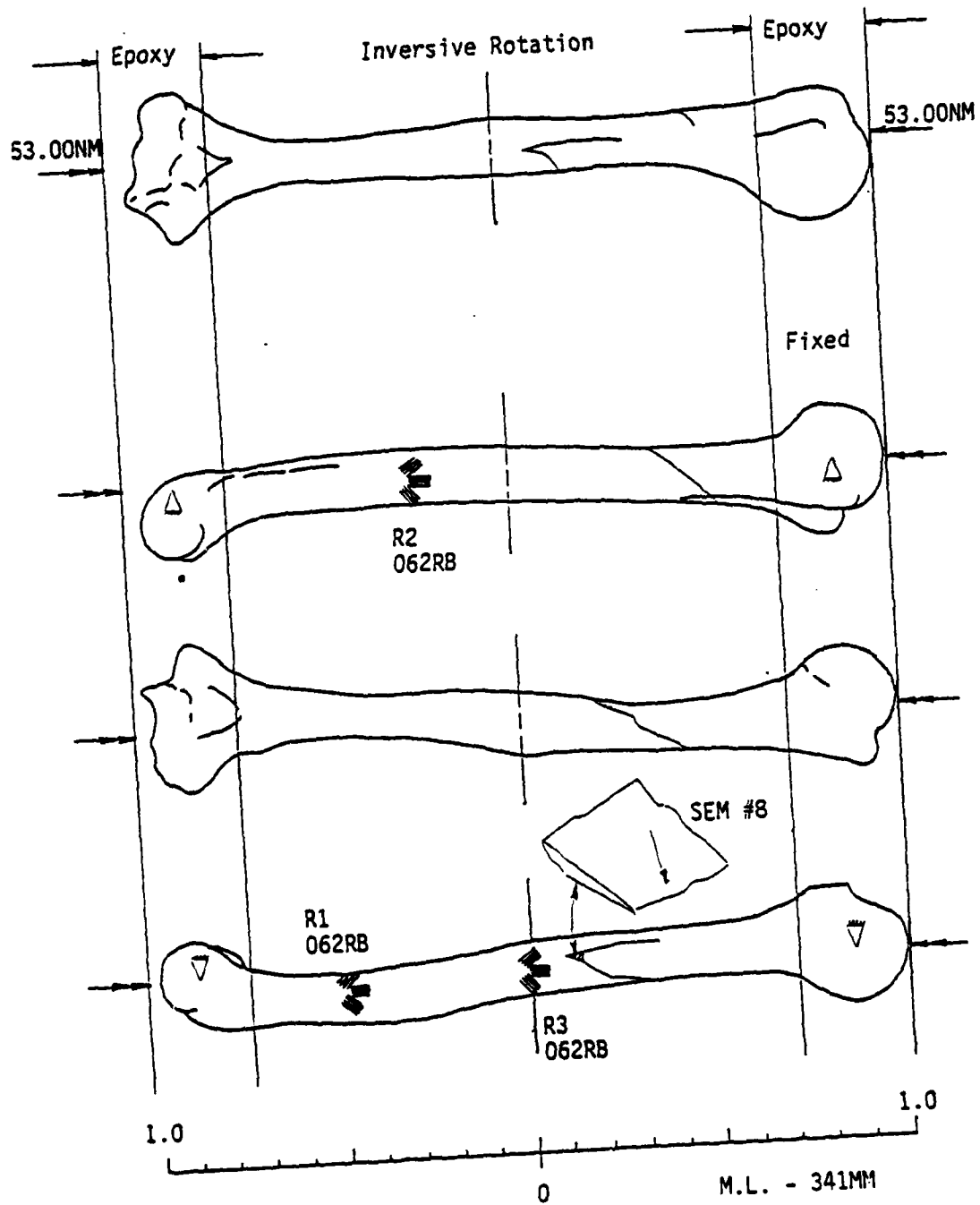


Figure 2.56 Test results for RH3793.

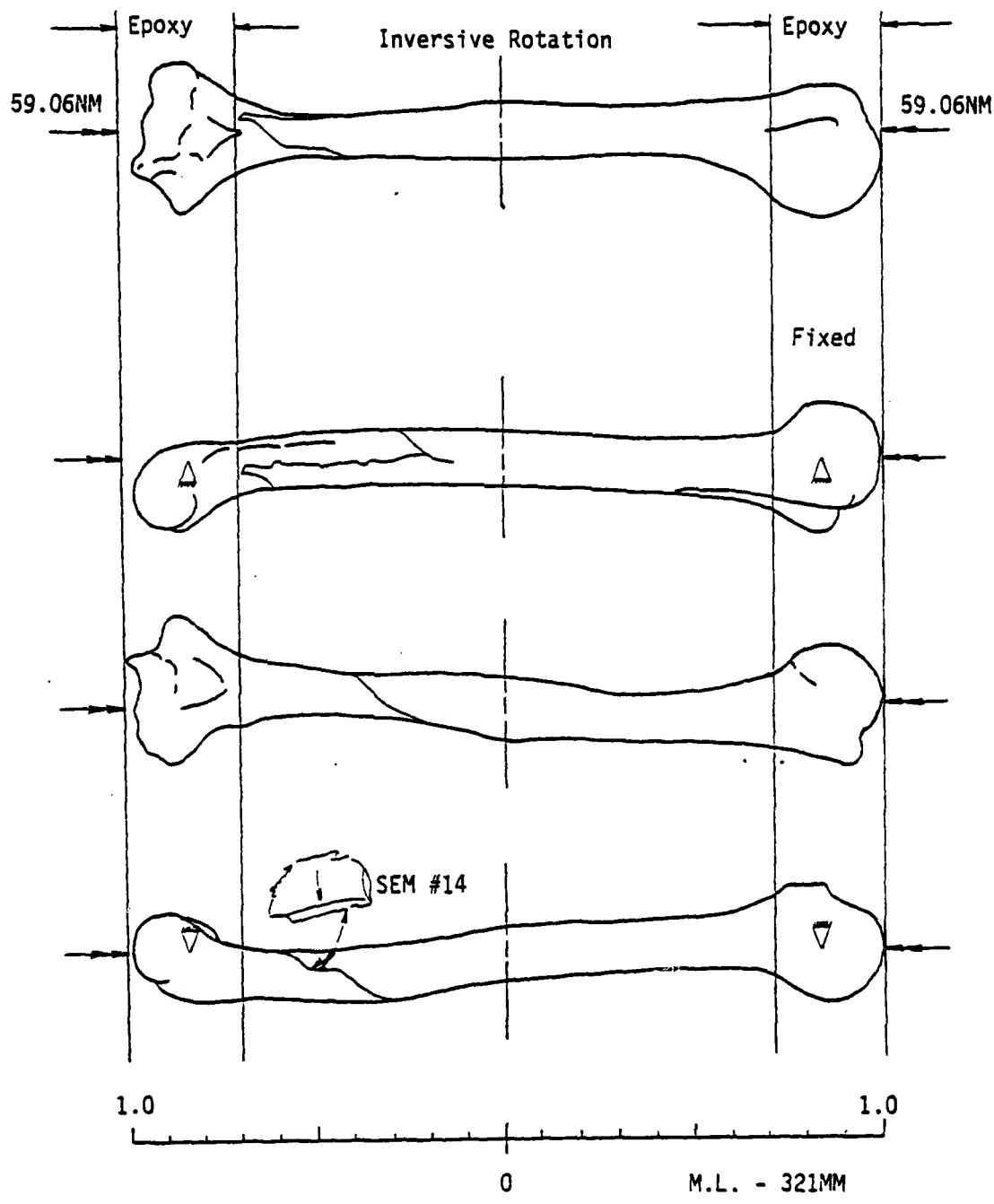


Figure 2.57 Test results for RH3753.

Three of the humeri, RH3753, LH3782 and LH3792, had regions of the spiral fracture that were parallel to the torsional axis. RH3793 had a region that was normal to the torsional axis. In addition, LH3782 had one fracture that ran parallel to the CSO fracture on the medial side. All these fracture regions are believed to be caused by shearing forces.

#### Fibulae:

Three fibulae were tested under torsion only loading conditions. Two were involved in the torsion only test of the tibia, but did not display any fractures. Two of the three bones, RFb3793 and LFb3753 (Figures 2.58 - 2.59) exhibited the spiral fracture; however, only LFb3753 separated by the CSO mode. LFb3792 (Figure 2.60) exhibited a fracture that began in the spiral mode but quickly transformed in a longitudinal crack (shearing failure) parallel to the torsional axis. Two of the fractures occurred in the proximal third and one in the proximal half of the diaphysis.

#### Bending Only Fractures:

Each of the four bone types failed under the four point bending load beginning on the convex side of the bending diaphysis. Here the fracture started as a tension failure with the stress aligned with the osteon axis. The fracture traveled normal to the neutral axis and bifurcated. The bifurcation usually appeared near the neutral axis; however it was also observed to begin quite a distance above or below. Once the fracture bifurcated, it followed a curved path until parallel with the diaphysis axis and terminated either blindly or with complete separation of the bone. With reference to the osteon axes, the bifurcation transitioned from a fracture surface oblique to the axes to one in line with the axes.

#### Femora:

Of the four femora tested under bending only conditions, all four exhibited a fracture configuration similar to that described above. For the one femur RF3753, tested with a narrow roller spacing (more bending than shear), the fracture (Figure 2.61) occurred in the distal third of the diaphysis directly below one of the rollers. Of the two femora tested using a medium roller spacing (more shear--less bending), one, LF3793, displayed the typical bifurcation while the other, RF3792, did not.

AD-A111 090

KANSAS UNIV/CENTER FOR RESEARCH INC LAWRENCE  
MECHANICAL PROPERTIES OF FOUR HUMAN LONGBONES. (U)  
NOV 81 C R KULP, H W SMITH, H C ANDERSON

F/G 6/16

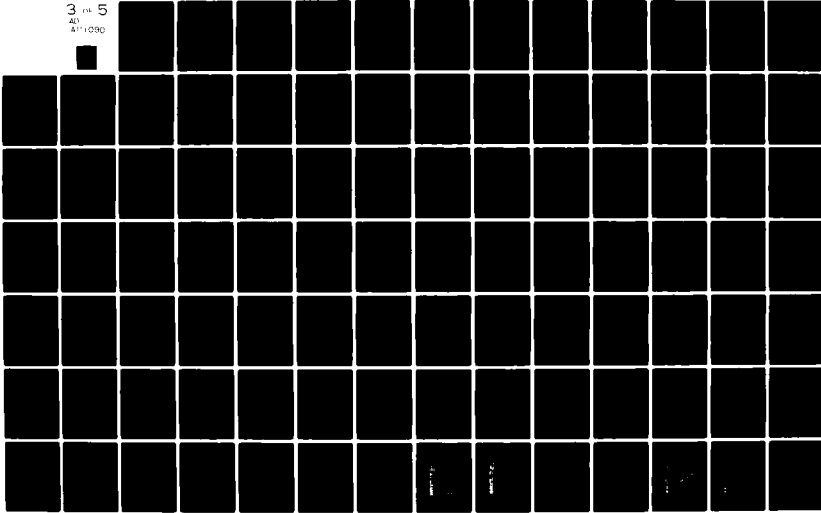
F59620-79-C-0183

UNCLASSIFIED

AFOSR-TR-82-0040

NL

3 of 5  
AD  
A111090



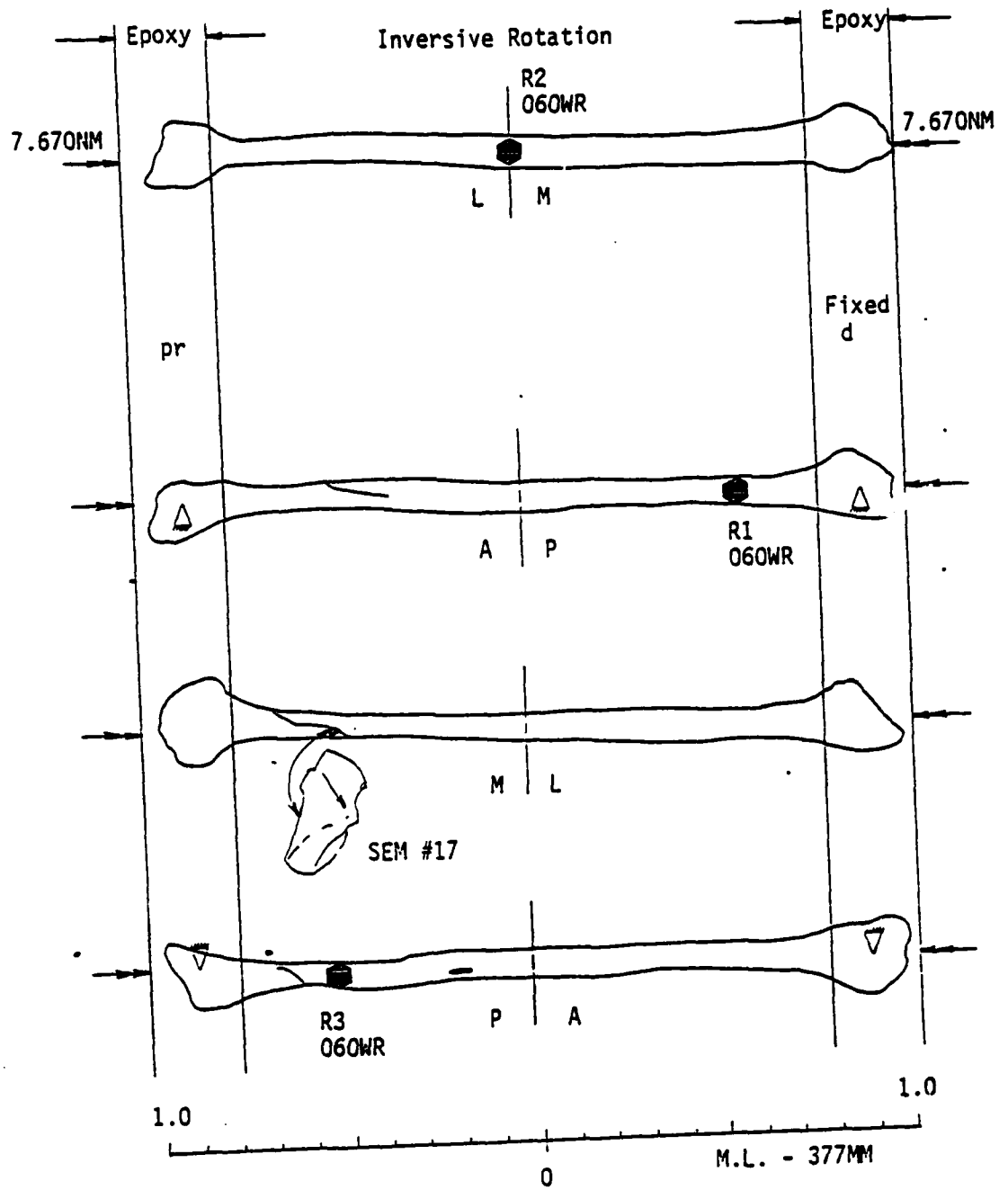


Figure 2.58 Test results for RFB3793.

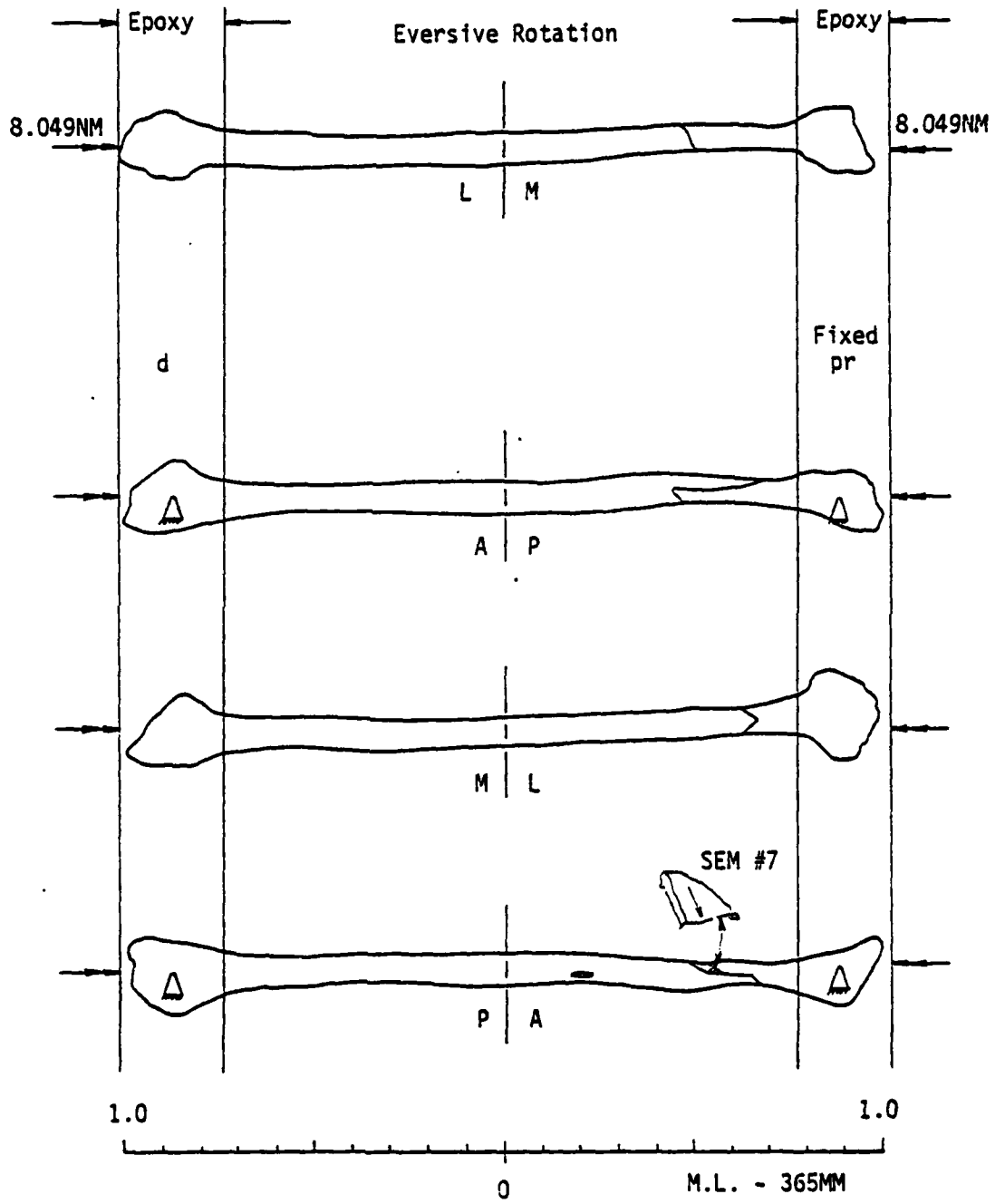


Figure 2.59 Test results for LFB3753.

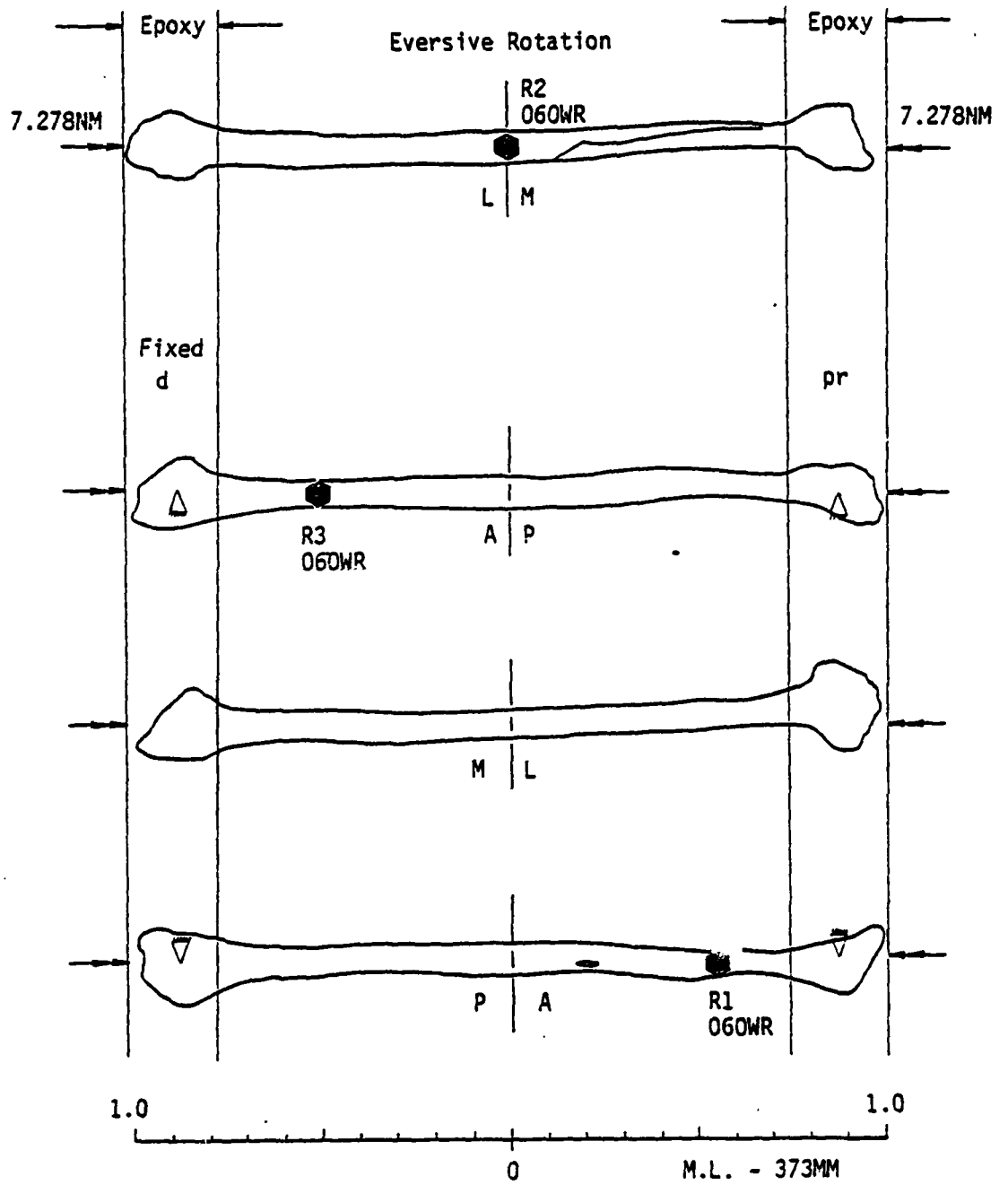


Figure 2.60 Test results for LFB3792.

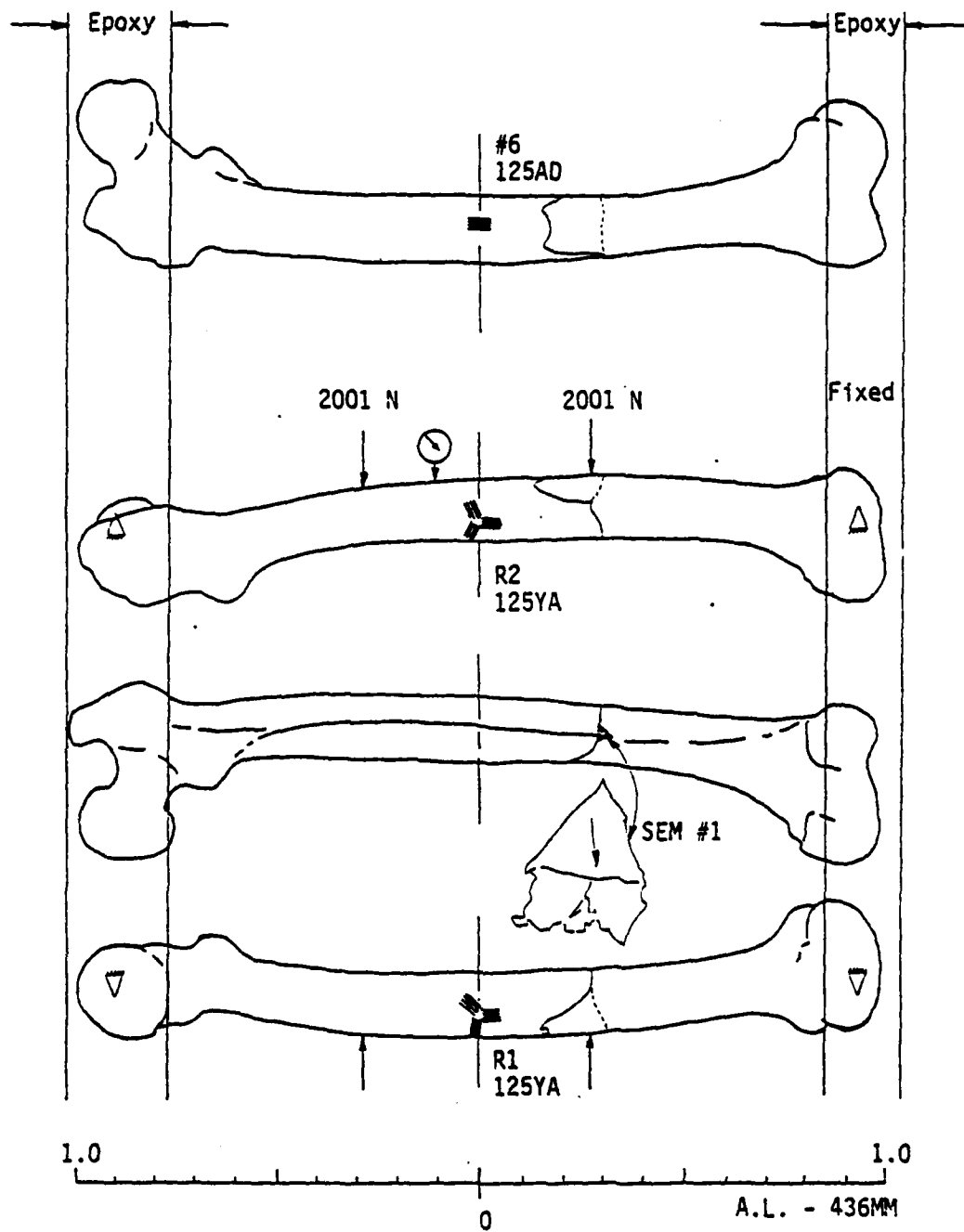


Figure 2.61 Test results for RF3753.

not bifurcate but did have one branch following a path similar to those occurring with bifurcation. Both of these fractures began inside the rollers--one (Figure 2.62) at the distal third and the other (Figure 2.63) at the proximal third of the diaphysis. For the last femur, LF3782, tested under a bending only condition, the roller spacing was wide causing the most shear and the least bending possible. This bone failed with two bifurcated fractures as described above, but with more branching (Figure 2.64). One of these fractures began on the distal end outside the roller while the other occurred on the proximal end inside the roller.

#### Tibiae:

Of the three tibiae that failed under bending only, two, RT3792 and RT3753, displayed the same fracture configuration. Their configuration was similar to the patterns described above with the exception of having only one obvious branch--no bifurcation. Both of these fractures occurred in the distal third of the diaphysis and are shown in Figures 2.65 and 2.66. RT3792 was bent using a medium roller spacing and RT3753 with a narrow spacing. The third tibia, LT3793 (Figure 2.67), was also bent with a medium spacing, but displayed a configuration that was an exaggerated form of the above with several longitudinal fractures. These multiple fractures occurred in the distal third of the diaphysis and one traveled over half the diaphysis.

#### Humeri:

All of the five humeri tested in bending were fractured using the same roller spacing which produced primarily a bending loading condition. The fracture configurations that resulted were comparable to those observed in general for bending. One humerus, RH3792, did not display a bifurcation, but did have the curved path that resulted after the initial fracture caused by the normal bending stresses (Figure 2.68). The other four humeri did exhibit bifurcation with much branching. For RH3782, RH3790, LH3787, the paths after branching (Figure 2.69-71) were typical of those observed with the other bone types; however, LH3753 had paths that ran oblique and parallel (Figure 2.72) to the humerus axis implying that a large amount of shear was present. RH3790 and LH3787 were the two humeri selected for the rapid rate

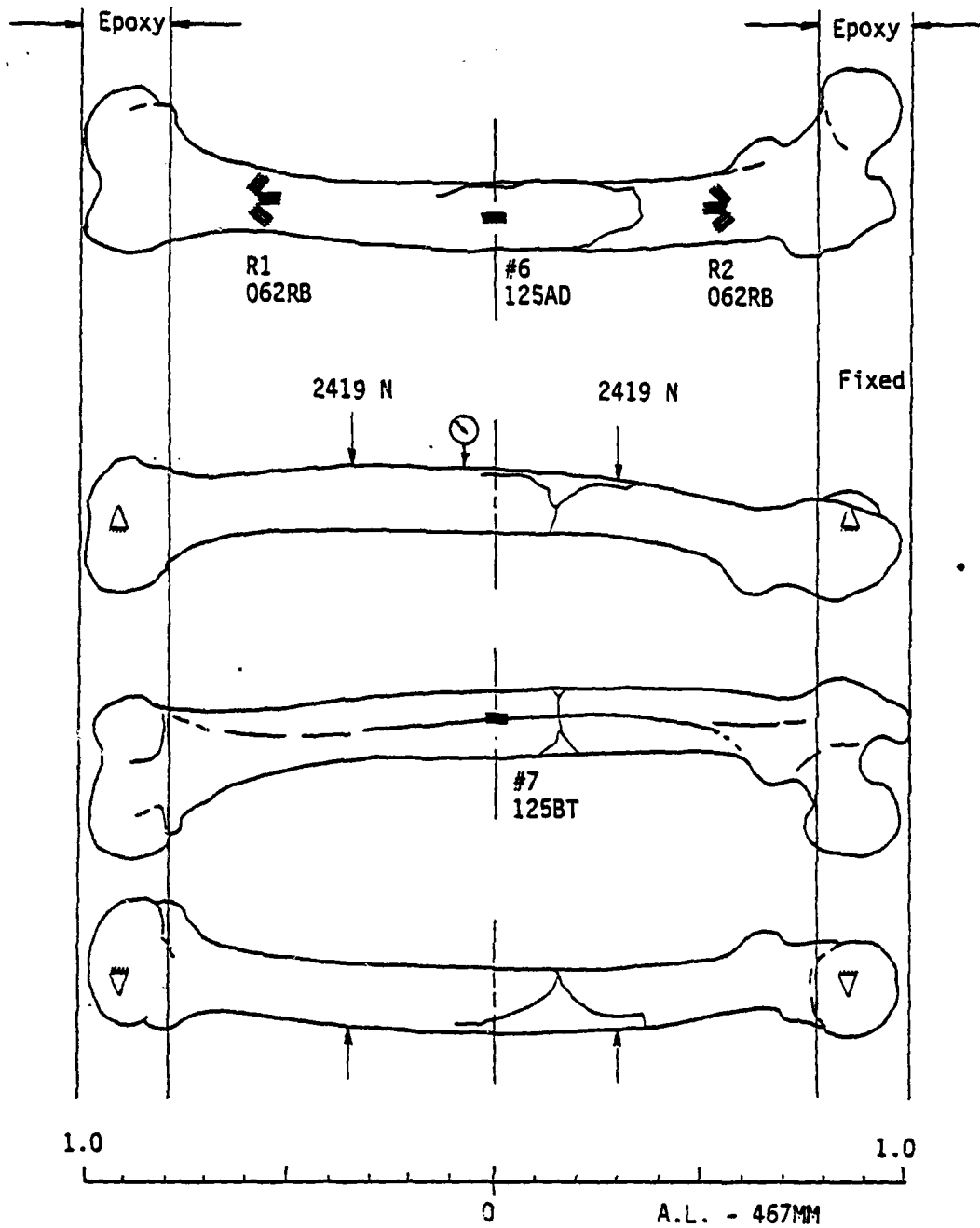


Figure 2.62 Test results for LF3793.

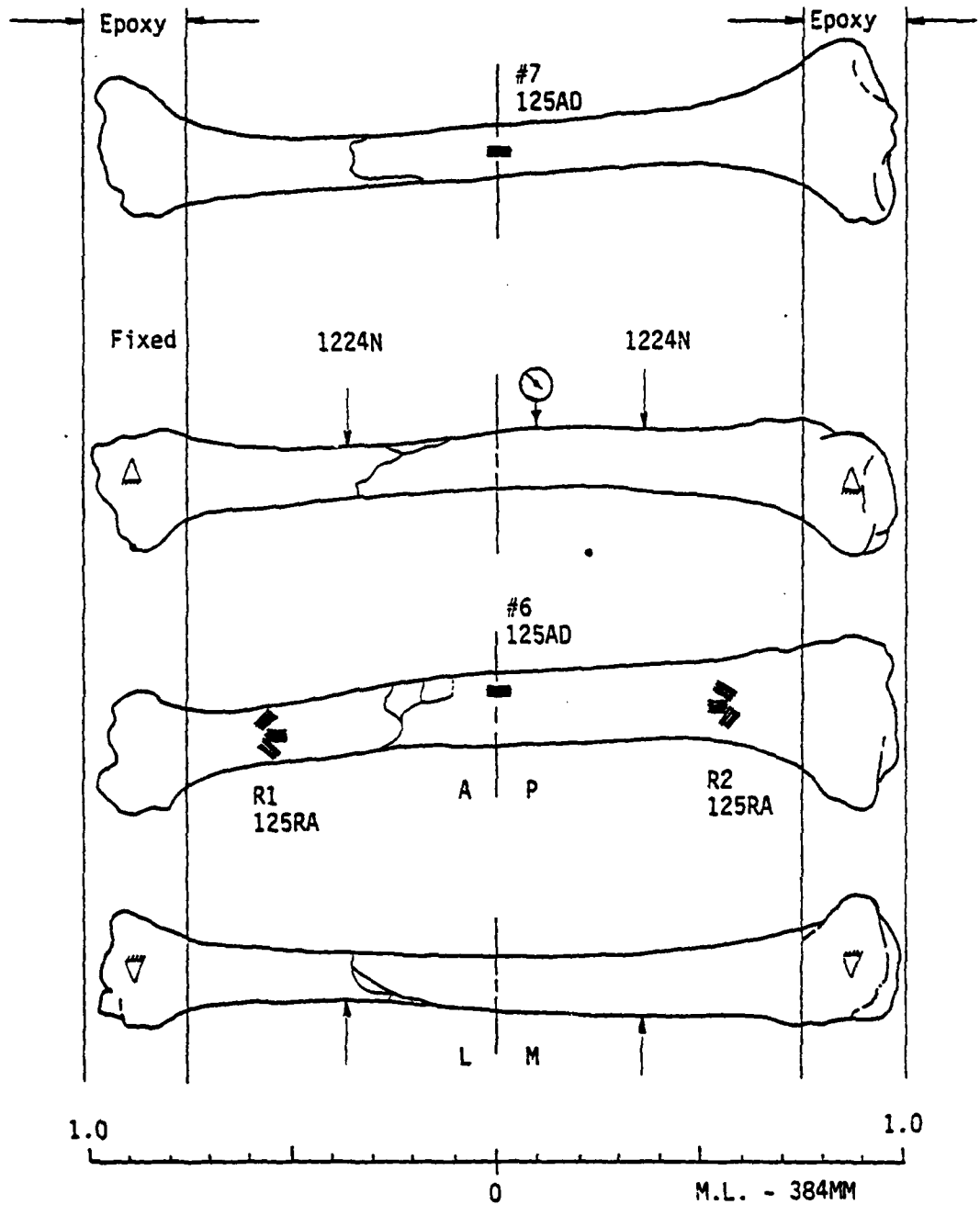


Figure 2.63 Test results for RT3792.

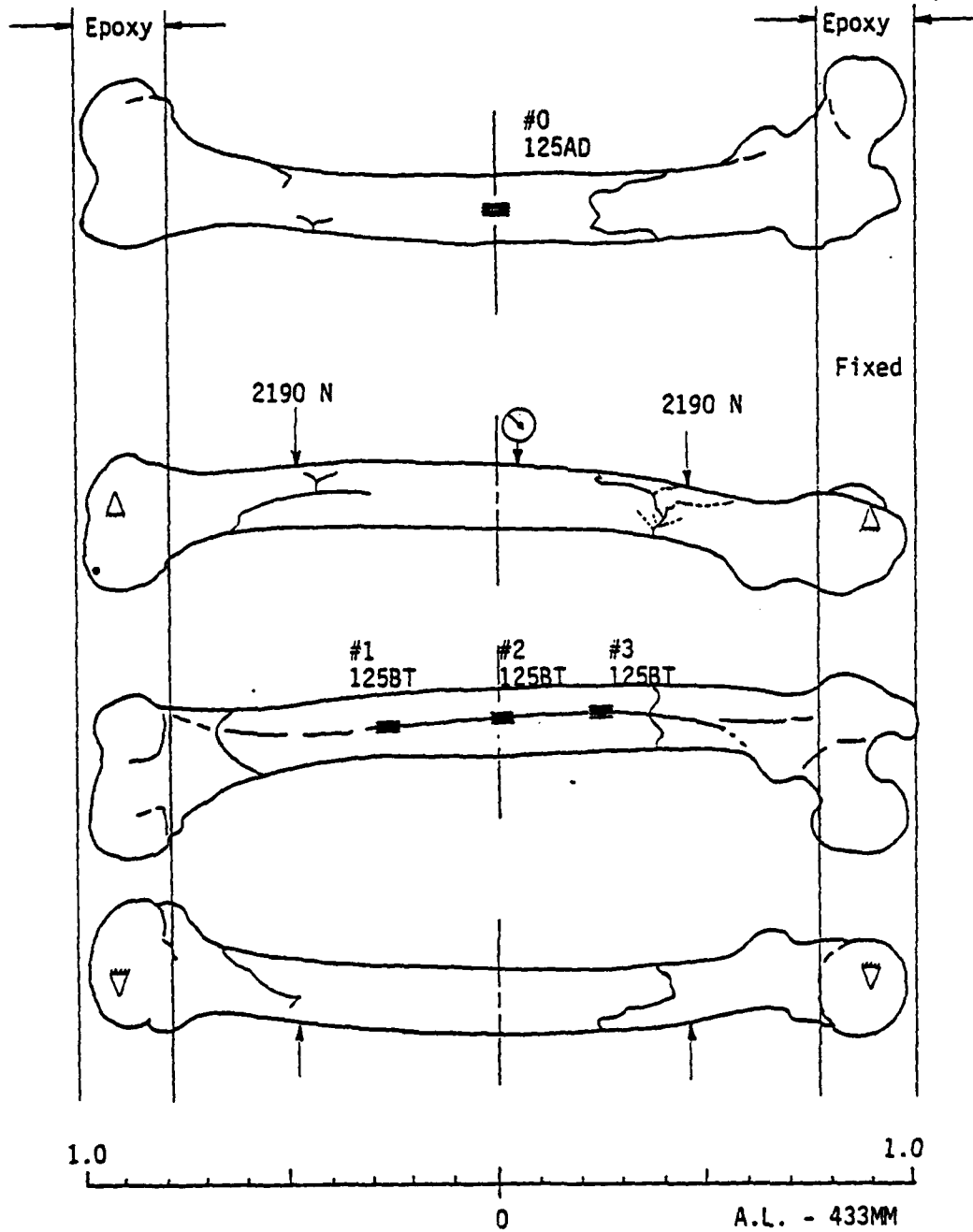


Figure 2.64 Test results for LF3782.

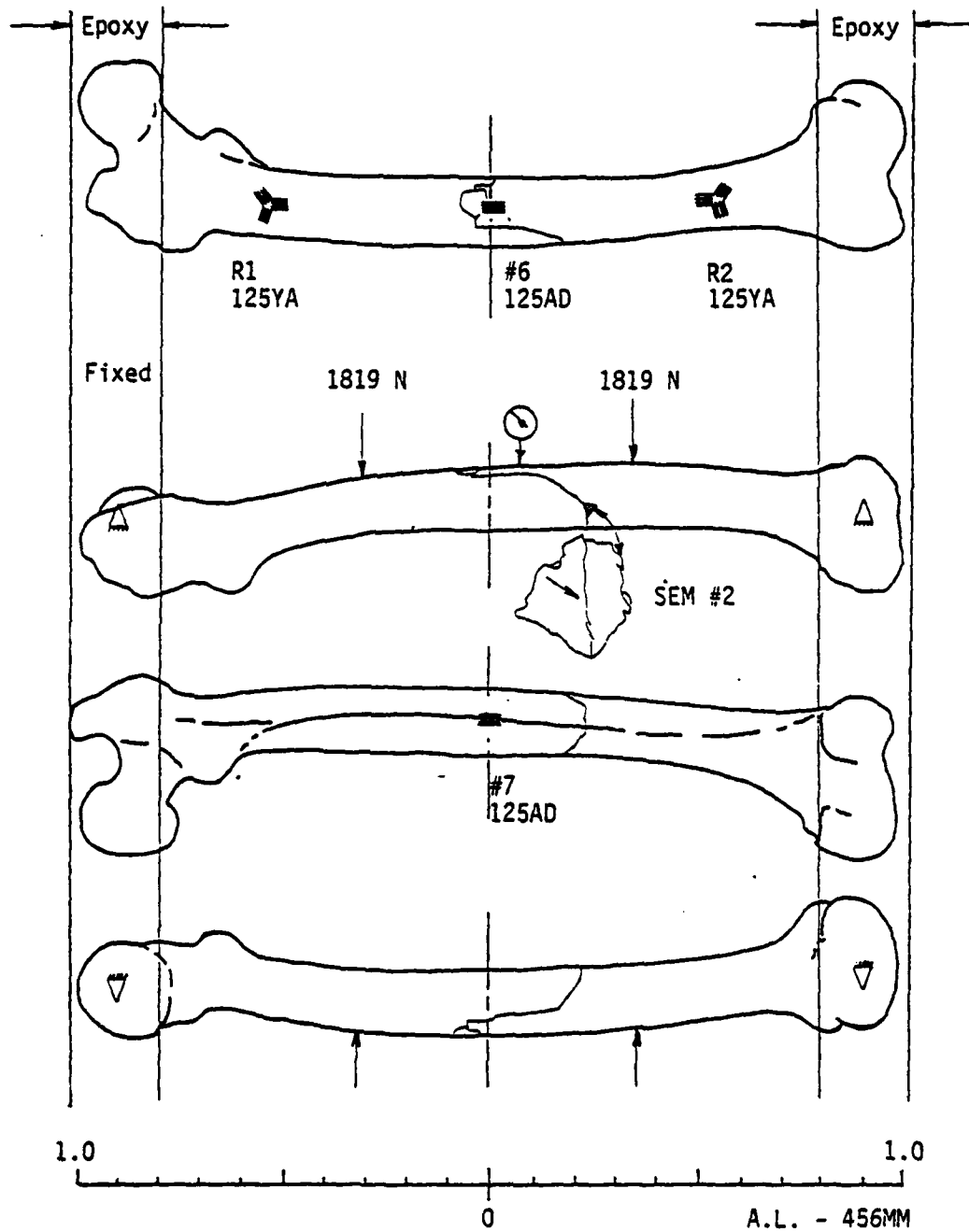


Figure 2.65 Test results for RF3792.

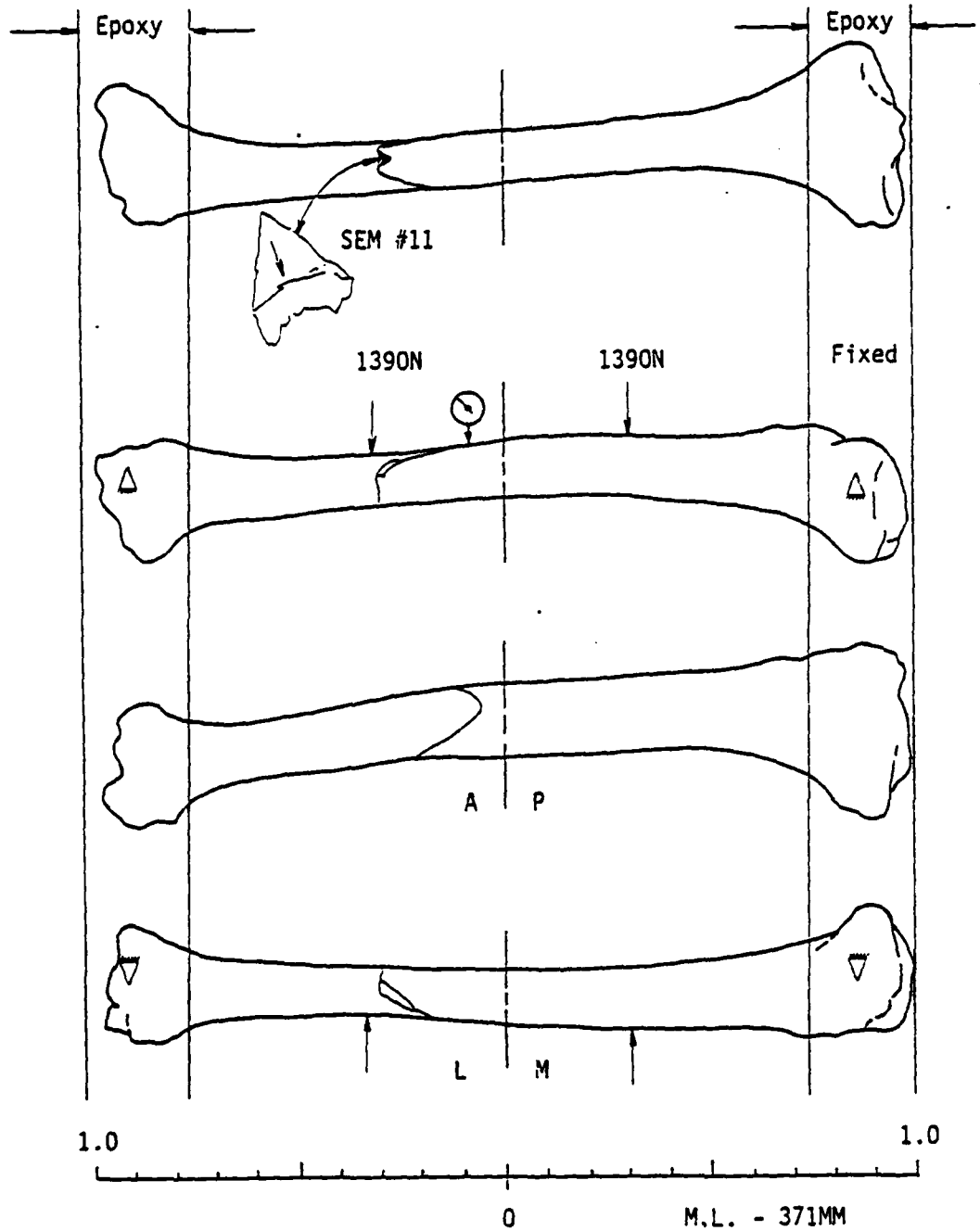


Figure 2.66 Test results for RT3753.

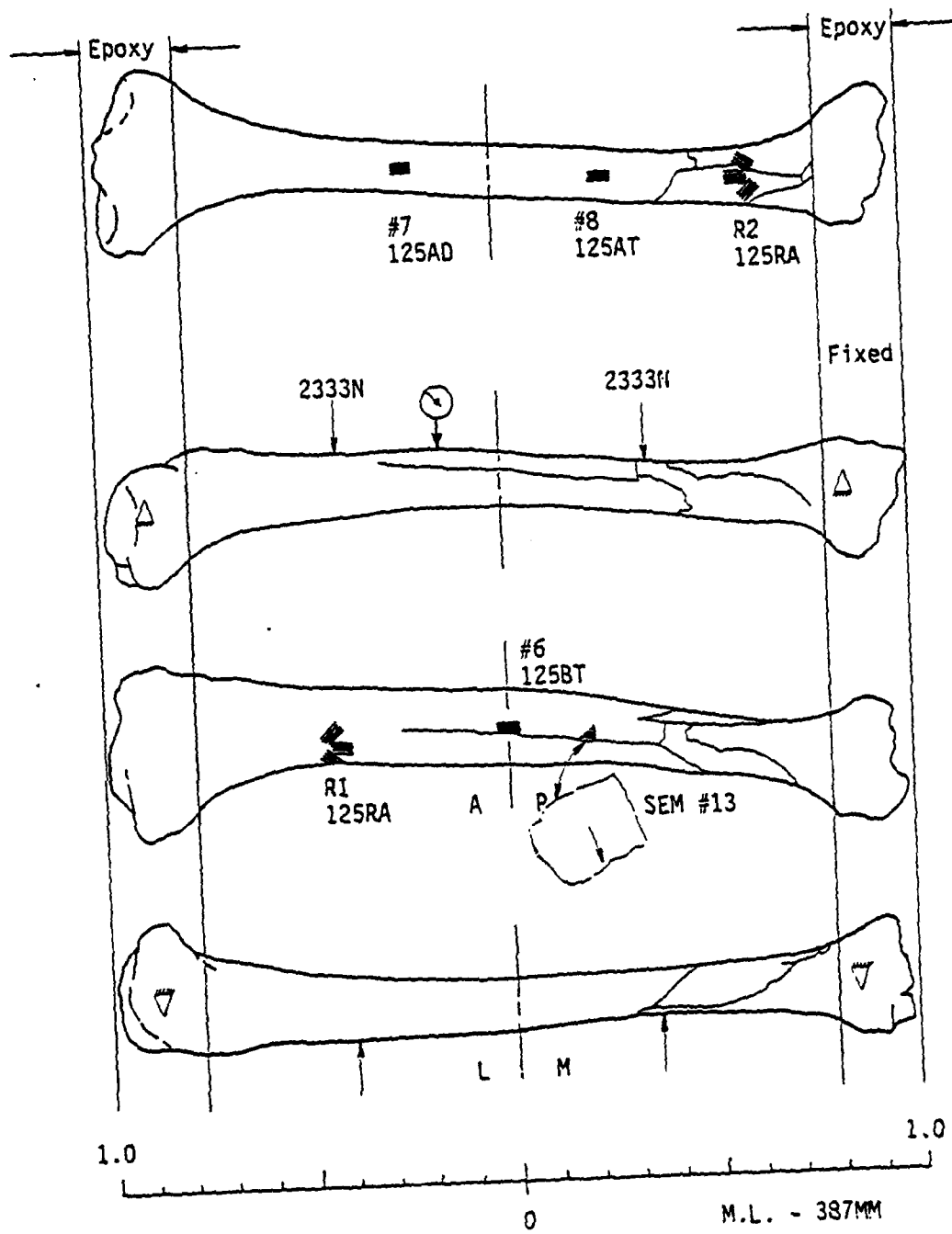


Figure 2.67 Test results for LT3793.

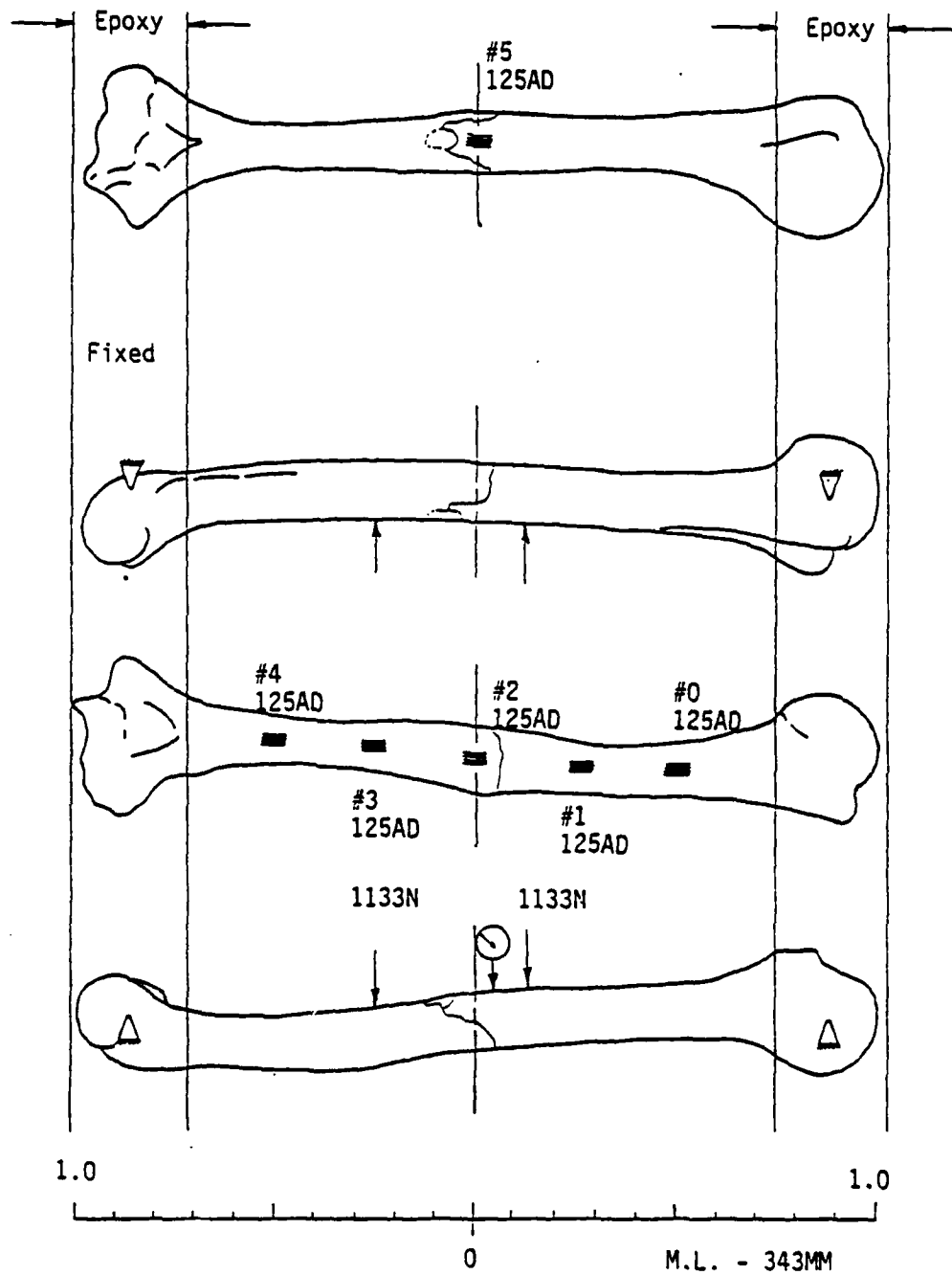


Figure 2.68 Test results for RH3792.

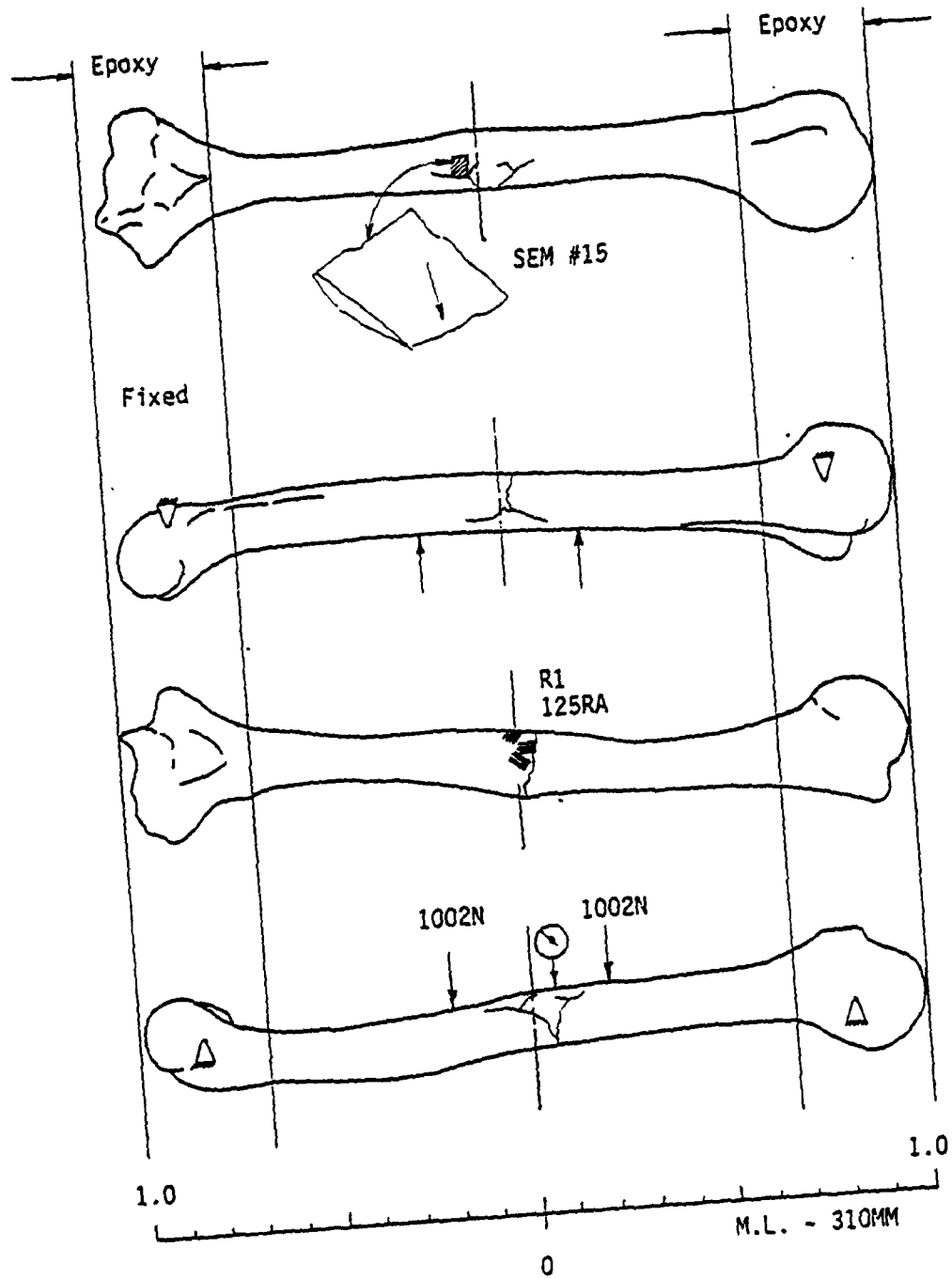


Figure 2.69 Test results for RH3782.

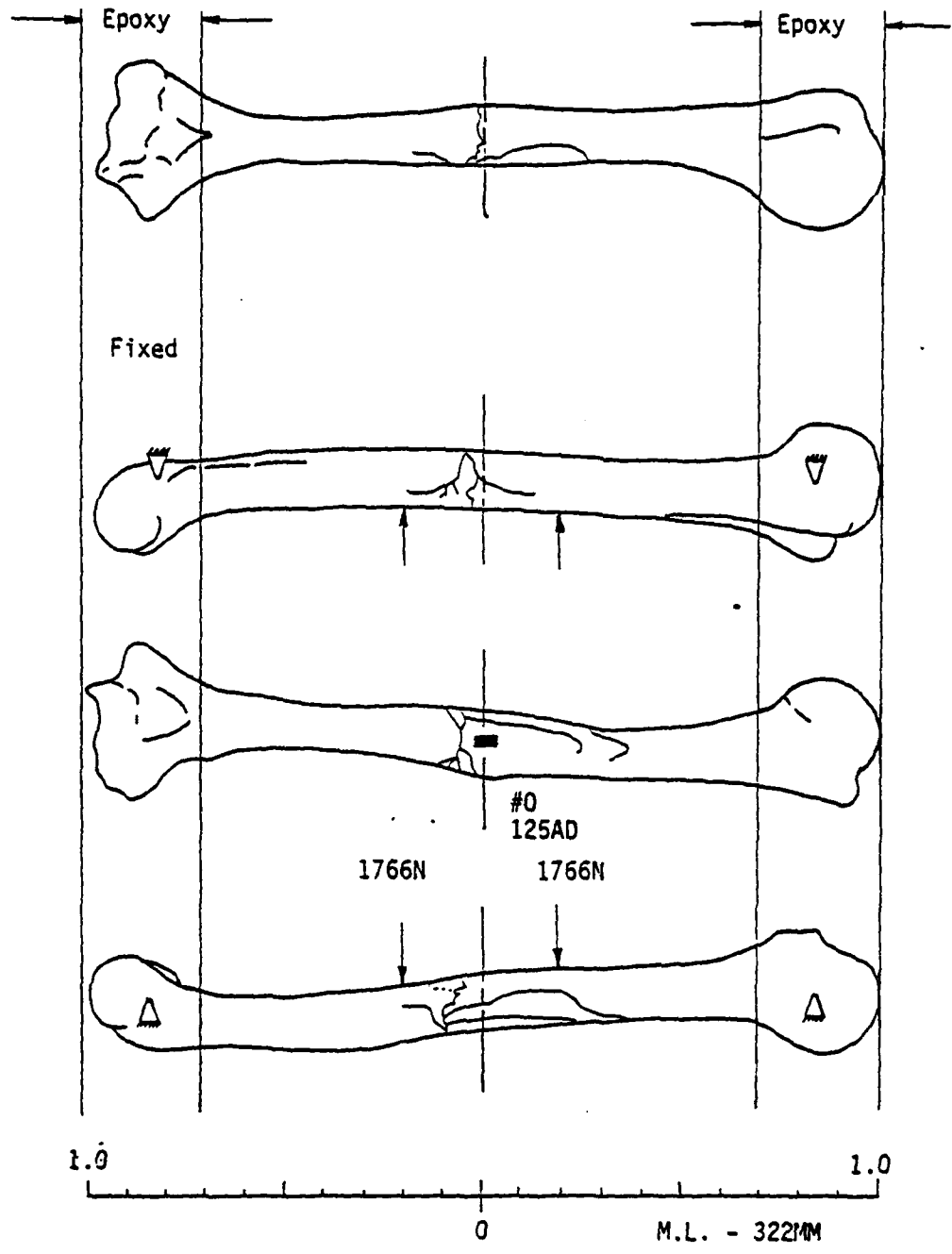


Figure 2.70 Test results for RH3790.

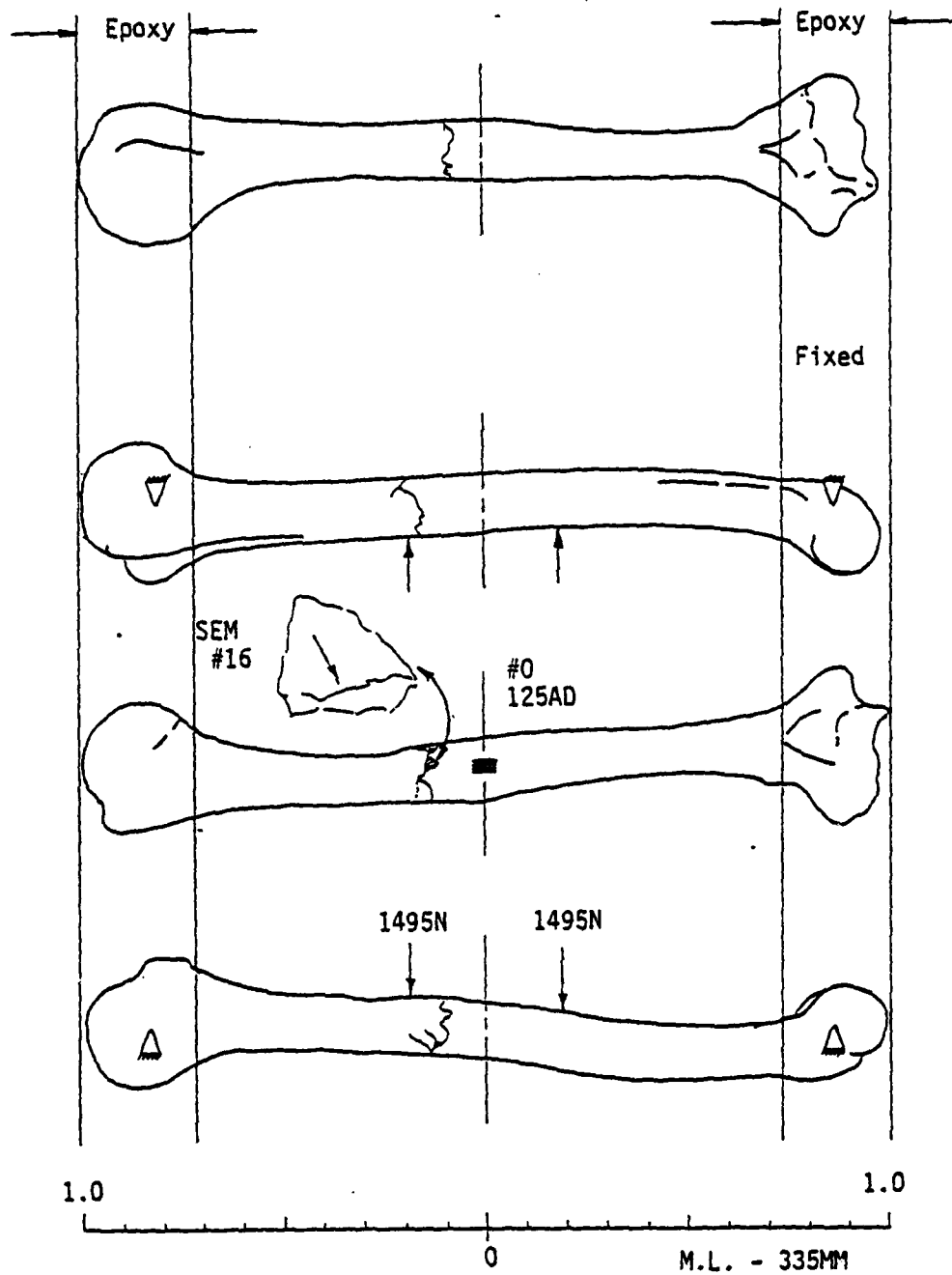


Figure 2.71 Test results for LH3787.

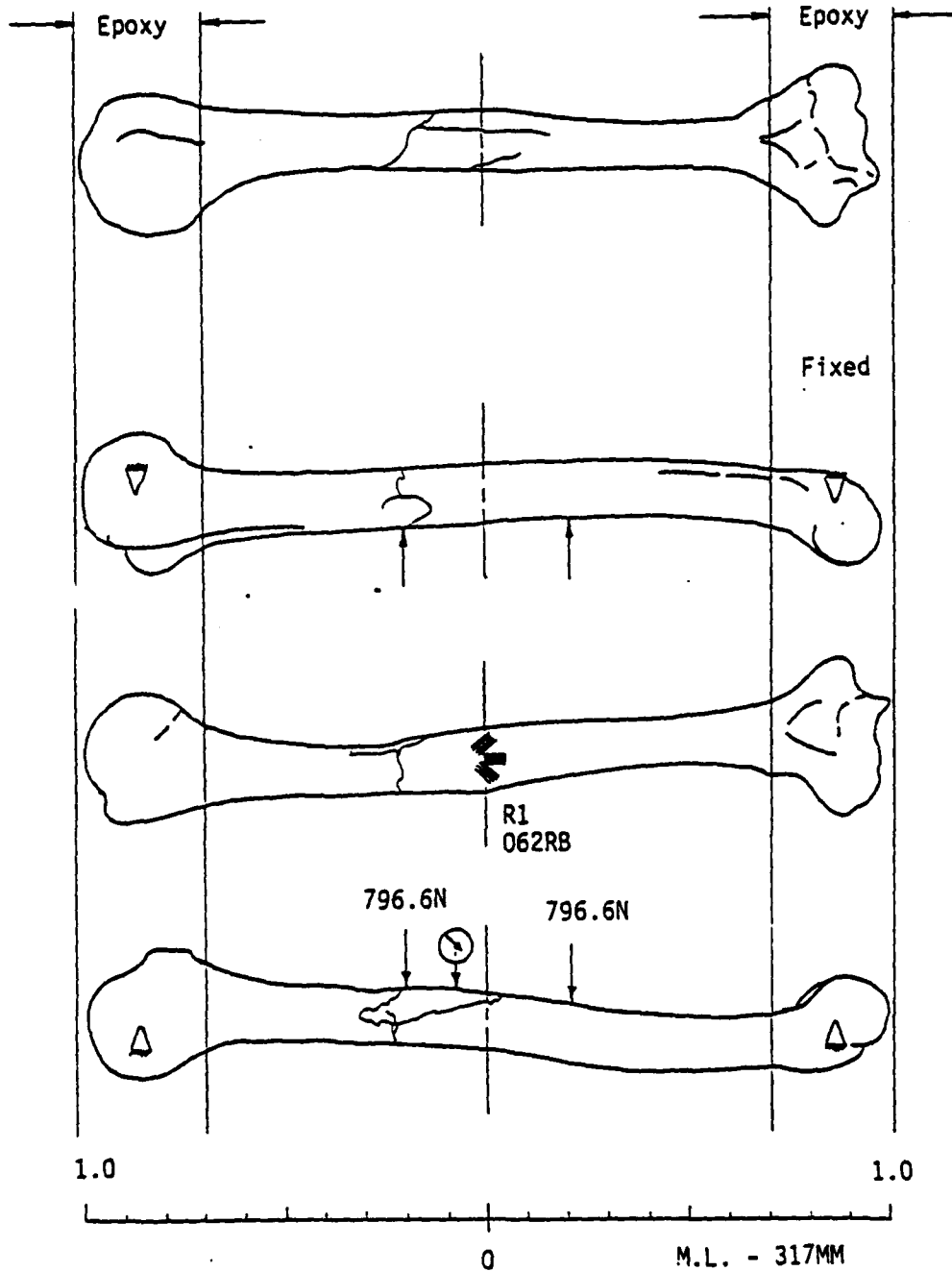


Figure 2.72 Test results for LH3753.

tests. RH3790 displayed considerable branching with some branches running 25% of the diaphysis and parallel to diaphyseal axis.

#### Fibulae:

Of the three fibulae tested in bending only, one, LFB3793, fractured under indeterminate loading conditions. (The bending carriage suspension chain was not slack and carried a large portion of the bending load.) However, even though the load at fracture is unknown, the fracture pattern should be representative of the patterns expected for the fibulae. Figure 2.73 shows the fracture for this fibula. Notice that they are essentially of the same configuration as those of the other bone types; however, some local crushing beneath the roller is probably involved. RFB3792 in Figure 2.74 shows a similar fracture pattern, but with no apparent bifurcation; the typical curvature occurring after the bending fracture is present. Both of these bones were bent using a medium roller spacing.

The only fibula, RFB3753 (Figure 2.75), tested using a narrow roller spacing was the first fibula fractured and it did not exhibit any obvious fracture. It was tested prior to the installation of the compensating spring on fixed end clamp and, therefore, contains an unwanted boundary condition--the end moment caused by the center of gravity of the fixed end clamp not passing through the support axis (see Section 2.2.3.2).

#### Combined Loadings:

The combined loading conditions consisted of two basic loading plans--torsion dominant and bending dominant. In the torsion dominant test, the bending load and torsional load were applied simultaneously in predetermined increments until a certain bending load was achieved. Then the torsional load was increased further incrementally while the bending load was adjusted to remain essentially constant. The bending dominant plan was similar with the torsional load held constant at some level while the bending load was increased until fracture occurred. The results of these two loading conditions will be discussed separately.

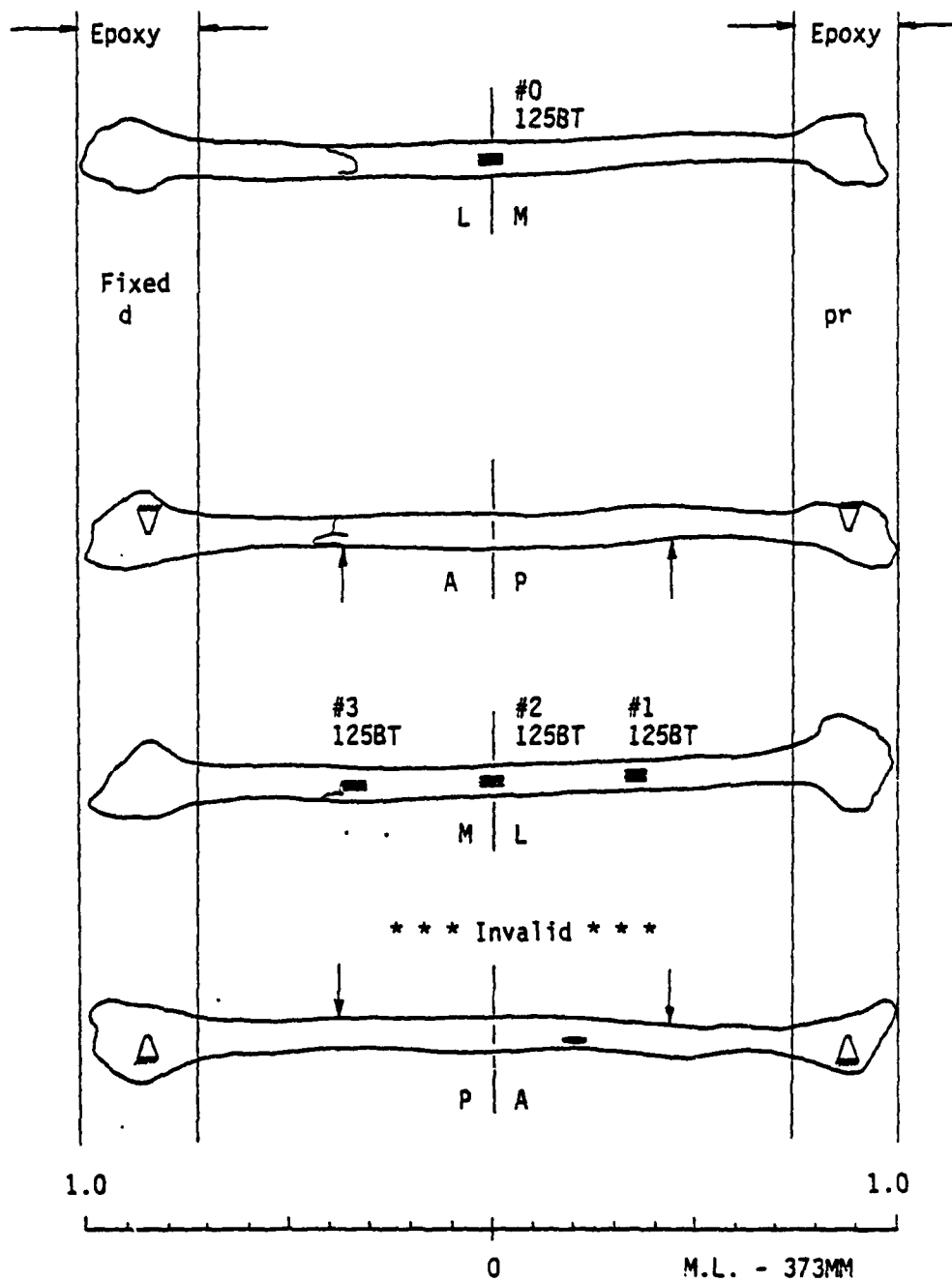


Figure 2.73 Test results for LFB3793.

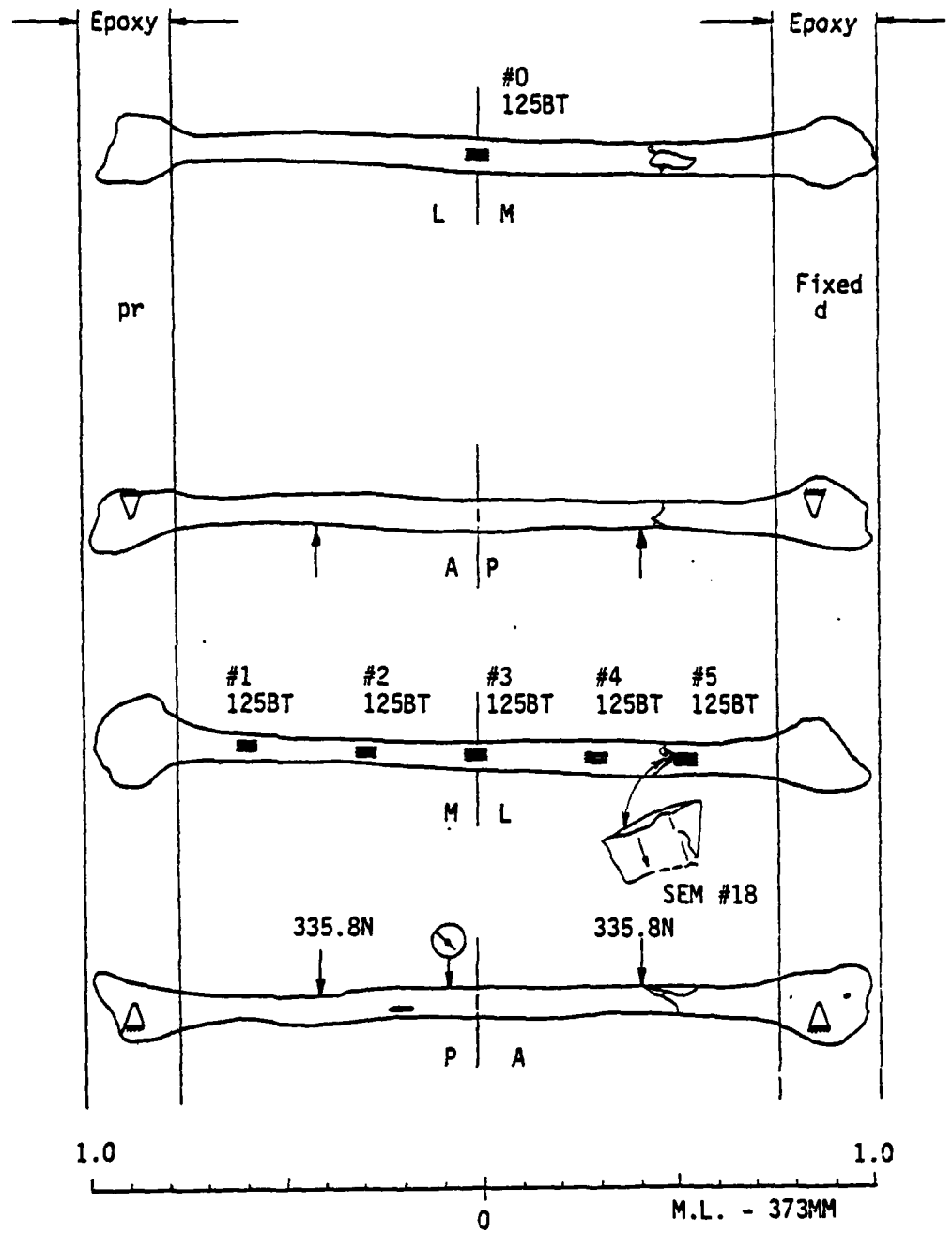


Figure 2.74 Test results for Rfb3792.

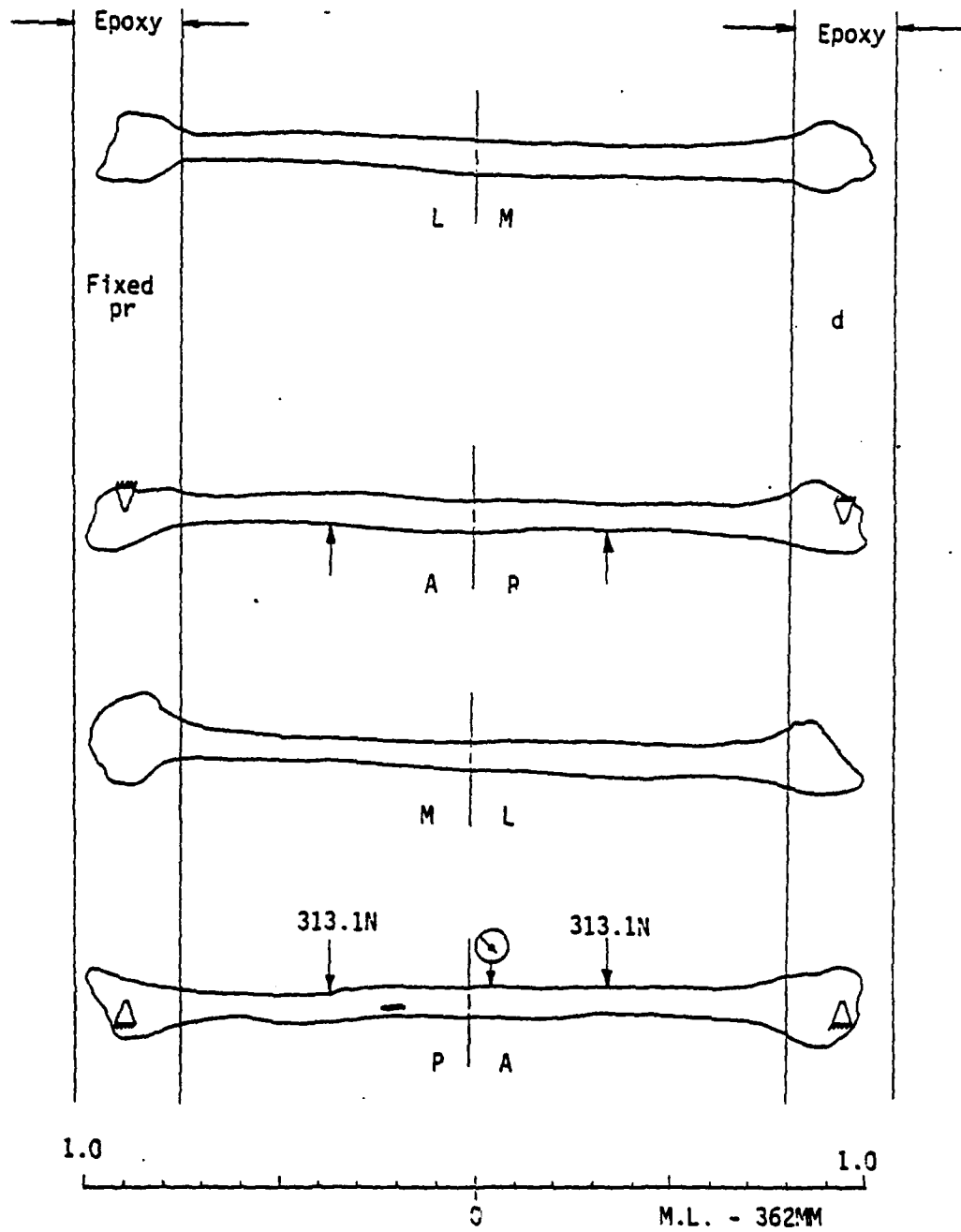


Figure 2.75 Test results for Rfb3753.

Torsion Dominant:

Femora: For the two femora tested under a torsion dominant combined loading condition, one, LF3790, had a fracture configuration that one would expect from a torsion only loading condition; the other femur, RF3790, definitely displayed the effects of both bending and torsion. LF3790 (Figure 2.76) had a spiral fracture that traveled once around the diaphysis as well as the CSO fracture connecting the start and finish of the spiral fracture. RF3790 (Figure 2.77) had the same configuration plus the bifurcation observed for the bending only loading condition. Note how the location of these bifurcations are slightly rotated opposite to the direction of twist when compared to the bifurcations observed in the bending only fractures. Since the fracture occurred while the bone was in a twisted state and since the bone surface rotates relative to the bending carriage, the bifurcations all displaced in azimuth counter to the direction of twist as the twisting moment is removed. The probable reason for bifurcations in the one femur and not the other, is that RF3790 was tested with a wide roller spacing while LF3790 was bent using a narrow roller spacing. Note also that the spiral fracture occurred in the distal half of the left femur and proximal half of the right. This is probably the result of the differences between eversive and inversive rotation.

Tibiae: As with the femora, one tibia tested under the torsion dominant loading condition had a fracture configuration typical of the torsion only loading condition while the other tibia had pattern with characteristics of both bending and torsion. LT3790 (Figure 2.78) had two parallel, longitudinal fractures on the posterior side at the proximal end. Intuitively, these two fractures seem more the result of bending shear stresses than of normal bending stresses. Anyway, they are the result of bending and not twisting. One of the fractures transforms into the typical spiral fracture associated with the torsion only condition. The spiral travels once around the diaphysis and ends with no CSO. The other tibia, RT3790 (Figure 2.79), exhibited only the spiral fracture with a partial CSO. The fracture of the first tibia spanned the proximal half while the fracture of the latter was concentrated in the distal third. The difference in configuration was

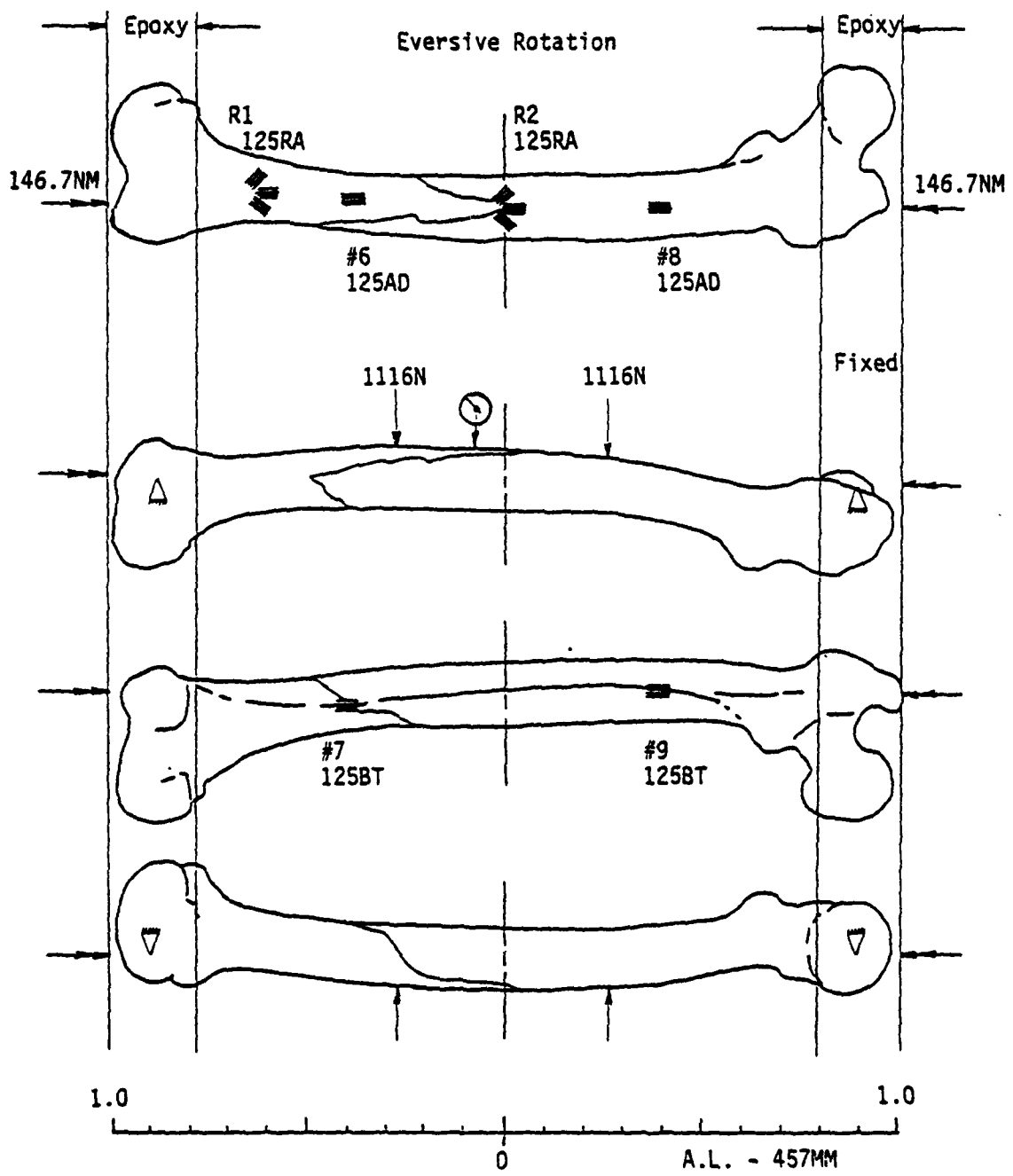


Figure 2.76 Test results for LF3790.

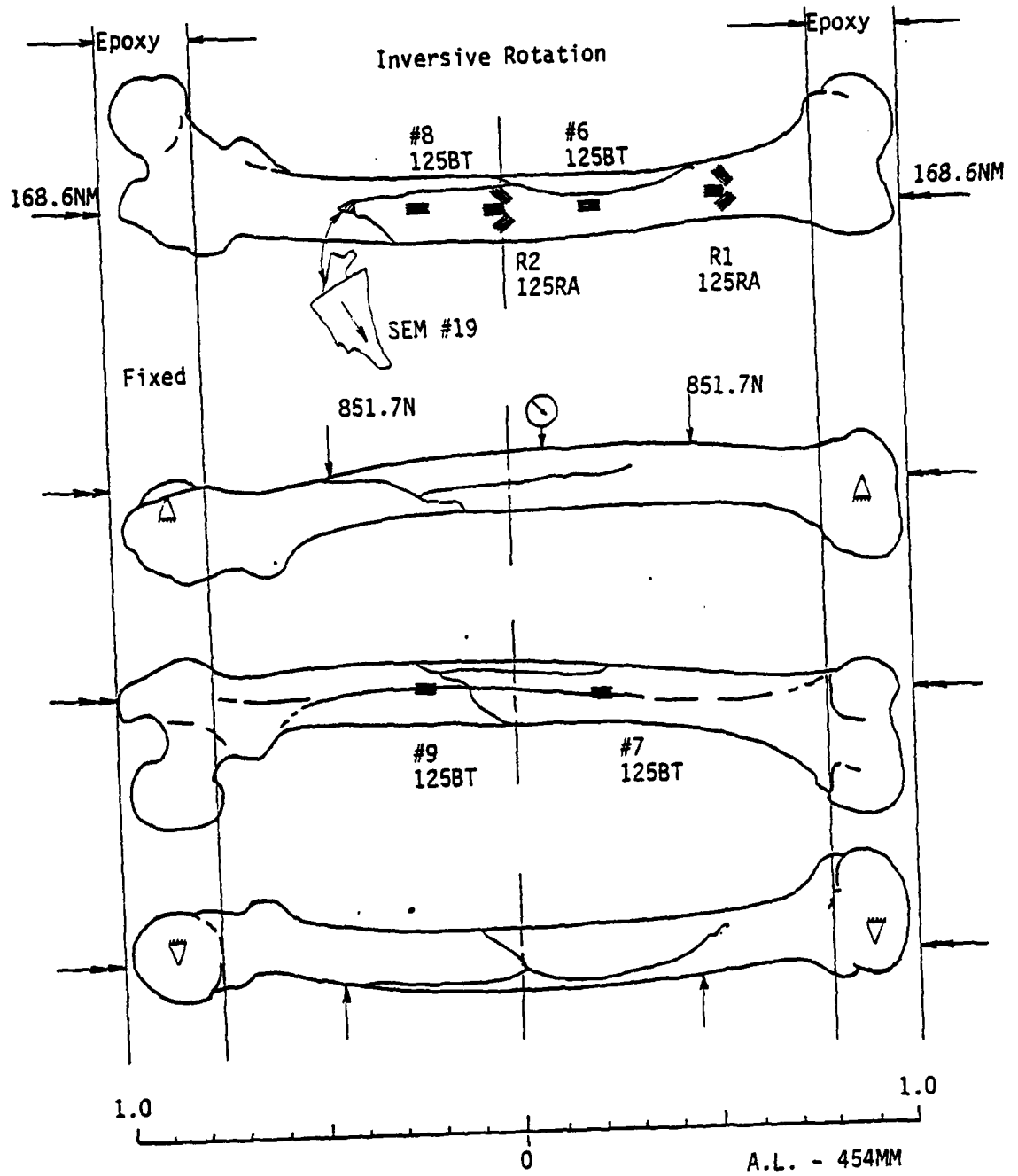


Figure 2.77 Test results for RF3790.

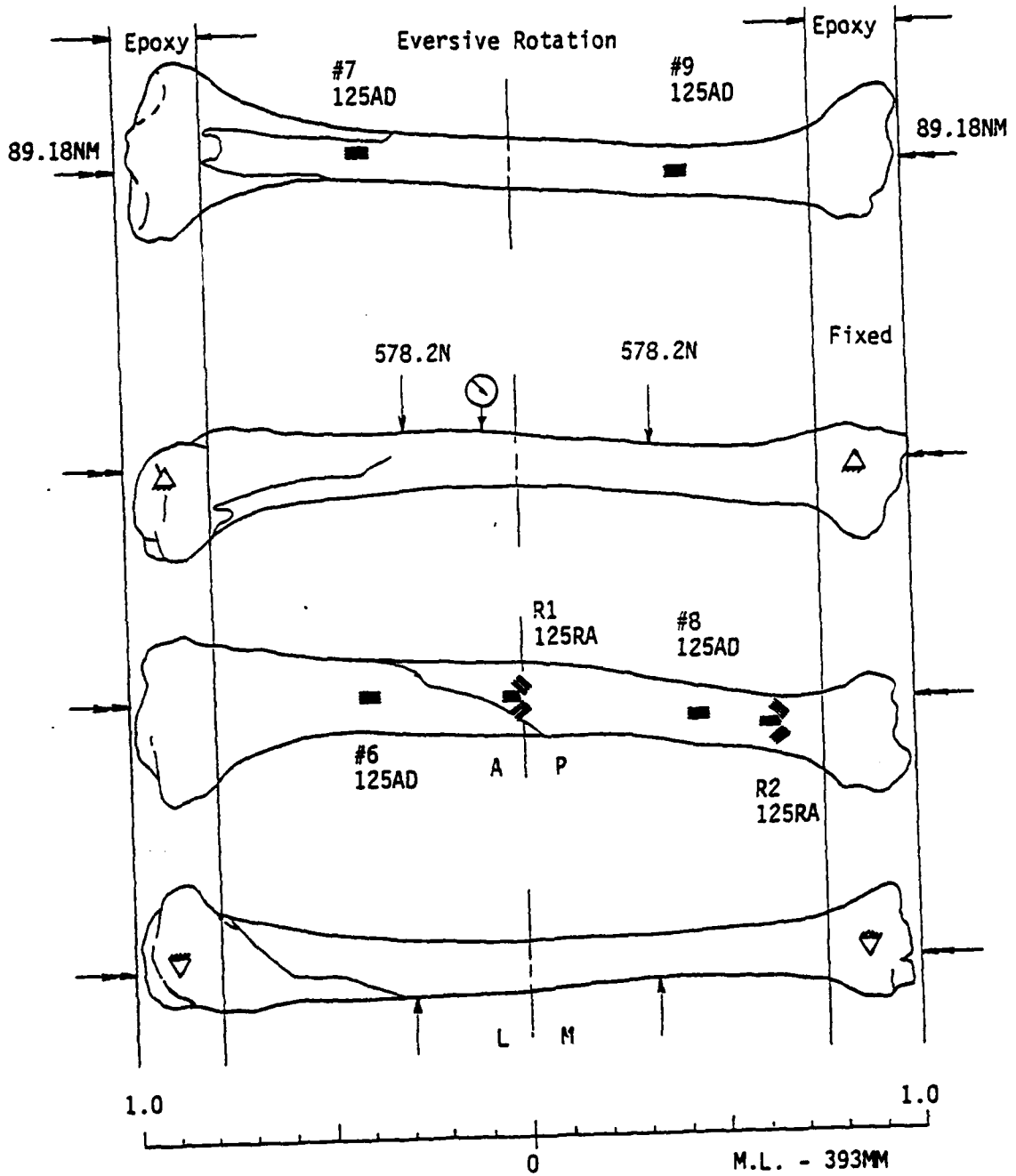


Figure 2.78 Test results for LT3790.

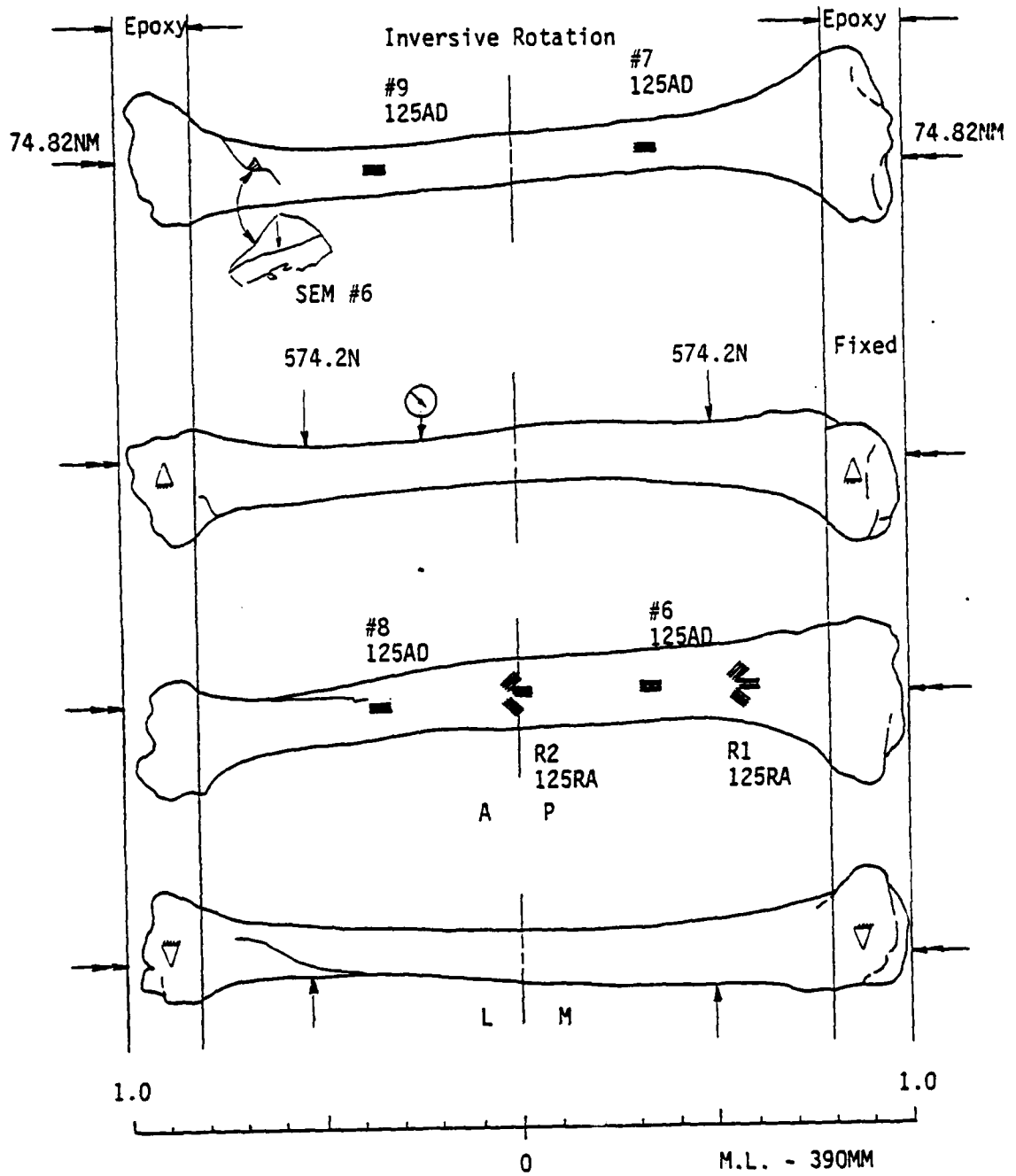


Figure 2.79 Test results for RT3790.

probable due to difference in load spacing. LT3790 was bent with a narrow roller spacing and twisted eversively while RT3790 was with a wide spacing and inversive rotation.

Humeri: A slight difference in behavior was observed for the two humeri than was discussed for the tibiae and femora. RH3787 (Figure 2.80) had a spiral fracture in the proximal half of the diaphysis with no CSO. LH3790 (Figure 2.81) had a spiral fracture in the second quarter of the diaphysis from the proximal end, but with a complete CSO fracture. Since both of these were bent with the same roller spacing, the reason for different locations along the diaphysis is probably the result again of inversive rotation versus eversive rotation.

Fibulae: Of the three fibulae tested under the torsion dominant loading condition, two had characteristics of the bending only situation while the other exhibited torsion only characteristics. RFb3790 (Figure 2.82) had a bending tension fracture on the medial side that curved toward and bifurcated close to the lateral surface. The fracture occurred directly below the roller (load) in the distal first quarter at fixed end clamp where there was little rotation relative to the bending carriage. The branching on both sides of the load had long fracture lines parallel to the axis of rotation. RFb3787 (Figure 2.83) also exhibited a fracture characteristic of bending only which began as a tension failure in the medial side, distal end well outside the roller (load). The fracture then curved proximally toward the lateral surface on both the anterior and posterior sides, but did not bifurcate. It approached an orientation parallel to the lateral surface before separating the diaphysis. The distal end was also at the fixed end clamp for this fibula so there was little rotation relative to the bending carriage. LFB3790 (Figure 2.84) fractured spirally and separated with a CSO.

General: Regions existed in the spiral fractures described above which were oriented parallel to the torsional axis. The regions were observed in almost all of the spiral fractures and occasionally were entered and exited with rather sharp changes in direction.

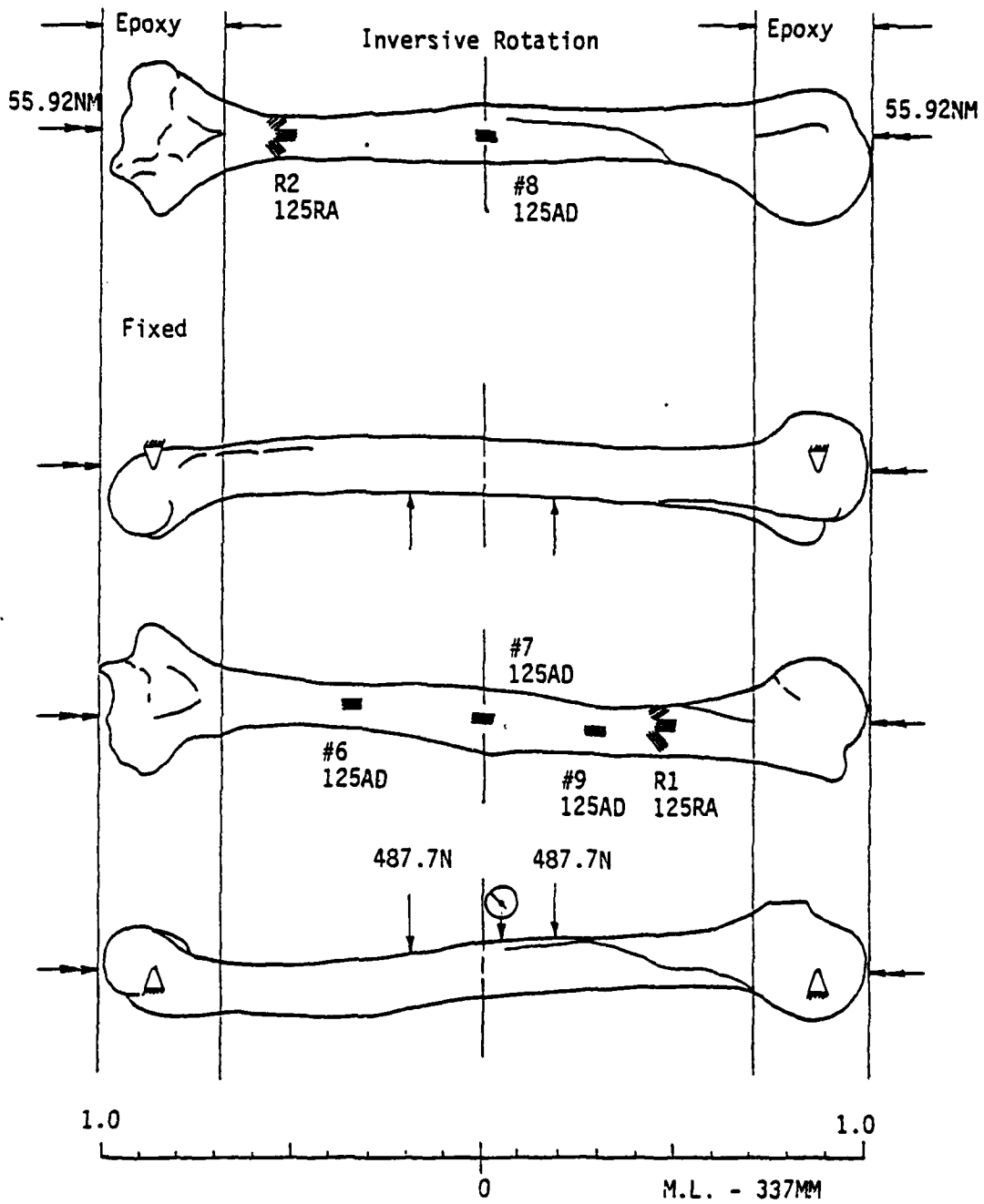


Figure 2.80 Test results for RH3787.

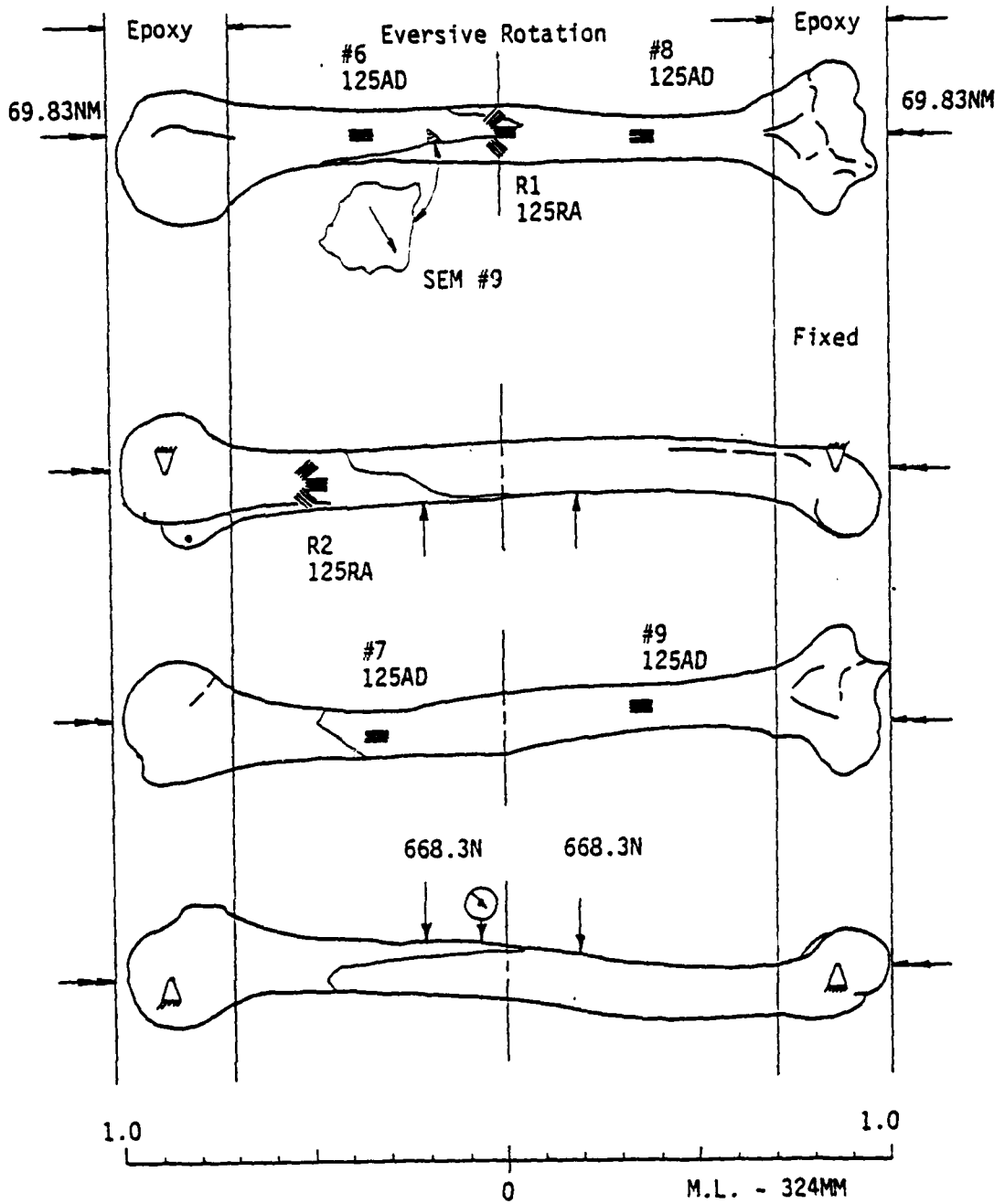


Figure 2.81 Test results for LH3790.

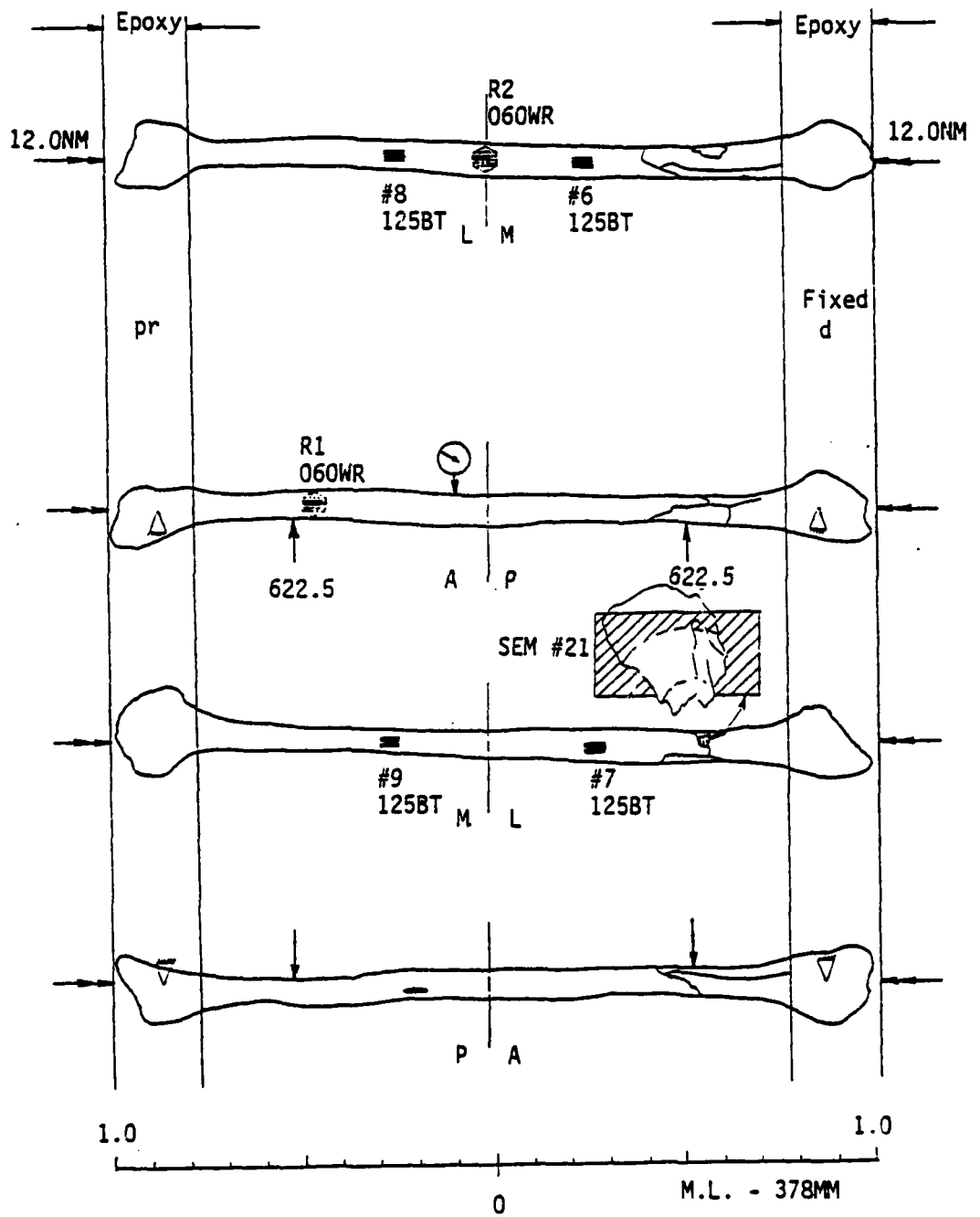


Figure 2.82 Test results for RFB3790.

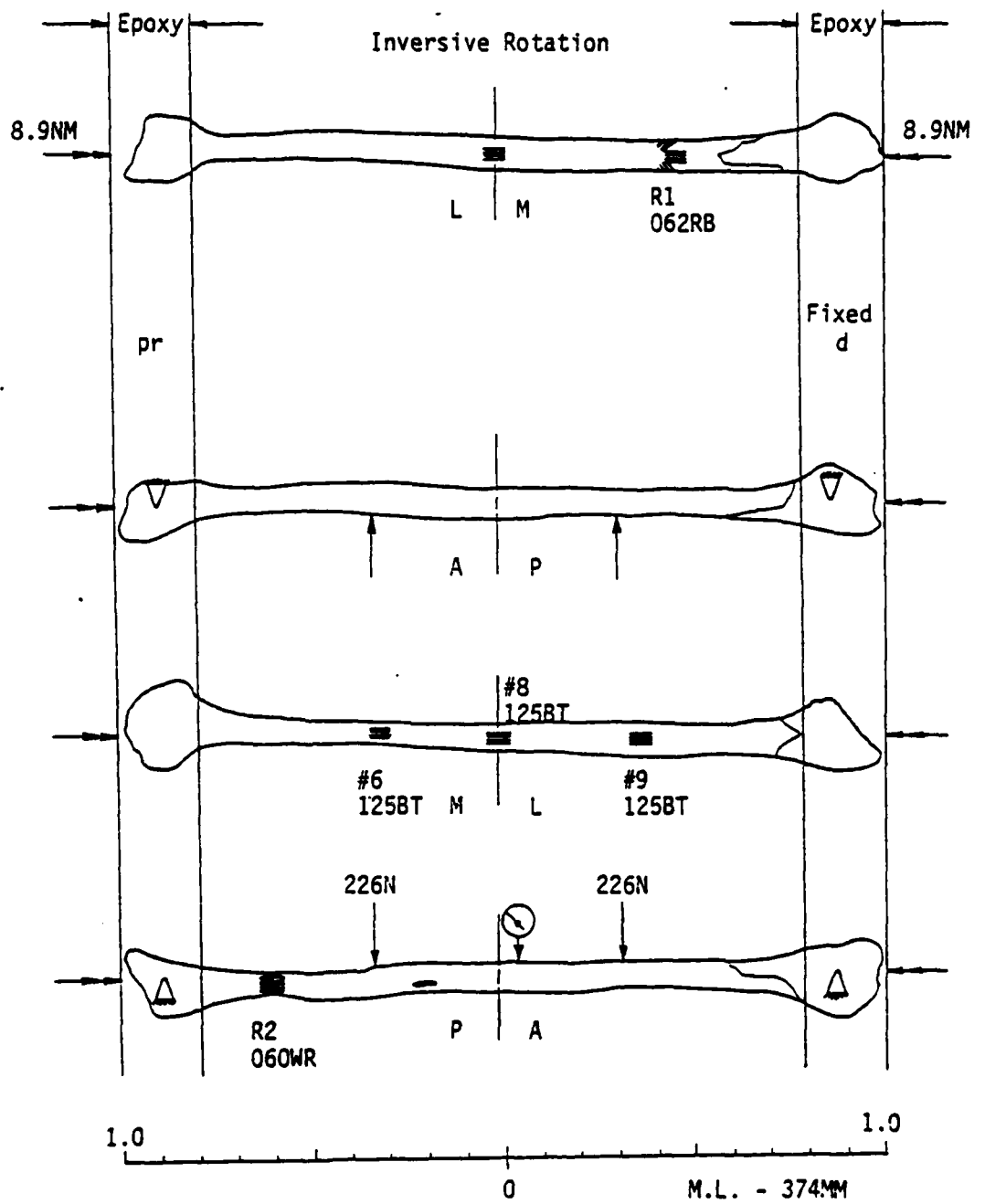


Figure 2.83 Test results for RFB3787.

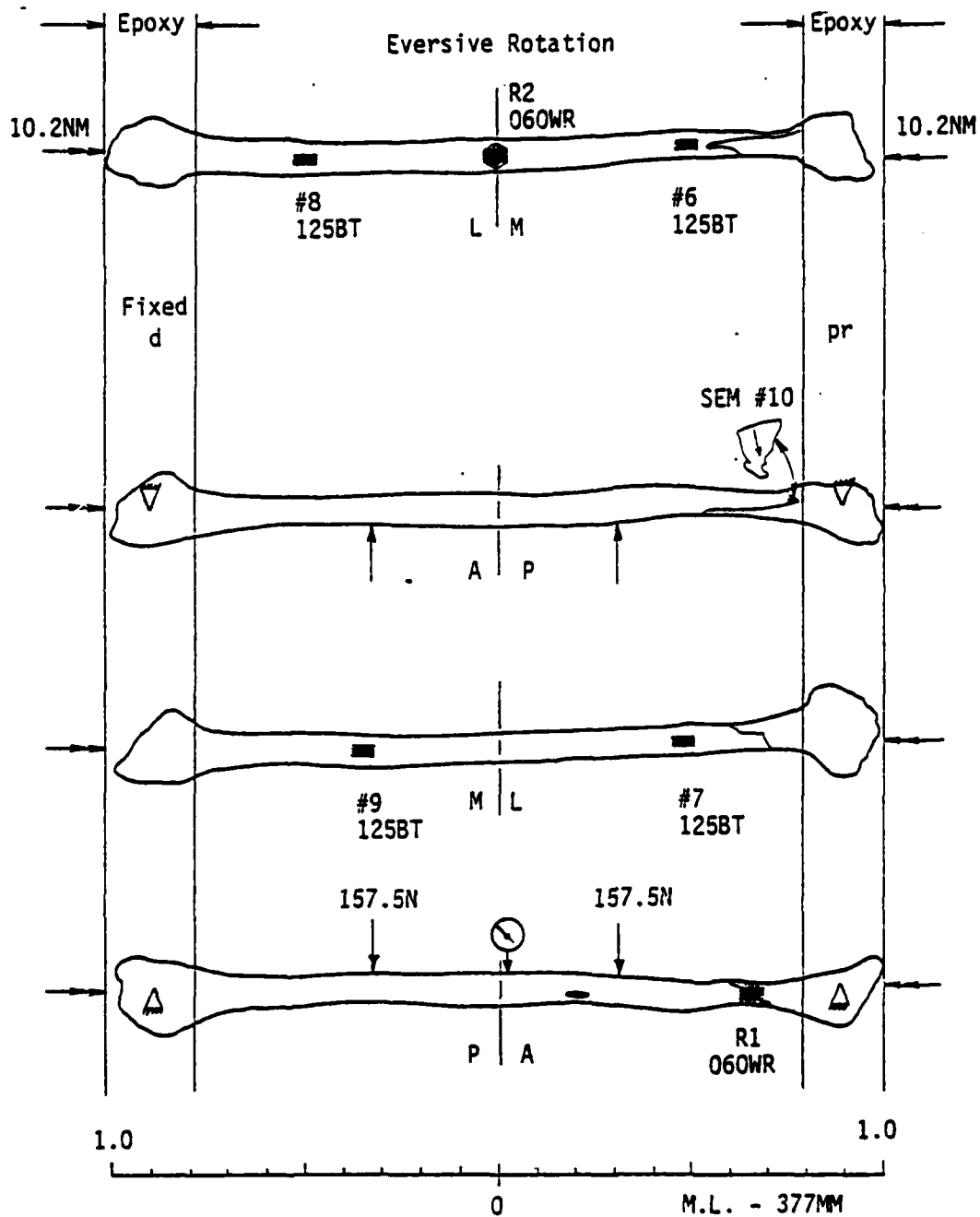


Figure 2.84 Test results for LFB3790.

Bending Dominant:

Femora: Two femora were tested under bending dominant loading conditions. Both of these had fractures characteristic of the bending only situation with fracture beginning on the convex side of the bending bone as a tension failure. The fracture then proceeded vertically normal to the neutral axis and, at approximately the neutral axis, bifurcated in RF3787 (Figure 2.85) while only curving in LF3787 (Figure 2.86). The fracture continued to curve proximally in LF3787 until parallel to anterior surface before separating the diaphysis. In RF3787, one branch traveled parallel to the neutral axis angling off to the anterior surface; the other branch traveled to the anterior surface along a path almost normal to the neutral axis. In LF3787 the bone was bent using a narrow roller spacing and the fracture occurred at the distal third well outside the roller. In RF3787, the roller spacing was at the widest separation and here the fracture occurred directly below the roller at the distal third of the diaphysis.

Tibiae: Neither of the two tibia tested under the bending dominant condition displayed fracture patterns similar to the torsion only or bending only situations. They were more similar to those configurations associated with pure torsion, but they traveled only half way around the diaphysis and, therefore, had no CSO mode. LT3787 (Figure 2.87) was bent using a narrow roller spacing and its fracture began at the proximal end, spiraling toward the distal third of the diaphysis and ending blindly beneath the applied load. RT3787 (Figure 2.88) had a fracture which followed a similar path, but occurred at the distal end of the bone.

Humeri: The only humerus, LH3793 (Figure 2.89), tested under the bending dominant loading condition exhibited fracture configurations characterized by the bending only loading condition. Two fractures occurred; each started opposite one of the rollers on the posterior side and traveled a curve path towards the proximal end which was oblique to torsional axis. The fracture beneath the proximal roller bifurcated on the medial side but not on the opposite, lateral side. The other, beneath the distal roller, curved upwards towards the anterior surface on the lateral side, only, following a path parallel to the proximal fracture.

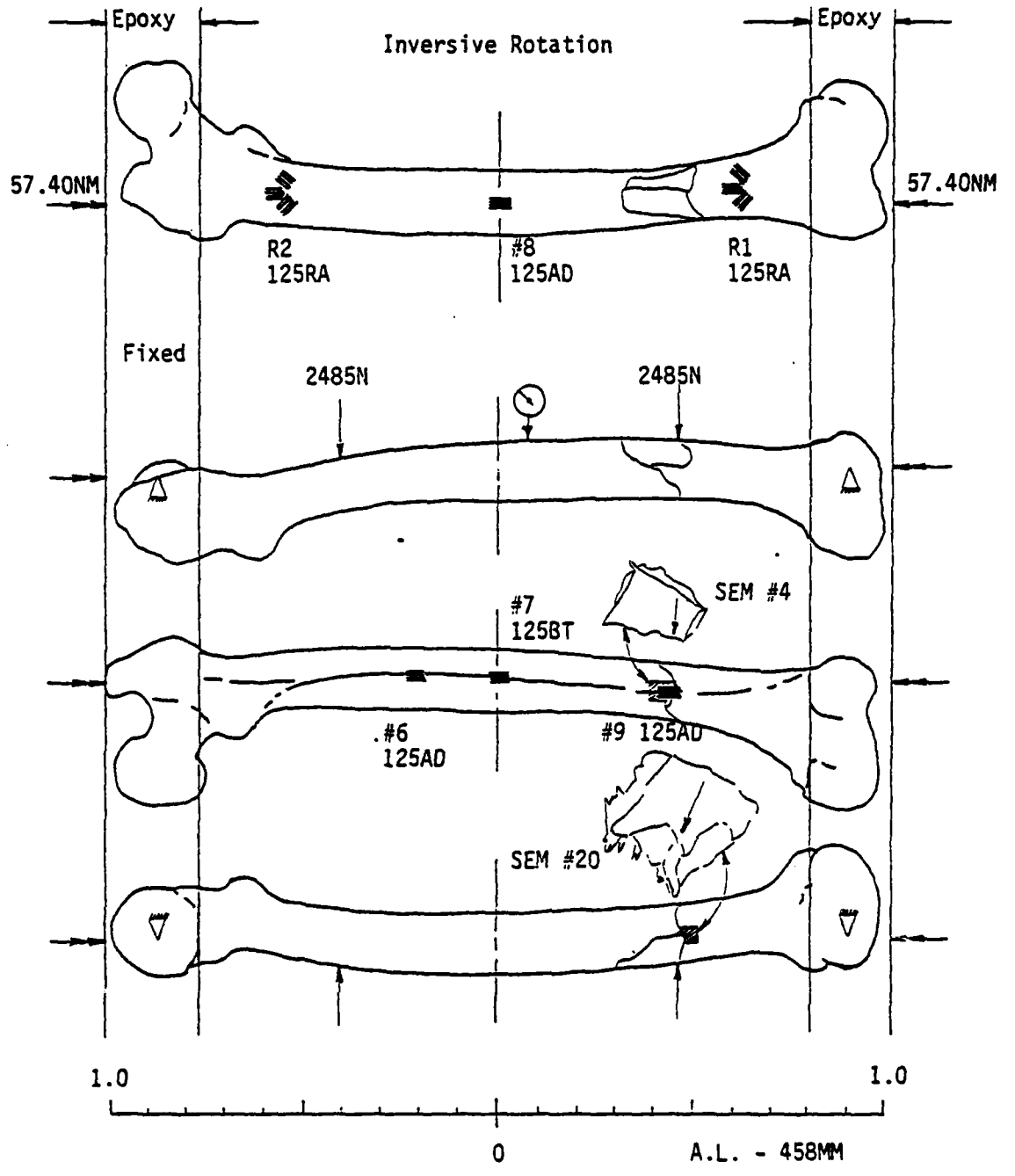


Figure 2.85 Test results for RF3787.

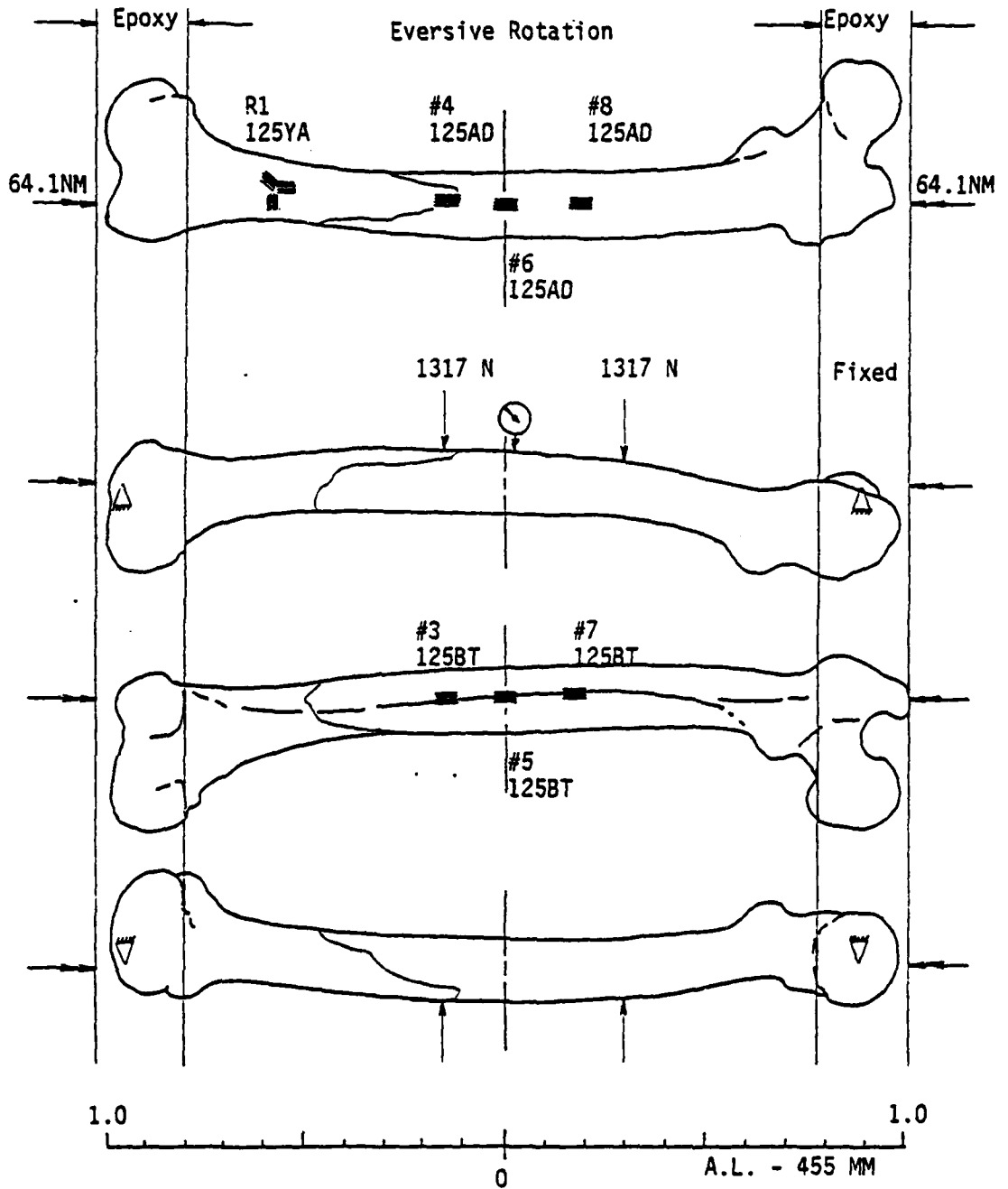


Figure 2.86 Test results for LF3787.

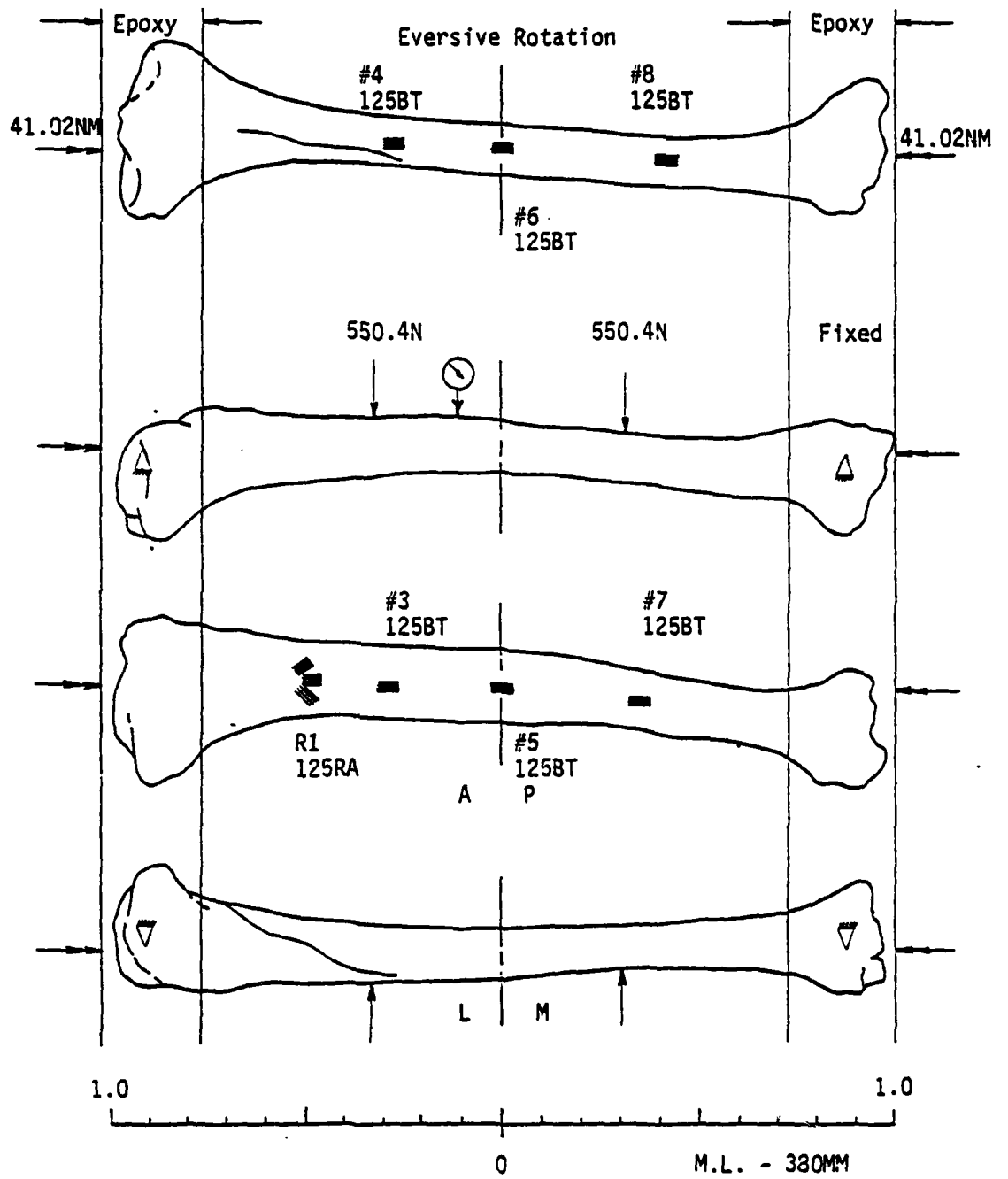


Figure 2.87 Test results for LT3787.

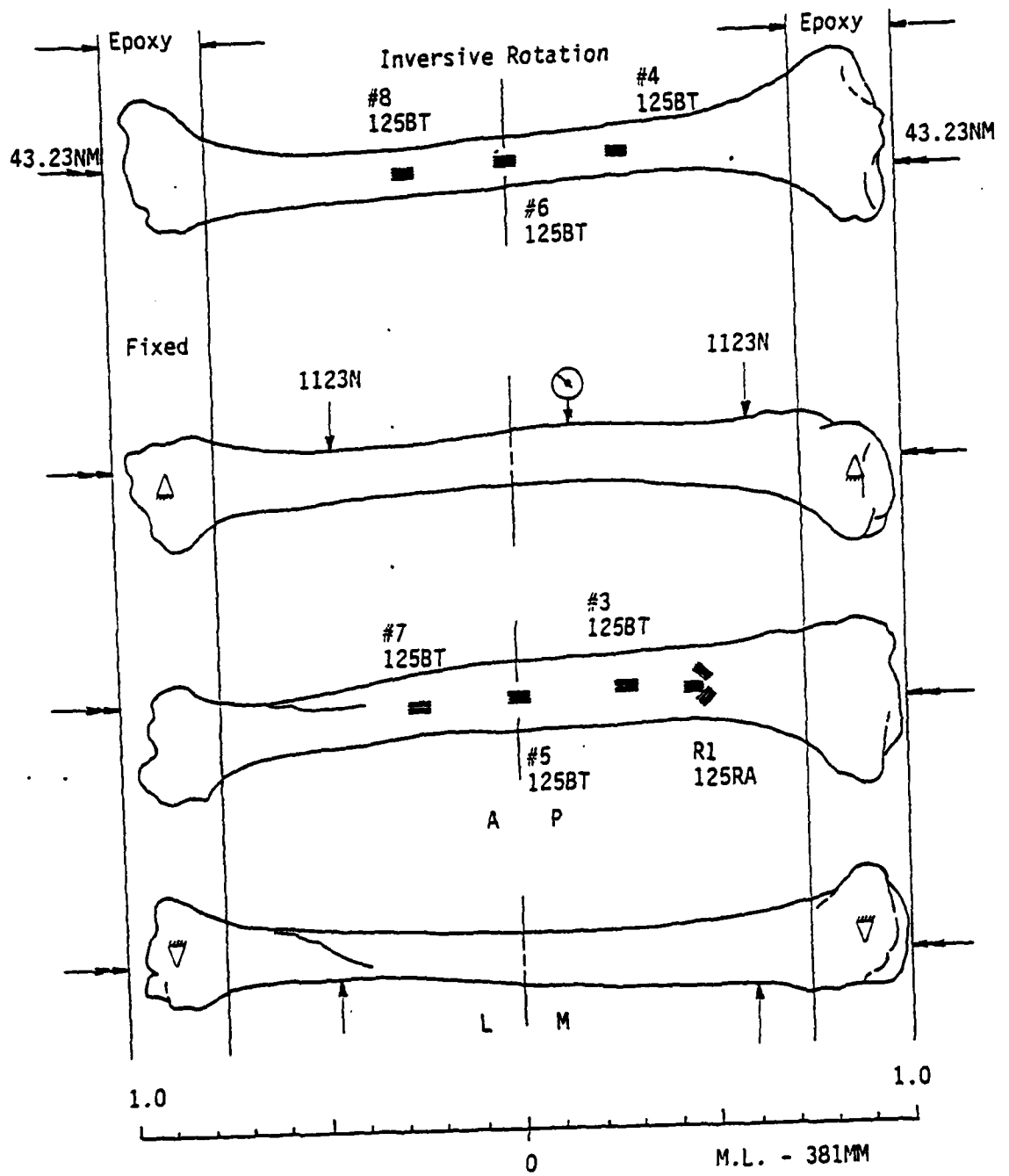


Figure 2.88 Test results for RT3787.

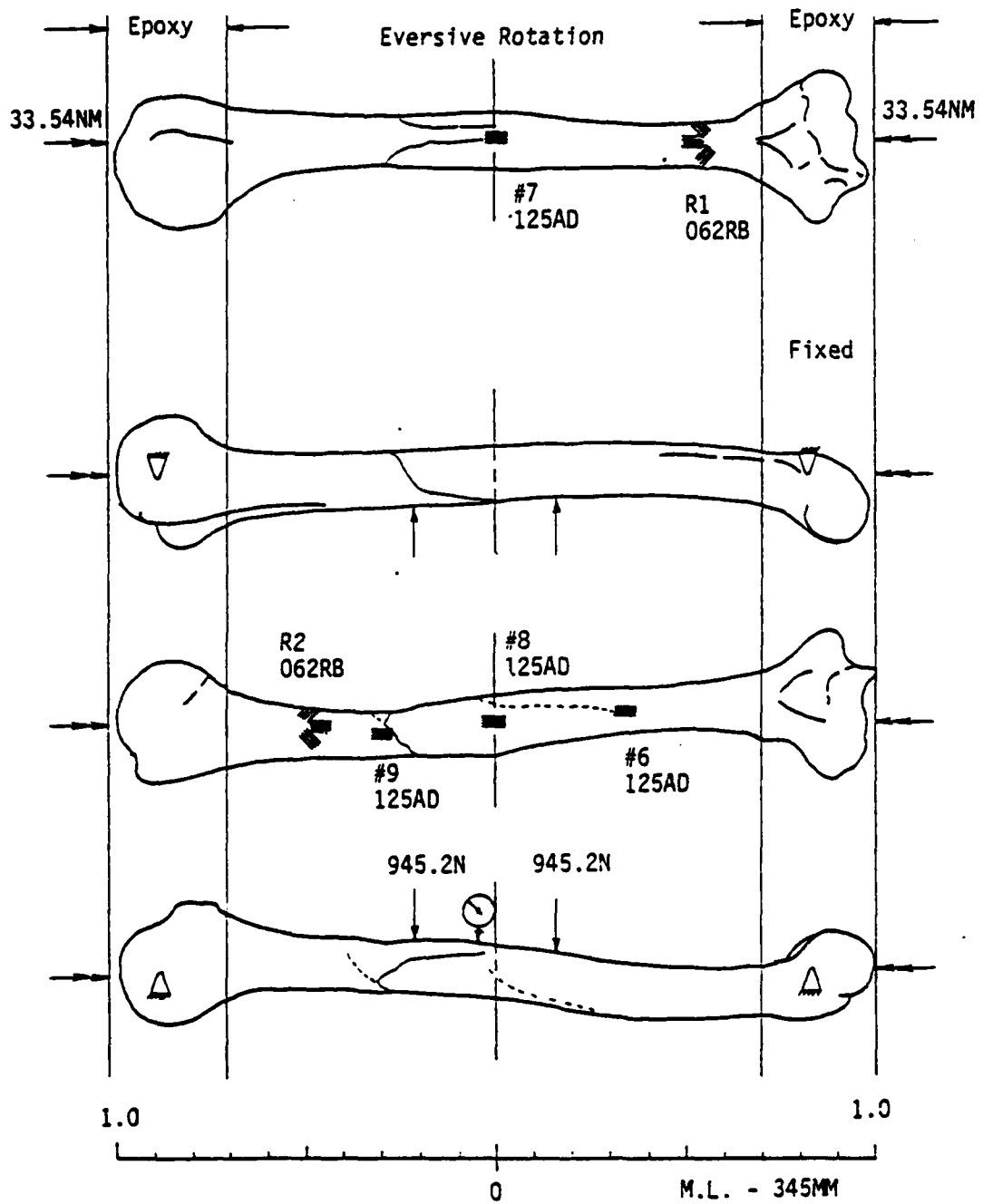


Figure 2.89 Test results for LH3793.

Fibulae: The only fibula tested under bending dominant loading conditions was LFB3787 (Figure 2.90). The fracture that resulted was very similar to that observed for LFB3787 under torsion dominant conditions. The fracture began as a bending tension failure on the medial side at the proximal third. The path then curved toward the distal end until almost parallel with anterior surface before the diaphysis finally separated. They began between the support point and the roller. The roller spacing was set to a narrow separation.

Summary:

Considering those fracture configurations observed for the torsion only condition, they all confirm tension stresses as the primary mode of failure. The tension stress occurs normal to the principal stress planes that result from the pure shear created by the twisting of the bone diaphysis. Nevertheless, there are regions in the crack geometry which are attributed to failure by shearing action. These regions appear normal or parallel to the axis of rotation about which the twisting moment is applied. All of these fractures occurred in the distal half of the bone for the femora and tibiae, but in the proximal half for the humeri and fibulae. One humerus did fracture in the distal half. For torsion only the location of the fracture appears independent of whether eversive or inversive rotation was applied. The two tibia which were twisted while articulated with their fibulae also had fractures consistent with these observations.

For those bones fractured under bending only loading conditions, all displayed a bifurcated fracture except for one femur, one humerus and two tibiae. The fracture began as bending tension failure on the convex side of the bending bone within the middle third of diaphysis of all the bones except for the fibulae. In the fibulae the fracture began on the convex side but at the distal third below the roller. The fracture path usually was normal to the neutral axis and traveled approximately to the neutral axis before bifurcation occurred or the crack changed direction. At this point whether it bifurcated or curved off at an angle with the diaphysial axis, the fracture eventually became parallel to the upper diaphyseal surface. A majority of the fractures were noticed to start in close proximity of one of the rollers in the

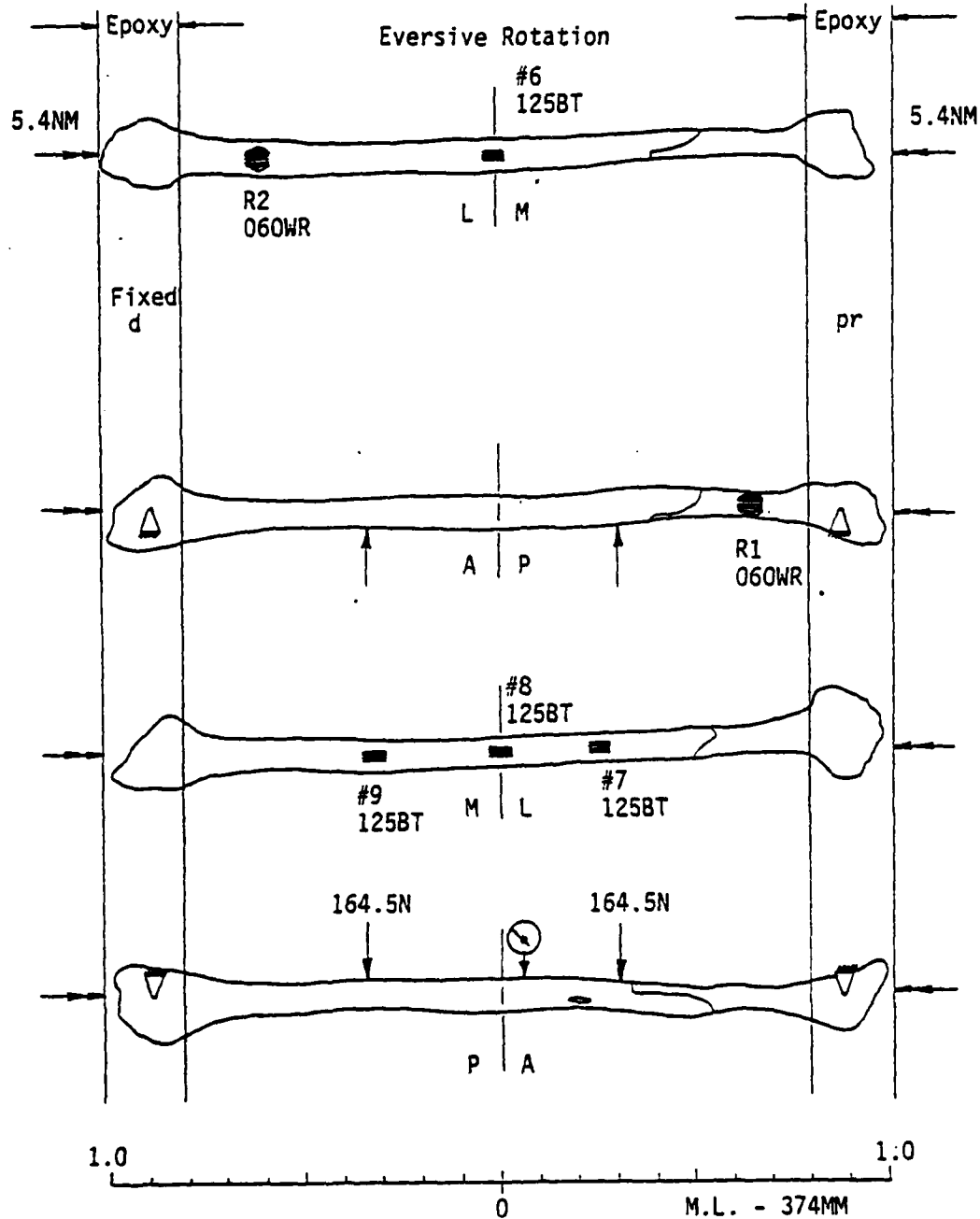


Figure 2.90 Test results for Lfb3787.

bending carriage--a location of concentrated loading. For those bones that did not bifurcate, the path curved towards the mid-diaphysis after changing direction at the neutral axis.

In general, the combined loadings displayed configurations that were characteristic of the dominant loading condition. One femur, one tibia and one humerus did exhibit characteristics of both bending and torsion; the femur and tibia were subjected to torsion dominant loadings while the humerus to bending dominant conditions. Fracture location appeared dependent upon direction of rotation for all the bones except the humeri. The fractures in the femora subjected to narrow and medium load spacings favored the mid-diaphysis during eversive rotation and the distal third when subjected to inversive rotation. One femur which was inversely rotated, but bent with a wide roller spacing did fracture in the proximal half. The tibiae fractures occurred in the proximal half for eversive rotation and the distal half for inversive rotation regardless of the load spacing. The fibulae fractured in the proximal half when subjected to eversive rotation and the distal half for inversive rotation. The humeri fractured in proximal half for all of their combined loading conditions.

#### STRESS STATES:

A considerable amount of effort was involved in determining the strain and stress state at various locations along the diaphysis of the bones during the three loading conditions. The effort has proven well worthwhile in that the stress states offer some insight into failure modes and the magnitudes of the stresses along the diaphysis as well as how these may change as loading conditions change.

The computer programs discussed in Section 2.2.5.1. was used to plot the strains and stresses against the loads that were applied. Strains in the direction of the axes depicted in Figure 2.42 were plotted for each rosette along with the principal strains and stresses. The principal angles with reference to these axes were also included in the plots of principal strains and stresses and were plotted against the applied load. For the combined loading conditions, the strains, stresses; principal angles and fixed load were plotted against the dominating load. If the material axes did not coincide with the

middle gage leg (the x-axis in Figure 2.43) then the stress principal angle was not the same as the strain principal angle.

Bending Only Stress States:

At the beginning of the testing, rosettes were placed at various locations along the bone diaphyses to determine whether the diaphyseal curvature would tend to rotate the bone under bending only condition. The rosettes were also expected to expose the magnitudes of the stresses and possibly display any unexpected, unusual stress situations. The gages were placed away from the suspected neutral axis to avoid any null indications and at locations which were considered simple stress distributions. The precise gage locations are shown in Figures 2.91 - Figures 2.138.

Femora:

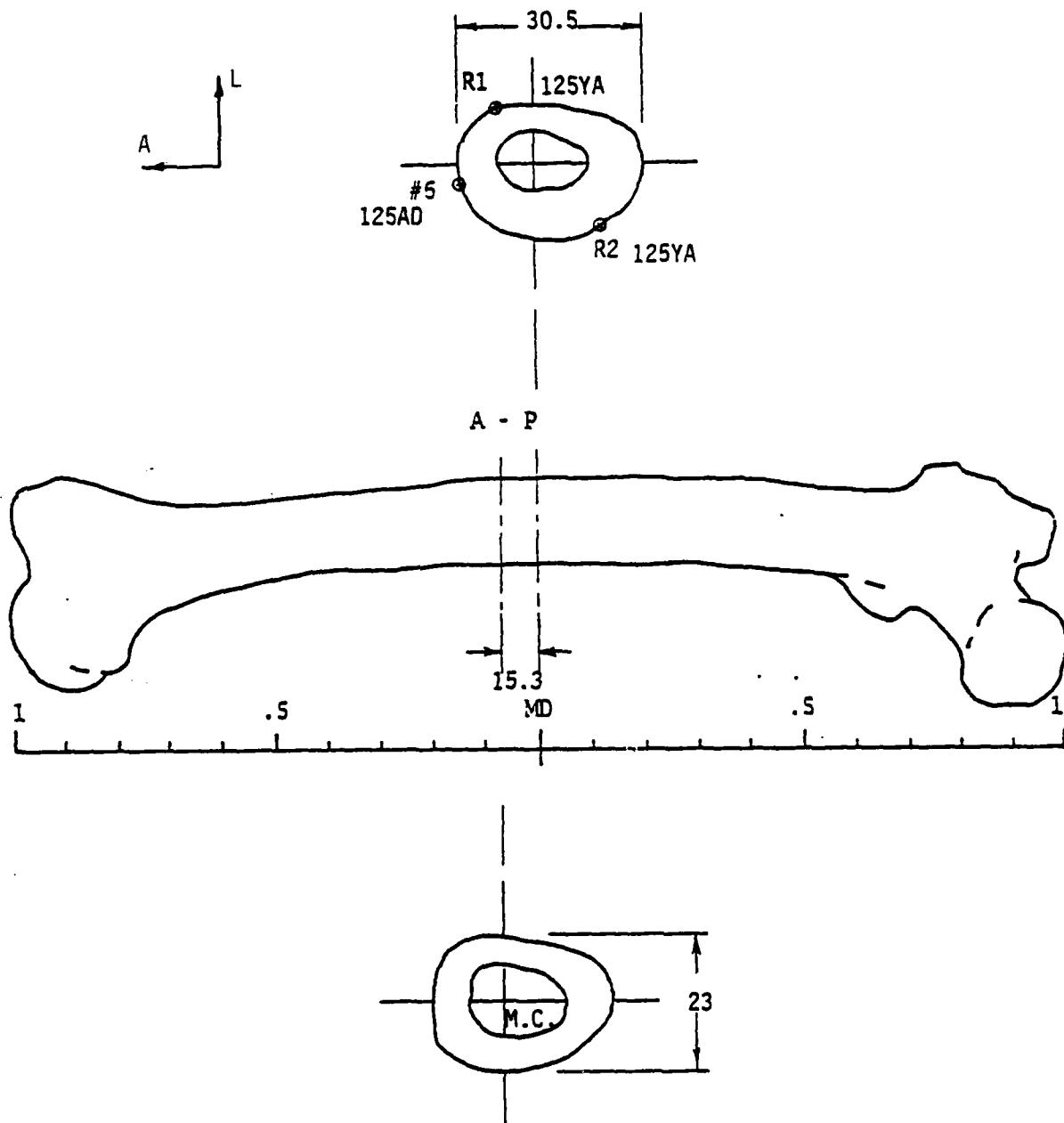
Three femora were gaged with rosettes for the bending only loading configuration. LF3793 and RF3792 had two rosettes each (one on the anterior surface at each end) which were placed at locations proportional between the two bones. The third femur, RF3753 also had two rosettes, but these were located about the periphery at the mid-diaphysis.

The two femora with rosettes in proportional locations indicated compression as expected with a relatively large amount of shear which was unexpected. LF3793 exhibited values of the compression and shear at failure that were almost twice those of RF3792. This difference was the same regardless whether stress or strain was considered or whether gage strain or principal strain were compared. Also of significance was the difference in the direction of the shearing strain measured at the distal rosette as compared to that measured at the proximal rosette (Figure 2.139, 140). The distal rosette implied a tendency for the diaphysis to rotate inversively while the proximal gage inferred an eversive tendency. RF3792 also exhibited the same behavior, but not as extremely. Both ends of this femur seem to rotate inversively, but the proximal end less than the distal. Although the principal stresses and maximum shearing stresses agreed well between the gages at opposite ends of each bone, the principal angles were either of opposite sign or differed in magnitude by a factor of two.

DISK AND STRAIN GAGE SECTIONS

RIGHT FEMUR NO. 3753 BN 9

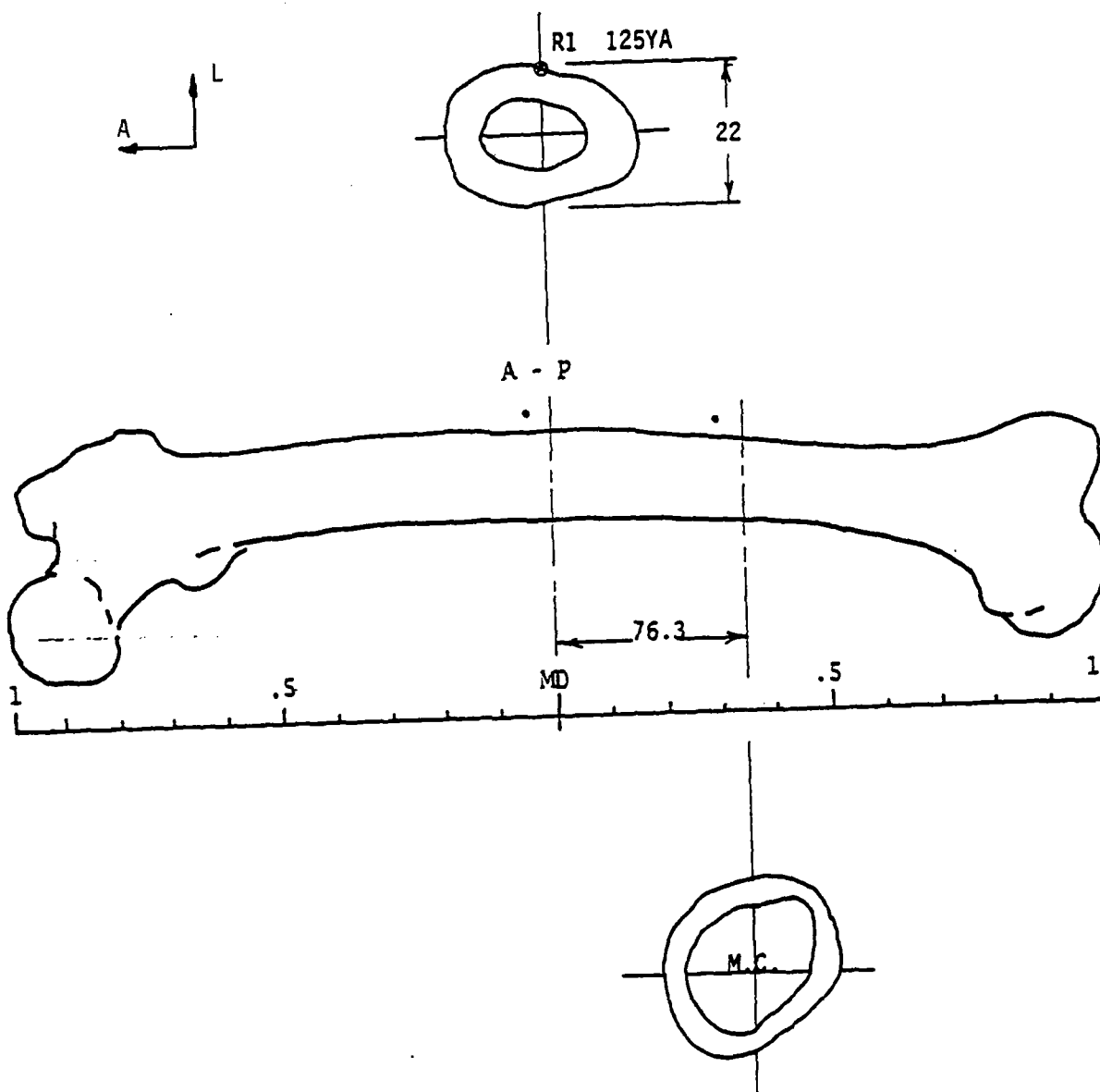
Figure 2.91 Locations of M.C. sections and strain gages for RF3753.



DISK AND STRAIN GAGE SECTIONS

LEFT FEMUR NO. 3753 T8

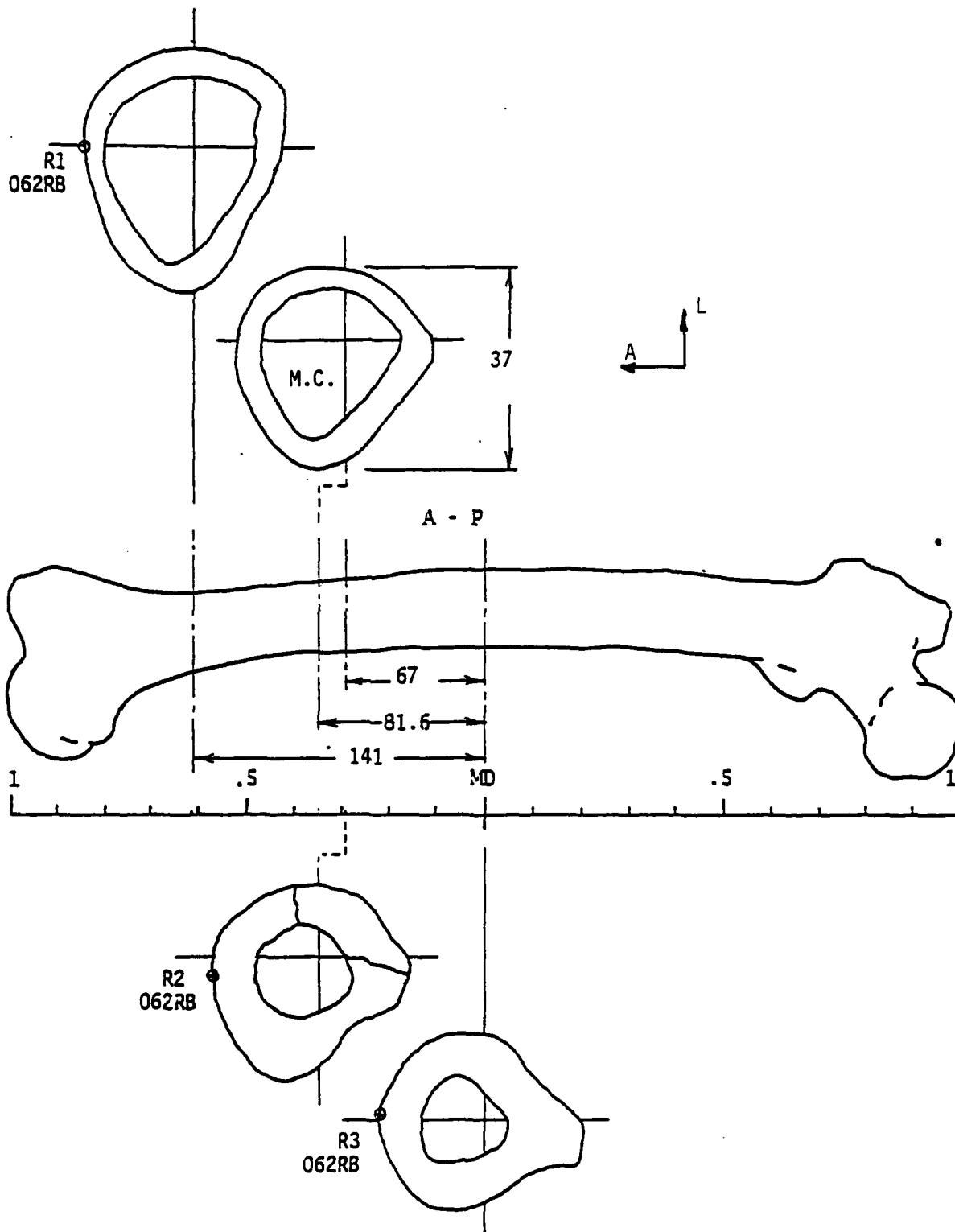
Figure 2.92 Locations of M.C. sections and strain gages for LP3753.



DISK AND STRAIN GAGE SECTIONS

RIGHT FEMUR NO. 3793 T 18

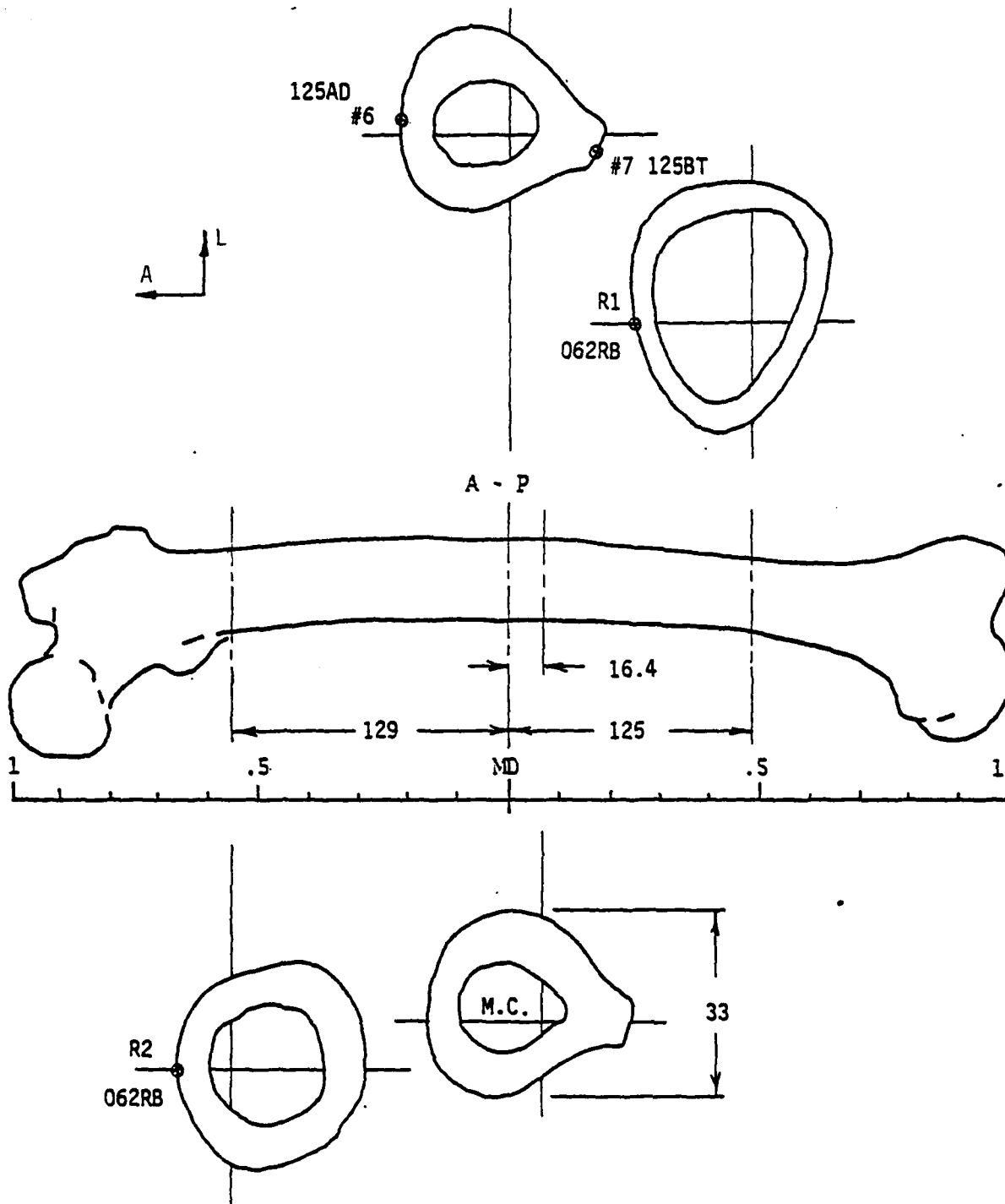
Figure 2.93 Locations of M.C. sections and strain gages for RF3793.



DISK AND STRAIN GAGE SECTIONS

LEFT FEMUR NO. 3793 8M 19

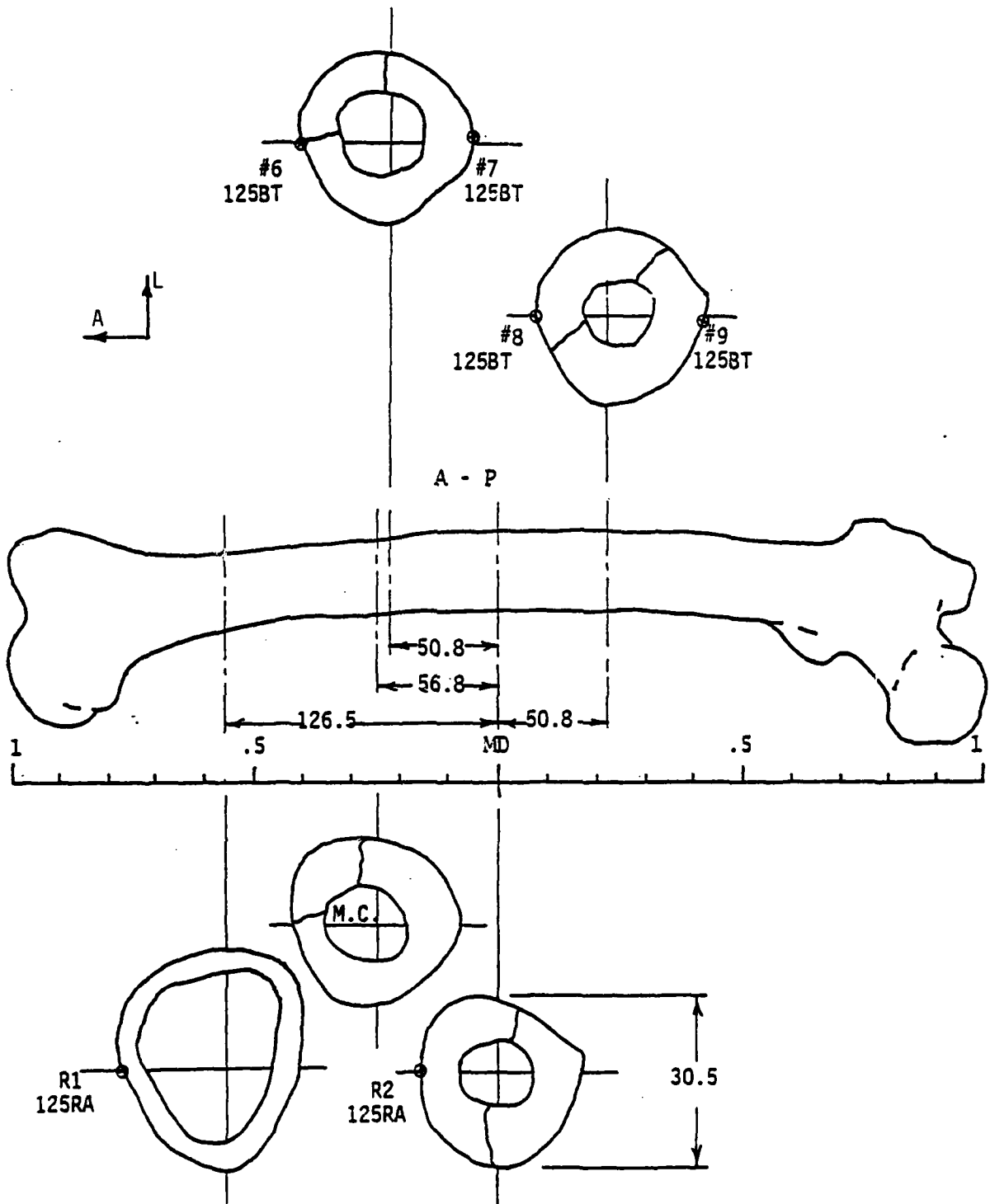
Figure 2.94 Locations of M.C. sections and strain gages for LF3793.



DISK AND STRAIN GAGE SECTIONS

RIGHT FEMUR NO. 3790 CTW 14

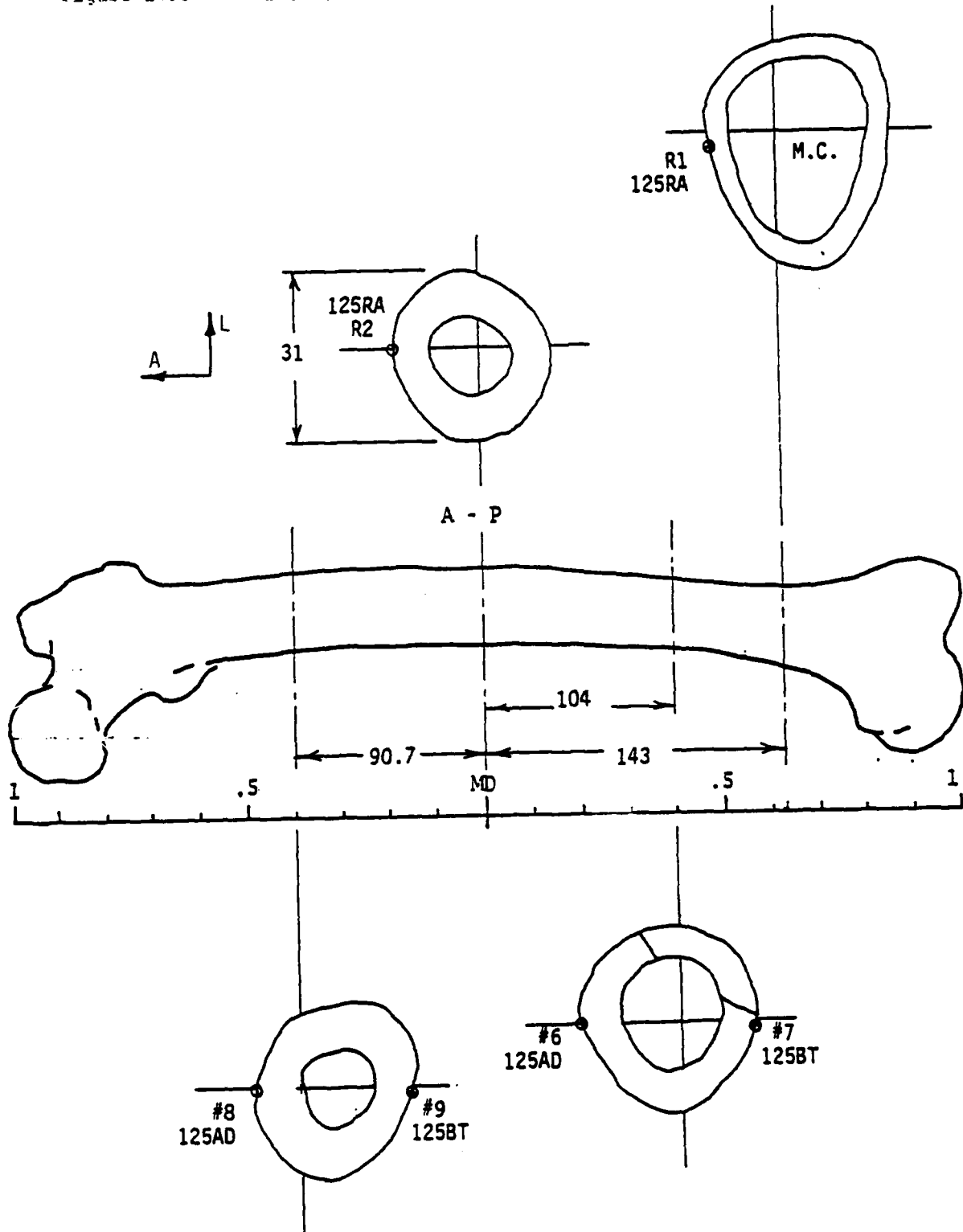
Figure 2.95 Locations of M.C. sections and strain gages for RF3790.



# DISK AND STRAIN GAGE SECTIONS

LEFT FEMUR NO. 3790 CTN 14

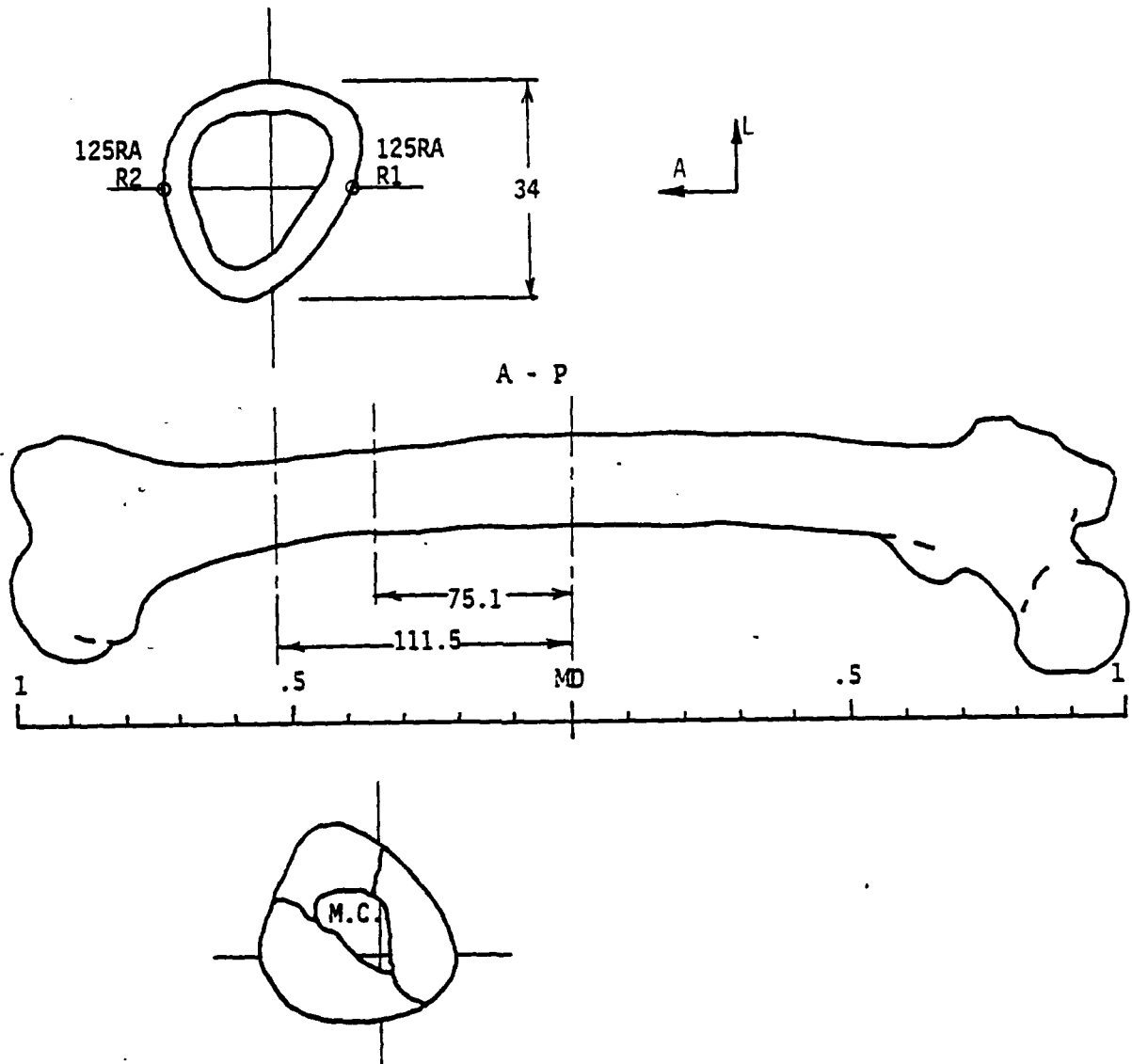
Figure 2.96 Locations of M.C. sections and strain gages for LF3790.



DISK AND STRAIN GAGE SECTIONS

RIGHT FEMUR NO. 3782 T 15

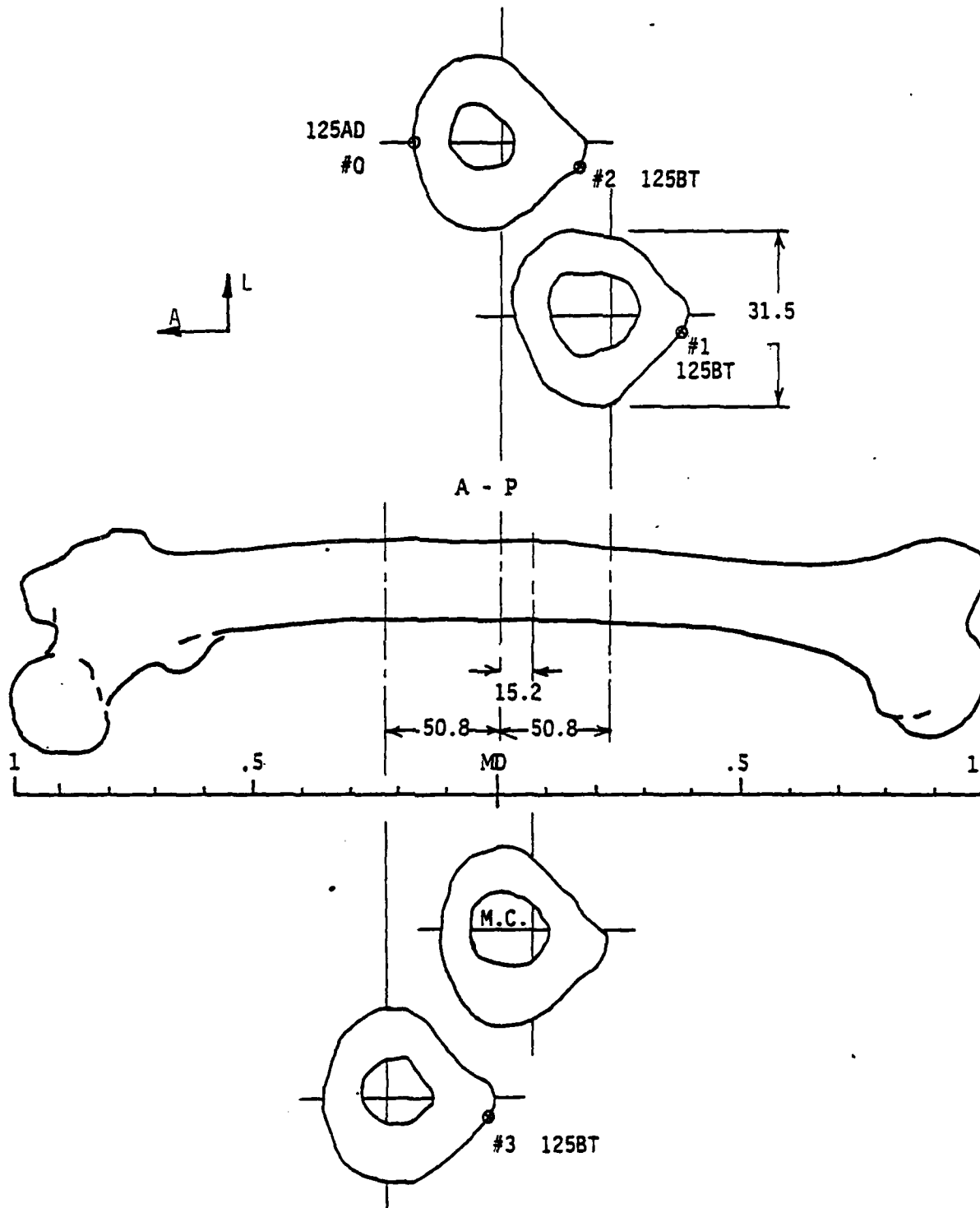
Figure 2.97 Locations of M.C. sections and strain gages for RF3782.



DISK AND STRAIN GAGE SECTIONS

LEFT FEMUR NO. 3782 BW 13

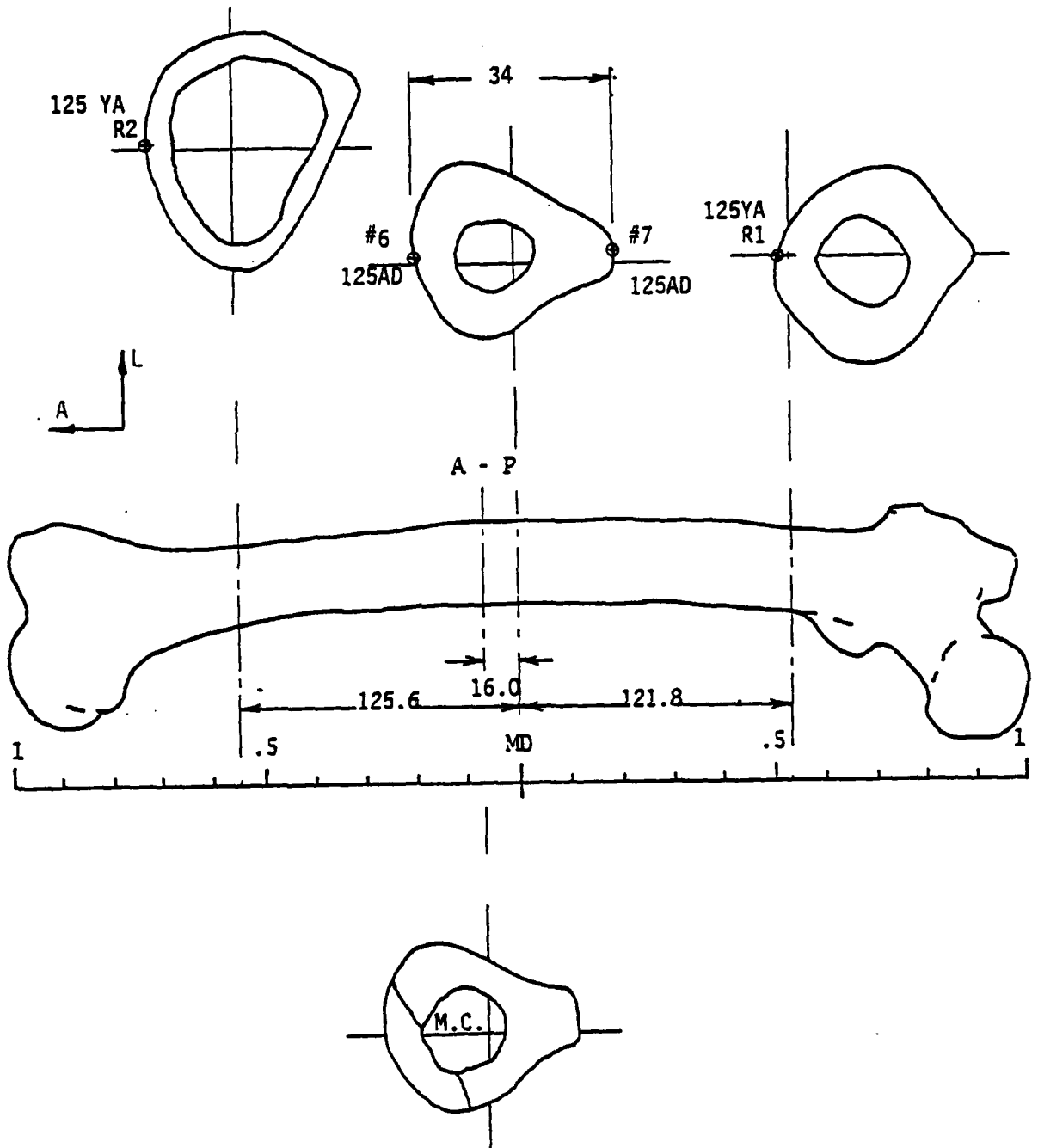
Figure 2.98 Locations of M.C. sections and strain gages for LF3782.



DISK AND STRAIN GAGE SECTIONS

RIGHT FEMUR NO. 3792 BM 10

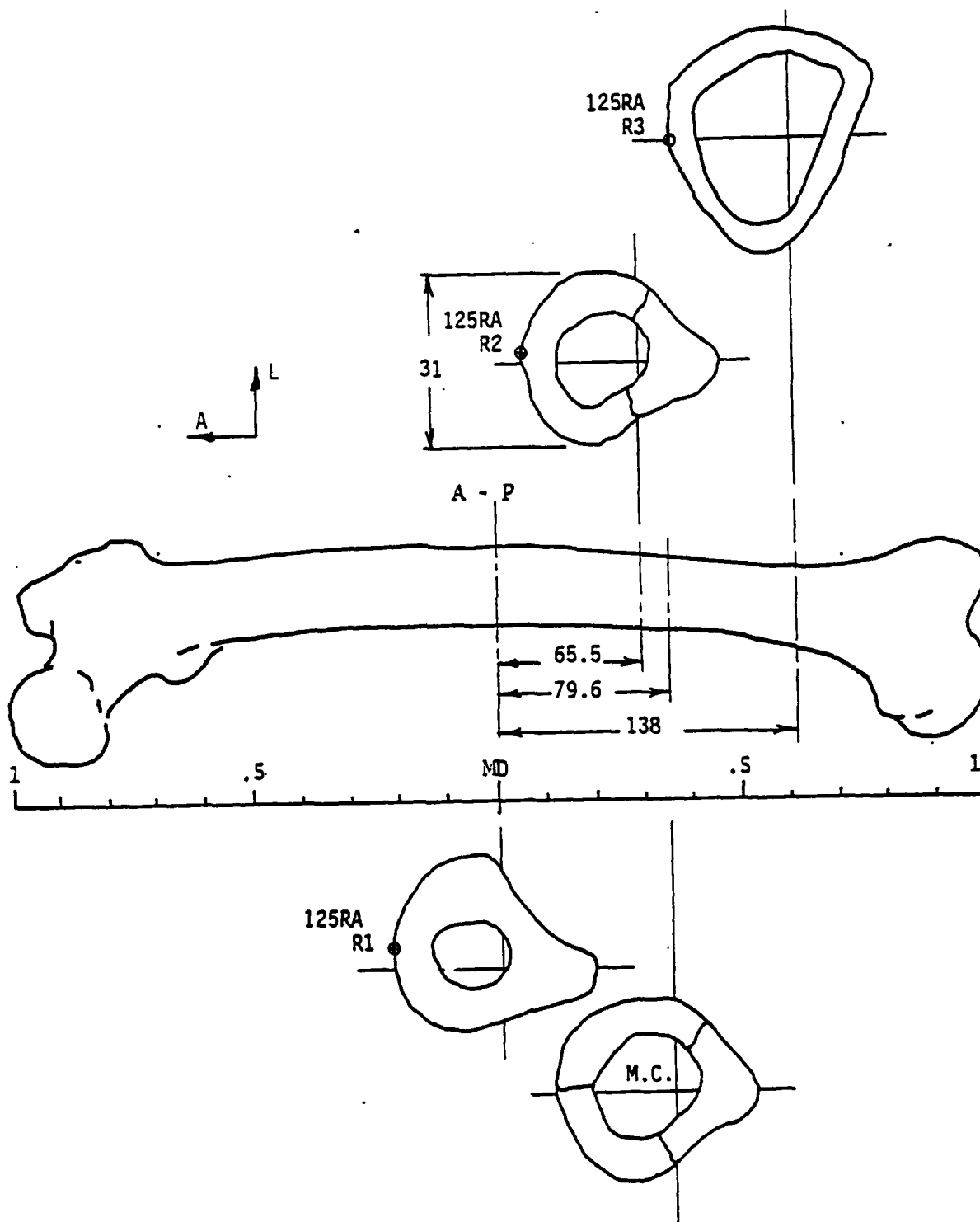
Figure 2.99 Locations of M.C. sections and strain gages for RF3792.



DISK AND STRAIN GAGE SECTIONS

LEFT FEMUR NO. 3792 T 11

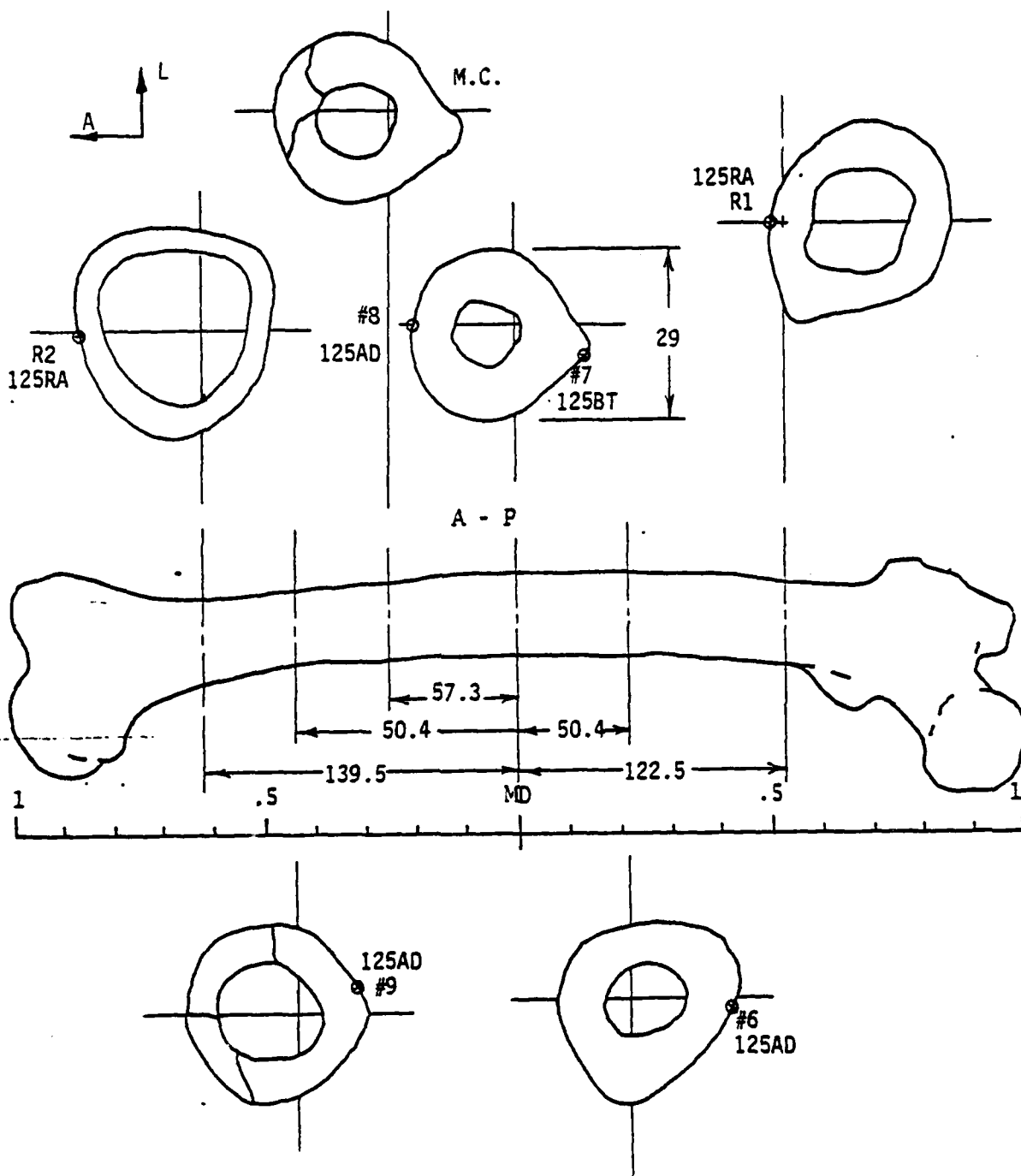
Figure 2.100 Locations of M.C. sections and strain gages for LF3792.



DISK AND STRAIN GAGE SECTIONS

RIGHT FEMUR NO. 3787 CBN 47

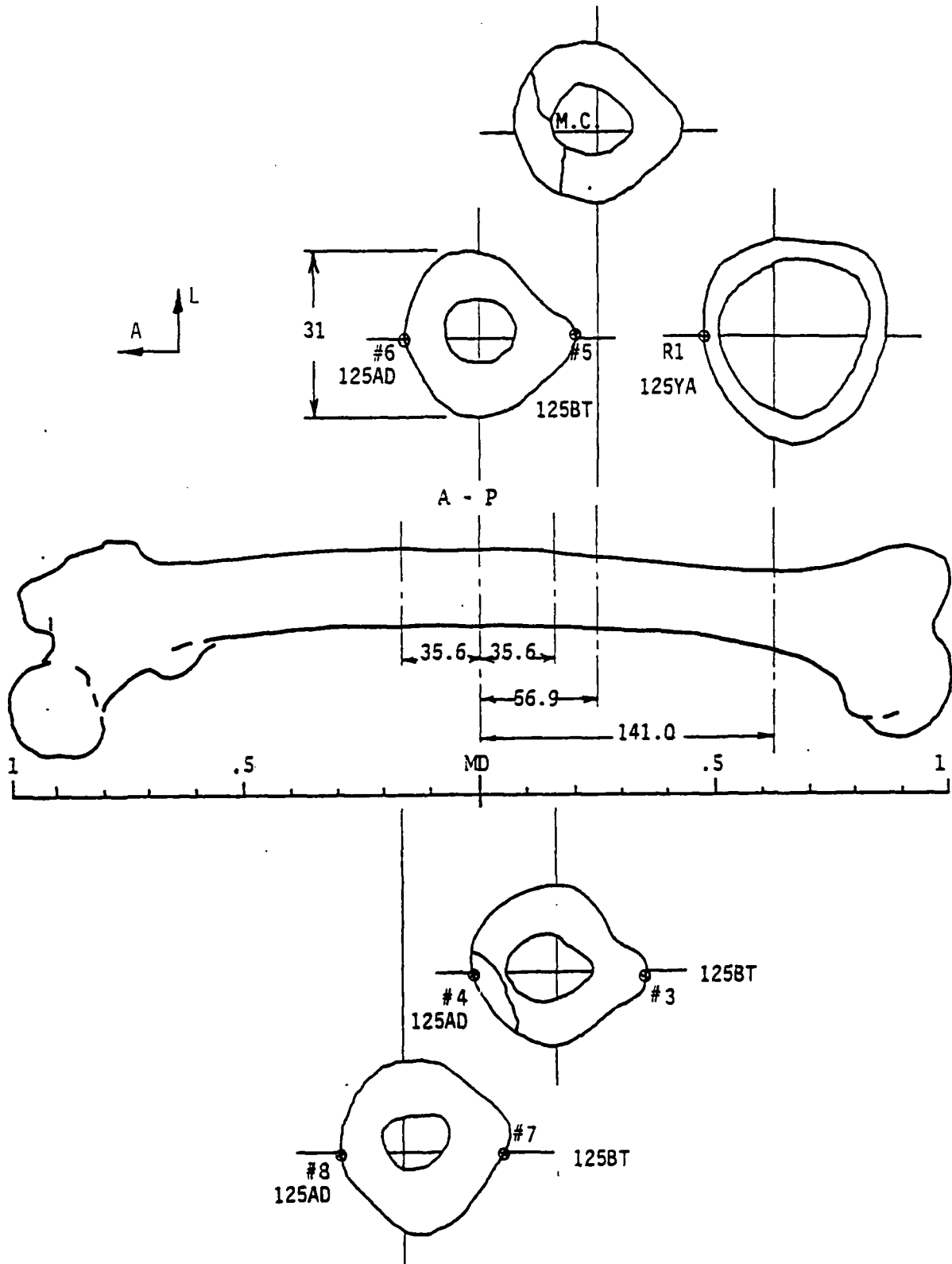
Figure 2.101 Locations of M.C. sections and strain gages for RF3787.



DISK AND STRAIN GAGE SECTIONS

LEFT FEMUR NO. 3787 CBN 12

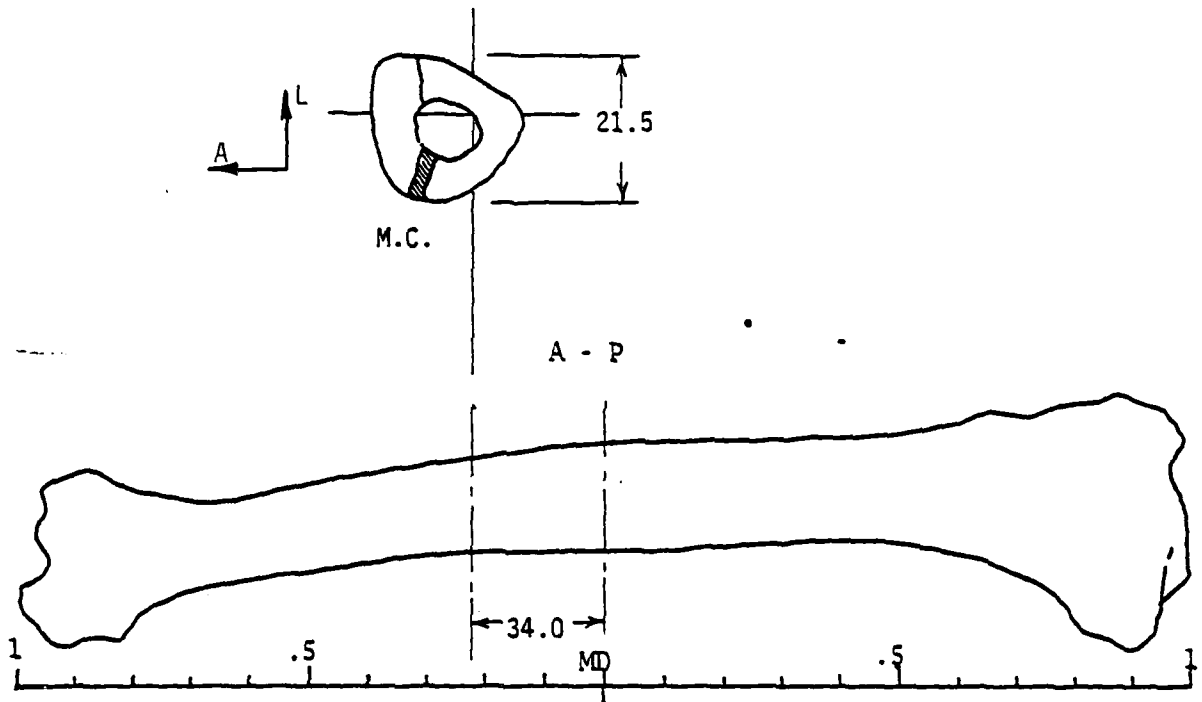
Figure 2.102 Locations of M.C. sections and strain gages for LF3787.



DISK AND STRAIN GAGE SECTIONS

RIGHT TIBIA NO. 3753 BN3

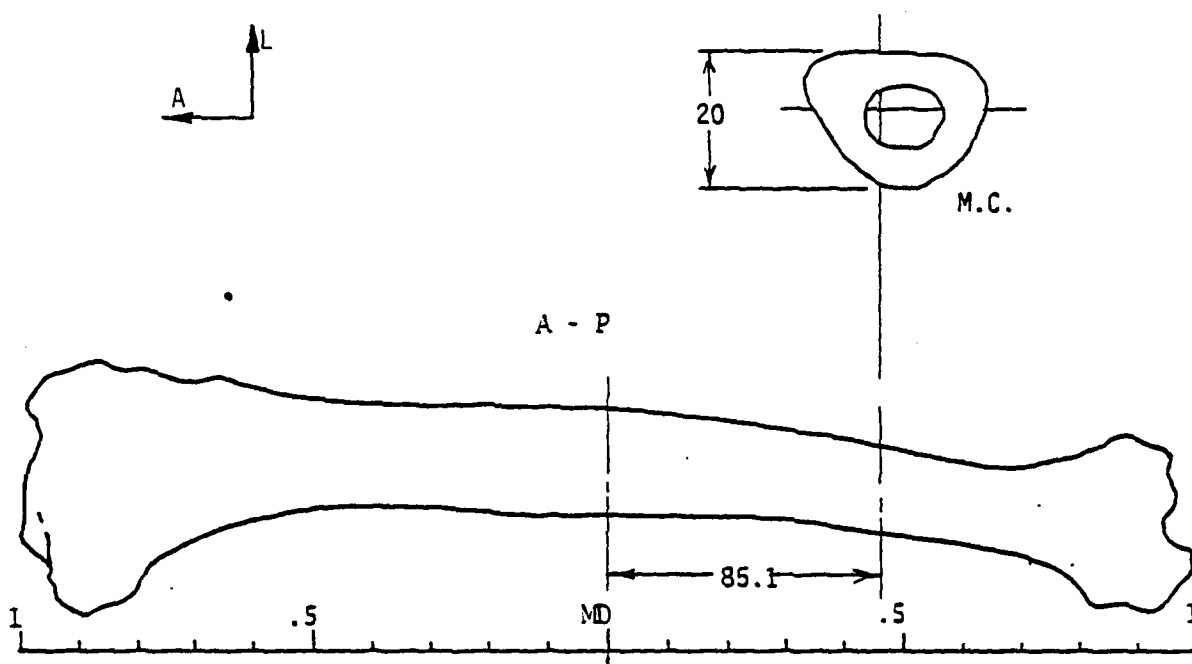
Figure 2.103 Locations of M.C. sections and strain gages for RT3753.



DISK AND STRAIN GAGE SECTIONS

LEFT TIBIA NO. 3753 T 5

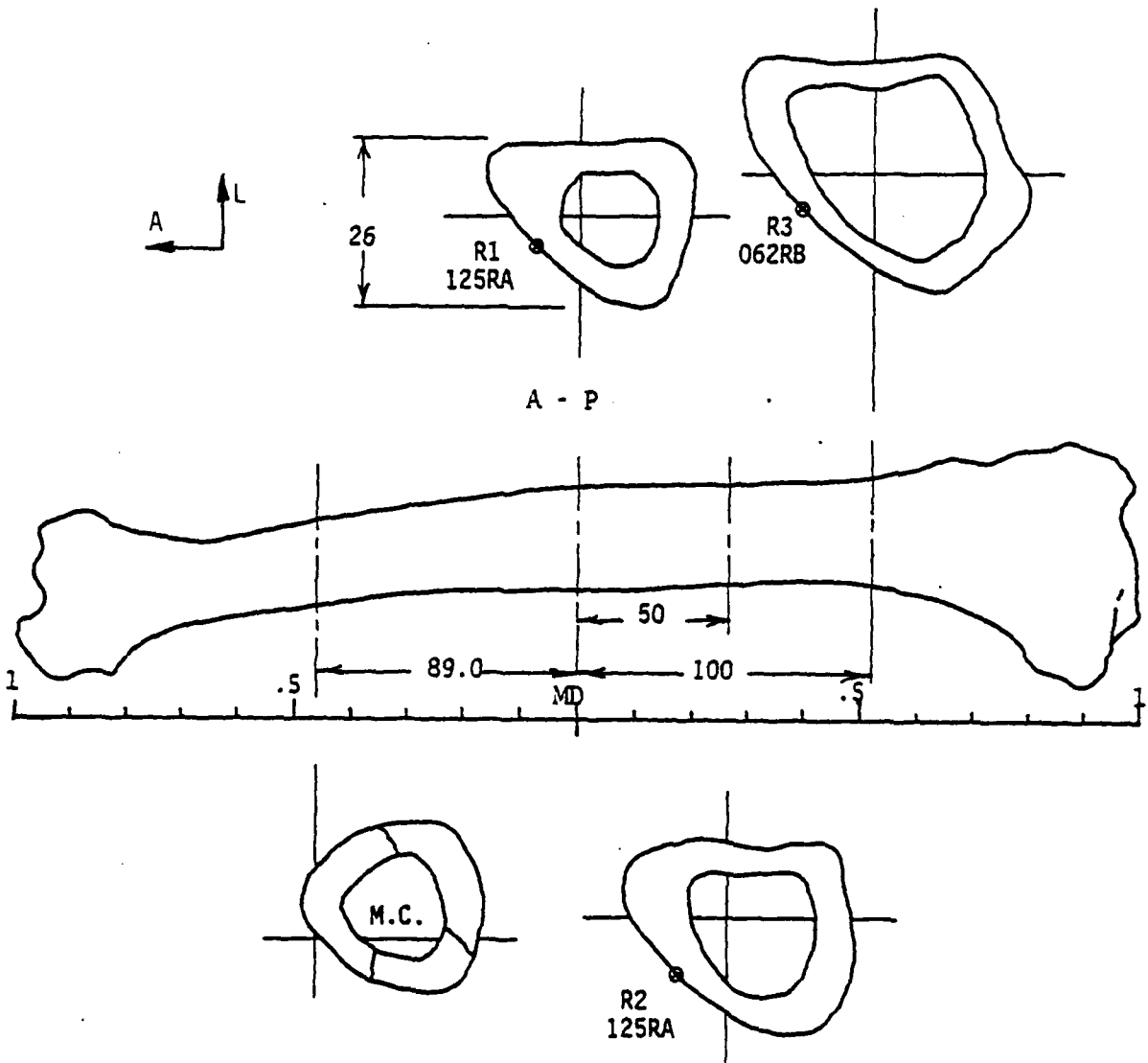
Figure 2.104 Locations of M.C. sections and strain gages for LT3753.



DISK AND STRAIN GAGE SECTIONS

RIGHT TIBIA NO. 3793 T 21

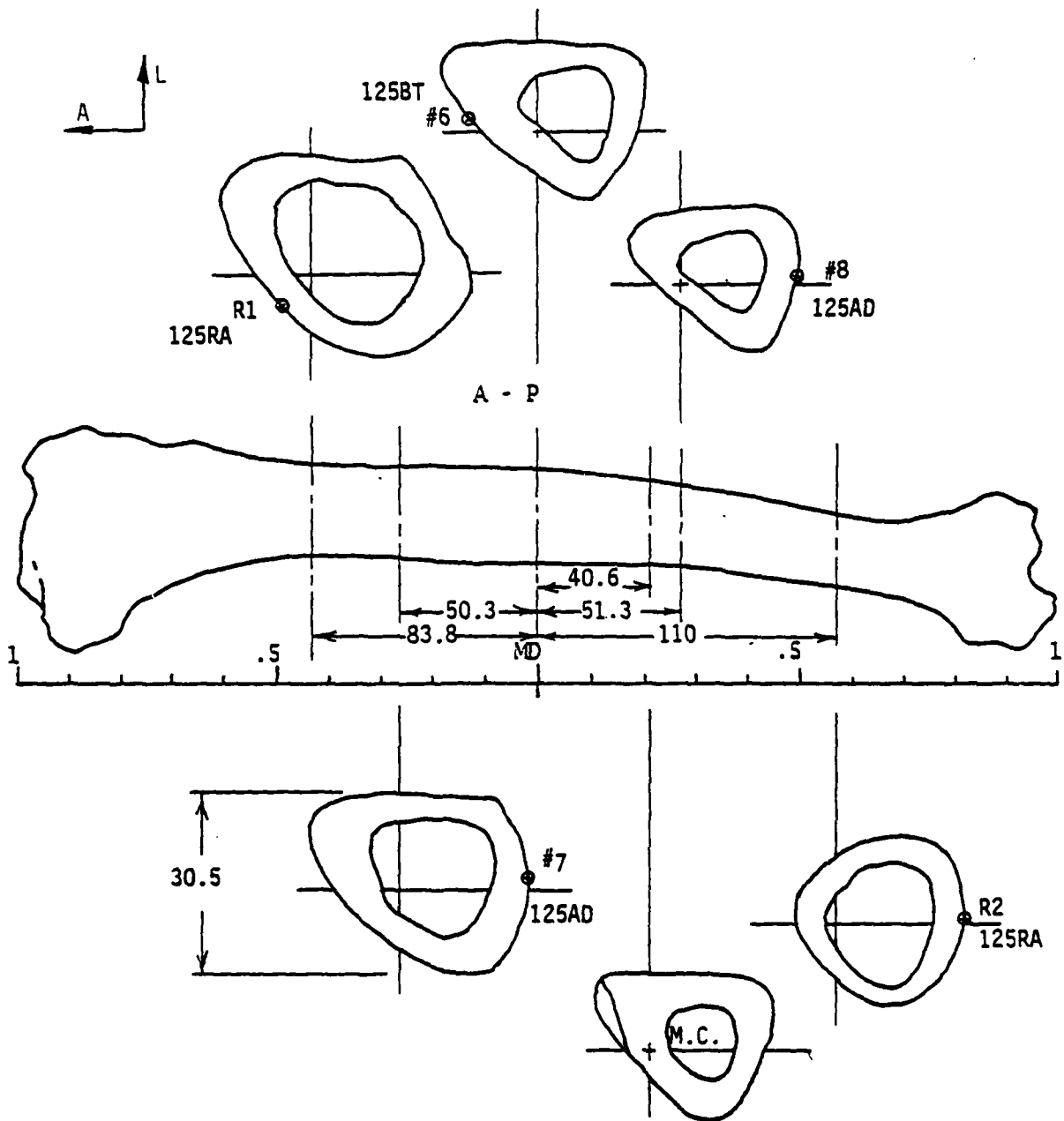
Figure 2.105 Locations of M.C. sections and strain gages for RT3793.



DISK AND STRAIN GAGE SECTIONS

LEFT TIBIA NO. 3793 9M 27

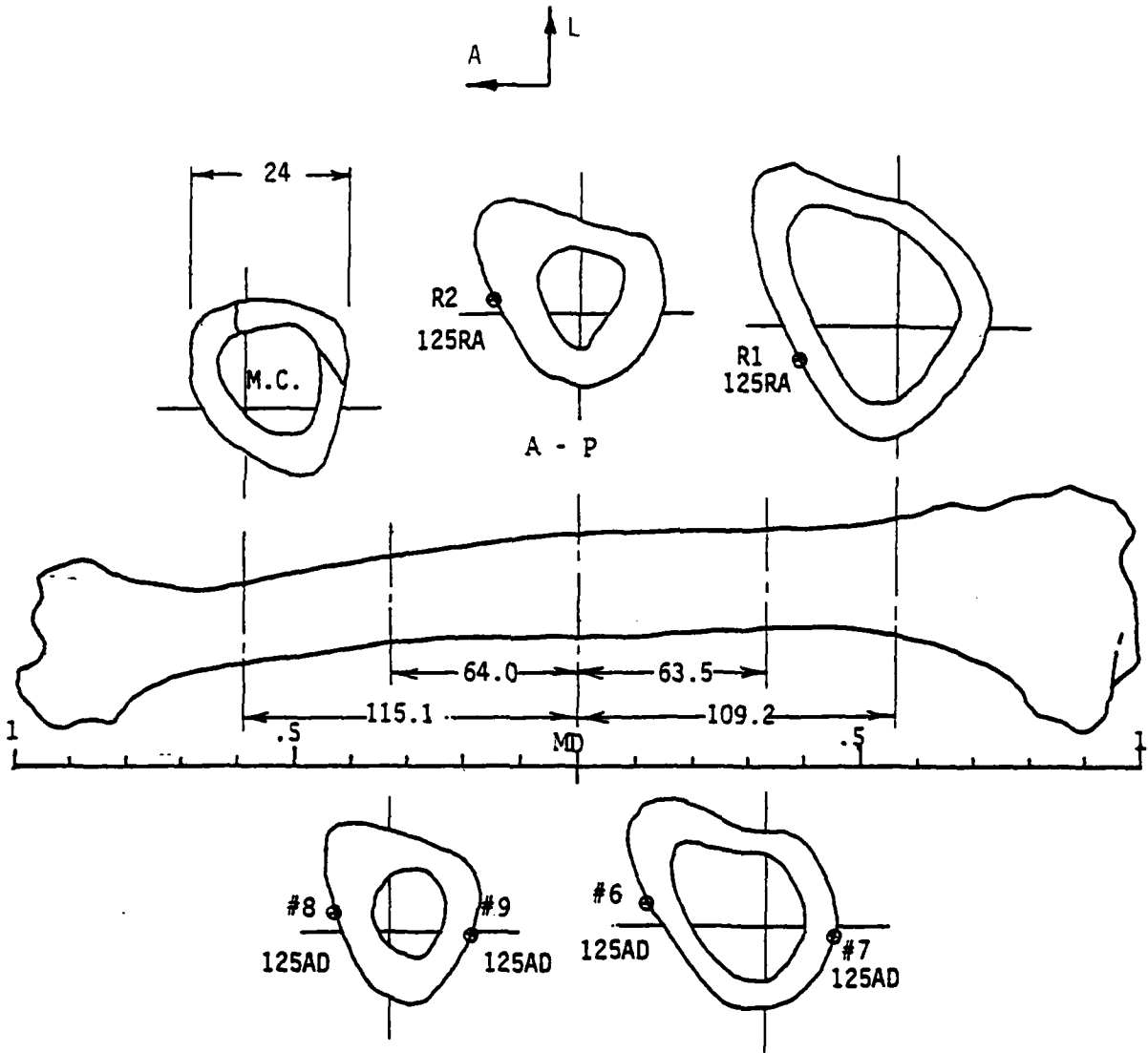
Figure 2.106 Locations of M.C. sections and strain gages for LT3793.



DISK AND STRAIN GAGE SECTIONS

RIGHT TIBIA NO. 3790 CTW 25

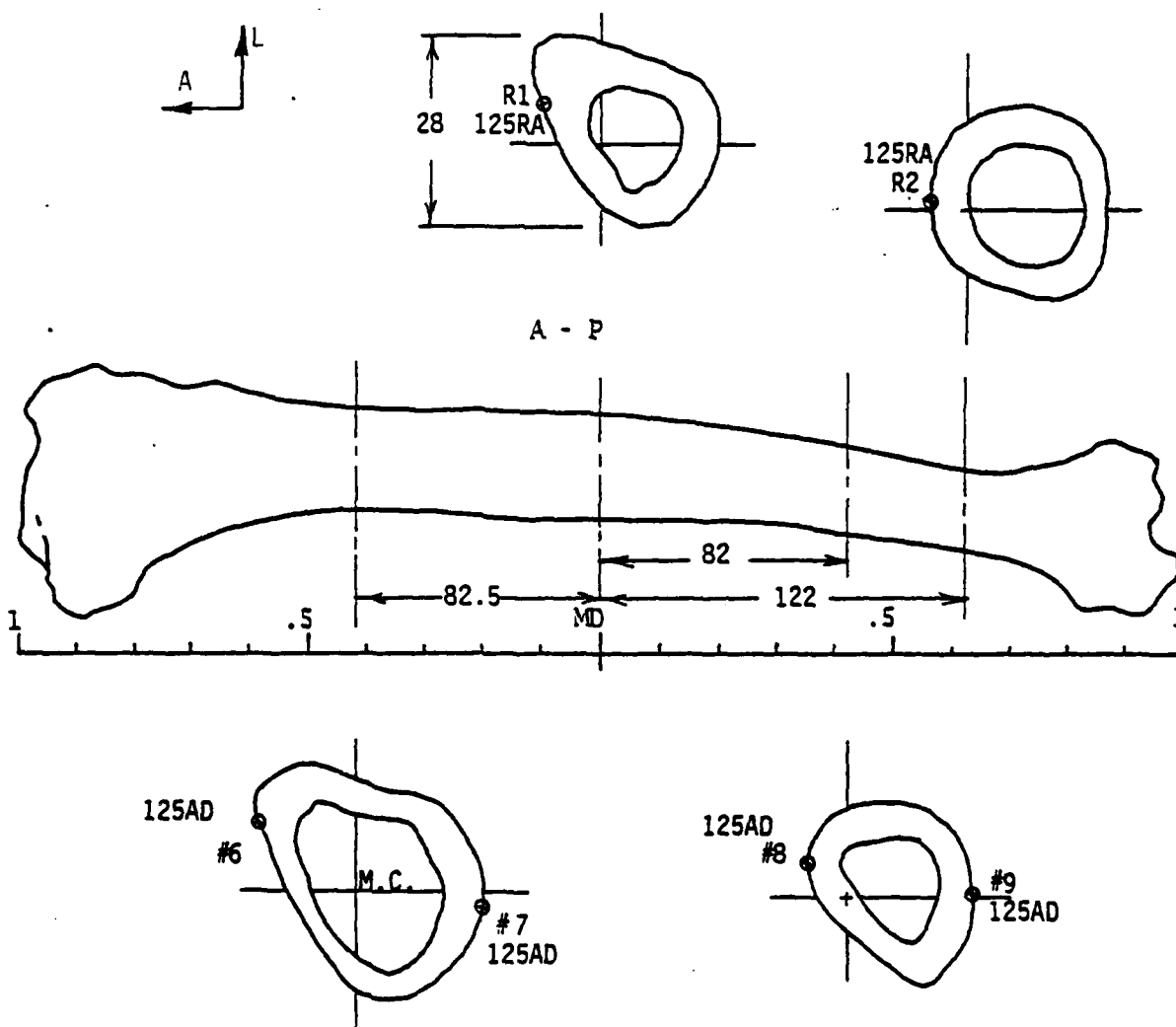
Figure 2.107 Locations of M.C. sections and strain gages for RT3790.



DISK AND STRAIN GAGE SECTIONS

LEFT TIBIA NO. 3790 CTN 26

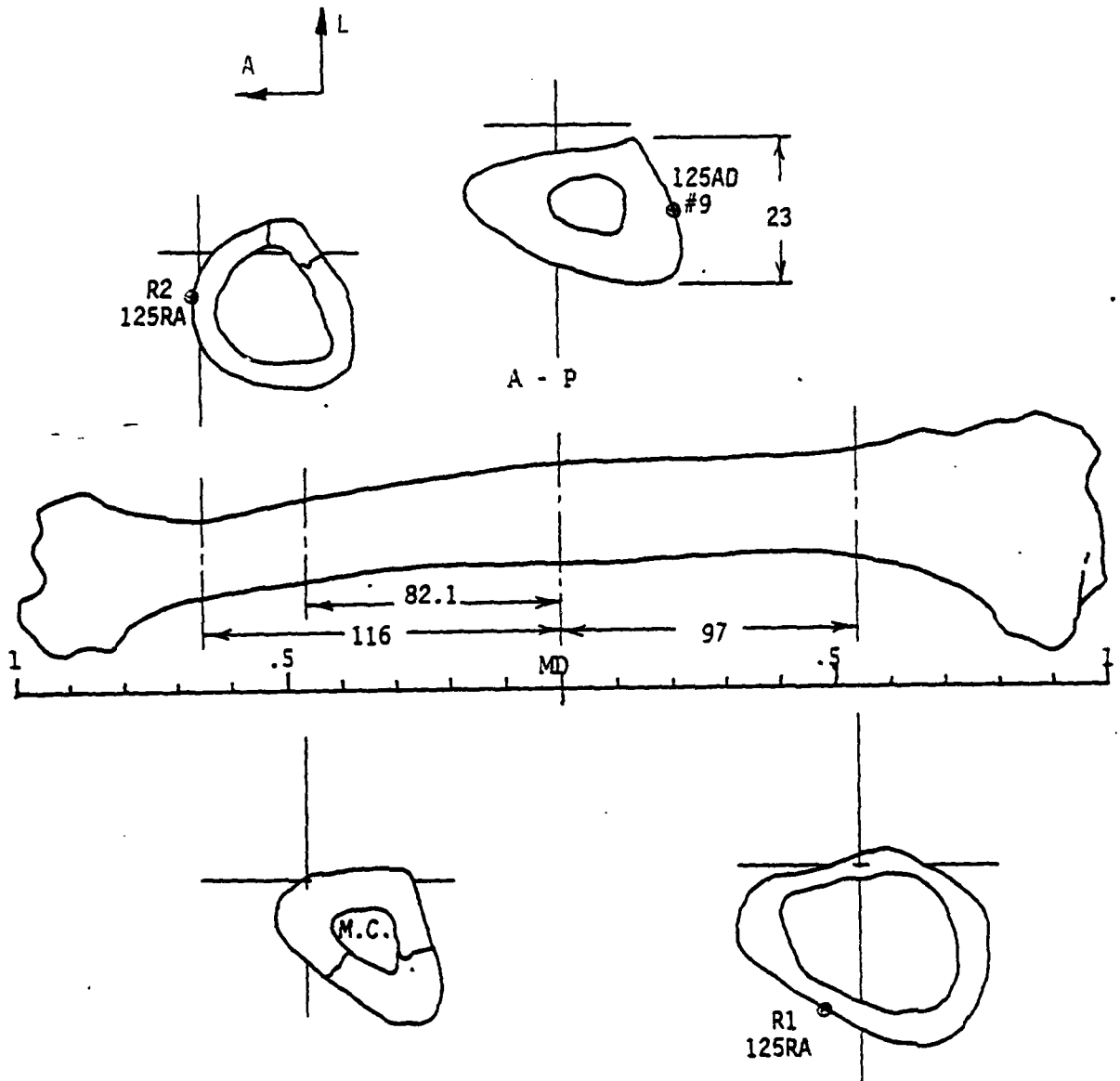
Figure 2.108 Locations of M.C. sections and strain gages for LT3790.



DISK AND STRAIN GAGE SECTIONS

RIGHT TIBIA NO. 3782 T 31

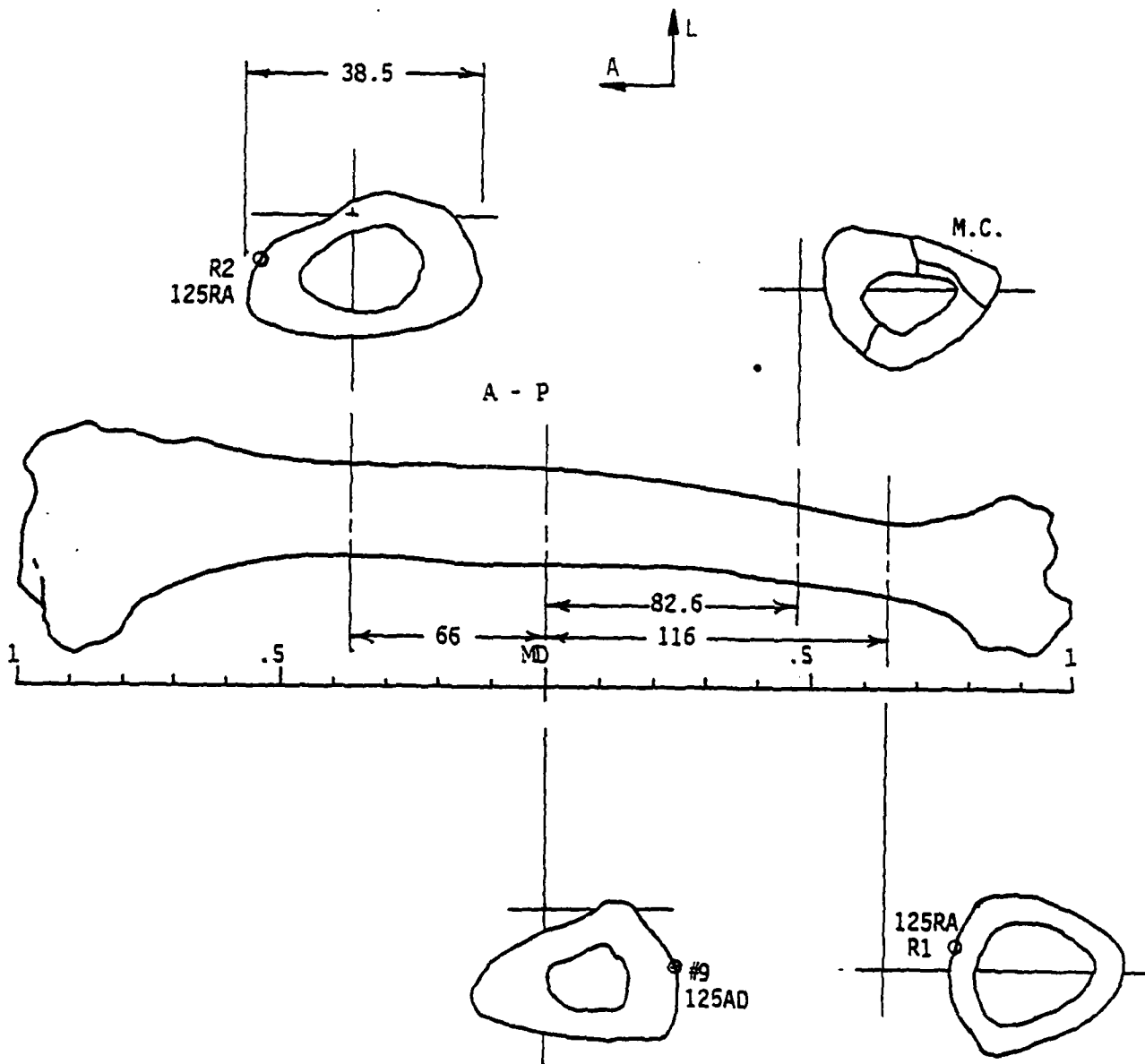
Figure 2.109 Locations of M.C. sections and strain gages for RT3782.



DISK AND STRAIN GAGE SECTIONS

LEFT TIBIA NO. 3782 T 32

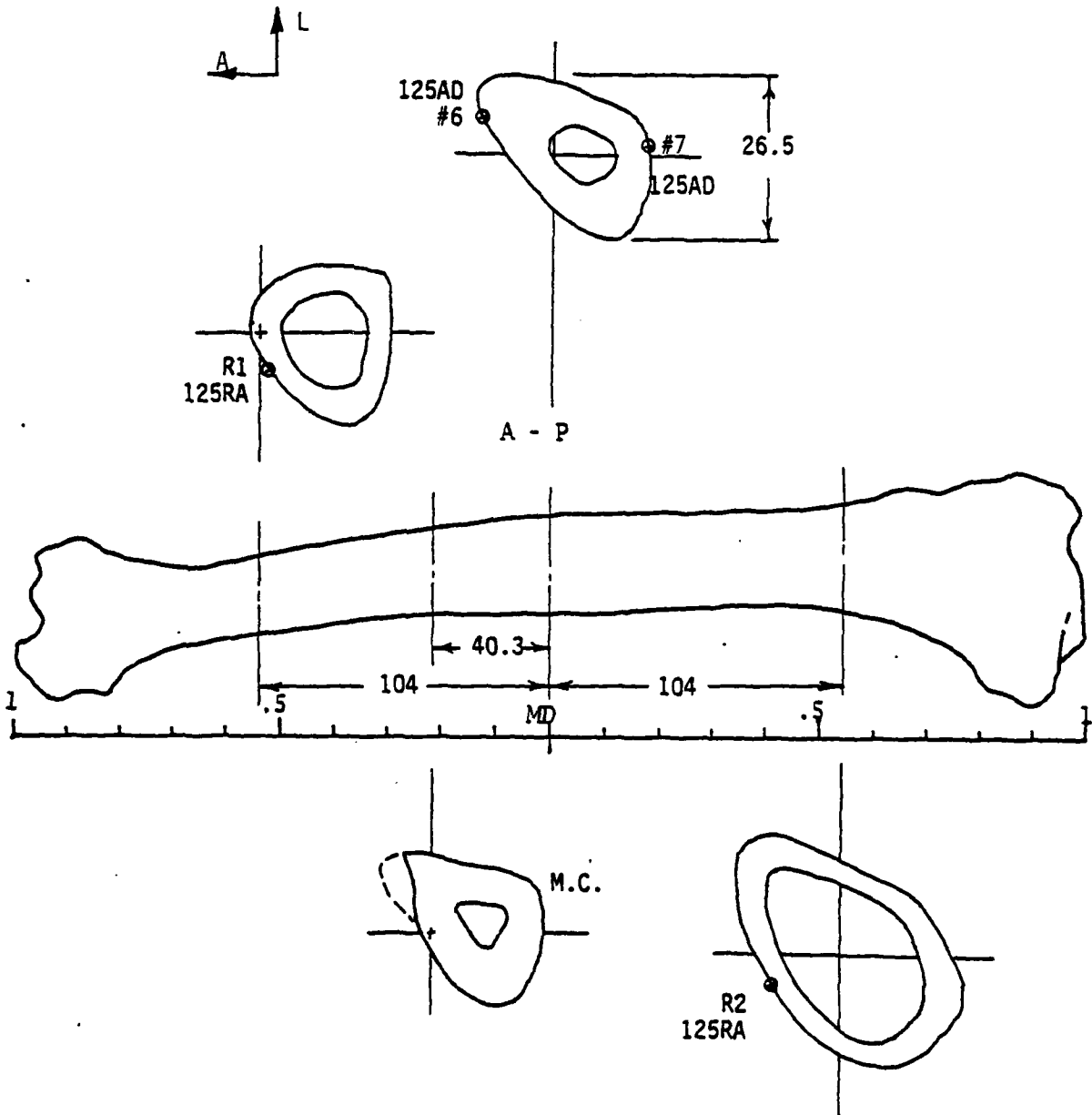
Figure 2.110 Locations of M.C. sections and strain gages for LT3782.



DISK AND STRAIN GAGE SECTIONS

RIGHT TIBIA NO. 3792 BM 24

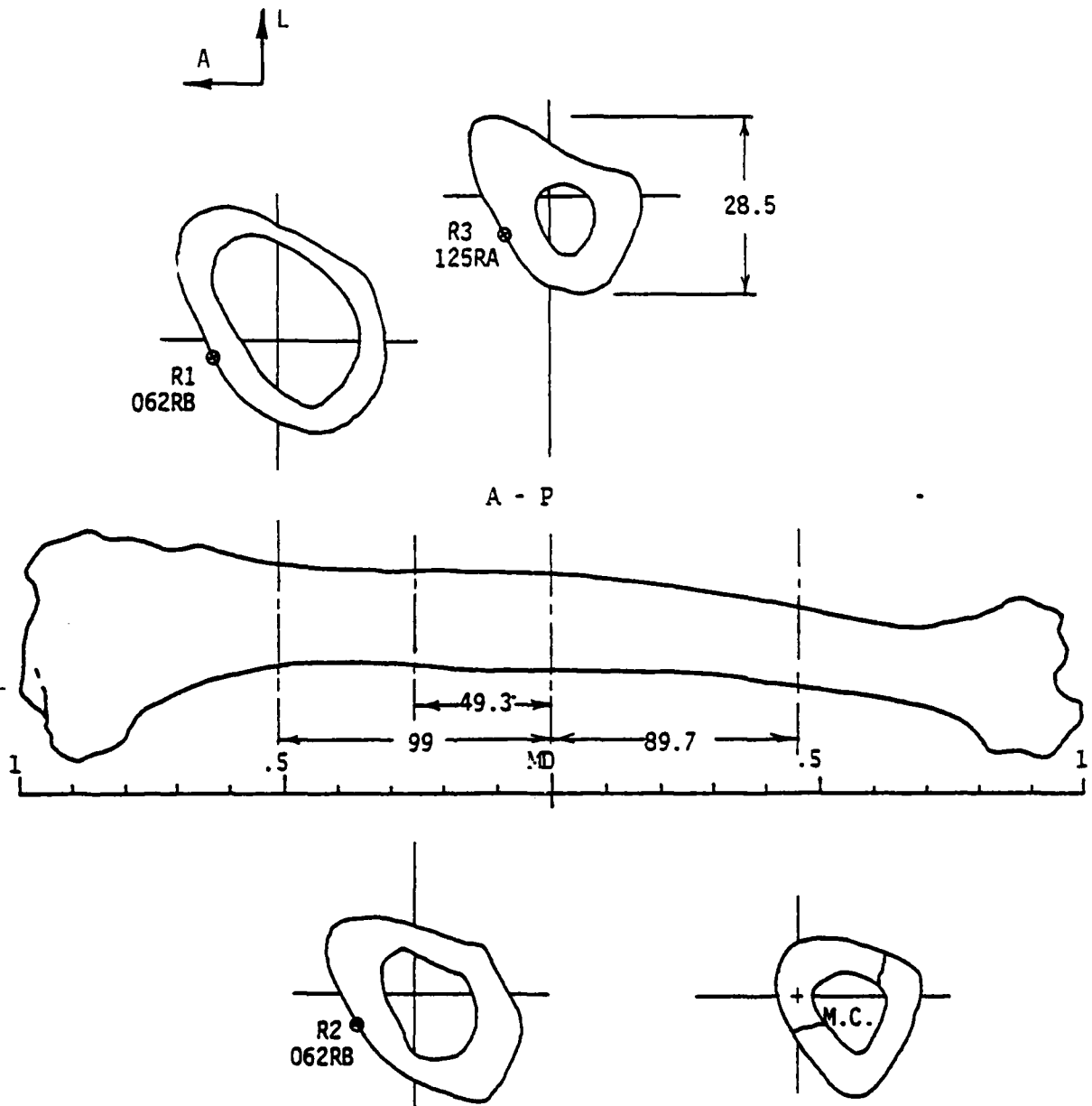
Figure 2.111 Locations of M.C. sections and strain gages for RT3792.



DISK AND STRAIN GAGE SECTIONS

LEFT TIBIA NO. 3792 T 20

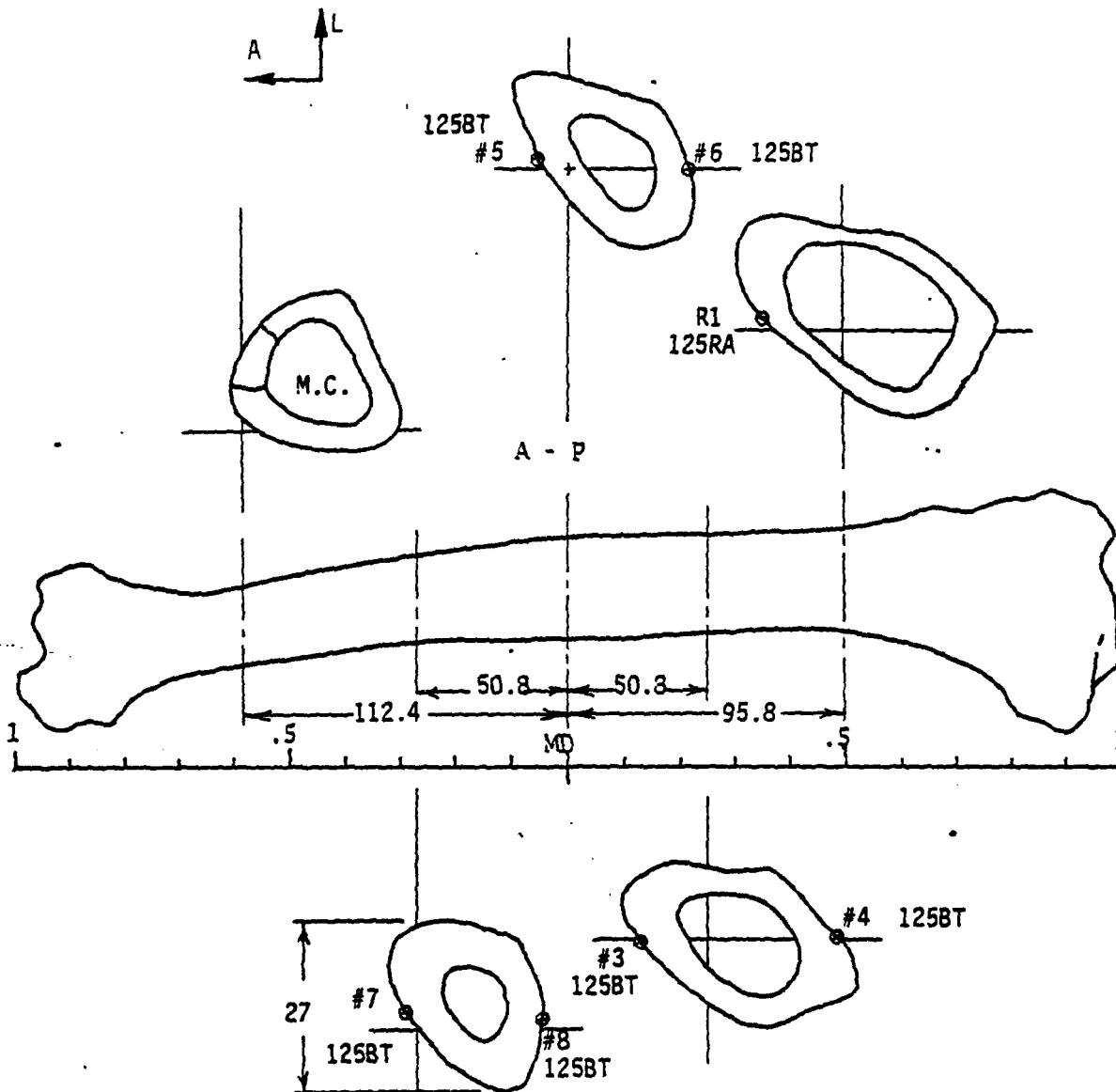
Figure 2.112 Locations of M.C. sections and strain gages for LT3792.



DISK AND STRAIN GAGE SECTIONS

RIGHT TIBLA NO. 3787 CBW 17

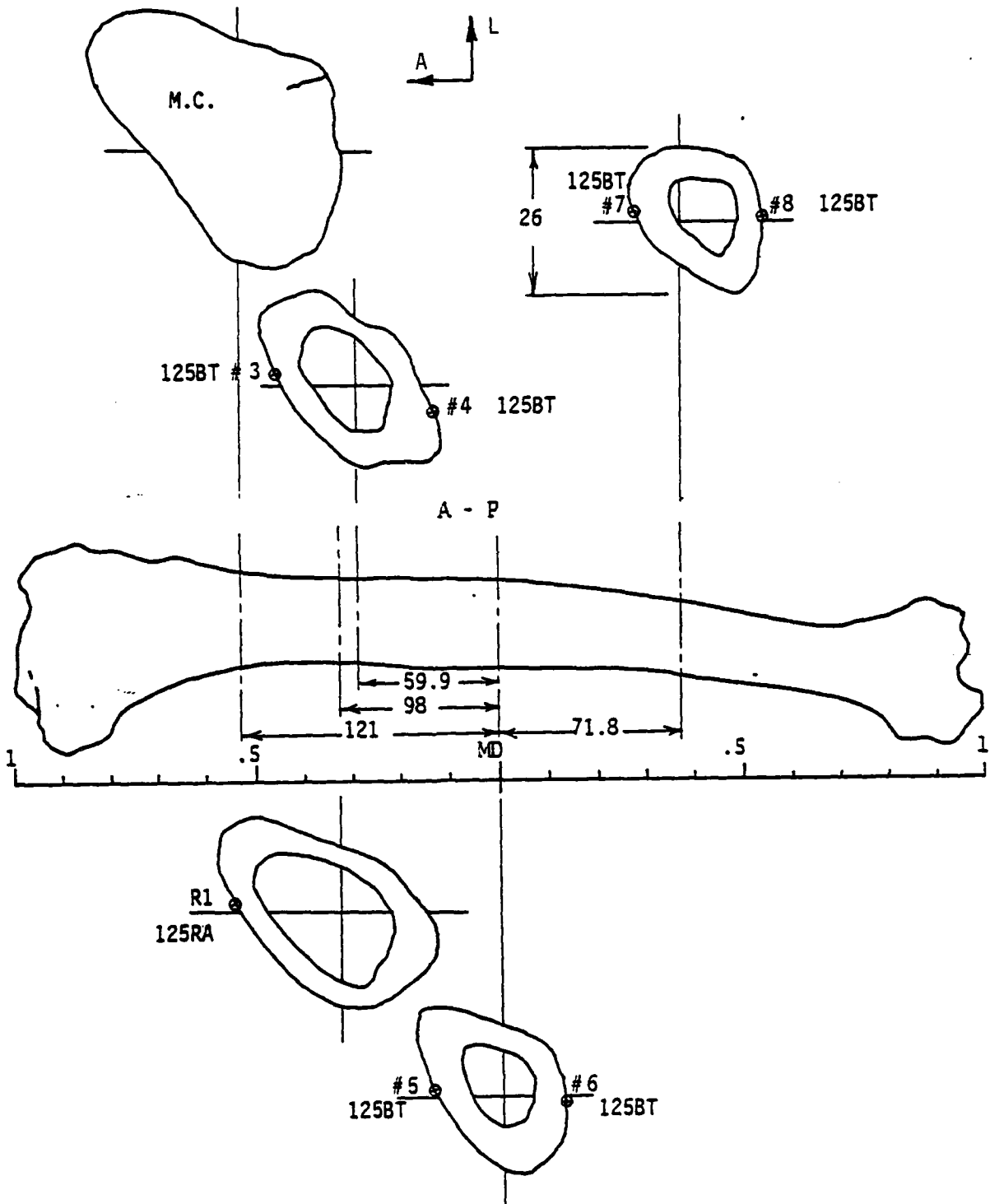
Figure 2.113 Locations of M.C. sections and strain gages for RT3787.



DISK AND STRAIN GAGE SECTIONS

LEFT TIBIA NO. 3787 CBN 16

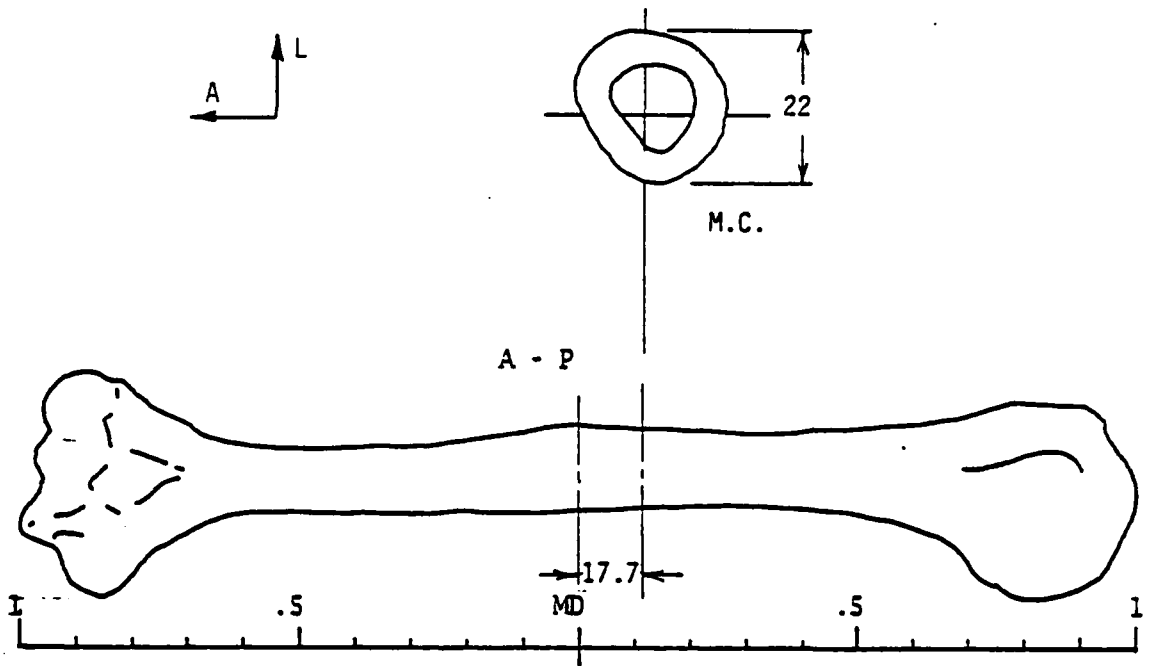
Figure 2.114 Locations of M.C. sections and strain gages for LT3787.



DISK AND STRAIN GAGE SECTIONS

RIGHT HUMERUS NO. 3753 T 6

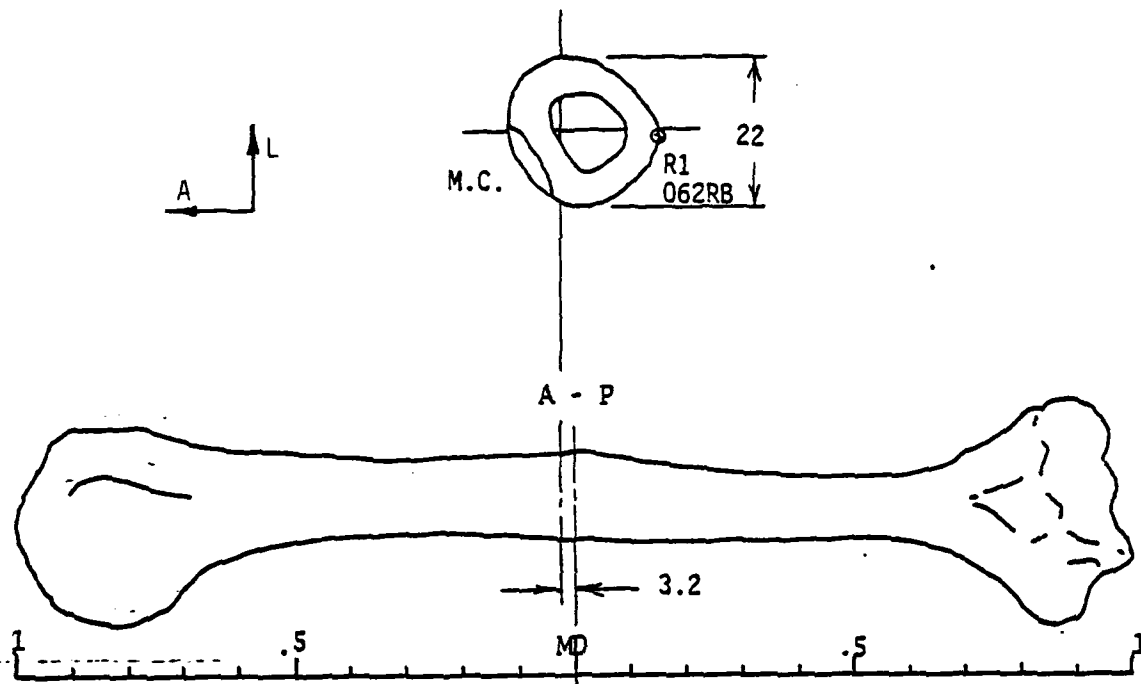
Figure 2.115 Locations of M.C. sections and strain gages for RH3753.



DISK AND STRAIN GAGE SECTIONS

LEFT HUMERUS NO. 3753 B 34

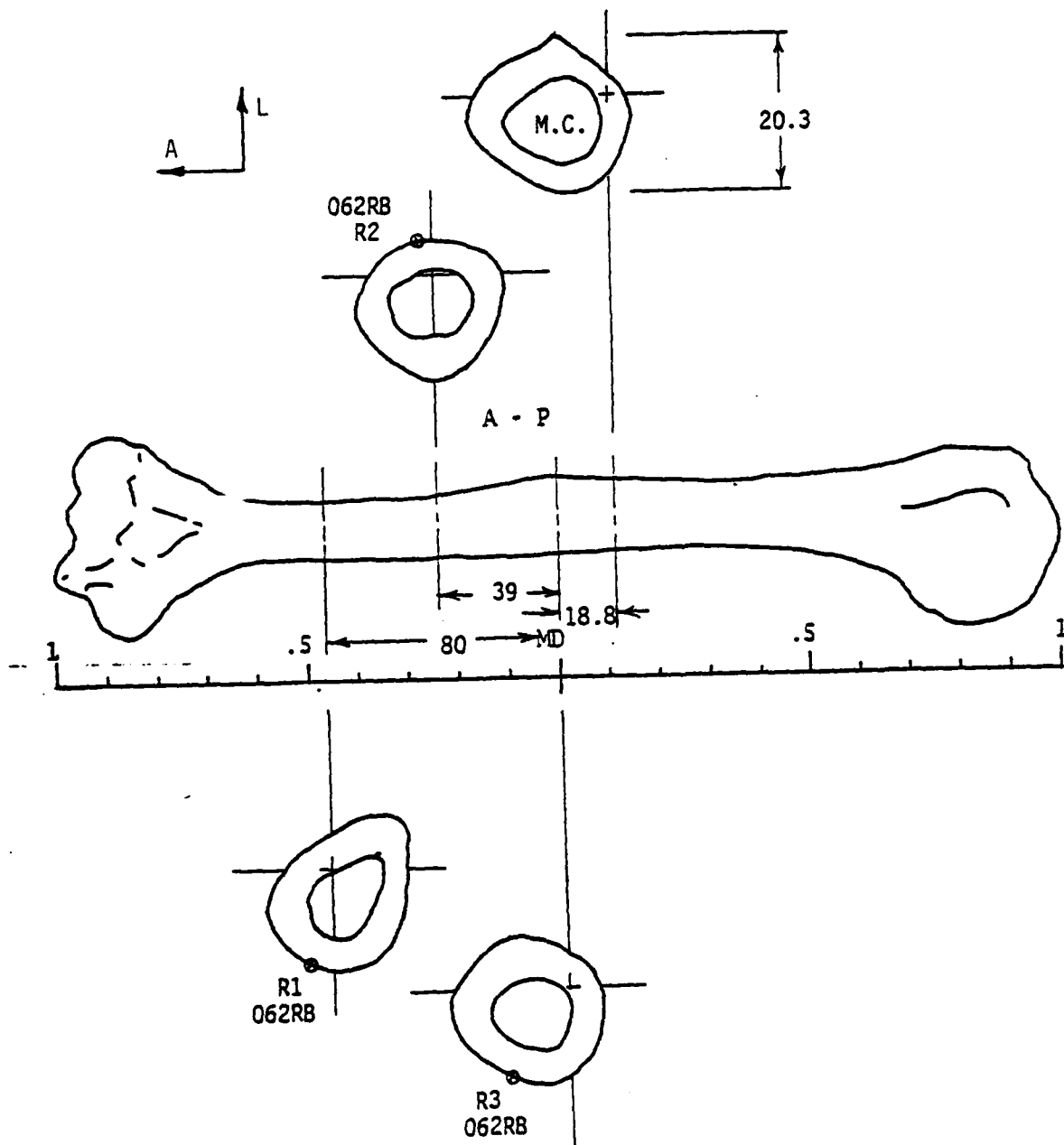
Figure 2.116 Locations of M.C. sections and strain gages for LH3753.



DISK AND STRAIN GAGE SECTIONS

RIGHT HUMERUS NO. 3793 T 23

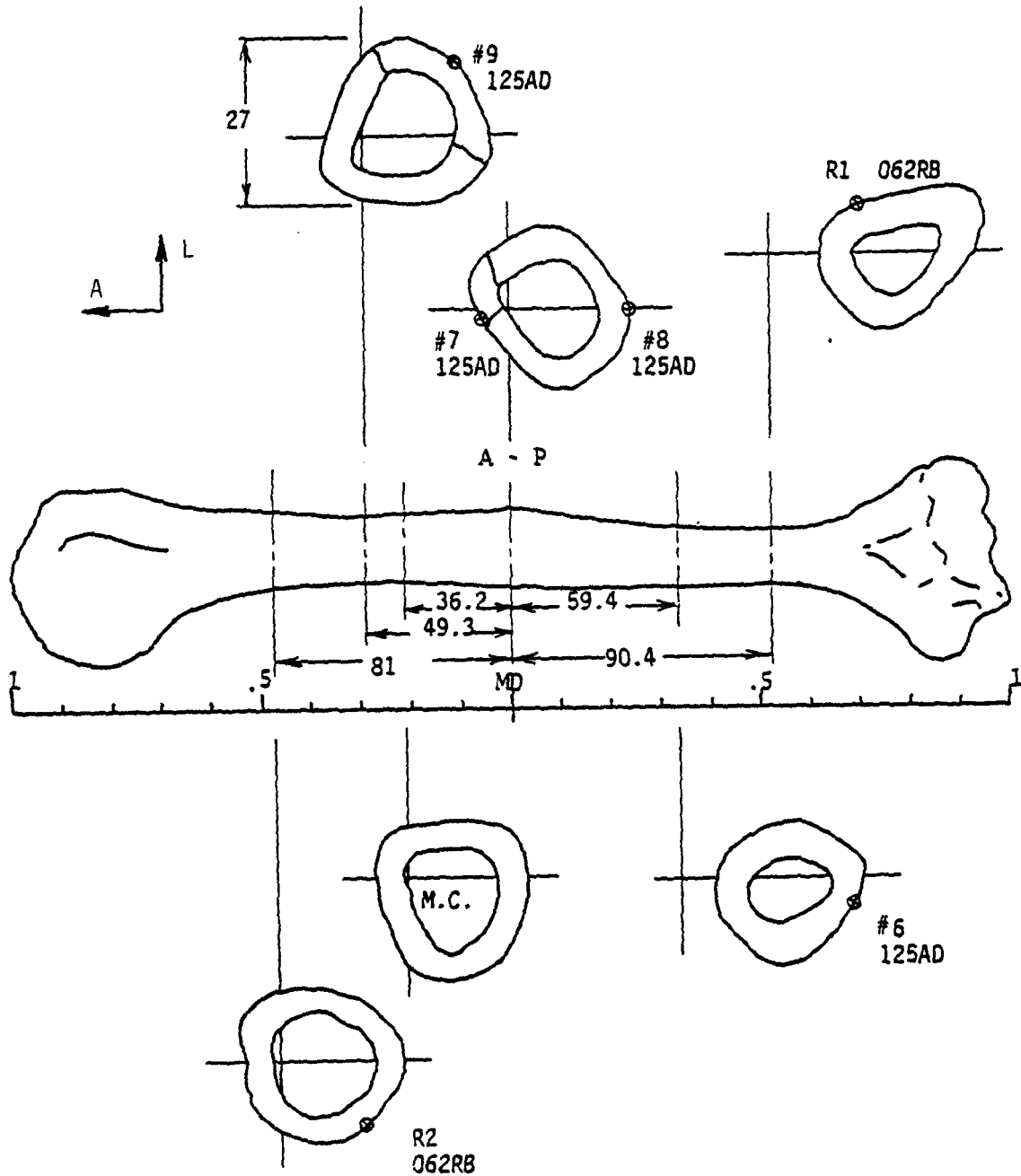
Figure 2.117 Locations of M.C. sections and strain gages for RH3793.



DISK AND STRAIN GAGE SECTIONS

LEFT HUMERUS NO. 3793 CBN 36

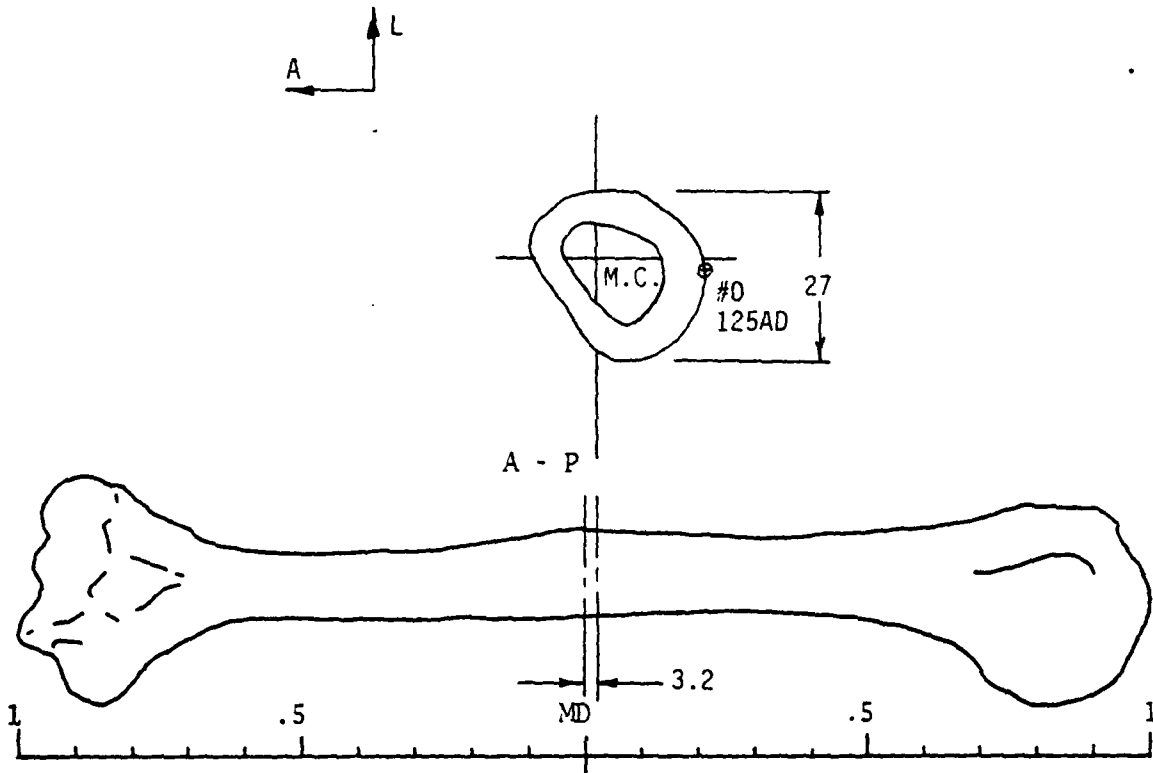
Figure 2.118 Locations of M.C. sections and strain gages for LH3793.



DISK AND STRAIN GAGE SECTIONS

RIGHT HUMERUS NO. 3790 Rapid 45

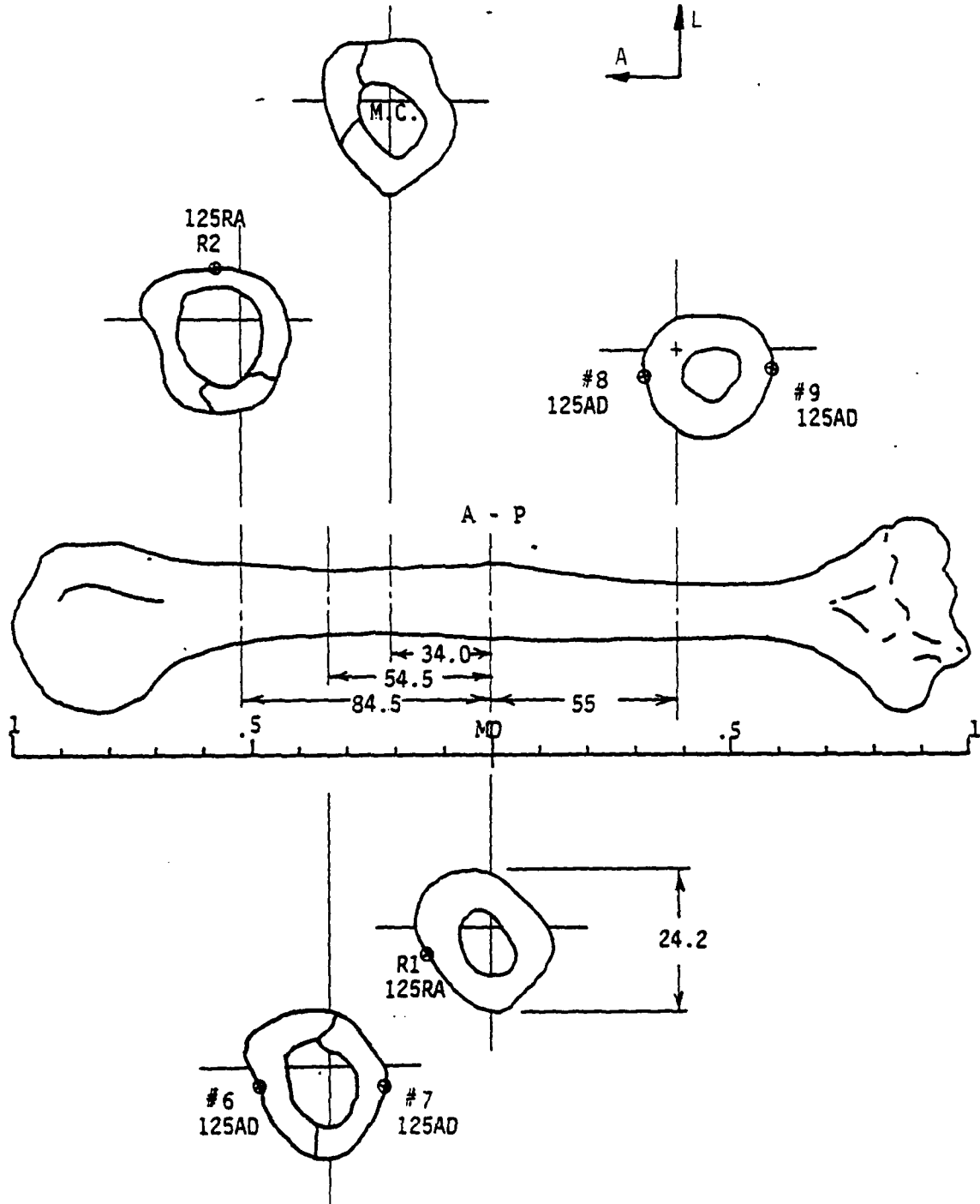
Figure 2.119 Locations of M.C. sections and strain gages for RH3790.



DISK AND STRAIN GAGE SECTIONS

LEFT HUMERUS NO. 3790 CT 40

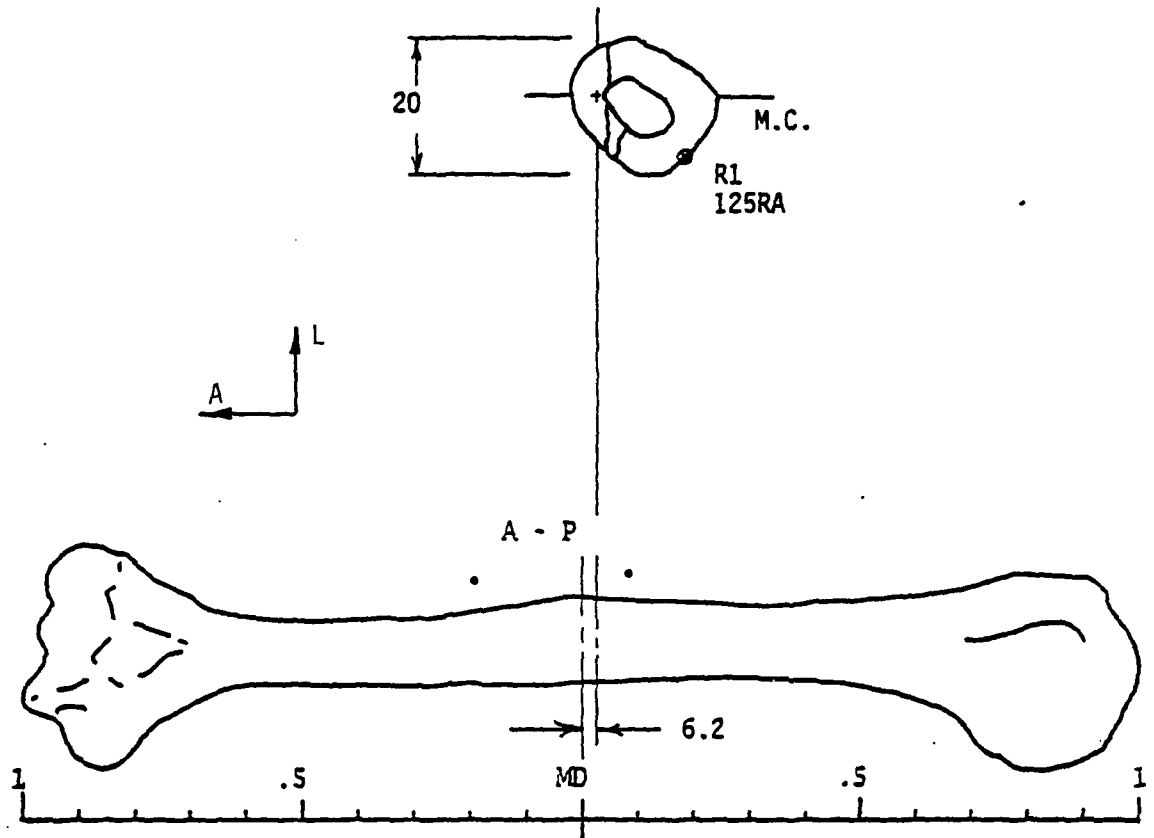
Figure 2.120 Locations of M.C. sections and strain gages for LH3790.



DISK AND STRAIN GAGE SECTIONS

RIGHT HUMERUS NO. 3782 B33

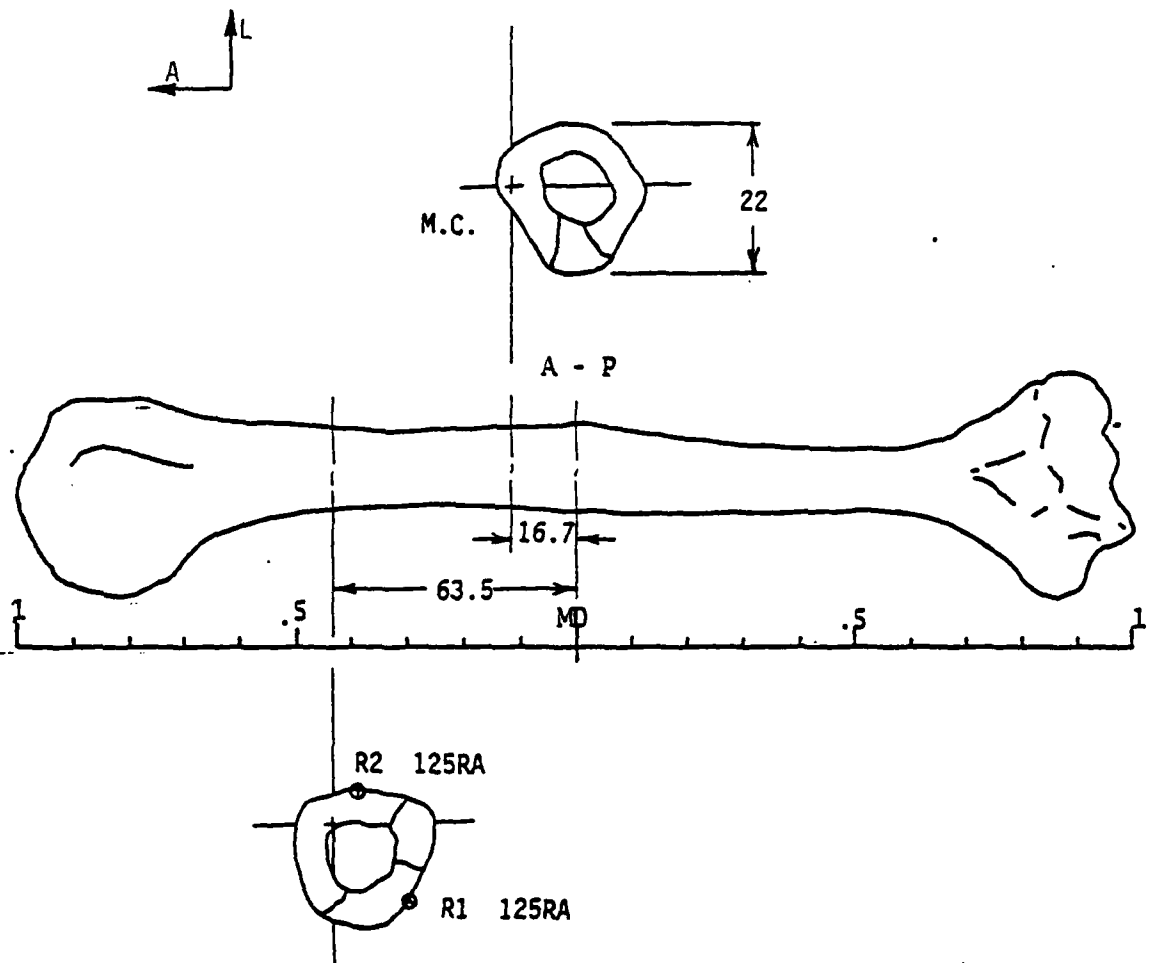
Figure 2.121 Locations of M.C. sections and strain gages for RH3782.



DISK AND STRAIN GAGE SECTIONS

LEFT HUMERUS NO. 3782 T 28

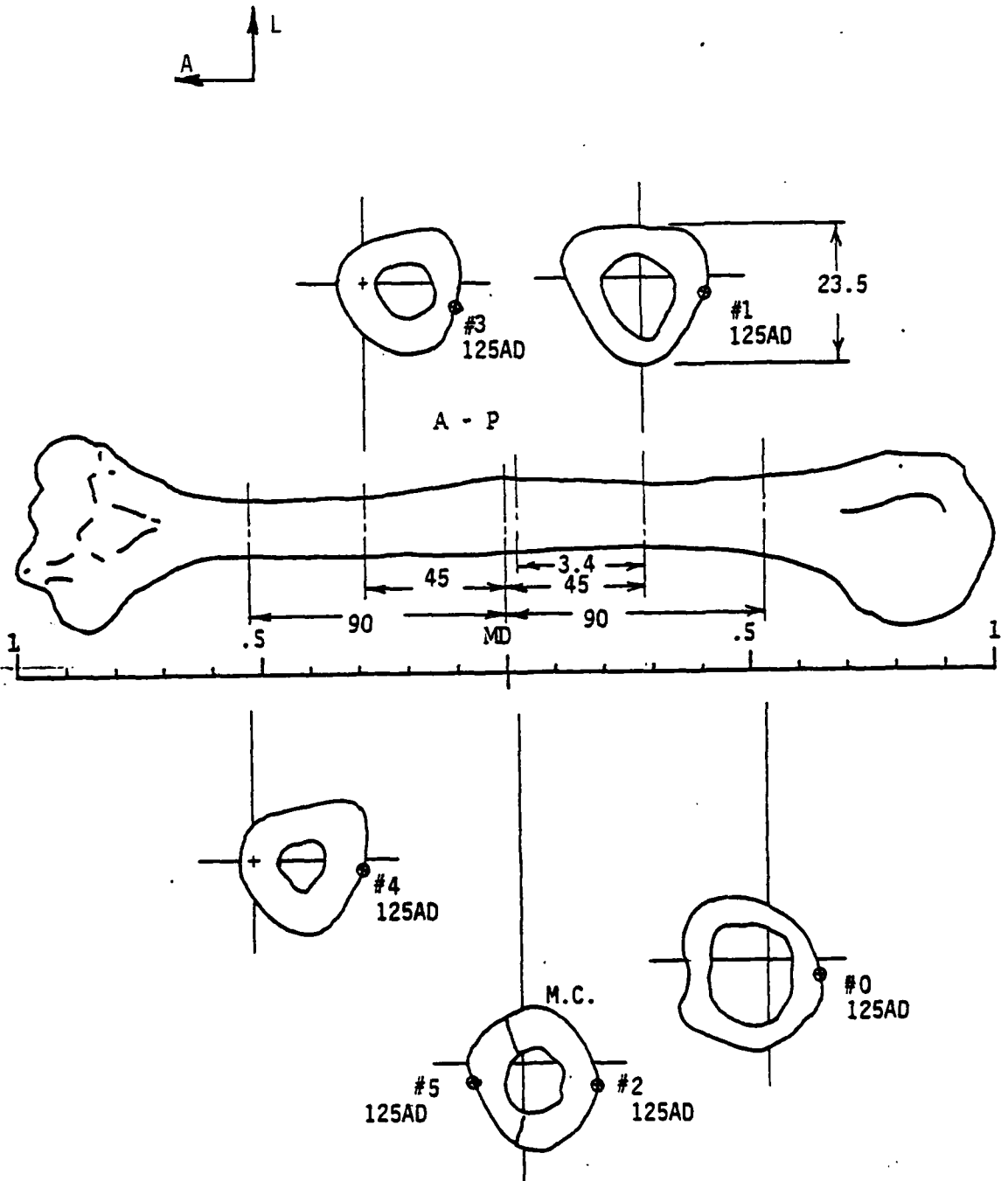
Figure 2.122 Locations of M.C. sections and strain gages for LH3782.



DISK AND STRAIN GAGE SECTIONS

RIGHT HUMERUS NO. 3792 B 35

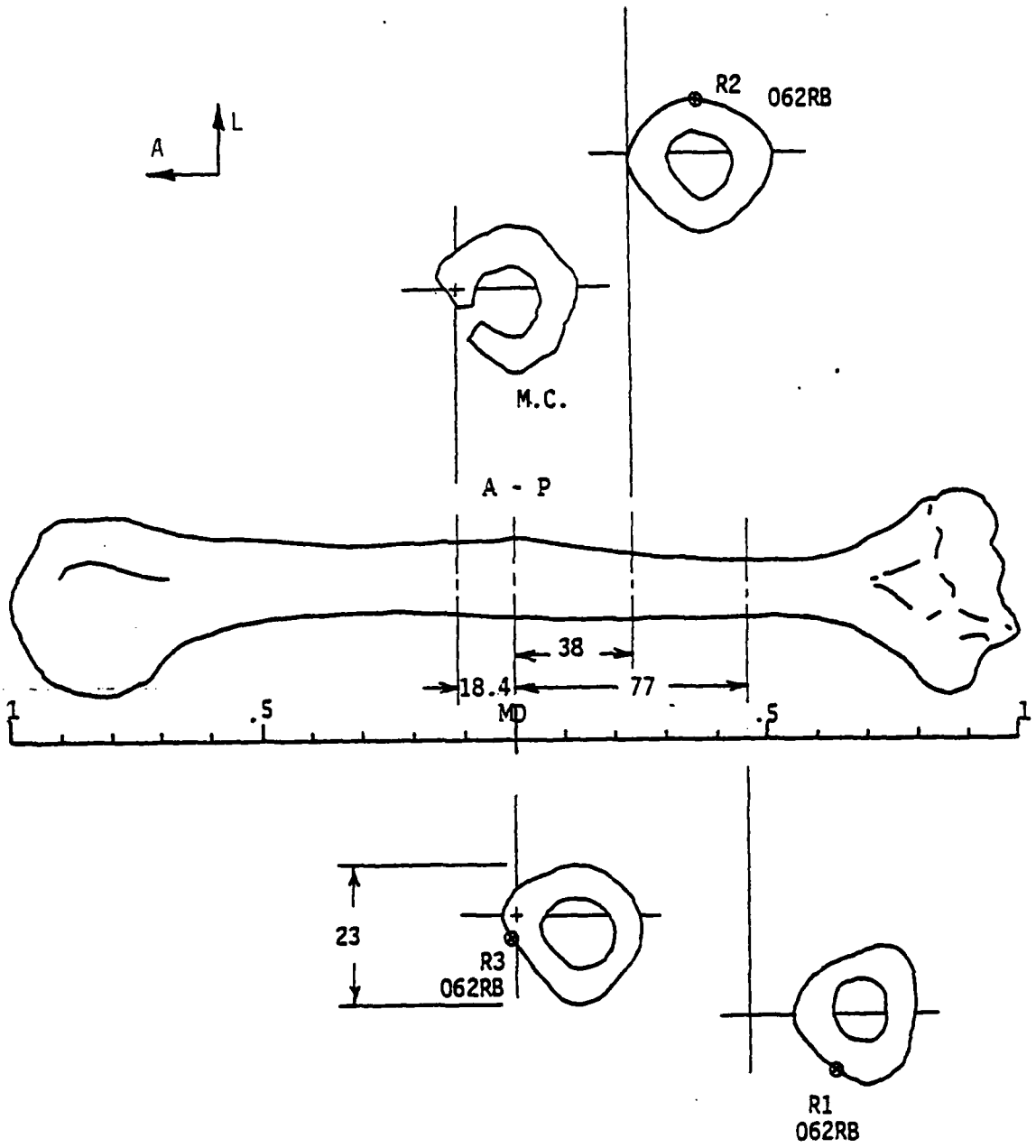
Figure 2.123 Locations of M.C. sections and strain gages for RH3792.



DISK AND STRAIN GAGE SECTIONS

LEFT HUMERUS NO. 3792 T 22

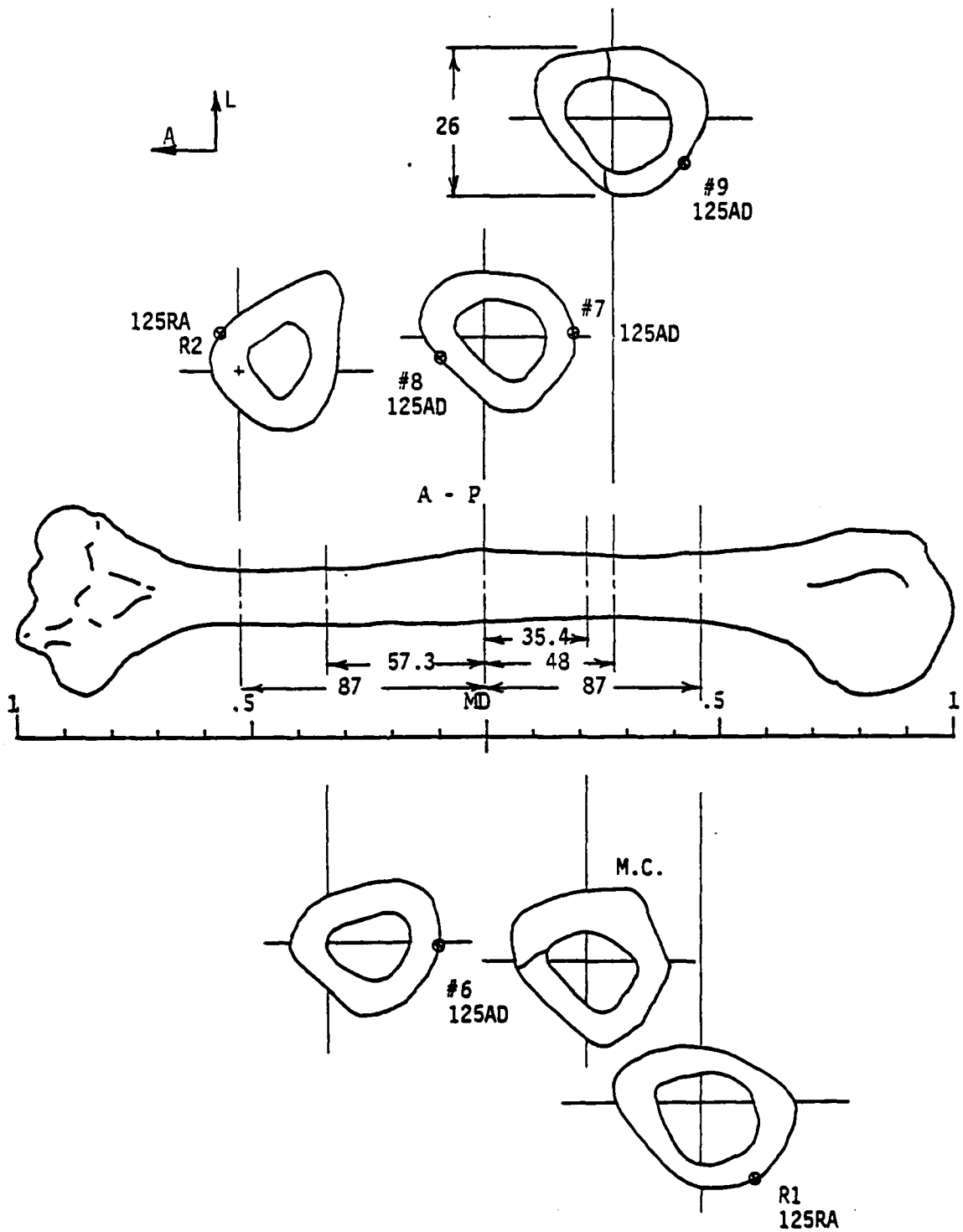
Figure 2.124 Locations of M.C. sections and strain gages for LH3792.



DISK AND STRAIN GAGE SECTIONS

RIGHT HUMERUS NO. 3787 CT 38

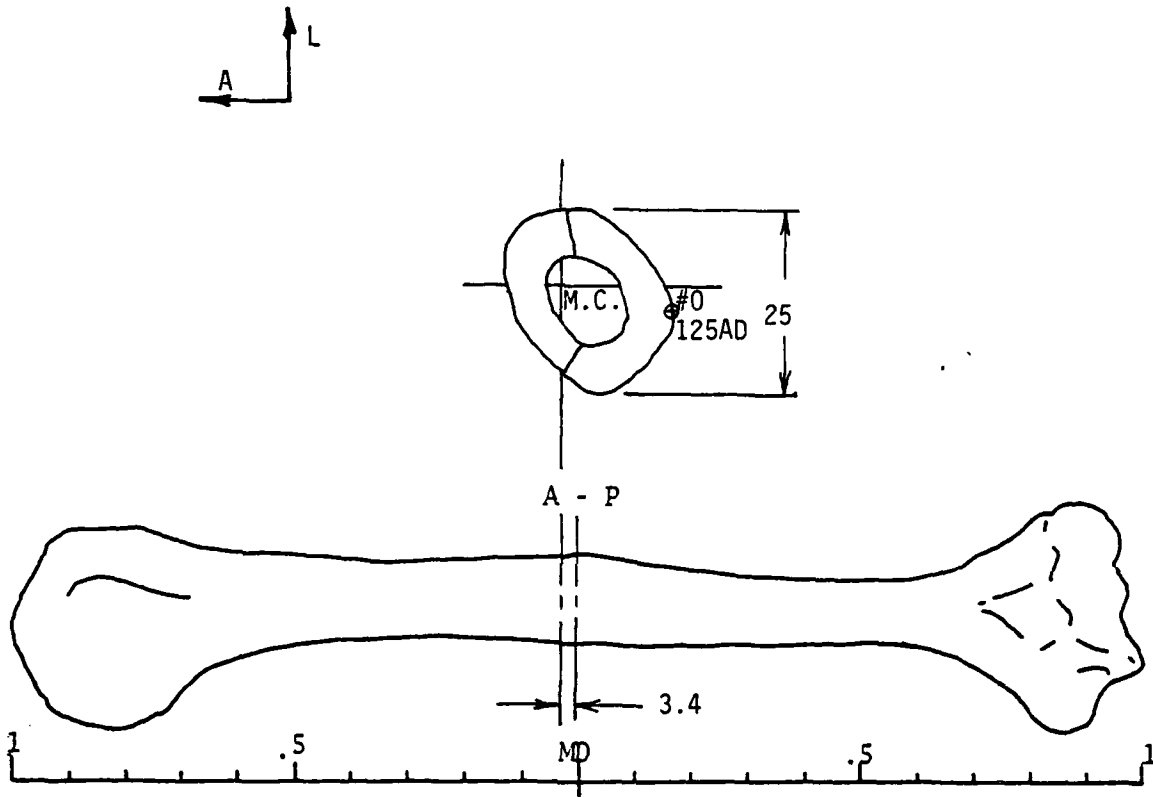
Figure 2.125 Locations of M.C. sections and strain gages for RH3787.



DISK AND STRAIN GAGE SECTIONS

LEFT HUMERUS NO. 3787 Rapid 46

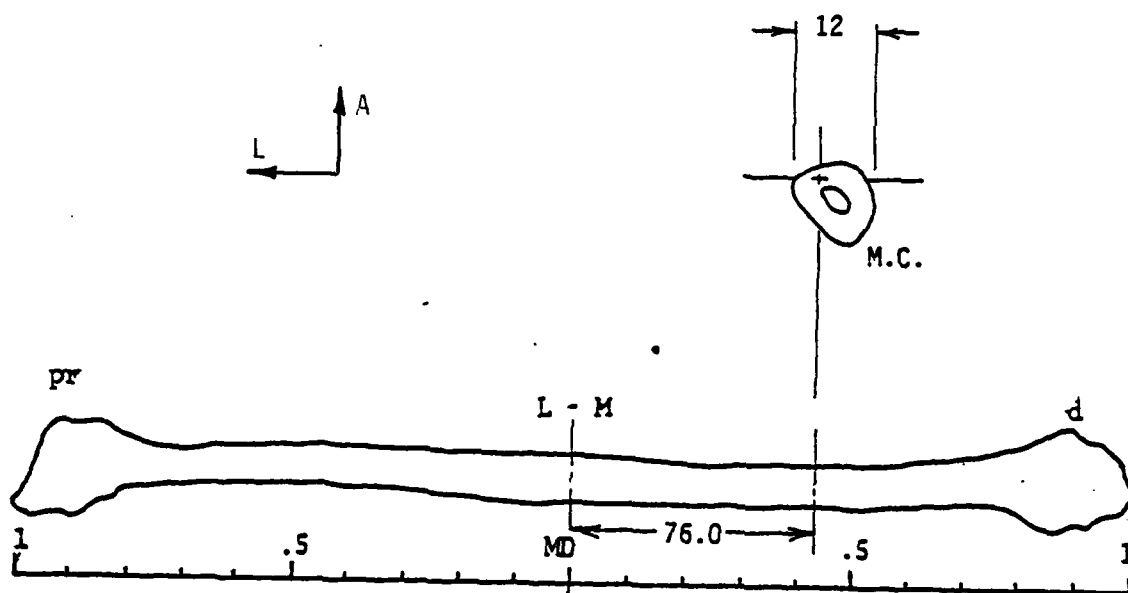
Figure 2.126 Locations of M.C. sections and strain gages for LH3787.



DISK AND STRAIN GAGE SECTIONS

RIGHT FIBULA NO. 3753 BN 4

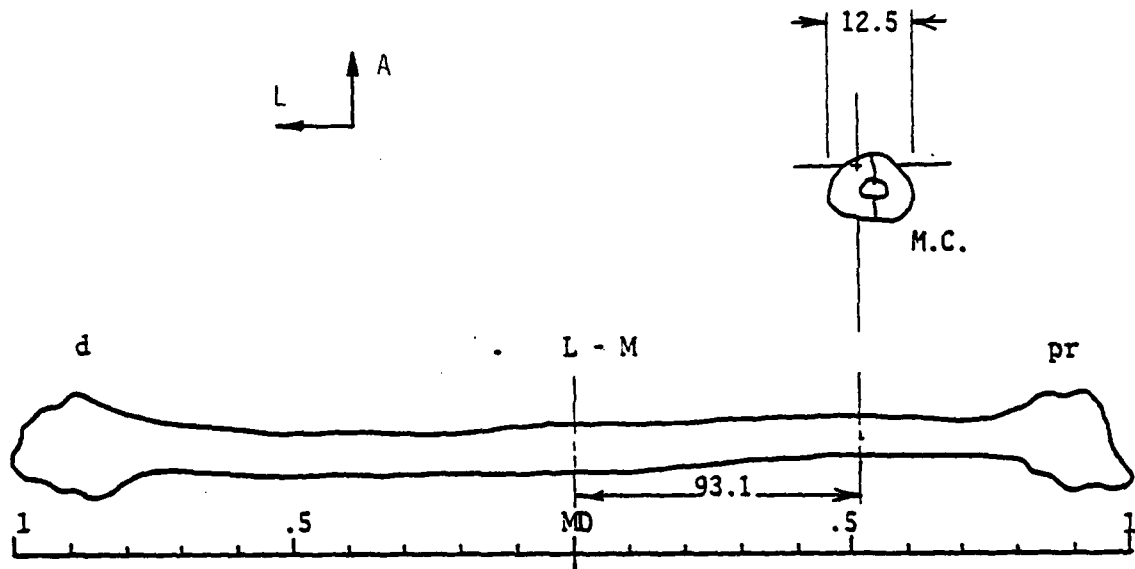
Figure 2.127 Locations of M.C. sections and strain gages for Rfb3753.



DISK AND STRAIN GAGE SECTIONS

LEFT FIBULA NO. 3753 T 7

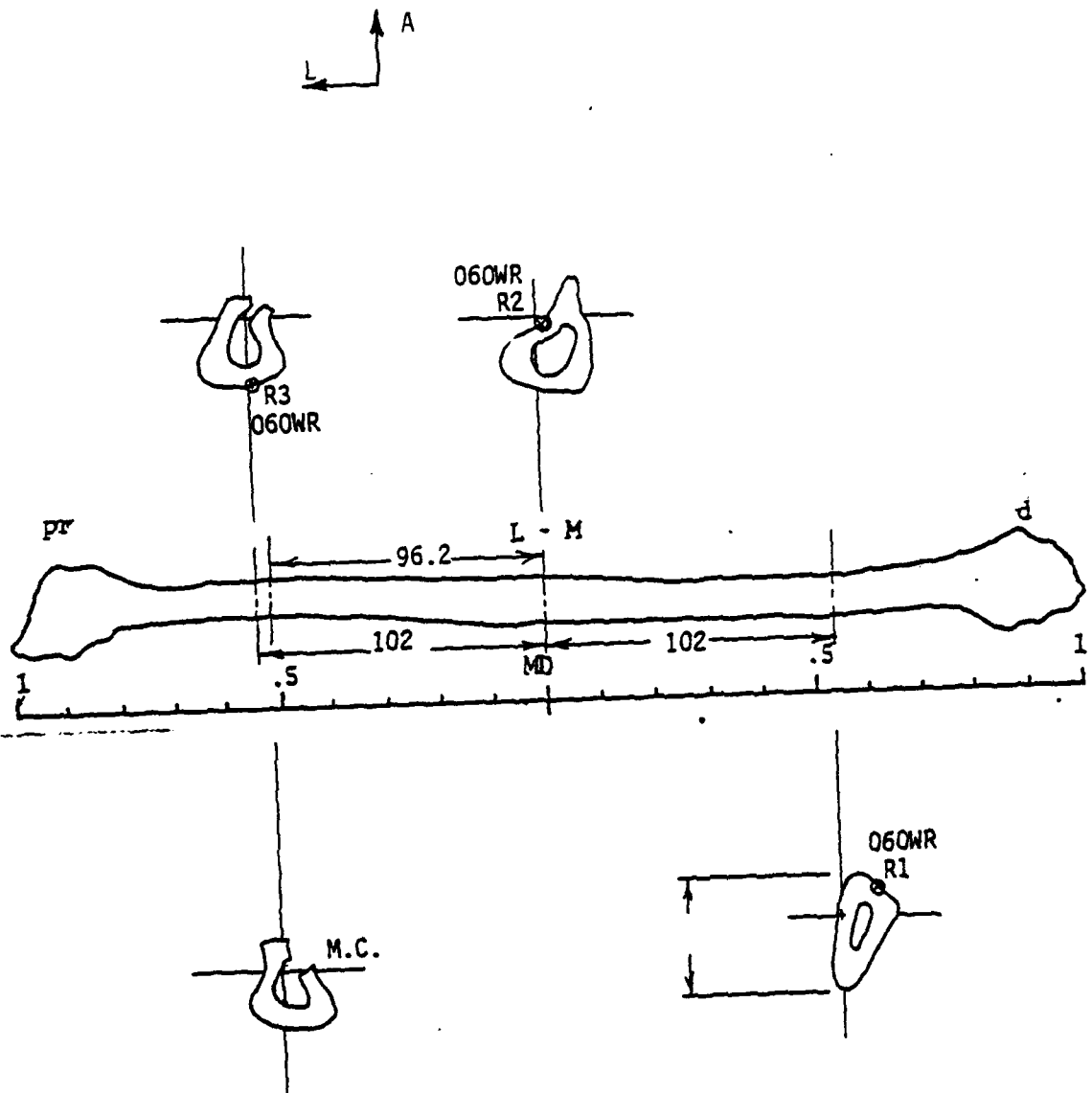
Figure 2.128 Locations of M.C. sections and strain gages for LFB3753.



DISK AND STRAIN GAGE SECTIONS

RIGHT FIBULA NO. 3793 T 30

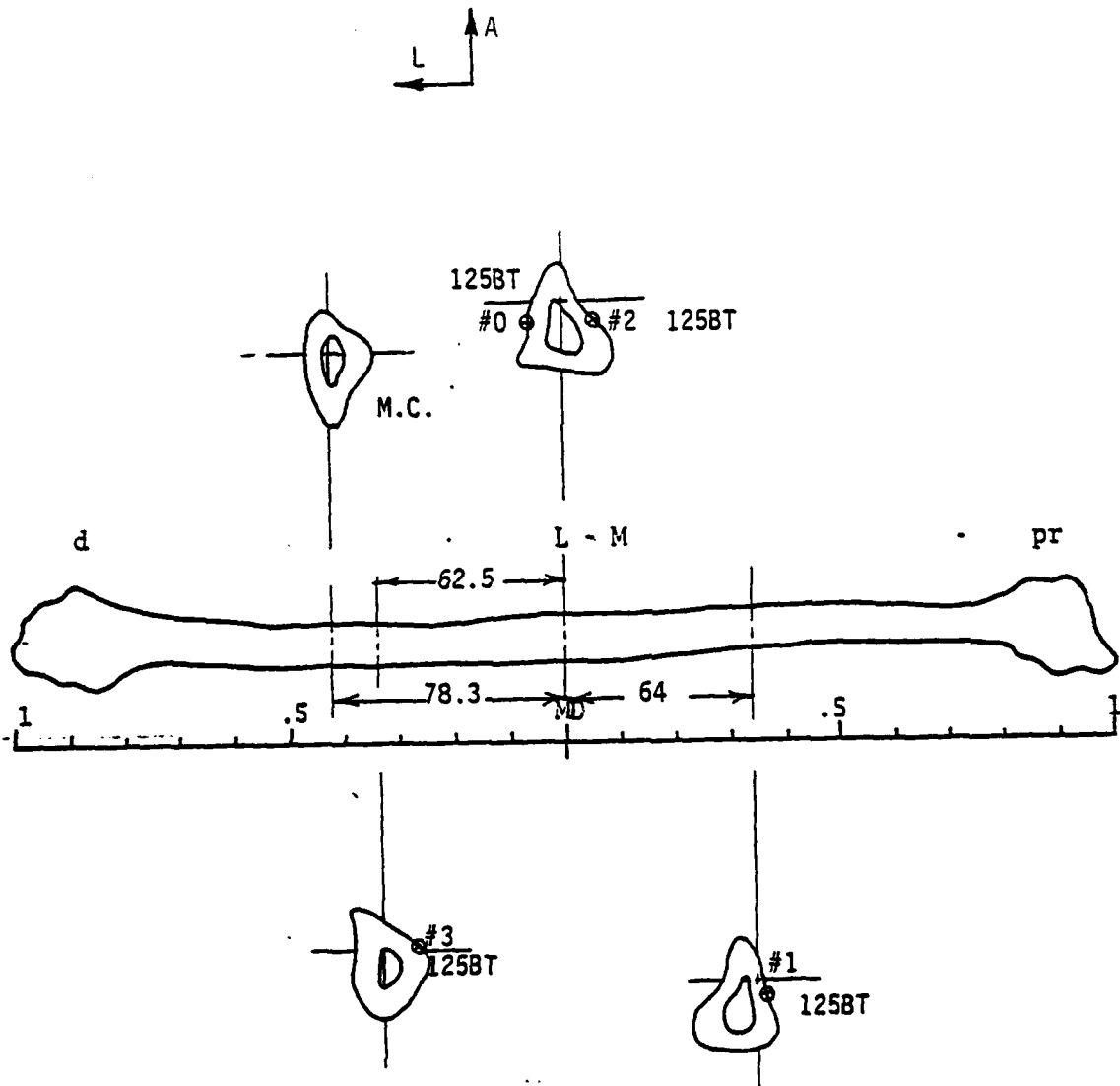
Figure 2.129 Locations of M.C. sections and strain gages for Rfb3793.



DISK AND STRAIN GAGE SECTIONS

LEFT FIBULA NO. 3793 BM 37

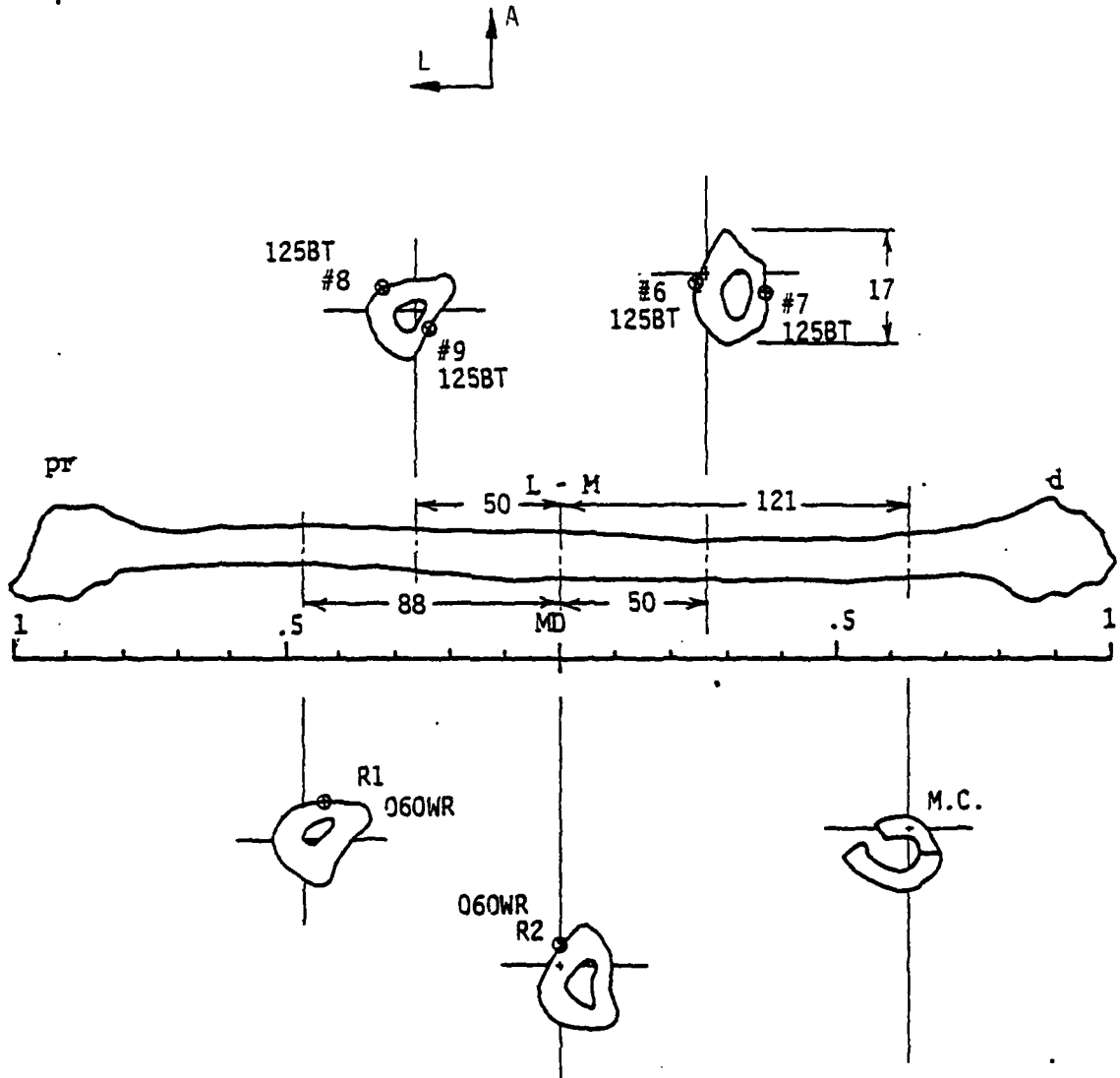
Figure 2.130 Locations of M.C. sections and strain gages for LFb3793.



DISK AND STRAIN GAGE SECTIONS

RIGHT FIBULA NO. 3790 CTW 41

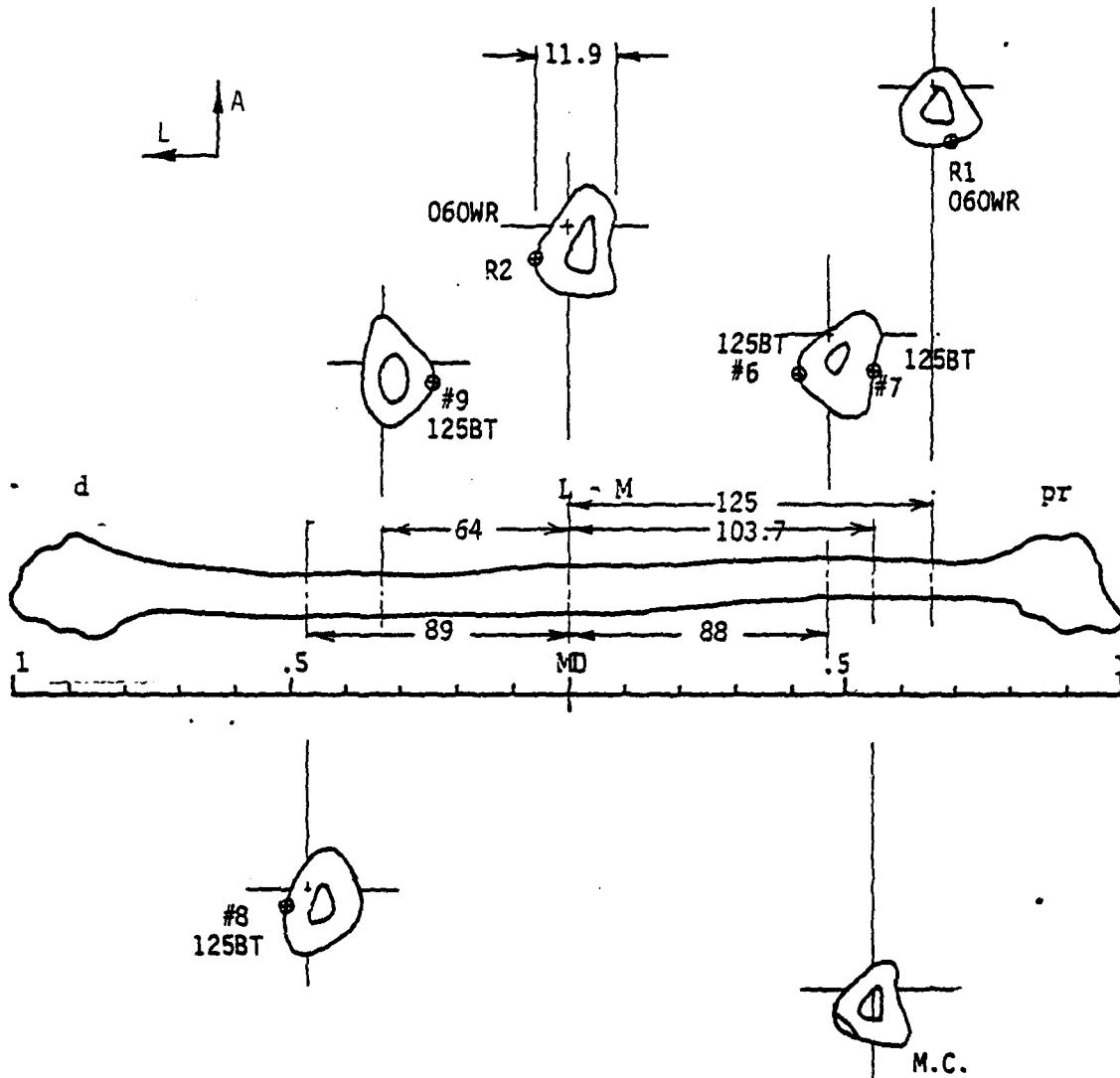
Figure 2.131 Locations of M.C. sections and strain gages for Rfb3790.



DISK AND STRAIN GAGE SECTIONS

LEFT FIBULA NO. 3790 CTN 42

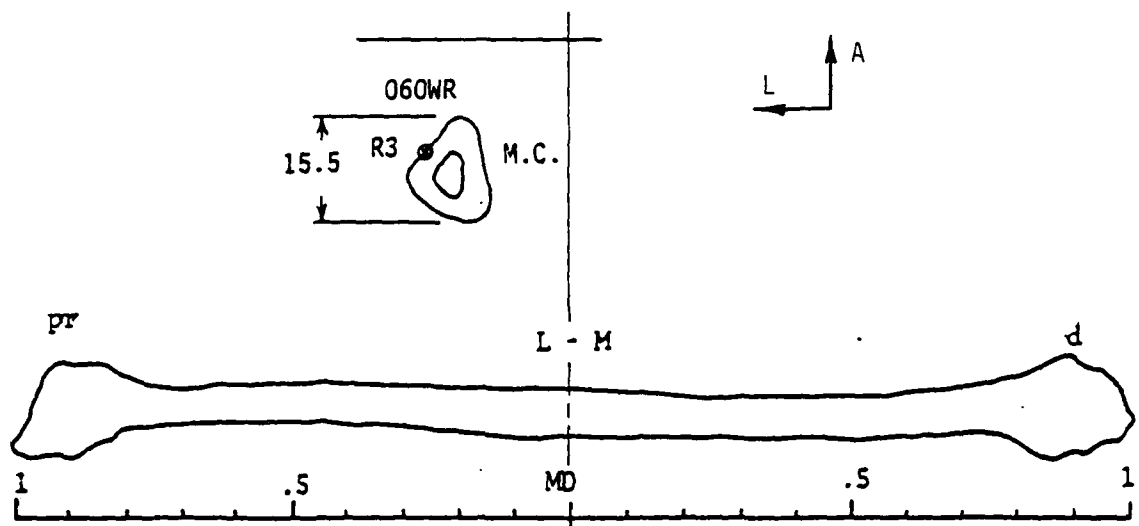
Figure 2.132 Locations of M.C. sections and strain gages for LFb3790.



DISK AND STRAIN GAGE SECTIONS

RIGHT FIBULA NO. 3782 TOR 31

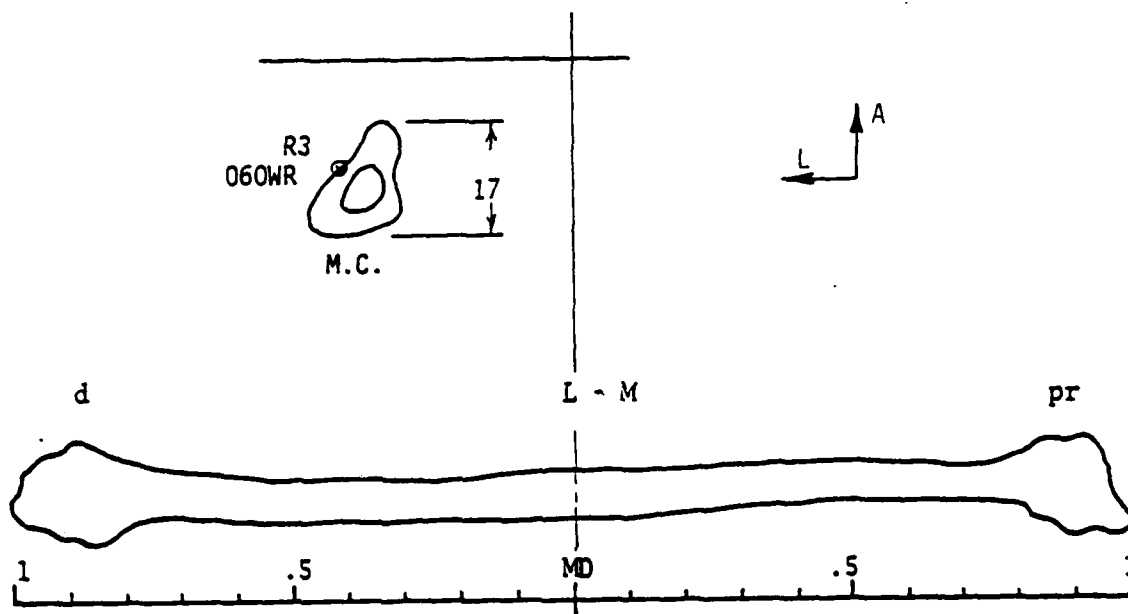
Figure 2.133 Locations of M.C. sections and strain gages for Rfb3782.



DISK AND STRAIN GAGE SECTIONS

LEFT FIBULA NO. 3782 TOR 32

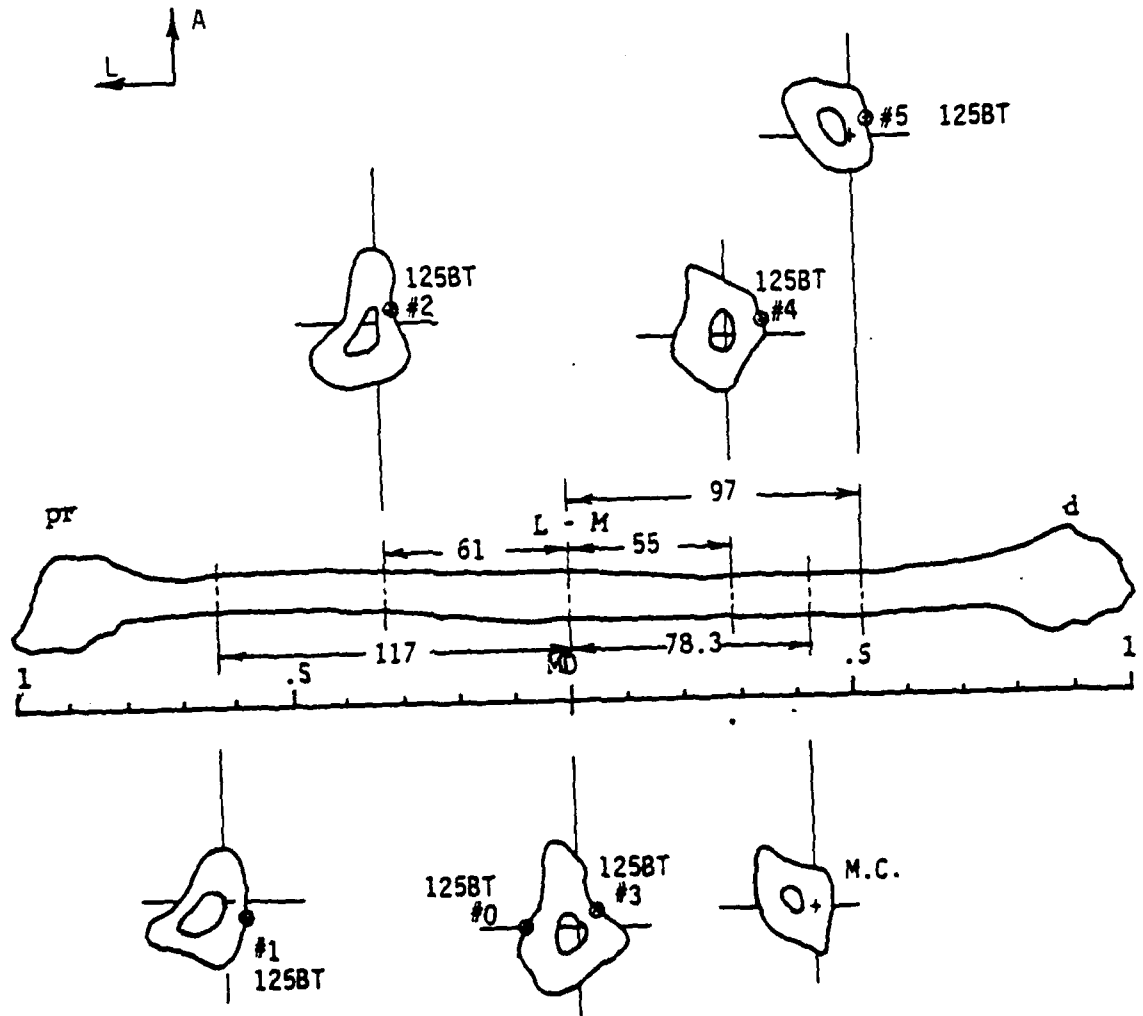
Figure 2.134 Locations of M.C. sections and strain gages for Lfb3782.



DISK AND STRAIN GAGE SECTIONS

RIGHT FIBULA NO. 3792 BM 39

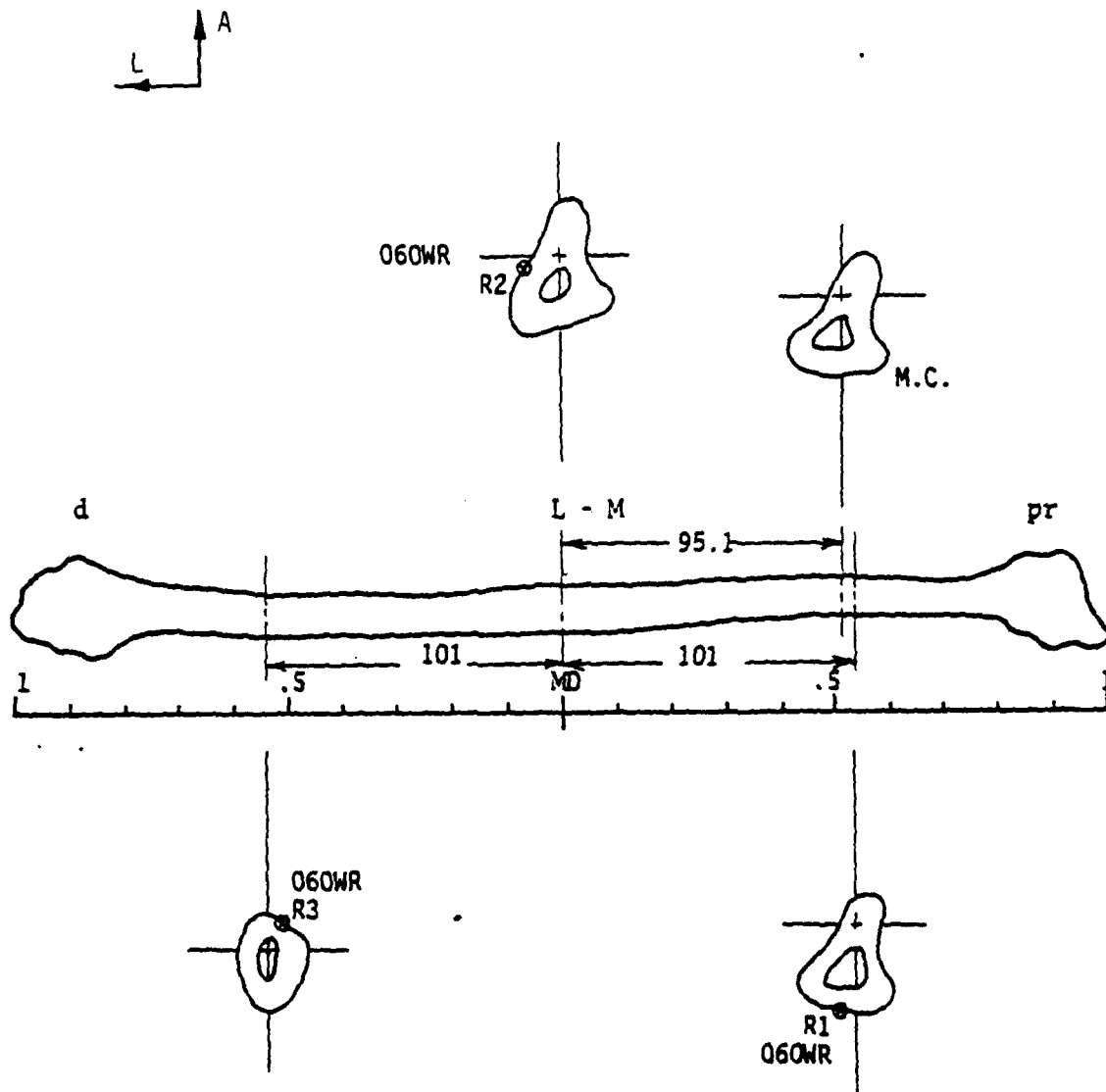
Figure 2.135 Locations of M.C. sections and strain gages for RFB3792.



DISK AND STRAIN GAGE SECTIONS

LEFT FIBULA NO. 3792 T 29

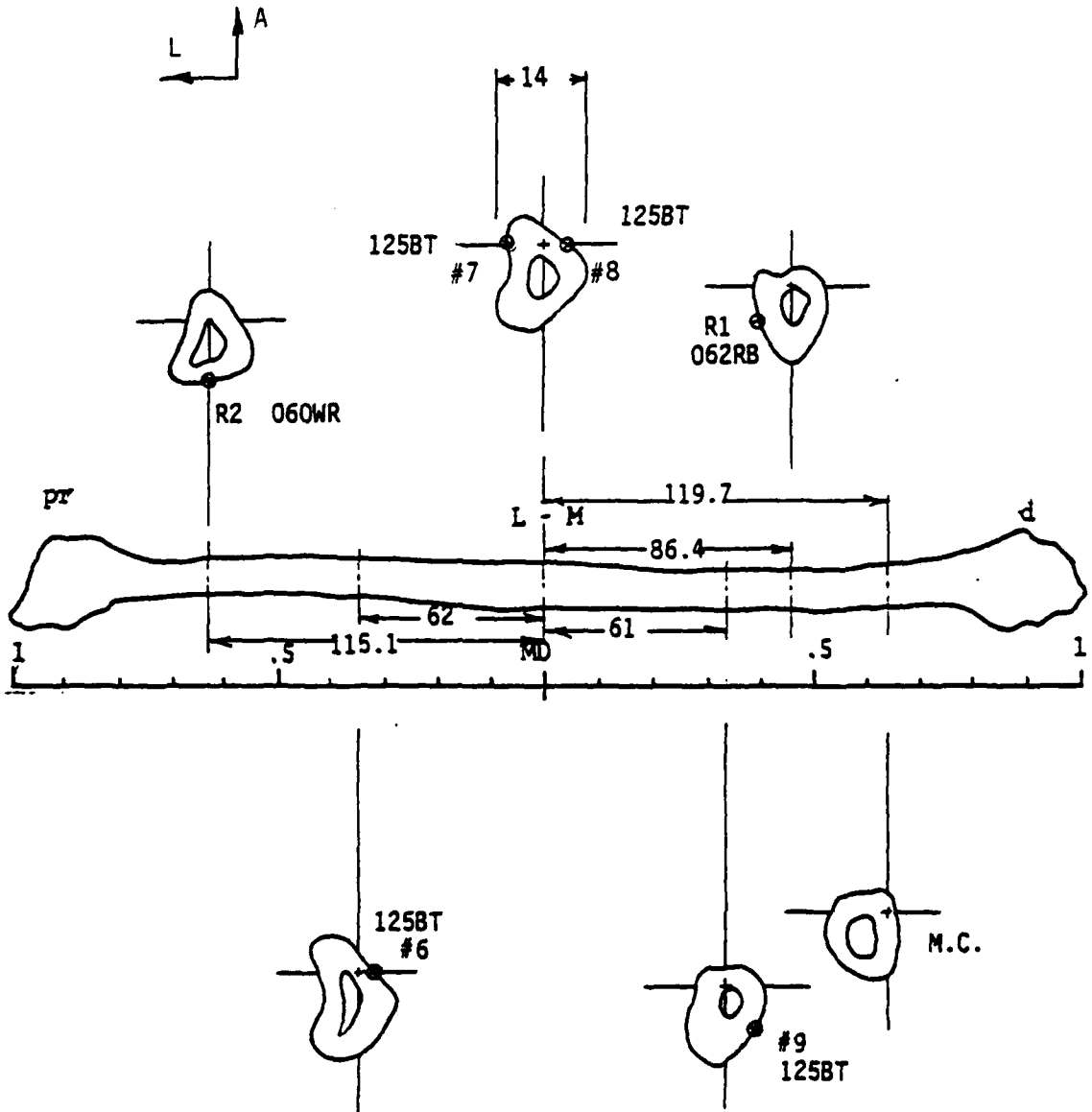
Figure 2.136 Locations of M.C. sections and strain gages for LFb3792.



DISK AND STRAIN GAGE SECTIONS

RIGHT FIBULA NO. 3787 CTN 44

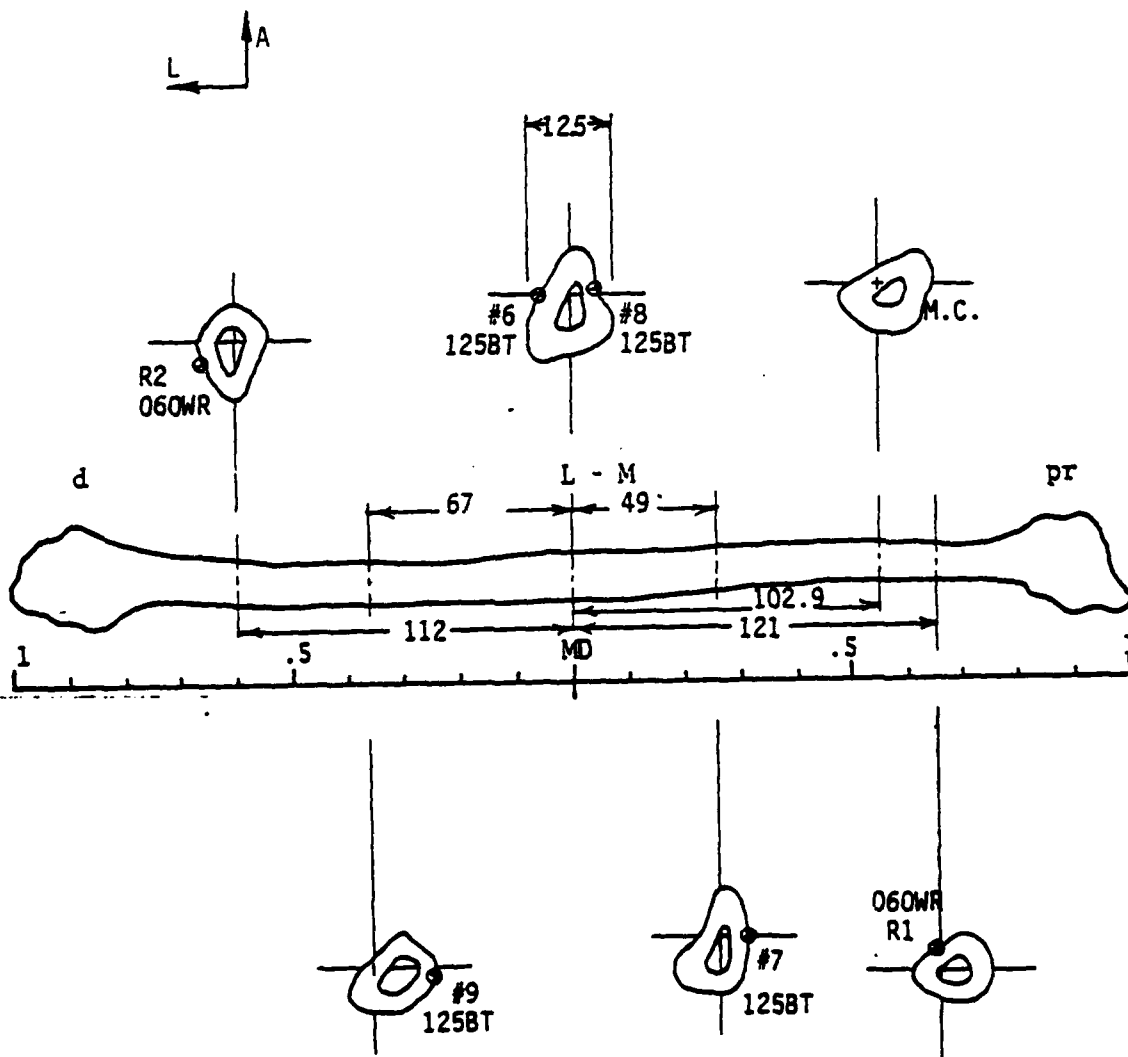
Figure 2.137 Locations of M.C. sections and strain gages for Rfb3787.



DISK AND STRAIN GAGE SECTIONS

LEFT FIBULA NO. 3787 CBN 43

Figure 2.138 Locations of M.C. sections and strain gages for Lfb3787.



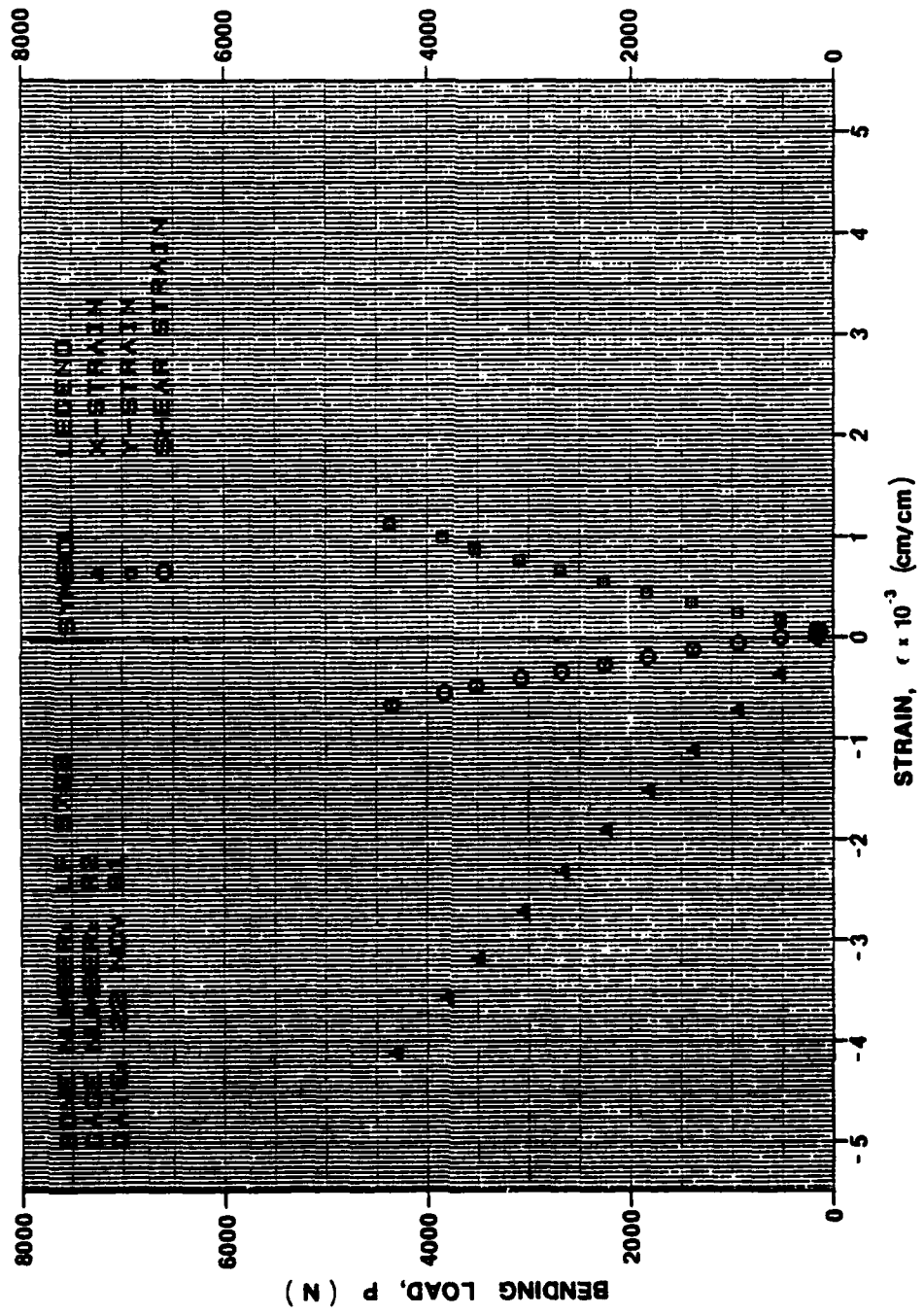


Figure 2.139 Gage strain for LF3793, concave side, proximal end, bending only.

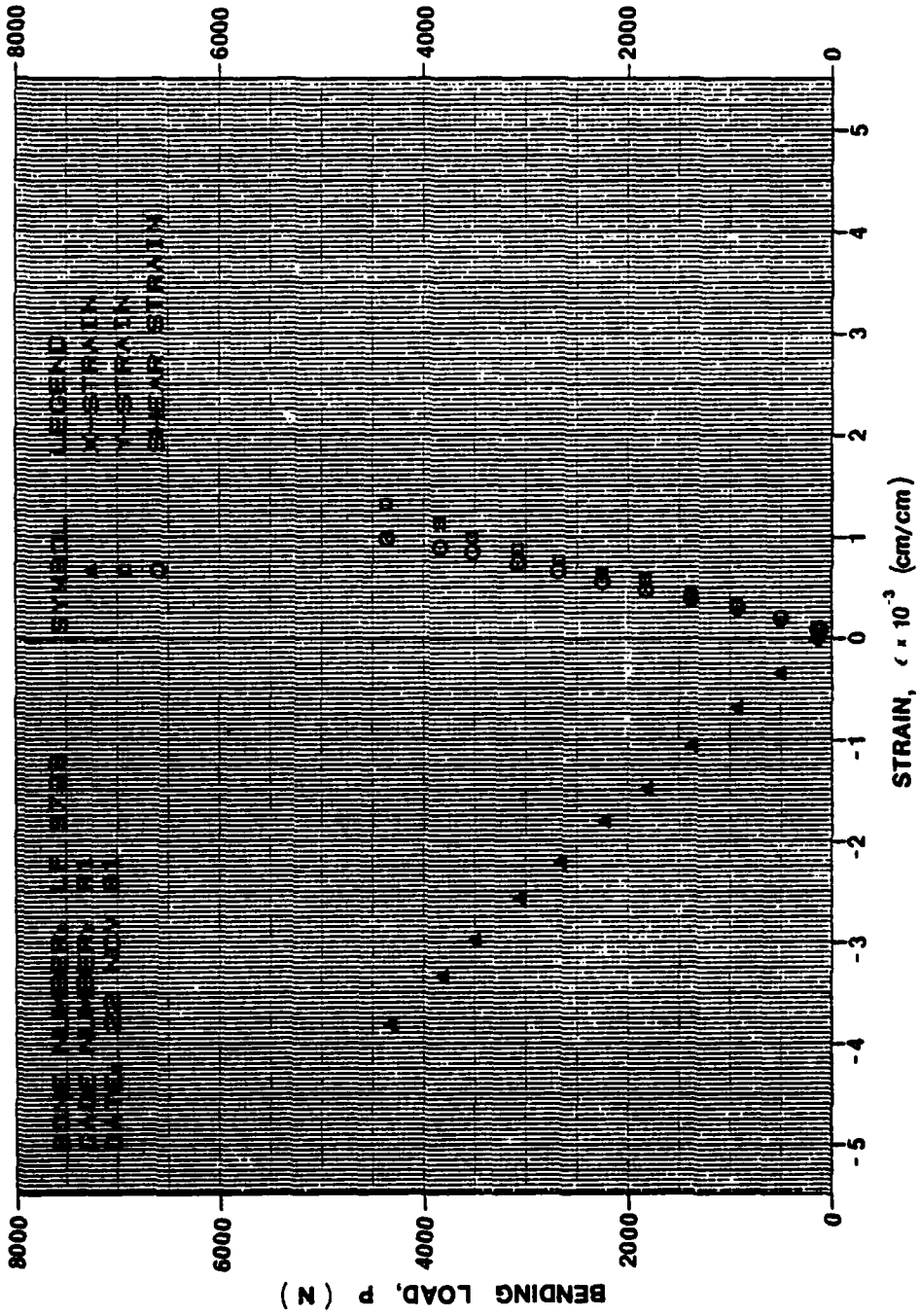


Figure 2.140 Gage strain for LF3793, concave side, distal end, bending only.

The femur with the two rosettes at its mid-diaphysis strained as one would expect for the bending only condition with the exception of some shear present between the two rollers (load points). With four point bending, shearing forces should not exist between the two center concentrated loads unless these loads are not equal or unless simple bending is not present. In this case, the shear present at the two rosettes implies a tendency for the femur to rotate inversively when bent. Note also for this femur the principal strain orthogonal to the diaphyseal axis was a tensile strain which could account for the path that the propagating crack assumed after bifurcation or when it started to curve toward a path parallel to the concave bending surface.

One femur, LF3782, was gaged only with axial gages for bending only. One gage was placed on the concave (anterior) side of bending bone and three were bonded on the opposite, convex (posterior side). One of posterior gages was at the mid-diaphysis; one was at the proximal third and the other was at the distal third. This femur fractured on the posterior surface due to bending tension at two locations. One fracture was relatively close to the axial gage at the proximal third. The stress at this gage, accounting for the material direction [4], using the technical constants of Reilly and Burstein [1], was 98.3 MPa. This was less than the stress sensed by the gage at the distal third which was 127.6 MPa. The stresses at the mid-diaphysis were -99.0 MPa on the anterior surface and 130.2 MPa on the posterior surface. All of the stresses were available at fracture and are within 27% of the rupture tensile stress of 133 MPa, proposed by Reilly and Burstein. Note that the initial tangent modulus of Reilly and Burstein was used here to approximate the failure stress; this approximation is reasonable since the load-strain curves were mildly nonlinear.

#### Tibiae:

Two tibiae were gaged for the bending only loading condition. One, RT3792, had two rosettes on the concave side (anterior) of the bending bone at the distal and proximal quarters. In addition there were two axial gages at the mid-diaphysis: one as close to the crest as possible and the other in the center (lateromedially) on the posterior side. The other tibia, LT3793, had a rosette on the convex (posterior) side of the

bending diaphysis at the distal quarter with a second rosette on the medioanterior side near the proximal third. This tibia also had two axial gages centered mediolaterally on the posterior side at the distal and proximal thirds as well as a third axial gage close to the crest on the anterior side.

The shearing strain at the distal rosette on RT3792 inferred a tendency for the diaphysis to twist eversively at that location while the shearing strain at the proximal rosette implied a tendency to twist inversively. This follows intuitively if one considers the cross-sectional shape (Figure 2.5) in conjunction with the constraint of the bone at its ends. The compressive strain at the distal gage of this tibia was twice as great as the compressive strain sensed by the proximal gage. This result is also acceptable when the geometry is compared between the two ends. Since the difference in the magnitude of the tensile strain on the posterior side of the two ends should be comparable to that of the compressive strain, bending fractures should be expected to occur in the distal half (as observed) rather than the proximal half. The axial gages at the mid-diaphysis of the bone indicated a stress of -96.8 MPa on the anterior side and a tensile stress of 142.2 MPa on the posterior side.

LT3793 also exhibited a tendency to twist while undergoing pure bending. The shearing strain at its proximal gage implied an inverse rotation at that location while the shearing strain at the distal end indicated an eversive rotation. This twisting was opposite in direction with that discussed above because this tibia was a left instead of a right and the crest was offset to the opposite side of axis of twist. Note also (Figure 2.141, 142) that the shearing action at the proximal gage was 25 times the magnitude of that at the distal gage; this was a result of the greater offset of the crest from the axis at the proximal end than the distal end. RT3792 did not display such a large difference in shearing strain since its crest was not offset as much from the torsional axis of the Osteoclast as this tibia.

The stresses sensed at the axial gages on the posterior side of LT3793 were of course tensile and measured 145.9 MPa at the proximal gage and 269.2 MPa at the distal gage. The compressive strain measured on the anterior surface at the mid-diaphysis was -96.8 MPa. Note the

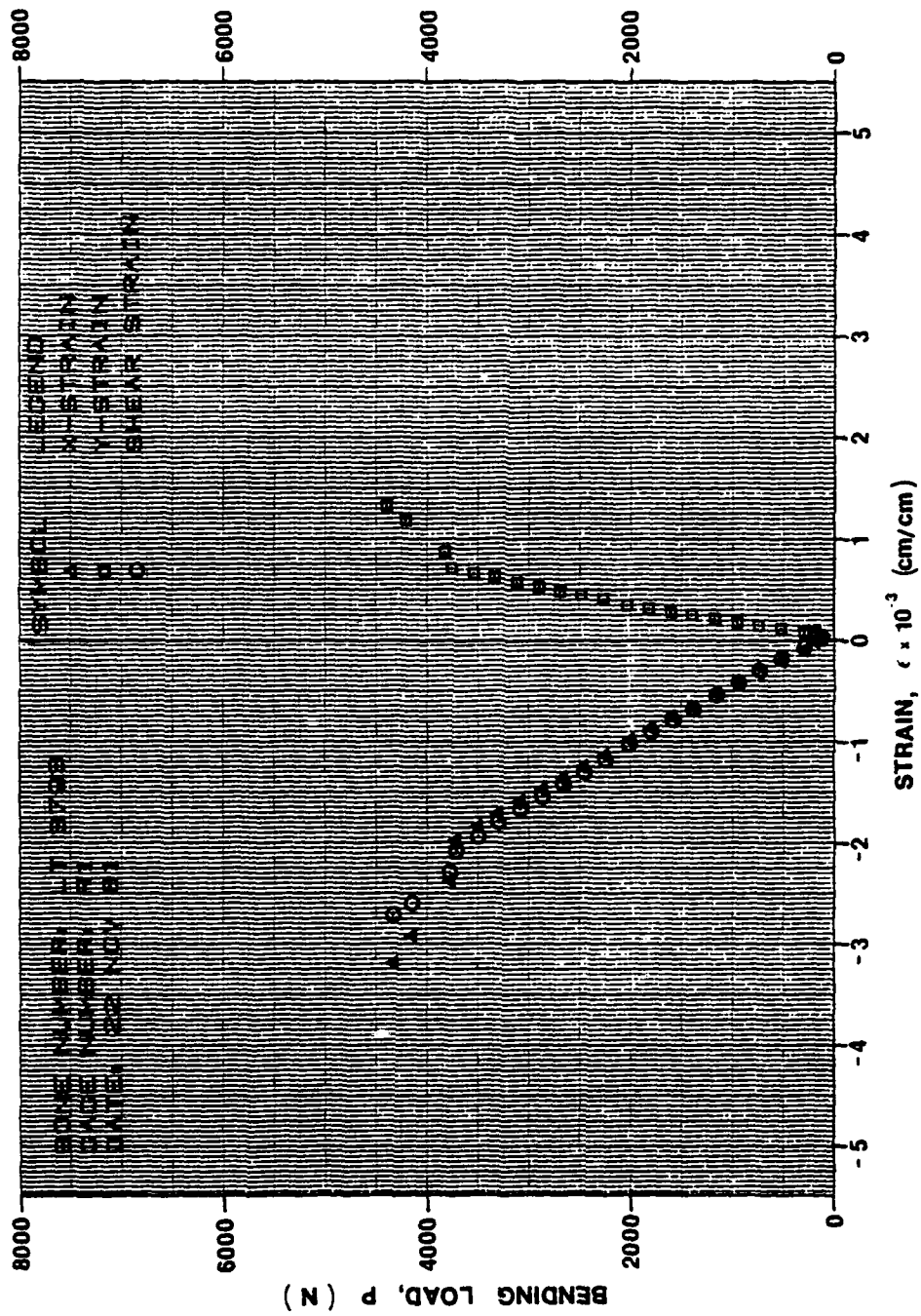


Figure 2-141 Gage strain for LT3793, concave side, proximal end, bending only.

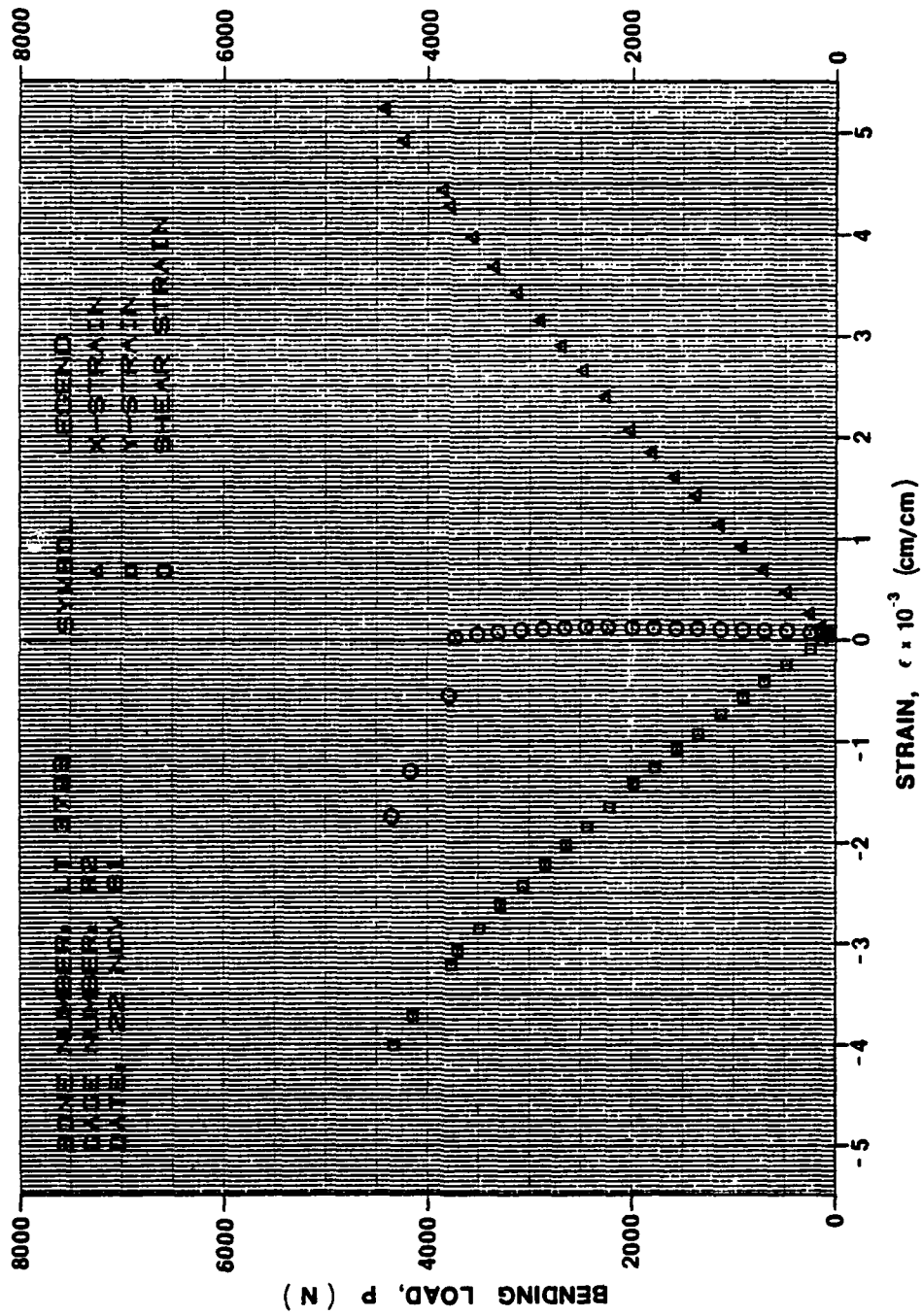


Figure 2.142 Gage strain for LT3793, convex side, distal bending only.

first two of these are almost twice the tensile rupture stresses reported [1] for bone and are not acceptable because of the nonlinear characteristics of the load-strain plots from which they were taken; however, realistic stresses at the time of failure can be extrapolated from the load-strain plots using a ratio of slope of the curve at failure  $P'(f)/\epsilon'(f)$ , to the slope of the curve at zero load,  $P'(0)/\epsilon'(0)$ . Multiplying this ratio with the modulus reported by Rielly and Burstein results in an approximation of the tangent modulus at fracture. Then, the strain extrapolated from the load-strain plot multiplied by this tangent modulus should give a stress at the gage at fracture which should be reasonable as long as the fracture occurred while the load was increasing.

If the material axes were not parallel with the gage axes, the stresses were determined using the equation,

$$\sigma = (19.72 \cos^4 \alpha + 25.16 \sin^2 \alpha \cos^2 \alpha + 13.43 \sin^4 \alpha) (\text{GPa}) \epsilon$$

where  $\alpha$  is the angle between the material axes and the gage axes. Since this equation is in terms of the initial tangent modulus, multiplying it by the ratio of the slopes (discussed above) leads to an equation,

$$b = \frac{P'(f)}{\epsilon'(f)} \frac{\epsilon'(0)}{P'(0)} (19.72 \cos^4 \alpha + 25.16 \sin^2 \alpha \cos^2 \alpha + 13.43 \sin^4 \alpha) (\text{GPa}) \epsilon$$

which adjusts for material nonlinearity and accounts for a material direction skewed from the gage axes. Remember, the stress so determined is an approximation to that actually in existence at the time of fracture since both the strain and tangent modulus at the time of fracture were extrapolated. Using the equation, the stresses were extrapolated (Figure 2.143) for the posterior axial gages of LT3793. The resulting stresses, 22.4 MPa and 22.8 MPa compared to 269.2 MPa, were much more reasonable and are closer to what one would expect for two gages located at equal distances from the mid-diaphysis. The strains which were normal to the axis of the diaphysis and tangent to its circumference at the rosettes also propose an important fact. These strains at the distal end were four times larger than they were at the proximal end -- a result of the difference in magnitude of the nominal strains parallel to the diaphyseal axis and Poisson's effect. On the

AD-A111 090

KANSAS UNIV/CENTER FOR RESEARCH INC LAWRENCE  
MECHANICAL PROPERTIES OF FOUR HUMAN LONGBONES. (U)  
NOV 81 C R KULP, H W SMITH, H C ANDERSON

F/8 6/16

UNCLASSIFIED

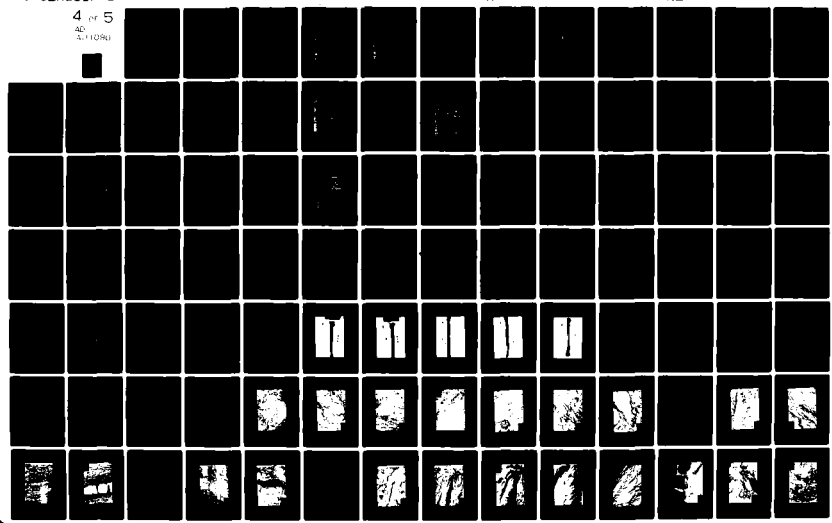
AFOSR-TR-82-0040

F49620-79-C-0183

NL

4 of 5

AD  
A111090



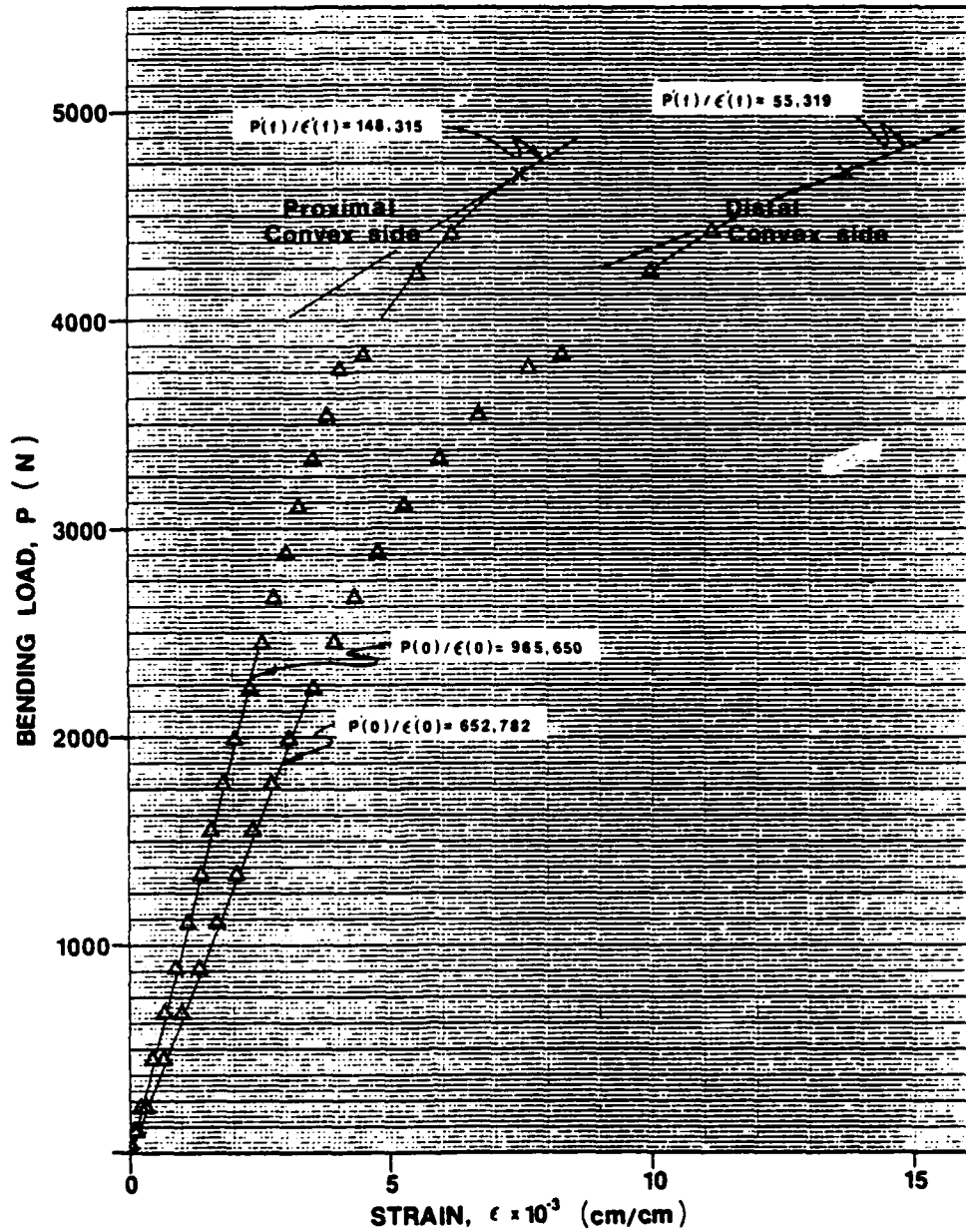


Figure 2.143 Axial strains for LT3793, convex side, near mid-diaphysis, bending only.

convex side of the bending bones, the strains were compressive; but, on the concave they were tensile and could have accounted for the fractures parallel to the diaphyseal axis on the anterior side of LT3793. Contradicting this possibility were the principal stresses (Figure 2.144) which account for material direction. The principal stresses closest to being normal to the diaphyseal axis and tangent to the diaphyseal circumference were tensile, but negligible, on the anterior surface and compressive on the posterior surface. If the principal stresses are transformed back to a reference axis parallel and normal to the diaphyseal axis they average 4.3 MPa in magnitude on the anterior (compression) surface and 15.2 on the posterior (tension) surface. The shear on the posterior surface was sensed only at the distal end of LT3793 and was much higher due to the larger roller (load) spacing and the resulting higher loads. Still this, the largest, shearing stress, was far below that of 68 MPa reported by Rielly and Burstein.

#### Humeri:

Five humeri with strain gages were tested in the bending only configuration. Two of the humeri, RH3782 and LH3753, had a rosette bonded to the convex side of the bending bone at the mid-diaphysis and two, LH3787 and RH3790, used for the rapid rate tests, had an axial gage at the same location. The fifth humerus, RH3792, was statically tested and had six axial gages. Five of the gages were placed on the convex (posterior) side of the bending bone at the distal and proximal quarters, the distal and proximal thirds and the mid-diaphysis. The sixth gage was at mid-diaphysis on the opposite (anterior) side. The strains measured during the static tests implied a behavior quite different from that inferred by strains of the rapid rate tests.

The plots of the principal strains of the two humeri, RH3782 and LH3753 (Figure 2.145, 146), indicate a definite nonlinear, material behavior and possibly even a plastic behavior past a certain strain. At first when principal stresses are considered, the rupture stresses for the two humeri appear to be four times that reported in literature; however, these stresses were determined using Rielly and Burstein's technical constants which include an initial tangent modulus for Young's modulus. As the load passes 50% of fracture load this modulus no longer

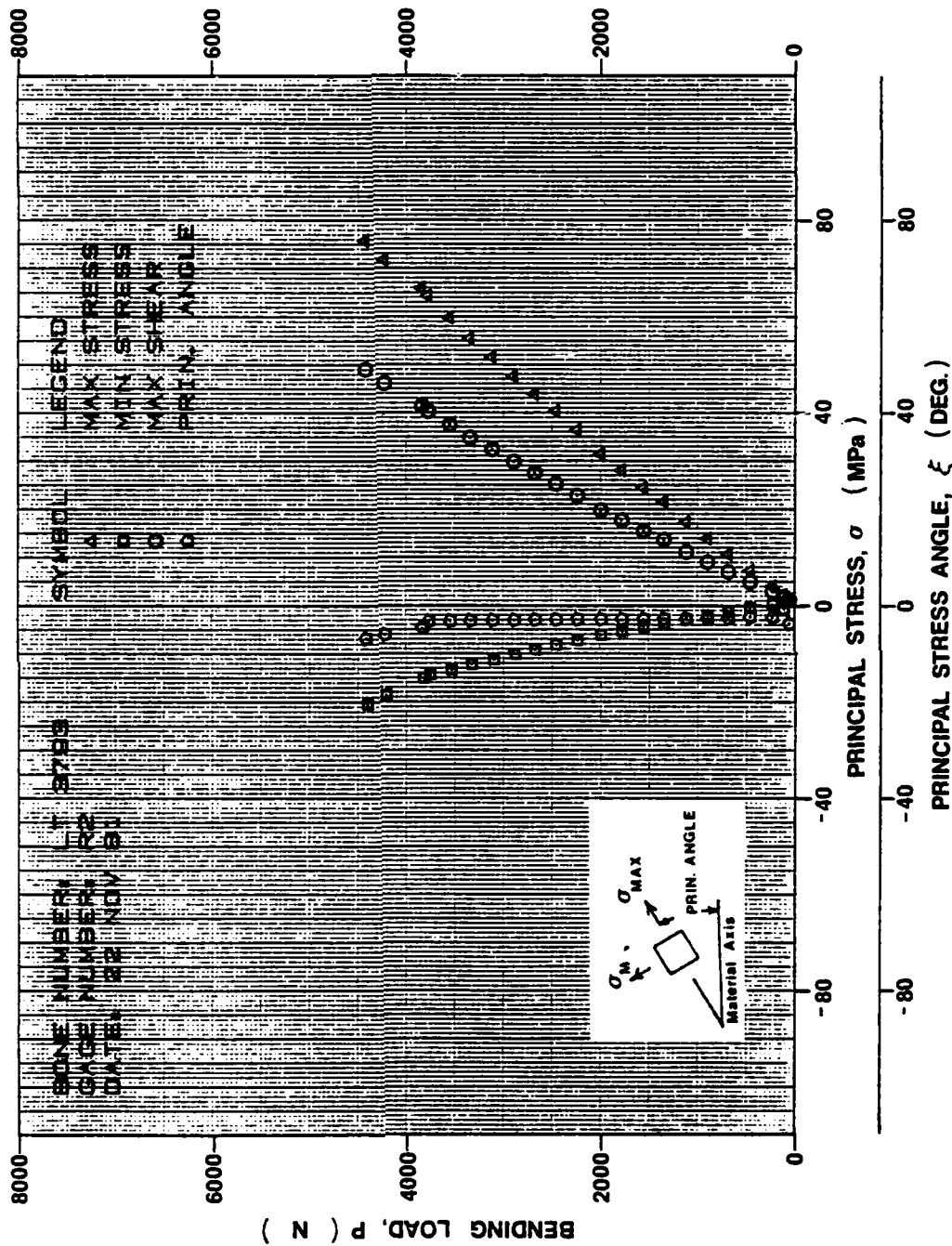


Figure 2.144 Principal stresses for LT3793, convex side, distal end, bending only.

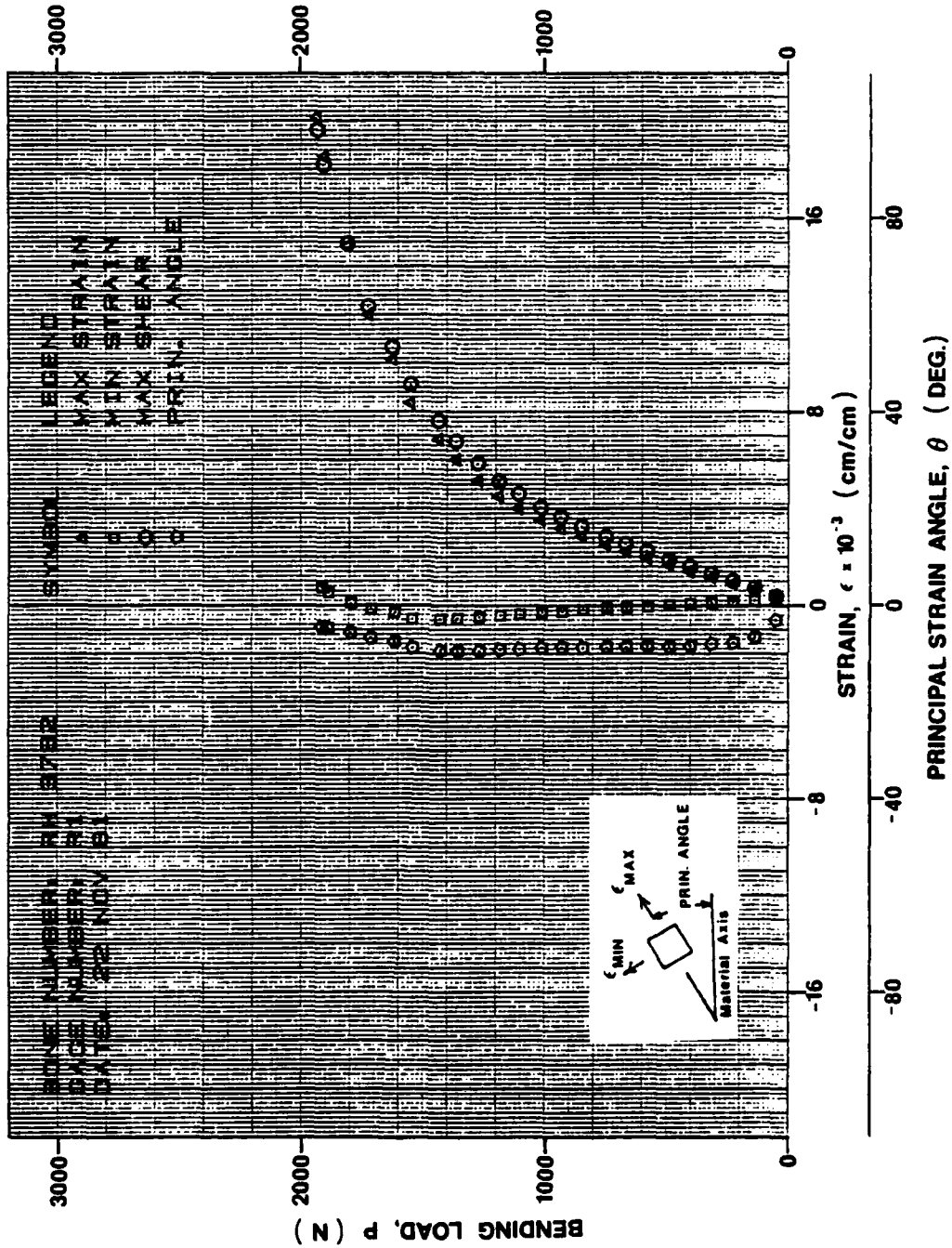


Figure 2.145 Principal strains RH3782, convex side, mid-diaphysis bending only.

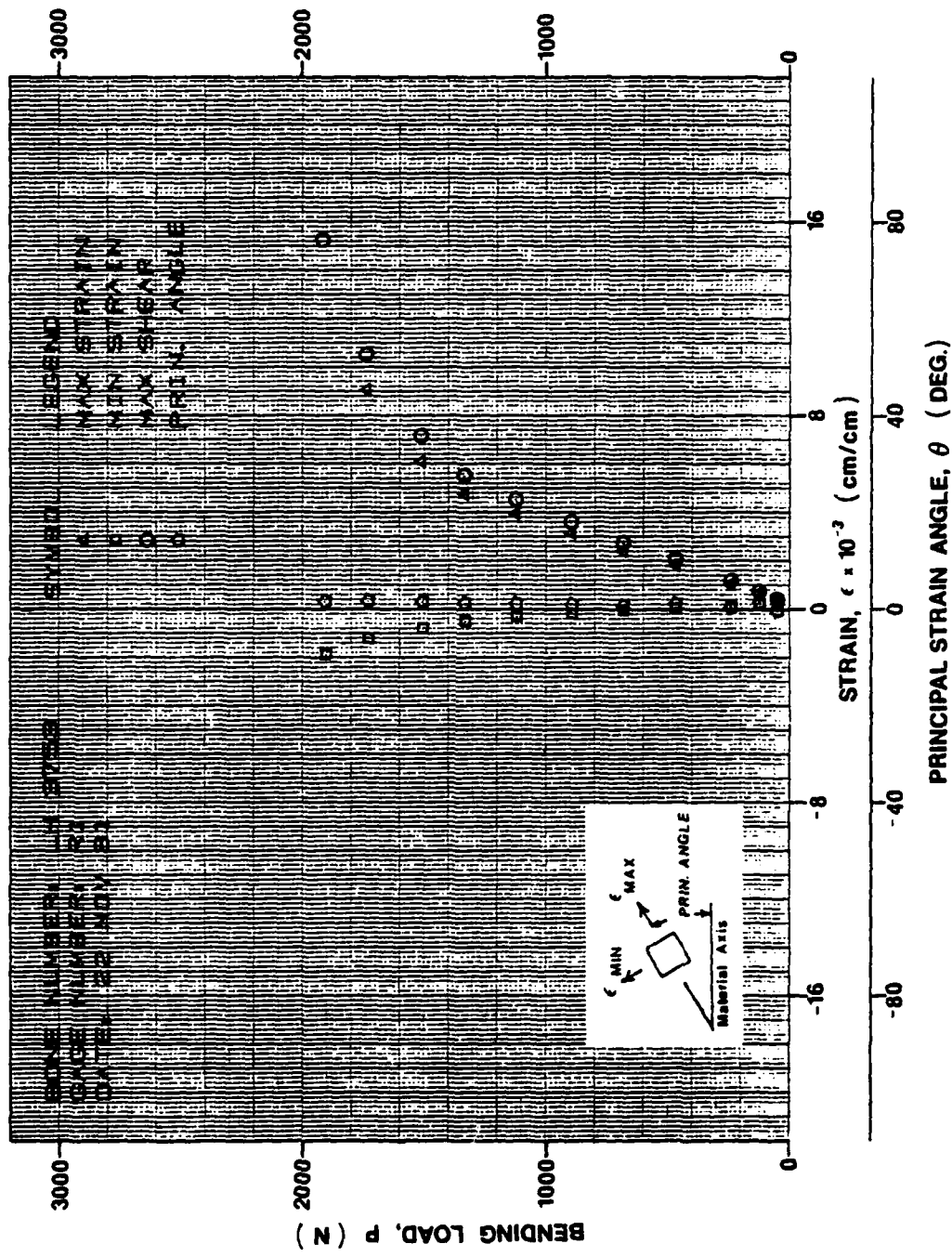


Figure 2.146 Principal strains LH3753, convex side, mid-diaphysis, bending only.

can be used reasonably; the local tangent modulus can be applied at each load increment to estimate the principal stresses. Since the tangent modulus decreases significantly as the load increases, the values of stresses calculated using such a modulus would also decrease, bringing us back to a reasonable stress level. If the cross-sections at the mid-diaphysis of the two humeri are used to approximate a moment of inertia about the neutral axis as well as a distance to the most extreme fiber in tension, the stresses, calculated using the largest moment possible before or at failure, produces a rupture stress within 2% of that reported for failures where the tensile stresses are aligned with the osteon axes. Nevertheless, the load-strain plots do characterize the material behavior and will display any nonlinear and plastic response to load; but without a correct modulus for the plastic region of these plots, the stresses at rupture are indeterminate from the strains.

Concerning the possibility of twist due to the bending of a curved diaphysis, the shearing strains at the two gages which were normal to and parallel with the torsional axis of the osteoclast implied a tendency for RH3782 to twist eversively while LH3753 showed little tendency to twist at all. The tendency of RH3782 to twist was small compared with the result of diaphyseal curvature on the femora and result of cross-sectional shape on the tibiae. Since humeri are almost circular in cross-section and have almost straight diaphyses, this observation was expected.

The load strain plots (Figure 2.147, 148) of the two humeri of the rapid rate tests, exhibited an interesting behavior. As the load increased the strain increased as expected until about 80% of the rupture load in LH3787 and 50% of the rupture load in RH3790 when the strain began to decrease. The only explanation for the decrease is that these humeri began to strain plastically at another location, presumably the location where fracture occurred.

Using the same method of adjusting the stresses that was explained in for the tibiae the stresses at the gages at fracture on RH3792 were derived from the load-strain plots. These stresses were:

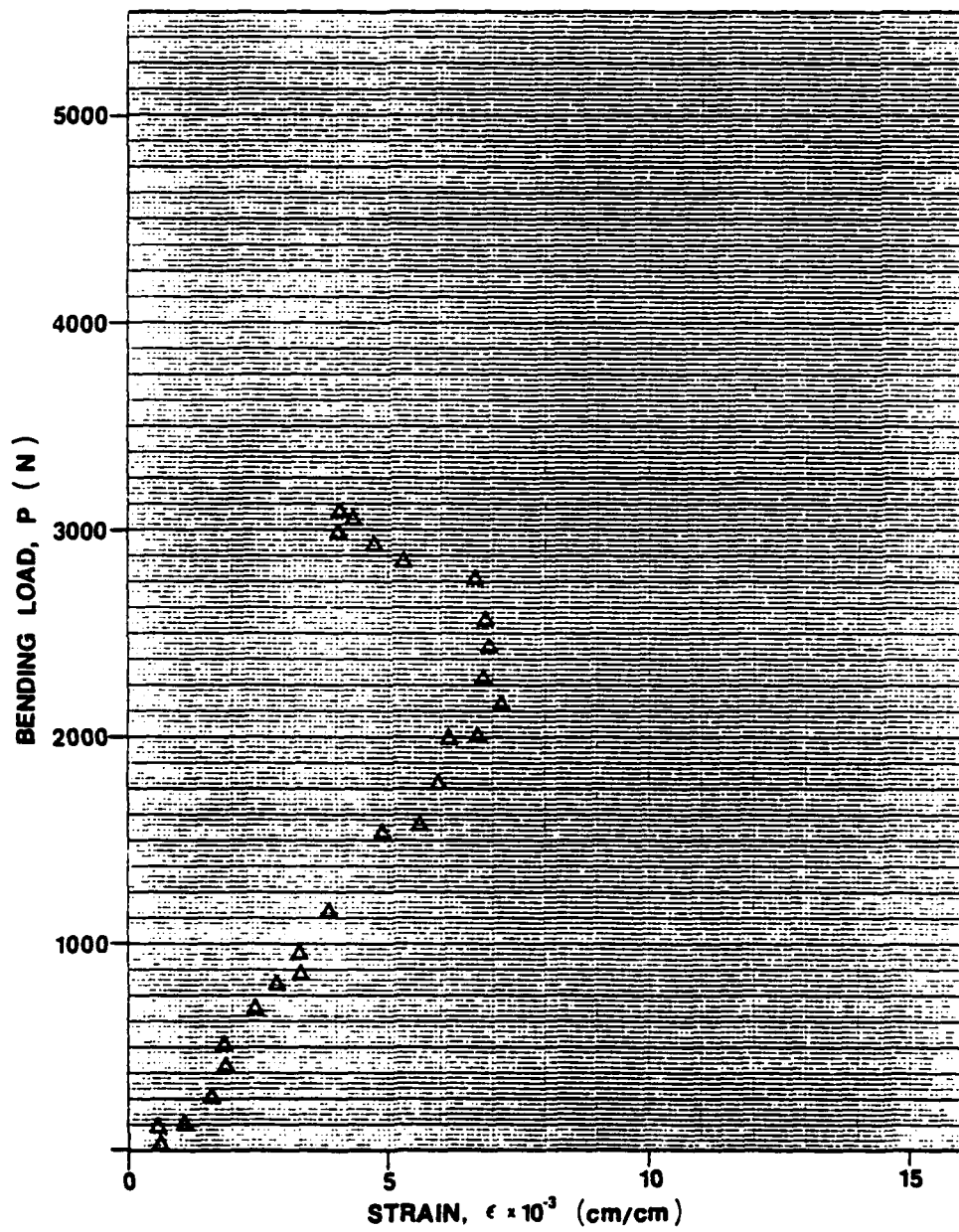


Figure 2.147 Axial strains from rapid rate test of LH3787, convex side, mid-diaphysis.

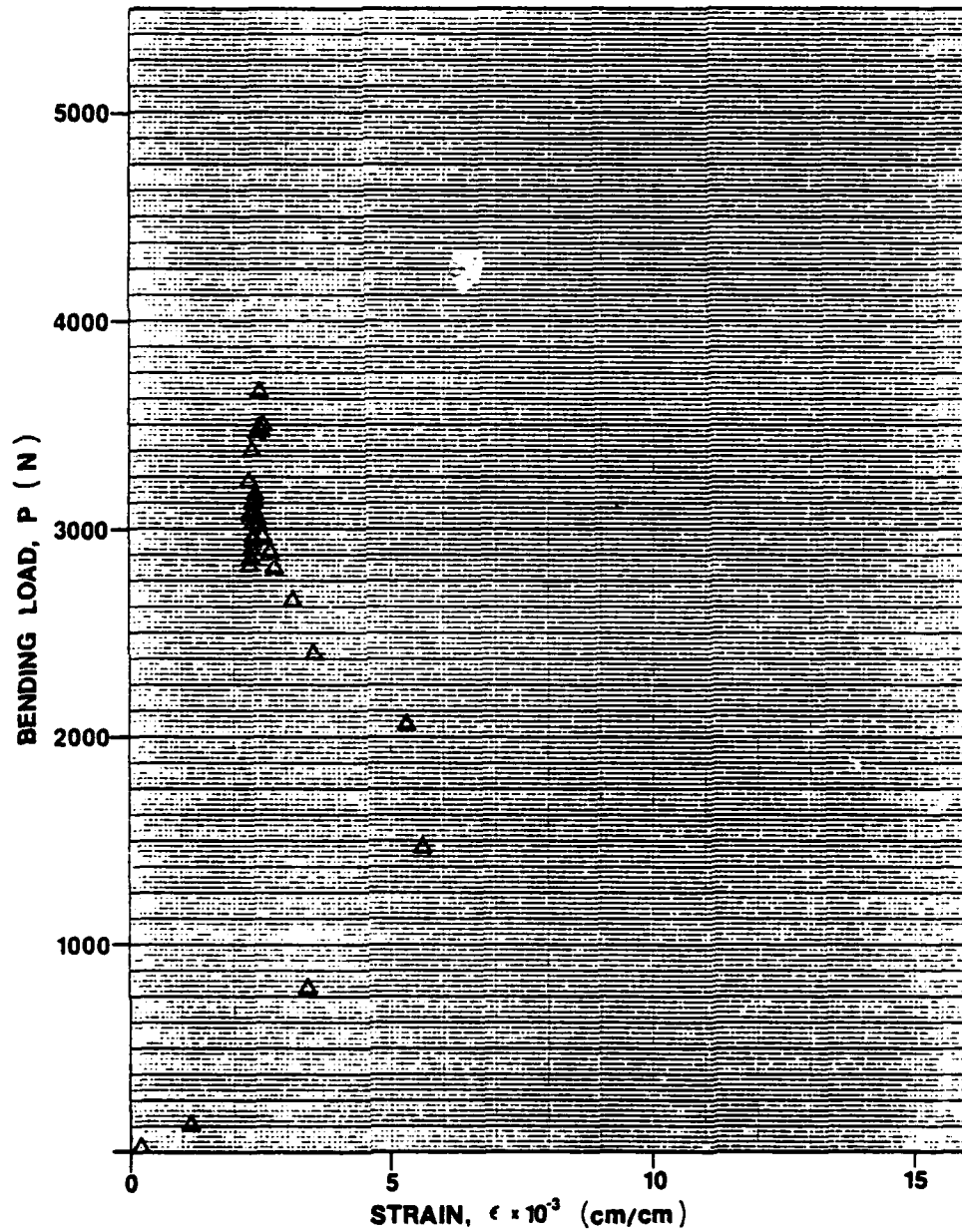


Figure 2.148 Axial strains from rapid rate test of RH3790, convex side, mid-diaphysis.

Distal quarter	Distal third	Mid-diaphysis	Proximal Third	Proximal Quarter
		-202.3 MPa (concave side)		
53.3 MPa	97.5 MPa	115.8 MPa	62.98 MPa	66.1 MPa

Notice that the compressive stress was 50% greater than reported (-133 MPa) by Reilley and Burstein. This is possible, more than likely, due to the constraint of the surrounding material. Notice also that the stress at the proximal third is 65% of the stress at the distal third. This difference is reasonable when the geometry at the two locations is compared.

#### Fibulae:

Only one fibula, Rfb3792, was gaged for the bending only loading condition. All the gages were axial gages with five on the convex (medial) side of the bending bone and one on the concave (lateral) side. The gages on the medial side were placed at the distal and proximal quarters, distal and proximal thirds and at the mid-diaphysis. The one gage on the lateral side was placed at the mid-diaphysis. The stresses at the gages were again adjusted as explained earlier to account for material direction and material nonlinearity. The stresses were:

Distal Quarter	Distal Third	Mid-Diaphysis	Proximal Third	Proximal Quarter
		-100.4 MPa (concave side)		
53.2 MPa	64.1 MPa	81.2 MPa	18.6 MPa 61.3 MPa	15.3 MPa 49.9 MPa

The stresses at the proximal third and proximal quarter varied between the ranges shown depending on the extrapolation of the load-strain plot in this highly nonlinear part of the curve. The stress at the distal quarter gage was low considering the fracture occurred very near the gage. The load-strain plot for this gage was rather straight and the extrapolation of the fracture strain was rather straight forward allowing little variation in interpretation. The reason for the low value is not obvious.

### Torsion Only Stress States

Only rosettes were bonded to those bones tested under torsion only loading conditions. The gages were located to sense any bending if present and to indicate the strain and stress variation along the diaphyseal axis. Of major interest were the strains and stresses along diaphysis of the tibia with its tear drop cross-sectional shape.

#### Femora:

Four femora were gaged for torsion only loading conditions. One femur, LF3753, had one rosette at the mid-diaphysis on the lateral surface. Two femora, LF3792 and RF3793, had three rosettes bonded to the anterior surface at mid-diaphysis, distal third and distal quarter. The remaining femur, RF3782, had two rosettes at the distal quarter--one on the anterior side and one on the posterior side.

Four femora were gaged for torsion only loading conditions. One femur, LF3753, had one rosette at the mid-diaphysis on the lateral surface. Two femora, LF3792 and RF3793, had three rosettes bonded to the anterior surface at mid-diaphysis, distal third and distal quarter. The remaining femur, RF3782, had two rosettes at the distal quarter--one on the anterior side and one on the posterior side.

The strains in line with the gage axes of LF3753 were as expected for a tubular shape subjected only to a twisting moment. The minimal strains parallel and normal to the torsional axis were negligible with shear dominating.

The maximum stresses (Figure 2.149) were as expected also. The principal tensile and compressive stresses were equal to the maximum shear stress and existed at a principle angle of  $39^\circ$ . The load-strain plots were definitely linear and implied that the stresses at fracture, extrapolated from the load-stress plot, would be feasible. The tensile stress at the gage (mid-diaphysis) was only 11.0 MPa--considerably lower than expected in accordance with the reported values of 68 MPa [1]. Even though the gage lay in between the spiral fractures, the stresses should have been somewhat greater.

The two femora, LF3792 and RF3793, which had the three rosettes on the anterior surface from the mid-diaphysis to the distal quarter also displayed stress states similar to the above. The stresses at the mid-

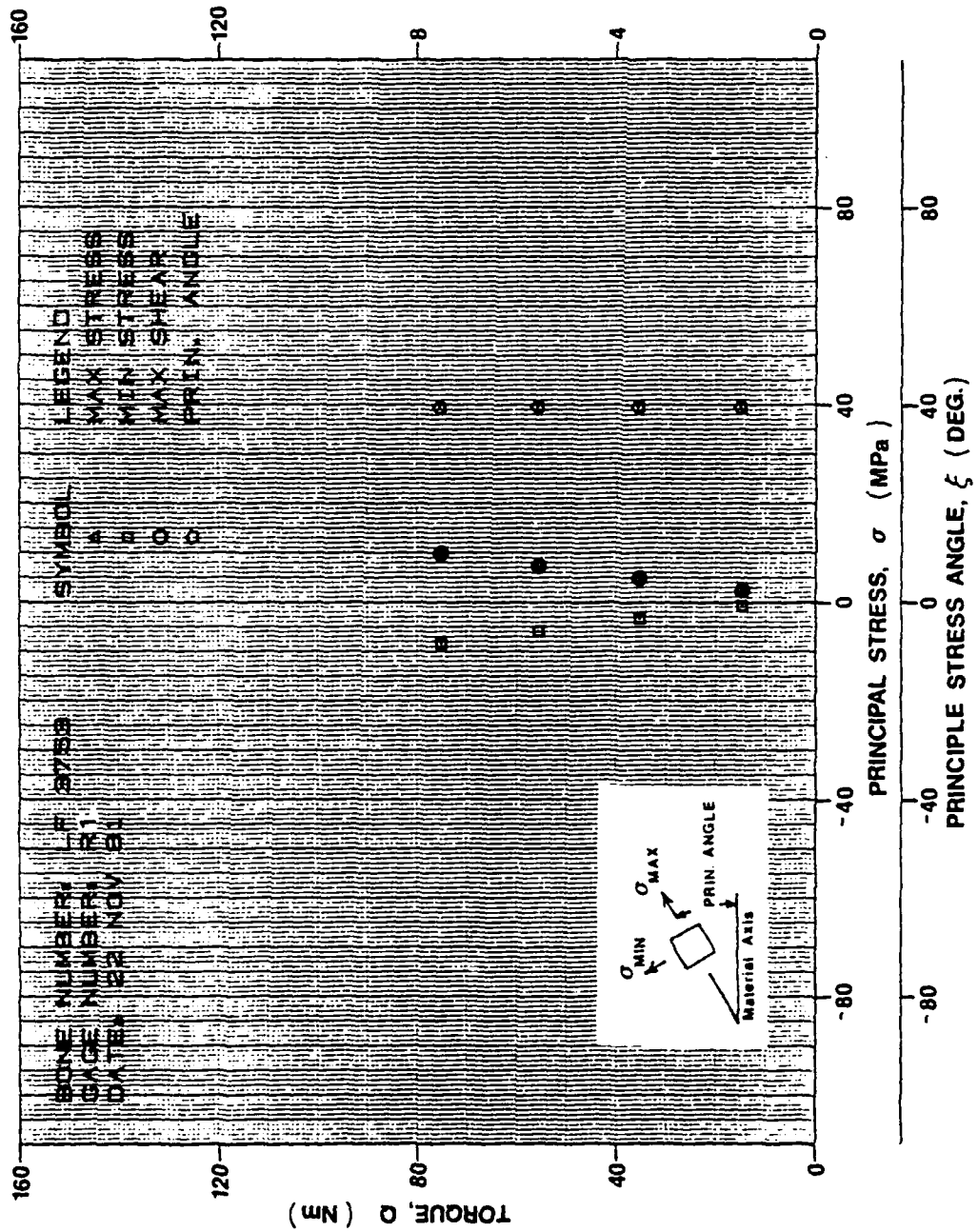


Figure 2.149 Principal stresses for LF3753 at the mid-diaphysis, torsion only.

diaphysis at fracture in RF3793 and LF3792 were twice the magnitude of those observed in LF3753, but the nominal strains aligned with the gage axes were negligible, once again, with the shearing strain dominating. At the mid-diaphysis, the magnitudes of the shearing, tensile and compressive stresses were equal in magnitude; however, near the distal end, the magnitude of the tensile stress was less than the shearing stress on RF3793 and greater than the stress on LF3792. This indicates there was some bending present along the diaphysis. The stresses alone do not indicate the true deformation of the bone. Since the osteoclast induces stress through deformation, the strains are caused and the stresses result according to the orthotropic behavior of the bone; therefore, the strains aligned with gage axes should indicate the loading applied. These strains imply a straightening out of both RF3793 and LF3792.

RF3793 had a rosette (Figure 2.45) near a portion of its spiral fracture which was parallel to the torsional axis. The cause of the fracture is uncertain but the principal angle of principal stresses at this gage was only 45 deg--less than would be required for principal tensile stresses to have caused the longitudinal fracture. The principal shearing strains and calculated stresses at this gage were greater than those measured at the other two gages that were closer to the mid-diaphysis. Also the strains at this rosette, which were normal to the torsional axis and tangent to the periphery of the diaphysis, were compressive indicating that the fracture was not due to tension. Considering these interpretations, this longitudinal fracture may be a failure caused by shearing forces.

The femur, RF3782, which had two rosettes, one anterior and one posterior, at the distal quarter, verified that bending did indeed exist for the femora under the torsion only conditions. The posterior gage, showed a tensile strain in the direction of diaphyseal axis while the anterior gage showed a compressive strain. This implies, RF3782, was straightening out under the application of pure torsion.

Notice in Figure 2.48, that this femur also has a fracture path parallel to the torsional axis at gage R1. Different from RF3793, the principal angle (Figure 2.150) for the stresses at this gage is close to 60 deg. and, therefore, the principal tensile stress is almost normal to

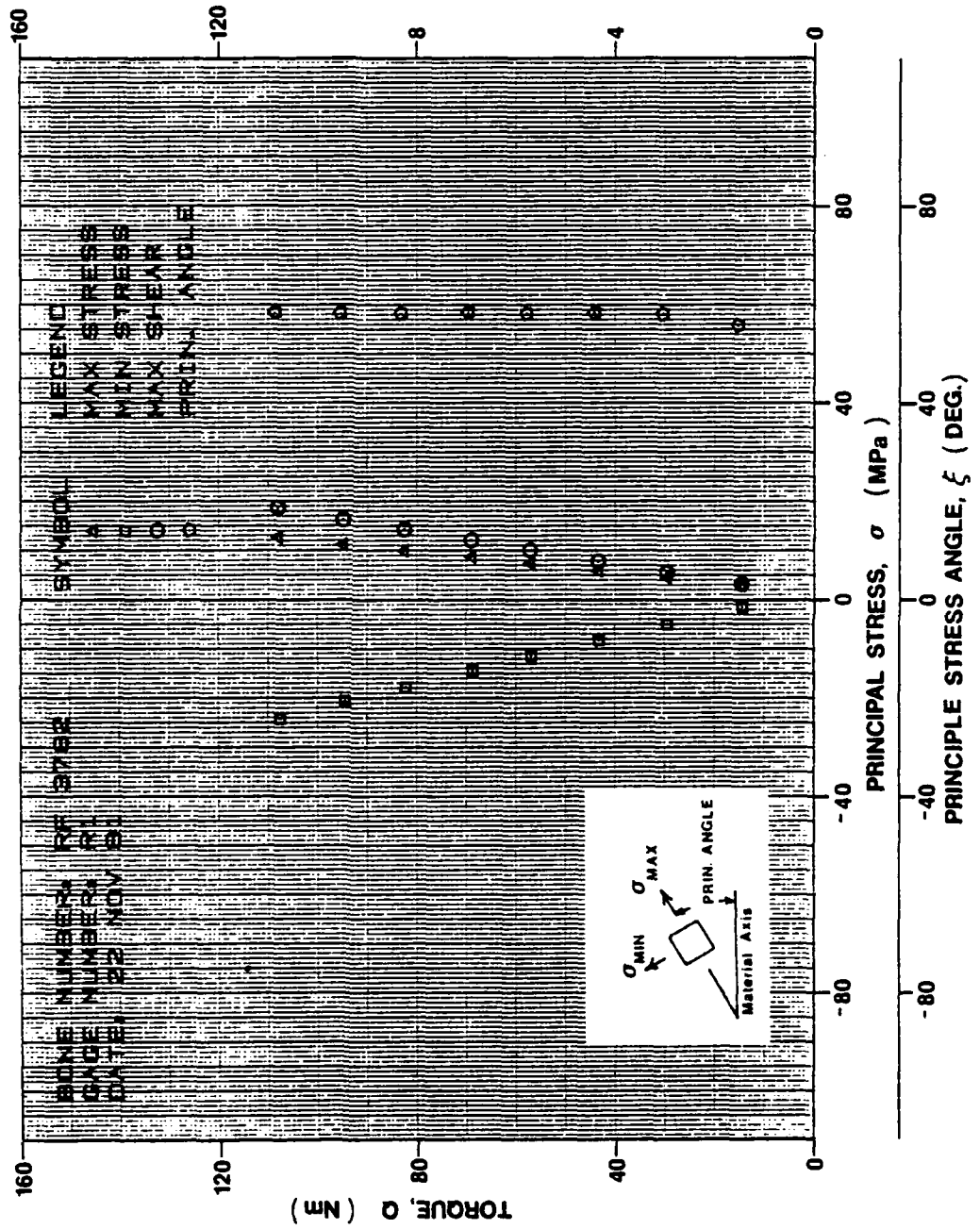


Figure 2.150 Principal stresses of R1782, anterior side, distal end, torsion only.

the fracture. In addition, the strains normal to the torsional axis were tensile rather than compressive (as was the case for RF3793). So, for this case, the longitudinal crack is assumed to be a tension failure.

**Tibiae:**

Two tibiae, RT3793 and LT3792, tested under the torsion only loading condition, each had three rosettes on the medioanterior surface; one was at the mid-diaphysis; one at proximal third and one at the proximal quarter. They were placed as close to the crest of the tibia as their backings would allow. Two additional tibiae, RT3782 and LT3782, were subjected to a twisting moment only but were tested articulated with their fibulae. Both of these had a rosette at the distal and proximal quarters on the anterior surface and one axial at their mid-diaphysis on the posterior surface.

Both, RT3793 and LT3792, had strains along the gage axes that implied some bending due to torsion. RT3793 had compressive strains parallel to the torsional axis and, since the gages were in the medioanterior surface, these strains indicate a tendency for the tibia to curve, bend, in medioanterior direction. On the other hand, LT3792 had compressive strains at the mid-diaphysis gage and tensile strains at proximal third which were in the direction of the torsional axis. The strains indicate bending toward the lateroposterior direction at the proximal end with the bending reversing to an opposite direction at the mid-diaphysis. The bending is probably caused by the curvature of the tibiae in conjunction with the constraint and the warping effect of their odd shaped cross-sections when twisted. The difference in the bending behavior between RT3793 and LT3792 is more than likely a result of their different directions of twist--RT3793 was twisted inversively while LT3792 was twisted eversively.

The principal strains and stresses increased from the mid-diaphysis toward the proximal end on RT3793, but decreased from the mid-diaphysis to the proximal end on LT3792. This difference again was probably the effect of inversive versus eversive rotation. The shearing stresses were observed to be significantly lower than the reported ultimates--22 MPa as compared to 68 MPa [1]; however, since the fracture occurred at

the distal end where the section modulus ( $J/\rho$ ) is lower, this is acceptable. The principal angle varied between 36 deg. at the proximal end and 45 deg. at the mid-diaphysis.

The rosettes at the proximal ends of the two tibiae tested articulated displayed stress states similar to those discussed above for comparable gage locations. There was a slight difference in the bending behavior in the RT3782 was twisted inversively resulting in a slight bending toward the latero-posterior side while LT3782 was twisted eversively and tended to bend medio-anteriorly. This is opposite to the indications of the comparable gages on the unarticulated tibiae under the same rotations. This difference may be the result of the shift of the twist axis from the center of the mid-diaphysis cross-section for the unarticulated tests to a location lateral to the tibia (between the tibia and fibula) for the articulated tests. Otherwise the principal stresses and strains as well as the principal angles are similar to the unarticulated tibiae.

The two rosettes at the distal end of RT 3782 and LT3782 show strains and stresses that are approximately twice those observed at the proximal end. The principal stresses (although not a good approximation of the stress state because of the slight nonlinearity) show that as the twisting moment is increased the stress state becomes more involved and is no longer pure shear. The strains along the gage axes show no bending for RT3782, but a considerable bending toward the anterior side of the bone for LT3782. A tensile strain normal to the torsional axis increases drastically for no comparable increase in the slight compressive strain which is in the direction of the torsional axis--obviously this tensile strain is not due the Poisson effect. The ultimate principal stresses for both bones were again below those reported--40 MPa compared to Reilley and Burstein's 68 MPa. The ultimate stress for RT3787 was 30% greater than that of LT3787, but its spiral fracture passed beneath the rosette.

The axial gages at mid-diaphysis on the posterior side of both tibiae also implied bending was present. The compressive strains at the gage on RT3782 show that the bone bends posteriorly under the twisting moment confirming the bending implication of the proximal rosette

discussed above. The axial gage on LT3782 shows bending in the anterior direction which also agrees with proximal rosette discussed above.

Humeri:

Three humeri tested under torsion only conditions were strain gaged. Two humeri, LH3792 and RH3793, had three rosettes bonded at locations which were proportioned between the two bones. Two of the rosettes were on the medial side at the mid-diaphysis and distal quarter while the third was on the lateral side at the distal third. The third humerus had two rosettes at the proximal third--one on the medial side and one on the lateral side.

LH3792 was clamped in the Osteoclast with the center of the mid-diaphyseal section 12.7 MM below the torsional axis of machine. It displayed a state of pure shear at each of the gage locations with the principal stresses equal in magnitude to the maximum shear stresses. The tensile strains parallel torsional (gage) axis at mid-diaphysis and distal quarter in conjunction with the compressive strain at the distal third inferred a bending in the lateral direction. Even though the distal-quarter gage was near a fracture line, none of the stresses at any of the gages were close to the reported ultimate. The principal angles were between 35 and 40 degrees.

RH3793, with rosettes at locations which were proportional to LH3792, displayed slightly different stress states. This bone was tested with the torsional axis of the osteoclast passing through the center of the cross-section of the mid-diaphysis; however, none of the stress states indicated that pure shear was present. All three gages sensed a tensile strain parallel to the torsional axis. Since all three gages were placed anterior to the "neutral axis"\* at their location and considering that the gage at the distal third was on the opposite side of the diaphysis from the other two, these tensile strains imply a tendency for this humerus to bend anteriorly when pure torsion is applied. The maximum shear stress for one of the rosettes near the fracture was close to 50 MPa and, since it seemed to behave plastically

---

\*The position of the neutral axis was assumed.

just prior to fracture (rupture twisting moment less than the ultimate twisting moment), the fracture stress, intuitively, could have approached 60 MPa. The principal angles again varied between 40 degrees at the most distal gage to 45 degrees at the distal third. Note also that this humerus was twisted inversively while LH3792 was twisted eversively.

LH3782, which had the two rosettes that opposed each other at the proximal third, exhibited unusual strain and stress plots. Both of these gages were located on top of a fracture and displayed small load-strain slopes with those plots corresponding to the lateral side appearing quite nonlinear. Comparing the strains in line with the gage axis, there was considerable bending toward the medial surface. Since the strains parallel to the torsional axis were tensile at both gages (with the strains on the medial side negligible compared to those on the lateral side) and since one gage was anterior to neutral axis and one posterior, there appears to be an axial force present--probably poor adjustment of the Osteoclast prior to testing. The gage on the medial side was on top of two fractures suspected to be caused by a shearing action rather than tensile. Figure 2.151 shows the load-principal-strain plot for this gage. Notice its nonlinearity plus the fact the principal angle never exceeds 45 degrees. The nonlinear behavior indicates an area of large distortion compared to the load-strain plots of the other two humeri. The fact that the principal angle is less than 45 deg. infers that the fractures did not occur in an opening, tensile mode.

#### Fibulae:

Two of the fibulae, LFb3792 and RFb3793, tested under torsion only conditions were gaged with stacked rosettes. Both bones had three rosettes each. Each bone had a rosette at the distal end on the anterior surface, one at the mid-diaphysis on the lateral surface, and one at the proximal end on the posterior surface. Although these gages were placed in similar locations between the two bones, they were not located at proportional dimensions.

LFb3792 exhibited bending at the distal and proximal ends (according to the strains parallel to the torsional axis at these locations),

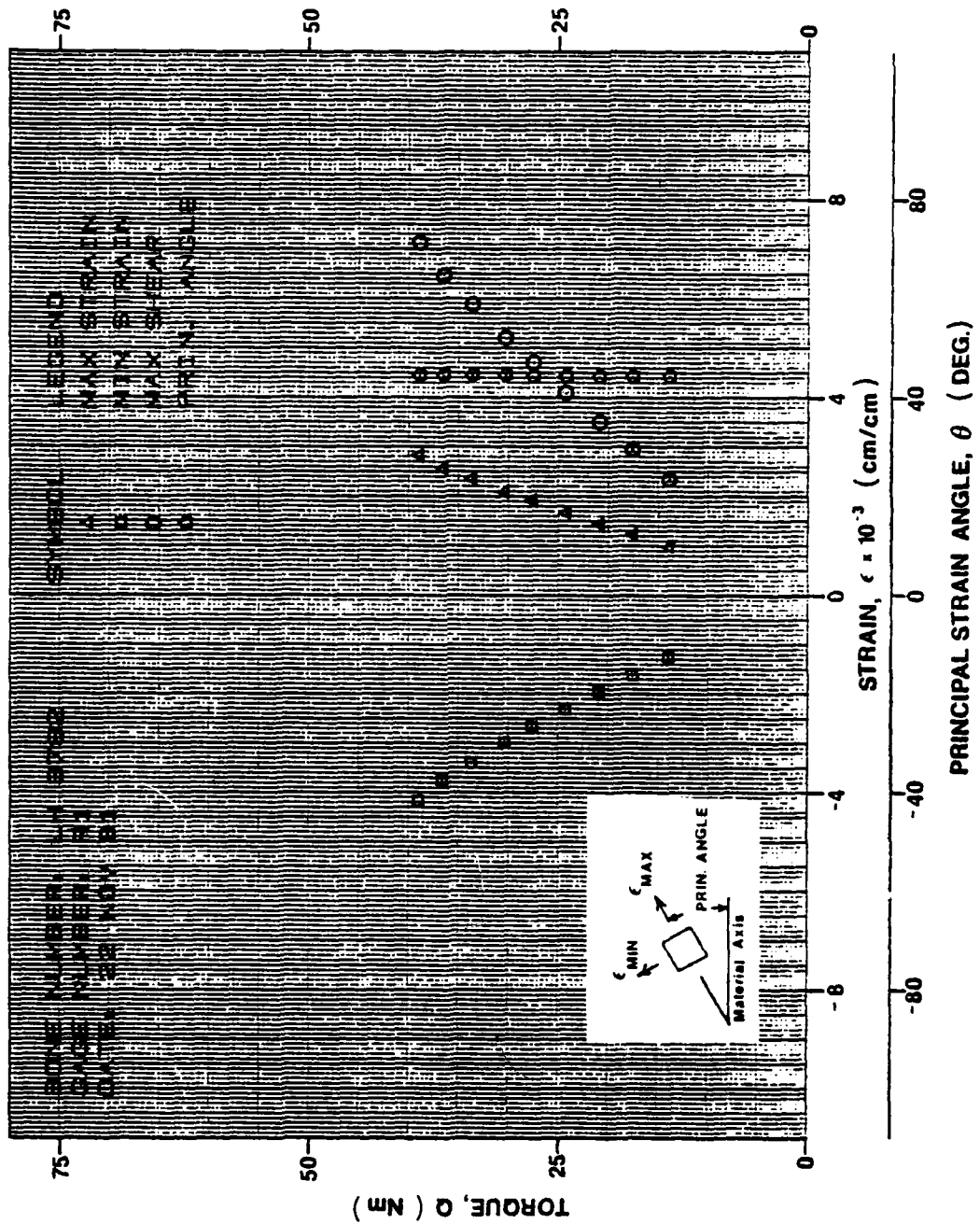


Figure 2.151 Principal strains for LH3782, medial side, proximal end, torsion only.

but the gage at the mid-diaphysis intimated no bending at all. Since the strains at the distal and proximal locations were tensile and since these gages were located on opposite sides of the diaphysis, the only bending possible requires an inflection point at the mid-diaphysis. Rfb3793 had negligible nominal strains along the gage axes, and therefore, any bending if present was minimal.

As with the other bone types, the maximum stresses calculated for the strains measured at the gage locations for the two fibulae were quite small, only 20 MPa at the largest. The only gage in the vicinity of a fracture sensed a meer 10 MPa. The only other interesting observation for these two bones was the large principal angle of 60 degrees which occurred at the onset of the loading schedule. This angle occurred at the distal gage on Lfb3792 and at the proximal gage of Rfb3793 and decreased immediately to 55 degrees as the load was advanced. The reason for its appearance at different ends of the two bones is that Lfb3792 was twisted eversively while Rfb3793 was twisted inversively. The cause of the large principal angle might be attributable to the interosseus crest which would cause considerable warping of the cross-section.

#### Anisotropic Behavior:

Unexplicable behavior strains which were normal to the axis of twist and observed at certain locations along the diaphyses of tibiae, humeri and fibulae, implied cross-coupling between these strains and the shearing strains caused by the twisting moments. Specifically, the lateral strains at the rosettes on the following bones exhibited this unusual increase, some more severely than others:

Rosette #3	RT 3793
2	RT 3782
1, 2	RH 3793
2	LH 3792
2	LH 3782
1	Rfb 3793

Figure 2.152 illustrates the deviation from normal isotropic behavior. Other than anisotropic behavior, the only other explanation is the alteration of the strain state by geometrical constraint.

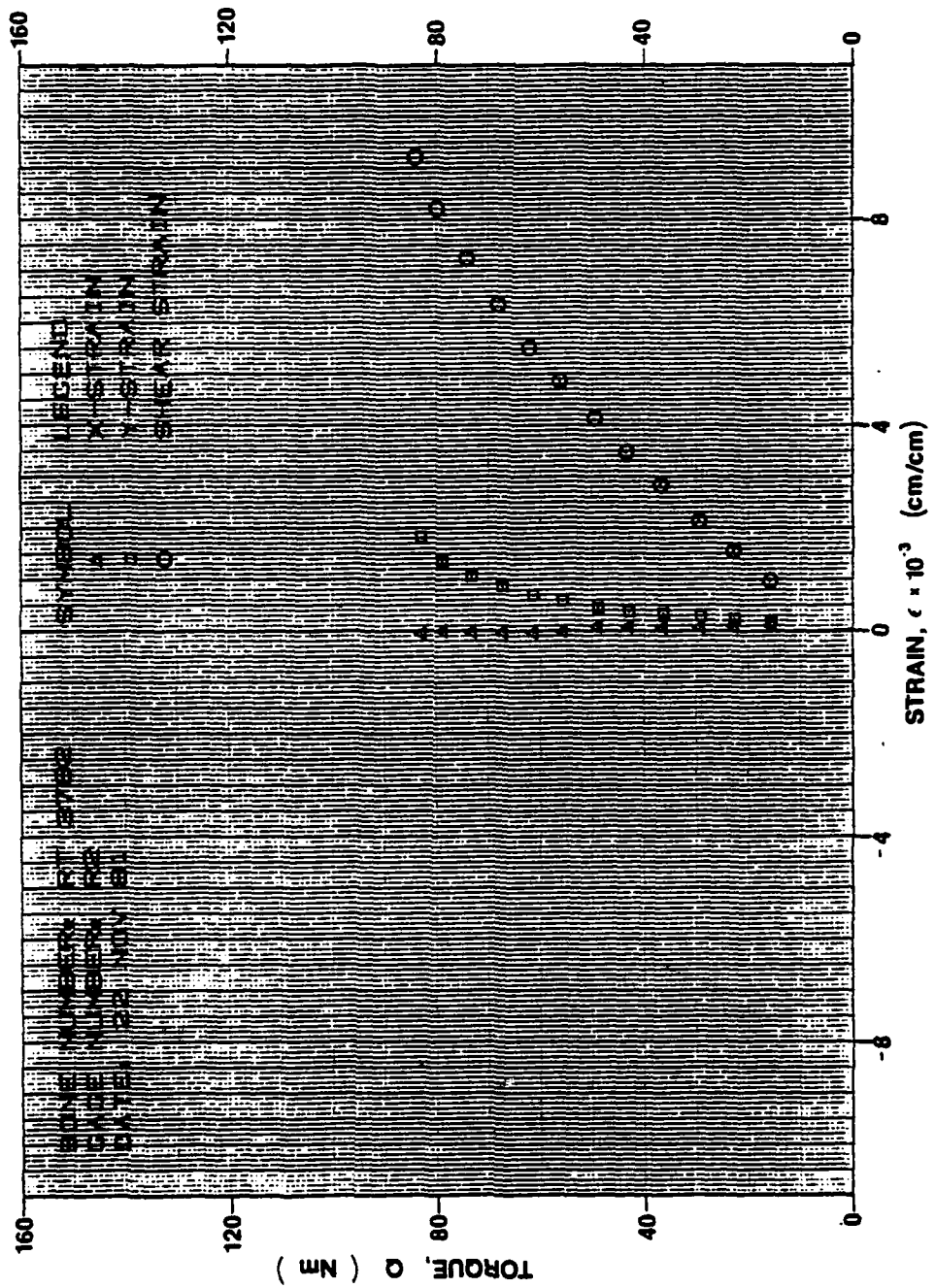


Figure 2.152 Unexplained increase of lateral strains RT3782.

### Combination Loadings

All of the bones tested under combined loading conditions, were gaged with different configurations of rosettes and axial strain gages. Each had at least one rosette, and two axial gages, but most of them had two rosettes and four axial gages. The configuration selected for each test was determined according to the type of loading applied (narrow load spacing versus wide, torsion dominant versus bending dominant, etc.) and scientific curiosity. The observations are discussed according to bone type and not respective of loading condition (torsion dominant versus bending dominant).

To describe the stress states and the manner in which they change as the loads are advanced, it is advantageous to discuss Mohr's circle and its alteration with changes in the applied loads. Consider a rosette on the concave surface of a bending bone. Figure 2.153 shows a Mohr's circle for three stages of loading: initial load step; point of dominance where the one load is held fixed and the other increased; and fracture.

In the bending dominant situation Mohr's circle shows, that both the principal stresses should increase as well as, of course, the maximum shear stress. The principal angle also increases when the bending load is increased and the twisting moment is held constant because the principal stresses approach those typical of the bending only situation where the principal stress of the greatest magnitude coincides with the normal bending stress and that of the smallest approaches zero.

For the torsion dominant situation, Mohr's circle again shows that the principal stresses and, consequently, the maximum shearing stress must increase as the loading is advanced. However, in this case, the principal angle declines from its initially large value towards 40 deg. which is associated with the pure shear state of stress.

With such behaviors in mind, the stress states observed in the combined loading conditions are easily evaluated.

#### Femora:

Three of the four femora tested in combined loading situations had two rosettes and four axial gages; the fourth had one rosette and 6

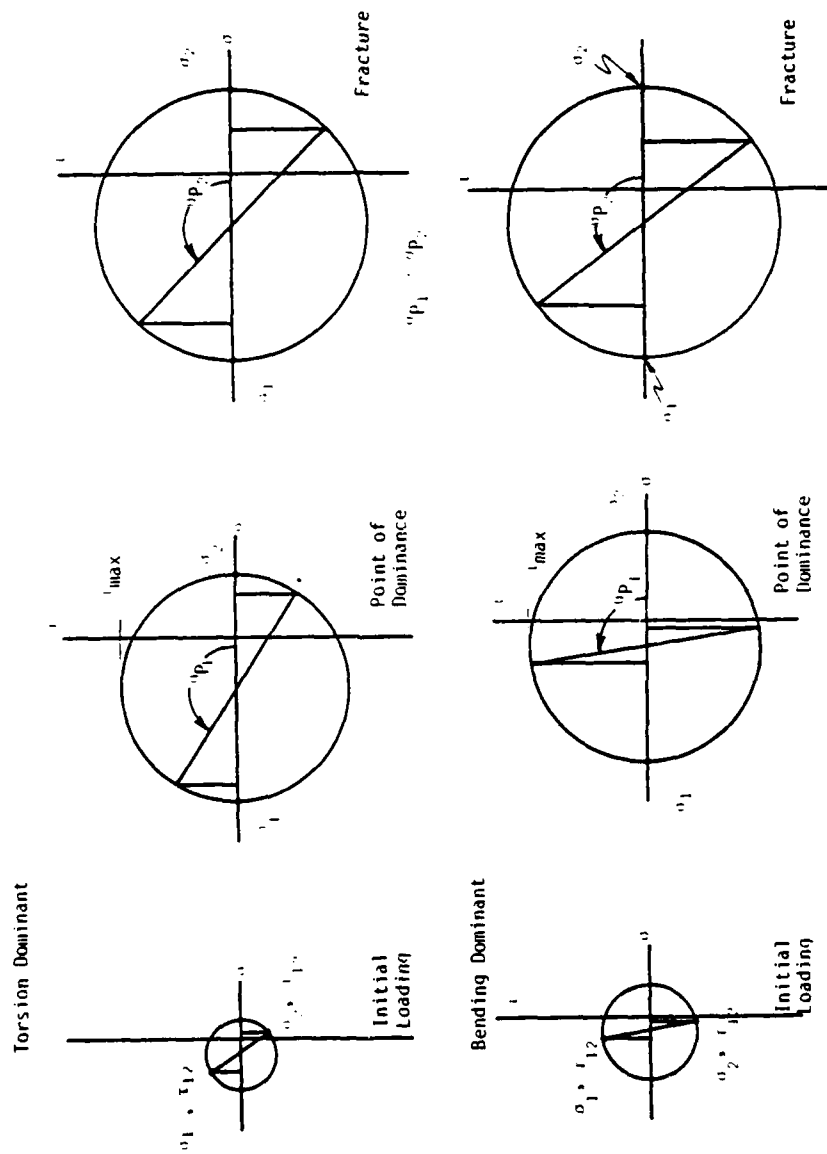


Figure 2.153 Mohr's circle depiction of stress alteration under torsion dominant and bending dominant loading conditions.

axial gages. Two, LF3790 and RF370, had similar configurations with a rosette on the concave (anterior) side of the bending bone at the mid-diaphysis and distal quarter. The axial gages of these two bones were placed on the anterior and posterior sides near the distal and proximal third of the diaphysis. The third bone, RF3787, had one rosette on the concave (anterior) surface of the bending bone at the distal quarter and one on the anterior surface at the mid-diaphysis and three on the posterior side at the mid-diaphysis and near the distal and proximal thirds. The last femur, LF3787, was gaged with only one rosette at the distal quarter on the anterior surface and three axial gages at the mid-diaphysis, slightly displaced distally and proximally from the mid-diaphysis on anterior and posterior surface.

Both RF3790 and LF3790 were fractured under torsion dominant loading conditions--the former inversively and latter eversively. The middle leg of the mid-diaphyseal gage on LF3790 was lost at the start of testing and the strains recorded were of no value. The other three rosettes for the two bones implied strain and stress states as should be expected. The principal angle initially is larger than 45 deg. and then approaches 45 deg. as the stress state approaches that of pure shear. The normal principal stresses and strains of the mid-diaphyseal gage of RF3790 were approximately twice those of LF3790--a result of the increasing shearing strain in conjunction with the higher bending stress. The bending strain at the distal rosette was approximately 67% of that sensed at the mid-diaphysis and the shearing strain probably varies because of a difference in cross-sectional geometry. The axial gages verified the bending strains sensed by the rosettes and implied that the tensile strains due to bending were 41% larger than the compressive strains due to bending.

For the two femora, LF3787 and RF3787, tested under bending dominant conditions, the strains parallel and normal to torsional axis behaved as would be expected. The bending strain increased, as did the lateral strain (Poisson's effect), as the bending was increased while the shearing strains remained relatively constant. The principal strains and stresses and maximum shearing strain and stress as well as the principal angle increased as the loading advanced and appeared approximately equivalent when comparing rosettes even though the loading was

widely spaced for RF3787 and narrowly spaced for LF3797. Of interest is the strain behavior at the proximal gage of RF3787. Near the fracture load, the strains sensed by this gage began to decrease while those at the distal gage continued to increase linearly. The cause for the decrease is not readily apparent.

The axial gages showed that the strains sensed at similar locations along the diaphysis between the two bones are reasonably matched considering possible variations in geometry. The load-strain plot of the axial gage on top of the fracture on the posterior side at the distal end of RF3787, behaves nonlinearly while the gage on top of the fracture on the anterior side distal third of LF3787 remains linear. This response is odd since the former is in tension and the latter compression and Reilly and Burstein have shown the compression behavior of osteon bone more plastic than the tension behavior. The only possible explanation is that the fracture mode is quite different between the two sites.

Generally, the bending stresses associated with failure appear to be close to those reported as ultimate (strains approaching 8000 micro-strain for linear behavior). For the two bones subjected to a torsion dominant loading where the fractures were spiral in nature, the stresses appeared considerably lower than those reported as ultimate (strains approaching 12,600 microstrain for a linear behavior) except for those at the mid-diaphyseal rosette, of RF3790. The strains at this location did approach 10,000 microstrain. The probable reason for the apparently low stress indications was the inappropriate gage locations.

#### Tibiae:

Two tibiae, tested under the torsion dominant loading condition, were strain gaged with two rosettes and four axial gages. RT3790 had a rosette at the mid-diaphysis and the proximal quarter. LT3790 had a rosette at the mid-diaphysis and the distal quarter. The rosettes on both bones were bonded on the anterior side, the concave side of the bending bone, as near the tibial crest as possible. The axial gages were located on both bones at the distal and proximal thirds on the posterior and anterior surface (again as near the crest as possible).

The two other tibiae, RT3787 and LT3787, tested under bending only loading conditions, were strain gaged with one rosette and six axial gages on each. The rosette was placed at the proximal end of each bone on the concave (anterior) side of the bending diaphysis as near the crest as was possible. The axial gages were placed anteriorly (as near the crest as was possible) and posteriorly at the distal and proximal thirds and at the mid-diaphysis.

The strains which were parallel to the torsional axis at the rosettes behaved as expected for the torsion dominant loading condition, remaining constant after the bending load was fixed; however, the strains normal to the axis increased with the increase in shearing strain as the twisting moment was advanced (Figure 2.154). Such behavior was observed for the torsion only case and discussed earlier. This departure from isotropic behavior was more noticeable in LT3790 which was twisted eversively with a narrow roller spacing than RT3790 which was twisted inversively with a wide roller spacing. Otherwise the principal strains and stresses continued to increase as the loading was advanced while the principal angles decreased. The principal strain behavior of LT3790 was considerably more non-linear than that of RT3790-- a result probably of the strains normal to the torsional axis increasing nonlinearly.

The strains sensed by the axial gages were insignificant. They were rather constant after the bending load was held constant and larger in magnitude at the distal third where the section modulus is smaller.

The two tibiae, RT3787 and LT3787, subjected to the bending dominant conditions also displayed rather insignificant strain behavior at their gages. At the rosettes, strains parallel to the torsional axes increased as the bending loads were advanced and the twisting moments held constant. The strains normal to the torsional axis did not increase proportionally as expected from Poisson's effect, again possibly the result of anisotropy. The shearing strain at the rosette on RT3787 made a sudden jump as the bending was increased, but this was attributed to a twisting moment caused by the offset of the bending load from the torsional axis due to the tibial crest. Principal strains and stresses increased as expected as did the principal angle. The strains at the axial gages were also insignificant except for their verification that

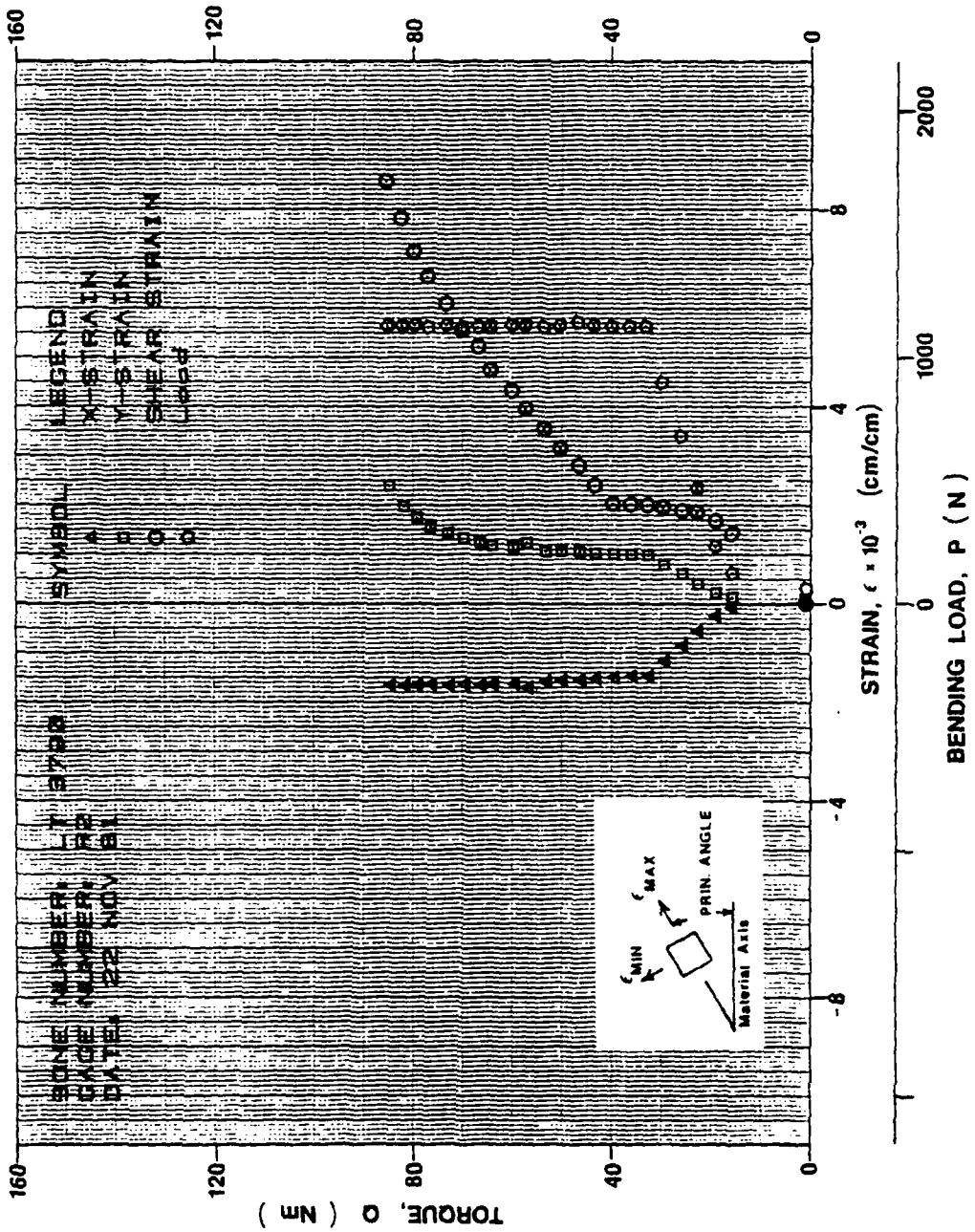


Figure 2.154 Gage strains for LT3798, concave side, distal end, torsion dominant.

the section modulus decreases from the proximal to the distal end. The loading for RT3787 was applied with a wide roller spacing while the bone was twisted inversively. LT3787 was bent using a narrow spacing and twisted eversively.

#### Humeri:

Three humeri were gaged with two rosettes and four axial gages for the combined loading situation. Two humeri, LH3793 and RH3787, each had a rosette at the proximal third on the convex (posterior) side of the bending bone and at the distal quarter on the anterior side. Their axial gages were placed at the mid-diaphysis on the anterior and posterior surface and at the distal third and proximal third on the posterior side. The third humerus, LH3790, had a rosette at the mid-diaphysis on the concave (anterior) side of the bending diaphysis and at the proximal end on the lateral side. Its axial gages were at the distal third and proximal third on the anterior and posterior sides. All three bones were loaded with a narrow load spacing. The two left humeri were twisted eversively while the right was twisted inversively.

The gages on RH3787 were placed at locations which were proportional to the locations of similar gages on LH3793. RH3787 was fractured under a torsion dominant loading condition while LH3793 was fractured under a bending dominant loading condition. Both bones were bent with the same, narrow roller spacing but RH3787 was twisted inversively while LH3793 was twisted eversively. The strains normal and parallel to the torsional axis at the distal rosette were ideal for a torsion dominant situation; however, those strains at the proximal gage depicted a deviation from Poisson's effect. The strain normal to the torsional axis (Figure 2.155) increased as the twisting moment increased while the strains parallel to the axis remained reasonably constant as would be expected. The cause in this case was not a result of anisotropy as suggested earlier for the torsion only condition but an effect of the rosette's rotation about the centroidal axis of cross-section. This rosette was at the suspended end of the Osteoclast and, therefore, its angular displacement relative to bending load was much larger than that of the rosette at the fixed end. Specifically, as the twisting moment was advanced, this rosette rotated from a position

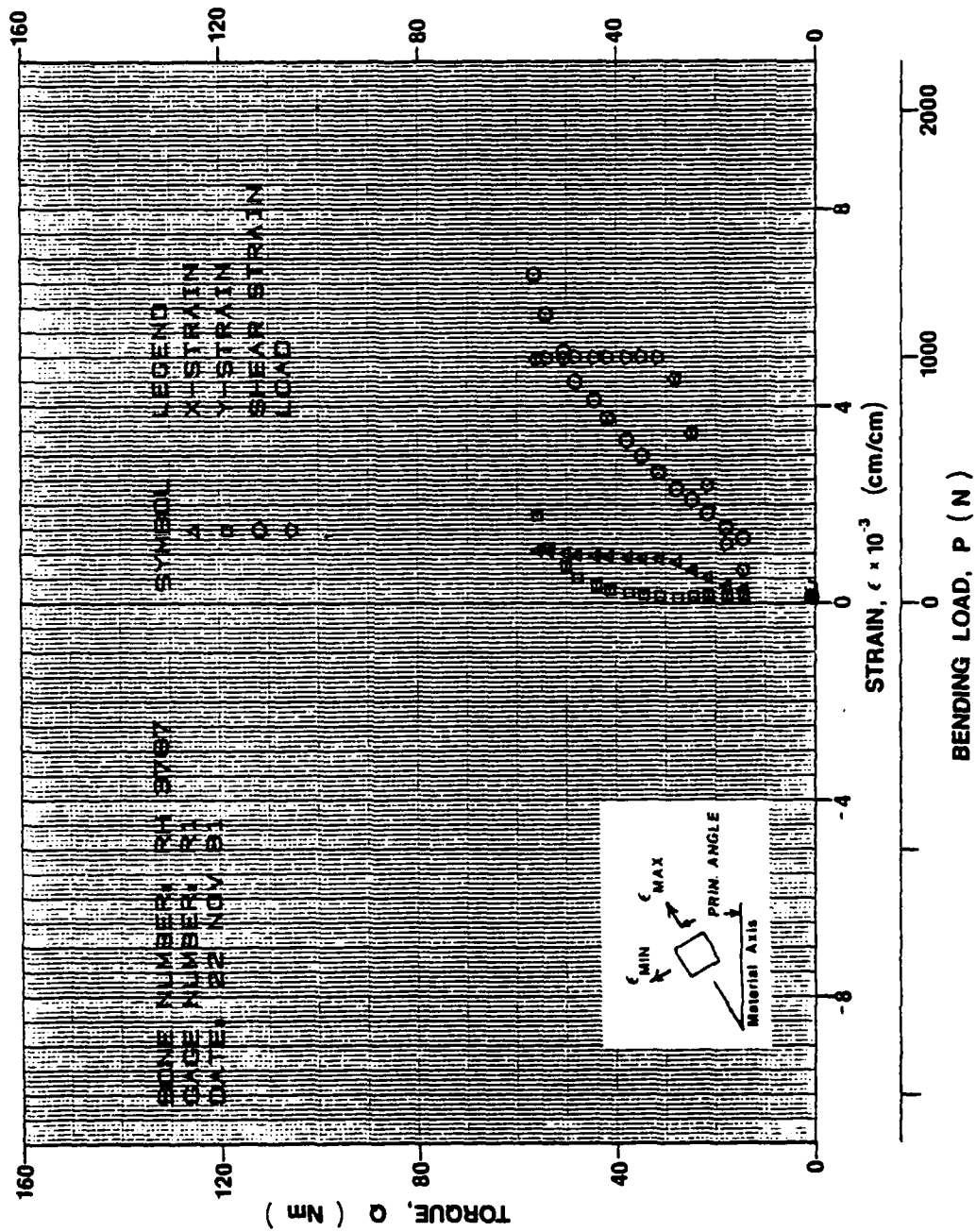


Figure 2.155 Gauge strains for RH3787, convex side, proximal end, torsion dominant.

sensing pure bending and shearing strains to one showing compression as well as bending and shearing (Figure 2.156). So the nonlinear increase is an artifact associated with the nonconservative loading by the Osteoclast. The principal strains and stresses and the principal angle all increase as the loads are advanced.

The complementary arrangement of gages on LH3793 produced strains as expected for a bending dominant condition with the exception of the shearing strain. The strains parallel and normal to the torsional axis increased due to the increase in bending moment and Poisson's effect, respectively, but the shearing strain normal and parallel to the torsional axis decreased when it should have remained constant as the bending load increased. At first, this decrease was also believed to be an artifact, a result of the design of the Osteoclast. The cause of the decrease was thought to be the bending slope at the suspended end decreasing the torsional component of the applied torsional load (Figure 2.157). However, for this to be the case, the slope would have to be approximately 15 deg. to cause the first 5% decrease in strain. The maximum slope measured at this end was only 4.74 deg. After examining the location of the rosettes relative to the assumed "neutral axis", the cause was apparent. The torsional shear was reduced by the increasing bending shear as the bending load was advanced. The principal strains and stresses increased as expected. The principal angle at the proximal rosette decreased while the principal angle at the distal rosette increased; a behavior that is acceptable when the decreasing shearing strains and their normal strains are represented with a Mohr's circle.

The load strain plots from the axial gages on RH3787 were insignificant except for indicating the section modulus at the mid-diaphysis was less than the section modulus at the distal third which was less than that at the proximal third. The compressive strain at the mid-diaphysis was slightly less than the tensile strain.

The load-strain plots from the axial gages on LH3793 were nonlinear for all the locations except the distal third. For this bone the section modulus at the mid-diaphysis was less than that at the proximal third which was less than that at distal third. Using the approximation discussed earlier, the stress at the proximal gages, which was near the fracture, was estimated at 107 MPa. The stress at mid-diaphysis on the

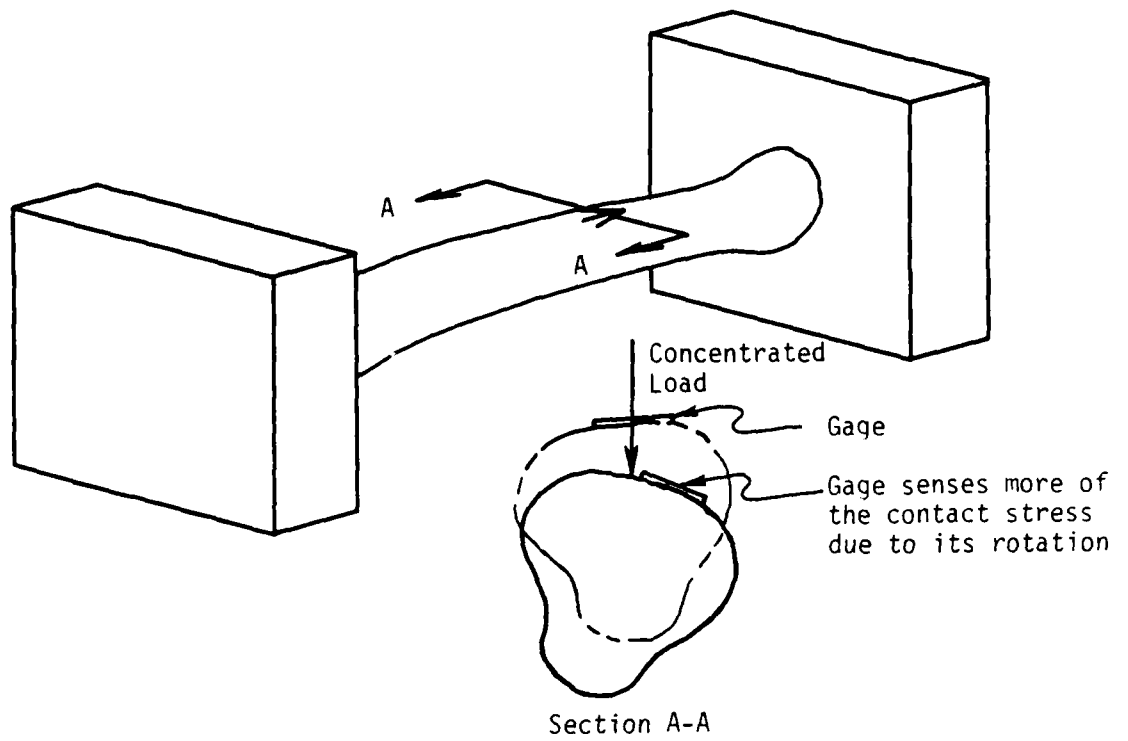


Figure 2.156 Increase in lateral strain due to the rotation of the section.

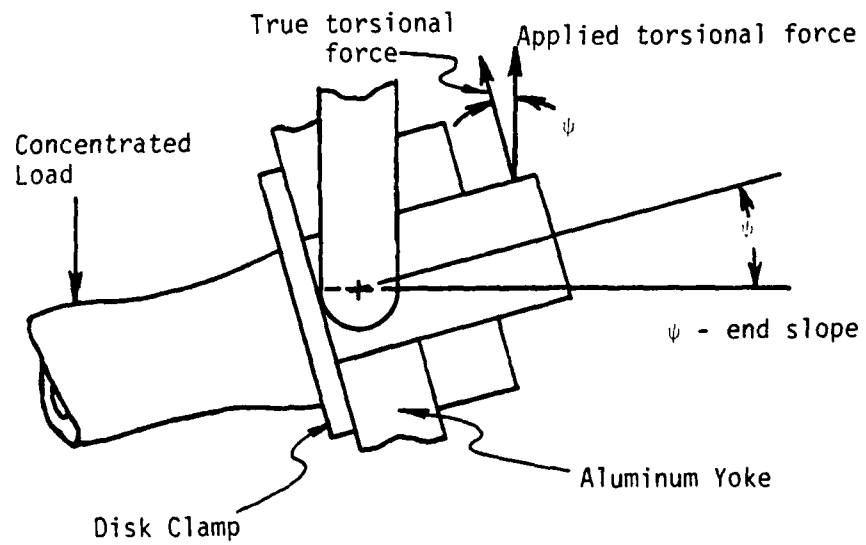


Figure 2.157 Effect of bending slope on true torsional force at the suspended end disk/clamp.

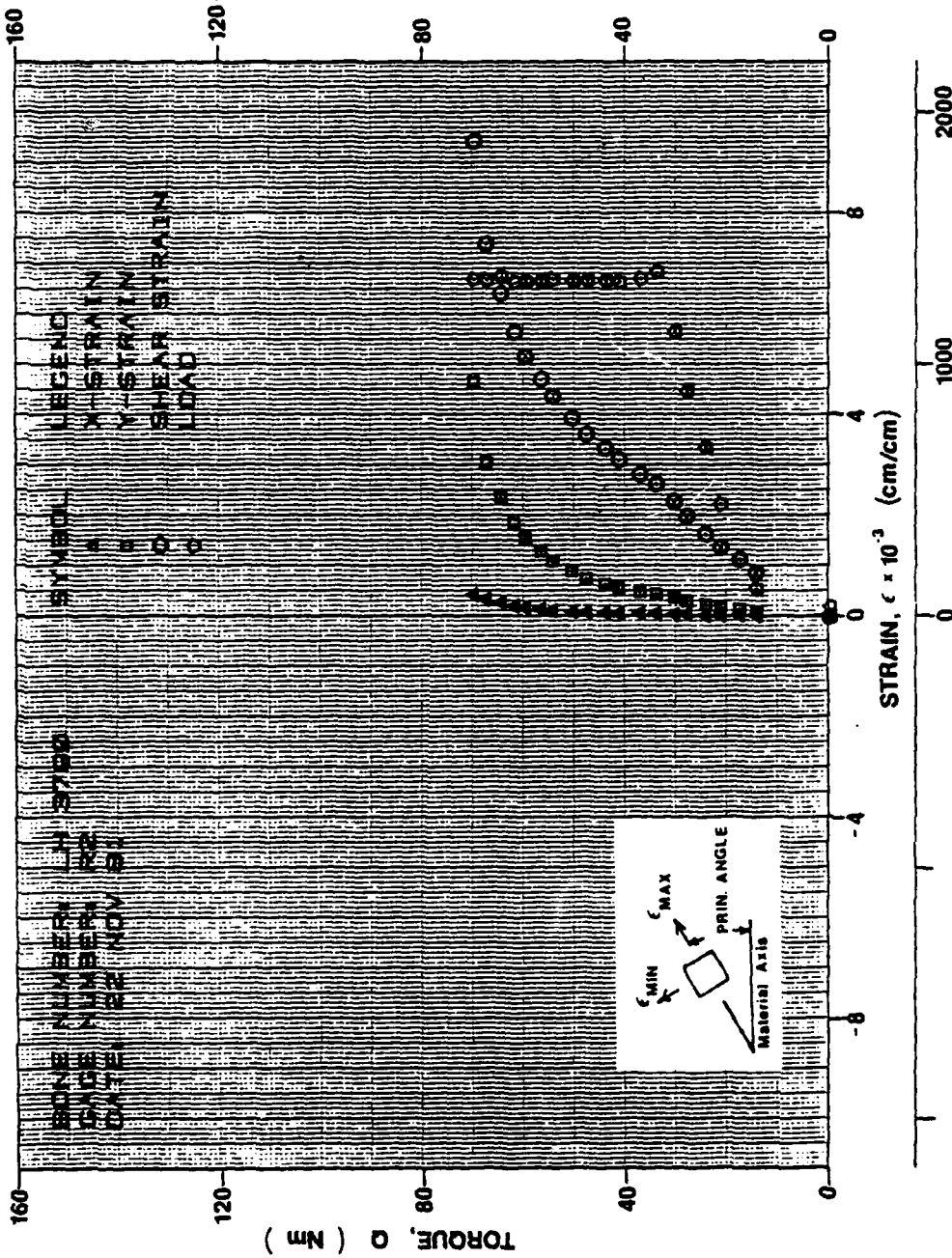
posterior side was estimated at 151 MPa.

LH3790 was twisted eversively under torsion dominant loading conditions and had strains normal to the parallel with the torsional axis at both rosettes which were consistent with the theories of mechanics of materials. The rosette at the mid-diaphysis on the anterior side displayed bending strains that remained constant after the bending load was fixed and the torsional load advanced while the shearing strains continued to increase. The rosette at the proximal end on the lateral side near the "neutral axis" displayed bending strains which were negligible until the twisting moment was sufficient to rotate the gage away from the neutral axis (Figure 2.156). The strains at this gage normal to the torsional axis behaved as described earlier in that, as the twisting moment increased, these strains (Figure 2.158) increased very nonlinearly. Plots of principal strains and stresses as well as the principal angle against the dominant loads were as expected considering the above observations. All increased as the twisting moment was advanced. The strains from axial gages were insignificant; however, they did indicate that the section modulus is less at the distal third than the proximal third.

#### Fibulae:

Four fibulae were strain gaged for testing under combined loading conditions. However, during one of the tests (that of Rfb3790) the maximum contraction of the turnbuckle controlling the dominant load was reached before fracture occurred and the test was continued by increasing the fixed load. Consequently, the load-strain plots were quite random and quite scattered and, therefore, very confusing. This particular bone was not evaluated.

Two of the remaining three were tested using torsion dominant loading conditions with one, Lfb3790, twisted eversively and the other, Rfb3787, inversively. Both of these were gaged with two rosettes and four axial gages; however, their gage configurations were different. Lfb3790 had a rosette at the mid-diaphysis on the concave (lateral) side of the bending diaphysis and one at the proximal quarter on the posterior side. Both of these gages were stacked rosettes. The axial gages on this fibula were on the lateral and medial sides at the distal



and proximal thirds. Rfb3787 had a rectangular rosette near the distal third on the concave (lateral) side of the bending diaphysis and a stacked rosette at the proximal quarter on the posterior side. This fibula had three axial gages on the convex (medial) side of the bending diaphysis at the distal and proximal thirds and mid-diaphysis as well as an axial gages on the lateral side at the mid-diaphysis. The third fibulae, Lfb3787, was tested under bending dominant loading conditions while twisted eversively. Its gage configuration was the same as that of Rfb3787 except the locations were not proportional and varied slightly.

After the first run during the testing of Lfb3790, the middle leg of the rosette at the mid-diaphysis was lost. The remaining gage at the proximal end exhibited nothing unusual. The bending and lateral strains, indicated that the gage was slightly above the neutral axis and, as the twisting moment was held constant, these strains approached zero when the gage was rotated toward the applied load. The shearing strains normal and parallel to the torsional axis were nonlinear throughout the test. The principal strains increased as the test progressed while the principal angle decreased approaching 45 deg.

The strains sensed by the axial gages implied little about the section modulus. The neutral axis at the distal gage was apparently much closer to the lateral surface than it was at the proximal gage.

The load-strain plots of Rfb3787, which was also tested under torsion dominant conditions, were insignificant. The axial gages did imply that the section modulus at the distal third was less than that at the proximal third which was less than the section modulus at the mid-diaphysis. The neutral axis also appears to be closer to the lateral surface than the medial surface at the mid-diaphysis.

The last fibula, Lfb3787, was planned for bending dominant conditions; however, the bone failed at a loading condition which was less than predicted and, therefore, the bending load was still being advanced when fracture occurred. Nothing unusual was noticeable in the load-strain plots. The strains from the axial gages did indicate the section modulus at proximal third was less than it was at the distal third. The neutral axis of the diaphysis also appears to be nearer the lateral surface than the medial surface.

#### LOADS:

Forty-six of the 48 bones fractured were loaded quasi-statically at a strain rate less than  $10^{-5}$  cm/cm/sec. The other two, both humeri, were loaded at a more rapid rate of  $5 \times 10^{-4}$  cm/cm/sec to demonstrate the increase in the fracture strength expected of whole bone when loaded "dynamically." This section describes the fracture loads and associated displacements observed for the 48 bones fractured using the three loading conditions, bending only, torsion only and combinations of torsion and bending. Graphs for estimating the fracture loads and displacements of the four human long bones are presented.

#### Fracture Loads and Displacements:

The magnitudes of the loads causing fracture varied markedly with bone type -- as discussed earlier this variation is a result of the bone geometry as well as the load configuration (wide versus narrow load spacing). Likewise variations in magnitude were also observed for the displacements -- a result of their dependence on the bending and torsional stiffness of the bone, both of which are functions of the geometry as well as the material properties. Table 2.24 compares the mean fracture loads with displacements among the four bone types for the bending and torsion only loading condition. The fracture loads are presented as the forces sensed by the "controlling" load cells (Section 2.2.3.3) and as the bending/twisting moments derived from those forces. Tables 2.25 - 2.27 list all the fracture loads and all the displacements derived for each of the 48 bones tested. The fracture loads in these tables again are given as the force sensed at the "controlling" load cell as well as the bending/twisting moments derived from the forces.

All the fracture loads, except for those of two humeri, were attained through quasi-static loading rates  $\epsilon < 10^{-5}$  cm/cm/sec). Although still far from dynamic, the two humeri were bent at a more rapid rate ( $\epsilon < 5 \times 10^{-4}$  cm/cm/sec) to discern an increase, if any, in the fracture load. Consistent with other findings [6] the rapidly attained fractures were 75% greater than those reached statically.

The calculation of twisting moments listed in the tables is described earlier in the section titled "Data Corrections." The bending

Table 2.24 Mean fracture values for the four human long bones.

Bone	Mb (NM)	$\delta b$ (cm)	Distal Slope (DEG)	Proximal Slope (DEG)	T (NM)	$\phi$ (DEG)
Femur	258.5	1.463	3.38	4.23	125.0	13.91
Tibia	160.9	1.065	4.86	3.60	67.1	20.66
Humerus	104.5	1.357	7.34	5.94	52.7	23.81
Fibula	29.2	2.179	10.06	8.59	7.67	29.45
Humerus (Rapid Rate)	179.4	2.928	--	--	--	--
Tibia (Articulated)	--	--	--	--	83.9	18.24

Table 2.25 Fracture bending moments and bending deflections for the bending only loading condition.

Cadaver	Side/ Bone	$P_b$ (N)	$M_b$ (NM)	$\delta_b^*$ (cm)	Distal Slope (DEG)	Proximal Slope (DEG)	Load Spacing	Test Rate
3753	RF	4003	272.3	1.705 (Pr)	6.59	6.77	N	Static
3793	LF	4838	320.2	1.770 (d)	4.68	7.32	M	Static
3792	RF	3638	236.8	1.275 (d)	4.07	5.16	M	Static
3782	LF	4381	204.5	1.100 (d)	4.87	4.41	W	Static
3753	RT	2780	144.2	1.320 (d)	5.40	3.36	N	Static
3793	LT	4666	214.8	0.990 (Pr)	4.27	3.79	M	Static
3792	RT	2448	123.6	0.884 (Pr)	4.92	3.55	M	Static
3753	LH	1593	82.0	1.638 (Pr)	8.46	7.07	N	Static
3782	RH	2004	98.9	1.368 (Pr)	8.04	6.52	N	Static
3792	RH	2267	132.7	1.065 (Pr)	5.53	4.24	N	Static
3753	Rfb	626	30.6	2.640 (d)	10.97	11.11	N	Static
3792	Rfb	672	27.8	1.718 (Pr)	9.14	6.06	M	Static
3790	RH	3532	189.5	3.752	--	--	N	Rapid
3787	LH	3008	169.2	2.103	--	--	N	Rapid

\*Deflections were measured at a point from the mid-diaphysis toward one end of the bone at a mean distance of 1.62 cm for the femora, tibiae and fibulae and at a mean distance of 7.4 mm for the humerus. The abbreviation in parentheses denotes toward which end of the bone the deflection was measured.

Table 2.26 Fracture twisting moments and corresponding angles of twist for the torsion only loading condition.

<u>Cadaver</u>	<u>Side/ Bone</u>	<u>P<sub>T</sub> (N)</u>	<u>T (NM)</u>	<u>φ (DEG)</u>	<u>Direction of Rotation</u>
3753	LF	320	94.4	13.67	E
3793	RF	514	152.0	13.56	I
3782	RF	413	122.5	13.32	I
3792	LF	447	130.9	15.09	E
3753	LT	225	44.7	30.59	E
3793	RT	296	86.1	16.56	I
3792	LT	240	70.4	14.83	E
3753	RH	232	59.1	23.98	I
3793	RH	198	53.0	24.69	I
3782	LH	150	41.9	18.47	E
3792	LH	223	56.6	28.11	E
3753	LFb	37	8.05	33.67	E
3793	RFb	29	7.67	24.79	I
3792	LFb	32	7.28	29.89	E
Articulated:					
3782	RT/Fb	324	87.7	21.12	I
3782	LT/Fb	274	80.0	15.35	E

Table 2.27 Fracture loads and displacements for the combined loading conditions.

Cadaver	Side/ Bone	P <sub>b</sub> (N)	M <sub>b</sub> (NM)	δ <sub>b</sub> (cm)	Distal Slope (DEG)	Proximal Slope (DEG)	P <sub>T</sub> (N)	T (NM)	φ (DEG)	Load Spacing	Direction of Rotation
Torsion Dominant:											
3790	RF	2233	117.7	0.449	1.62	2.34	648	181.4	18.57	W	I
3790	LF	1701	121.6	0.573	1.80	2.50	501	146.7	14.32	N	E
3790	LT	1151	41.2	0.128	0.67	0.71	248	74.8	9.78	W	I
3790	LT	1159	63.9	0.134 (Pr)	1.07	0.72	309	89.2	15.29	N	E
3790	LH	1337	71.6	0.516 (Pr)	2.80	1.86	248	69.8	16.93	N	E
3787	RH	975	54.8	0.297 (Pr)	1.22	0.91	180	55.9	15.17	N	I
3790	RFb	1245	78.8	1.993 (Pr)	20.57	13.04	6.5	12.0	35.14	W	I
3790	LFb	315	16.3	1.74 (Pr)	4.39	0.96	38	10.2	20.61	N	E
3787	RFb	452	23.6	1.660(Pr)	5.91	5.94	31	8.9	12.95	N	I
Bending Dominant:											
3787	RF	4790	256.9	1.596	8.36	6.14	195	55.6	5.34	W	I
3787	LF	2633	194.8	0.809	2.96	3.07	208	64.1	6.44	N	E
3787	RT	2245	75.0	0.480 (Pr)	2.74	1.34	141	43.8	8.04	W	I
3787	LT	1101	59.8	0.28 (Pr)	1.52	1.76	132	41.0	4.07	N	E
3793	LH	1890	109.6	0.950 (Pr)	4.57	4.74	110	34.0	7.55	N	E
3787	LFb	329	16.7	1.620 (Pr)	6.13	6.52	17	5.4	4.12	N	E

\*deflections were measured at a point from the mid-diaphysis toward one end of the bone at a mean distance of 1.62 cm for the femora, tibiae and fibulae and at a mean distance of 7.4 mm for the humerus. The abbreviation in parentheses denotes toward which end of the bone the deflection was measured.

moments were calculated by multiplying the average distance, in meters, between the loads nearest the supports and the supports (Figure 2.159), by one half of the fracture load recorded at the bending load cell.

The calculation of the twist angles and bending displacements were also described in the section, "Data Corrections." The slope angles were calculated by finding the arc-tangent of the quotient of the slope deflection, indicated by the slope dial indicator, divided by the distance from the support axis to the contact point of the indicator probe (Figure 2.159).

To offer some means of predicting mid-diaphyseal deflections, slopes at the supports and the twist angles, each value in Tables 2.25 - 2.27 was plotted against its corresponding load in terms of bending and twisting moment. For the bending only and torsion only loading conditions, these points are the moments and displacements at fracture. For the combined loading conditions, they are either the values of the dominant load at fracture or the moments and corresponding displacements of the fixed load which was held constant as the dominant load was advanced. Curves were also generated using least squares, linear regression to fit polynomial equations to the points.

Graphs of the bending moments as functions of mid-diaphyseal displacement and end slopes are presented in Figures 2.160 - 2.162, respectively. Graphs of twisting moments as a function of twist angle are presented in Figure 2.163. Once the bending moments or twisting moments are known, these graphs allow a prediction of the displacements that would result from a bending or twisting load. The estimated accuracy of the prediction is  $\pm 10\%$  to  $\pm 20\%$  of the actual measured value. Although the curves are very approximate, they are the only known means available to estimate whole bone displacements.

#### Estimation of Fracture Loads:

The bending and twisting moments from all the valid tests ending in fractures were reduced to provide interaction boundaries. The purpose of these boundaries is to provide a means of predicting the loads necessary to cause a fracture in any one of the four human long bones. The interaction diagrams are presented in terms of synthetic stresses. The synthetic stress,  $\tau$ , along the ordinate of the diagram represents

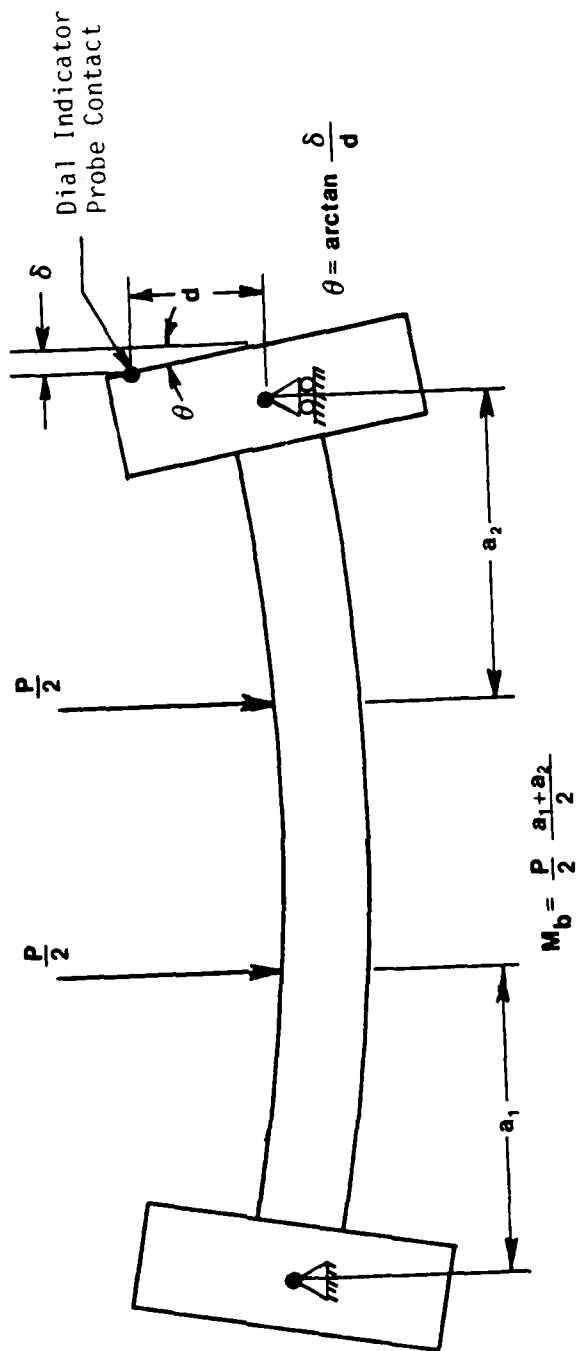


Figure 2.159 Calculation of bending moments from fracture loads.

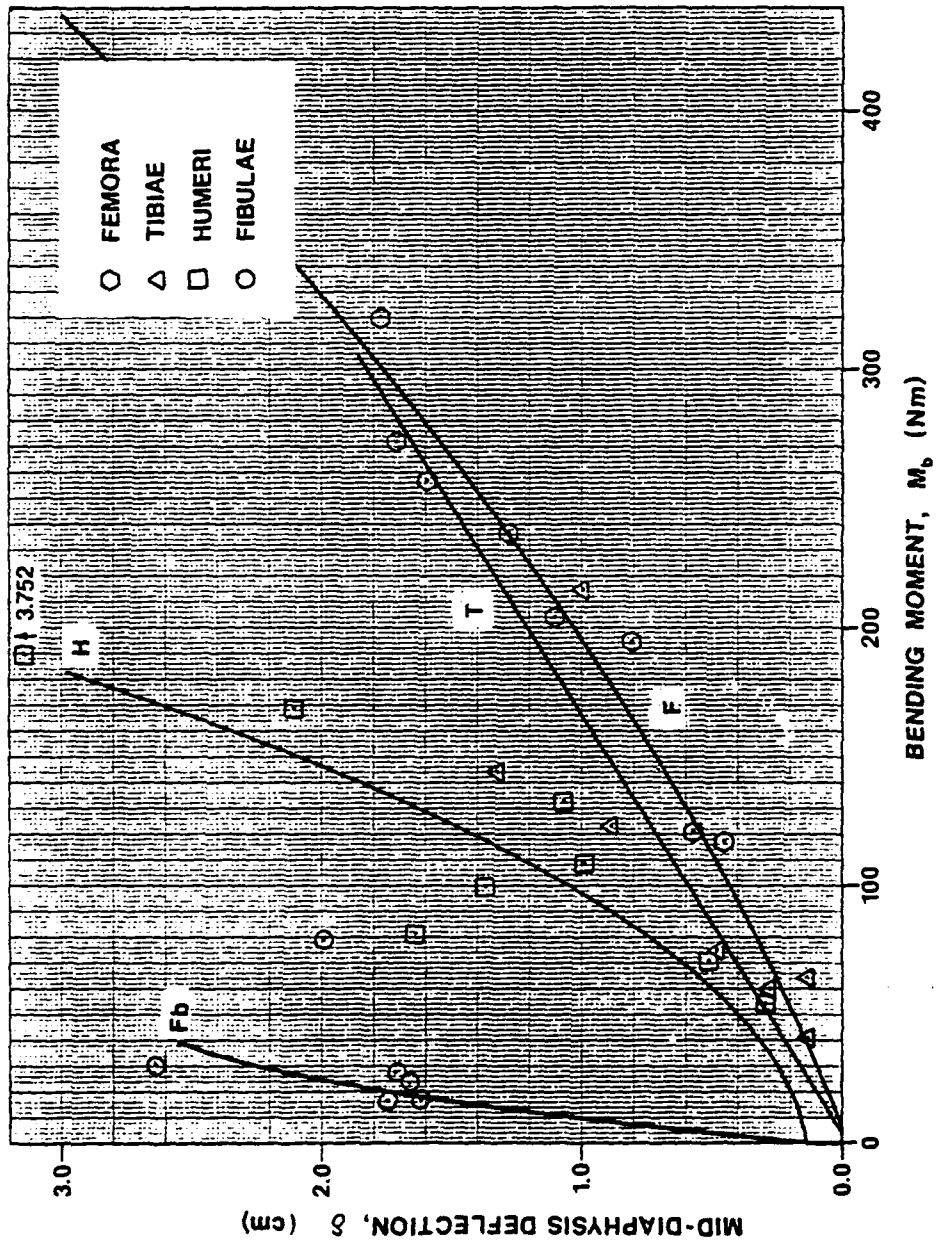


Figure 2.160 Bending deflections of the four human long bones.

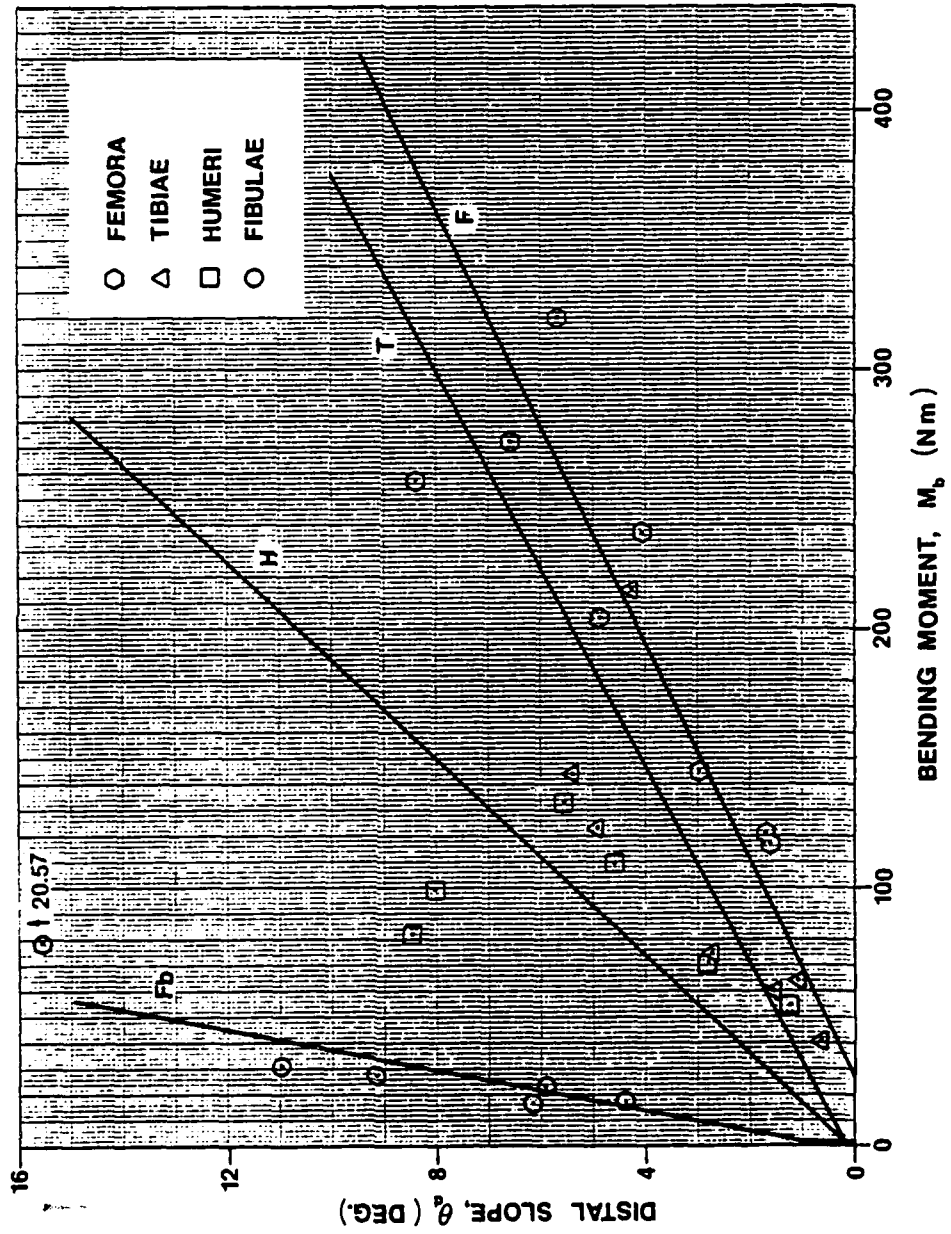


Figure 2.161 Distal end bending slopes of the four human long bones.

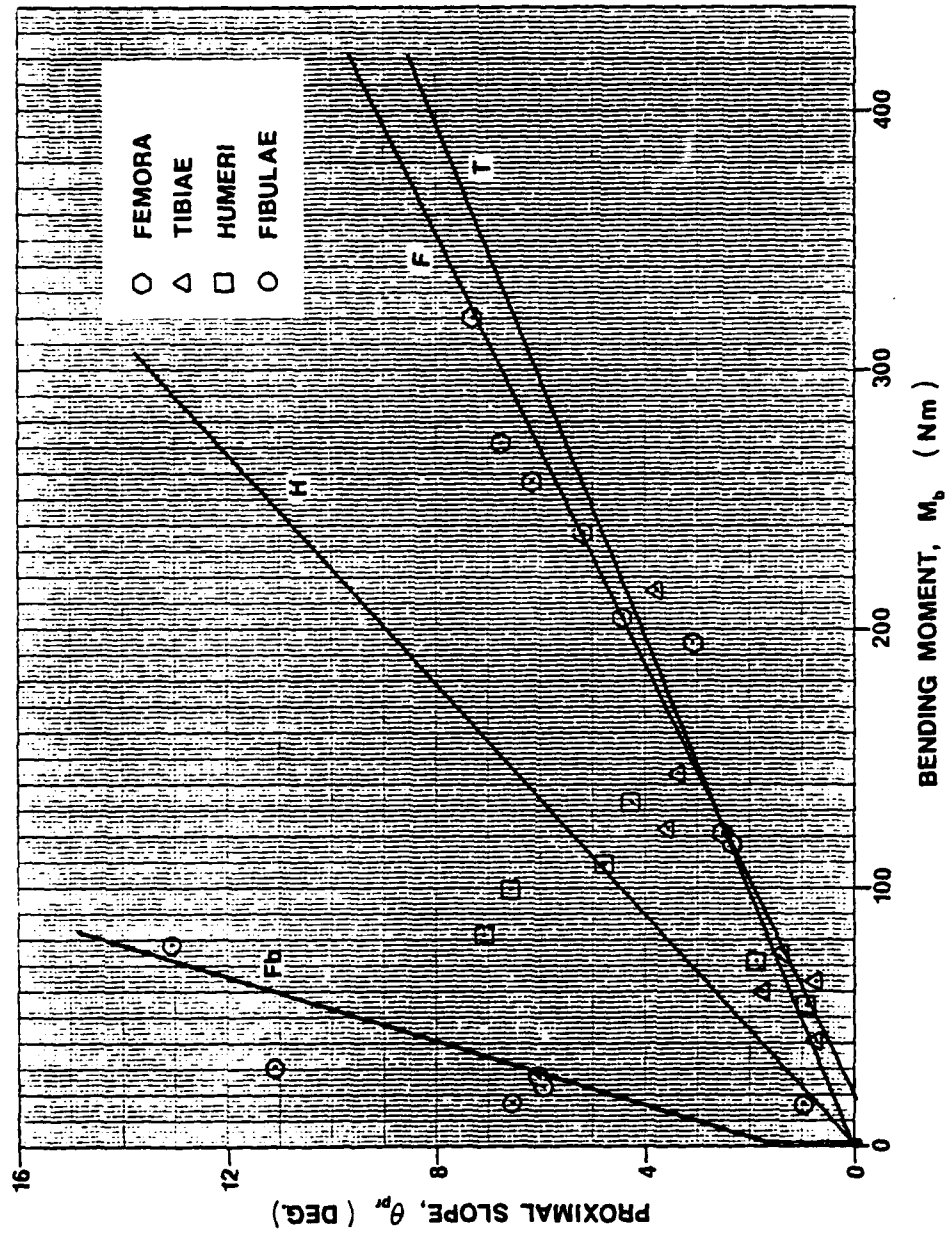


Figure 2.162 Proximal end bending slopes of the four human long bones.

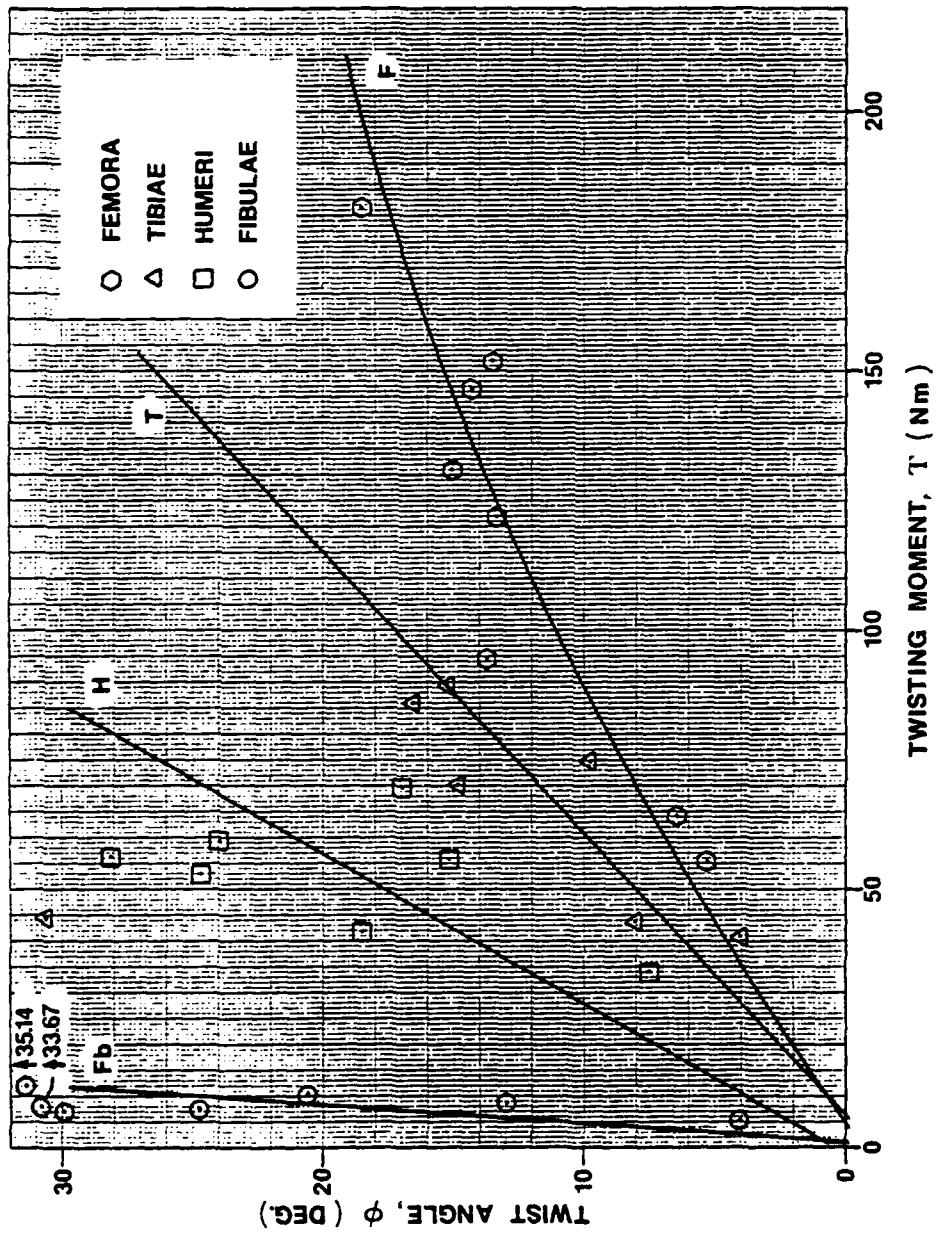


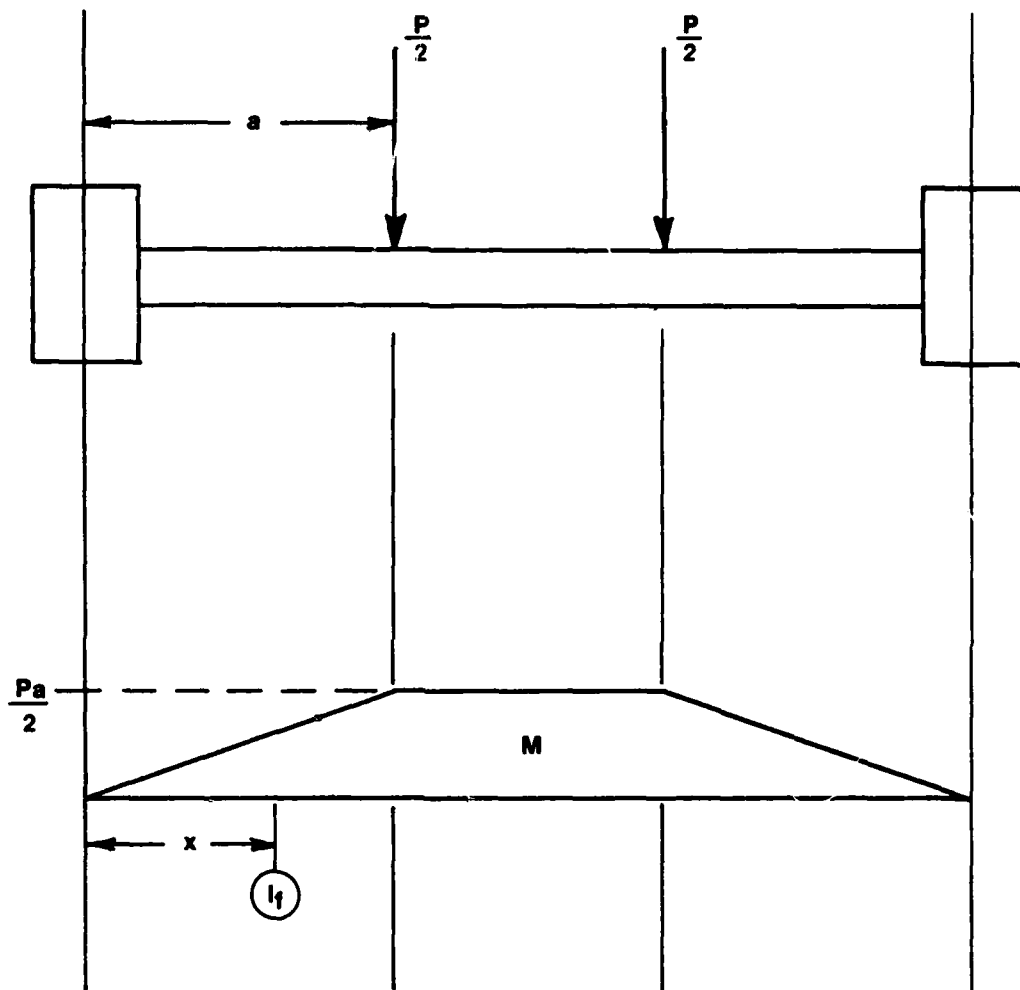
Figure 2.163 Twist angles of the four human long bones.

the contribution of a twisting moment towards the fracture of a particular bone type. The synthetic stress,  $\sigma$ , along the abscissa represents the contribution of a bending moment towards the fracture of the same bone. The point where the boundary intersects the ordinate is the synthetic shearing stress which will cause the bone to fracture without any bending applied. Similarly, the point where the boundary crosses the abscissa is the synthetic bending stress which will cause fracture in the absence of any torsion. A point along the boundary in the quadrant then becomes the combination of stresses which are necessary for the bone to fracture when the two loading conditions are combined.

The boundaries are useful in two ways. First, if one of the four long bones is twisted and the twisting moment known, the synthetic stress  $\tau$  may be determined. Selecting the appropriate interaction boundary one enters with  $\tau$  and finds its intersection on the boundary. The synthetic stress,  $\sigma$ , corresponding to the intersection then becomes the synthetic "bending" stress that should cause fracture. With this fictitious bending stress known the fracture bending moment is then readily available. The second approach to the curve concerns the susceptibility of a loaded bone to fracture. In this case, the synthetic torsional stress,  $\tau$ , and bending stress,  $\sigma$ , are determined and plotted on the intersection diagram respective of bone type. If the point lies below the curve, the bone "probably" will not fail. If it lies above, fracture is possible.

To generate the curves the synthetic stresses were calculated using bending and twisting moments derived from the test results. The bending moments were determined at a location,  $l_f$ , (Figure 2.164) along the diaphysis where a fracture is most likely to initiate. These locations were selected as explained in the section titled "Nondimensionalization" and are in terms of percentages of total bone length. The percentages are,

Femora	79% A.L. measured from the proximal end
Tibiae	19% M.L. measured from the proximal end
Humeri	77% M.L. measured from the proximal end
Fibulae	82% M.L. measured from the distal end



$$M_b = \frac{Px}{2}$$

Figure 2.164 Calculation of fracture bending movements for the interaction boundaries.

where A.L. is the anatomical length and M.L. is the morphological or maximum length.

Using these locations, the bending moments were derived by applying simple mechanics of material theory as shown in 2.164. These bending moments were different from those in Tables 2.25 - 2.27. However, the twisting moments are those listed in Table 2.26 which were derived as explained in "Data Corrections."

The "nondimensionalization" of the moments involved a fictitious section modulus. The section modulus is labeled fictitious because it is calculated using a tubular shape for the cross-section at station,  $l_f$ , instead of the true section shape. The stresses that evolve when the fracture moments are divided by this fictitious modulus are fictitious themselves -- thus the terminology, "synthetic" -- and are essentially the fracture loads independent of bone geometry. They represent the ultimate stress for a bone type in the general sense and may be used to predict the fracture load for any bone, respective of type and certain geometry.

To derive the section moduli, diameters were averaged at station,  $l_f$ , to define the tubular shape approximating the cross-section at the station. The cross-section at station,  $l_f$ , was selected because it supposedly locates the point of fracture initiation as described in the section, "Nondimensionalization." The diameters were measured in the mediolateral and anteroposterior views of roentgenograms of each bone. The inside diameters of the cortical wall in each view were averaged as were the outside wall diameters. These were then used to calculate the polar moment of inertia and to approximate the distance from the neutral or torsional axis to the extreme fiber stressed in tension or shear. Both quantities are necessary to compute the section moduli,

$$S_b = S_t = \pi \frac{(D_o^4 - D_i^4)}{\frac{32}{D_o}} \frac{1}{2}$$

where  $S_b$  is the bending modulus,  $S_t$  the torsion modulus,  $D_o$  the average outside diameter and  $D_i$  is the average inside diameter.

To derive the synthetic stresses, the moments were divided by the section moduli in accordance with the mechanics of material relationships for bending stress,

$$\sigma_b = \frac{M_b}{S_b}$$

and for torsional stress,

$$\tau = \frac{T}{S_\tau}$$

Theoretically, if the section shapes at station,  $l_f$ , are the same for any bone of a particular bone type, if the loads applied are the same, and if fracture occurs consistently when a certain stress level is attained, then the synthetic stresses should agree among the tests of a particular bone type. Such agreement should occur for the bending only as well as the torsion only loading conditions (even when the load spacing is varied) as long as the fracture initiates at the same ultimate bending tension stress. However, since in actuality the section shapes at station,  $l_f$ , vary markedly among bones of the same type and since fracture initiation is also a function of discontinuities as well as stress level, one should expect some "scatter" of the synthetic stresses. The scatter of the bending synthetic stresses calculated using the approximations discussed so far was indeed large--especially when compared to the synthetic shear stresses. On the contrary, the shear stresses agreed quite well among bone types as well as among bones of the same type. There was an apparent dependency on the direction of twist for the humerus, but no evidence of such a dependency for the other bone types.

The close agreement among the shear stresses is attributed to the close approximation of the diaphyseal cross-section by the tubular shape. Conversely, the agreement was poor among the bending stresses because the tubular shape is poor approximation when used to calculate the second moment of inertia. Using half of the average diameter,  $D_o$ , for the distance from the neutral axis to the extreme tension fiber only adds to this error, especially for cross-sectional shapes of the femur or tibia.

To account for such losses in accuracy and reduce the scatter of the synthetic bending stress, a bias factor was estimated by comparing actual bone cross-sections with their tubular approximations. The synthetic bending stresses were simply multiplied by the factor to bring their values into closer agreement.

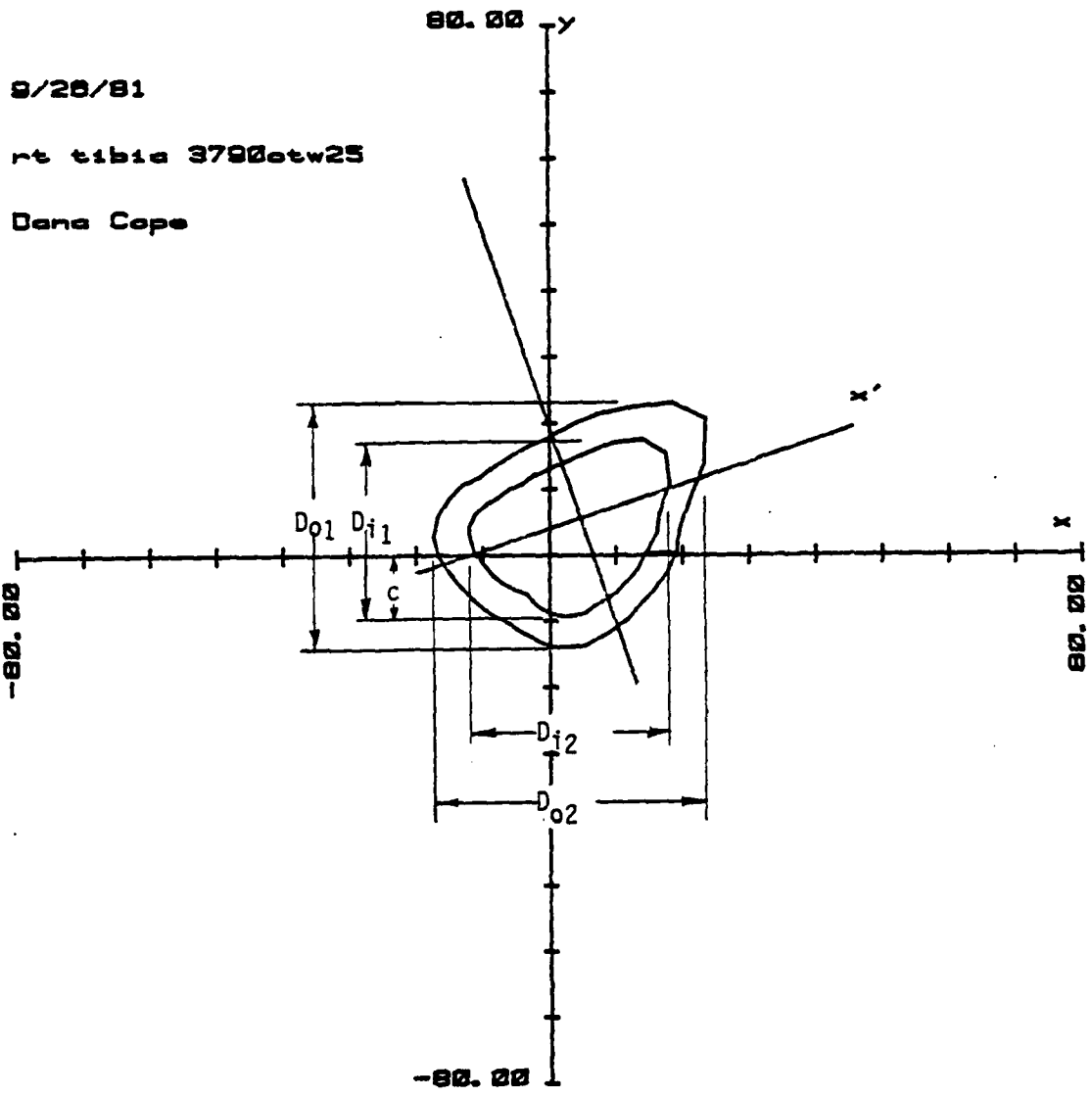
For the exact cross-sectional shapes, sections were selected from those sketched of the cuts made in the bones to show the peripheral locations of strain gages and the shapes of the specimens sent for the medical evaluation (Figures 2.91 - 138). Since the locations of the sections sketched did not coincide with those at station,  $l_f$ , sections at locations as close as possible to  $l_f$  were chosen. Fortunately, sections were available at locations within 5% - 10% of  $l_f$ . The second moments of inertia of the sections were estimated using the computer program described in the section, "Section Properties." Figure 2.165 shows the output from the program and depicts the measurement of the inside and outside diameters used for a tubular approximation of the section. Also shown in the figure is the measurement used for the actual distance from the neutral axis to the extreme tension fiber occurring when the bone is bent in a plane similar to that of the tests. For the bias factor, the fictitious section modulus, calculated for a tubular approximation of the average diameters from the true cross-section, was divided by the actual section modulus of the true cross-section,

$$F = \frac{\pi (D_o^4 - D_i^4)}{32D_o} \div \frac{I_{xx}}{C}$$

where  $D_o$  and  $D_i$  are the average outside and inside diameters,  $I_{xx}$  is the estimated second moment of inertia of actual bone cross-section at  $l_f$ , and  $C$  is the measured distance to the extreme tension fiber. Three such factors were calculated using a cross-section near  $l_f$  for three different bones of each bone type. The sections selected are shown in Figures 2.93, 95, 99, 107, 109, 111, 118, 123, 125, 132, 135, 137. The factor used to decreased the scatter of the bending synthetic stresses was the average of the three factors for each bone type.

In summary, the final synthetic stresses are given by the equations,

Figure 2.165 Section approximation from the computer output described in section properties.



$I_{xx} = 75305.10 \text{ mm}^4$

$I_{xx'} = 40128.82 \text{ mm}^4$

$I_{yy} = 84402.80 \text{ mm}^4$

$I_{yy'} = 85023.29 \text{ mm}^4$

$I_{xy} = 33271.78 \text{ mm}^4$

$\theta = 18.53 \text{ deg}$

$I_{x'} = 0.00 \text{ mm}^3$

$I_{y'} = 0.00 \text{ mm}^3$

AREA = 485.08 mm<sup>2</sup>

$$\sigma_b = \frac{F M_b}{S_b}$$

$$\tau = \frac{T}{S_\tau}$$

These stresses are listed in Table 2.28, 29 and plotted in Figures 2.166 - 169. The boundary curves in the figures are first and second order polynomials derived using least squares, linear regression applied to the points plotted. The boundaries are presented for each bone type irrespective of the direction of twist. A total of three boundaries are provided for each bone type with the exception of the fibula. The three boundaries represent an upper and lower boundary derived from selected points and the mean of these extremes. Because the behavior of the fibula while separated from the tibia is merely academic, only one boundary is provided which incorporates all the points. The two tibiae and fibulae tested articulated and the two humeri tested under rapid rate conditions were not included in the development of the interaction boundaries.

#### 2.2.6 References:

1. Reilly, D. T., Burstein, A. H., "The Elastic and Ultimate Properties of Compact Bone Tissue," J. Biomechanics, 1975, pp. 393-405.
2. Taylor, H. L., Orthopedic Surgery, 1909, p. 339.
3. Kobayashi, A. S., Manual on Experimental Stress Analysis, 34d Ed., Society for Experimental Stress Analysis, 1978.
4. Carter, D., "Anisotropic Analysis of Strain Rosette Information from Cortical Bone," Journal of Biomechanics II, 1978, pp. 199-202.
5. Popov, E. P., Mechanics of Materials, Prentice-Hall, Inc., 1976.
6. Currey, J. D., "The Effects of Strain Rate, Reconstruction and Mineral Content on Some Mechanical Properties of Bovine Bone," Journal of Biomechanics, Vol. 8, 1975, pp. 81-86.

### 2.3 Brittle Coat

#### 2.3.1 Introduction

Brittle coating is an experimental stress analysis technique used to determine stress distributions in materials, especially points of

Table 2.28. Synthetic stresses for the femora and tibiae.

Cadaver	Side/ Bone	Bias Factor	$\sigma_b$ (MPa)	$\sigma_r$ (MPa)	Roller Spacing
3753	LF	--	--	44.3	--
3792	LF	--	--	47.0	--
3782	RF	--	--	40.0	--
3793	RF	--	--	40.2	--
3753	RF	1.17	140.3	--	N
3787	LF	1.17	32.2	9.6	N
3790	LF	1.17	33.4	39.8	N
3782	LF	1.17	80.6	--	W
3787	RF	1.17	122.7	18.5	W
3790	RF	1.17	35.4	51.4	W
3792	RF	1.17	62.0	--	M
3793	LF	1.17	69.3	--	M
3753	LT	--	--	43.7	--
3792	LT	--	--	77.8	--
3793	RT	--	--	59.0	--
3753	RT	1.17	65.7	--	N
3787	LT	1.17	9.7	14.2	N
3790	LT	1.17	21.0	62.4	N
3787	RT	1.17	25.5	11.1	W
3790	RT	1.17	15.6	34.2	W
3792	RT	1.17	49.9	--	M
3793	LT	1.17	39.7	--	M

Table 2.29 Synthetic stresses for the humeri and fibulae.

<u>Cadaver</u>	<u>Side/ Bone</u>	<u>Bias Factor</u>	$\sigma_b$ <u>(MPa)</u>	$\sigma_r$ <u>(MPa)</u>	<u>Roller Spacing</u>
3753	RH	--	--	48.7	--
3792	LH	--	--	68.6	--
3793	RH	--	--	45.0	--
3782	LH	--	--	67.8	--
3782	RH	1.38	233.4	--	N
3753	LH	1.38	78.2	--	N
3792	RH	1.38	199.5	--	N
3793	LH	1.38	80.1	24.0	N
3787	RH	1.38	28.4	29.8	N
3790	LH	1.38	71.2	52.7	N
3753	LFb	--	--	55.7	--
3792	LFb	--	--	21.0	--
3793	RFb	--	--	26.8	--
3787	LFb	1.04	96.7	33.4	N
3790	LFb	1.04	43.7	39.6	N
3787	RFb	1.04	86.4	27.4	N
3753	RFb	1.04	198.4	--	W
3793	LFb	1.04	297.2	--	M
3792	RFb	1.04	120.0	--	M



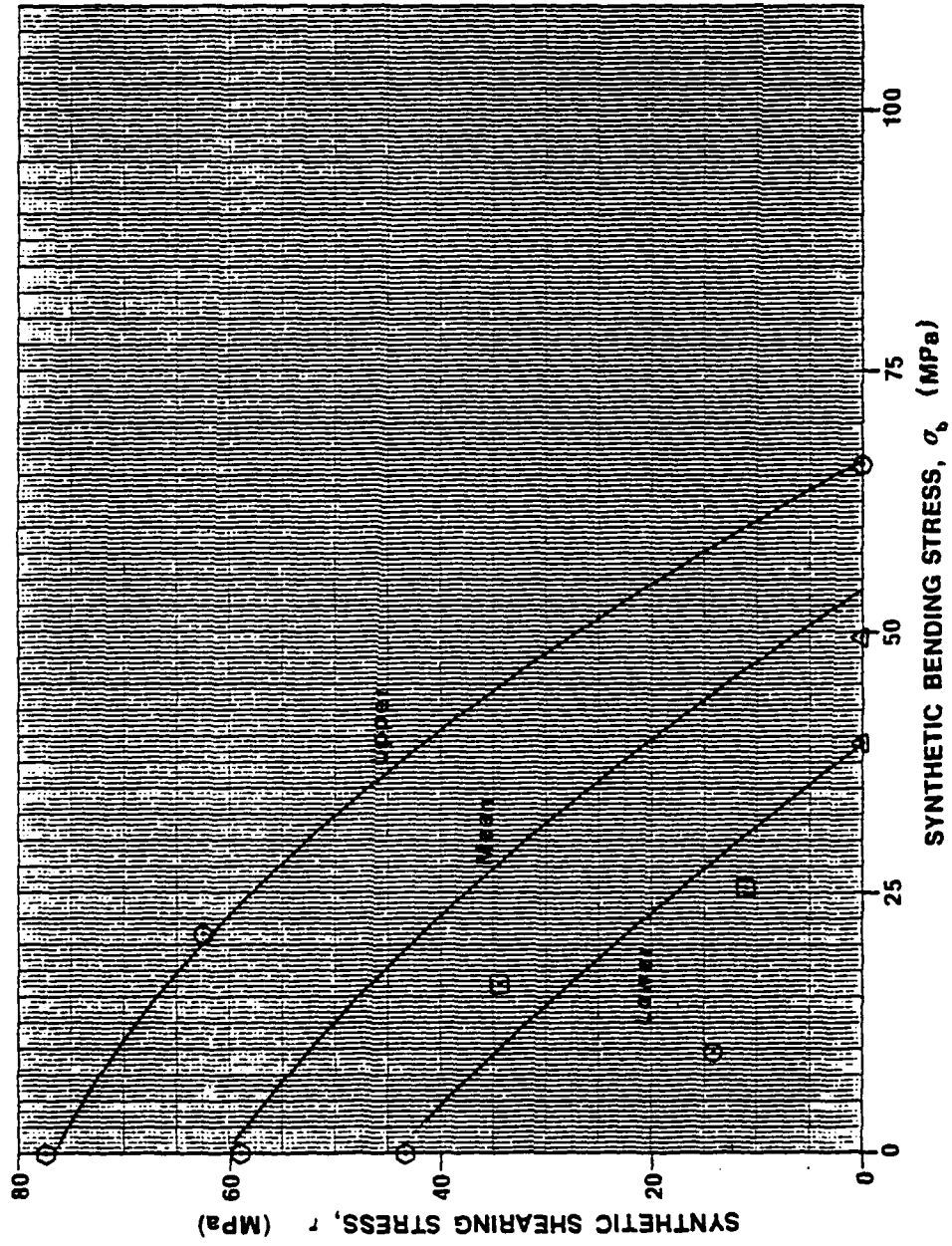


Figure 2.167 Interaction boundary for the tibia.

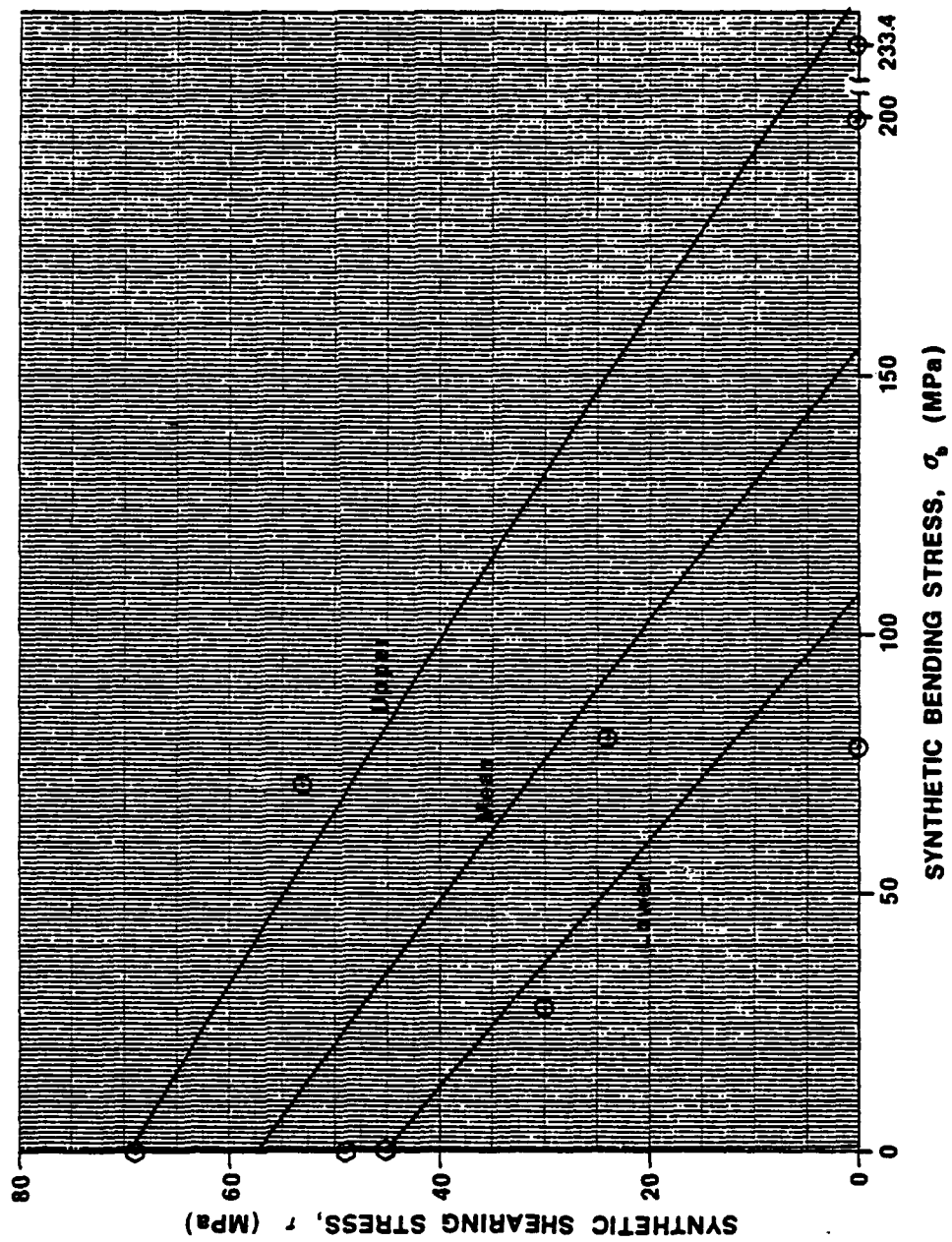


Figure 2.168 Interaction boundary for the humerus.

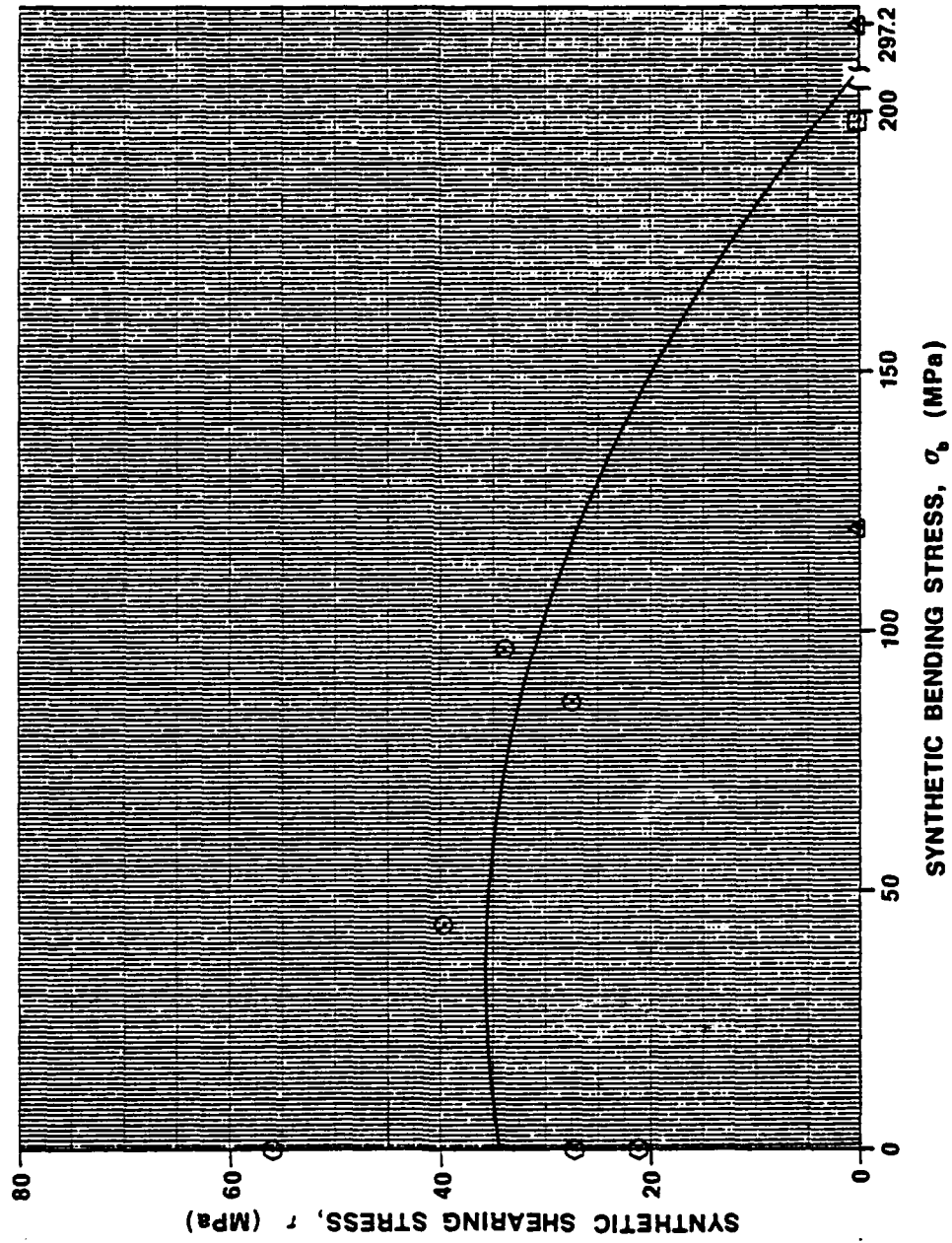


Figure 2.169 Interaction boundary for the fibula.

maximum stress and stress concentrations. In this study, brittle lacquer was used on a femur loaded in torsion to determine the location and direction of the maximum stress. It was hoped that the test would isolate the fracture initiation point as the bone was twisted to failure.

### 2.3.2 Theory

The brittle coating stress analysis technique is based on Hooke's Law -- stress is directly proportional to strain and the area of greatest strain is also the site of highest tensile stress. The low tensile strength of the lacquer coating results in its cracking at stresses far below the elastic limit of the bone. These cracks emphasize places of greatest tension and lie perpendicular to the direction of tension in the bone. The coating thus indicates the direction of the principal strains at a point and the magnitude of the largest principal strain.

### 2.3.3 Test Specimen

The test specimen was an embalmed human left femur of unknown sex and weight. The femur was measured and molded with epoxy putty.

#### 2.3.3.1 Surface Preparation

The femur was exposed for two days to the room environment allowing it to dry prior to the surface preparation. The surface preparation consisted of scraping away all the fleshy tissue and degreasing the bone with acetone, followed by Chlorothene Nu degreaser. After this, the procedure was the same as that used for strain gage application.

#### 2.3.3.2 Coating

Before the lacquer coating, an undercoat of aluminum paint (Tenslac U-10-A) was applied to the bone to provide a reflective surface and highlight the cracks. The calibration bars [1] were also sprayed at this same time. After the undercoat was dry (20-30 min.), a coating of Tenslac TL-500-80A was sprayed onto the bars and the bone in layers while waiting two minutes between each layer to allow for solvent evaporation. This lacquer was determined appropriate for temperature and humidity conditions of 74°F and 52%, respectively, in accordance with reference [1]. Each layer was applied consecutively until a uniform color on the bone and the bars approximately matched that for the correct thickness of .003 per reference [1]. The complete coating on the femur and calibration

bars was allowed to dry in a constant temperature and humidity environment for 24 hours prior to testing.

#### 2.3.4 Equipment

The coated femur was twisted in the Osteoclast to different load levels before it was finally fractured. Loads and displacements were recorded as explained in Section 2.2.3.

#### 2.3.5 Test Procedure

The first step in the test was to load the calibration bars and determine the threshold strain of the lacquer application. Since it was estimated to take 3-5 sec. to reach a load level, the first bar was loaded in 3 sec. and the second in 5 sec. Hence, the calibration bars were loaded at a rate approximating that for the bone.

The bone failure load was estimated at 85 lb. using data from previous tests on fresh bones. Since this corresponds to a limit load of 57 lb., the first test was run in 5 lb. increments to 60 lb. after setting the zeros of the dial gages at a 10 lb. load. The method used for loading was multiple increments of increasing load [2] which involved applying each increment, searching for cracks and recording data, and then removing the load for twice the time required to achieve the previous load cycle (the unloading allows creep relaxation of residual stresses in coating). The next increment was then applied and the process repeated up to the limit load. At this point the cracks were marked and photographed. For the second test the bone was loaded in 5 to 10 lb. increments to failure without releasing the load.

#### 2.3.6 Observations

Both calibration bars indicated a threshold strain of 600  $\mu\epsilon$ . The first cracks in the lacquer occurred near the proximal third on the posterior side at 40 lb. as shown in Figure 2.170 followed by cracks at the lesser trochanter at 50 lb. and cracks on the anterior surface as shown in Figure 2.171. The crack patterns in the figures have been highlighted with ink for emphasis. At a load of 150 lb. the bone fractured violently as shown in Figures 2.172 - 2.174.

#### 2.3.7 Data Reduction

The threshold strain of 600  $\mu\epsilon$  was used to calculate the stress at the point where the coating first cracked using a value for Young's modulus,  $E$ , of 14.25 GPa. This value implies that bone is an isotropic

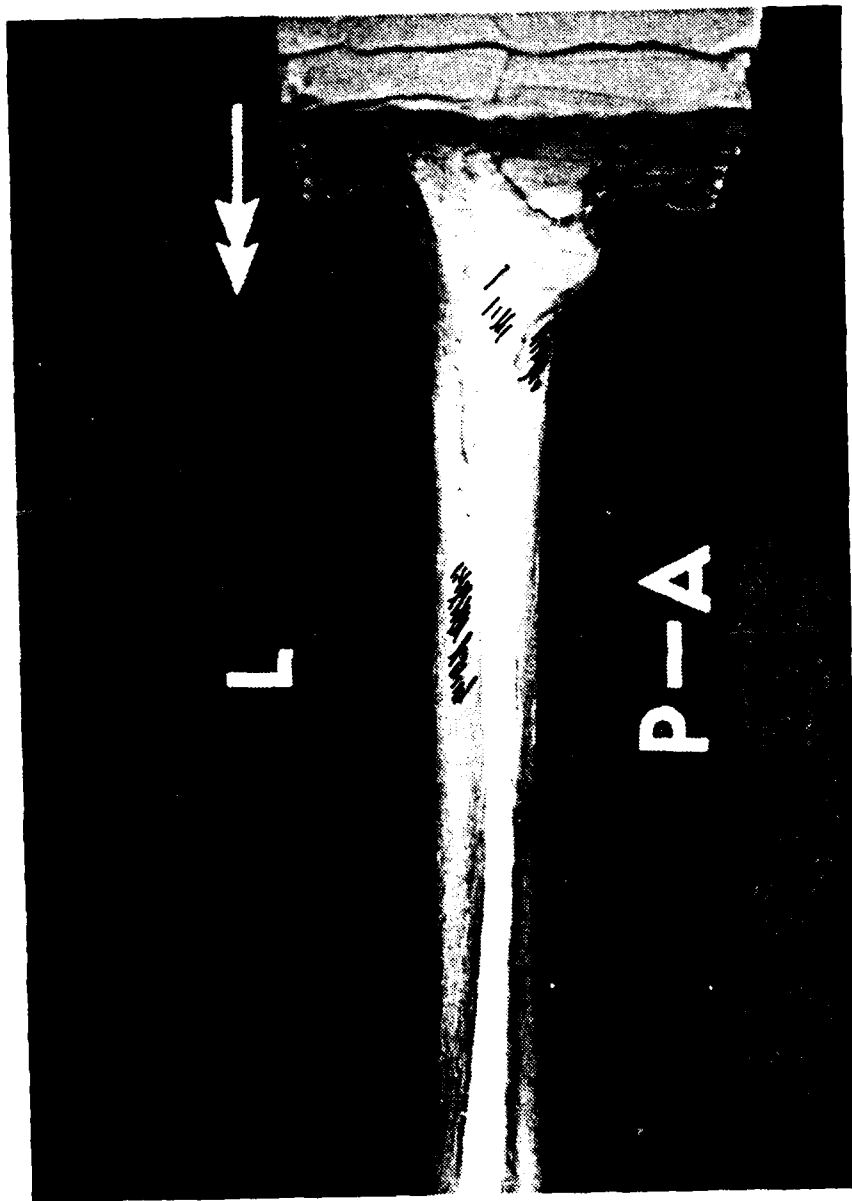


Figure 2.170 First brittle lacquer cracks observed at the proximal end on the posterior side.

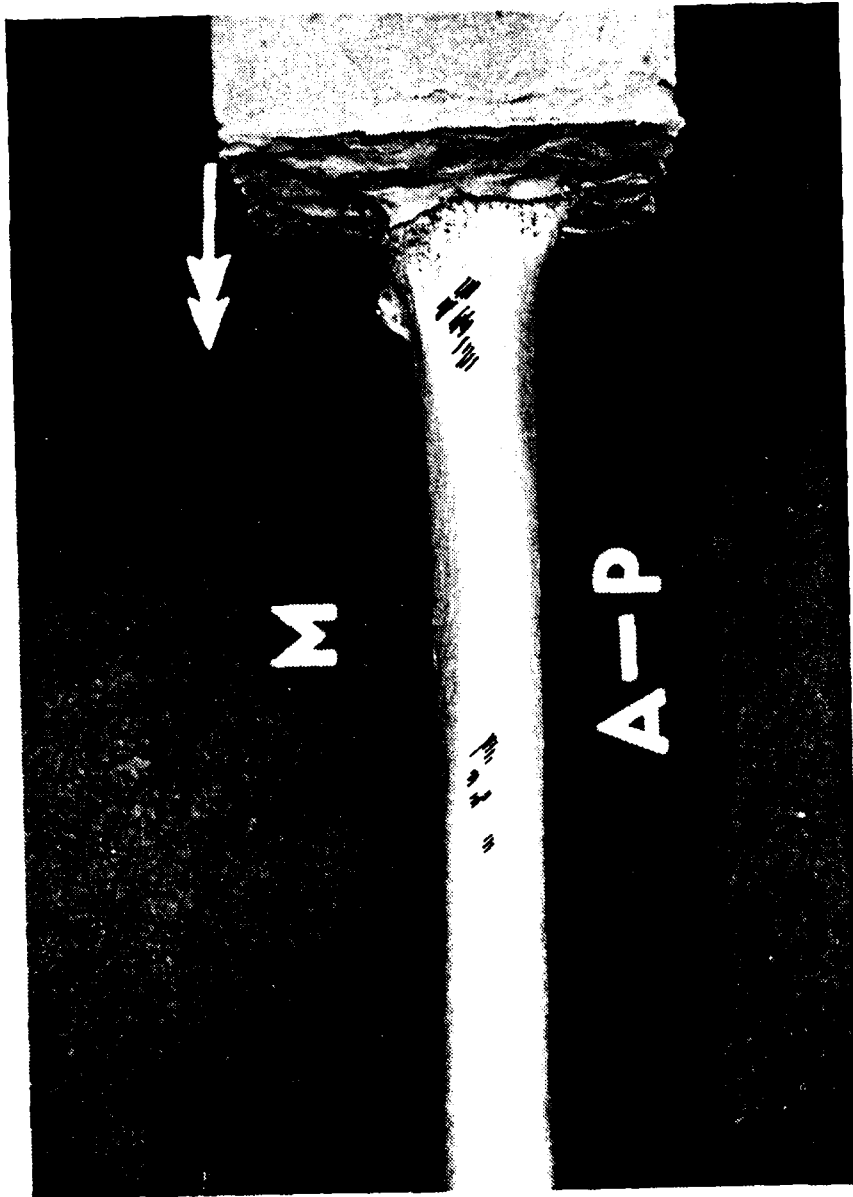


Figure 2.171 Cracks observed at the proximal end anterior surface after additional loading.

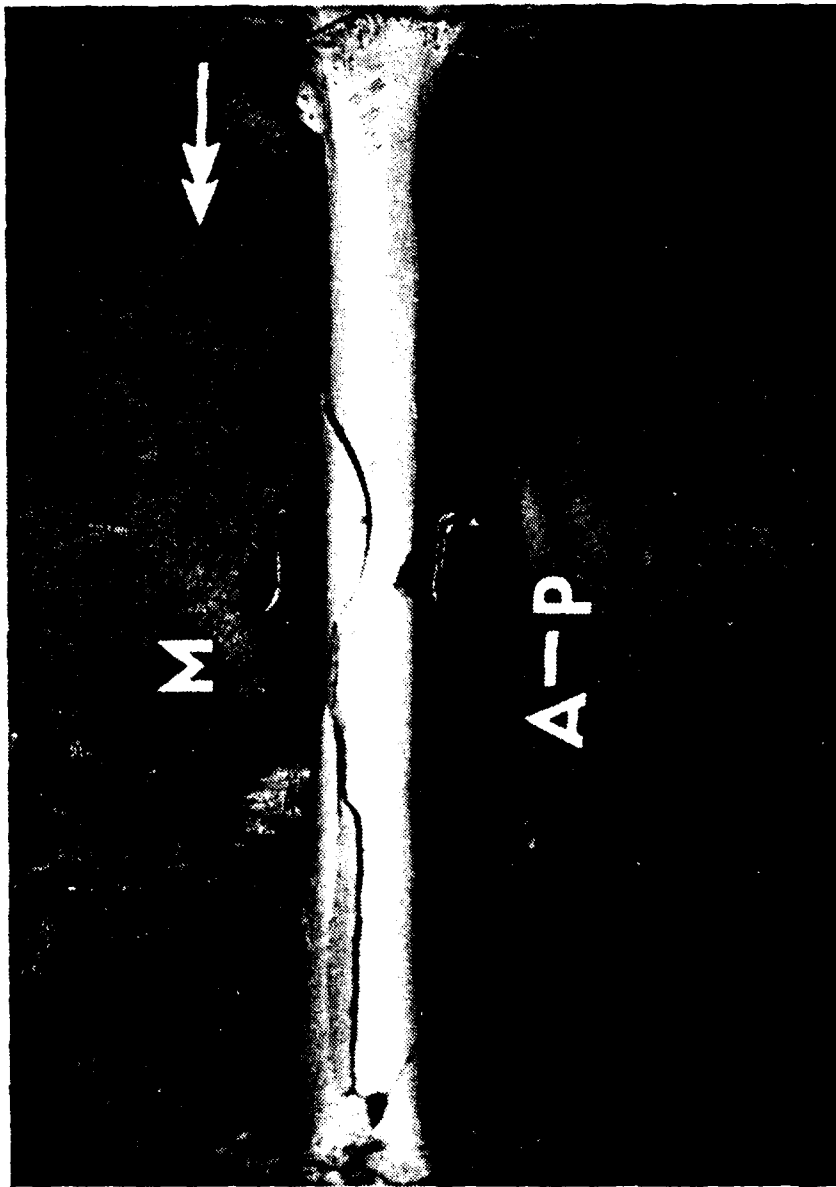


Figure 2.172 Fracture pattern anterior view.

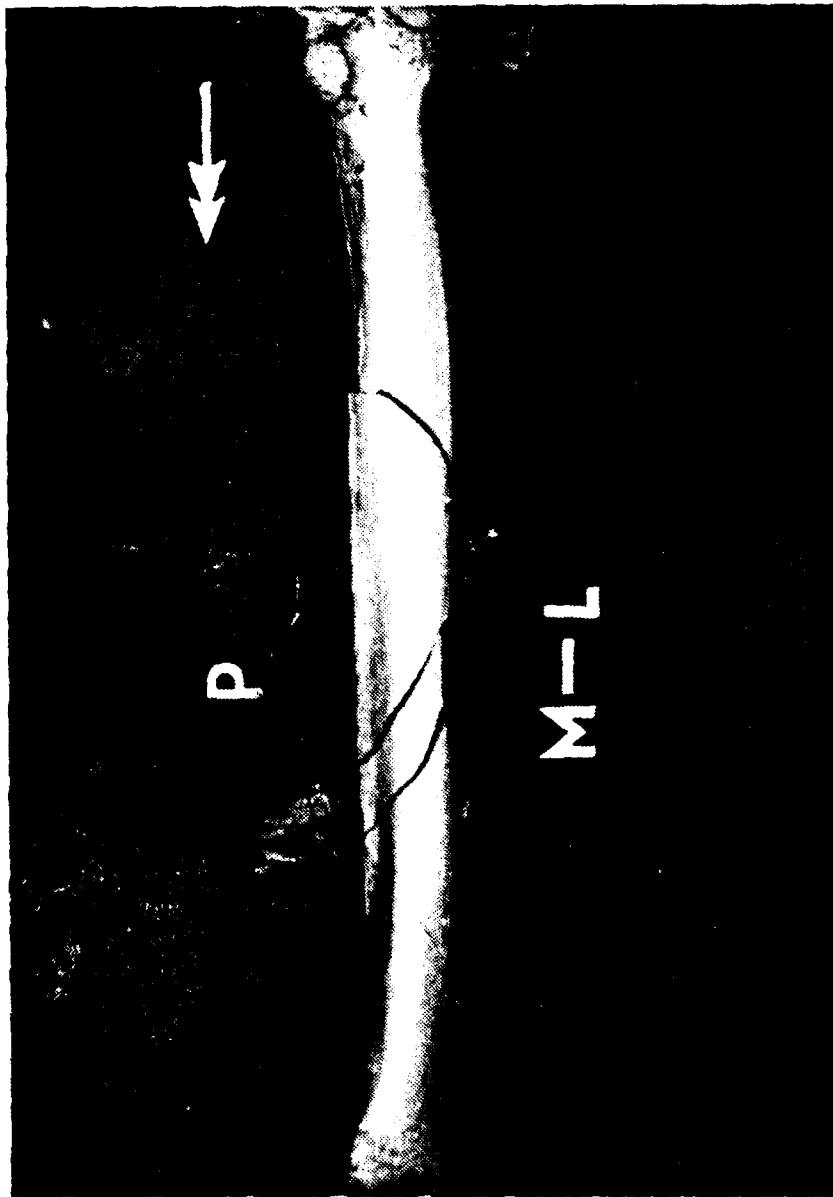


Figure 2.173 Fracture pattern medial view.

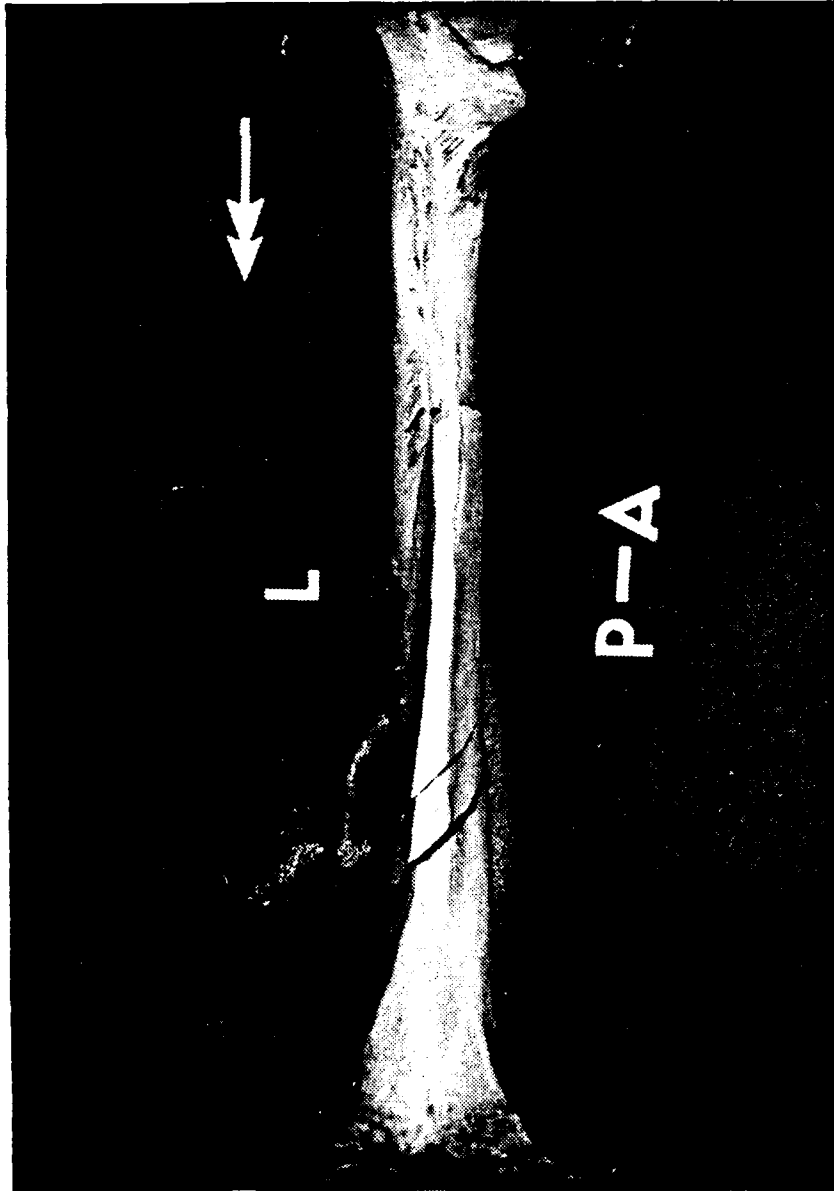


Figure 2.174 Fracture pattern posterior view.

material but, since only the maximum principal strain  $\epsilon_1$  is known, it is applicable. The principal stress  $\sigma_1$  is then:

$$\sigma_1 = \epsilon_1 E$$

$$\sigma_1 = 8.55 \text{ MPa}$$

From Figures 2.170 and 2.171 the angle of the principal strains was found to be 40-45°. This agrees very well with the 45° angle which would be expected from a pure torsion loading as shown in Figure 2.4.

### 2.3.8 Results

From Figure 2.170 it is seen that the lacquer cracks first occurred near the proximal end. The fracture pattern is a predominantly spiral fracture with a clamshell opening on the distal anterior surface as described in section 2.2.5.2. This fracture seemed to occur at about the distal third of the diaphysis opposite to the end from where it was expected to fracture considering the crack patterns in the lacquer coating. This discrepancy could be the result of several factors. The fracture may have started at the proximal third and propagated toward the distal end. Or, possibly, for this oddly shaped structure, the coating thickness was not constant and the first cracks occurred at a point which was not a point of the highest stress. Or, then again, the difficulty of spotting the cracks when they first appeared might have resulted in an incorrect determination of the regions of highest strain.

The results may have been improved if the lacquer coating were allowed to dry more thoroughly. Furthermore, the nonuniform thickness of the coatings could be accounted for by increasing the sample size and, thus, allowing a statistical analysis of the stress.

### 2.3.9 References

1. Tenslac Instruction Bulletin, TL-201.
2. Easley, John T.; CE 721 Class Notes; Summer 1981.

## 2.4 Scanning Electron Microscope (SEM) Study

### 2.4.1 Introduction

The main intent of the SEM study was to determine the primary micromechanical failure mode along particular fracture faces. Fracture configurations that are associated with tensile and shear states of stress were examined by removing sections from specific locations along the fracture line. Specifically, the spiral fractures resulting from pure torsion were not examined because they are known to be caused by tensile states of stress. Locations were selected that would typify tensile failures with planes parallel or transverse as well as normal to the osteons' axes. These were compared to fracture faces where shear was to be a suspected cause of failure. Finally, using conclusions drawn from the above, sections taken from fracture surfaces of unknown origin were examined for cause of failure.

### 2.4.2 Theory

Historically, engineers have expected certain types of loading conditions to cause particular stress states. Bending theoretically causes compression on the concave side of a deflected beam and tension on the convex side. Pure torsion causes pure shear in planes normal and parallel to the axis of rotation. Such shear will cause materials weak in tension (as is normally the case) to fail along spiral fractures (Figure 2.175). On the other hand, materials weak in shear will fail in planes normal and parallel to the axis of rotation when subject to torsion. Tension is associated with the parting of material planes and shear is associated with the sliding of material planes.

During the fracturing of the four human long-bones, possible shear fractures as well as the known tension fractures were observed under both bending and torsion conditions. During tests of bending only, fractures were observed that began on the tension side of the bending bone, normal to the neutral axis, and progressed, following a smooth curve, toward a plane that was parallel to the neutral axis. These fracture patterns could have been caused by one of two different types of stress states: (1) tension along the entire fracture line (Figure 2.176); (2) tension initially, as expected, progressing to shear and again ending in tension in the remaining bone area (Figure 2.176). For

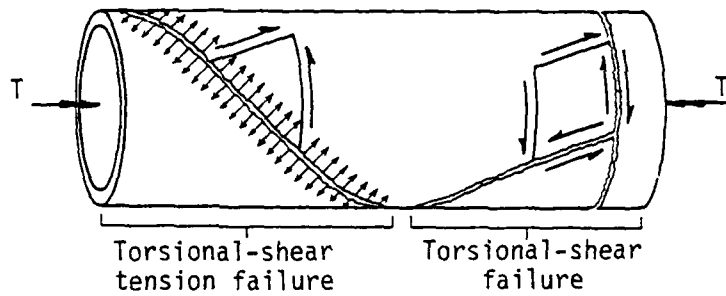


Figure 2.175 Fractures expected of tubular shapes subjected to pure torsion.

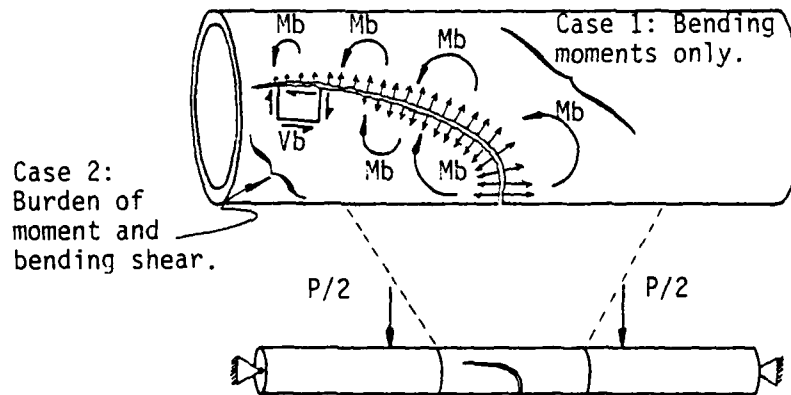


Figure 2.176 Fractures expected of tubular shapes under pure bending.

the second case to occur, the support conditions must change. Figure 2.177 shows that with four-point bending, there is zero shear between the center concentrated loads; the second case is impossible. However, as also shown in Figure 2.176, if, after the initial bending failure, the support now becomes the remaining material, the loading condition becomes three-point bending and shear exists across the entire loaded area. This is possible because immediately after the bending fracture has progressed to the neutral axis, the bone cannot, at that instant, resist the existing bending moment and a plastic hinge essentially forms momentarily in the remaining material. On the contrary, those fractures observed in the torsion only tests, that were parallel or normal to the torsional axis, could have been caused only by shear.

For either type of fracture, one can expect to observe osteons on the fracture face that have been separated along planes that are normal, parallel or oblique with respect to the osteon axis. However, the fractured osteons and lamellar (interstitial) bone should appear different for a tension state of stress than it would for a shear state. For a tension situation, the overall topography should appear irregular with the remnants of some osteons protruding away from the fractured surface and the remnants of others recessed into the surrounding lamellar bone. On the other hand, for shear one should expect rather flat surfaces since the sliding of one plane with respect to the other is difficult for fracture planes that are irregular. But, regardless of the overall surface appearance, the deciding factor should be the arrangement of the mineralized collagen fiber bundles. Since these bundles should be brittle and break easily under a bending load, any bundles that would have been pulled from their neighboring bundles by a tension force normal or oblique to the osteon axis should appear broken and pointing normal to the fracture surface. Likewise, any shear force acting normal to an osteon axis, should break these fiber bundles and bend them flat against the fracture plane if that plane is normal to the osteon axis. Furthermore, any tension fracture in a plane parallel to the osteon axis should show sheets of lamella pulled up and away from the fracture surface.

In order to determine whether shear failures occurred at such locations as discussed above, 21 SEM sections were cut from the four

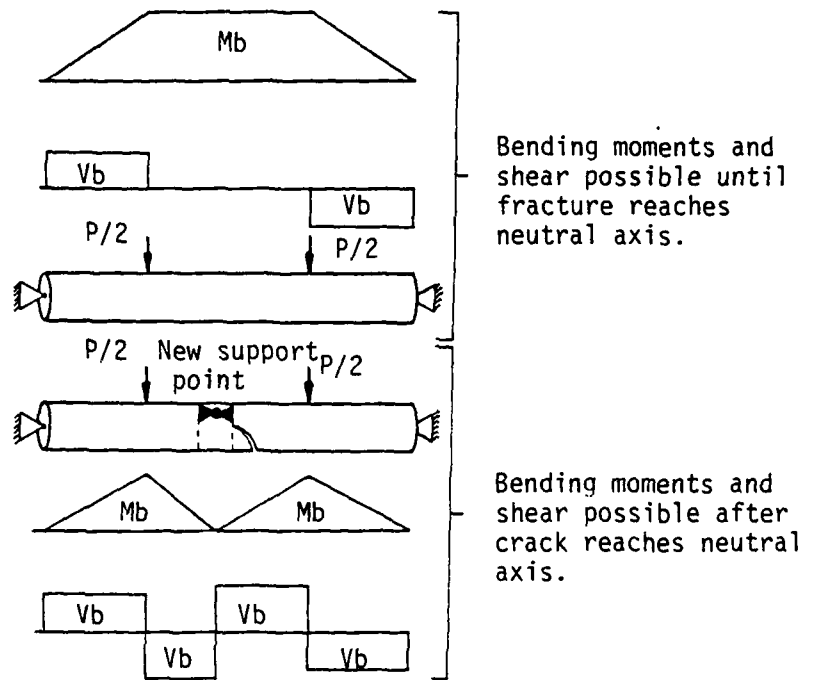


Figure 2.177 Change in support conditions during fracture causing shear between the loads in four point bending.

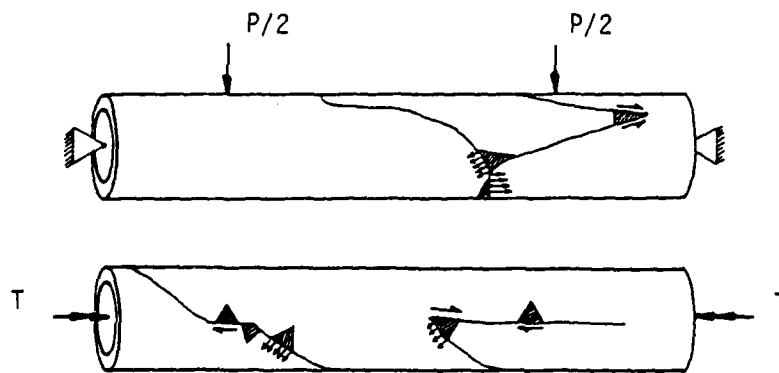


Figure 2.178 Schematic of the select SEM locations in the study.

long-bones at three specific locations along the fracture configurations (Figure 2.178). Eight sections were removed from areas known to involved tension; several were removed from those locations where shear was suspected to have caused failure; and, six were cut from locations where the state of stress was unknown. Figures 2.91 - 2.138 show the exact locations of these sections.

#### 2.4.3 Specimen Preparation

The 21 sections were removed from 20 fresh human long-bones which were fractured during the whole bone testing with the Osteoclast. Table 2.31 lists the bones along with the type of test performed and the type of failure surface expected.

Each section was cut from the surrounding hard tissue using a coping saw or a jewelers' saw depending on the delicacy of the situation. These specimens were cut generally 3 mm to 10 mm in overall length in order to remain in the viewing window of the SEM.

All sections were immediately and individually placed in 60 ml, capped bottles labeled with the bone number. Each jar contained five to ten drops of Ringer's to keep the fragment moist and maintain vapor pressure. The bottles were placed in a freezer within 30 minutes after the section was removed. They were not quick-frozen, since the soft tissues were not of interest.

The sections were prepared for the SEM as well as viewed at the University of Kansas Medical Center SEM laboratory. Initially the preparation was not to involve dehydration. However, during "pump down" of the gold coating chamber, it was realized that the specimens were too moist to achieve the vacuum necessary. Therefore the entire specimen preparation consisted of the following steps:

1. Degreasing in FREON 113 for 10 minutes.
2. Ultrasonic vibration in the FREON 113 for 20 minutes.
3. Dehydration in graded aqueous solutions of 30%, 70%, 80% and 95% ethanol (by weight) for 30 minutes at each grade followed by immersion in 100% ethanol for 16 hours.
4. Mounting on aluminum stubs using "double-sticky" tape.

Table 2.30 SEM sections.

<u>Section No.</u>	<u>Cadaver No.</u>	<u>Test Type</u>	<u>Suspected Fracture Surface</u>	<u>Suspected Fracture Plane</u>
1	RF 3753	Bend N	Tension	Normal
2	RF 3792	Bend M	Tension	Oblique
3	LF 3792	TOR	Tension	45° Oblique
4	RF 3787	CTW	Tension	Oblique
5	LT 3792	TOR	Tension	>45° Oblique
6	RT 3790	CTW	Shear	Parallel
7	LFb 3753	TOR	Shear	Parallel
8	RH 3793	TOR	Dubious	Dubious
9	LH 3790	CTN	Dubious	Dubious
10	LFb 3790	CTN	Dubious	Dubious
11	RT 3753	Bend N	Tension	Normal
12	RT 3793	TOR	Shear	Oblique
13	LT 3793	TOR	Shear	Parallel
14	RH 3753	TOR	Shear	Parallel
15	RH 3782	Bend N	Shear	Parallel
16	LH 3787	Rapid-bend	Tension	Normal
17	RFb 3793	TOR	Tension/Shear	Oblique
18	RFb 3792	Bend	Tension	Normal
19	RF 3790	CTW	Dubious	Dubious
20	RF 3787	CTW	Dubious	Dubious
21	RFb 3790	CTW	Dubious	Dubious

5. Gold coating in a TECHNICS gold coating chamber for 30 minutes at 100 millitorr and 100 mamps/10 volts D.C. (Note: This treatment should result in approximately 150 Å of gold coated.)

#### 2.4.4 Equipment/Technique

The specimens were examined in a JOEL, JSM-35 scanning electron microscope. All those specimens known to have failed under tension were examined first. Those expected to have failed in shear were examined next and those sections taken from a fracture location of unknown cause were examined last. Polaroid pictures with negatives were taken of all exemplary or unique sites. All repetitive observations were described in written records.

#### 2.4.5 Results

##### 2.4.5.1 Tension Surfaces

For those fracture surfaces known to be the result of a tension state of stress, the appearance was as theorized. Figure 2.179 shows an osteon photographed on a fracture surface of section number 1 which occurred in a plane normal to the osteon axis. Notice that the spicules (mineralized collagen fiber bundles) parallel to the osteon axis are sharp, slender and numerous. Compare these with those of the surrounding lamellar bone which do not run parallel to the osteon axis. These are more rounded in appearance with fewer sharp projections protruding from remaining material. On a lower magnification and larger scale, this type of fracture surface may have a highly stepped topography or the surface may be quite flat with some of the remaining osteons protruding from the surface and some recessed. Usually, if stepped, the fracture occurs along a fracture line that is oblique, but only at a slight angle, with the normal to the osteon axis. Figures 2.180(a) and (b) show such a plane as photographed on section number 2.

If the fracture is on a plane 45 deg. to the osteon axis, the surface appears as shown in Figures 2.181 and 2.182. Notice how these surfaces show large plates of lamella and lamellar bone pulled from the remaining material. Figure 2.181 contains photographs of the fracture surface from section number 2 where the bending has caused a tension



Figure 2.179 Osteon failing normal to its axis in a bending tension state of stress (section 1, 240x).

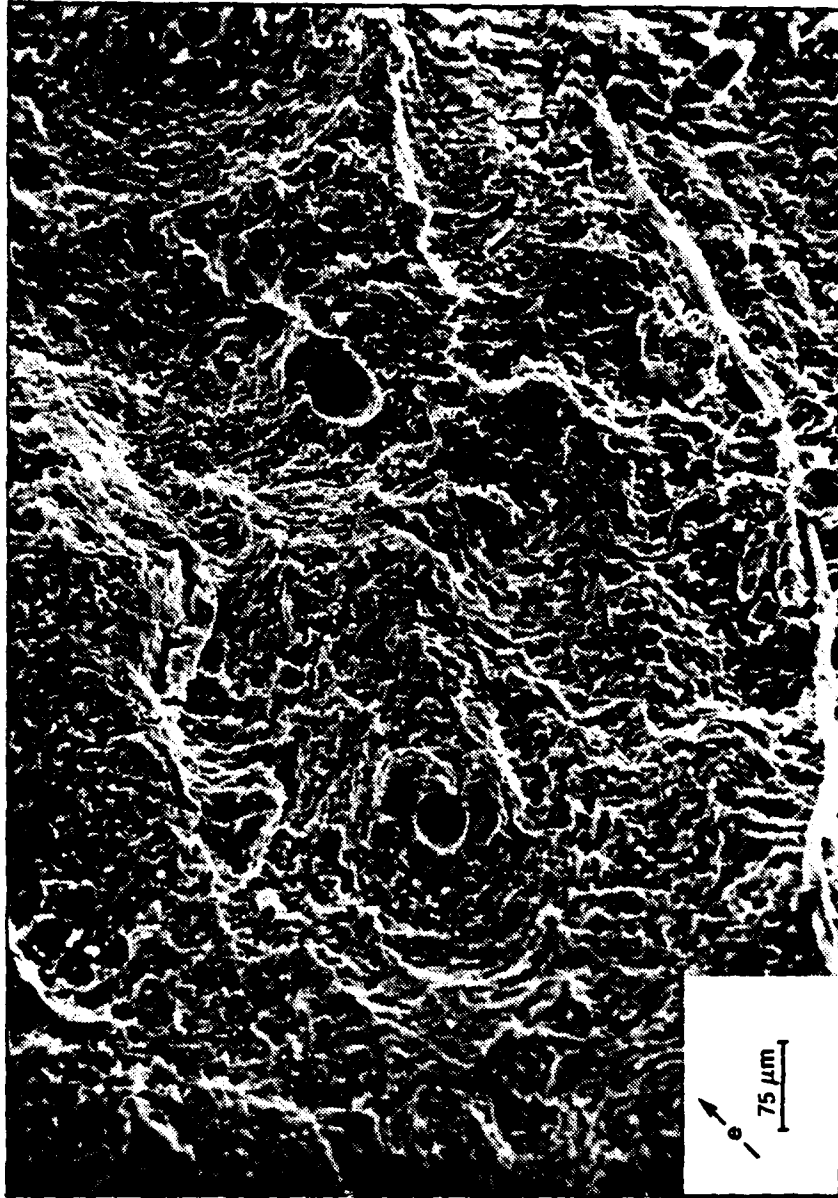


Figure 2.180(a) Stepped fracture surface caused by bending tension slightly oblique to the osteon axis (section 2, 100x).

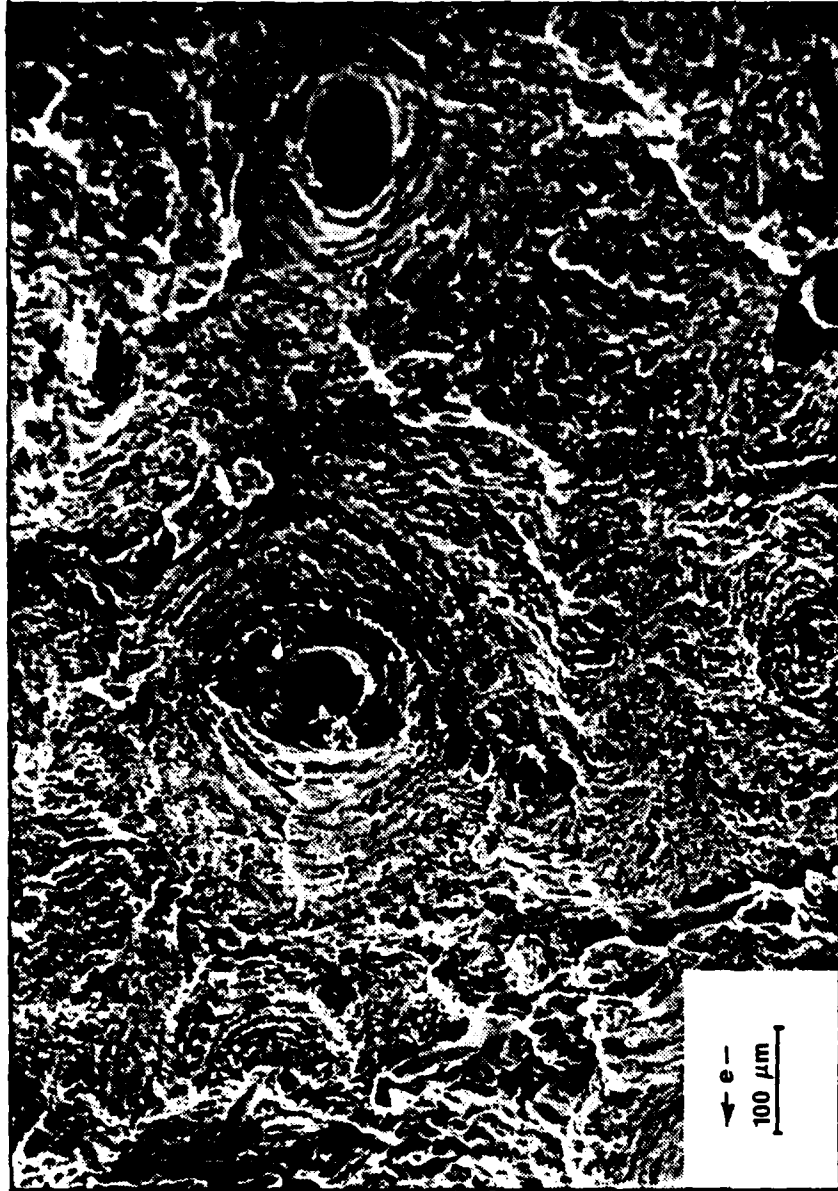


Figure 2.180(b) Stepped fracture surface caused by bending tension at a more oblique angle to the osteon axis (section 2 90x).



Figure 2.181(a) Bending tension fracture on a 45° plane to the osteon axes (section 2, 39X)..



Figure 2.181(b) Osteon in the frame in Figure 2.181(a) (150x).



Figure 2.182(a) Torsional-shear tension fracture on a 45° plane to the osteon axes (section 3, 75x).

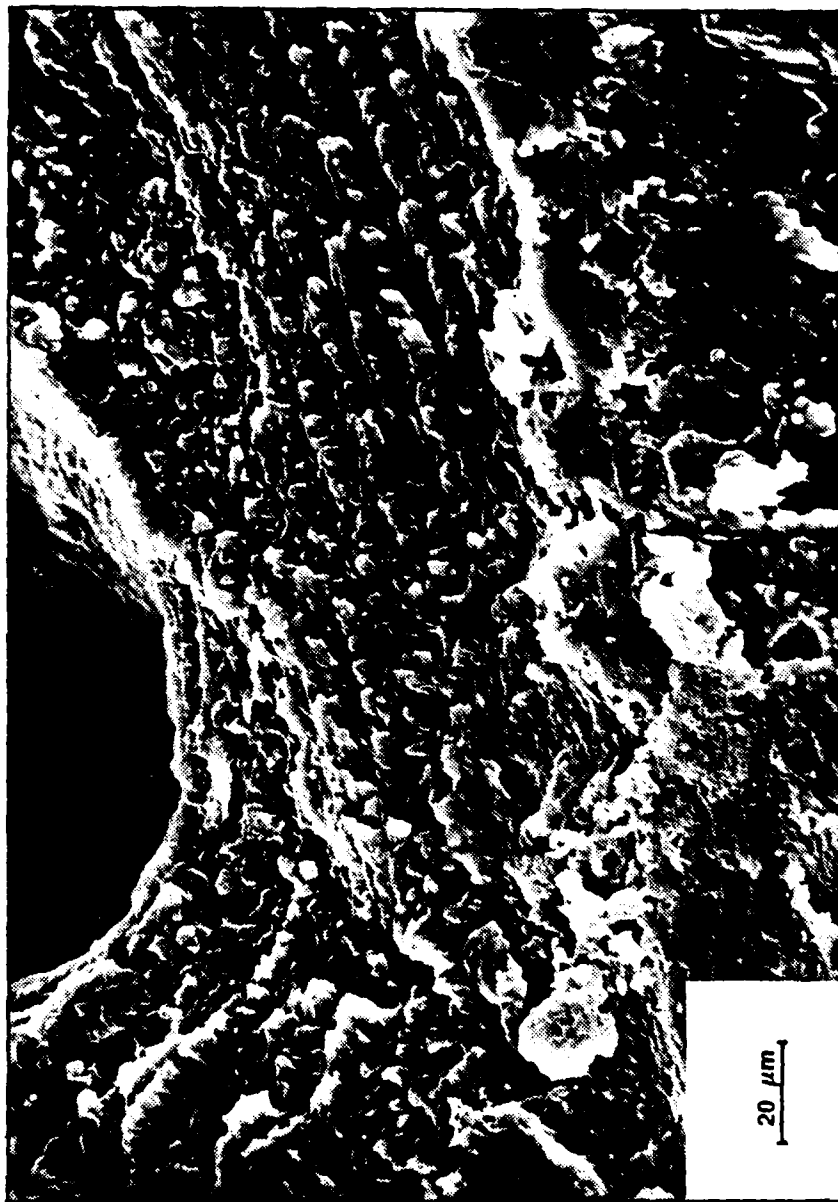


Figure 2.182(b) Osteon in the frame in Figure 2.182(a) (430x).

failure. Figure 2.182 contains photographs from section number 3 where the failure was caused by tension along a spiral fracture resulting from pure torsion. Notice in Figures 2.181(b) and 2.182(b) that the spicules are short and stubby and do not lie flat against the remaining material. If these two osteons had been photographed at a moderately acute angle to their planes, the bending of spicules would have appeared as in Figure 2.183 where they are definitely bent up and away from the fracture surface. This photograph was along a fracture surface that occurred at an angle greater than 45 deg. with the osteon axes and was caused by tension resulting from the bending that occurred in Section 4. A smaller magnification and larger scale view of this type of surface is shown in Figure 2.184 which was also the result of the tension associated with bending.

#### 2.4.5.2 Shear Surfaces

For the fractures surfaces that were suspected to be the result of shear, the appearances were again as theorized. Figure 2.185 shows the fracture surface that is parallel to the osteon axes. This fracture is believed to be the result of shearing forces rather than tensile forces because of its topography as well as because of its orientation with respect to bone axis. The section was removed from a segment of the fracture line of Section 5 which resulted from pure torsion and was parallel to the torque vector (Figure 2.178). Its fracture surface at a smaller magnification and on a larger scale is flat. Notice in Figure 2.185(a) that fiber bundles in the lamellar bone appear to have been pulled from the surrounding material in the direction of the arrow (depicted in the photograph) which is direction that this surface would have moved due to shearing forces existing at the time of failure. Now, granted, at the top of Figure 2.185(a) and within the cement line of the osteon in Figures 2.185(a) and (b) the spicules indicated movement normal to the surface; however, this movement could have occurred after the initial movement parallel to the surface as the fracture continued toward the distal end (refer to Section 2.2.2) in a tension mode. In other words, the mating surfaces initially slid with respect to each other until weakened and then opened up under the influence of the tensile forces.

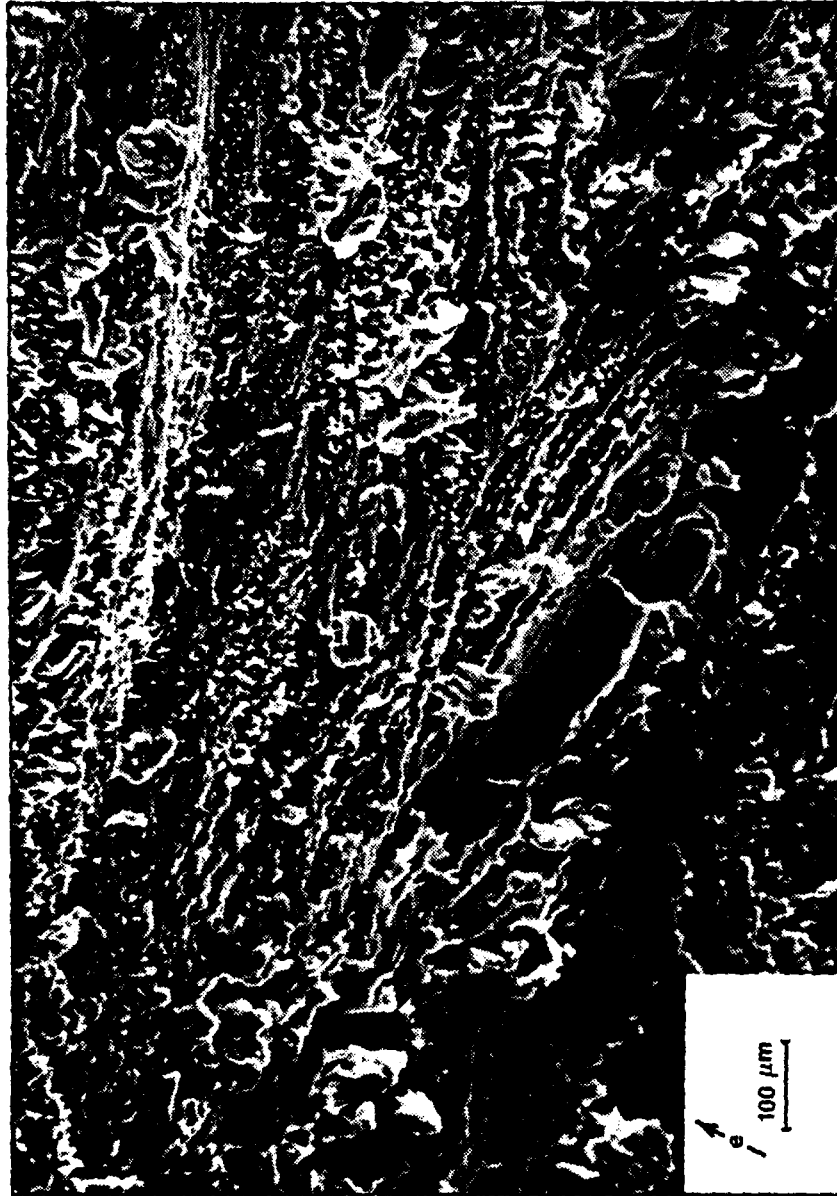


Figure 2.183 Tilted view of a bending tension's failure on an oblique plane to the osteon axes (section 4, 75x).

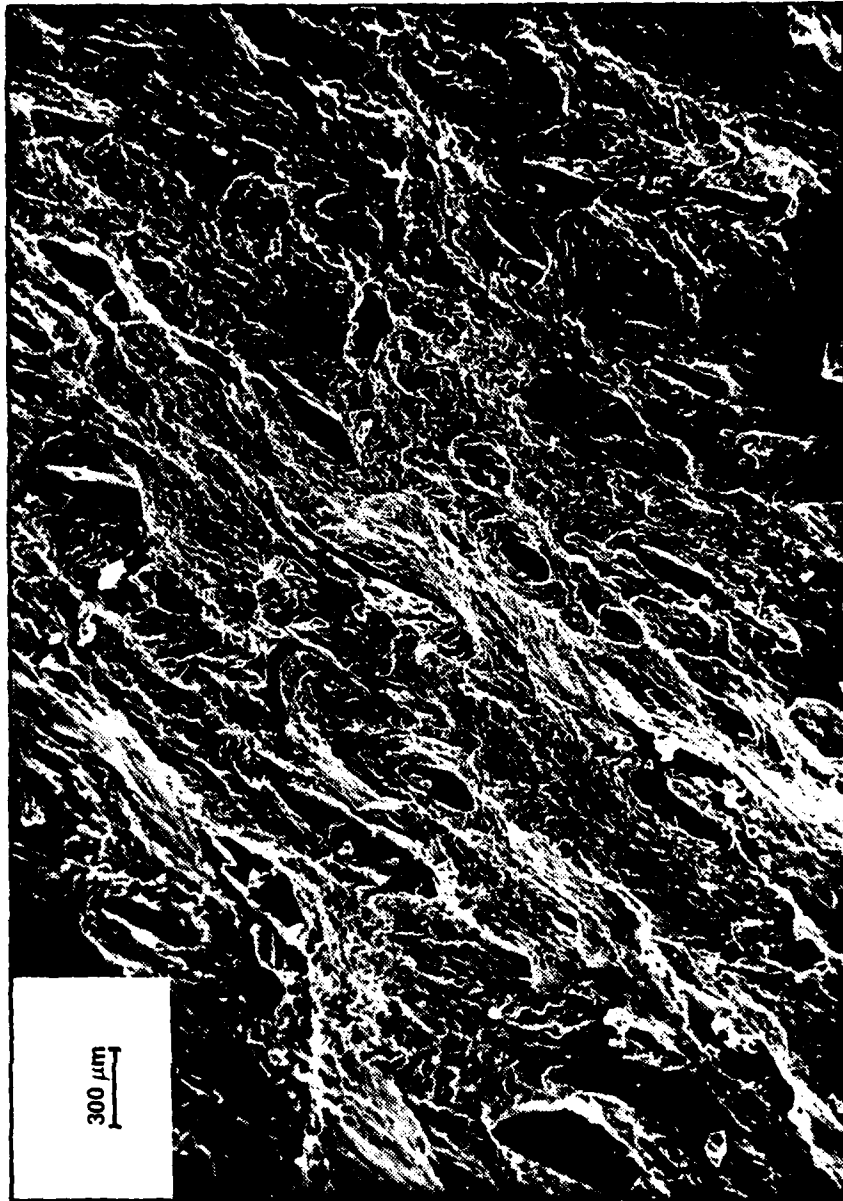


Figure 2.184 Larger scale view of a torsion-shear tension failure on a plane greater than  $45^\circ$  to the osteon axes (section 5,24x).

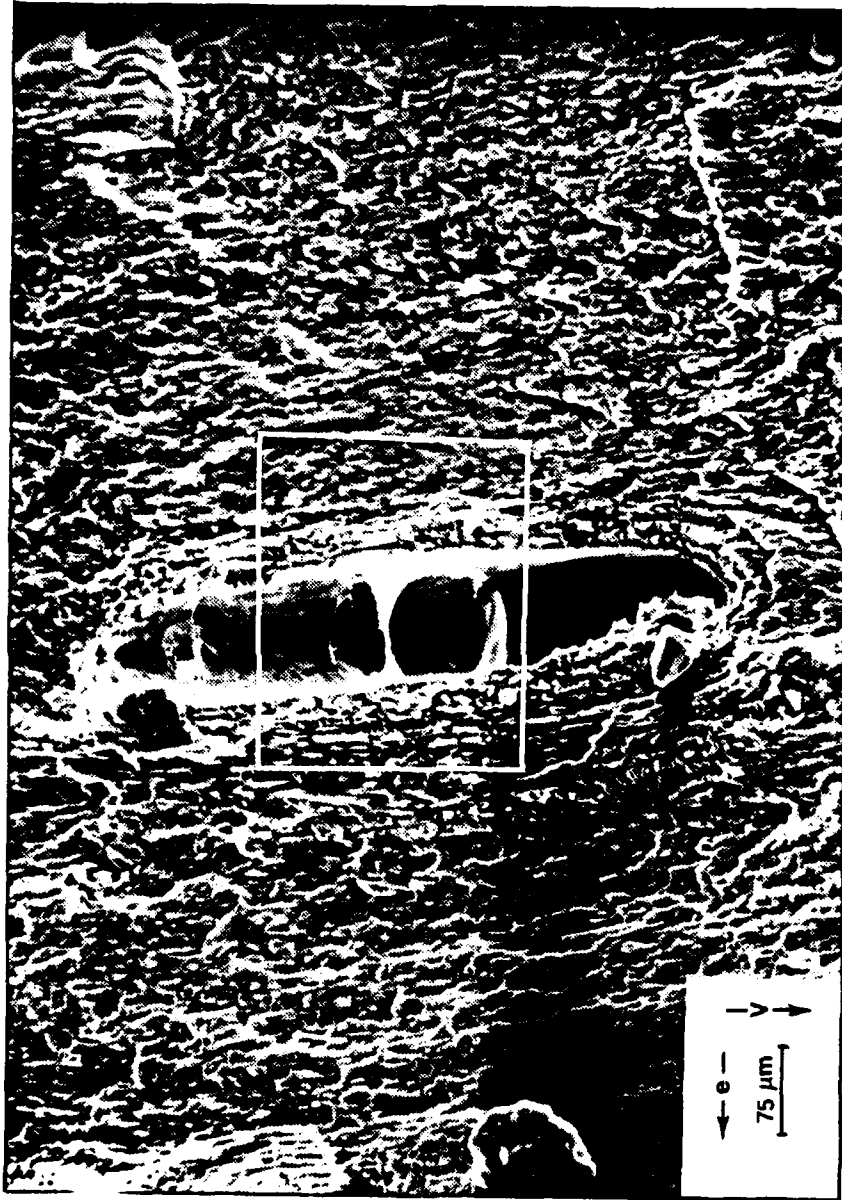


Figure 2.185(a) Shear failure parallel to the osteon axes (section 6, 100x).



Figure 2.185(b) Osteon in the frame of Figure 2.185(a) (320x).

Figure 2.186 also shows a fracture surface that is believed to be the result of shearing forces. This section, number 6, was removed from a fracture location similar to that of Section 5 above -- parallel to the torque vector. Again these two photographs of different locations along the section surface imply, for reasons discussed above, the slippage of material planes rather than their pulling apart. The arrows in the figure show the directions of movement of the surfaces that would have resulted from the shearing forces possible during the torsional loading.

#### 2.4.5.3 Fracture Surfaces of Unknown Origin

After examining those fractures surfaces known to be caused by a tension state of stress and those suspected of shear, the sections cut from locations of unknown states of stress were scanned. Of these six sections, the modes of failure of five were proposed and these are listed in Table 2.32. The sixth was covered with a film that obscured the surface details and, therefore, the mechanical reason for the fracture was indiscernable.

Of special interest was section number 7. This section occurred at a location along the fracture configuration where a shear face met a tension face. The fracture occurred as the result of pure torsion. Figure 2.187 shows an osteon on the tension face. Notice that the surrounding lamellar bone has the characteristics associated with a tensile force acting on an oblique plane to the osteon axis. Figure 2.187(b) - (e) shows the mineralized collagen fiber bundles of the endosteal lamella. Figure 2.187(f) shows the broken fiber bundles of this lamellae along the fracture plane.

Figure 2.188 shows the fracture surfaces of section number 8 caused by tensile forces of a combined loading condition. Figure 2.189 shows a probable shear surface from section number 9 which occurred during a combined loading condition.



Figure 2.196(a) Shear in a plane parallel to the osteon axes (section 7, 110x).



Figure 2.186(b) Shear in a plane parallel to the osteon axes in lamellar bone (section 7, 150x).

Table 2.31 Proposed causes of fracture surfaces of unknown origin.

<u>Section No.</u>	<u>Cadaver No.</u>	<u>Test Type</u>	<u>Fracture Surface</u>	<u>Fracture Plane</u>
8	RH 3793	TOR	Tension/shear	Oblique
9	LH 3790	CTN	Tension	Normal
10	LFb 3790	CTN	Shear	Oblique
19	RF 3790	CTW	Tension	Oblique
20	RFb 3790	CTW	Tension/shear	Normal/ parallel
21	RF 3787	CTW	Indiscernable	



Figure 2.187(a) Osteon on a torsion-shear tension face (section 8, 100x).



Figure 2.187(b) End of the same osteon, 220x.



Figure 2.187(c) End of the same osteon, 1000x.



Figure 2.187(d) Endosteal lamella showing mineralized collagen fiber bundles (section 8, 5000x).



Figure 2.187(e) Mineralized collagen fiber bundles (section 8, 11,000x).



Figure 2.187(f) Fractured end of mineralized fiber bundles (section 8, 9000x).

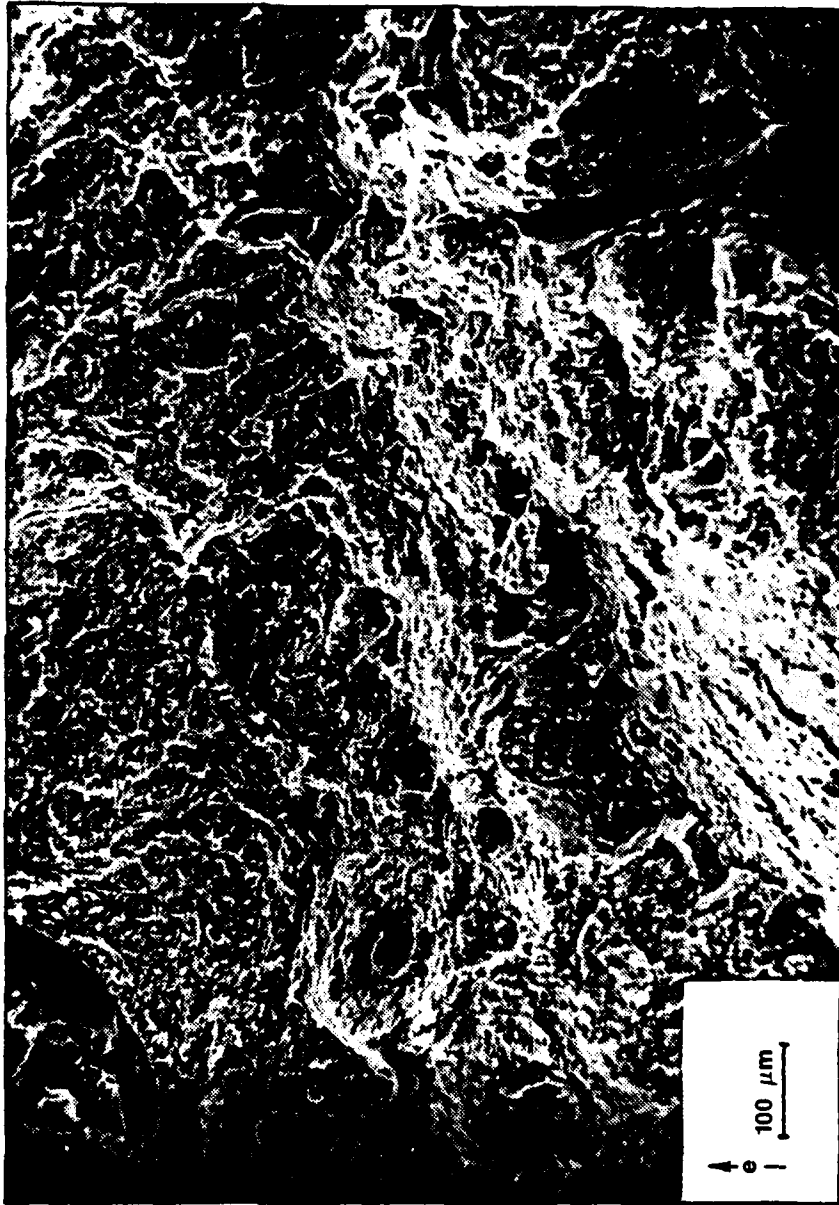


Figure 2.188(a) Bending tension failure along a 45° plane (section 9, 80x).



Figure 2.188(b) Bending tension failure along a plane less than 4° to the osteon axes (section 9, 75x).

AD-A111 090

KANSAS UNIV/CENTER FOR RESEARCH INC LAWRENCE.  
MECHANICAL PROPERTIES OF FOUR HUMAN LONGBONES. (U)  
NOV 81 C R KULP, H W SMITH, H C ANDERSON

F/8 6/16

F49620-79-C-0183

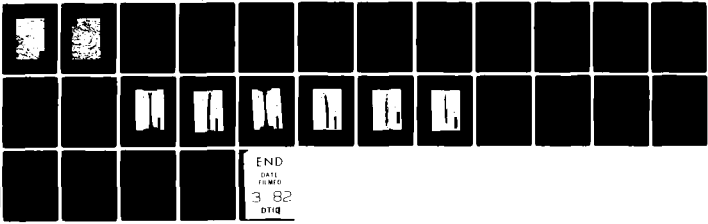
AFOSR-TR-82-0040

NL

UNCLASSIFIED

5 of 5

AD-A11-090



END

DATE

FILMED

3 82

DTIC

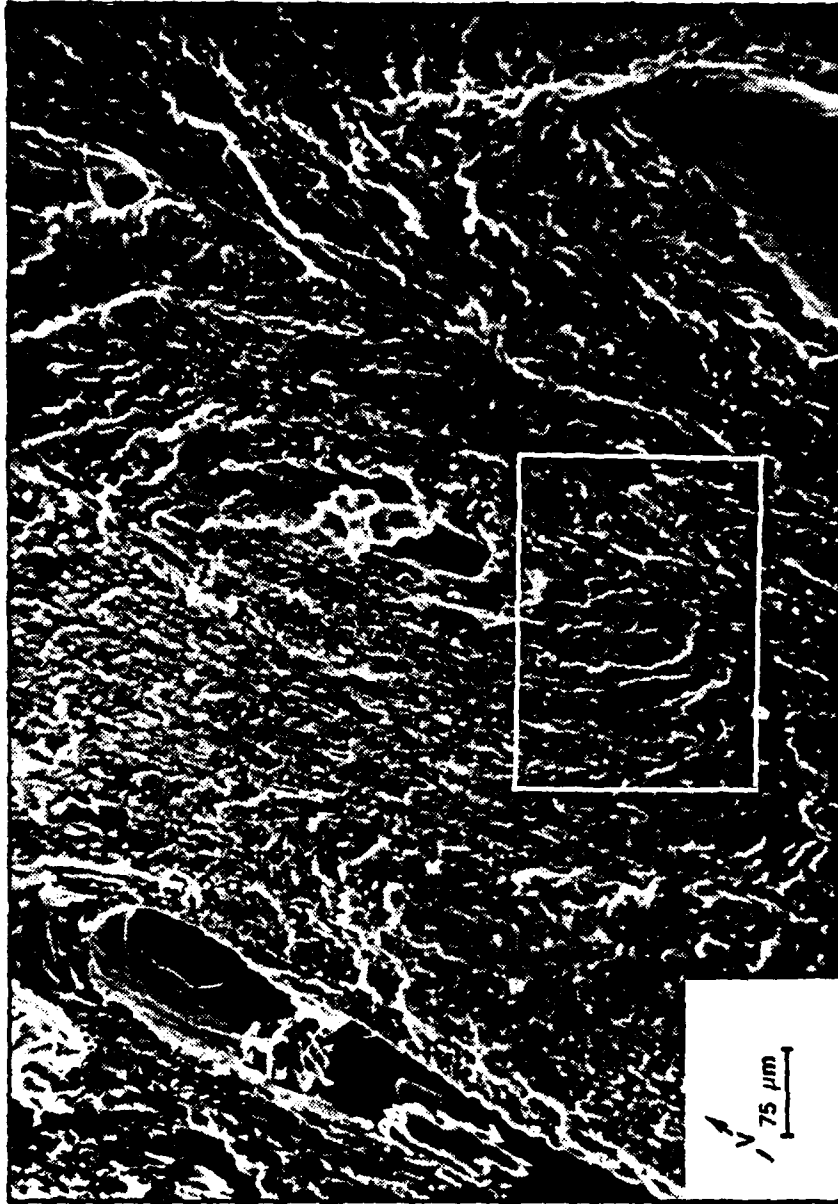


Figure 2.189(a) Shear fracture 45° to the osteon axes (section 10, 100x).

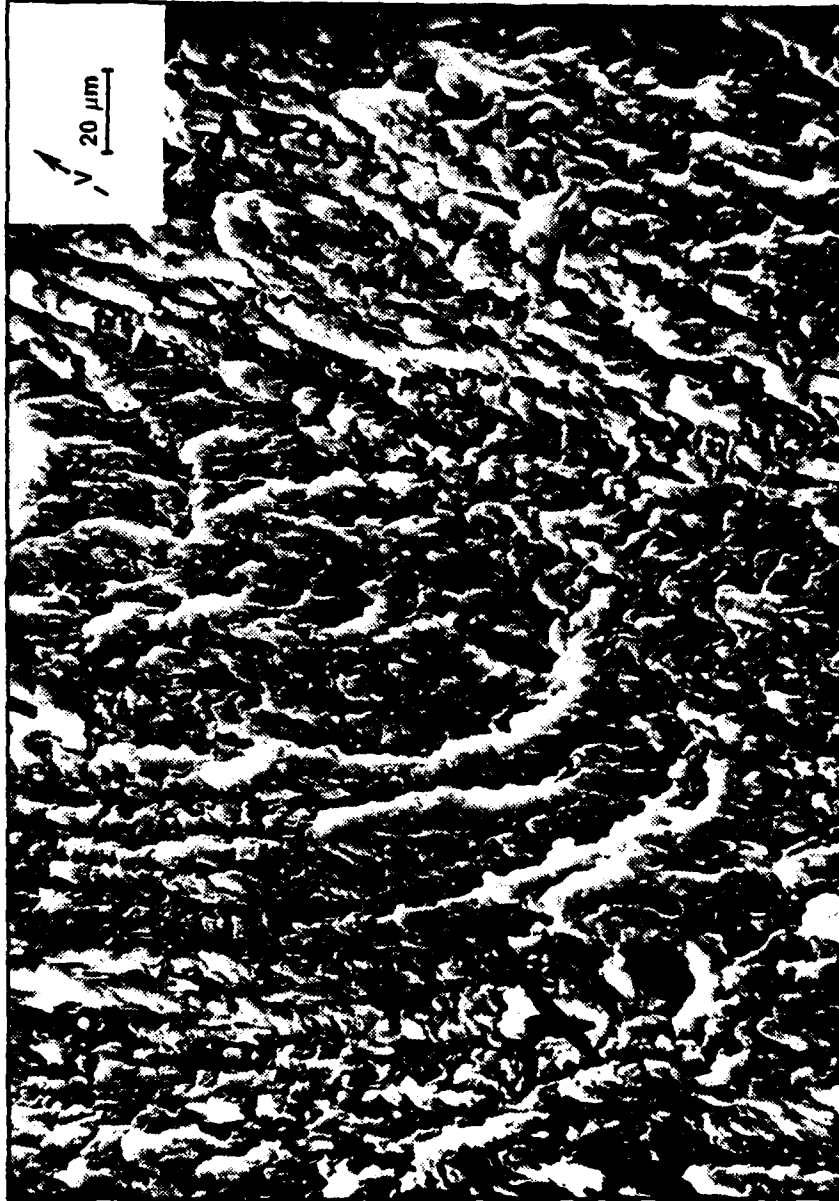


Figure 2.189(b) Lamellae within the frame in Figure 2.193(a) (360x).

## 2.5 Medical Analysis

### 2.5.1 Methods

Left and right femora, tibiae, humeri and fibulae were resected, fresh at autopsy, from six cadavers at the Kansas University Medical Center. The bones were frozen immediately and remained essentially in a frozen state until they were fractured in the Osteoclast. Following fracture, slabs of cortical bone, near the fracture faces, were dehydrated and ashed to determine ash weight, water content, and amounts of Ca and  $PO_4$  or they were acid hydrolyzed and analyzed for protein and hydroxproline content. Undecalcified micro-sections of cortical bone were also analyzed morphometrically for porosity. Table 2.32 lists the personal data for the cadavers involved in the study.

#### 2.5.1.1 Mineral Content

The samples were initially placed in an oven for 48 hours at 105°C to remove water. Weights were measured before and after this procedure to determine the water content of the samples. The samples were then placed in a muffle furnace for 48 hours at 750°C. Again the weight of the samples was measured and the mineral content of the bone calculated. The ash was analyzed for the amount of calcium and phosphate.

1. Calcium content: The ash was dissolved in a minimal amount of 6N hydrochloric acid. Distilled water was added to make a 10 ml stock solution. A 1:100 dilution of the stock solution was made and the calcium level determined by a direct method based on the o-cresolphthalein complexation reaction [1]. All reagents and standards for this assay were supplied by Sigma Chemical Company.

2. Phosphate content: The 10 ml stock solution was diluted 1:1000. Phosphate levels were then measured by a spectrophotometric assay [2].d

#### ACID HYDROLYSIS:

Bone samples were dried for 48 hours at 105°C and then hydrolyzed in 6N hydrochloric acid overnight at 110°C. A flask evaporation technique was employed to remove the acid. The subsequent washes with distilled water were used to insure that the acid had totally been

Tables 2.32. Personal Data of Human Subjects

Cadaver No.*	Age (years)	Sex	Race	Height (cm)	Weight (N)
3753	32	F	W	162.6	489-511
3793	64	M	W	184.2	734
3790	54	M	W	177.8	778
3782	61	F	W	--	2002
3792	63	M	W	172.7	712
3787	58	M	W	182.8	801

\*These numbers are control numbers assigned by the Anatomy Department at the Kansas University Medical Center. When prefixed by the side and bone type abbreviation, they refer to the specimen numbers used throughout the study.

removed, and would not effect pH sensitive assays. The total residue was solubilized in distilled water to a total volume of 10 ml.

1. Protein content: Total protein levels were determined in the 10 ml stock solution by the Lowry method [3].

2. Hydroxyproline content: The spectrophotometric method of Woessner was used [4]. A 50  $\mu$ l sample of the 10 ml stock was added to 500  $\mu$ l of distilled water. 250  $\mu$ l of a chloramine-T solution was added and mixed well then left at room temperature for 20 minutes. Next, 250  $\mu$ l of 3.15M perchloric acid was added and mixed well then left at room temperature for 5 minutes. Finally 250  $\mu$ l of 20% P-dimethylamino-benzaldehyde was added and mixed then left at room temperature overnight. The next day the absorbancies at 565 nm were determined for the samples, blanks and standards (100 mg/ml, 75 mg/ml, 50 mg/ml, 35 mg/ml).

For histological study, the bone samples were embedded in a methyl methacrylate medium and were sectioned by a Jung Model K Sledge microtome. A modified Masson stain was then applied. The bone microstructure was then studied by bone morphometry, more specifically the porosity of the cortex and determination of cortical width.

## 2.5.2 Results

### 2.5.2.1 Bone Ash

The ashing data for the bone specimens analyzed showed very little variation from bone to bone or from donor to donor (Table 2.33). Water content was approximately 10% in our specimens and ash content was approximately 65%. This is comparable to what has been determined for normal mammalian bones by other investigators using similar techniques [5-7]. The mean Ca/PO<sub>4</sub> molar ratio was approximately 1.65 which would fit for most mineral being Present as hydroxyapatite whose theoretical Ca/PO<sub>4</sub> ratio is 1.67.

### 2.5.2.2 Protein and Hydroxyproline Content

Table 2.34 shows that the average fraction of total bone content consisting of protein was remarkable consistent at approximately 25.4 mg/g of dehydrated bone, and that hydroxyproline, a specific amino acid of collagen, was prominent.

Legends for Table 2.33

ASHING DATA

RH - Right Humerus  
LH - Left Humerus  
RF - Right Femur  
LF - Left Femur  
RT - Right Tibia  
LT - Left Tibia  
RFb - Right Fibula  
LFb - Left Fibula

Sample weight, Sample minus H<sub>2</sub>O, and Ash weight in grams

Sample minus H<sub>2</sub>O weight recorded after 48 hours at 105°C

Ash weight recorded after 48 hours at 750-800°C

% H<sub>2</sub>O = (Sample) - (Sample - H<sub>2</sub>O) / Sample x 100

% Ash = Ash / Sample H<sub>2</sub>O x 100

PO<sub>4</sub> and Ca-weight in grams as determined spectrophotometrically

Ca/PO<sub>4</sub> = moles of PO<sub>4</sub> / moles of Ca

Table 2.33 Ashing Data.

Sample Identity	Sample Weight	Sample minus H <sub>2</sub> O	Ash weight	% H <sub>2</sub> O	% ASH	PO <sub>4</sub>	Ca	PO <sub>4</sub> /ASH X 100	Ca/ASH X 100	Ca/PO <sub>4</sub>
3753-RH	0.4825	0.4314	0.2847	10.6	66.0	0.145	0.105	50.9	36.9	1.47
3753-LH	0.4607	0.4136	0.2757	10.2	66.7	0.146	0.0936	53.0	33.9	1.52
3753-RF	1.1448	1.0389	0.7174	9.2	69.1	0.3490	0.258	52.7	36.0	1.63
3753-LF	0.6196	0.5528	0.3589	10.8	64.9	0.2137	0.123	59.6	34.3	1.32
3753-RT	0.5703	0.5148	0.3293	9.7	64.0	0.2268	0.230	53.5	33.7	1.52
3753-LT	0.4167	0.3759	0.2395	9.8	63.7	0.1410	0.087	58.9	36.3	1.54
3753-RFb	0.1065	0.0974	0.0626	8.5	64.3					
3753-LFb	0.1635	0.1490	0.0990	8.9	66.4	0.0623	0.031	62.9	30.8	1.20
3782-RH	0.6344	0.5596	0.3623	11.8	64.7	0.1710	0.126	47.2	34.8	1.75
3782-LH	0.3619	0.3260	0.2171	9.9	66.6	0.1319	0.0752	60.8	34.6	1.36
3782-RF <sup>1</sup>	0.8400	0.7388	0.4632	12.0	62.7	0.2338	0.1776	50.5	38.4	1.82
3782-RF <sup>2</sup>	0.7995	0.6988	0.4540	12.6	64.9	0.2109	0.1725	46.5	38.0	1.96
3782-RF <sup>3</sup>	0.6371	0.5567	0.3651	12.6	65.6	0.1943	0.1431	53.2	39.2	1.75
3782-LF	1.0849	0.9721	0.6614	10.4	68.0	0.3225	0.230	48.8	34.8	1.69
3782-LT	0.5671	0.5137	0.3283	9.4	63.9	0.1616	0.1219	49.2	37.2	1.75
3782-RT	0.6464	0.5874	0.3803	9.4	64.7	0.1689	0.1443	44.4	37.9	2.04
3787-RH	0.3018	0.2711	0.1724	10.2	63.6	0.0864	0.0611	50.1	35.4	1.69
3787-LH	0.4485	0.4055	0.2490	9.6	61.4	0.1336	0.0929	53.7	37.3	1.64
3787-RF	0.5530	0.4962	0.3210	10.3	64.7	0.1800	0.1167	56.1	36.3	1.54
3787-RT	1.6485	1.4880	0.9816	9.7	65.9	0.4855	0.3780	49.5	38.5	1.85
3787-LF	0.5353	0.4837	0.2866	9.6	59.3	0.1354	0.1042	47.3	36.3	1.82
3787-LT <sup>1</sup>	0.6697	0.5985	0.2871	10.6	48.0	0.1359	0.1090	47.3	37.9	1.89
3787-LT <sup>2</sup>	0.7193	0.6402	0.3737	11.0	58.4	0.1907	0.1435	51.0	38.4	1.75
3787-RFb	0.2334	0.2117	0.1306	9.3	61.6	0.0631	0.0433	48.3	33.1	1.64
3787-LFb	0.1310	0.1192	0.0748	9.0	62.8	0.0358	0.0221	47.9	29.6	1.47
3790-RH	0.4259	0.3841	0.2506	9.8	65.2	0.1296	0.0962	51.7	37.4	1.72
3790-LH	0.7923	0.7037	0.4431	11.2	63.0	0.2210	0.1680	49.9	37.9	1.82
3790-RF	0.7464	0.6708	0.4242	10.1	63.2	0.2134	0.1490	50.3	35.1	1.67
3790-LF	0.3736	0.3240	0.1903	13.3	58.7	0.0996	0.0698	52.3	36.6	1.67
3790-RT	0.7191	0.6512	0.4025	9.4	61.8	0.2393	0.1492	59.5	37.1	1.49
3790-LT	0.5874	0.5322	0.3287	9.4	61.8	0.1516	0.1290	46.1	39.1	2.00
3790-RFb	0.2119	0.1927	0.1246	9.1	64.7	0.0619	0.0418	46.0	33.6	1.72
3790-LFb	0.1425	0.1296	0.0822	9.1	63.4	0.0409	0.0269	49.8	33.0	1.56
3792-RH	0.2659	0.2400	0.1586	9.7	66.1	0.0825	0.0535	51.9	33.7	1.54
3792-LH	0.7485	0.6714	0.4373	10.3	65.1	0.2190	0.1560	50.1	35.7	1.69
3792-RF	0.2855	0.2527	0.1656	11.5	65.5	0.0962	0.0616	58.1	37.2	1.52
3792-LF	1.4052	1.2705	0.8419	9.6	66.3	0.4389	0.305	52.1	36.2	1.64
3792-RT	0.2250	0.2008	0.1310	10.8	65.2	0.0698	0.0491	53.3	37.5	1.67
3792-LT	0.4722	0.4280	0.2769	9.4	64.7	0.1362	0.1027	49.2	37.2	1.79
3792-RFb	0.2629	0.2386	0.1545	9.2	64.8	0.0790	0.0528	51.2	34.2	1.59
3792-LFb	0.4000	0.3636	0.2255	9.1	62.0	0.1160	0.0780	51.4	34.6	1.59
3793-RH	0.5606	0.5007	0.3072	10.7	61.4	0.1640	0.1158	53.4	37.7	1.67
3793-LH	0.4075	0.3673	0.2302	9.9	62.7	0.1190	0.0790	51.7	34.3	1.59
3793-RF	0.3329	0.2954	0.1885	11.3	63.8	0.1044	0.0695	55.4	36.8	1.59
3793-LF	1.0291	0.9253	0.5815	10.1	62.8	0.2840	0.2110	48.9	36.3	1.75
3793-RT	0.5678	0.5146	0.3280	9.4	63.7		0.1223		37.3	
3793-LT	0.7738	0.6987	0.4630	9.7	66.3	0.2430	0.1800	52.5	38.9	1.75
3793-RFb	0.1458	0.1335	0.0834	8.4	62.5	0.0460	0.0295	55.2	35.5	1.54
3793-LFb	0.2500	0.2264	0.1503	9.4	66.4	0.0751	0.0490	49.9	32.6	1.56

Legends for Table 2.34

ACID HYDROLYSIS DATA

Sample minus  $H_2O$  - weight in milligrams after 48 hours at  $105^{\circ}C$ .

Hydroxyproline and Protein weight in milligram was spectrophotometrically determined.

Table 2.34 Acid Hydrolysis Data

Sample Identity	Sample minus-H <sub>2</sub> O	Hydroxyproline	Protein	OH-proline + sample weight	Protein + sample wt.
3753-RH	14.1	0.4407	0.3033	31.0	22.0
3753-LH	15.1	0.5258	0.3984	35.0	26.0
3753-RF	24.3	0.7195	0.6045	30.0	25.0
3753-LF	21.7	0.2670	0.6589	12.0	30.0
3753-RT	26.0	0.2618	0.7334	10.0	28.0
3753-LT	29.8	0.9028	0.8607	30.0	29.0
3753-RFb	19.0	0.6237	0.4951	33.0	26.0
3753-LFb	22.8	0.7283	0.6411	32.0	28.0
3782-RH	16.7	0.5131	0.3620	31.0	22.0
3782-LH	38.6	1.0985	1.2145	29.0	31.0
3782-RF(1)	23.0	0.6608	0.5282	29.0	23.0
3782-RF(2)	23.2	0.6761	0.5516	29.0	24.0
3782-RF(3)	22.9	0.6655	0.5389	29.0	23.0
3782-LF	28.7	1.0628	0.8371	37.0	29.0
3782-RT	19.0	0.5721	0.4180	30.0	22.0
3782-LT	19.6	0.6488	0.4932	33.0	25.0
3787-RH	29.8	0.9468	0.8629	32.0	29.0
3787-LH	33.8	0.9624	0.8784	29.0	26.0
3787-RF	20.5	0.6543	0.5187	32.0	25.0
3787-LF	25.2		0.6123		24.0
3787-LT(1)	26.0	0.7743	0.6025	30.0	23.0
3787-LT(2)	31.2	0.9315	0.7117	30.0	25.0
3787-RFb	19.9	0.6174	0.4983	31.0	25.0
3787-LFb	21.3	0.6496	0.5675	31.0	27.0
3787-RT	19.5	0.2117	0.7579	11.0	38.0
3790-RH	30.3	0.9257	0.6556	31.0	22.0
3790-LH	15.4	0.5234	0.3661	34.0	24.0
3790-RF	22.3	0.6900	0.6184	31.0	28.0
3790-LF	22.4	0.6549	0.5456	29.0	24.0
3790-RT	23.4	0.0900	0.3125	08.0	13.0
3790-LT	25.4	0.1983	0.6089	08.0	24.0
3790-RFb	34.6	0.0088	0.9236	29.0	27.0
3790-LFb	30.5	0.9626	0.8093	32.0	27.0
3792-RH	19.0	0.9219	0.6250	30.0	32.0
3792-LH	24.9	0.7158	0.6089	29.0	24.0
3792-RF	33.3	0.9507	0.8436	29.0	25.0
3792-LF	30.6		0.7120		23.0
3792-RT	31.0	0.9219	1.2713	30.0	41.0
3792-LT	25.5	0.2206	0.7513	09.0	29.0
3792-RFb	52.3	1.4571	1.4184	28.0	27.0
3792-LFb	25.2	0.7585	0.5971	30.0	24.0
3793-RH	18.8	0.5777	0.4303	31.0	23.0
3793-LH	13.7	0.4245	0.2500	31.0	18.0
3793-RF	28.7	0.8735	0.8245	30.0	29.0
3793-LF	11.8	0.3708	0.2193	31.0	19.0
3793-RT	26.2	0.0900	0.3125	08.0	13.0
3793-LT	18.1	0.5496	0.3627	30.0	20.0
3793-RFb	23.9	0.7232	0.6196	30.0	26.0
3793-LFb	23.3	0.6971	0.6512	30.0	28.0

### 2.5.2.3 Morphometric Analysis

Measurements of cortical bone porosity and thickness by MOP-3 analysis (Table 2.35) show that the variation in porosity from site to site and from bone to bone is fairly high. The usual porosity, i.e. the percentage of sectioned surface occupied by Haversian spaces and other non-mineralized substituents of the bone, varied from approximately 6.9% to 8.8%, and there were no statistically significant differences from bone to bone.

As would be anticipated, the mean cortical thickness varied significantly from one type of bone to another, so that, for example, mean cortical thickness of fibulas (approximately 2.01 mm) is significantly less than mean cortical thickness of femurs (approximately 4.62 mm), etc. Only the mean cortical width of humeri was not significantly different from that of tibias, but since these are bones with similar overall dimensions, a lack of difference is not too surprising.

### 2.5.3 Discussion

Uniformity of bone composition from specimen to specimen, the similarity of bone composition to what has been reported as normal [6,7], and the lack of great variation in cortical porosity suggests that the human bones donated for this study were similar enough to be compared as to their mechanical properties.

The testing of mechanical properties was carried out by Professor Smith's lab at Lawrence. Since the bones were very similar in composition and structure, it has not been possible to relate variations in mechanical resistance or variations in fracture site to the composition and structure of individual bones.

It is notable that when the induced fracture sites were examined by scanning electron microscopy, the surfaces showed changes involving shearing as well as a tension characteristic (Kulp, et al., unpublished data). Exactly the opposite has been observed and reported by others in animal bones which were mechanically stressed to the point of fracture. This observation represents a very interesting difference, and should be studied further.

Table 2.35 % Porosity and cortical width (analyzed by MOP 3)

	<u>Position</u>	<u>Humerus</u>	<u>% Porosity</u>	<u>Mean Width (mm)</u>
3753 RH	.11P		5.27	2.76
3753 LH	.03P		3.67	3.02
3782 RH	.03P		4.40	3.55
3782 LH	.11P		4.28	3.34
3787 RH	.21P		5.74	3.27
3787 LH	.03P		10.30	3.05
3790 RH	.03P		14.00	5.43
3790 LH	.21P		5.75	4.18
3792 RH	.02P		9.02	4.07
3792 LH	.11P		12.12	3.63
3793 RH	.11P		6.49	3.43
3793 LH	.21P		4.51	2.57
		<u>Femur</u>		
3753 RF	.07D		2.91	4.80
3753 LF	.34D		6.95	3.44
3782 RF(1)	.53D		6.27	3.15
3782 RF(2)	.35D		7.28	4.67
3782 RF(3)	Midshaft		7.23	5.40
3782 LF	.08D		4.68	4.87
3787 RF	.22D		7.22	4.99
3787 LF	.25D		5.23	5.46
3790 RF	.25D		11.51	5.75
3790 LF	.62D		5.60	2.75
3792 RF	Midshaft		5.65	4.69
3792 LF	.36D		10.19	4.66
3793 RF	.35D		8.93	3.74
3793 LF	.07D		6.82	6.34
		<u>Tibia</u>		
3753 RT	.22D		2.07	4.31
3753 LT	.46D		2.89	2.65
3782 RT	.47D		8.13	4.97
3782 LT	.48D		7.62	4.16
3787 RT	.59D		8.26	3.01
3787 LT(1)	.64P		11.29	2.19
3787 LT(2)	.33P		15.19	2.91
3790 RT	.59D		7.49	2.86
3790 LT	.42D		5.15	2.06
3792 RT	.22D		11.76	4.88
3792 LT	.46D		10.26	3.72
3793 RT	.46D		5.88	3.27
3793 LT	.21D		7.03	3.74
		<u>Fibula</u>		
3753 RFb	.43D		2.94	2.93
3753 LFb	.52P		5.57	1.84
3787 RFb	.63D		18.84	1.97
3787 LFb	.55P		14.20	1.62
3790 RFb	.53D		9.38	1.75
3790 LFb	.55P		4.28	1.83
3792 RFb	.42D		8.50	2.92
3792 LFb	.52P		10.68	1.37
3793 RFb	.52P		8.42	1.54
3793 LFb	.43D		5.74	2.32

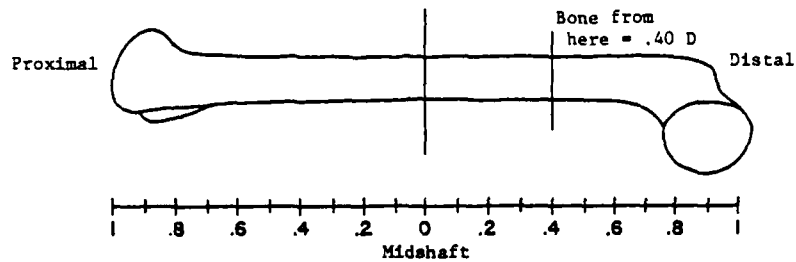
Table 2.35 % Porosity and cortical width (analyzed by MOP 3) continued

AVERAGE DATA							
	Mean % Porosity	SD	SE	(n)	Mean Cortical Width	SD	SE
Humerus	7.129	3.409	0.984	12	3.525	0.766	0.221
Femur	6.891	2.216	0.592	14	4.622	1.023	0.274
Tibia	7.925	3.617	1.003	13	3.441	0.948	0.263
Fibula	8.855	4.814	1.522	10	2.009	0.546	0.173

STATISTICS			
% Porosity	t	p	n
Humerus vs Femur	0.2073	ns	24
Humerus vs Tibia	0.5665	ns	23
Humerus vs Fibula	0.9523	ns	20
Femur vs Tibia	0.8878	ns	25
Femur vs Fibula	1.2026	ns	22
Tibia vs Fibula	0.5102	ns	21
<u>Mean Cortical Width</u>			
Humerus vs Femur	3.1163	< 0.005	24
Humerus vs Tibia	0.2445	ns	23
Humerus vs Fibula	5.4016	< 0.001	20
Femur vs Tibia	3.1096	< 0.005	25
Femur vs Fibula	8.0637	< 0.001	22
Tibia vs Fibula	4.5489	< 0.001	21

Legend for Table 3

Position refers to relative distance from midshaft to Proximal (P) or Distal (D) end of bone, where the whole distance = 1 from midshaft to either end, e.g. below



SD = Standard Deviation  
SE = Standard Error

n = number of observations  
ns = not significant

#### 2.5.4 References

1. Cohnerty, H., Briggs, A, "Determination of Serum Calcium by Means of Orthocresolphthalein Completone," Am. J. Clin. Pathol., 45:290, 1966.
2. Fiske, C.H. and Subbarow, Y, "The Colorimetic Determination of Phosphorus," J. Biol. Chem., 66:375-400, 1925.
3. Lowry, O.H., Rosenbrough, N.J., Farr, A.L. and Randall, R.J., "Protein Measurement with the Folin Phenol Reagent," J. Biol. Chem., 193:265-275, 1951.
4. Bergman, I., Loxley, R., "Two Improved and Simplified Methods for the Spectrophotometric Determination of Hydroxyproline," Analytical Chemistry 35:1961-1965, 1963.
5. Eastoe, E. and Eastoe B, "The Organic Constitutents of Mammalian Compact Bone," Biochem. J. 57:455-459, 1954.
6. McLean, F.C. and Urist, M.R., "Bone: Fundaments of the Physiology of Skeletal Tissue," Univ. of Chicago Press, Chicago, 1973.
7. Vaughan, J.M, Physiology of Bone, Clarendon Press, Oxford, 1970.

### 3.0 Conclusions

#### 3.1 Introduction

From the indications of the literature search in preparation for this research program, little has been done to study the mechanical behavior of whole bone. Some research has been accomplished concerning the effects of twisting whole bone but little else has been reported about the effects of bending and almost nothing exists concerning combinations of these loadings. As of this report, methods for predicting the fracture loads and associated displacements of whole bone have not been found. Furthermore, reports correlating fracture patterns and strain data also seem to be scarce.

In an attempt to fill this void, the following conclusions offer methods for the prediction of whole bone behavior and generalized the types of fractures to expect when the four human long bones are twisted, bent, or twisted and bent simultaneously. Summaries of the osteometric, histological and morphological studies attempt to qualify the proposed methods. The microscopic summary suggests failure modes for the propagating fractures.

#### 3.2 Osteometry

The present study simply does not include a large enough sample to reliably test the mechanical responses of a wide range of bones of differing morphological types. It probably does, however, include the "average" type of bones found in modern white populations. The average stature of the males in the present study is approximately 172 cm (67.9 inches). The average stature of the females is 162 cm (63.8 inches).\*

#### 3.3 Fracturing

##### 3.3.1 Fracture Patterns

###### 3.3.1.1 Torsion Only

Fractures occurring when any one of the human long bones is twisted typically spiral in course. In general they are believed to begin near the ends of diaphysis and travel toward the mid-diaphysis of the bone.

\*Based on Trotter and Gleser's stature reconstruction for femur length (1952).

Some fractures are also thought to initiate at the mid-diaphysis and at one end of the diaphysis, simultaneously, and then converge on a common point. Nonetheless, the spiral fractures only complete one revolution around the diaphysis before terminating.

Termination involves either the arrest of the propagating fracture or the complete separation of the diaphysis. If arrest occurs the fracture ends blindly in the cortical wall and the bone remains in one piece. If separation occurs, it results from a plate bending failure of the cortical wall termed the "clam shell opening" (CSO) mode. This failure occurs after the spiral fracture has completed the one revolution around the diaphysis, leaving as the only material to resist the twisting moment, a ribbon of the diaphyseal wall. The ribbon under the influence of the twisting moment tries to straighten out and the resulting extreme deformation causes the CSO fracture. This final fracture connects the ends of the spiral fracture and allows the complete separation of the diaphysis.

The only characteristics of the spiral fracture peculiar to bone type are the locations of the fracture with respect to length and periphery of the diaphysis. The femora and tibiae consistently fracture in the distal half, while the humeri and fibulae tend to fracture towards the proximal end. Only the tibia displays any correlation to the direction of twist with the CSO occurring on the anterior side when twisted eversively and on the posterior side when inversively.

The spiral fractures frequently exhibit temporary changes in the direction as they propagate around the diaphysis. The deviations from a helical path generally occur mid-way between the start and finish of the spiral and in areas of diaphysis where drastic changes in cross-sectional shape occurs. Apparently, the fracture initiates in a region of the cortical wall where the tensile stresses are large and a discontinuity exists. It then propagates along a path that permits a maximum energy release to obtain a minimum of internal energy. The release in energy occurs primarily through the opening mode of fracture, but when the stress field changes the mode may switch to a tearing or slipping action. The changes in direction of the fracture are attributed to the changes in fracture mode. Therefore, as the fracture spirals around the diaphysis, the tension resulting from the shearing forces normal to and

parallel with the axis of twist cause the fracture to propagate in the opening mode; but when the fracture reaches a region where the tension is not sufficient to sustain that mode of failure, the fracture switches to a shearing mode under the influence of the ever present shearing forces induced by the applied twisting moment. The fracture then continues along a new path, parallel to the axis of twist, until the tension stresses are once again sufficient for the fracture to revert back to a spiral course in an opening mode. Figures 2.190 - 193 show a typical spiral fracture.

#### 3.3.1.2 Bending Only

Fractures in the four human long bones caused by four point bending in the absence of a twisting moment begin on the convex side of the bending diaphysis. The fracture initiates as a result of a tension stress, aligned with the axis of curvature, acting in the vicinity of some discontinuity. The fracture then travels normal to the axis of curvature on both sides of the bone until it reaches the "neutral axis" where it bifurcates. After bifurcating, the fractures follows a curved path until it parallels the axis of curvature. At this point, it either ends blindly in the cortical wall or continues as a plate bending failure, ending with complete separation of the diaphysis. Bending fractures initiate within the middle third of the diaphysis for femora and humeri, but in the distal third for the fibulae and tibiae.

As in the case of pure torsion, the fracture propagates along a path of maximum energy release to attain a minimum of potential energy. Initially, the mode of fracture is an opening action, but due to the changes in the stress field, the mode could change to a shearing or tearing action. As to the exact mode of fracture after bifurcation one can only speculate. The stress field after the bifurcation is not obvious; however it does not seem to support the opening mode. The present contention is the fracture continues in a shearing mode shortly after the bifurcation, especially when the fracture becomes aligned with the axis of curvature. Figure 2.194 - 195 illustrates the bending only fracture configuration.

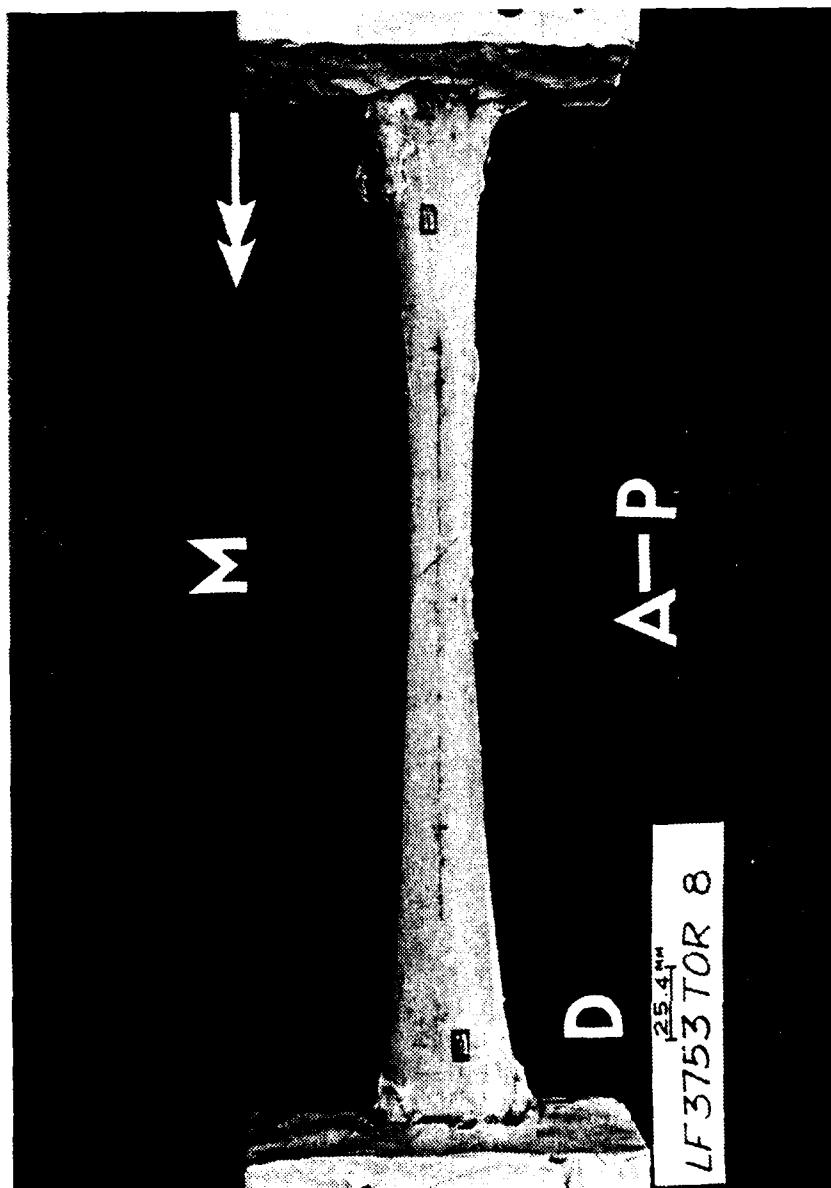


Figure 2.190 Anterior view of the spiral fracture in a femur.

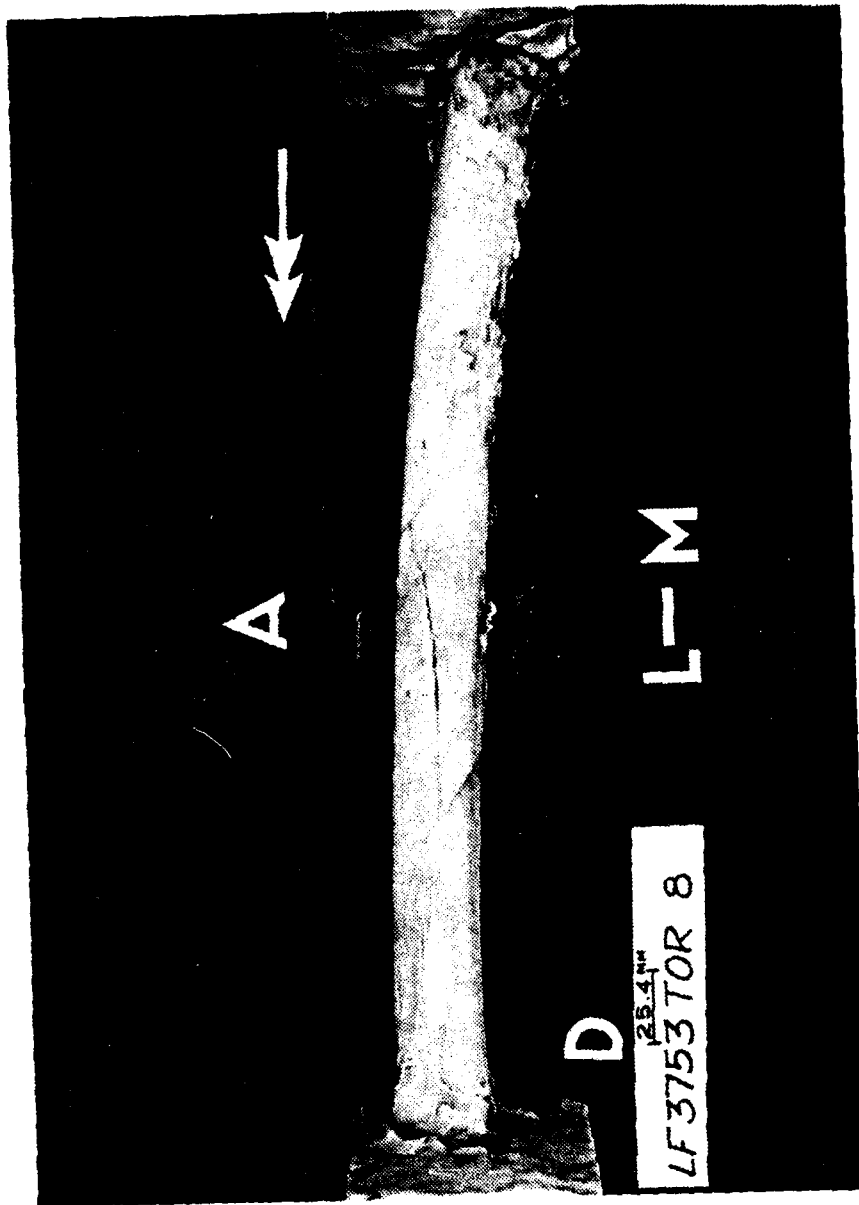


Figure 2.191 Lateral view of the CSO mode in a femur.

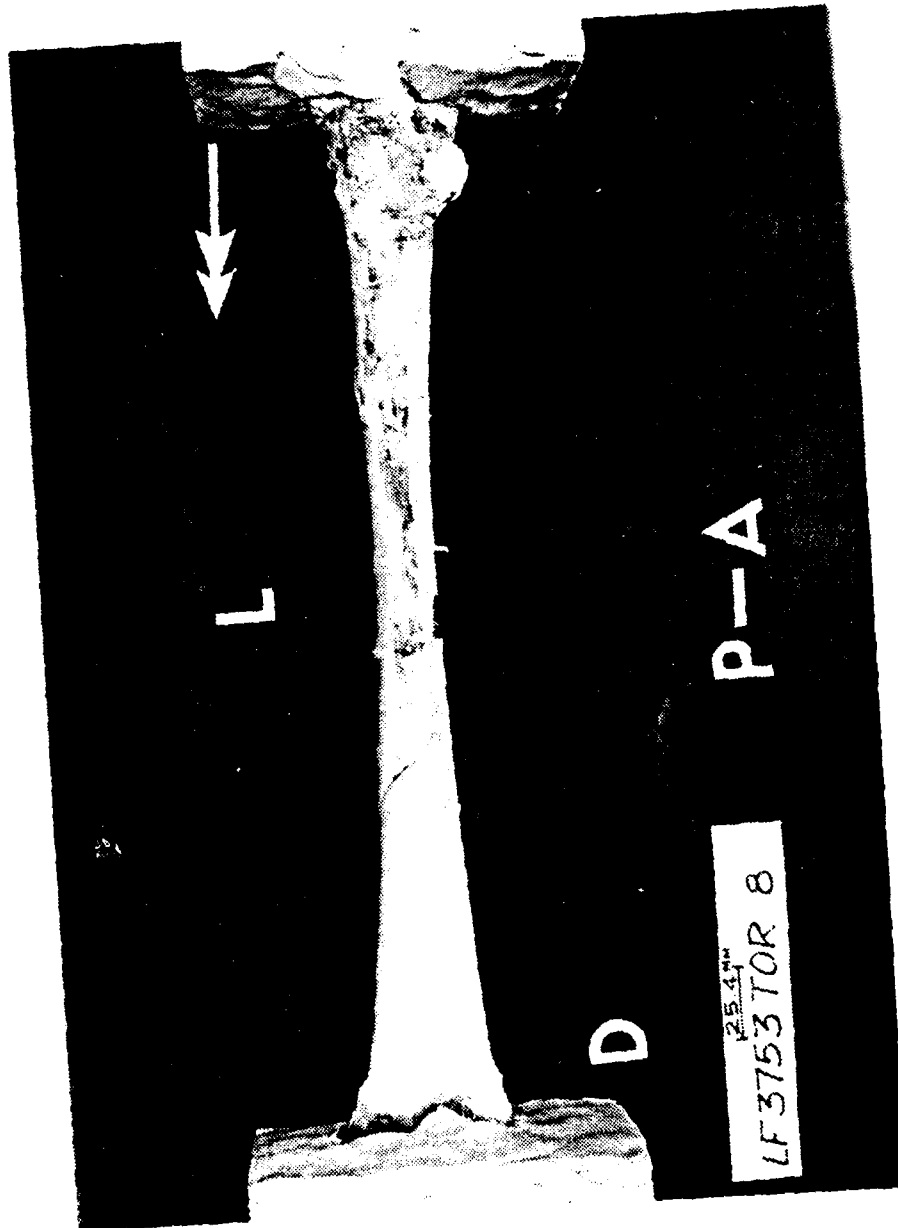


Figure 2.192 Posterior view of the spiral fracture in a femur.

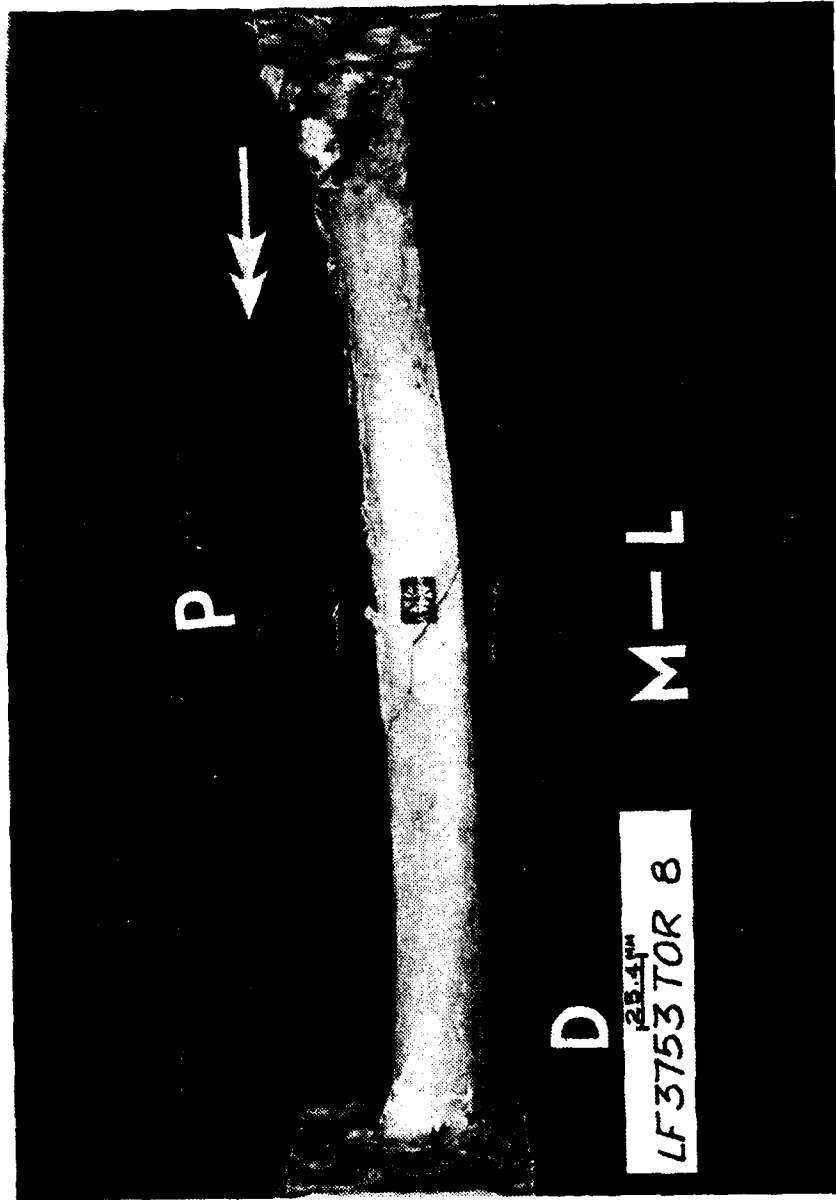


Figure 2.193 Medial view of the change in direction of the spiral fracture.

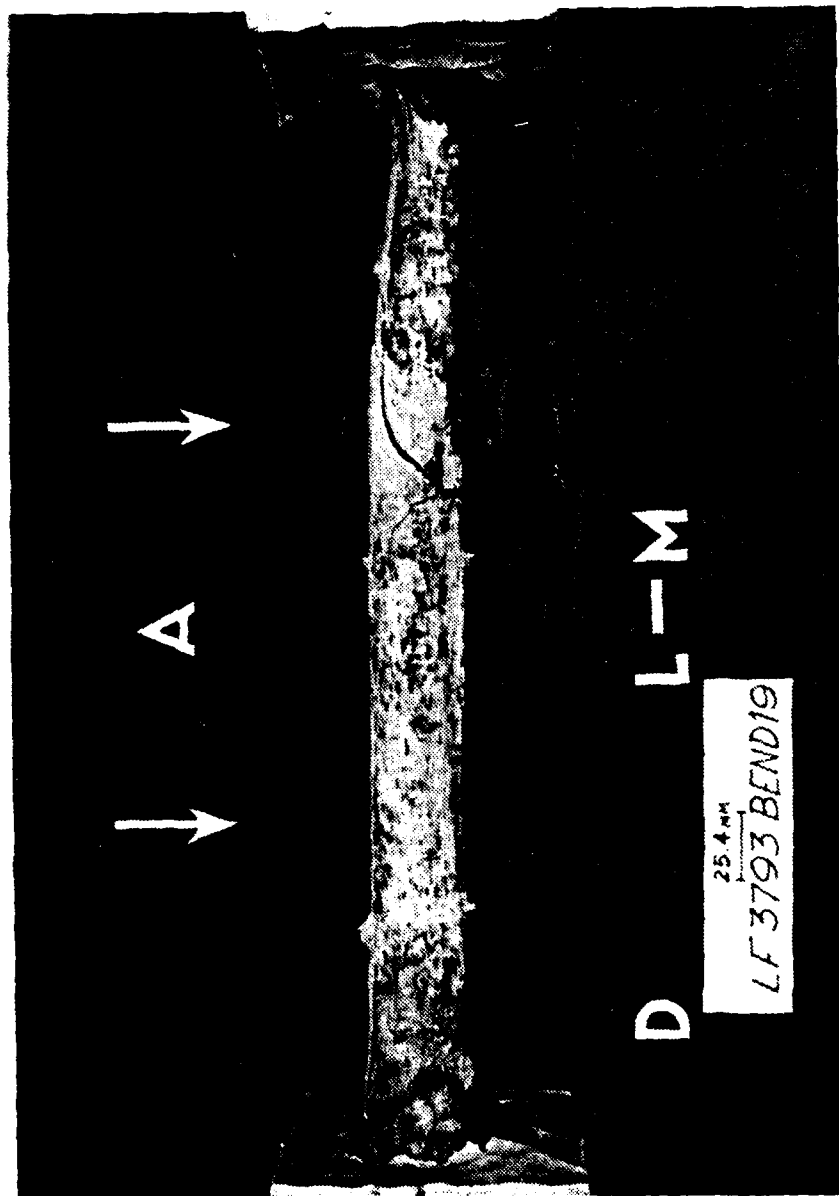


Figure 2.194 Lateral view of a typical bending fracture.

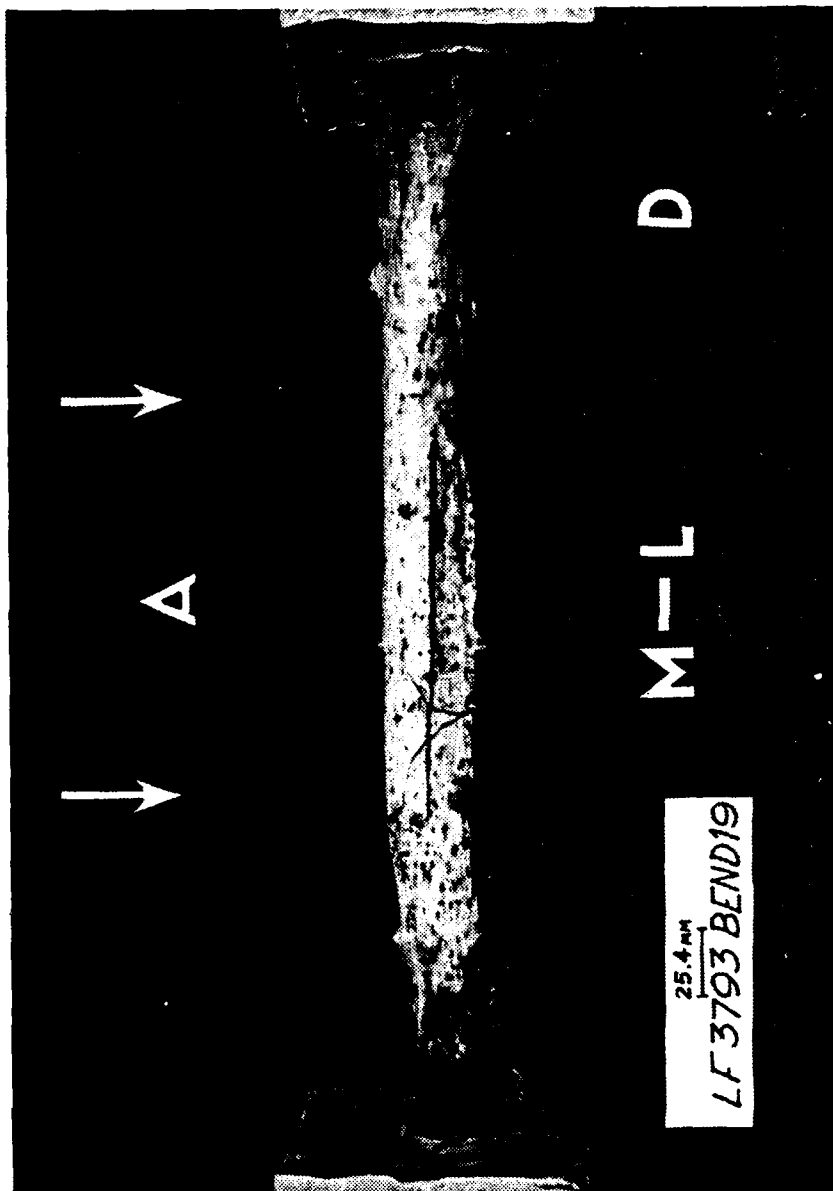


Figure 2.195 Medial view of the same fracture in Figure 2.194.

### 3.3.1.3 Combined Loadings

The fractures which occur in the four long bones when they are bent and twisted simultaneously tend to have characteristics associated with the dominant loading condition. If the dominating load is torsion, the fractures spiral around the diaphysis. If the dominant load is bending, then the fracture pattern is that observed when only bending loads are applied. Although these configurations are expected in general, the tibiae tends to exhibit a spiral fracture when the dominant load is bending. Mixed configurations can occur if the loadings are such that neither twisting or bending dominate.

### 3.3.2 Strain States

Although the implications of the strains sensed at various locations around and along the diaphysis of the four long bones are not astounding, they do offer some indication of the strain magnitudes of deforming, whole bone. The strains have also verified some speculations concerning the performance of whole bone as well as provided some comparisons between the material behavior of whole bone with that of small specimens.

Strains recorded for the femora, humeri and tibiae indicate these bone types tend to twist under static bending, introducing shearing strains along with the expected bending strains. These two bone types also tend to bend when twisted, introducing bending strains where they are unexpected. Causes for these responses are different for each bone type. The femur and humerus twist while bent due to the curvature of their diaphysis. However, the tibia twists because its "tear drop" shaped cross-section offsets the applied bending loads from the axis of twist and this moment arm creates a twisting moment. In the case of pure torsion, the femur and humeri straighten out because the distances between the ends of their curved diaphysis are increased when the bones are twisted. On the other hand, the tibia bends when twisted mainly due to the reaction of the cross-sections attempting to warp while constrained by surrounding material. The strains caused by these geometrically induced deformations are usually small in the case of the bending strains caused by twisting; but the shearing strains introduced by bending are occasionally significant, altering the strain state

normally expected for pure bending. The fibulae also bends in the presence of a twisting moment but the tendency is not quite as pronounced.

Comparisons of ultimate bending stresses with reported ultimates [1] indicate good agreement between large and small scale test results. However, ultimate tension stresses estimated for fractures caused by pure torsion are only 20% to 60% of the reported shear ultimates experienced in small scale tests. Since stresses are determined accurately from strains only when a material behaves linearly and since most of the load-strain plots recorded during the whole bone tests are nonlinear, the stresses in this study often had to be estimated from the load-strain plots and therefore are questionable.

Gage strains along axes parallel and normal to the axis of twist, behave in accordance with mechanics of materials theories -- for both pure bending and pure torsion. The maximum principal strain (tensile) resulting from pure torsion acts on a plane whose normal is 45 deg. to the axis of twist when a right-hand torque is applied. This fact verifies a tension failure as the cause of the spiral fracture. Strains in the vicinity of longitudinal fractures, which occur occasionally along the path of a spiral fracture imply that tension is not the cause of such fractures; the maximum tensile strain in these regions still acts on a plane 45° to the axis of twist.

The different slopes of the load strain plots from the axial gages indicate the variation of section modulus along the bone. A decrease in slope corresponds to a decrease in section modulus and vice versa. If a section modulus is known at one location, this fact allows the calculation of the section modulus at a different location if load strain plots are available at both locations.

Strain states of the combined loading conditions always approach states characteristic of the dominant load. Regardless of the loading condition, the principal strains (maximum shearing strains) always increase as the dominant load is advanced. The significant change in the strain state is the variation of the principal angle. When torsion dominates bending, the principal angle is initially larger than 45 deg. (with respect to the axis of twist) on the compression side and less than 45 deg. on the tension side of the bent diaphysis. Then as the

twisting moment is increased the principal angle approaches 45 deg. Conversely, when bending dominates, the principal angle is initially near 45 deg. (possibly slightly larger on the compression side or less on the tension side, depending on the initial amount of bending) and approaches 90 deg. on the compression side or zero on the tension side. More explicitly, the principal angle changes to bring the biaxial strain state into correspondence with the state that would exist if the dominating load existed by itself. Therefore, the fracture that results when torsion and bending are combined depends on the magnitude of the principal angle as well as the principal strains.

Strains measured on the surface of whole bone are in general congruous with a plane stress, orthotropic material assumption. Nevertheless, unexplainable increases in strains normal to the axis of twist were observed on the diaphyseal surface under conditions of pure torsion. The only explanations available for their increase is a cross-coupling of these lateral strains with the shearing strains due to the anisotropic behavior of the material.

### 3.3.3 Fracture Loads

The mean values of fracture loads expected of fresh, human femora, tibiae, humeri, and fibulae when they are bent or twisted statically are listed in Table 2.24. Along with fracture loads are the fracture displacements. Rapid rate tests (also listed in the table) when considered with other published findings imply dynamic fracture loads are usually 75% greater than the fracture loads occurring under static conditions. Therefore, if the values in the Table are used to bound dynamic fracture characteristics, they should be increased by at least 75%.

The interaction boundaries presented in Figures 2.166 - 2.169 provide a means of estimating the fracture loads of the four human long bones when bending and twisting are combined. Steps for predicting the magnitudes of these moments follow:

#### A. Bending or Twisting Applied Individually:

1. Using the boundary of the bone of interest, read the synthetic stress along the appropriate axis ( $\sigma_b$  for a bending fracture load and  $\tau$  for a twisting moment to cause fracture)

2. Measure the inside and outside diameters at following locations along the diaphysis:

Femora 79%	A.L. measured from the proximal end
Tibiae 19%	M.L. measured from the proximal end
Humeri 77%	M.L. measured from the proximal end
Fibulae 82%	M.L. measured from the distal end

A.L. - anatomical length

M.L. - maximum length

Measure the diameters from an anterioposterior as well as mediolateral view if possible. Find the average of the inside and outside diameters, separately. If only one view is possible, the mediolateral view is the more conservative.

3. Calculate a section modulus for the bone. For bending use the equation,

$$S_b = \frac{F \pi}{32} \frac{D_o^4 - D_i^4}{D_o}$$

but for a twisting situation use,

$$S_t = \frac{\pi}{16} \frac{D_o^4 - D_i^4}{D_o}$$

where  $D_o$  is the average outside diameter from step 2,  $D_i$  the average inside diameter from step 2, and  $F^*$  is the bias factor,

Femora	-	$F = 1.17$
Tibia	-	$F = 1.17$
Humerus	-	$F = 1.38$
Fibula	-	$F = 1.04$

\* $F$  may be found more exactly as

$$F = \frac{\frac{\pi}{32} \frac{D_o^4 - D_i^4}{D_o}}{\frac{I_{xx}}{c}}$$

if the second moment of inertia about the neutral axis  $I_{xx}$ , and the distance from the neutral axis to the extreme tension fiber,  $c$ , are known for the actual cross-section at the locations in A(2). However, the increase in accuracy that occurs may not warrant the time involved.

If step 2 is not possible, the following section moduli may be used in place of the above, but a decrease accuracy is probable.

Femora	$S_b = 1998 \text{ mm}^3$	$S_t = 2870 \text{ mm}^3$
Tibiae	$S_b = 2840 \text{ mm}^3$	$S_t = 1148 \text{ mm}^3$
Humeri	$S_b = 815 \text{ mm}^3$	$S_t = 892 \text{ mm}^3$
Fibulae	$S_b = 112.1 \text{ mm}^3$	$S_t = 271 \text{ mm}^3$

Note: The  $S_b$  values given above were determined from the actual section moduli of the selected sections discussed in the section "Estimation of Fracture Loads." The  $S_t$  values are the mean values of all the section moduli calculated using the average diameters measured from the roentgenograms.

- Using the synthetic stress and section modulus calculate the failure moment, for bending,

$$M_b = \sigma_b S_b$$

and for twisting,

$$T = \tau S_t$$

Where  $\sigma_b$  and  $\tau$  are the bending and shearing synthetic stresses, respectively.

- Using the appropriate loading configuration, determine the appropriate formulation for the fracture force as a function of fracture moment and calculate the fracture force.

#### B. Bending and Twisting Combined

- Establish the dominating load or the load which is held fixed whichever is more convenient. Calculate the synthetic stress representing its moment.
  - Perform step A(2) and A(3) above.
  - Calculate the synthetic stress for bending,

$$\sigma_b = \frac{M_b}{S_b}$$

and for shearing,

$$\tau = \frac{T}{S_\tau}$$

where  $M_b$  is the bending moment and T the twisting moment or torque.

2. Using the synthetic stress from B(1) enter the interaction boundary for the bone of interest. Where the synthetic stress intersects the boundary find the synthetic stress corresponding to the supplemental load.
3. Using step A(4) find the moment of the supplemental load. This moment in conjunction with that of step B(1) will probably cause the bone to fracture.
4. Using step A(5) the fracture forces which depend on the loading configuration may be found.

Note: If both the twisting moment and bending moment are known, the interaction boundaries are also useful in determining whether or not fracture is probable. This approach also accommodates an estimation of the margin of safety between fracture and an existing loading condition.

With the predicated fracture moments available, the displacements possible at fracture are read from Figures 2.160 - 163. These figures also apply to loads other than fracture. Displacements for loading situations which cause synthetic stresses within the interaction boundaries are also predictable with these curves. Beware that the mid-diaphyseal deflection was measured 1 to 2 cm from the true mid-diaphysis; therefore, when this curve is used, the values may be 5% to 10% less than the actual mid-diaphyseal displacements. One must also understand that all the curves may result in values which are in error  $\pm 20\%$ .

#### 3.4 Brittle Coat

Although the accuracy of strain measurements using brittle coatings is questionable, the method does give a good picture of where the stress concentrations occur as well as directions for the principal strains.

If accurate strain measurements are required, the brittle lacquer cracks isolate areas of maximum stress where the gages should be applied.

The cracking of the brittle coating indicated that the proximal quarter and proximal third regions of the diaphysis are locations the greatest initial strain and, thus, stress. Comparing this observation with the fracture patterns that occurred during the testing, the spiral fractures in the femur apparently start at either the proximal quarter or proximal third and travel to the proximal third or quarter, respectively. Again the possibility exists where the fracture may begin at both locations and then converge on a common point.

### 3.5 SEM

The scanning electron microscope study, as limited as it was, inferred that a shearing mode does exist along particular regions of the fracture. These regions are those where the opening modes seems inconsistent with the loading conditions--specifically, when fractures are parallel or normal to the torsional axis during torsion only or when they are parallel to the neutral axis during bending only. This finding is congruous with the interpretation of the strain data, but requires an extensive SEM study before it is totally credible.

The SEM work also illustrated the unusual structure of bone tissue. Much is required involving micromechanical theories before bone can be adequately represented in terms of its constituents.

### 3.6 Medical Analysis

The uniformity of bone composition from specimen to specimen, the similarity of bone composition to what has been reported as normal, and the lack of great variation in cortical porosity suggests that the human bones donated for this study should have comparable mechanical properties. Their normalcy also suggests that they should have mechanical properties comparable to those of the general population. In fact, the bones were so similar, bone response and fracture sites could not be related to tissue composition or bone structure.

### 3.7 General

Although the bones strain gaged were exposed to ambient conditions of the laboratory for periods of time in excess of that allowed for

small scale tests of bone tissue, the performance of the four human long bones described above accurately typifies the behavior of wet, fresh bone. Except during strain gaging, the bones were kept hydrated in Ringer's solution or encapsulated in highly humid air to retain a moist state. Furthermore, different from small bone coupons, whole bone is an essentially closed system laced with canals filled with and connected to fluids. Such a porous structure does not lose enough moisture to the surrounding environment through evaporation over a period of a few hours to cause a monumental change in its hydrous compositions. This fact is verified by the results of the histological analysis and, thus, supports the contention that the behavior observed for those bones tested is indeed that of fresh, wet bone.

### 3.8 References

1. Reilly, D. T., Burstein, A. H., "The Elastic and Ultimate Properties of Compact Bone Tissue," J. Biomechanics, 1975, pp. 393-405.

#### 4.0 Recommendations

Further research will be necessary to gain a complete understanding of the biomechanical ramifications of the tremendous amount of variation in human skeletal populations. Long bone metrics vary greatly among individuals. For instance, in Parsons' study [9], the longest maximum femur length was 543 mm. This same femur had a platymeric transverse diameter of 35 mm which was below the mean value for the entire population of 36 mm. The present sample had two specimens with platymeric transverse diameters greater than 35 mm but no femur was even close to 543 mm in length.

Ideally, a large number of bones from individuals from different racial groups of both sexes should be tested. In this study both embalmed and fresh bone has been tested. A large sample of embalmed bone could be obtained relatively easily from medical schools after the cadavers have been dissected. Testing would then reveal the responses of bones of various morphological types. The responses of fresh bones could then be inferred based on the mechanical differences of fresh and embalmed bones used in this study.

In addition to the need for more tests to increase the data base, tests involving dynamic loadings of whole bones are imperative. Other investigators have shown substantial increases above the static values of ultimate strains and ultimate loads when bone tissue is failed dynamically. Since bone fractures rarely occur at low strain rates, the need for whole bone dynamic loads and displacements is obvious.

Furthermore, although less information is available concerning the performance of whole bone than exists describing the behavior of bone tissue, additional information about bone as a structural material is required. More information verifying the technical constants is necessary to accomplish the simple mechanics of materials analyses as well as the more sophisticated finite element models. Finally, more experiments followed by microscopic studies are essential to actually understand how the seemingly, loosely constructed collagen fibrils can offer such strength to random assemblages of the higher organized lamellar and osteon systems.

Obviously, the ultimate goal for any engineer involved with the behavior of a structure is an accurate representation of that structure

in an abstract, mathematical sense. If he can achieve such a model, then he can determine its characteristics under the influence of various environmental factors applied in different combinations. If only one whole bone were modeled effectively mathematically using computer technology, then the door would be open to such representation of other skeletal members. Eventually, with experience, the modeling of other human organs would be possible until components of the human anatomy, or complete anatomies, could be assembled into human simulations appropriate for medical and human factors research. The implications of such capabilities are overwhelming, but with the present rate of advancement in the design of computing systems and with a greater knowledge of human tissue such modeling will become a reality.

**DAT  
FILM**